Vieillissement et maladies neurodégénératives : nouvelles contraintes apportées par la métallomique

Lucie Sauzéat

Numéro National de Thèse : 2018LYSEN005

THESE de DOCTORAT DE L'UNIVERSITE DE LYON

opérée par

l'Ecole Normale Supérieure de Lyon

Ecole Doctorale N° 52
Physique et Astrophysique de Lyon (PHAST)

Spécialité de doctorat : Géochimie isotopique – Applications médicales
Discipline de doctorat : Sciences de la terre

Soutenue publiquement le 18/04/2018, par :

Lucie SAUZÉAT

Vieillissement et maladies neurodégénératives : Nouvelles contraintes apportées par la métallomique

Devant le jury composé de :

Mattielli Nadine
Professeure – ULB, Bruxelles – Rapporteure

Weis Dominique
Professeure – UBC, Vancouver – Rapporteure

Vanhaecke Frank
Professeur - Ghent University, Ghent – Examinateur

Schneider Bernard
Maître d'enseignement et de recherche - EPFL, Lausanne – Examinateur

Bulteau Anne-Laure
Chargée de recherche - IGFL, Lyon – Examinatrice

Balter Vincent
Directeur de recherche - ENS, Lyon - Directeur de thèse

REMERCIEMENTS

C′est avec grand plaisir, mais aussi avec un peu de soulagement je dois l'avouer que j′en arrive à écrire ces quelques lignes de sincères remerciements à toutes les personnes qui m′ont aidée, soutenue et encouragée durant ces trois années de thèse.

En premier lieu, je souhaite remercier Vincent Balter à qui je dois beaucoup et sans qui je ne serai pas là. Merci tout d'abord de t'être battu dès mon arrivée avec l'administration pour que je puisse débuter cette thèse et merci également de m'avoir soutenue pendant ces trois années passée à l'ENS. Tu m'as permis de travailler sur des sujets novateurs en collaboration avec divers corps de métiers alliant médecins et biologistes, une expérience très enrichissante que je n'oublierai pas. En me laissant une grande liberté de travail, tu m'as également offert la possibilité d'évoluer librement et de façon autonome dans mes recherches, ce en quoi je te suis très reconnaissante.

Je remercie aussi très sincèrement Philippe Gillet, pour son intérêt et son immense soutien financier dont ma thèse a amplement bénéficié.

J'adresse également ma reconnaissance à Nadine Mattielli et Dominique Weis, mes deux rapporteurs ainsi qu'à mes examinateurs Anne-Laure Bulteau, Bernard Schneider et Frank Vanhaecke pour avoir accepté de relire et juger mon manuscrit et faire partie de mon jury de thèse.

Un grand merci également à Emmanuelle Albalat, Aline Lamboux et Mélanie Simon pour avoir pris le temps de répondre à mes questions et de m'avoir conseillée sur les techniques analytiques. Pas de chimie sans acide et pas d'acide sans Florent, merci donc à Florent Arnaud pour son temps passé à la distillation. Merci également à Philippe Télouk qui m'a épaulée pendant ces 3 années de thèse sur les spectromètres de masse. Avec ton assistance non stop 24h/24, tu m'as permis de surmonter pas mal de problèmes ce qui m'a valu d'obtenir un bon nombres de résultats.

Une autre personne à qui je dois énormément c'est Anne Laurençon pour avoir pris le temps de m'initier à la biologie des vers. N'ayant aucune connaissance dans ce domaine, les débuts n'étaient certes pas faciles mais tu as su me faire progresser au détriment, il est vrai, de plusieurs vers mis à la poubelle ! Toute ma sympathie va également à toutes les autres personnes de l'équipe de l'IGFL qui m'ont épaulé, conseillé sur des questions biologiques et qui m'ont ainsi permis d'avoir des résultats concluants. Je pense notamment à Alexia Buis, Mélanie Salamito et Christian Lamy sans qui mes tests à l'IGFL n'auraient probablement pas encore abouti.
Merci aussi à Pooja Jha pour son temps passé à prélever les organes de souris et avec qui j 'ai eu des discussions très enrichissantes. Je lui suis aussi très reconnaissante d'avoir accepté de m'accueillir à Lausanne pour me faire découvrir et visiter leur laboratoire.
Je suis également très reconnaissante envers toutes les autres personnes avec qui j'ai pu collaborer à savoir Emilien Bernard, Pascal Leblanc, Armand Perret-Liaudet, Isabelle Quadrio, Emmanuel Broussolle, Johan Auwerx et Christine Ferrier.

Merci également à toutes les personnes qui ont contribué de près ou de loin à l'avancée de cette thèse et particulièrement à Marie-Jeanne Barrier. Tu es une gestionnaire plus que super sans qui je

serai probablement toujours en train de me battre avec des problèmes administratifs. Le labo a vraiment de la chance de t'avoir !

Parce que sans elles tout aurait été certainement très diffèrent, j'adresse également tous mes remerciements à Catherine Chauvel et Roberta Rudnick. Grâce à Catherine j'ai pu acquérir la rigueur et la précision analytique requise en géochimie tandis que Roberta m'a offert la chance de faire une expérience à l'étranger, deux choses dont je vous suis très reconnaissante.

Une autre personne à qui je dois beaucoup dans cette thèse c'est ma co-bureau Fanny, que je remercie pour tous les bons moments passés à ses cotés. Qu'aurait été ma thèse sans tous nos papotages, soirées Françaises et Zurichoises et toutes nos longues discussions sur l'avenir qui m'ont tellement aidée à aller de l'avant et à relativiser dans les moments de doutes! Merci aussi pour les cours de cuisine macarons, avec ta recette et tes astuces je ne peux plus les rater ;)
Toute ma sympathie va également à l'ensemble du laboratoire et plus particulièrement à mes anciens et nouveaux co-bureaux Marie, Eloïse, Jean-Loup et Nathalia qui ont su me supporter pendant ces trois années de thèse. Je remercie aussi tous les autres thésards et postdocs et plus particulièrement Théo, Mélanie (IGFL), François, Hélène, Anne-Céline etc... pour les supers moments/soirées passés à leurs cotés.
Il n'est plus au labo et ne lira probablement pas ces remerciements, mais je tiens aussi à remercier très sincèrement Victor, mon tout premier co-bureau ! Merci pour ta bonne humeur et tes conseils précieux...je te souhaite le meilleur pour la suite et espère que tout se passera comme tu le voudras.

Toute ma reconnaissance va aussi à mes amis hors labo qui sont à mes yeux une réelle bouffée d'oxygène. Quoi de mieux que de rigoler et partager un bon verre de vin avec eux sans parler de boulot ! Merci donc à Inès, Gaëtan, Laura, Marina, Camille, Seb et Cerise, Mathieu & Eunyeng, Emily, Nolwenn, Hélène & Bruno ...

Je terminerai par les personnes les plus importantes pour moi pendant ces trois années de thèse, à savoir ma famille. Tout d'abord, je remercie bien évidemment mes parents, mon frère et mes beaux-parents pour leur immense soutien. Merci aussi a mes cousin(es), oncles, tantes et grand-parents. Pour finir, un immense merci aussi à mon petit chou. Tu m'as tellement soutenue et aidée à aller de l'avant pendant ces 3ans de thèse que les mots ne sont pas à la hauteur pour te dire à quel point je te suis reconnaissante ... mais je ne doute pas que tu sais ce que je pense ;)

Résumé

Caractérisé par le déclin progressif et irréversible des fonctions biologiques vitales, le vieillissement est un processus biologique complexe qui s'accompagne souvent par l'apparition de maladies neurodégénératives. D'ici 2050, plus de 1.5 milliards de personnes dans le monde seront définies comme vieillissantes. L'amélioration de la qualité de vie des personnes âgées constitue donc un enjeu majeur pour notre société.

Encore mal connue, la dégradation progressive du métallome est associée au vieillissement et à l'apparition de maladies neurodégénératives et en est probablement l'une des causes. L'objectif de cette étude est de mieux caractériser l'évolution du métallome chez deux modèles animaux au cours du temps *i.e.* la souris et le vers ainsi que chez l'humain atteint de sclérose latérale amyotrophique (SLA). Pour ce faire, nous avons analysé une vingtaine d'éléments traces et majeurs ainsi que les compositions isotopiques du cuivre ($\delta^{65}Cu$) et du zinc ($\delta^{66}Zn$) d'organes de souris, de différentes souches de nématodes, et de liquides céphalo-rachidiens (LCRs) humains.

L'analyse des organes de souris montre que d'importants dérèglements chimiques et isotopiques se développent dans l'organisme avec l'âge, chaque organe ayant sa propre signature élémentaire et isotopique. On observe par exemple une hausse de la concentration en Cu dans le cerveau associée à une diminution de $\delta^{65}Cu$ dans le foie au cours du vieillissement. Grâce à l'analyse métabolomique et à l'utilisation de mélanges isotopiques, nous montrons que ces variations pourraient s'expliquer par des dysfonctionnements physiologiques et métaboliques majeurs comme des dérèglements de flux hépatique et/ou la dégradation de la barrière hémato-encéphalique avec l'âge. Cela suggère que l'analyse temporelle du métallome pourrait être un marqueur de l'âge biologique.

L'analyse de nématodes a révélée qu'un animal génétiquement modifié pour vivre plus longtemps se distinguait des autres nématodes à plus courte durée de vie par une baisse de sa concentration et de sa composition isotopique en Cu dès son plus jeune âge. Le suivi temporel de ces biomarqueurs devrait permettre de détecter un vieillissement précoce.

Finalement, l'analyse de LCRs de patients atteints de SLA, une maladie neurodégénérative sévère pour laquelle il n'existe aucun biomarqueur ni traitement, montre qu'une personne atteinte de SLA se distingue de sujets sains et de patients touchés par la maladie d'Alzheimer par des compositions isotopiques en Cu plus positives. Cette spécificité, laissant entrevoir de nouvelles perspectives concernant l'identification de biomarqueurs spécifiques de la SLA, pourrait s'expliquer par la formation d'agrégats protéiques toxiques dans le cerveau.

Abstract

Characterized by the progressive and irreversible decline of vital biological functions, ageing is a complex biological process that often comes with neurodegenerative disorders. In 2050, more than 1.5 billion elderly are expected in the world. Improve the quality of life of these ageing people is therefore a major challenge for our society.

Still poorly known, the progressive degradation of the metallome is asscociated with ageing and neurodegenerative diseases development and is probably one of their causes. The objective of this study is to better characterize the metallome evolution in two animal models over time *i.e.* the mouse and the worm as well as in human affected by amyotrophic lateral sclerosis (ALS). To do this, we analyzed twenty trace and major elements as well as the isotopic compositions of copper ($\delta^{65}Cu$) and zinc ($\delta^{66}Zn$) of mouse organs, different strains of nematodes, and human cerebrospinal fluid (CSFs).

The analysis of mouse organs shows that important chemical and isotopic changes develop in the body over time, each organ having its own elemental and isotopic signature. For example, we observe an increase of the Cu concentration in the brain associated with a decrease of the $\delta^{65}Cu$ in the liver over time. Based on the analysis of metabolomic parameters and the use of isotopic mixings, we show that these variations may be explained by major physiological and metabolic dysfunctions, such as the deregulation of hepatic fluxes and/or the degradation of the blood-brain barrier with age. This suggests that the temporal analysis of the metallome could be used as a potential marker of the biological age.

The analysis of nematodes revealed that long-lived animals differ from short-lived nematodes by an early-age decrease in their Cu isotopic composition and Cu concentration. The temporal monitoring of these biomarkers could therefore be used to detect premature ageing conditions.

Finally, the analysis of CSFs of patients with amyotrophic lateral sclerosis (ALS), a severe neurodegenerative disease for which there is currently no reliable biomarker or treatment, shows that ALS patients have a higher $\delta^{65}Cu$ compared to healthy subjects and Alzheimer's disease patients. This feature, offering new perspectives to identify ALS-specific biomarkers, may be explained by the formation of toxic protein aggregates in the brain.

INTRODUCTION

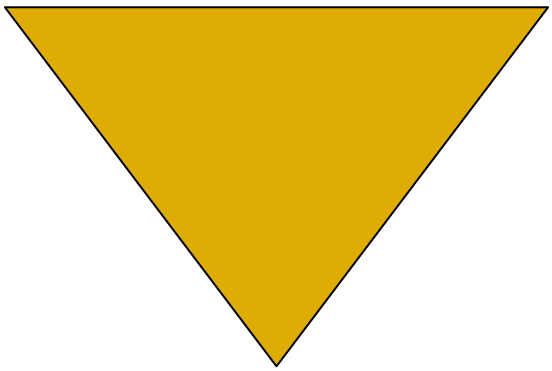

Depuis déjà plusieurs années, le vieillissement de la population mondiale s'accélère à un rythme sans précédent et ce phénomène est en constante évolution. D'ici 2050, le nombre de personnes âgées (*i.e.* > 65 ans) devrait en effet doubler, voire tripler selon les sources (Insee, OMS) dépassant ainsi les 1.5 milliards soit plus de 16% de la population mondiale contre seulement 5% en 1950 (World Health Organization, 2011) (Figure 1).

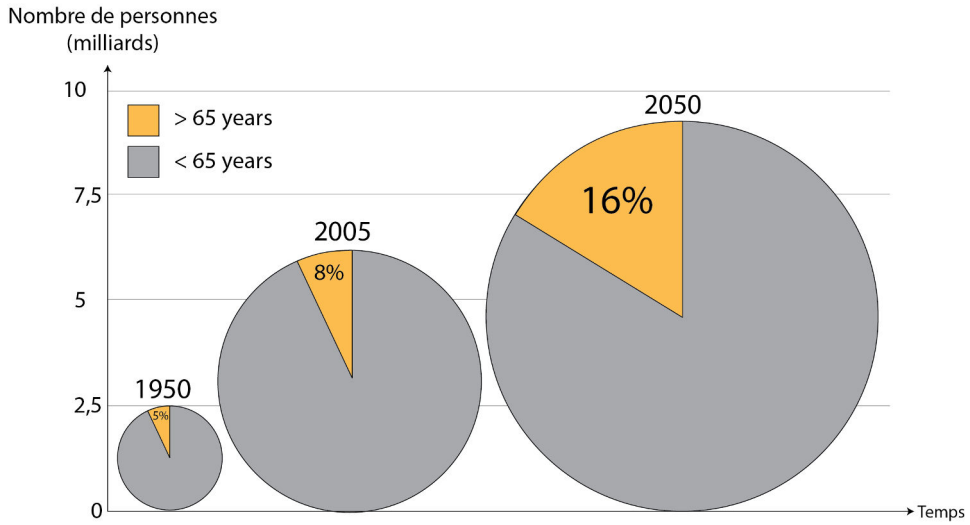

Modified from WHO (World Health Organization, 2011)

Figure 1 : Accroissement du vieillissement de la population mondiale entre 1950 et 2050. Modifié d'après l'organisation mondiale de la santé, WHO, (2011).

Pour autant, force est de constater que si les gens vivent de plus en plus longtemps, ils ne vieillissement pas toujours en bonne santé. Le vieillissement de la population représente donc un enjeu majeur de santé publique ayant également un impact considérable sur notre système socio-économique auquel la société future devra faire face. Sur le plan économique, pour ne citer qu'un exemple, le vieillissement de la population va accroitre les besoins en terme de dépendance. A ce jour, la France alloue plus de 24 milliards d'euros pour couvrir l'ensemble des dépenses publiques consacrées à la santé, l'hébergement et la prise en charge médico-sociale des personnes âgées, mais cette somme devrait atteindre les 35 milliards d'euros en 2060 (source Insee). Sur le plan des politiques sociales, cela nécessitera de repenser les systèmes de retraites et d'aides à la personne. En effet, avec seulement 600 000 places aujourd'hui disponibles en maison de retraite en France et environ 26 millions de personnes âgées attendues en 2050, il est évident qu'en l'absence de réforme, seulement une partie de la population aura accès à ces aides publiques ; ce qui ne fera qu'accroître les inégalités sociales déjà existantes. C'est toutefois sur le plan médical que les changements seront probablement les plus importants et qu'ils nécessiteront des modifications importantes comme la hausse du nombre d'aidants et de soignants. De ce

point de vue, il est intéressant de noter que les aidants sont pour la plupart des membres de la famille proche (dont plus de 85% sont actuellement des femmes ; source Inge Cantegreil-Kallen (AP-HP)). Bien que leur volonté soit simplement d'assister le patient vieillissant dans les tâches de la vie courante, la pression psychologique ainsi que la fatigue physique et nerveuse générées par ces situations sont encore trop souvent sous-évaluées pouvant conduire à des dépressions et des morts prématurées. En moyenne, 30% des aidants, tout âge confondu, décèdent avant la personne âgée dont ils prennent soins (source : Inge Cantegreil-Kallen (AP-HP) et Emmanuelle Duron (Universités Paris Descartes), conférence 'Aging' 2017). Un autre défi de santé majeur contre lequel la société devra lutter est le développement progressif de pathologies sévères comme les maladies cardio-vasculaires et/ou neuro-dégénératives (Qiu et al., 2009; Querfurth and LaFerla, 2010; Roth et al., 2015; Sanuade et al., 2014) (Figure 2) dont le nombre ne cessent d'augmenter au cours du temps.

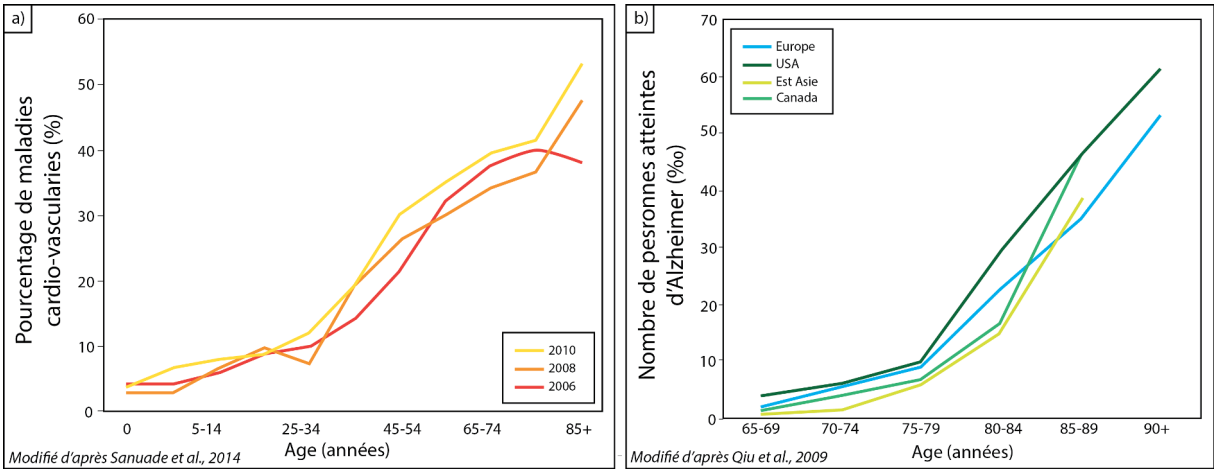

Figure 2: Augmentation des maladies cardio-vasculaires (a) et de la maladie d'Alzheimer (b) avec l'âge. Modifié d'après Sanuade et al. (2014) *et Qiu et al.* (2009).

Si la maladie d' Alzheimer reste à ce jour la plus courante avec 800 000 cas diagnostiqués en France (source : frm.org) suivie par la sclérose en plaque et la maladie de Parkinson qui touchent environ 100 000 personnes âgées chacune (source : arsep.org et inserm.fr), d'autres maladies, plus rares mais non moins dévastatrices, existent telles que la sclérose latérale amyotrophique (SLA, aussi appelée Maladie de Charcot) (~7000 patients diagnostiqués) et la maladie de Creutzfeldt-Jakob (MCJ) (prés d'une centaine de patients atteints) (source : arsla.org et who.int). C'est donc plus d'un million de personnes qui sont atteintes de maladies neuro-dégénératives en France; un chiffre qui devrait encore s'accentuer avec le vieillissement de la population démontrant une fois de plus à quel point l'accroissement du nombre de personnes âgées constituera une charge pour les générations à venir si aucune mesure n'est mise en place.

Il arrive cependant que certaines exceptions se produisent. C'est notamment le cas des 'supers seniors' comme la gymnaste Johanna Quaas et le cycliste Robert Marchand. A 91 et 105 ans respectivement, ils sont des sportifs en excellente santé physique et mentale dont les performances sportives peuvent avoisiner celles de personnes trentenaires. Cela soulève plusieurs questions : Pourquoi certaines personnes vieillissent-elles en bonne santé et d'autres non? Pourquoi certaines développent-elles des pathologies neurodégénératives ?

La réponse à ces questions se trouve vraisemblablement dans l'identification des mécanismes à l'origine du vieillissement et des maladies associées. Cependant, les symptômes associés aux pathologies chroniques tels que les maladies neurodégénératives sont bien souvent masqués par les effets du vieillissement affectant ainsi nos capacités à les détecter et comprendre leur cause. Le vieillissement étant un processus extrêmement complexe, les mécanismes responsables de son développement et de sa progression sont eux aussi difficiles à identifier. L'environnement extérieur (e.g. pollution, tabac) (Beach et al., 2015), le stress (Betteridge, 2000; Finkel and Holbrook, 2000; Kregel and Zhang, 2006; Stadtman, 2004; Sun and Tower, 1999), le régime alimentaire (Gkogkolou and Böhm, 2012; Gusarov et al., 2017; Lakowski and Hekimi, 1998; Schlotterer et al., 2009) mais également la place occupée dans la société (e.g. degré hiérarchique au travail, pauvreté, éducation, niveau social) (Singh and Siahpush, 2006), les dérèglements métaboliques (Houtkooper et al., 2011) et les facteurs génétiques (Arantes-Oliveira et al., 2003; Kenyon, 2005; Kenyon et al., 1993; Lee et al., 2003) sont susceptibles de jouer un rôle sur le développement et la progression du vieillissement. Il semblerait également qu'un dérèglement chimique soit impliqué dans ce processus tout comme dans l'apparition des maladies neurologiques.

Récemment, plusieurs études ont identifié un lien entre la quantité d'éléments chimiques présente dans le corps et l'évolution de ces pathologies (Azhdarzadeh et al., 2013; Giacconi et al., 2016; Hozumi et al., 2011; Malavolta et al., 2010; 2015; Mezzetti et al., 1998; Rembach et al., 2014; Roos et al., 2012; 2013; Turnlund et al., 1986). Les processus biologiques et les réactions métaboliques à l'origine de ces dérèglements chimiques ne sont cependant pas encore bien compris. De la même manière, il a récemment été démontré qu'un dérèglement isotopique pouvait être associé au vieillissement de la population comme par exemple une diminution de la composition isotopique en cuivre ($\delta^{65}Cu$) et à l'inverse une augmentation de celle en zinc ($\delta^{66}Zn$) dans le sang (Jaouen et al., 2013a) (Figure 3).

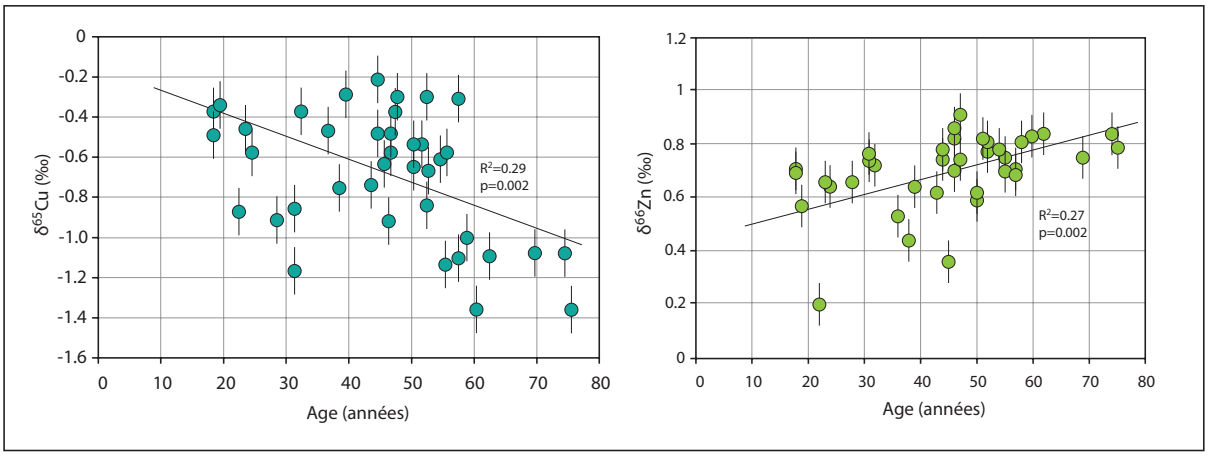

Figure 3: Composition isotopique en cuivre ($\delta^{65}Cu$) et en zinc ($\delta^{66}Zn$) mesurées dans du sang humain. Modifié d'après Jaouen et al.(2013a).

Cependant, là encore, la cause de ces dérèglements isotopiques reste inconnue et l'influence qu'ils peuvent avoir sur le vieillissement et potentiellement sur le développement des maladies neuro-dégénératives comme la sclérose latérale amyotrophique (SLA ou Maladie de Charcot) n'a jamais été profondément étudié. Mesurés avec une précision de l'ordre du pour mille (‰), les isotopes s'avèrent pourtant très prometteurs dans divers domaines de recherche tels que l'archéologie, l'anthropologie, la médecine ou encore la biologie. En ce sens, ils ont notamment permis de mieux percevoir la complexité de certaines maladies telles que le cancer (Albarède et al., 2016; Balter et al., 2015; Bondanese et al., 2016; Chamel et al., 2016; Larner, 2015; Larner et al., 2015; Lobo et al., 2017; Telouk et al., 2015), la maladie de Wilson (Aramendía et al., 2013), du Prion (Büchl et al., 2008; Miller et al., 2016) et d'Alzheimer (Moynier et al., 2017). Ils ont également permis d'apporter des informations supplémentaires sur des maladies touchant les reins (Anoshkina et al., 2017) et le foie (Lauwens et al., 2016) comme la cirrhose (Costas-Rodríguez et al., 2015; 2016), ainsi que sur la ménopause (Jaouen and Balter, 2014; Van Heghe et al., 2014), les conditions d'allaitement (Tacail et al., 2017) ou encore du régime alimentaire (Costas-Rodríguez et al., 2014; Jaouen et al., 2016a; 2013b; 2016b; Van Heghe et al., 2012).

Comprendre les dérégulations chimiques et isotopiques associées au processus de vieillissement et à ses pathologies sont des enjeux majeurs pour en comprendre les origines mais également pour développer de futurs traitements thérapeutiques et même peut-être ralentir le processus de vieillissement. La modulation et/ou la supplémentation d'éléments chimiques comme le cuivre (Cu), le zinc (Zn) mais aussi le lithium (Li) a d'ores et déjà été suggérée, et même utilisée, comme traitement potentiel pour limiter la progression de certaine maladie telle que la maladie d'Alzheimer (Bush and Tanzi, 2008; Nuttall and Oteiza, 2014), la maladie de Wilson (Hedera, 2017; Rodriguez-Castro et al., 2015), la maladie

bipolaire (Roux and Dosseto, 2017; Vestergaard and Licht, 2001) ou encore l'anorexie (Bakan, 1979; Birmingham and Gritzner, 2006; McClain et al., 1992; Safai-Kutti, 1990; Su and Birmingham, 2001) et la dépression (Chasapis et al., 2012; Gabriel Nowak et al., 2003; Whittle et al., 2009). Cependant, les métaux sont toxiques à forte dose (Calafato et al., 2008; Chen et al., 2013; Larner et al., 2013) et peuvent entraîner d'importants effets secondaires nuisibles à la santé (Okusa and Crystal, 1994; Pauze et al., 2007; Vestergaard and Licht, 2001). C'est pourquoi il est primordial de quantifier ces dérèglements chimiques et isotopiques afin de pouvoir les utiliser à bon escient pour dépister et/ou soigner les individus vieillissant en mauvaise santé ou développant des pathologies complexes telles que les maladies neurodégénératives.

Au regard de ces résultats prometteurs et des progrès considérables qu'ils restent encore à faire concernant notre compréhension globale du vieillissement, cette étude a pour but premier de mieux contraindre la nature des liens existants entre le vieillissement et les dérèglements chimique et isotopique. Comment sont induits ces dérèglements ? Sont-ils spécifiques à un réservoir donné comme le sang ou peut-on observer des variations similaires dans tous les organes? Les dérèglements chimiques et isotopiques sont-ils la cause du vieillissement ou sont-ils simplement une conséquence résultant de dysfonctionnements métaboliques précoces? Pouvons-nous utiliser ces variations comme biomarqueurs fiables pour détecter des pathologies et ainsi ralentir les détériorations biologiques contribuant au vieillissement en mauvaise santé? Enfin, pouvons-nous contrôler les variations chimiques et isotopiques liées au vieillissement pour améliorer les conditions de vies des personnes âgées ?

Pour apporter des éléments de réponses à ces questions, j'ai analysé les concentrations en éléments traces et majeurs ainsi que les compositions isotopiques en cuivre ($\delta^{65}Cu$) et en zinc ($\delta^{66}Zn$) chez deux modèles animaux *i.e.* la souris et le vers (*C.elegans*) à différents stades de leur vie. A l'inverse des vers sur lesquels les analyses ont été réalisées sur l'organisme entier, nous nous sommes concentrés sur différents organes de souris (foie, muscle, cœur, cerveau et rein), le but étant de contraindre l'évolution chimique et isotopique à différentes échelles allant de l'organe à l'organisme total (vers) en fonction de l'âge. Notons que le génome humain présente 99% de similitude avec celui de la souris et entre 60 et 80% avec celui du vers (Andreux et al., 2012; Lai et al., 2000; Shaye and Greenwald, 2011) faisant de ces animaux des modèles idéals pour étudier le vieillissement chez l'Homme. Des tests visant à réguler la quantité d'éléments chimiques présente dans l'organisme ont également été effectué sur les vers dans le but de

comprendre et quantifier l'implication de ces dysfonctionnements chimiques vis à vis du vieillissement.

Au delà du processus de vieillissement observé chez tous les êtres vivants, je me suis aussi intéressée en détails à une maladie neurodégénérative encore mal comprise : la sclérose latérale amyotrophique (SLA) ou Maladie de Charcot. Cette maladie foudroyante conduit dans 100% des cas à la mort des patients en moyenne en moins de 5 années. La cause de cette maladie est inconnue, les marqueurs de dépistage et les traitements sont quasiment inexistants. Or, plus la maladie est dépistée tôt, plus les chances sont grandes de pouvoir freiner son évolution et la stabiliser. Les objectifs de cette étude sont donc aussi d'évaluer le potentiel des compositions chimiques et isotopiques comme futurs marqueurs de dépistage de la SLA mais également comme outils pour comprendre le rôle et l'importance qu'occupent ces dysfonctionnements dans la maladie et cibler les mécanismes qui en sont à l'origine. Bien que des variations chimiques et isotopiques aient été observés chez des patients atteints de la maladie d'Alzheimer (Azhdarzadeh et al., 2013; Bucossi et al., 2011; Moynier et al., 2017), qu'en est-il concernant les patients atteints de SLA ? Ces variations chimiques et particulièrement isotopiques sont-elles spécifiques d'une maladie donnée ? Si oui, à partir de quand ces dérèglements sont-ils visibles ?

Pour répondre à ces questions, j'ai mesuré les concentrations en éléments traces et majeurs et les compositions isotopiques ($\delta^{65}Cu$ et $\delta^{66}Zn$) de liquides céphalo-rachidiens (LCR) de patients sains ou atteints de maladies neuro-dégénératives regroupant la sclérose amyotrophique latérale (SLA) et la maladie d'Alzheimer (AD). Produits et localisés dans le cerveau, ces liquides sont supposés refléter les perturbations biochimiques qui s'y opèrent. Quantifier les perturbations chimiques des LCRs des patients malades pourrait donc permettre d'apporter des informations supplémentaires et utiles à la détection de cette pathologie et d'élucider la où les causes qui en sont à l'origine.

Le travail de thèse présenté dans ce manuscrit se divise en 4 grands chapitres :

- Le premier chapitre est consacré à la mise en contexte du lecteur. Il définit le vieillissement et la sclérose latérale amyotrophique (SLA) et présente l'état des connaissances médicales sur ces deux sujets. Ce chapitre dresse également un bilan sur l'importance des éléments chimiques tels que le cuivre et le zinc dans notre corps, et met en évidence l'intérêt des compositions isotopiques dans la compréhension de certaines pathologies complexes.

- Le deuxième chapitre présente l'ensemble des échantillons et des méthodes d'analyses utilisées dans cette étude. La provenance des échantillons, les protocoles de prélèvement, les procédures visant à mettre les échantillons en solution ainsi que les techniques d'analyses chimiques et isotopiques sont détaillées dans cette partie. Enfin, l'évaluation de la qualité des données acquises est longuement discutée notamment à travers un article publié pendant ma thèse et visant à identifier et quantifier les principales sources de contamination externe pouvant biaiser nos résultats.

- Le troisième chapitre, divisé en deux manuscrits, s'intéresse aux variabilités chimiques et isotopiques induites au cours du temps à l'échelle de l'organe chez la souris et de l'organisme dans sa globalité chez le vers. Le lien entre dysfonctionnement chimique et dérèglement métabolique est discuté en détails dans cette partie ainsi que l'intérêt que pourrait représenter ces outils comme nouveaux traitements thérapeutiques pour améliorer les conditions de vie des personnes vieillissantes.

- Le quatrième chapitre de cette thèse a pour but d'apporter des informations supplémentaires concernant la sclérose latérale amyotrophique (SLA). Dans une première partie sous forme de manuscrit, nous montrons que les variations chimiques et principalement celles des compositions isotopiques en cuivre peuvent s'avérer utiles pour détecter cette pathologie rare. Dans une deuxième partie, nous tentons de comprendre l'origine de ses variations isotopiques à travers des modèles cellulaires.

Cette étude s'achève par une conclusion permettant de résumer brièvement l'ensemble des résultats et interprétations fondamentaux de cette étude.

VERS UNE NOUVELLE APPROCHE MÉTALLOMIQUE DES SCIENCES MÉDICALES

CHAPITRE I

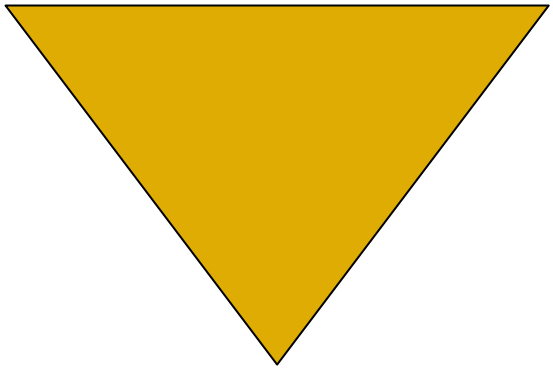

CHAPITRE I : VERS UNE NOUVELLE APPROCHE MÉTALLOMIQUE DES SCIENCES MÉDICALES

Divisé en deux parties, l'objectif de ce chapitre est de situer le contexte biomédical et chimique dans lequel s'insère cette étude. Dans une première partie sont ainsi présentés deux des principaux enjeux médicaux auxquels la médecine actuelle doit faire face et sur lesquels notre étude s'est basée ; à savoir le vieillissement de la population et le développement de la sclérose latérale amyotrophique (SLA). A travers une approche métallomique, la deuxième partie tend à démontrer l'importance des éléments chimiques dans le corps humain mais également le danger qu'ils peuvent représenter pour l'organisme lorsque leur métabolisme est déréglé.

I.1. Vieillissement et Sclérose latérale amyotrophique (SLA) : Les limites de la médecine

I.1.1. Le vieillissement

I.1.1.a. Définition

I.1.1.b. Principaux facteurs contribuant au vieillissement

I.1.2. La sclérose latérale amyotrophique (SLA)

I.1.2.a. Définition

I.1.2.b. Diagnostic et traitement

I.2. Importance des métaux dans le corps humain

I.2.1. Exemple du cuivre (Cu) et du zinc (Zn)

I.2.1.a. Métabolisme du Cu et du Zn dans l'organisme

I.2.1.b. Dérèglement homéostatique du Cu et Zn: Quelles conséquences ?

I.2.1.c. Isotopie du Cu et Zn

I.2.2. Rôle et importance d'autres métaux dans l'organisme

I.1. Vieillissement et sclérose latérale amyotrophique (SLA) : Les limites de la médecine

I.1.1. Le vieillissement

I.1.1.a. Définition

Lorsque l'on parle de vieillissement, il ne faut pas confondre l'âge chronologique et l'âge métabolique. L'âge chronologique n'est autre que le nombre d'années écoulées depuis la naissance. Il évolue de façon similaire chez tous les individus et est totalement indépendant de notre santé physique. A l'inverse, l'âge ou vieillissement métabolique dépend comme son nom l'indique de notre métabolisme et donc de notre santé. C'est la raison pour laquelle certaines personnes peuvent paraître plus jeune que leur âge (*i.e.* âge métabolique < âge chronologique) et inversement. Si l'âge chronologique est simple à contraindre, le vieillissement métabolique apparaît quant à lui comme un phénomène complexe et multifactoriel pouvant résulter de l'interaction de divers paramètres biologiques, génétiques, environnementaux et socioculturels. Bien qu'à ce jour il n'y ait pas de définition universelle acceptée, ce dernier se caractérise en général par le déclin progressif et fonctionnel de l'ensemble de nos réactions métaboliques et de notre système immunitaire entraînant des dysfonctionnements et des dégradations irréversibles à l'échelle cellulaire et moléculaire au cours du temps. Avec l'âge, l'organisme n'étant plus apte à assurer l'ensemble de ses fonctions biologiques et physiologiques se trouve ainsi plus vulnérable face au développement de certaines maladies. C'est pourquoi le nombre de maladies chroniques augmente de façon considérable chez les personnes âgées.

I.1.1.b. Principaux facteurs contribuant au vieillissement

Malgré toutes les théories qui ont été suggérées pour tenter d'expliquer les détériorations observées au cours du vieillissement, la cause principale du vieillissement reste encore une énigme. Parmi ces théories on compte par exemple l'immunoscenescence (altération du système immunitaire) (Fulop et al., 2010; Lang et al., 2012), l'apoptose (dégénération cellulaire) (Muradian and Schachtschabel, 2001; J.-H. Zhang et al., 2003), la méthylation de l'ADN (Horvath, 2013), le dysfonctionnement des mitochondries (Lee et al., 2003; Ryu et al., 2016; Tosato et al., 2007) ou encore le dérèglement homéostatique des protéines (Sands et al., 2017). Si plusieurs observations biologiques attestent aujourd'hui de l'existence de ces dégradations, il semble néanmoins que ces phénomènes ne soient pas les causes principales du vieillissement, certains de ces dérèglements pouvant simplement être les

conséquences d'autres perturbations plus importantes. A l'inverse, la formation de radicaux libres (1) (*i.e.* théorie des radicaux libres connue aussi sous le nom de théorie du stress oxydatif) (Finkel and Holbrook, 2000; Kregel and H. J. Zhang, 2006; Stadtman, 2004), le raccourcissement des télomères (2) (Bellot and X. Wang, 2013; Cawthon et al., 2003; Jiang et al., 2007; Meissner and Ritz-Timme, 2010; Tomás-Loba et al., 2013) et la glycation non enzymatique des protéines induite par un régime alimentaire trop riche (3) (Gkogkolou and Böhm, 2012; Luevano-Contreras and Chapman-Novakofski, 2010; Stitt, 2001) pourraient jouer un rôle plus important dans le vieillissement.

(1) La théorie des radicaux libres

La théorie des radicaux libres, appelée aussi théorie du stress oxydatif est souvent l'hypothèse la plus mise en avant par les scientifiques qui tentent d'expliquer pourquoi et comment nous vieillissons. Le stress oxydatif se caractérise par un déséquilibre entre la quantité de radicaux libres (ou dérivés réactifs de l'oxygène) et le taux de protéines anti-oxydantes (Betteridge, 2000) comme la superoxide dismutase (SOD1) et la métallothionéine (Fukai and Ushio-Fukai, 2011; Valentine et al., 2005). Ces radicaux libres, secrétés à la fois par des facteurs exogènes (e.g. UV, cigarettes) ou endogènes (e.g. NADPH oxydase) au niveau de la chaîne de respiration cellulaire dans les mitochondries (Stadtman, 2004) sont des espèces chimiques oxygénées ayant une configuration très instable qui s'explique par la présence d'électrons libre de valence non appariés. Parmi ces radicaux libres, on trouve par exemple l'anion superoxyde O_2^-, le peroxyde d'hydrogène H_2O_2 ou encore l'ion hydroxyle OH^-. Toutes ces espèces, cherchant à atteindre une configuration électronique stable vont oxyder des protéines, des acides désoxyribonucléiques (ADN) et des lipides en leur dérobant un électron. Cela va affecter leurs propriétés fonctionnelles et de ce fait favoriser le vieillissement de l'organisme (Finkel and Holbrook, 2000; Kregel and H. J. Zhang, 2006; McCord and Aizenman, 2014; Stadtman, 2004). Le dérèglement homéostatique des protéines, l'apoptose et l'immunosenescence précédemment suggéré comme des causes à l'origine du vieillissement pourraient donc être que des conséquences secondaires faisant suite à l'activité toxique des dérivés réactifs de l'oxygène (ROS).

(2) Le raccourcissement des télomères

Les télomères (*i.e.* séquences répétées de nucléotides) sont des parties non codantes de l'ADN situés aux extrémités des chromosomes qui permettent d'éviter d'éventuels

dysfonctionnements génétiques pouvant être causés par la fusion des chromosomes entre eux (O'Sullivan and Karlseder, 2010). Avec l'âge, le taux de l'ADN polymérase et l'expression de l'ADN télomérase, deux enzymes qui permettent respectivement la réplication et la restauration des télomères au cours de chaque division cellulaire diminuent (Tomás-Loba et al., 2013). Cela entraîne alors un raccourcissement progressif des télomères au cours du temps. A terme, ce raccourcissement des télomères provoque d'importantes instabilités génétiques puis la mort cellulaire (*i.e.* apoptose) (Cawthon et al., 2003; O'Sullivan and Karlseder, 2010) favorisant ainsi un vieillissement prématuré et limitant l'espérance de vie moyenne de l'Homme (Cawthon et al., 2003; Tomás-Loba et al., 2013) (Figure 1).

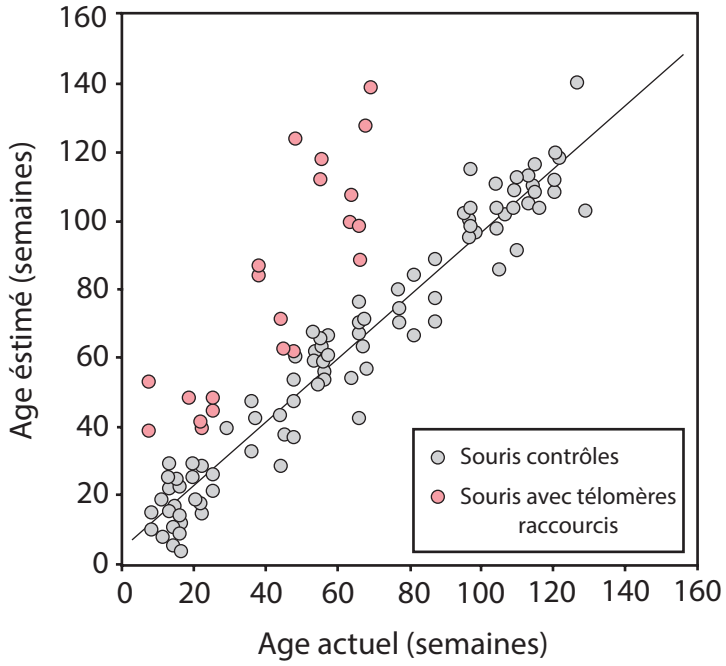

Figure 1: Effet du raccourcissement des télomères sur l'espérance de vie de souris; modifié d'après Tomàs-Loba et al.(2013). *Les points roses représentent des souris avec des télomères raccourcis (i.e. ayant une télomérase déficiente, Terc$^{-/-}$) et les points gris des souris 'contrôles' (i.e. télomères de longueur normale, WT). L'âge estimé a été calculé en comparant un ensemble de métabolites mesurés dans le sérum des souris WT et Terc$^{-/-}$.*

(3) Régime alimentaire trop riche

La troisième théorie communément mise en avant pour expliquer le ralentissement du vieillissement est la restriction calorique (CR). Les premiers effets bénéfiques de la restriction calorique, qui consistent à restreindre les apports nutritionnels journaliers ont été

confirmés pour la première fois chez des rats en 1935 (McCay et al., 1935) (Figure 2) puis chez de nombreuses espèces comme la levure (Guarente, 2005; Leonov et al., 2017), le vers (Houthoofd and Vanfleteren, 2006; Lakowski and Hekimi, 1998), la mouche (Partridge et al., 2005) ou encore le singe (Ramsey et al., 2000).

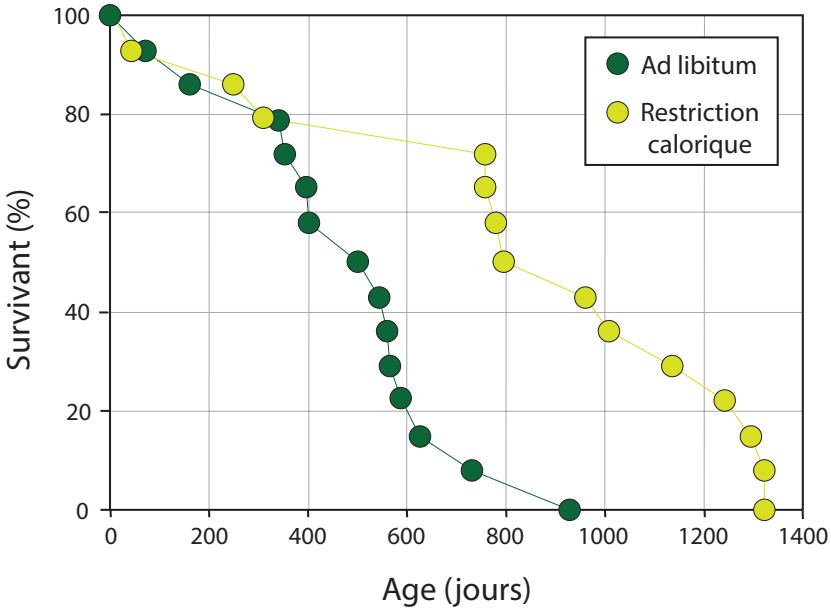

Figure 2: Effet de la restriction calorique sur la longévité de rats, modifié d'après McCay et al(1935).

Bien que les mécanismes associés à ce régime hypocalorique soient encore mal contraints et puissent s'avérer complexes, plusieurs hypothèses sont actuellement mise en avant (McDonald and Ramsey, 2010). Tout d'abord, il semblerait que la restriction calorique, en réduisant simultanément le taux de glucose (sucre) et d'insuline (hormone favorisant l'absorption depuis le sang des sucres vers les cellules) dans l'organisme ait un effet bénéfique sur le métabolisme énergétique (Heilbronn et al., 2006; Masoro, 2005; Schlotterer et al., 2009) ainsi que sur le métabolisme protéique intracellulaire et la protection cellulaire (via l'activation du facteur de transcription daf-16) (Kenyon et al., 1993) contribuant à ralentir le vieillissement. Plusieurs études génétiques ont en effet montré que des organismes mutants (daf-2, age-1, eat-2), caractérisés par une voie défectueuse de signalisation de l'insuline, avaient par exemple une protection cellulaire renforcée et une durée de vie prolongée (Arantes-Oliveira et al., 2003; Jia, 2004; Kenyon et al., 1993; Lakowski and Hekimi, 1998; Schlotterer et al., 2009) comparés à des organismes contrôles.

Bien que les sucres soient nécessaires pour le bon fonctionnement de l'organisme, ils peuvent s'avérer toxique à trop haute dose et entrainer l'accumulation de corps gras (Jia,

2004) et la formation de glycotoxines (AGEs, advanced age glycation products) (Gkogkolou and Böhm, 2012; Luevano-Contreras and Chapman-Novakofski, 2010) nocifs pour l'organisme. En se liant aux molécules, ces produits induisent leur glycation et la modification de leur configuration spatiale ce qui, à terme, entraine la perte de leur fonctions métaboliques et d'importants dérèglements physiologiques comme l'accroissement du taux d'inflammation favorisant le vieillissement (Gkogkolou and Böhm, 2012; Luevano-Contreras and Chapman-Novakofski, 2010).

Plusieurs études ont également montré que la restriction calorique pouvait avoir un effet sur la méthylation de l'ADN (Maegawa et al., 2017), la production de radicaux libres (Ramsey et al., 2000; Schlotterer et al., 2009; Sohal and Weindruch, 1996), le cycle cellulaire (Leonov et al., 2017) et l'autophagie (Kroemer, 2015) mettant en avant les effets multiples d'un régime hypocalorique notamment sur la réponse immunitaire et anti-oxydante, la réparation cellulaire et le maintien de l'information génétique.

La restriction calorique permet également d'activer la formation de sirtuines, des enzymes appartenant à la famille des déacétylases qui ralentissent le vieillissement (Guarente, 2005) en agissant sur divers mécanismes cellulaires comme par exemple la réparation de l'ADN ou la résistance au stress oxydatif et permettent ainsi d'éviter la mort cellulaire (Michan and Sinclair, 2007).

Au vu de ces résultats, il apparaît que le vieillissement est un phénomène compliqué dont les causes restent encore vagues. Notons que depuis peu, des études ont également révélé la présence d'importants dérèglements chimiques au cours du temps (Coudray et al., 2006; Malavolta et al., 2015; Mezzetti et al., 1998; Rembach et al., 2014) venant complexifier une fois de plus notre compréhension du sujet mais laissant néanmoins entrevoir de nouvelles pistes d'étude.

I.1.2. La sclérose latérale amyotrophique (SLA)

I.1.2.a. Définition

Affectant environ 250 000 personnes dans le monde (source : santé publique), la sclérose latérale amyotrophique (SLA) appelée plus couramment maladie de Charcot ou maladie de Lou Gherig est une maladie neurodégénérative qui se caractérise par une destruction progressive des neurones moteurs (cellules nerveuses spécialisées dans la motricité) présents dans le cortex cérébral primaire (neurones supérieurs), le tronc cérébral et la moelle épinière (neurones inferieurs) (Figure 3).

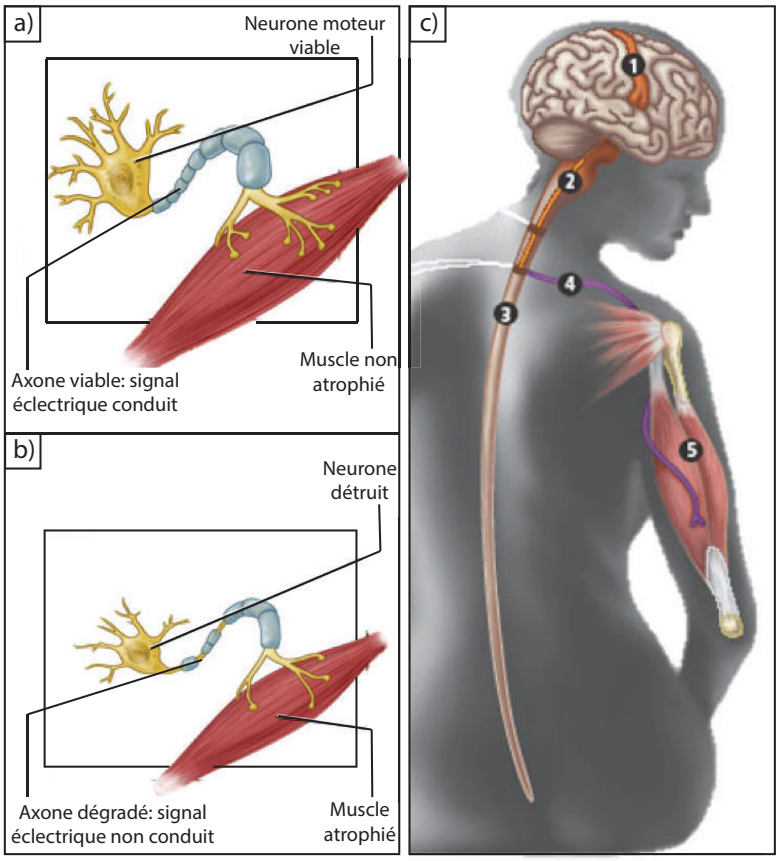

Figure 3 : a) Muscle non atrophié (patient sain), b) Muscle atrophié (patient SLA) et c) Trajet du message nerveux contrôlant la motricité musculaire : (1) Neurone moteur supérieur localisé dans le cortex moteur (cerveau), (2) Neurone moteur inferieur localisé dans le tronc cérébral et (3) la moelle épinière, (4) Axone conduisant le signal électrique au muscle (5). Source image: karmanhealthcare.com

Étant donné que ces neurones sont impliqués dans la transmission des signaux électriques du cerveau vers la moelle épinière et de la moelle épinière vers les muscles, cette dégénérescence neuronale, qui s'effectue à deux niveaux (forme bulbaire et spinale) provoque une atrophie musculaire qui s'avère mortelle. Dans la forme bulbaire, où la dégénérescence commence par affecter les neurones moteurs supérieurs de la face et du pharynx, ce sont les muscles de la langue et des lèvres qui sont touchés en premier, ce qui entraîne des troubles du langage (difficulté à parler/articuler) et de la déglutition (difficulté à s'alimenter). La maladie s'intensifie progressivement avec l'atteinte des muscles impliqués dans la motricité volontaire comme ceux des jambes, des bras et des mains. Cela provoque des crampes et des chutes jusqu' à la paralysie complète du patient. L'atrophie des muscles du pharynx apparaît finalement à un stade avancé de la maladie provoquant d'importantes complications respiratoires qui précipitent bien souvent l'aggravation de la maladie et le risque de décès. Pour la forme spinale, le résultat final est similaire bien que ce soit les

neurones moteurs innervant le tronc et les membres qui dégénèrent en premier affectant d'abord la motricité.

L'âge à partir duquel les premiers symptômes de la maladie apparaissent varie considérablement. Si en moyenne il se situe entre 50 et 60 ans, plusieurs cas précoces (30 ans) ont pu être observés. En général la durée de vie maximum d'un patient diagnostiqué de SLA varie entre 3 et 5 ans (Narasimhan, 2015), ce qui s'explique par un diagnostic tardif et une évolution rapide de la maladie. Il est également important de noter que plus de 90% des cas sont sporadiques contre seulement 5 à 10% d'origine familiale (Taylor et al., 2016) ce qui rend l'identification des mécanismes responsables de la dégradation neuronale extrêmement difficile.

I.1.2.b. Diagnostic et traitement

Similaires à d'autres maladies et/ou au vieillissement 'normal', les premiers symptômes de la SLA peuvent facilement passer inaperçus et rendre le diagnostic difficile. De nos jours, lorsqu'une personne est suspectée d'avoir la SLA, elle est dans un premier temps soumise à des tests non spécifiques cherchant à évaluer le degré de la déficience fonctionnelle. Pour cela, le patient réalise 12 tâches de la vie quotidienne en lien avec différentes fonctions comme la parole et la motricité (ALS Functional Rating Scale, ALSFRS) (Cedarbaum et al., 1999). A la fin du test, le patient se voit attribuer une note variant entre 0 et 48 (0 pour probablement malade et 48 pour non atteint de SLA). Dans le cas ou le patient obtient une note basse, il va alors subir toute une batterie de tests médicaux comprenant des électromyogrammes (EMG), des imageries par résonnance magnétique (IRM) du cerveau et de la moelle épinière ainsi que des prélèvements de sang et de liquides céphalo-rachidiens (LCRs). Réalisés en premier lieu, l'EMG mesure l'intensité de l'activité électrique échangée entre les nerfs crâniens et les muscles tandis que l'IRM vise à mettre en avant une atrophie cérébrale décelable par des lésions ischémiques et inflammatoires le plus souvent au niveau des lobes frontaux. Cependant, l'aspect en imagerie est bien souvent normal et lorsque des anomalies sont visibles elle sont rarement quantifiables. Pour compléter le diagnostic, des analyses chimiques sont alors réalisées sur des liquides céphalo-rachidiens et du sang total afin de quantifier le niveau de certaines protéines, enzymes et chémokines impliquées dans les processus neurotrophiques et inflammatoires (X. Chen and Shang, 2015; Kuhle et al., 2009; Lind et al., 2016; Tarasiuk et al., 2012; Ticozzi et al., 2012) ainsi que le taux de neurofilaments (Lu et al., 2015) souvent plus élevés chez les patients malades. En comparant les résultats avec ceux de patients sains, il est possible d'exclure la présence de la maladie ou, dans le cas contraire, d'assigner un diagnostic variant entre 'cliniquement

certain', 'probable' ou 'possible' basé sur les critères d'Awaji (AC) et d'El Escorial (rEEC) (Li et al., 2017). Cependant, le test de dépistage n 'est pas exclusif à la maladie. Une personne atteinte de la maladie d'Alzheimer présentera aussi une atrophie cérébrale bien qu'elle soit hippocampique et non localisée dans le cortex moteur et aura également un taux élevé de neurofilaments mesuré dans le liquide céphalo-rachidien (Zetterberg et al., 2016). De plus, le diagnostic étant majoritairement fait par élimination d'autres pathologies, sa fiabilité est souvent compromise. Depuis peu, l'utilisation d' algorithmes (Bede et al., 2017; Savage, 2017) prenant en compte un plus large spectre de paramètres et reposant sur d'importantes bases de données laissent à penser qu'ils pourraient fournir des informations cruciales concernant le dépistage précoce de la SLA, bien que cela nécessite tout d'abord de finaliser les banques de données.

En plus des marqueurs de dépistage peu fiables qui retardent le diagnostic de la maladie, aucun traitement permettant de stopper complètement son évolution n'a encore vu le jour. L'absence de traitement ciblé découle inéluctablement de notre méconnaissance des mécanismes à l'origine de la SLA. L'accumulation cytoplasmique dans les cellules neuronales de protéines mal-conformées comme la TDP-43 (TAR DNA-binding protein 43), la Cu-Zn SOD1 (Copper-zinc superoxyde dismutase) ou encore la FUS/TLS (Fused in Sarcoma/Translocated in Sarcoma) est définit comme un critère pathologique spécifique de la SLA (Chen-Plotkin et al., 2010; Nonaka et al., 2013; Parker et al., 2012; Smethurst et al., 2015; Valentine et al., 2005; Wiedau-Pazos et al., 1996) qui pourrait entraîner la dégénérescence et l'inflammation neuronale. Cependant, les causes et les mécanismes d'agrégation de ces protéines restent encore à comprendre. Plusieurs études ont mis en avant des causes génétiques (Cirulli et al., 2015; Dolgin, 2017; Taylor et al., 2016), la dernière identifiée étant la mutation du gène C90ORF72 (Dolgin, 2017). Cependant, ces mutations ne permettent d'expliquer que 20 à 40% des cas familiaux et seulement 10% des cas sporadiques (Dolgin, 2017; Valentine et al., 2005). D'autres facteurs comme le taux de radicaux libres ou encore les paramètres environnementaux (e.g. exposition a des substances toxiques comme le formaldéhyde) pourraient également être impliqué dans la dégradation neuronale (Brown, 2017) bien que leur rôle ne soit pas encore très bien compris. Malgré cela, certains traitements ont néanmoins vu le jour comme l'Edavarone, une molécule antioxydante permettant de lutter contre les dérivés réactifs de l'oxygène (ROS); le Masitinib, une substance chimique qui vise à inhiber les enzymes augmentant l'inflammation nerveuse ; le Riluzole qui agit sur le taux de glutamate (un messager nerveux) ; ou encore le Tirasemtiv, une molécule qui vise à stimuler les tissus musculaires (Scott, 2017). Or, si ces traitements permettent de ralentir l'évolution de la maladie et d'en atténuer les symptômes, ils ne permettent pas de la soigner. Au delà de ces traitements médicamenteux souvent

remis en cause en raison de leur efficacité variable, d'autres traitements alternatifs sont disponibles sur internet mais restent pour la plupart des « produits charlatans » souvent toxique pour l'organisme (Bedlack, 2017). Depuis peu, l'espoir repose sur de nouvelles thérapies géniques qui développent la modulation (on/off) et le remplacement des gènes codant pour des protéines mal conformées ou encore la suppression des ARN messagers (intermédiaire entre le gène et la protéine) (Scott, 2017). Malheureusement, ces essais ne reposent aujourd'hui que sur la théorie et nécessitent encore de nombreux tests avant d'aboutir à un traitement fiable et efficace de la SLA.

I.2. Importance des métaux dans le corps humains

I.2.1. Exemple du cuivre (Cu) et du zinc (Zn)

Juste après le fer (Fe), le cuivre (Cu) et le zinc (Zn) sont les deux métaux de transitions les plus abondants dans le corps humain, représentant respectivement 0,8% et 0,03% des éléments traces, soit 3g de Zn et 0.1g de Cu au total dans notre organisme (Institute of Medicine, 2002) (Figure 4).

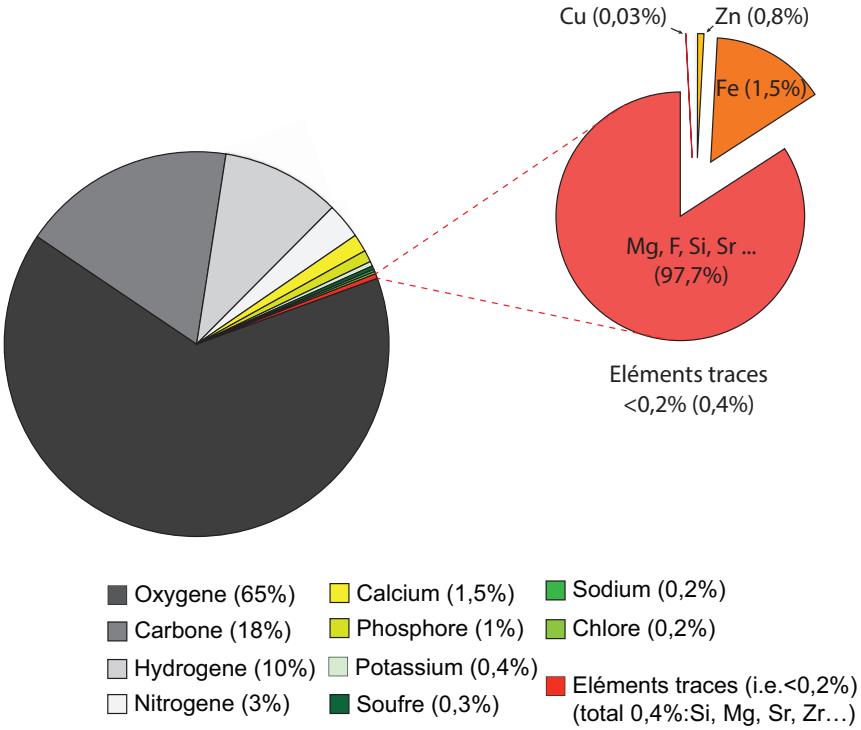

Figure 4: Représentation schématique du pourcentage des différents éléments chimiques présents dans le corps humain

Considérés comme des éléments vitaux pour notre santé, il est recommandé d'avoir une consommation journalière stable et régulière qui varie en fonction du sexe et de l'âge des individus. En moyenne, une femme adulte devrait ingérer 0.9 mg de cuivre et 8 mg de zinc par jour tandis qu'un homme adulte aura besoin de 1.2 mg de cuivre et 11 mg de zinc en moyenne (Institute of Medicine, 2002; Madej et al., 2013; National Research Council, 1989). Les principaux apports nutritifs proviennent de la viande rouge, du foie, des œufs et des fruits de mer pour le zinc et du foie de veau, des huîtres et autres fruits de mer ainsi que des fruits à coques et des graines de sésame pour le cuivre (Gropper and Smith, 2012; National Research Council, 1989; Squitti et al., 2014).

I.2.1.a. Métabolisme du Cu et du Zn dans l'organisme

- Le cuivre:

Une fois ingéré dans l'organisme par le tractus gastro-intestinal (Turnlund et al., 1984), le cuivre est réduit (Cu^{2+} à Cu^{+}) par des enzymes réductrices (métallo-réductase) telle que la cytochrome b (558) Fe/Cu réductase ou la STEAP2 (Collins et al., 2010). Cela lui permet de se lier à un transporteur (Ctr1) présent dans la membrane apical des entérocytes (cellules intestinales) qui va favoriser son transport du lumen (cœur de l'intestin) vers l'intérieur des entérocytes (Kim et al., 2008) (Figure 5). Le cuivre qui n'est pas utilisé par les entérocytes est expulsé dans le sang grâce à une enzyme présente dans la membrane basolatérale de ces cellules appelée ATP7A (ATPase) (Kim et al., 2008). Dès lors qu'il se retrouve dans le sang, le Cu est acheminé vers l'ensemble des organes et autres parties du corps via la céruloplasmine (80%) et l'albumine (20%) ; les deux principaux réservoirs du cuivre dans le sang (Collins et al., 2010; Gaetke and Chow, 2003). C'est le foie qui reçoit le cuivre en premier, ce dernier étant le principal organe de stockage du cuivre, qui par la suite, est en charge de le redistribuer en fonction des besoins à tous les autres organes comme le cœur, les muscles, le cerveau et les reins (Figure 5). Le cuivre excédentaire, qui n'est pas utilisé par l'organisme et qui peut représenter un danger si il s'accumule, est excrété par la bile (~0.5 mg/day), l'urine (<0.1 mg/day) ainsi que les selles (1.5 mg/day) (Figure 5).

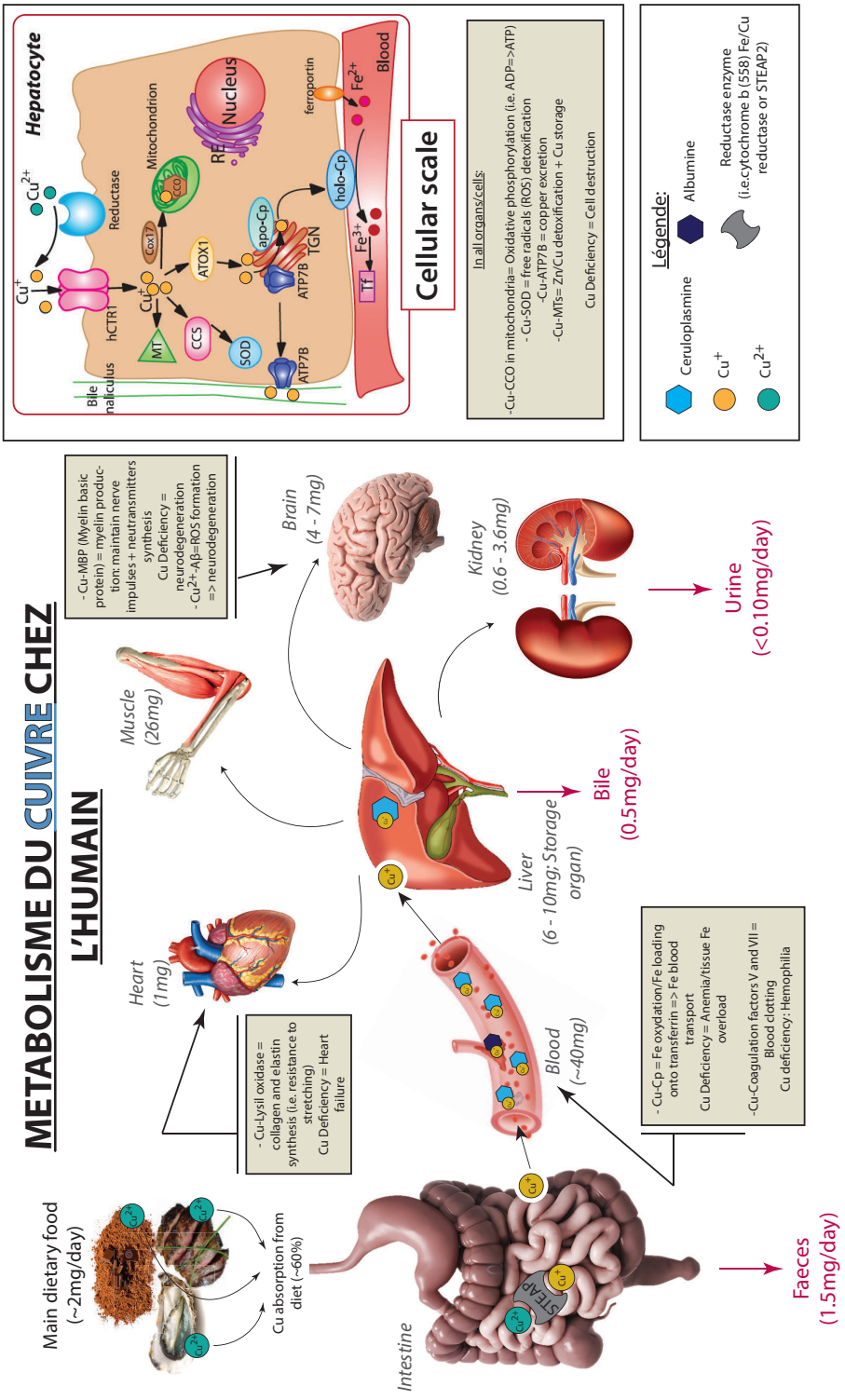

Figure 5 : Métabolisme du cuivre chez l'Homme à l'échelle de l'organisme et de la cellule; modifié d'après Kim et al.(2008)*; Turski and Thiele* (2009)*; Collins et al.*(2010)*; Angelova et al.*(2011)*; Ibrahim* (2013)*; Balter et al.*(2013)*; Squitti et al.*(2014)*; Gil-Bea et al.* (2017). *Abréviations: MT: metallothionéine, Cox17: cytochrome c oxidase Cu-chaperone, CCO: cytochrome c oxidase, ATOX1: protéine antioxidante 1, Cp: céruloplasmine, CCS: superoxide dismutase Cu-chaperone, SOD: superoxide dismutase, ATP7A/B: Cu-transporteur ATPase, TGN: appareil de Golgi, hCTR1: Cu-transporteur 1. Dans les encadrés beiges sont répertoriés des exemples de protéines et d'enzymes dans lesquelles le cuivre joue le rôle de cofacteur catalytique ainsi que les fonctions associées.*

A l'échelle de la cellule, le cuivre est acheminé vers l'ensemble des organelles via des protéines dites « chaperones » parmi lesquelles on retrouve ATOX1, COX17 et CCS (Gil-Bea et al., 2017; Kim et al., 2008) (Figure 5). Au sein de ces organelles, le cuivre est lié à un ensemble de protéines fonctionnelles comme la CcO (cytochrome c oxidase); une protéine présente dans la membrane interne des mitochondries qui est impliquée dans la respiration cellulaire (Iwata et al., 1995) ou encore la protéine Cu-Zn SOD1 (Cu-Zn superoxyde dismutase); un antioxydant contre l'accumulation de dérivés réactifs de l'oxygène (ROS) (Gil-Bea et al., 2017; Kim et al., 2008) (Figure 5). Les métallothionéines (MTs) permettent quant à elles de stocker le cuivre excédentaire et ainsi de réguler le taux intracellulaire (Banci et al., 2010; Turnlund, 1998) ; un processus appelé homéostasie. Notons que la métallothionéine (MT), avec la céruloplasmine (Cp) représente également la protéine principale de stockage du cuivre dans le milieu extracellulaire (sang) (Collins et al., 2010; Hellman and Gitlin, 2002; Turnlund et al., 1984).

Impliqué dans un grand nombre de protéines et d' enzymes, le cuivre apparaît donc comme un excellent cofacteur catalytique de plusieurs réactions métaboliques et processus physiologiques vitaux tels que la production d'énergie (ATP) via sa liaison avec la protéine CcO, le transport d'oxygène (via l'hémocyanine), la détoxification des dérivés réactifs de l'oxygène (ROS) (via la SOD) ou encore la pigmentation de la peau (via la tyrosinase, T) (Kim et al., 2008; Turski and Thiele, 2009) (Table 1).

Enzyme/Protein	Function	Consequence of Deficiency
Cu,Zn Superoxide Dismutase	Superoxide disproportionation; signaling	Oxidative stress; hepatocellular carcinoma; neurodegeneration
Cytochrome Oxidase	Mitochondrial oxidative phosphorylation; ATP production	Respiratory deficiency; cardiomyopathy; lethality
Tyrosinase/Laccase	Melanin synthesis; virulence and pathogenicity in fungi; innate immunity	Pigmentation Defects/Albinism; reduced fungal virulence
Peptidylglycine α-amidating monooxygenase	Peptide amidation/maturation	Heart rate defects; endocrine dysfunction; lethality
Dopamine β-Hydroxylase	Norepinephrine synthesis	Hypoglycemia; hypotension
Ceruloplasmin	Ferroxidase: Fe loading onto transferrin	Aceruloplasminemia: progressive anemia, neurodegeneration, diabetes
Hephaestin	Ferroxidase for ferroportin-mediated iron efflux	Anemia; impaired Fe aborption by peripheral tissues
Lysyl Oxidase	Covalent crosslinking of collagens and elastin	Aortic aneurisms, cardiovascular dysfunction
Lysyl Oxidase-like Proteins	Oxidation of snail transcription factor resulting in E-cadherin silencing and promoting EMT	Altered cell-cell contacts
Coagulation Factors V and VIII	Blood Clotting	Hemophilia
Nitrous Oxide Reductase	Catalyzes reduction of N_2O to N_2 in denitrification pathway of bacteria	Respiratory deficiency; Imbalance in nitrogen cycle
Ethylene Receptor	Ethylene signal transduction	Plant senescence, fruit ripening, growth
XIAP	Inhibitor of apoptosis	Copper deficiency in mouse knock-out
Ace1	*S. cerevisiae* transcription factor active under condtions of high intracellular copper	Inability to grow on high copper media
Copper Amine Oxidase	Deamination of primary amines to aldehyde	Impaired immune responses (in AOC3 knock-out mouse); reduced fat deposition in obese mice

Table 1: Exemples de protéines et d'enzymes dans lesquelles le cuivre est impliqué en tant que cofacteur catalytique. Les fonctions métaboliques associées ainsi que les conséquence engendrés par un déficit sont également présentées ; d'après Turski and Thiele (2009).

Il est également nécessaire pour d'autres processus physiologiques plus importants en relation par exemple avec les fonctions du système nerveux central (Banci et al., 2010; Kim et al., 2008; Turski and Thiele, 2009). En effet, dans le cerveau ou il est incorporé dans les astrocytes (cellules de la matière grise et blanche) et les cellules épithéliales des plexus choroidaux (CSF) il va, de par sa liaison avec l'enzyme dopamine-β-monoxygénase (DβM) catalyser la noradrénaline ; un neurotransmetteur qui assure la transmission des messages nerveux entre les neurones (Scheiber and Dringen, 2013; Scheiber et al., 2014). Dans le cerveau, il peut également se lier à d'autres enzymes spécifiques comme la tyrosinase (T), la céruloplasmine (Cp), la peptiglycine α-amidating monoxygenase (PαM) ou encore la lysyl oxidase (LOX) (Scheiber et al., 2014) participant ainsi au métabolisme énergétique (CcO, mitochondrie, ATP production), au métabolisme du fer (Cp), aux défenses antioxydantes (SOD) ou encore a la synthèse d'autres neuropeptides (DβM) nécessaires au bon fonctionnement des fonctions neuronales (Scheiber et al., 2014; Scheiber and Dringen, 2013).

- Le zinc:

Tout comme le cuivre, le zinc est un métal essentiel pour notre organisme qui est absorbé au niveau du tractus gastro-intestinal grâce à des protéines de transport (e.g. Zip 4). Il est ensuite distribué à l'ensemble du corps à travers le système de circulation centrale c'est à dire le sang (Eide, 2006; Foster et al., 1984; Osredkar and Sustar, 2011; Roh et al., 2012) ou il est complexé à l'albumine à plus de 60% (Kambe et al., 2015) (Figure 6). A l'inverse du cuivre, le foie n'est pas un organe de stockage même si, suite à son incorporation, le zinc semble être directement transporté vers cet organe avant d'être redistribué dans le reste du corps (Figure 6). En général, le zinc est préférentiellement stocké dans les muscles (environ 90% du zinc total de notre corps), les os et la peau (Kambe et al., 2015) à l'intérieur desquels il se trouve fixé à des métallothionéines (MTs) ainsi que dans l'intestin ou il est concentré au sein de « gut granules (intestinal lysosome-like organelles) » (Cabrera, 2015; Roh et al., 2012). Ce sont principalement ces deux protéines qui contrôlent l'homéostasie du zinc et qui permettent d'éviter un excès ou un déficit de zinc en stockant ou relâchant le zinc dans l'ensemble de l'organisme en fonction de ses besoins.

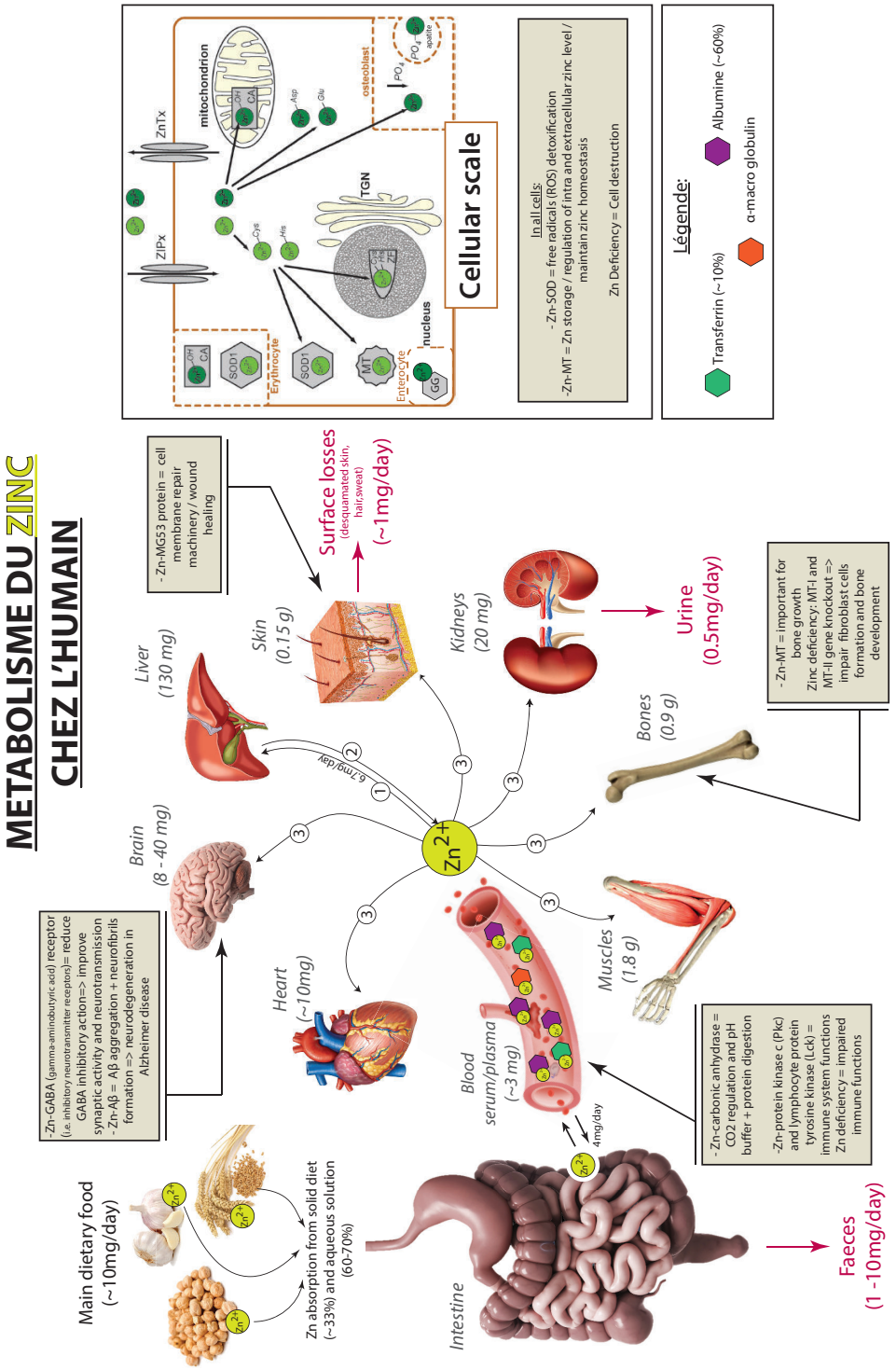

Figure 6 : Métabolisme du zinc chez l'Homme à l'échelle de l'organisme et de la cellule; modifié d'après Prasad (1995)*; Smart et al.* (2004)*; Maynard et al.* (2005)*; Eide et al.* (2006)*; Lansdown et al.* (2007)*; Murakami et al.* (2008)*; Haase et al.* (2009)*; Fong et al.* (2009)*; Gower-Winter et al.* (2012)*; Solomons et al.* (2013)*; Balter et al.* (2013)*; Roohani et al.* (2013)*; Kambe et al.* (2015)*; Cai et al.* (2015)*; Bonaventura et al.* (2014)*. Abréviations: MT: métallothionéine, CA: cysteine; SOD1: superoxide dismutase 1, GG: gut granules (i.e. organelles similaires aux lysosomes), TGN: appareil de Golgi, Cys: cystéine, His: histidine, ZF: zinc finger, Asp: asparate, Glu: glutathione, ZIPx and ZnTx: transporteurs du zinc. Dans les encadrés beiges sont répertoriés des exemples de protéines dans lesquelles le cuivre joue le rôle de cofacteur catalytique ainsi que les fonctions associées.*

A l'échelle cellulaire, le transport endogène ou exogène du zinc est régit par deux familles de protéines de transport : 1) les CDF (Cation Diffusion Facilitor) (par exemple CDF/ZnT/SLC30) qui permettent de diminuer le niveau de zinc dans le cytoplasme intracellulaire en excrétant le zinc hors de la cellule ou en le transportant dans les organites de la cellule et 2) les ZIP (Zrt-like, Irt-like Protéines) (par exemple Zip7, Zrt1) qui permettent d'acheminer le zinc vers l'intérieur de la cellule et d'augmenter le niveau de zinc cytoplasmique (Eide, 2006). Dans ces deux familles de transporteurs, le zinc est relié à des ligands (atomes de liaisons) d'histidine (atome de nitrogène) et de cystéine (atome de soufre) (Eide, 2006; Solomons, 2013).

Une fois dans la cellule, le zinc joue le rôle de cofacteur structural et catalytique dans plus de 300 enzymes (Auld, 2001; Eide, 2006; Osredkar and Sustar, 2011; Roh et al., 2012; Vallee and Falchuk, 1993) comme la Cu/Zn SOD1, l'Adh1 (déshydrogénase) (Eide, 2006) et les metallothionéines (Solomons, 2013). Tout comme le cuivre, il a donc un rôle crucial dans un grand nombre de fonctions physiologiques et de processus cellulaire tels que la synthèse d'ADN et la division cellulaire (Prasad, 1995), la spermatogénèse (Vallee and Falchuk, 1993), les fonctions immunes (il permet l'activation et la prolifération des cellules impliquées dans la réponse immunitaire *i.e.* lymphocytes T et B et monocytes) (Bonaventura et al., 2014; Murakami and Hirano, 2008), la cicatrisation de la peau (Lansdown et al., 2007) ou encore la régulation des glandes endocrines (Cabrera, 2015; Solomons, 2013). Il participe également au bon développement des os ainsi qu'à la croissance des tissus conjonctifs comme ceux présents dans le coeur et le système nerveux (Roohani et al., 2013; Solomons, 2013) et assure aussi des fonctions neurologiques dans le cerveau. Relâché par les vésicules synaptiques dans lesquelles il est stocké au sein du cerveau (Bonaventura et al., 2014), il peut en effet activer des récepteurs de neurotransmetteurs tels que NMDA (acide N-méthyl-D-aspartique) et GABA (acide gamma-aminobutyric) qui vont moduler l'activité synaptique et la neurotransmission (Smart et al., 2004).

Il est important de noter qu'avec plus de 99% de similitude existant entre le génome de la souris et celui de l'Homme (source: NIH, National Human Genome Research Institute), le métabolisme des métaux et particulièrement celui du cuivre et du zinc présenté ci-dessus chez l'humain est similaire à celui de la souris d'ou proviennent les organes analysés au cours de cette thèse. De la même manière, le génome humain compte entre 60 et 80% de gènes homologues à celui du vers *C.elegans* (nématode), également étudiés dans ce projet (P. Chen et al., 2013; Shaye and Greenwald, 2011) suggérant que leur métabolisme devrait s'apparenter à celui de l'Homme. Bien que le métabolisme des métaux chez le nématode

reste encore peu contraint et que son anatomie soit moins complexe que celle de l'Homme, ce dernier ayant seulement un système digestif (bouche, pharynx, rectum et anus), un système reproducteur (gonade, utérus, spermathèque, vulve, vésicule séminale et cloaque) et un système nerveux (302 neurones, synapses), il possède tout de même d'importantes similitudes avec l'être humain concernant par exemple les tissus musculaires ou encore les neurones (Hulme and Whitesides, 2011). De grande ressemblances au niveau des processus biochimiques impliqués dans la transduction du signal intracellulaire (e.g. insuline/IGF1/FOXO ; *C.elegans* INS1 protéine ≈ insuline humaine *i.e.* une protéine régie par la mutation daf-2), la dégradation des nutriments, le métabolisme énergétique, la synthèse des protéines ou encore le métabolisme (*i.e.* transport, excrétion/détoxification) des métaux ont également été observé (Anderson and Leibold, 2014; Aschner et al., 2017; Hulme and Whitesides, 2011; Martinez-Finley and Aschner, 2011). Par exemple, un ensemble de protéines de transport permettant de réguler la quantité intracellulaire des métaux comme le Fe, le Mn, le Cu et le Zn présentent des homologues chez l'humain (*i.e.* Cu : CUA 1_{vers} = $ATP7A/B_{humain}$ (Chun et al., 2017); Fe et Mn: $SMF\text{-}3_{vers}$ = $DMT1_{humain}$; FTN-1,2,3 = $Ferritine_{humain}$; FPN-1,2,3 = $Ferroportine_{humain}$ (Anderson and Leibold, 2014; Au et al., 2009; Chakraborty et al., 2015); Zn : $TTM1B_{vers}$ = CDF $transporter_{humain}$ (Roh et al., 2013). D'autres molécules impliquées dans le stockage et la régulation de métaux comme le glutathione et les métallothionéines ont également leurs analogues chez l'humain (*i.e.* mtl-1 et mtl-2) (Kowald et al., 2016). Par conséquent, bien que le métabolisme des métaux chez le nématode puisse paraître bien plus simple que celui de l'Homme et/ou de la souris, de grandes ressemblances existent, notamment en ce qui concerne le métabolisme des métaux.

I.2.1.b. Dérèglement homéostatique du Cu et Zn: Quelles conséquences ?

Compte tenu de l'importance que représentent le cuivre et le zinc dans les réactions métaboliques essentielles à la croissance, au développement et à la santé, il est évident qu'un dérèglement homéostatique (accumulation, déficit ou mauvaise localisation des éléments chimiques) représente un facteur de risque non négligeable pour l'organisme. Des hausses de concentrations en cuivre et en zinc ont déjà été identifiées dans un ensemble de pathologies neurodégénératives comme la maladie de Wilson (Bandmann et al., 2015), la maladie d'Alzheimer (Huang et al., 2000; Sastre et al., 2015; Squitti et al., 2014), la maladie de Parkinson (Larner et al., 2013; Pall et al., 1987), la sclérose latérale amyotrophique (SLA) (Dang et al., 2014; Hozumi et al., 2011; Roos et al., 2013) ou encore la maladie du Prion (Siggs et al., 2012) (Figure 7).

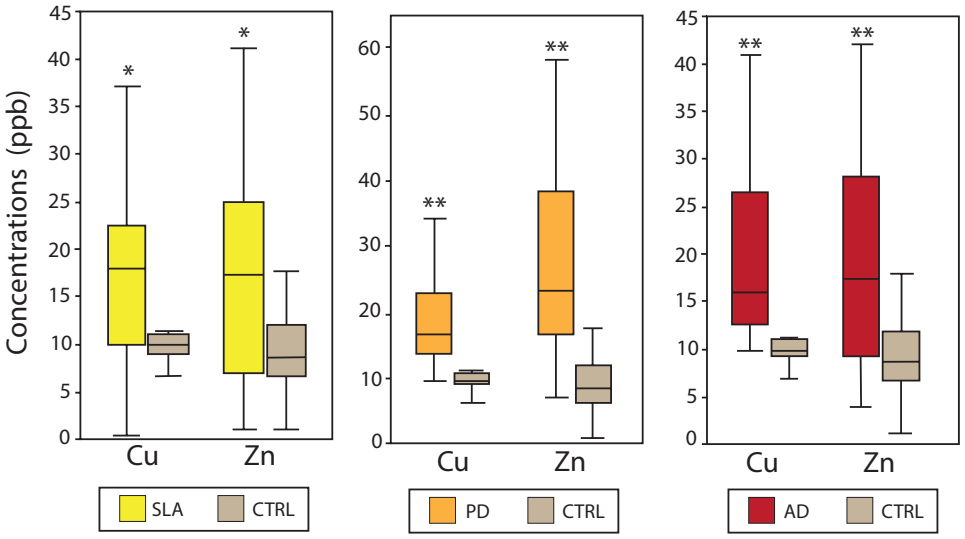

Figure 7: Augmentation des concentrations en cuivre (Cu) et en zinc (Zn) dans les liquides céphalo-rachidiens de patients atteints de a) sclérose latérale amyotrophique (SLA), b) maladie de Parkinson (PD) et c) maladie d'Alzheimer (AD); modifié d'après Hozumi et al.(2011). **p<0.05 et **p<0.01.*

En excès, ces deux métaux peuvent contribuer à la formation de radicaux libres (ROS) (Ahuja et al., 2015; Bush, 2000; Gaetke and Chow, 2003; Manzl et al., 2004) et à l'agrégation de protéines mal conformées comme la β-amyloïde (Barnham and Bush, 2008; Barnham et al., 2004; Bush and Tanzi, 2008; Huang et al., 2000; Kepp, 2017; Maynard et al., 2005; Nuttall and Oteiza, 2014; Sastre et al., 2015; Strozyk et al., 2009), l'α-synucléine (Bharathi et al., 2007), la TDP-43 (TAR-DNA binding protéine 43) (Gil-Bea et al., 2017) et la protéine Prion (PrP) (Jones et al., 2004); pouvant ainsi favoriser la dégénérescence neuronale de certaines pathologies comme la maladie d' Alzheimer, la SLA et la maladie du Prion.

Une augmentation des concentrations en cuivre a également été reportée dans plusieurs types de cancer (sein, cervicales, poumons et estomac (Gupte and Mumper, 2009)) soulignant l'implication d'un dysfonctionnement des voies métaboliques du cuivre dans les processus de tumorigénèse (formation des tumeurs). En excès, le cuivre peut en effet favoriser le développement et la prolifération de cellules cancéreuses (Brady et al., 2014; Gupte and Mumper, 2009; Hainaut et al., 1995; Ishida et al., 2013; 2010). Un déficit en cuivre et en zinc a également été observé dans d'autres pathologies comme la maladie de Menkes (Kaler, 2011), les maladies chroniques du foie comme la cirrhose (Ibrahim, 2013; Rahelić et al., 2006) ou encore l'anorexie (Bakan, 1979; Safai-Kutti, 1990).

D'importantes variations sont aussi reportées avec l'âge chez l'Homme. On note par exemple une augmentation de la concentration en cuivre et une diminution de celle en zinc dans le sang/plasma/sérum (Cabrera, 2015; Coudray et al., 2006; Haase and Rink, 2009; Madej et al., 2013; Malavolta et al., 2015; 2010; Mezzetti et al., 1998; Milanino et al., 1986;

Mocchegiani et al., 2012; Rembach et al., 2014; Sullivan et al., 1979) au cours du temps. Des variations sont aussi visibles dans les organes de souris. On note par exemple une hausse de la quantité de cuivre dans le cerveau (Fu et al., 2015; L.-M. Wang et al., 2010; Zatta et al., 2008) et une baisse de celle en zinc dans le cœur de modèles murins (Morita et al., 1994) au cours du temps, ainsi que chez le vers où une hausse du cuivre a été remarquée (Klang et al., 2014) avec l'âge. Puisque le zinc est impliqué dans la réponse immunitaire (Bonaventura et al., 2014) et que le cuivre catalyse la formation de radicaux libres (ROS) (Ahuja et al., 2015; Bush and Tanzi, 2008; Gaetke and Chow, 2003; Manzl et al., 2004), leur mauvaise régulation pourrait accélérer le vieillissement et donc l'incidence de maladie graves.

I.2.1.c. Isotopie du Cu et Zn

Comme tous les éléments chimiques, le cuivre (Cu) et le zinc (Zn) reposent sur le même modèle à savoir : un atome composé d'un noyau lui même constitué de protons (charge positive) et de neutrons (électriquement neutres) autour duquel gravitent des électrons (charge négative). L'égalité entre le nombre de protons et d'électrons permet d'assurer la neutralité de chaque atome. Ainsi, chaque atome se distingue par son nombre de proton appelé numéro atomique (Z) et son nombre de neutrons.

$$ {}^{A}_{Z}X $$

X : Elément chimique
A : Masse atomique (nombre de protons + neutrons)
Z : Numéro atomique (nombre de protons)

Un élément chimique peut avoir différents isotopes c'est à dire des atomes qui ont le même nombre de protons mais un nombre de neutrons différent et donc une masse atomique différente. C'est notamment le cas du cuivre et du zinc.

Le cuivre possède deux isotopes stables ; le ^{63}Cu et le ^{65}Cu dont les abondances naturelles sont respectivement de 69,7% et 30,8%. Ces deux isotopes partagent le même nombre de protons (29) mais se distinguent par leur nombre de neutrons (34 pour le ^{63}Cu et 36 pour ^{65}Cu). Plus il y a de neutrons, plus la masse atomique de l'atome est élevée : le ^{65}Cu (M = 64.9278 g/mol) est donc plus « lourd » que le ^{63}Cu (M = 62.9296 g/mol).

Le zinc, quant à lui, possède 30 protons et 5 isotopes stables : le ^{64}Zn, le ^{66}Zn, le ^{67}Zn, le ^{68}Zn et le ^{70}Zn ayant respectivement 34, 36, 37, 38 et 40 neutrons et dont les abondances naturelles sont de 48,6%, 27,9%, 4,1%, 18,8% et 0,6% (Figure 8).

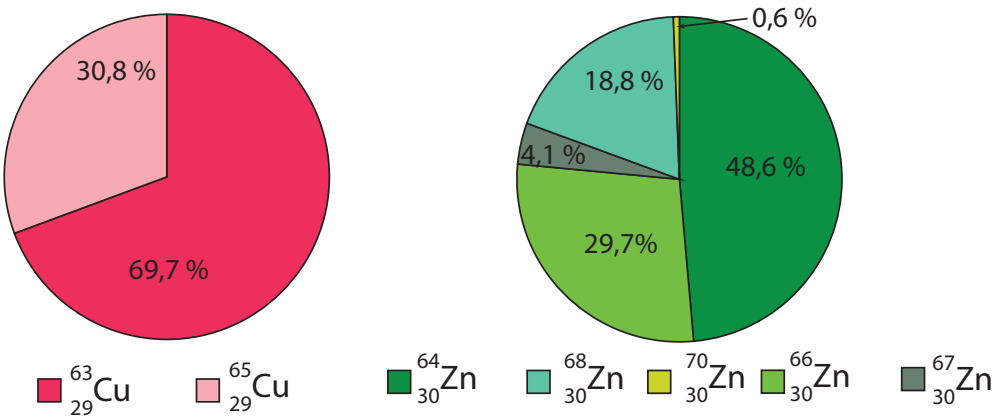

Figure 8 : Abondances naturelles des isotopes du cuivre et du zinc

Pendant les processus biochimiques et les réactions métaboliques, les isotopes qui ne possèdent pas les mêmes masses et qui ont donc des propriétés physico-chimiques distinctes, sont incorporés de manière différente dans les réservoirs biologiques (par exemple dans le sang ou les liquides céphalo-rachidiens) et dans les composés (protéines, molécules). Cette différence de comportement génère une variabilité des abondances isotopiques que l'on appelle « fractionnement isotopique ». L'amplitude du fractionnement se quantifie par la mesure de composition isotopique (‰) qui n'est autre que le rapport de deux isotopes d'un même élément chimique normalisé par rapport à un standard de référence. Pour le cuivre, le standard de référence est une solution de cuivre pur (NIST 97) et la composition isotopique d'un échantillon est calculée avec la formule suivante:

$$\delta\,^{65}Cu = \left[\frac{\left(\frac{^{65}Cu}{^{63}Cu}\right)_{ech.}}{\left(\frac{^{65}Cu}{^{63}Cu}\right)_{std}} - 1\right] * 1000$$

Pour le zinc, le standard de référence est JMC 3-0749-L avec une composition isotopique notée :

$$\delta\,^{66}Zn = \left[\frac{\left(\frac{^{66}Zn}{^{64}Zn}\right)_{ech.}}{\left(\frac{^{66}Zn}{^{64}Zn}\right)_{std}} - 1\right] * 1000$$

ech : abréviation pour échantillon

std : abréviation pour standard

Par définition, les compositions isotopiques en Cu et Zn des deux standards de référence sont donc égales à zéro. δ^{66}Zn et δ^{65}Cu sont positifs lorsque les compositions isotopiques de l'échantillon analysé sont plus lourdes que le standard de référence et négatifs lorsque qu'elles sont plus légères.

En biologie, le fractionnement isotopique est contrôlé principalement par deux paramètres qui sont (1) l'état d'oxydation de l'ion métallique et (2) la nature des ligands qui lient le métal (Schauble, 2004). Des calculs *ab initio* ont récemment démontré que les espèces (molécules, protéines et enzymes) liant les métaux par des ligands à forte électronégativité comme l'oxygène (O, lactate) ou l'azote (N, histidine) étaient préférentiellement enrichies en isotopes lourds (e.g. ^{65}Cu et ^{66}Zn) ; à l'inverse, les métaux liés à des espèces à plus faible électronégativité comme le soufre (S, cystéine et metallothionéine) sont préférentiellement enrichis en isotopes légers (e.g. ^{63}Cu et ^{64}Zn) (Albarède et al., 2016). De façon similaire, les espèces oxydées (*i.e.* liant les ions oxydés comme Cu^{2+}) ont des compositions isotopiques plus lourdes que les espèces réduites (*i.e.* liant les ions réduits comme Cu^{+}) (Albarède et al., 2016; Balter et al., 2013). Notons que le zinc ; qui ne possède qu'un seul état d'oxydation se trouve en général moins fractionné que le cuivre, qui en possède deux (Albarède et al., 2016).

Au fil du temps, la mesure des rapports isotopiques en cuivre et en zinc s'est révélée très prometteuse dans divers domaines comme l'archéologie où ils ont par exemple été utilisés pour déterminer le sexe d'individus appartenant à des civilisations anciennes (Jaouen et al., 2012) ou pour reconstruire l'évolution de niveau trophique ancien (Jaouen et al., 2013a). En biologie et en médecine, ils ont permis de mieux percevoir la complexité de certaines pathologies telles que la maladie de Wilson (Aramendía et al., 2013), du Prion (Büchl et al., 2008; Miller et al., 2016) et d'Alzheimer (Moynier et al., 2017) ou encore de l'hémochromatose (Stenberg et al., 2005). Ils ont également permis d'apporter des informations supplémentaires sur des maladies affectant le foie (Lauwens et al., 2016) comme la cirrhose (Costas-Rodríguez et al., 2015; 2016) ou encore d' apporter des informations constructives permettant de mieux contraindre différents types de cancers. Par exemple, Larner et al. (2015), Balter et al. (2015), Bondanese et al. (2016), Télouk et al. (2015), Lobo et al. (2017) ou encore Chamel et al. (2016) ont montré que les rapports isotopiques en cuivre (δ^{65}Cu) et en zinc (δ^{66}Zn) étaient significativement altérés dans le sang et/ou les tissus cancéreux d'humains et d'animaux atteints de cancer colorectal, de carcinome hépatocellulaire et épidermoïde et de cancer du sein ; les tissus tumoraux étant notamment enrichies en isotopes lourd du cuivre et à l'inverse en isotope léger du zinc. Des variations de compostions isotopiques en cuivre et en zinc ont également été observées

avec l'âge (Jaouen et al., 2013b) ainsi qu'entre des espèces végétariennes, omnivores et carnivores (Costas-Rodríguez et al., 2014; Jaouen et al., 2013a; 2016a; 2016b; Van Heghe et al., 2012), apportant dans ce dernier cas des informations sur le régime alimentaire des populations. Des variations ont également été observées au cours de la ménopause (Jaouen and Balter, 2014; Van Heghe et al., 2014). Notons que ces informations pourraient par la suite s'avérer utiles pour déceler des problèmes en lien avec l'alimentation ou des dérèglements physiologiques comme par exemple l'anorexie.

I.2.2. Rôle et importance d'autres métaux dans l'organisme

Outre le cuivre et le zinc, d'autres métaux comme le fer (Fe) et le calcium (Ca) sont également essentiels pour l'organisme. Le fer est par exemple un oligo-élément qui intervient dans le cycle respiratoire des cellules musculaires, la fabrication de globules rouges et qui joue un rôle fondamental dans la production d'hémoglobine ; une protéine contenue dans les globules rouges et qui assure le transport d'oxygène dans le sang (Walczyk and Blanckenburg, 2002). Bien qu'il soit vital pour l'organisme, il arrive cependant qu'il se révèle toxique lorsqu'il se trouve mal régulé. Un déficit en fer pourra par exemple conduire à une anémie caractérisée par une baisse des compositions isotopiques en Fe dans le sang (Van Heghe et al., 2013), tandis qu'un excès de Fe conduira à une hémochromatose identifiable par une hausse du rapport isotopique $\delta^{56}Fe$ (Krayenbuehl et al., 2005; Stenberg et al., 2005; Van Heghe et al., 2013), une hausse isotopique également observée dans le sang de personnes ayant développée une maladie chronique des reins (Anoshkina et al., 2017). Une augmentation des concentrations en Fe dans le cerveau (Pithadia and Lim, 2012), contrebalancée par une diminution dans le sérum (Azhdarzadeh et al., 2013; Paglia et al., 2016) a également été observée chez des personnes atteintes de la maladie d'Alzheimer. En participant à la formation de radicaux libres et en favorisant l'agrégation de protéines mal conformées comme la β-amyloïde (Bush and Tanzi, 2008; Kepp, 2017), l'accumulation de fer dans le cerveau pourrait tout comme le cuivre et le zinc être responsable de la dégénérescence neuronale dans la maladie d'Alzheimer. D'autres pathologies telles que les maladies chroniques du rein ou encore d'importantes pertes de sang sont également relier à un dérèglement homéostatique du fer se traduisant par une augmentation des compositions isotopiques dans le sang/sérum (Anoshkina et al., 2017; Hotz et al., 2012).

Le calcium (Ca) est aussi un élément indispensable à l'organisme. Principalement essentiel pour la croissance osseuse et la dentition, il intervient aussi dans diverses réactions métaboliques impliquées dans la sécrétion hormonale, la conduction nerveuse, les

fonctions musculaires ou encore la coagulation sanguine (Beto, 2015). Une dérégulation de la teneur en calcium peut, tout comme le fer, le cuivre et le zinc, induire d'importantes perturbations. Par exemple, une baisse de la teneur en calcium dans l'organisme est à relier à une ostéoporose (Sunyecz, 2008). L'étude des rapports isotopiques ($\delta^{44}Ca$) à également permis de mettre en avant des changements physiologiques en lien notamment avec les pratiques alimentaires comme le sevrage (Tacail et al., 2017).

Outre le cuivre, le zinc, le fer et le calcium, d'autres éléments chimiques dont le métabolisme n'est pas toujours bien contraint, peuvent, lorsqu'ils sont mal régulés, contribuer au développement de certaines pathologies comme les maladies neuro-dégénératives (Azhdarzadeh et al., 2013; Hozumi et al., 2011; Paglia et al., 2016; Roos et al., 2013; 2012; Sastre et al., 2015) et les maladies chroniques du foie. Dans ce dernier cas, les patients malades ont des concentrations en Mn dans le sérum plus élevées que celles de patients sains (Rahelić et al., 2006). Concernant les maladies neuro-dégénératives, Paglia et al. (2016) ont démontré que les personnes atteintes de la maladie d'Alzheimer se distinguaient par une hausse de la teneur en vanadium (V), uranium (U), strontium (Sr) et molybdène (Mo) et à l'inverse une diminution de celle en manganèse (Mn), mercure (Hg) et sélénium (Se) dans leur sérum (Figure 9).

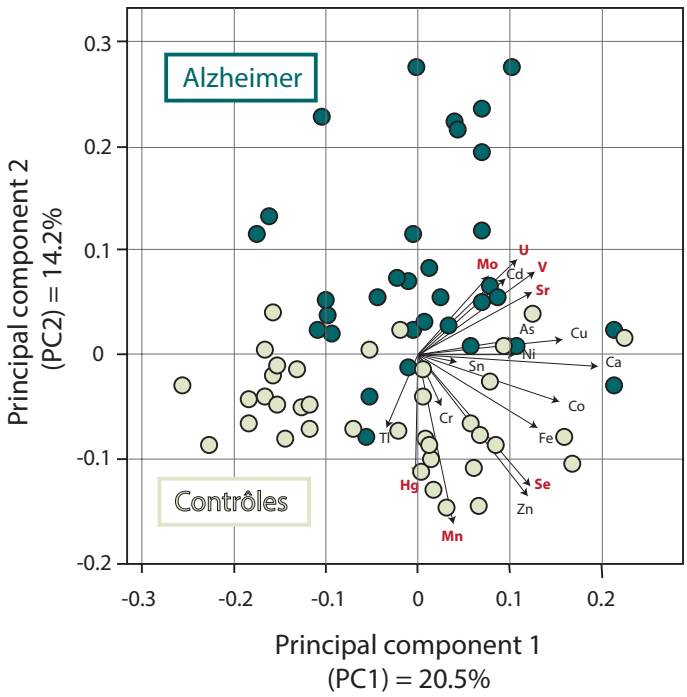

Figure 9 : Analyse en composantes principales (ACP) représentant les concentrations de divers éléments chimiques mesurés dans le sérum de patients avec la maladie d'Alzheimer (bleu foncé) et de sujets sains (vert clair). Les personnes malades ont des concentrations plus élevées en molybdène (Mo), uranium (U), vanadium (V) et strontium (Sr) et à l'inverse des concentrations plus basses en mercure (Hg), manganèse (Mn) et sélénium (Se) ; modifié d'après Paglia et al. (2016)

De la même manière, une hausse des concentrations en manganèse (Mn), uranium (U) (Roos et al., 2013; 2012), plomb (Pb) (Conradi et al., 1976; Roos et al., 2013; Vinceti et al., 2017), aluminium (Al), cadmium (Cd), cobalt (Co) et vanadium (V) (Roos et al., 2013) associée à une baisse de celles en magnésium (Mg) (Ostachowicz et al., 2006; Roos et al., 2013), sodium (Na) (Ostachowicz et al., 2006) et mercure (Hg) (Roos et al., 2013; Vinceti et al., 2017) a été notée dans les liquides céphalo-rachidiens de patients SLA (Figure 9). Cependant, il est intéressant de noter que les résultats obtenus par ces différentes études sur les variations de concentrations sont parfois contradictoires.

L'ensemble des études présentées ci-dessus souligne l'importance des éléments chimiques dans l'organisme et le danger qu'ils peuvent représenter lorsqu'ils sont dérégulés. Dans les chapitres suivants, nous verrons qu'ils occupent également un rôle important dans le processus de vieillissement et le développement de la sclérose latérale amyotrophique (SLA).

MATÉRIELS ET MÉTHODES

CHAPITRE II

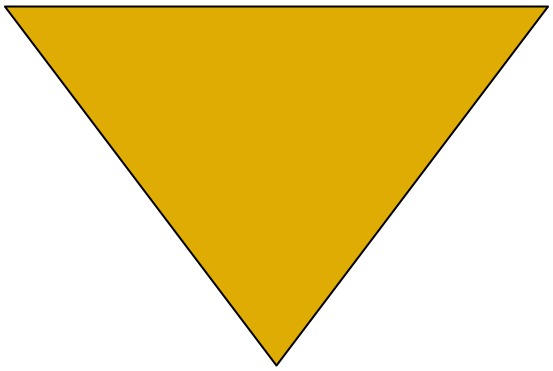

Ce chapitre, divisé en quatre grandes parties, est consacré principalement à la description détaillée des échantillons analysés dans cette étude ainsi qu'aux différentes techniques de préparation et d'analyses employées. L'évaluation de la qualité des données obtenues, jugée extrêmement importante dans cette étude y est également rigoureusement discutée. Dans la première partie sont ainsi développés le type et la provenance des échantillons sur lesquels ont portés cette étude ainsi que l'ensemble des méthodes de prélèvements. La deuxième partie de ce chapitre a pour but de décrire les protocoles de préparation des échantillons comprenant les étapes de lyophilisation, de mise en solution, de séparation et de purification des éléments chimiques par chromatographie ionique. La troisième partie vise à détailler les procédures analytiques suivies pour mesurer les concentrations en éléments traces et majeurs ainsi que les compositions isotopiques en Cu et en Zn et la quatrième partie discute précisément la qualité des résultats obtenus.

II.1. Provenance et protocole de prélèvement des échantillons

II.1.1. Les échantillons d'origine animale

II.1.1.a. Les organes de souris (C57BL/6)

II.1.1.b. Les vers (*C.elegans*)

II.1.2. Les échantillons d'origine humaine

II.1.2.a. Les liquides céphalo-rachidiens (LCRs)

II.1.2.b. Les cellules

II.2. Préparation des échantillons pour les analyses chimiques et isotopiques

II.2.1. Lyophilisation et mise en solution des échantillons

II.2.1.a. Protocole de lyophilisation

II.2.1.b. Mise en solution des échantillons

II.2.2. Séparation par chromatographie ionique

II.2.2.a. Principe de la chromatographie ionique

II.2.2.b. Isolation et purification du Cu et du Zn sur colonnes échangeuses d'ions

II.3. Analyses chimiques

II.3.1. Mesure des éléments traces et majeurs

II.3.1.a. Principe de la spectrométrie de masse à quadripôle et à émission optique

II.3.1.b. Mesure et calcul des concentrations

II.3.2. Les compositions isotopiques en Cu et Zn

II.3.2.a. Principe de la spectrométrie de masse à multi-collection et à source plasma

II.3.2.b. Mesure des rapports isotopiques en Cu ($\delta^{65}Cu$) et en Zn ($\delta^{66}Zn$)

II.4. Evaluation de la qualité des données acquises

II.4.1. Duplicats, réplicats et blancs d'acides

II.4.2. Standards de références biologiques

II.4.3. Evaluation des principales sources de contamination externe

II.4.3.a. Les tubes de prélèvement et stockage

II.4.3.b. Les gants de protection

ARTICLE

"Nitrile, latex, neoprene and vinyl gloves: a primary source of contamination for trace element and Zn isotopic analyses in geological and biological samples"

*Marion Garçon, **Lucie Sauzéat**, Richard W. Carlson, Steven B. Shirey, Mélanie Simon, Vincent Balter and Maud Boyet*

(published in Geostandards and Geoanalytical Research)

II.1. Provenance et protocole de prélèvement des échantillons

Dans cette étude, un ensemble d'échantillons biologiques d'origines diverses et variées ont été analysés dans le cadre de deux projets scientifiques étroitement reliés portant sur le vieillissement et les maladies neurodégénératives. Ils comprennent : (1) des échantillons d'origine animale, incluant des organes de souris et des vers (*C.elegans*) et (2) des échantillons d'origine humaine, à savoir des liquides céphalo-rachidiens (LCRs) et des modèles cellulaires.

II.1.1. Les échantillons d'origine animale

II.1.1.a. Les organes de souris (C57BL/6)

L'ensemble des organes étudiés dans cette étude a été prélevé sur une seule et même population de souris mâles appelée C57BL/6J, ou plus communément «Black 6». Les souris ont été élevées, tuées, et leurs organes ont été prélevés à l'École polytechnique de Lausanne (EPFL) par des biologistes avec qui j'ai collaboré tout au long de ma thèse.

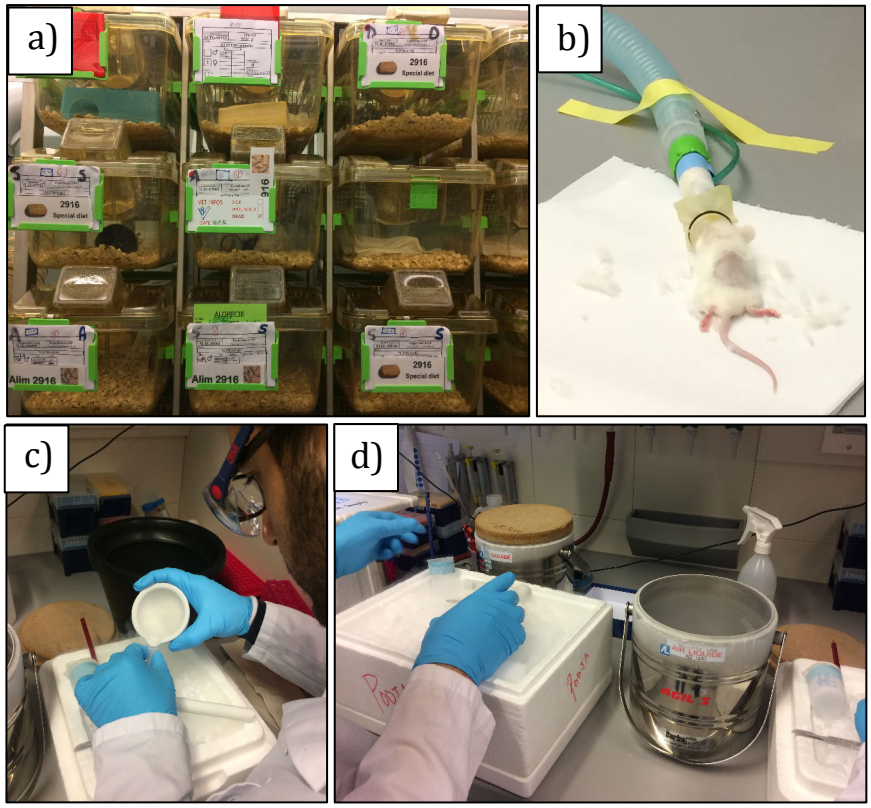

Figure 1: a) Élevage de souris (C57BL/6J), b) Euthanasie des souris par inhalation de dioxyde de carbone (CO_2), c) et d) Broyage et homogénéisation des organes avec de l'azote liquide

Avant d'être tuées, toutes les souris ont été nourries avec un régime alimentaire (chow diet) à base de graines et de céréales (e.g. farine de maïs, farine de soja, luzerne et alfafa)

et élevées dans des cages suivant des conditions similaires (*i.e.* température du milieu, temps d'exposition à une luminosité donnée et nombre de souris par cage identiques) (Figure 1a).

Parmi les organes collectés, on compte des foies, des muscles (quadriceps), des cœurs, des reins et des cerveaux dont les prélèvements ont été réalisés à des âges différents, à savoir 6 mois, 16 mois et 24 mois. La description détaillée (nom et nombre d'échantillons) pour chaque tranche d'âge est présentée dans la Table 1 ci-dessous.

Sample Name	Age (mois)	Organe
L2869	6	FOIE
L2870	6	
L2871	6	
L2872	6	
L2873	6	
L2874	6	
L2876	6	
L2860	6	
L2861	6	
L2862	6	
L2863	6	
L2864	6	
L2865	6	
L2866	6	
L2867	6	
L2868	6	
L2880	16	
L2883	16	
L2884	16	
L2886	16	
L2887	16	
L2888	16	
L2889	16	
L2890	16	
L2891	16	
L2892	16	
L2893	16	
L2894	16	
L2895	16	
L2896	16	
L2897	16	
L2898	16	
L2899	16	
L2900	24	
L2902	24	
L2903	24	
L2905	24	
L2906	24	
L2907	24	
L2908	24	
L2904	24	
L2910	24	
L2911	24	
L2913	24	
L2915	24	
L2916	24	
L2917	24	
L2918	24	
L2919	24	

Sample Name	Age (mois)	Organe
B2876	6	CERVEAU
B2870	6	
B2871	6	
B2872	6	
B2873	6	
B2874	6	
B2860	6	
B2861	6	
B2862	6	
B2863	6	
B2864	6	
B2880	16	
B2883	16	
B2884	16	
B2886	16	
B2887	16	
B2888	16	
B2889	16	
B2890	16	
B2891	16	
B2892	16	
B2893	16	
B2911	24	
B2913	24	
B2915	24	
B2916	24	
B2917	24	
B2919	24	
B2900	24	
B2902	24	
B2903	24	
B2904	24	
B2905	24	

Sample Name	Age (mois)	Organe
H2864	6	COEUR
H2870	6	
H2871	6	
H2872	6	
H2873	6	
H2895	16	
H2889	16	
H2890	16	
H2891	16	
H2892	16	
H2905	24	
H2900	24	
H2906	24	
H2907	24	
H2911	24	

Sample Name	Age (mois)	Organe
M2872 (Q)	6	MUSCLE QUADRICEPS
M2870 (Q)	6	
M2871 (Q)	6	
M2873 (Q)	6	
M2874 (Q)	6	
M2876 (Q)	6	
M2889 (Q)	16	
M2880 (Q)	16	
M2883 (Q)	16	
M2884 (Q)	16	
M2886 (Q)	16	
M2887 (Q)	16	
M2906 (Q)	24	
M2903 (Q)	24	
M2907 (Q)	24	
M2908 (Q)	24	
M2910 (Q)	24	
M2913 (Q)	24	

Sample Name	Age (mois)	Organe
K2870	6	REIN
K2871	6	
K2872	6	
K2873	6	
K2874	6	
K2860	6	
K2861	6	
K2883	16	
K2884	16	
K2886	16	
K2887	16	
K2888	16	
K2889	16	
K2890	16	
K2913	24	
K2915	24	
K2916	24	
K2917	24	
K2919	24	
K2900	24	
K2902	24	

Table 1 : Liste des organes de souris (C57BL/6J) analysés dans cette étude

Il est important de noter que toutes ces souris sont issues d'une même lignée et possèdent donc des caractéristiques communes telles que (1) un patrimoine génétique similaire; elles sont toutes homozygotes (*i.e.* deux allèles identiques pour un gène donné), et (2) un même phénotype (*i.e.* ensemble des caractères observables d'un individu). Cela signifie donc que le seul paramètre différant d'une souris à l'autre est leur âge.

Concernant les biopsies, ces dernières ont été effectuées dans des conditions d'hygiène et de sécurité règlementées par du personnel en Post doctorat hautement qualifié, notamment Pooja Jha sous la direction du Professeur Johan Auwerx au sein du laboratoire de physiologie (Laboratory of Integrative Systems Physiology ; LIPS) de l'EPFL. Brièvement, les animaux sont dans un premier temps asphyxiés par inhalation de dioxyde de carbone (CO_2) (Figure 1b) puis disséqués dans des conditions stériles. Les différents organes sont prélevés, broyés et homogénéisés dans un mortier en agate avec de l'azote liquide (N_2) (Figure 1c et 1d). Cette étape est extrêmement importante car la plupart des organes comme les muscles, les reins, les cœurs, et les cerveaux sont hétérogènes. Un échantillon non homogénéisé pourrait engendrer un prélèvement préférentiel d'une partie potentiellement enrichie ou appauvrie en certains éléments chimiques et ainsi entraîner un biais analytique. Après leur broyage, les organes sont stockés dans des tubes en polypropylène NALGENE® au sein de chambres froides à des températures inférieures à -80ºC dans le but d'optimiser leur conservation à long terme.

II.1.1.b. Les vers (*C.elegans*)

Avec une simplicité anatomique et un développement extrêmement rapide, le nématode *Caenorhabditis elegans* est depuis longtemps considéré comme un organisme modèle en biologie. Avec une phase de développement in-utero de 150 minutes et ex-utero d'environ 9 heures et seulement 38 heures pour devenir ensuite un jeune adulte (Figure 2), cet animal de taille millimétrique permet d'étudier de façon accélérer des processus biologiques beaucoup plus longs chez d'autres organismes comme la souris ou encore l'humain.

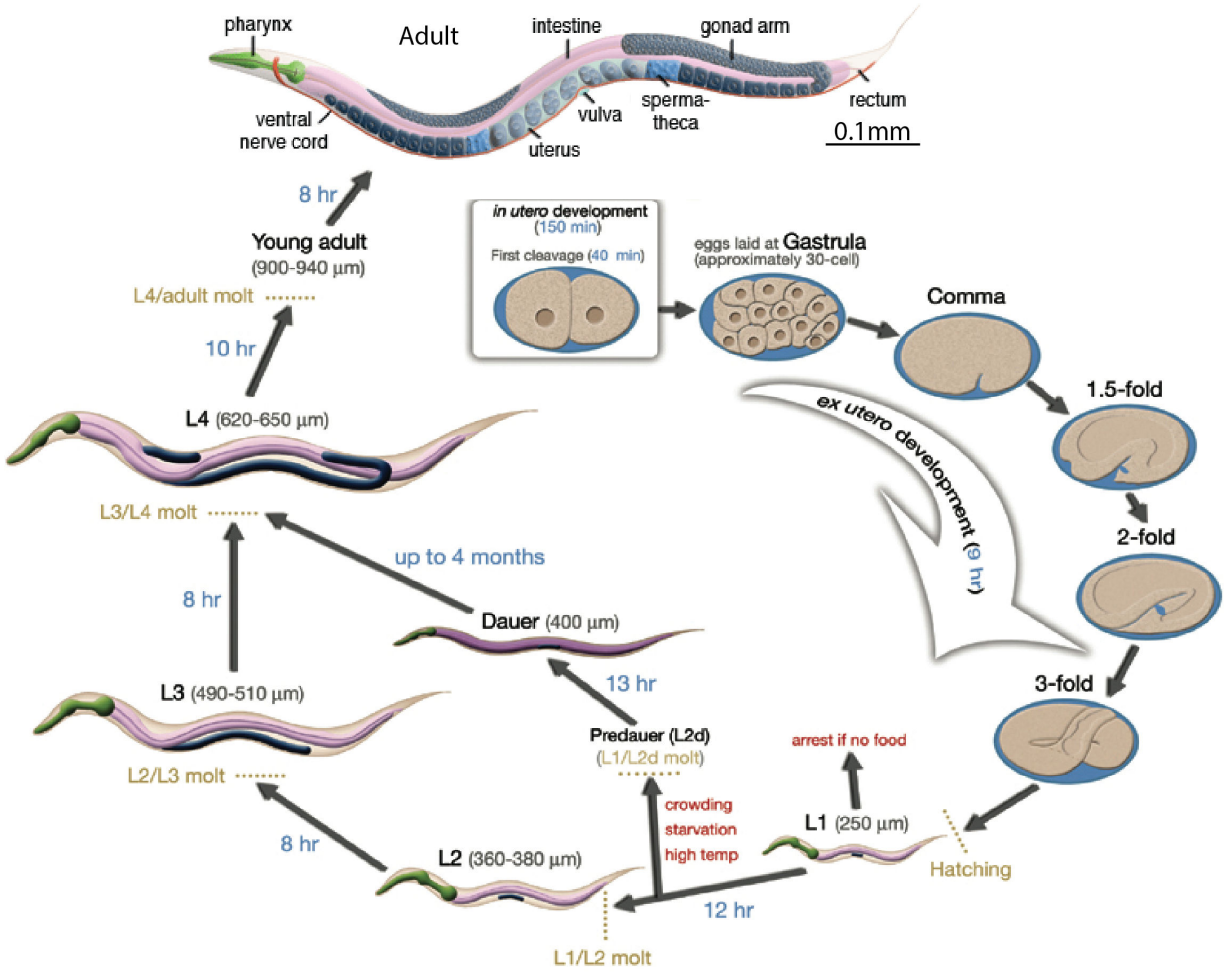

Figure 2 : Cycle de développement du nématode C.elegans d'après www.wormatlas.org

Dans cette étude, quatre types de vers ont été étudiés afin de mieux comprendre l'importance des dérèglements chimiques et isotopiques dans le vieillissement. Cela inclut une souche contrôle, c'est à dire non mutée (N2) et trois souches génétiquement modifiées: (1) e1370, un vers avec une longue durée de vie résultant d'une mutation sur le gène daf-2 *i.e.* un gène impliqué dans la régulation de l'insuline, (2) mu86, un vers à courte durée de vie portant une mutation sur le gène daf-16. Ce gène code pour un facteur de transcription (FOXO) impliqué dans la régulation de plusieurs centaines de gènes sous-jacents régulant la synthèse de molécules bénéfiques à l'organisme comme des espèces anti-oxydantes et des molécules favorisant la protection des cellules (Arantes-Oliveira et al., 2003; Kenyon, 2005; Kenyon et al., 1993) et (3) CF1588, un double mutant possédant à la fois la mutation sur le gène daf-2 et daf-16. Ce dernier a une durée de vie en moyenne similaire à celle du contrôle.

Tous les vers de cette étude proviennent du Centre Génétique Caenorhabditis (CGC). A l'exception des analyses chimiques et isotopiques que j'ai mené en salle blanche à l'ENS

de Lyon, j'ai réalisé la totalité des manipulations sur les vers (*i.e.* préparation, synchronisation, croissance, récolte et courbe de vie, Figure 3) au sein de l'IGFL (Institut Génomique Fonctionnel de Lyon) sous la tutelle d'Anne Laurençon.

Avant, pendant et entre chaque nouvelles expériences, les vers sont maintenus à une température constante de 20ºC au sein d'incubateur sur des boites de pétries contenant un milieu gélosé à base d'agar-agar (NGM) couplé à du FluoroUracil 3.95 mg/L (FU; Sigma F6627, une drogue limitant l'éclosion) sur lequel a été déposé une couche de bactéries vivantes (Escherichia coli, OP50) faisant office de nourriture (Figure 3 étape 1). Afin d'éviter un manque de nourriture, les vers doivent être changés de boîte tous les cinq jours. Concernant les bactéries, elles sont préparées dans un milieu de culture microbien stérile riche en nutriments (LB broth Lennox) contenant des peptides, des acides aminés et des glucides.

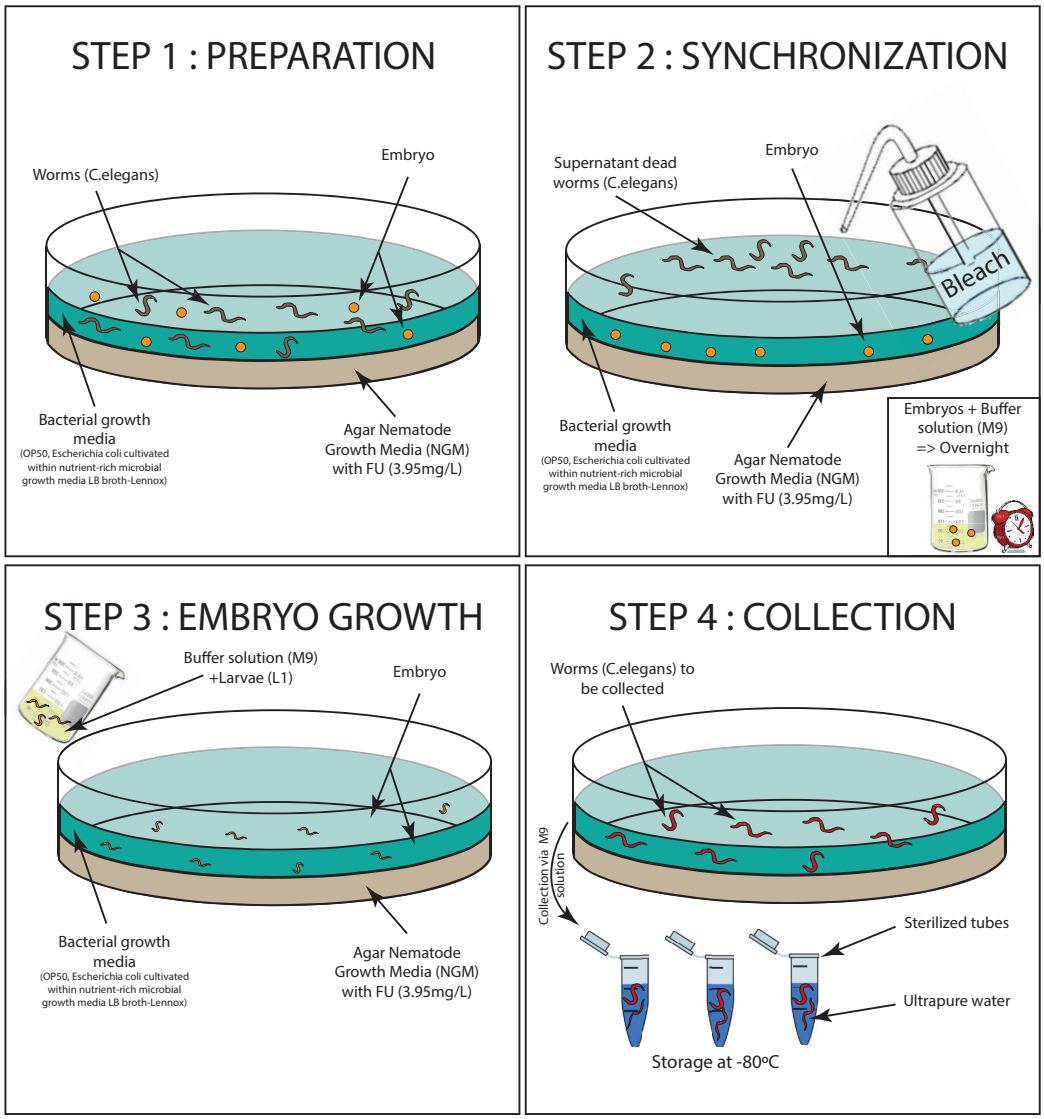

Figure 3 : Protocole de préparation des vers C. elegans. La concentration de FluoroUracil (FU) ajouté à la gélose est de 3.95 mg/L

En moyenne, une analyse chimique et isotopique précise requiert un minimum de 10000 vers, ce qui signifie que plus de 150 boites de pétries ont dû être préparées pour chaque test (soit plus de 450 boites au total *i.e.* 3 tests), une boite de pétrie de 85 mm de diamètre ne pouvant pas contenir plus de 1000 vers. En détail, la première étape consiste à synchroniser les vers, préalablement maintenus à 20ºC, avec une solution d'eau de javel (Figure 3, étape 2). Cette étape est réalisée sous un poste de sécurité microbiologique (PSM) afin d'assurer la protection optimale de l'opérateur, de la manipulation et de l'environnement. Elle permet de ne récolter que les embryons car les vers adultes ne résistent pas à la javel. Ces embryons sont ensuite stockés à 20ºC dans une solution à pH neutre (M9) au sein d'erlenmeyers pendant 1 nuit, une étape qui permet le passage du stade embryonnaire à celui de larves (stade L1, Figure 2). Après avoir déterminé le nombre de larves (stade L1) par millilitre de solution, ces dernières sont déposées par tranche de 1000 sur de nouvelles boites de pétrie de 85mm de diamètre (NGM, OP50) (Figure 3, étape 3) où elles vont se développer avant d'être récoltés à l'âge adulte aux périodes de temps voulues (*i.e.* 2, 10 et 17 jours) avec une solution à pH neutre (M9). Les vers sont ensuite congelés à -80ºC dans des tubes Eppendorf® préalablement stérilisés (Figure 3, étape 4).

II.1.2. Les échantillons d'origine humaine

II.1.2.a. Les liquides céphalo-rachidiens (LCRs)

Le liquide céphalo-rachidien (LCR), appelé aussi liquide cérébro-spinal, est un liquide biologique transparent sécrété par les cellules épithéliales présentes dans les plexus choroïdes (Damkier et al., 2013) et dans lequel baigne la moelle épinière et l'ensemble du cerveau. Il se trouve dans deux espaces distincts : 1) l'espace sous-arachnoïdien, une zone externe au système nerveux central, et 2) l'espace ventriculaire, un espace interne à l'encéphale divisé en quatre parties appelées les ventricules cérébraux (2 ventricules latéraux, le 3ème et le 4ème ventricule) (Figure 4).

Avec un volume moyen d'environ 150 mL, soit 10 à 20% du poids total de notre cerveau (Sakka et al., 2011) et un taux de production de 500 à 1200 mL par jour, ce liquide est renouvelé entre 3 et 4 fois par jour chez l'être humain (Sakka et al., 2011). Il se compose d'environ 99% d 'eau, le pourcentage restant étant constitué de protéines (*e.g.* albumine, α-,β- et γ-globulines) et de globules blancs et rouges. Le liquide céphalo-rachidien possède deux fonctions principales: un rôle de maintien mécanique luttant contre une hausse de pression afin de protéger le cerveau des chocs, et un rôle de protection immunitaire via l'élimination dans la circulation sanguine des substances toxiques et néfastes au système immunitaire.

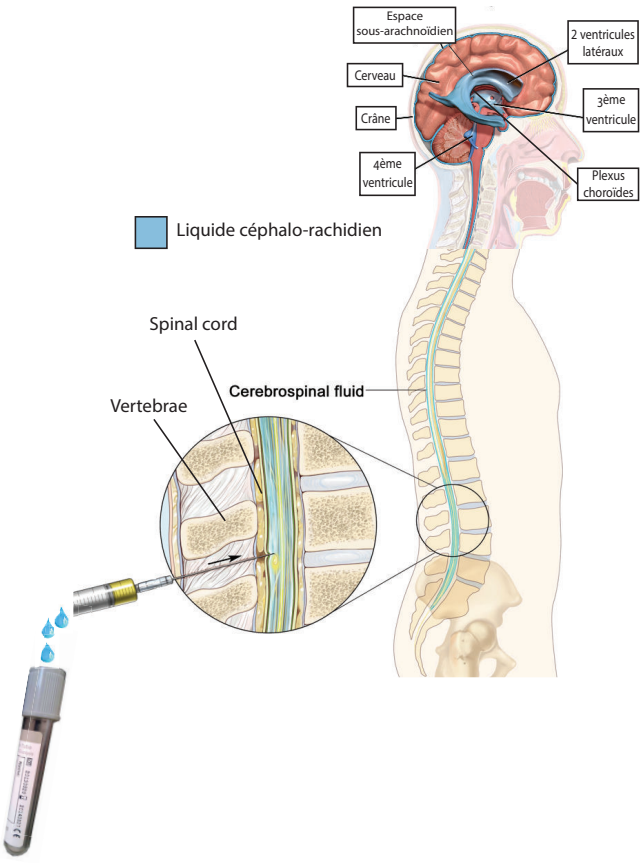

Figure 4 : *Représentation schématique indiquant la localisation du liquide céphalo-rachidien au sein du cortex sous-arachnoïdien et des espaces ventriculaires dans le cerveau humain ainsi que la méthode de prélèvement par ponction lombaire*

Dans cette étude, une soixantaine de LCRs ont été analysés dont l'ensemble des détails (*i.e.* sexe du patient, date de naissance et de prélèvement, diagnostic cognitif, nom de l'échantillon) est résumé dans la Table 2.

Ils proviennent de trois groupes de sujets distincts de sexe masculin ou féminin comprenant: (1) des patients atteints de la maladie d'Alzheimer (ALZ), et (2) de la sclérose latérale amyotrophique (SLA), et (3) de patients contrôles (CTRL) atteints d'aucune des deux précédentes maladies. Ce dernier groupe représente des personnes diagnostiquées positives à une démence mais dont l'étiologie serait reliée au domaine psychique et non biologique (bilan morphologique (IRM) et biologique (LCR) normaux).

Sexe	Date de naissance	Diagnostic	Date de prélèvement	Nom de l'échantillon
Masculin	13/08/1934	ALZ	15/03/10	ALZ4
Masculin	24/10/1931	ALZ	24/03/10	ALZ5
Masculin	25/04/1941	ALZ	14/04/10	ALZ6
Masculin	08/01/1942	ALZ	03/06/10	ALZ7
Masculin	03/09/1931	ALZ	07/06/10	ALZ8
Masculin	10/07/1947	ALZ	15/09/10	ALZ9
Masculin	21/12/1939	ALZ	18/11/10	ALZ10
Masculin	13/12/1950	ALZ	23/11/10	ALZ11
Masculin	30/11/1947	ALZ	26/01/11	ALZ12
Masculin	14/05/1943	ALZ	21/10/14	ALZ13
Masculin	23/12/1940	ALZ	15/09/14	ALZ14
Masculin	24/04/1940	ALZ	26/11/13	ALZ15
Masculin	03/10/1934	ALZ	04/06/14	ALZ16
Masculin	15/10/1935	ALZ	29/01/14	ALZ17
Masculin	29/09/1969	SLA	04/05/15	SLA1
Masculin	09/09/1952	SLA	16/04/15	SLA2
Masculin	13/03/1934	SLA	08/04/15	SLA4
Masculin	28/01/1967	SLA	25/11/14	SLA5
Masculin	10/04/1980	SLA	02/07/14	SLA6
Masculin	02/01/1949	SLA	12/06/14	SLA7
Masculin	20/12/1929	SLA	24/02/15	SLA8
Masculin	01/04/1946	SLA	09/10/14	SLA9
Masculin	23/06/1942	SLA	01/10/15	SLA10
Masculin	01/02/1951	SLA	03/11/15	SLA11
Masculin	02/01/1956	SLA	26/01/16	SLA12
Masculin	10/05/1955	SLA	27/01/16	SLA13
Masculin	18/06/1963	SLA	03/02/16	SLA14
Masculin	25/11/1965	SLA	28/01/15	SLA15
Masculin	29/04/1965	SLA	17/06/15	SLA16
Masculin	02/09/1945	SLA	29/07/15	SLA17
Masculin	14/08/1956	SLA	30/03/16	SLA18
Masculin	27/07/1967	SLA	02/05/16	SLA19
Masculin	01/07/1941	SLA	31/05/16	SLA20
Masculin	21/06/1946	SLA	02/06/16	SLA21
Masculin	21/09/1940	SLA	21/06/16	SLA22
Masculin	12/12/1962	SLA	05/07/16	SLA23
Masculin	11/02/1971	SLA	11/07/16	SLA24
Féminin	10/10/1943	SLA	23/09/14	SLA25
Féminin	23/05/1951	SLA	19/01/15	SLA26
Féminin	19/04/1951	SLA	05/05/15	SLA27
Féminin	05/09/1947	SLA	14/10/15	SLA28
Féminin	25/12/1947	SLA	26/01/16	SLA29
Féminin	23/09/1952	SLA	23/02/16	SLA30
Féminin	28/04/1971	SLA	14/06/16	SLA31
Féminin	29/11/1973	SLA	05/07/16	SLA32
Masculin	22/04/1960	CTRL	10/07/09	CTRL2
Masculin	03/04/1950	CTRL	12/12/12	CTRL3
Masculin	13/12/1943	CTRL	03/01/13	CTRL4
Masculin	29/08/1965	CTRL	25/09/13	CTRL5
Masculin	11/03/1968	CTRL	10/04/14	CTRL6
Masculin	29/07/1943	CTRL	23/06/11	CTRL7
Masculin	01/01/1954	CTRL	04/02/14	CTRL8
Masculin	10/01/1970	CTRL	26/05/14	CTRL9
Masculin	05/08/1943	CTRL	01/07/14	CTRL10
Masculin	08/03/1956	CTRL	13/12/14	CTRL11
Masculin	04/03/1935	CTRL	26/03/15	CTRL12

Table 2 : *Description détaillée des liquides céphalo-rachidiens analysés au cours de cette étude. ALZ=Alzheimer, SLA= sclérose latérale amyotrophique, CTRL= sujets contrôles*

Ces liquides biologiques, prélevés par ponction lombaire (*cf* figure 4) nous ont été fournis par le Dr Emilien Bernard du Centre de biologie Pathologie Est du CHU de Lyon (échantillons SLA et CTRL) et par la banque d'échantillons biologiques des Hospices Civils de Lyon (Hôpital neurologique P. Wertheimer) (échantillons ALZ). Tout comme les organes de souris, ils ont été conservés dans des tubes en polypropylène stérilisés (Figure 5) avant d'être stockés a -80ºC en chambre froide.

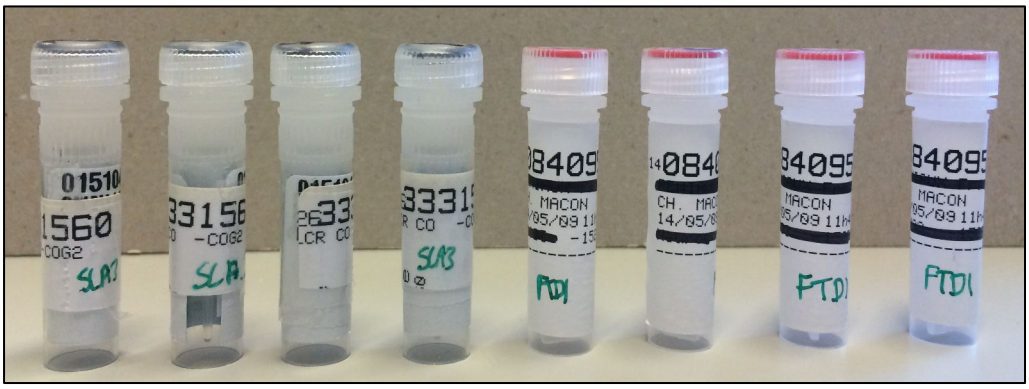

Figure 5 : Liquides céphalo-rachidiens de patients atteints de sclérose latérale amyotrophique (SLA) (bouchon noir) et de « contrôles, (CTRL) » (bouchon rouge) stockés dans des tubes en polypropylène stérilisés

II.1.2.b. Les cellules

La plupart des maladies neurodégénératives sont caractérisées par l'agrégation de protéines mal-conformées dans le cerveau comme la TDP-43 (TAR-DNA binding protein) pour la sclérose latérale amyotrophique (e.g. (Dang et al., 2014)) et la beta-amyloïde 42 (Aβ42) dans la maladie d'Alzheimer (e.g.(Reitz, 2012)). Bien que ces protéines soient présentes en grande quantité, leur implication dans ces maladies reste mal contrainte et il semblerait que leur toxicité soit dépendante d'importants dérèglements chimiques favorisant leur interaction avec des ions métalliques (e.g. Cu, Zn, Fe) et leur agrégation dans le cerveau (Bush and Tanzi, 2008; Kepp, 2017). Dans cette étude, nous avons tenté mieux comprendre le lien de cause à effet reliant dérèglements chimiques et isotopiques avec l'agrégation de TDP-43 afin d'élucider le rôle de cette protéine dans la SLA. Pour cela, nous avons analysés deux types de cellules humaines (neuroblastes : SHSY5Y, et cellules de reins : 293T) dans lesquelles ont été transfectées des gènes mutés (Q331K, G298S, G294A, NLS (78-74), NLS removal, NLS (78-74/187-192) codant pour différentes formes de la protéine TDP-43 mal-conformée. L'ensemble des détails relatifs à ces manipulations est présenté en Table 3.

Nom de l'échantillon	Condition de transplantation	Type de cellules mères transfectées	Proteines transfectées	Type de Mutations	Résultats	Quantité d'agrégats cytosoplamique
WT	Plasmid PEGFc1 (i.e. plasmid codant le TAG EGFP)	Cellule humaine de reins (293T) exprimant TDP43 endogene (propre a la cellule)	TDP-43 sauvage (normale/non mutée)		TDP43 endogene + TDP43normale transfectée fusionnée a EGFP	+
GFP			Transfecter que proteine EGFP non accolée a la TDP-43		TDP43 endogene + EGFP	-
T			Cellule non tranfectée/ exprime que TDP-43 endogene		TDP43 endogene	-
CTF			TDP-43 mutee	suppression du 'NLS' domaine	TDP43 endogene + TDP43mutée transfectée fusionnée a EGFP	++++
331				Q331K dans le 'glycine-rich C-terminal' domaine	TDP43 endogene + TDP43mutée transfectée fusionnee a EGFP	+
298				G298S dans le 'glycine-rich C-terminal' domaine	TDP43 endogene + TDP43mutée transfectée fusionnee a EGFP	+
294				G294A dans le 'glycine-rich C-terminal' domaine	TDP43 endogene + TDP43mutée transfectée fusionnee a EGFP	+
D				Mutation NLS (78-84)	TDP43 endogene + TDP43mutée transfectée fusionnee a EGFP	++
DD				Double mutation NLS (78-84 et 187-192)	TDP43 endogene + TDP43mutée transfectée fusionnee a EGFP	+++
S-400	DOX OFF + NO TAG	Neuroblastomes (cellules neuronales) SHSY5Y	Cellule infectée (i.e. transduite) avec DOX/ exprime que TDP-43 endogene		Expriment la forme TDP43 normale endogène	-
S-wt	DOX ON + TAG HA		TDP-43 sauvage (normale/non mutée)		Expriment après induction et en plus de la forme endogène la forme WT avec un tag HA	++/+
S-D	DOX ON + TAG HA		TDP-43 mutee	Mutation NLS (78-84)	Expriment après induction et en plus de la forme endogène la forme δNLS avec un tag HA	++/+
S-298	DOX ON + TAG HA			G298S dans le 'glycine-rich C-terminal' domaine	Expriment après induction et en plus de la forme endogène la forme G298S mutation familiale avec un tag HA	++/+

Table 3 : Conditions de transplantation des échantillons de cellules humaines (neuroblastes et cellules de reins) analysées dans cette étude. Transplantation/transfection = injection d'ADN. Plasmide = molécule circulaire d'ADN dans laquelle est inséré le gène à transfecter (e.g. plasmide PEGFc1 = plasmide contenant le gène TDP43 fusionné a un gène codant pour une protéine permettant de mettre en évidence la TDP43 telle que l'EGFP (Green Fluorescent Portein). HA (Human influenza hemagglutinin) est une protéine permettant d'activer le virus DOX qui régule la doxiciclyne (DOX), une molécule contrôlant l'expression et l'activation de la TDP43 transfectée.

Les transplantations ont été réalisées par Pascal Leblanc (ENS Lyon) en milieu stérile au sein du Laboratoire de Biologie Moléculaire de la Cellule (LBMC). Brièvement, les cellules sont isolées et conservées dans un milieu de culture (DNEM (Gibco/invitrogen) contenant 10% de sérum bovin, de la glutamine, de la pénicilline et des antibiotiques (streptomycine). Un gène codant pour la protéine TDP-43 conforme ou mutée leur est ensuite transplanté via un plasmide contenant un tag (tag eGFP (enhanced green fluorescent protein) ou tag HA) qui permettra de localiser et vérifier que la protéine est bien exprimée dans la cellule.

II.2. Préparation des échantillons pour les analyses chimiques et isotopiques

II.2.1. Lyophilisation et mise en solution des échantillons

L'ensemble de la préparation et des analyses chimiques (mesures des concentrations et mesures isotopiques) ont été réalisé au laboratoire de géologie de Lyon à l'ENS. A l'exception des liquides céphalo-rachidiens, tous les échantillons analysés dans cette étude ont été lyophilisés avant d'être dissous. Ceci permet de reporter des concentrations en éléments traces et majeurs par unité de masse sèche.

II.2.1.a. Protocole de lyophilisation

La lyophilisation est une technique couramment utilisée en biologie permettant de réduire le volume d'échantillon, d'optimiser la conservation des tissus et des organes disséqués (l'eau facilitant la dégradation par hydrolyse) (Day, 2007) tout en préservant leurs activités protéiques et enzymatiques ainsi que le maintien et la stabilité de leur ARN (Acide RiboNucléique) (Wu et al., 2012).
Cette méthode consiste à congeler l'échantillon à -80ºC pendant une période minimale de 12 heures. L'échantillon est ensuite placé dans un lyophilisateur où il est sublimé (transformation de la glace en vapeur d'eau) dans des conditions de pression et température fixe (~ -60ºC, < 0.8 mbar) (Day, 2007) (Figure 6).

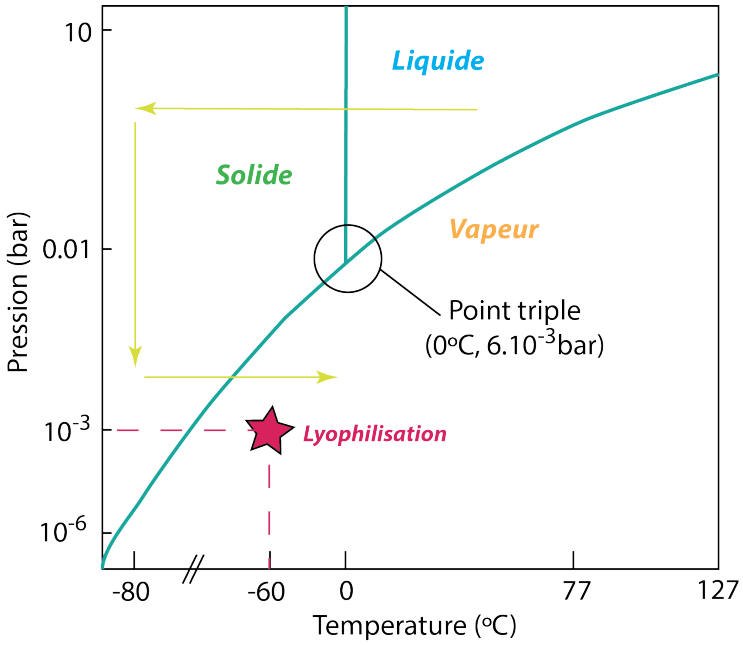

Figure 6 : Diagramme de phase montrant les étapes successives du processus de lyophilisation

Il est impératif de maintenir une pression inférieure à celle du point triple de l'eau (0ºC, 6.11 mbar) afin d'assurer la transformation direct de la glace en vapeur d'eau et d'éviter le réchauffement de l'échantillon pouvant entraîner son évaporation partielle et la perte de certaines substances volatiles.

Pour être complète, une lyophilisation doit durée au minimum 2 jours et 2 nuits pour des échantillons denses et compacts comme des organes. En deçà de cette période, des écarts de masses importants peuvent en effet être induits. Par exemple, dans le cas de foies de souris, ces écarts peuvent atteindre en moyenne 0.8 mg lorsque le temps de

lyophilisation varie entre 1 et 2 jours/nuits et plus de 45 mg si il est inférieur à 1jour et 1nuit (Figure 7). De telles différences peuvent alors engendrer des variations sur la concentration finale mesurée d'environ 4% si la différence de masse est de 0.8 mg et plus de 50% dans le cas extrême (écart de masse > 45 mg). A l'inverse, au delà de 2 jours et 2 nuits de lyophilisation, la masse reste inchangée (différence de masse < 0.1 mg *i.e.* précision de mesure sur la balance) (Figure 7).

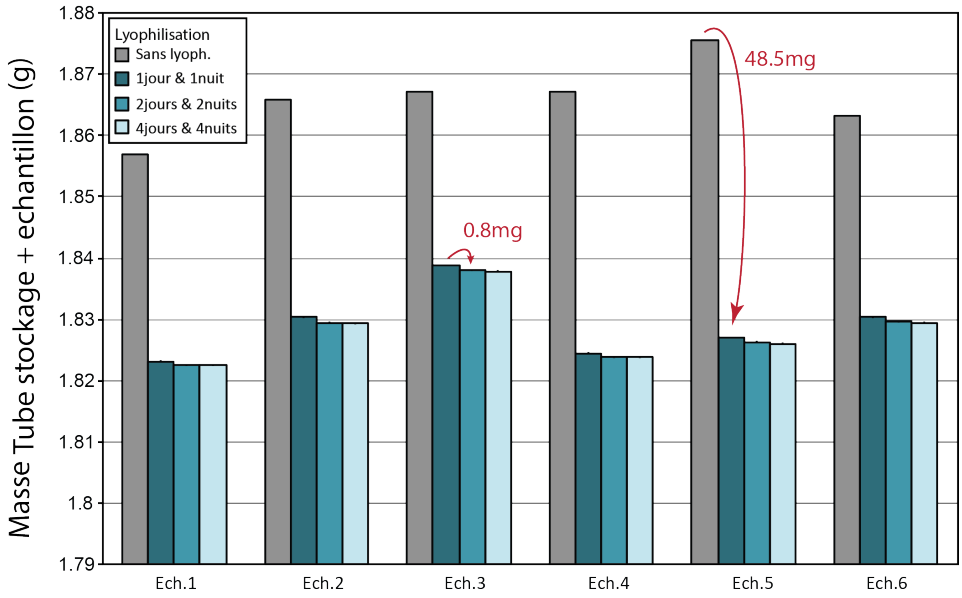

Figure 7 : Impact d'une lyophilisation incomplète sur la masse d'échantillon pesée. Les six échantillons testés sont des foies de souris.

II.2.1.b. Mise en solution des échantillons

La mise en solution est une étape cruciale à toute analyse chimique qui nécessite d'être totale, une dissolution incomplète pouvant engendrer un biais non négligeable dans les mesures de concentrations et de compositions isotopiques.

La première étape consiste à peser l'échantillon, préalablement déposé dans un bécher (Savillex®) propre d'une contenance moyenne de 15mL, à l'aide d'une balance de précision (0.1mg) en salle blanche (Figure 8a). Les masses pesées varient en fonction du type d'échantillon analysé et sont comprises entre ~10 mg pour les nématodes lyophilisés et ~2 g pour les liquides céphalo-rachidiens.

Une fois pesés, les échantillons sont attaqués avec 1 mL d'acide nitrique concentré ($\sim 15N, HNO_3^c$) + 200 µL d'eau oxygénée (H_2O_2) à 30% sous hottes à flux laminaire (Figure 8b). La dissolution s'effectue dans des béchers fermés sur une plaque chauffante à 90ºC pendant environ 12h (Figure 8c) en prenant soin de dégazer régulièrement pour éviter tout risque d'explosion ou de débordement, ce qui pourrait entrainer une perte d'échantillon.

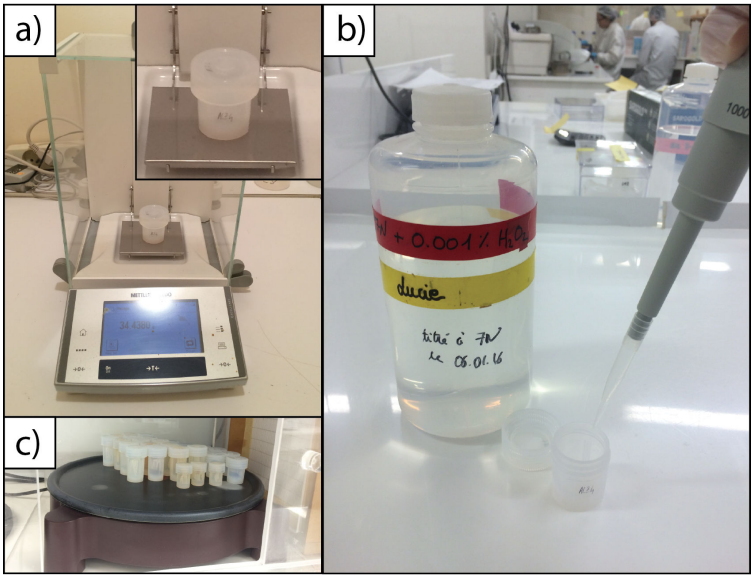

Figure 8 : a) Pesée des échantillons en salle blanche à l'aide une balance de précision, b) Etape de dissolution et reprise dans les acides adéquates (mélange HNO_3/H_2O_2 pour les attaques et HCl/H_2O_2 pour les reprises), c) Evaporation sur plaque chauffante à environ 130ºC sous hotte aspirante

Il arrive parfois qu'une seule attaque ne soit pas suffisante pour dissoudre totalement l'échantillon. Dans ce cas, une deuxième attaque, et si besoin un passage aux ultra-violets (UVs) pendant 4/5 heures pour détruire le reste de matière organique, est réalisé. Une fois la dissolution complète (*i.e.* solutions limpides et transparentes), les échantillons sont évaporés à 100ºC sur plaque chauffante sous hotte aspirante. Cette étape permet d'obtenir un résidu sec qui sera repris dans un volume défini d'HNO_3 0,5N. Afin de s'assurer d'une reprise totale des échantillons, les béchers sont passés dans un bain à ultrasons pendant environ 30 minutes. Un aliquot sera ensuite prélevé pour mesurer les concentrations en éléments traces et majeurs et le volume restant sera dédié à la mesure des compostions isotopiques en Cu et en Zn.

II.2.2. Séparation par chromatographie ionique

La séparation et la purification des échantillons sont deux étapes nécessaires si l'on souhaite mesurer avec précision les compositions isotopiques sur un spectromètre de masse à source plasma et à multi-collection (MC-ICP-MS). La non séparation des éléments chimiques pourrait engendrer des interférences isobariques (interférences entre deux éléments chimiques ayant le même nombre de masse ; tel que ^{64}Zn avec ^{64}Ni) ainsi que des effets de matrices et de doubles charges non négligeables affectant la précision et la justesse de mesure des rapports isotopiques en Cu et Zn.

Afin d'éviter toute contamination exogène par le milieu extérieur et/ou entre les échantillons,

plusieurs précautions sont prises pendant les étapes de séparation et purification. Toute la chimie est réalisée dans une salle blanche à air confiné sous des hottes à flux laminaire pour les élutions et sous des hottes aspirantes à reflux pour les phases d'évaporation. Par ailleurs, tous les acides utilisés sont doublement distillés et l'eau déionisée utilisée pour les phases d'élution et de lavage est de qualité ultra-pure (18.2 MΩ.cm). Enfin, le port de gants de protection est limité à ceux en matière vinyle uniquement; ces derniers ayant le plus faible potentiel de contamination (Garçon et al.(2017) ; voir ci-dessous).

II.2.2.a. Principe de la chromatographie ionique

La chromatographie ionique en phase liquide, appelée aussi chromatographie sur colonnes échangeuses d'ions, est une méthode qui permet la séparation de divers composants ioniques présents dans une même solution. La séparation dépend de l'affinité des ions envers une phase stationnaire, communément appelée résine et une phase mobile, appelée éluant. Les ions ayant des coefficients de partage élevés entre l'éluant et la résine (Kd > 1; forte affinité) vont migrer pus lentement que ceux ayant des coefficients de partage faible (Kd < 1; faible affinité). Par exemple, dans le cas d'une résine anionique avec comme éluant de l'acide chlorhydrique (HCl) fortement concentré (> 7N), le fer et le zinc seront retenus sur la colonne (Kd > 1) à l'inverse du Cu et de la majorité des éléments majeurs (Ca, Na, Mg ; Kd < 1) qui seront rapidement élués (Faris et al., 1964) (Figure 9a). Le zinc peut être élué et récupéré en présence d'acide nitrique (HNO_3) comme la plupart des autres éléments chimiques (Kraus and Nelson, 1958) (Figure 9b).

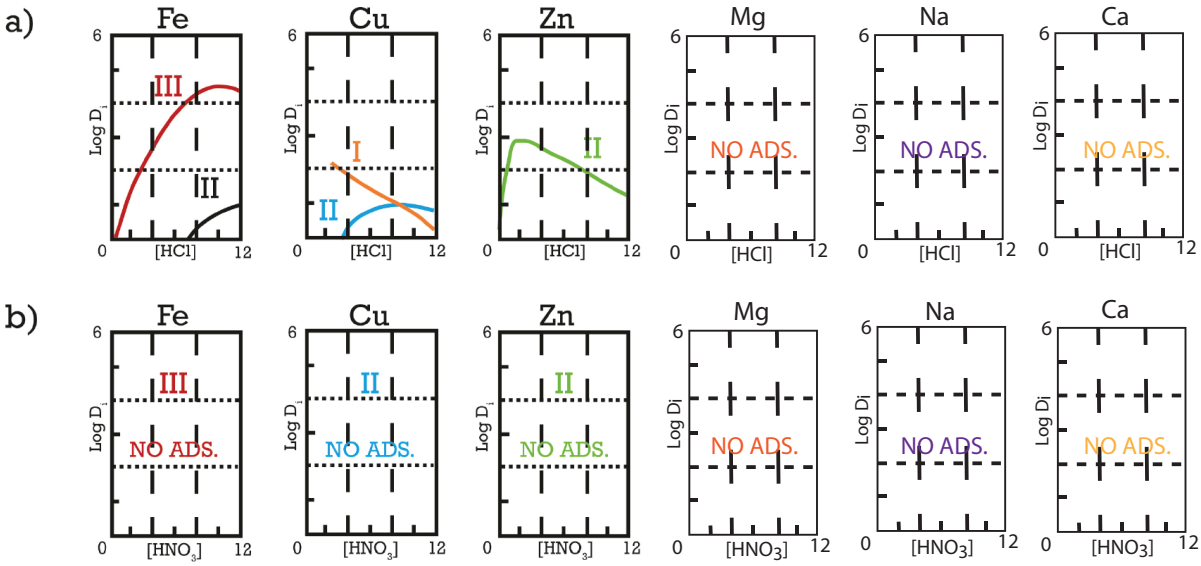

Figure 9 : Comportement des éléments chimiques sur résine anionique (AG MP-1) élué avec a) de l'acide chlorhydrique (HCl) et b) de l'acide nitrique (HNO_3) modifié d'après Faris et al.(1964) *et Kraus and Nelson* (1958) *respectivement. Log D_i correspond au coefficient de partage des éléments envers la phase stationnaire (résine).*

L'affinité d'un ion à l'égard de la résine, et donc sa vitesse de migration, dépend de plusieurs paramètres tels que: sa nature, le milieu d'introduction (acide ou basique), sa concentration en solution, le volume de résine, son degré d'oxydation mais aussi le degré de polymérisation, le maillage (taille des grains ou mesh) et le taux de réticulation (noté x.) de la résine (un taux de réticulation faible correspond à une structure plus perméable aux grosses molécules qu'un taux de réticulation élevé, mieux adapté à la séparation des ions). En général, les résines utilisées sont des groupements de polymères organiques de styrènes et divinylbenzènes électriquement neutres. Ces polymères (macromolécules) forment des réseaux tridimensionnels possédant à leur surface des groupements fonctionnels tels que NH_3^+ pour les résines anioniques et SO_3^{2-} pour les cationiques. Des contres-ions, fixés à ces groupements fonctionnels (comme l'ion Cl^- dans le cas des résines anioniques) assurent la neutralité de la résine et seront échangés avec les ions présents dans l'échantillon.

Dans cette étude, les résines utilisées sont des résines anioniques en forme chlorure Biorad AG MP-1 (100-200 mesh) ayant un maillage compris entre 150 et 75 µm. La retenue des éléments chimiques sur la phase stationnaire résulte de l'échange entre des chloro-complexes (formé par l'association des ions Cu^{2+} et Zn^{2+} oxydés avec les ions Cl^- de l'acide chlorhydrique dans lequel sont repris les échantillons) et des contre ions Cl^- rattachés aux groupements fonctionnels de la résine (Maréchal and Albarede, 2002).

II.2.2.b. Isolation et purification du Cu et du Zn sur colonnes échangeuses d'ions

La procédure de séparation et de purification du Cu et du Zn sur colonnes échangeuses d'ions est basée sur les techniques précédemment développées et décrites par Maréchal et al. (1999) et Maréchal and Albarède (2002).

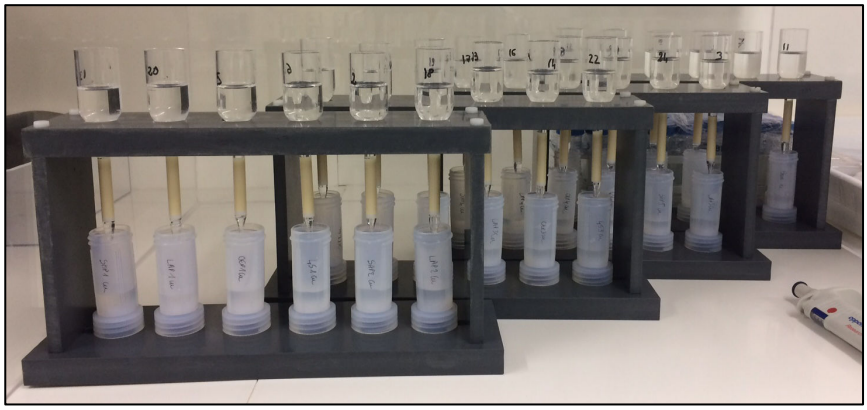

Figure 10 : Colonnes en quartz contenant 1,8 mL de résine anionique AG MP-1 (100-200 mesh) sous forme chlorure utilisée pour la séparation et la purification du Cu et du Zn

Dans un premier temps, des colonnes en quartz, ayant préalablement été remplies avec 1,8 mL de résine anionique AG MP-1 (100-200 mesh) en forme chlorure (Figure 10) et lavées par une série de 3 lavages alternant HNO_3 0.5N et eau distillée, sont décompactées.

S'en suit l'élution du Cu et du Zn dont la totalité du protocole analytique est détaillé dans la Figure 11. Brièvement, après avoir conditionné les colonnes en HCl 7N + 0.001% H_2O_2, l'échantillon, préalablement repris dans 1mL d'HCl 7N + 0,001% H_2O_2, est chargé sur la résine. La charge matricielle est premièrement éluée avec 10mL d'HCl 7N + 0,001% H_2O_2, suivie par le Cu récupéré avec 20mL de la même solution puis le Zn récupéré avec 10mL d'HNO_3 0,5N (Figure 11). Les deux fractions purifiées de Cu et de Zn sont donc collectées tour à tour dans deux béchers savillex® distincts puis évaporées avant d'être repris à nouveau dans 1 mL d' HCl 7N + 0,001% H_2O_2 et ultrasonnées.

Protocole de séparation du Cu et Zn

Etape	Eluant	Volume (mL)
Remoblisation de la résine	H_2O	~10
Lavage	HNO_3 0.5N	7 (1+6)
	H_2O	3
	HNO_3 0.5N	7 (1+6)
	H_2O	3
	HNO_3 0.5N	7 (1+6)
	H_2O	3
Conditionnement	7N HCl + 0.001% H_2O_2	7 (1+1+5)
Chargement échantillon	7N HCl + 0.001% H_2O_2	1
Elution de la matrice	7N HCl + 0.001% H_2O_2	10 (1+1+8)
Elution du Cu	7N HCl + 0.001% H_2O_2	20 (1+1+18)
Elution du Fe	2N HCl + 0.001% H_2O_2	10 (1+1+8)
Elution du Zn	HNO_3 0.5N	10 (1+1+8)
Lavage	H_2O	~10
	HNO_3 0.5N	~10

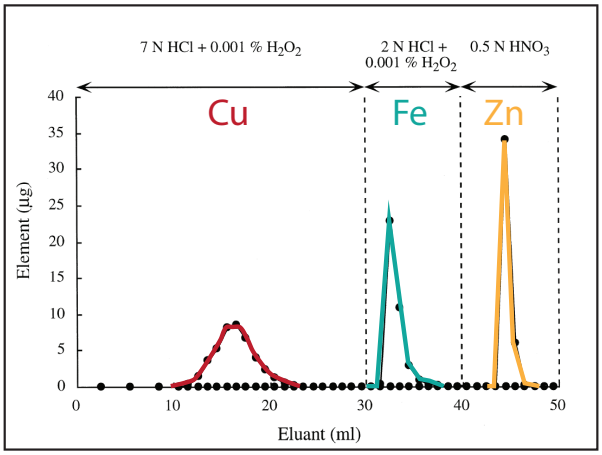

Figure 11 : Protocole de séparation et profil d'élution du Cu et Zn sur résine AG MP-1 100-200 Mesh modifié d'après Maréchal et al.(1999)

Une fois isolées, les fractions de Cu et de Zn doivent être davantage purifiées pour s'assurer qu'aucune trace d'éléments potentiellement interférents (comme le nickel, Ni) ne soit encore présents. Le protocole de purification réside simplement dans la répétition du protocole précédent (Figure 11) à trois exceptions près: (1) lors de la purification du Cu, la phase de lavage terminale est avancée directement après l'élution du Cu, (2) dans la purification du Zn, les phases d'élution du Cu et du Fe sont regroupées et éluées simultanément avec 10 mL d'HCl 2N + 0.001% H_2O_2 et (3) pour les deux purifications, une fois les résidus chargés sur colonne, les béchers de purification sont lavés avec ~1mL d'HCl 7N à 100ºC pendant environ 30 minutes puis rincés à l'eau distillée avant d'être réutilisés pour collecter les fractions de Cu et Zn. Cette étape permet d'éliminer les traces résiduelles de charge matricielle et donc d'optimiser la qualité de la purification.

Pour le Zn, un autre protocole a également été élaboré par Moynier et al.(2006). Cependant, dans cette méthode, de l'acide bromique (HBr) est utilisé pour conditionner la résine et éluer la charge matricielle, deux étapes précédant l'élution du Zn. L'HBr étant un acide moins propre que l'HCl 7N ultra-pure doublement distillé utilisé dans le protocole détaillé précédemment et analysant des échantillons très faiblement concentrés comme les liquides céphalorachidiens (LCR) ayant par conséquent un potentiel de contamination élevé, j'ai préféré ne pas utiliser la chimie en HBr pour minimiser le risque de contamination exogène.

II.3. Analyses chimiques

Après dissolution complète, l'échantillon est séparé en deux fractions distinctes: la première est utilisée pour mesurer les concentrations en éléments traces et majeurs tandis que la deuxième est consacrée à la mesure des compositions isotopiques en Cu et en Zn. Toutes les étapes de la procédure analytique suivie dans cette étude sont résumées dans la Figure 12.

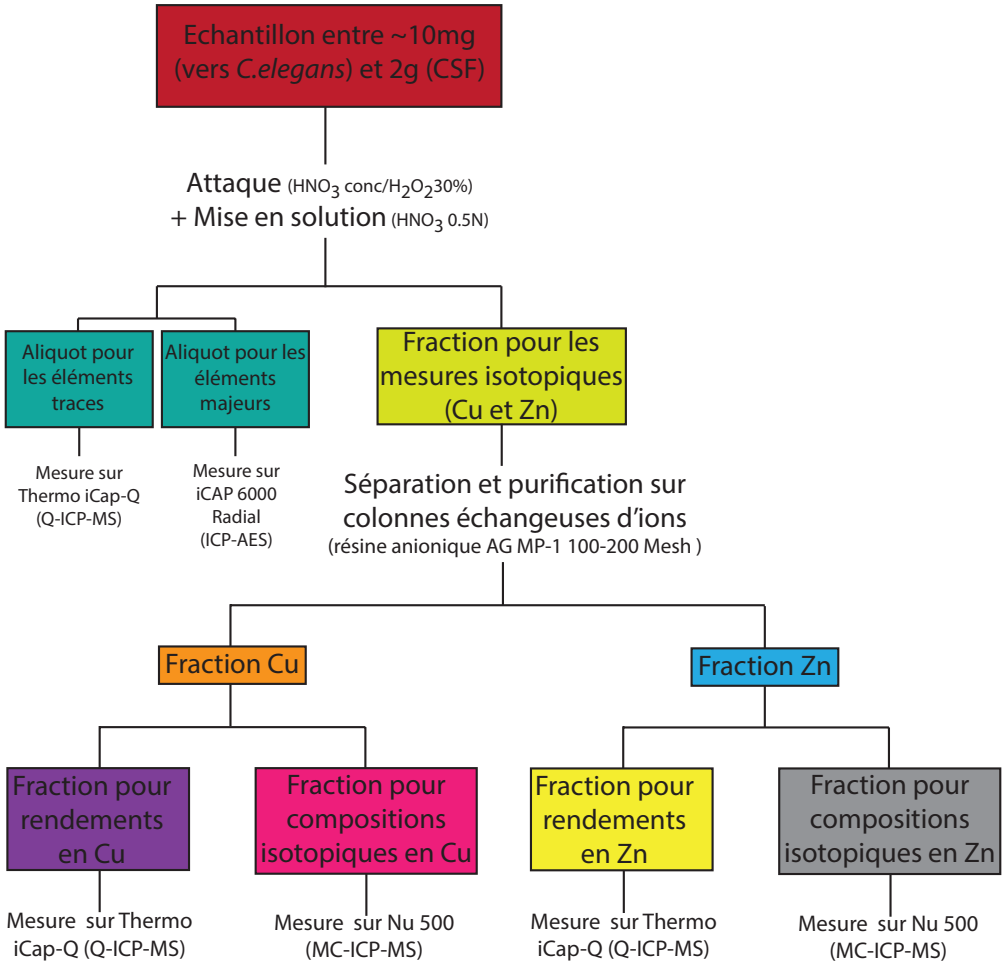

Figure 12: Organigramme résumant les étapes successives de la procédure analytique suivie pour mesurer les concentrations en éléments traces et majeurs, les rendements après chimie sur colonnes échangeuses d'ions et les compositions isotopiques en Cu et en Zn

II.3.1. Mesure des éléments traces et majeurs

II.3.1.a. Principe de la spectrométrie de masse à quadripôle et à émission optique

Les concentrations en éléments majeurs (Ca, K, Na, P, S, Fe et Mg) et en traces (~33 éléments) sont mesurées par un spectromètre à émission optique (ICP-AES, iCap 6000 Radial) et un spectromètre de masse à quadripôle (Q-ICP-MS) Thermo iCap-Q respectivement au sein du laboratoire de géologie de Lyon (Figure 13).

Figure 13 : Spectromètre à émission optique et à ionisation plasma (ICP-AES, iCap 6000 Radial) et spectromètre de masse à quadripôle (Q-ICP-MS, Thermo iCap-Q) *du laboratoire de géologie de Lyon*

De façon générale, l'analyse par spectrométrie se décompose en trois grandes étapes qui sont : 1) L'ionisation de l'échantillon, 2) la séparation des ions selon leur rapport masse/charge (m/z) ou selon leur énergie de désexcitation et 3) leur détection.

1) Ionisation de l'échantillon :

L'échantillon en phase liquide (dilué dans une solution d'HNO_3 0,5N) est introduit dans une chambre de nébulisation grâce à une pompe péristaltique ou il est nébulisé (*i.e.* transformé

en aérosol). Il est ensuite acheminé par un flux de gaz inerte (Argon) vers une torche à plasma où il est ionisé suite à son interaction avec un plasma d'argon (gaz inerte électriquement neutre formé par l'interaction d'un champ magnétique sur les particules initialement présentes dans le gaz d'argon). En général, la température du plasma se situe entre 6000 et 10 000 K d'ou la nécessité d'introduire un second gaz, également de l'argon qui va permettre de diminuer la température du système (cooling gas).

2) Système de séparation

Dans le cas des ICP-AES, ce n'est pas le faisceau ionique qui est directement mesuré mais l'énergie produite par l'excitation thermique des atomes ionisés. En retournant à leur état fondamental, les ions émettent des photons dont l'énergie est caractéristique d'un élément donné. La séparation des photons se fait à travers un réseau de diffraction (système de dispersion croisée).

Dans le cas des Q-ICP-MS, l'analyseur utilisé est un quadripôle. Le faisceau ionique passe à travers un ensemble de quatre électrodes soumises à des tensions continues et alternatives appelées quadripôles permettant la séparation des ions en fonction de leur rapport masse/charge (m/z).

3) Système de détection

Dans le cas de la spectrométrie à émission optique, les photons sont collectés grâce à des capteurs photos fixes utilisant un dispositif à transfert de charges (CCD ; Charge Couple Device).

Pour les spectromètres à quadripôles, après leur séparation les ions sont accélérés, focalisés et détectés sur des collecteurs fixes grâce à des multiplicateurs d'électrons (SEM Secondary Electron Multiplicator).

Il est important de noter que les modes de séparation et de détection employés dans les Q-ICP-MS sont eh général plus précis que ceux des ICP-AES. Un spectromètre à quadripôle permet de mesurer des concentrations variant entre 0.02 et 200 µg/L selon les éléments avec une gamme optimale comprise entre 1 et 30 µg/L. A l'inverse, la méthode optique présente des limites du fait de la proximité de certaines raies lumineuses (photons d'énergies proches). Elle permet donc de détecter des éléments dont la concentration en solution s'élève jusqu'à plusieurs mg/L avec un seuil de détection variable pour chaque élément chimique pouvant descendre par exemple jusqu'à 1 µg/L pour le magnésium (Mg) et seulement 20 µg/L pour le calcium (Ca).

II.3.1.b. Mesure et calcul des concentrations

Après leur dissolution, les échantillons sont repris dans un volume prédéfini d'HNO_3 0,5 N. Notons que plus ce volume est grand, plus la probabilité d'avoir des éléments non repris en solution est faible. C'est pourquoi il n'est, en moyenne, jamais inferieur à 5 mL. Deux aliquots de cette solution mère sont ensuite prélevés pour former des solutions « filles ». Le premier aliquot est dilué dans une solution d'HNO_3 0,5N + Indium (In) à 2µg/L et servira à estimer les concentrations en éléments traces. Le second est dilué dans une solution d'HNO_3 0,5N + Scandium (Sc) à 10 mg/L et sera quant à lui utiliser pour mesurer les concentrations en éléments majeurs. Le Sc et l'In sont ajoutés à titre d'étalons internes et servent à corriger de la dérive instrumentale au cours du temps ainsi que des effets de matrices pour les éléments majeurs et traces respectivement.

La procédure d'analyse complète des concentrations en éléments majeurs et traces repose sur l'analyse :

(1) de solutions étalons (*i.e.* des solutions de concentrations connues) variant entre 0 et 25-100 mg/L pour les éléments majeurs et entre 0 et 50-200 µg/L pour les éléments traces. Ces solutions permettent d'obtenir des droites de calibrations nécessaires aux calculs des concentrations et sont préparées le jour même à partir de solutions concentrées mono-élémentaire dans le cas des éléments majeurs et multi-élémentaires (SP33MS) dans le cas des éléments traces.
(2) des solutions filles (*i.e.* les échantillons),
(3) de blancs de chimie et/ou d'attaque (~1 blanc respectif par série d'échantillons) pour corriger d'une éventuelle contamination externe,
(4) de contrôles (*i.e.* solution étalon mesurée en début de séquence et remesurés en cours de séquence) pour contrôler l'éventuelle dérive de l'appareil de mesure dans le temps,
(5) des échantillons dupliqués, « dup » (*i.e.* mêmes échantillons issus de deux attaques différentes) et répliqués « bis » (*i.e.* mêmes solutions mesurées deux fois à intervalle de temps espacé) pour valider la procédure analytique et contrôler la dérive instrumentale,
(6) des standards biologiques maisons « in-house » et internationaux (*i.e.* certifiés) pour évaluer la qualité des données, c'est à dire contrôler la justesse (*i.e.* capacité à reproduire des valeurs certifiées de façon fiable) et la précision (*i.e.* variabilité entre plusieurs mesures d'une même solution) des données acquises.

Les concentrations finales sont calculées à partir des concentrations obtenues dans les solutions filles en prenant en compte leurs facteurs de dilutions. Pour les éléments traces, des interférences de masses peuvent se créer suite à la formation d'oxyde et/ou d'espèces poly-atomiques et ainsi biaiser les mesures. Ces interférences sont donc

contrôlées par la mesure simultanée du taux d'oxyde (rapport Ce/CeO i.e. métal/oxyde <2%) et par l'emploi d'une cellule de collision (gaz hélium). Le nombre de coups bruts obtenus sur le blanc d'attaque est également soustrait à celui obtenu pour l'échantillon afin de corriger de l'effet de contamination externe, mais cette correction est généralement négligeable.

Lorsque les quantités de Cu et Zn présentes dans l'échantillon sont suffisantes, les concentrations en Cu et en Zn sont mesurées avant et après la séparation des éléments par chromatographie sur colonnes échangeuses d'ions. Cela permet d'évaluer et de contrôler les rendements après chimie; autrement dit, de quantifier l'éventuelle perte de matière sur la résine pouvant être associée à des fractionnements isotopiques importants (Maréchal and Albarede, 2002). Un rendement de 100% est requis pour garantir des mesures isotopiques fiables. Pour cela, un aliquot (~3%) est prélevé après chimie dans les fractions purifiés reprises en HNO_3 0.5N puis dilué dans un volume final de 2mL d'HNO_3 0,5N + 2ppb d'In.

II.3.2. Les compositions isotopiques en Cu et Zn

L'ensemble des mesures isotopiques en Cu et Zn a été réalisé sur un spectromètre de masse à multi-collection et à source plasma (MC-ICP-MS ; Nu 500) au sein du laboratoire de géologie de Lyon de l'ENS (Figure 14).

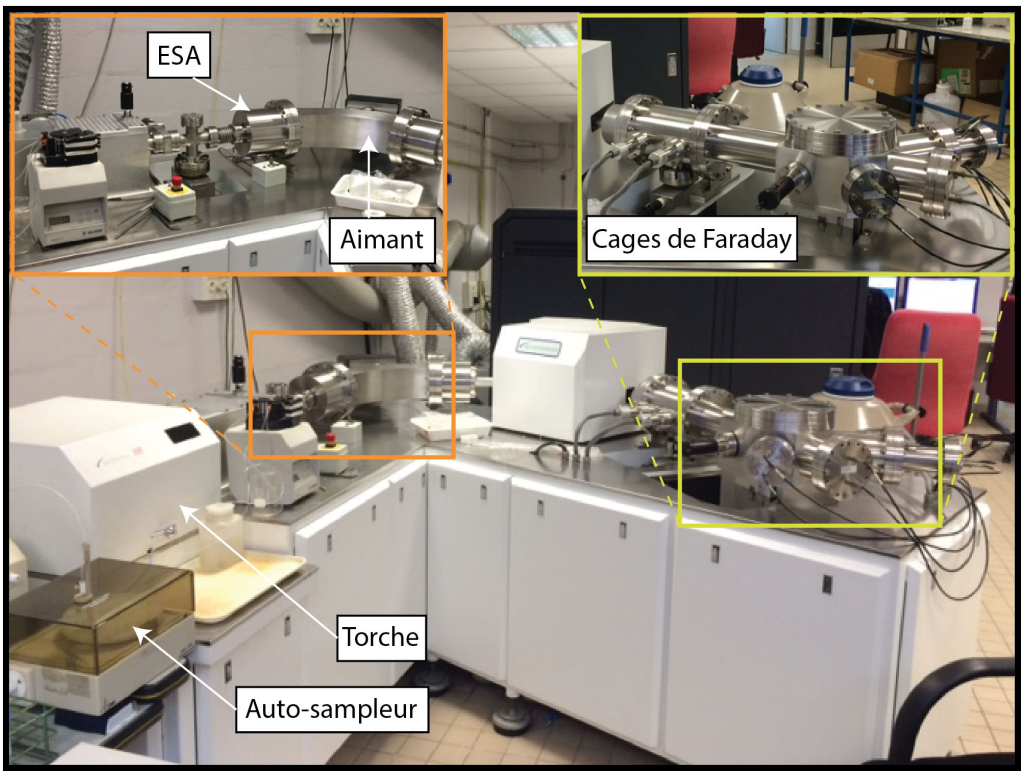

Figure 14 : Spectromètre de masse à multi-collection et à source plasma (MC-ICP-MS ; Nu 500) du laboratoire de géologie de Lyon (ENS)

II.3.2.a. Principe de la spectrométrie de masse à multi-collection et à source plasma

La spectrométrie de masse à multi-collection et à source plasma (MC-ICP-MS) repose sur les mêmes principes que la spectrométrie de masse par quadripôle (Q-ICP-MS) détaillée précédemment à savoir : (1) l'introduction de l'échantillon en phase liquide qui se fait en aspiration libre et avec un débit d'aspiration moyen de ~100 µL/min, (2) sa nébulisation et son ionisation au niveau de la torche à plasma, et (3) la séparation et la détection de ses ions en fonction de leur masse. Les seules différences avec la spectrométrie de masse par quadripôle résident dans cette dernière étape. Sur les MC-ICP-MS, les ions sont séparés au sein d'un secteur électrostatique (ESA ; ElectroStatic Analyser) puis d'un secteur magnétique (aimant) (Figure 14). Dans le secteur électrostatique, les ions sont différenciés en fonction de leur énergie cinétique (le rayon de trajectoire est proportionnel à l'énergie cinétique d'un élément donné) puis triés par leur rapport masse/charge (m/z) à travers le secteur magnétique (par effet d'inertie, les isotopes lourds sont moins déviés que les légers). Les ions sont ensuite collectés via un ensemble de cages de Faraday fixes. Ce type de détecteur est plus précis que celui utilisé dans les spectromètres à quadripôle (collecteur fixe + multiplicateurs d'électrons) mais s'avèrent être parfois moins sensibles. Dans cette étude, une mesure consiste, en général, en 1 cycle de 30 mesures de 10 secondes chacune; chaque mesure étant encadrée par deux phases de lavage successives d'environ 200 secondes (Wash Time) en HNO_3 0,5N puis HNO_3 0,05N.

II.3.2.b. Mesure des rapports isotopiques en Cu ($\delta^{65}Cu$) et en Zn ($\delta^{66}Zn$)

Une fois purifiées, les fractions de Cu et de Zn sont reprises dans des solutions d'acide nitrique très faiblement concentrées (HNO_3 0,05N) préalablement dopées en Zn (standard Zn JMC 3-0749L) pour les fractions de Cu, ou en Cu (standard Cu NIST SRM 976) pour les fractions de Zn; le Cu étant utilisé comme un standard interne pour corriger le fractionnement instrumental de masse dans les fractions de Zn et inversement (voir ci-dessous). Afin d'éviter un biais significatif des ratios isotopiques mesurés, il est impératif de vérifier trois conditions : (1) la mesure des compositions isotopiques doit se faire avec un plasma humide pour éviter le biais isotopique généré par un système de désolvatation (DSN), (2) la normalité des solutions de reprise des échantillons et des standards doit être identique; une différence de normalité ≥ 20% peut en effet engendrer des variations ≥ 0.1‰ pour $\delta^{66}Zn$ (Chen et al., 2016) et (3) les quantités de standard ajouté et de l'élément mesuré doivent être proche car un écart de concentrations trop important (*i.e.* $[Conc]_{ech}/[Conc]_{std} < 0.5$) peut

également entrainer des variations isotopiques pouvant avoisiner les 0.2‰ (Chen et al., 2016). En règle générale, une mesure isotopique optimale est obtenue lorsque la concentration dans l'échantillon est comprise entre 150 et 300 ppb et que le volume de solution avoisine les 0,7 mL (*i.e.* volume minimal de reprise en session automatique). Un certain nombre de corrections sont ensuite nécessaires pour obtenir des compositions isotopiques robustes. Ces corrections sont liées principalement à 1) la dérive instrumentale, 2) au fractionnement de masse instrumental, et 3) aux interférences isobariques. L'ensemble de ces corrections est détaillé ci-dessous :

1) Correction de la dérive instrumentale : méthode de « standard-bracketing »

Au cours du temps, il est fréquent d'observer une dérive des mesures reliée à l'instabilité temporelle du spectromètre de masse. Pour s'en affranchir, des standards de compositions isotopiques connus (Zn JMC 3-0749L, Johnson Matthey Royston, UK et Cu SRM 976, National Institute of Standards and Technology, Bethesda, MD, USA) sont analysés tous les deux échantillons, une méthode communément connue sous le nom de « standard-bracketing ». Les compositions isotopiques sont alors définies comme le rapport isotopique mesuré dans l'échantillon ($^{65}Cu/^{63}Cu$ ou $^{66}Zn/^{64}Zn$) normalisé par le barycentre des rapports isotopiques des deux standards le bracketant. Par exemple, dans le cas ou deux échantillons sont bracketés par deux standards (std 1 et std 2), les compositions isotopiques en Zn et en Cu du premier échantillon s'écriront :

$$\delta^{66}Zn_{sample} = \left[\frac{\left({}^{66}Zn/{}_{64}Zn\right)_{sample}}{\frac{1}{3}*\left({}^{66}Zn/{}_{64}Zn\right)_{std2} + \frac{2}{3}*\left({}^{66}Zn/{}_{64}Zn\right)_{std1}} - 1 \right] * 1000 \text{ in } ‰$$

$$\delta^{65}Cu_{sample} = \left[\frac{\left({}^{65}Cu/{}_{63}Cu\right)_{sample}}{\frac{1}{3}*\left({}^{65}Cu/{}_{63}Cu\right)_{std2} + \frac{2}{3}*\left({}^{65}Cu/{}_{63}Cu\right)_{std1}} - 1 \right] * 1000 \text{ in } ‰$$

2) Correction du fractionnement de masse instrumental

Au sein du plasma, les isotopes légers sont plus facilement déviés de l'axe optique que les isotopes lourds, ce qui entraine des fractionnements isotopiques variables. Une manière de corriger ce fractionnement est d'ajouter un standard (*i.e.* spike) de composition isotopique connue dans l'échantillon. Pour une efficacité optimale, il est primordial que l'élément chimique composant le spike soit différent de celui mesuré dans l'échantillon, de masse

proche, qu'il ne possède pas d'isotopes risquant d'interagir avec ceux de l'élément d'intérêt et qu'il possède au moins deux isotopes stables. Pour les mesures isotopiques en cuivre, on utilise généralement un spike de zinc (Zn JMC 3-0749L, Johnson Matthey Royston, UK) et inversement, un spike de cuivre (Cu SRM 976, National Institute of Standards and Technology, Bethesda, MD, USA) pour les mesures isotopiques de zinc.

La méthode de correction est basée sur les techniques décrites par Maréchal et al.(1999). Brièvement, elle repose sur le fait que les rapports isotopiques et les coefficients de fractionnement (***f***) du cuivre et du zinc ne sont pas indépendants l'un de l'autre mais sont reliés par des lois de fractionnements exponentielles selon les équations détaillées ci-dessous :

$$\left(\frac{^{65}Cu}{^{63}Cu}\right)_{réel} = \left(\frac{^{65}Cu}{^{63}Cu}\right)_{mesuré} * \left(\frac{M_{65_{Cu}}}{M_{63_{Cu}}}\right)^{f_{Cu}} \qquad (\text{Eq. 1})$$

$$\left(\frac{^{66}Zn}{^{64}Zn}\right)_{réel} = \left(\frac{^{66}Zn}{^{64}Zn}\right)_{mesuré} * \left(\frac{M_{66_{Zn}}}{M_{64_{Zn}}}\right)^{f_{Zn}} \qquad (\text{Eq. 2})$$

En combinant (Eq.1) et (Eq.2), on obtient :

$$f_{Cu}/f_{Zn} = \frac{\ln\left(\frac{^{65}Cu}{^{63}Cu}\right)_{réel} - \ln\left(\frac{^{65}Cu}{^{63}Cu}\right)_{mesuré}}{\ln\left(\frac{M_{65_{Cu}}}{M_{63_{Cu}}}\right)} \Bigg/ \frac{\ln\left(\frac{^{66}Zn}{^{64}Zn}\right)_{réel} - \ln\left(\frac{^{66}Zn}{^{64}Zn}\right)_{mesuré}}{\ln\left(\frac{M_{66_{Zn}}}{M_{64_{Zn}}}\right)}$$

ou encore,

$$\ln\left(\frac{^{65}Cu}{^{63}Cu}\right)_{mesuré} = \ln\left(\frac{^{65}Cu}{^{63}Cu}\right)_{réel} + \frac{f_{Cu}}{f_{Zn}} * \frac{\ln\left(\frac{M_{65_{Cu}}}{M_{63_{Cu}}}\right)}{\ln\left(\frac{M_{66_{Zn}}}{M_{64_{Zn}}}\right)} * \left[\ln\left(\frac{^{66}Zn}{^{64}Zn}\right)_{mesuré} - \ln\left(\frac{^{66}Zn}{^{64}Zn}\right)_{réel}\right] (\text{Eq. 4})$$

Cette équation est de la forme y = a*x + b avec a = $\frac{f_{Cu}}{f_{Zn}} * \frac{\ln\left(\frac{M_{65_{Cu}}}{M_{63_{Cu}}}\right)}{\ln\left(\frac{M_{66_{Zn}}}{M_{64_{Zn}}}\right)}$

b = $\ln\left(\frac{^{65}Cu}{^{63}Cu}\right)_{réel} - a * \ln\left(\frac{^{66}Zn}{^{64}Zn}\right)_{réel}$; y = $\ln\left(\frac{^{65}Cu}{^{63}Cu}\right)_{mesuré}$ et x = $\ln\left(\frac{^{66}Zn}{^{64}Zn}\right)_{mesuré}$

Ainsi, en mesurant simultanément les rapports isotopiques en Cu et en Zn, il est possible de quantifier précisément la pente ('a') de ces droites afin d'obtenir la relation existant entre le facteur de fractionnement du Cu et celui du Zn. Dans le cas d'une mesure isotopique en cuivre, le rapport corrigé sera ainsi calculé par :

$$\left(\frac{^{65}Cu}{^{63}Cu}\right)_{réel} = \left(\frac{^{65}Cu}{^{63}Cu}\right)_{mesuré} * \left(\frac{M_{^{65}Cu}}{M_{^{63}Cu}}\right)^{f_{Cu}} \text{ avec } f_{Cu} = f_{Zn} * \frac{a}{\ln\left(\frac{M_{^{65}Cu}}{M_{^{63}Cu}}\right)/\ln\left(\frac{M_{^{66}Zn}}{M_{^{64}Zn}}\right)}$$

Les différentes analyses de standards que j'ai réalisées au cours de ma thèse montrent que $\frac{f_{Cu}}{f_{Zn}}$ est constant quelque soit la séquence de mesures et/ou la configuration de l'appareil (Figure 15). En utilisant la pente des droites (Figure 15), nous avons estimé que le rapport f_{Cu}/f_{Zn} variait entre $0.95 < \frac{f_{Cu}}{f_{Zn}} < 1.09$ (*i.e.* $1.1097 < a < 0.9677$, Figure 15), ce qui montre que le fractionnement du cuivre est très proche de celui du zinc et que nous pouvons faire l'approximation que $f_{Cu} = f_{Zn}$. Un calcul de propagation d'erreurs montre que cette approximation engendre une erreur maximale de ±0.05 ‰ et ±0.02 ‰ pour les rapports isotopiques en Cu et en Zn respectivement. Ces erreurs sont inférieures à la reproductibilité externe à long terme estimé sur nos standards (0.09‰ pour $\delta^{65}Cu$ (n=351) et 0.07‰ pour $\delta^{66}Zn$ (n=481), 2sd).

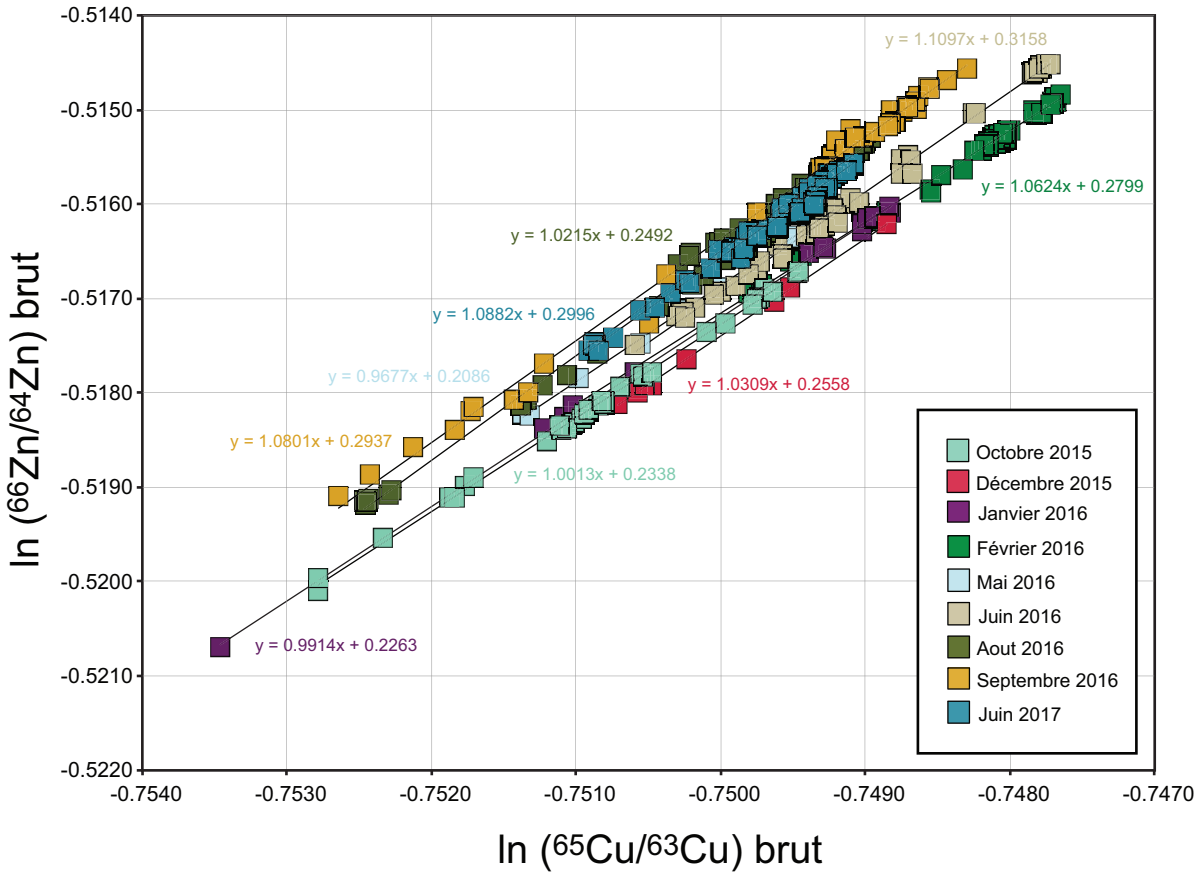

Figure 15 : Rapports isotopiques 'bruts' (i.e. non corrigés) en cuivre et en zinc simultanément mesurés dans les standards encadrant les échantillons pendant des périodes définies de ma thèse. Chaque couleur représente une séquence de mesure.

3) Interférences isobariques

On parle d'interférences isobariques lorsque deux éléments chimiques différents mais de même masse (isobares) sont mesurés simultanément sur le même détecteur. Le signal obtenu correspond alors à la somme de deux signaux. Par exemple, si nous mesurons un échantillon dans lequel se trouve du Ti, V et Cr (trois isobares de la masse 50 ; ^{50}Ti, ^{50}V et ^{50}Cr) (Figure 16), le collecteur dédié à la masse 50 comptabilisera la somme de ces 3 éléments et ne pourra pas faire de distinction.

	49	50	51	52	53	54	55	56	57	58	59	60	61	62	63	64	
Ti	5.41	5.18															Ti
V		0.250	99.75														V
Cr		4.345		83.79	9.501	2.365											Cr
Mn							100										Mn
Fe						5.845		91.75	2.119	0.282							Fe
Co											100						Co
Ni										68.08		26.22	1.140	3.634		0.926	Ni
Cu															69.17		Cu
Zn																48.63	Zn
	65	66	67	68	69	70	71	72	73	74	75	76	77	78	79	80	
Cu	30.83																Cu
Zn		27.90	4.10	18.75		0.62											Zn
Ga					60.11		39.89										Ga
Ge						20.84		27.54	7.73	36.28		7.61					Ge
As											100						As
Se										0.89		9.37	7.63	23.77		49.61	Se
Br															50.69		Br
Kr														0.35		2.28	Kr

Figure 16 : Tableau des abondances relatives de différents isotopes variant entre la masse 49 et 64.

Dans notre cas, il arrive parfois qu'il subsiste à l'état de traces certains éléments autres que ceux d'intérêts (*i.e.* Cu et Zn) malgré la séparation et purification par chromatographie sur colonnes échangeuses d'ions. Si les isotopes du Cu ne possèdent pas d'isobares, le ^{64}Zn possède un isobare majeur avec le ^{64}Ni (Nickel) (Figure 16). La correction de cette interférence se fait grâce à un autre isotope du Nickel (^{62}Ni). Connaissant le rapport ^{62}Ni/^{64}Ni naturel, le rapport ^{66}Zn/^{64}Zn corrigé peut être recalculé grâce à l'équation suivante :

$$\left(\frac{66_{Zn}}{64_{Zn}}\right)_{réel} = \left(\frac{66_I}{64_I}\right)_{mesuré} - \left(\frac{62_{Ni}}{64_{Ni}}\right)_{naturel} * \left(\frac{66_I}{62_I}\right)_{mesuré}$$

où $\left(\frac{62_{\mathrm{Ni}}}{64_{\mathrm{Ni}}}\right)_{\mathrm{naturel}} = 0{,}25247$; et ^{66}I,^{64}I et ^{62}I sont les intensités mesurées sur les masses 66, 64 et 62.

D'autres éléments comme le Xénon (Xe) et le Barium (Ba) peuvent également, si ils forment des doubles charges, induire des interférences sur le Cu et Zn. Par exemple, l'isotope de masse 130 du Ba (^{130}Ba), aura à l'état d'oxydation (+II) un rapport m/z (*i.e.* 130/2=65) similaire à celui de l'isotope ^{65}Cu. Tout comme le Ni, la correction d'interférence se fait *via* la mesure d'un autre isotope non interférent (*i.e.* ^{138}Ba et ^{131}Xe).

Le Titane (Ti) peut lui aussi induire des interférences isobariques sur le ^{64}Zn (Chen et al., 2016; Sossi et al., 2014). L'isotope 48 du Titane (^{48}Ti) en se complexant à un atome

d'Oxygène peut, par exemple, former un oxyde de Titane ($^{48}Ti^{16}O$), une espèce poly-atomique ayant une masse très proche de celle du ^{64}Zn dont l'appareil de mesure (Nu 500, basse résolution) ne peut pas faire la distinction. De manière générale, il est recommandé d'avoir un rapport Ti/Zn < 0.01 dans les fractions de Zn à analyser (Chen et al., 2016; Sossi et al., 2014) pour éviter une correction isobarique trop importante, une condition vérifiée dans cette étude au vu des quantités de Ti initialement très faible voire nulle dans les échantillons biologiques analysés. Notons que Chen et al. (2016) ont montré que lorsque le ratio $^{48}Ti/^{64}Zn$ était > 0.02, cela pouvait générer un biais non négligeable du rapport $\delta^{66}Zn$, jusqu'à ~0.2‰.

II.4. Evaluation de la qualité des données acquises

En bio-géochimie, comme dans la majorité des disciplines scientifiques, il n'existe pas de mesures « parfaites ». Les mesures de concentrations et de compositions isotopiques reportées dans cette étude sont donc entachées d'erreurs qui peuvent varier en fonction de la précision de l'opérateur, de la contamination exogène ou encore de la fiabilité des instruments de mesures. Il est donc nécessaire de contrôler la précision mais également la justesse des résultats obtenus via l'analyse de blancs d'acide, de réplicats, de duplicats et de standards certifiés. L'évaluation quantitative des principales sources de contaminations exogènes est également un critère d'évaluation important.

II.4.1. Duplicats, réplicats et blancs d'acides

Les blancs de chimie et d'attaque permettent de contrôler la propreté et d'évaluer les potentielles contaminations externes ou internes tout au long de la procédure analytique, de la dissolution de l'échantillon à la mesure sur les spectromètres de masse. Pour chaque série de mesure (soit environ 10 à 30 échantillons), un blanc d'attaque (*i.e.* mesuré avant le passage sur colonne) et un blanc de chimie (*i.e.* mesuré après le passage sur colonne) sont systématiquement analysés. Les « blancs » correspondent à des solutions d'acides (sans contact avec l'échantillon) qui ont subi la même procédure analytique que les échantillons, de la dissolution (blancs d'attaque) jusqu'à la mesure des rapports isotopiques (blancs de chimie). En moyenne, les quantités de Cu et Zn présentes dans les blancs d'attaque varient entre 40 pg et 80 pg et sont légèrement plus élevées dans les blancs de chimie variant entre <0.02 et 1.1 ng pour le Cu et entre <0.02 et 11.0 ng pour le Zn, ce qui représente en moyenne moins de 1% du Cu et du Zn présents dans les échantillons et isolés après chimie. Pour plus de clarté, l'importance et la proportion relative que représentent ces quantités mesurées dans les blancs par rapport à celles présentes dans les échantillons sont

discutées au cas par cas dans la suite du manuscrit. Nous avons également estimé l'impact de ces contaminations exogènes sur les mesures de compositions isotopiques des échantillons les plus pauvres en Zn et Cu, notamment les liquides céphalo-rachidiens (cf. Documents supplémentaires de l'article publié dans le Chapitre IV).

Les duplicats (« dup » ; deux échantillons identiques issus de deux attaques différentes) et réplicats (« bis » ; solution provenant de la même attaque et ayant subi la même chimie mais analysée deux fois) permettent d'évaluer la reproductibilité externe de la procédure analytique, ainsi que la reproductibilité interne associée à la stabilité des machines. L'ensemble des valeurs obtenues pour les échantillons répliqués (bis) et dupliqués (dup) est présenté dans les tables des manuscrits ci-dessous (voir chapitres IV et V). Qu'il s'agisse des analyses élémentaires (éléments majeurs et traces) ou isotopiques (δ^{65}Cu et δ^{66}Zn), les différences relatives entre les échantillons et leurs réplicats sont quasi-systématiquement inferieurs à 5% (2σ) pour les éléments traces et majeurs et inférieurs à 0.05‰ (2σ) pour les compositions isotopiques. Les différences entre échantillons et duplicats sont elles en moyenne inferieures à 10% et 0.1‰ (2σ), respectivement. Ces résultats démontrent la fiabilité et la robustesse des procédures analytiques utilisées et montrent que les résultats obtenus dans cette étude ont une bonne reproductibilité externe (duplicats reproductibles) et interne (réplicats reproductibles).

II.4.2. Standards de références biologiques

La justesse des données mais également la validité de la procédure analytique complète ne peut pas être évaluées par la simple mesure de duplicats et réplicats. Pour cela, il faut utiliser des standards de référence certifiés en concentrations et en compositions isotopiques analysés comme des échantillons inconnus. Cependant, si la composition chimique d'un vaste ensemble de standards de roche est relativement bien contrainte, c'est loin d'être le cas pour les standards biologiques, pour lesquels aucune donnée certifiée n'est actuellement disponible pour les rapports isotopiques en Cu et en Zn.
Aussi, afin d'assurer la fiabilité de nos résultats mais également ceux de l'ensemble la communauté scientifique, j'ai débuté une étude d'inter-calibration basée sur l'analyse de huit standards internationaux distincts et diversifiés comprenant des protéines de poissons (DORM-2 et DORM-4), du lait en poudre (BCR®-380R), du thon (ERM®-CE464), des haricots verts (BCR®-383), du sérum bovin fœtal (FBS), du foie bovin (SRM 1577c) et de l'hépatopancréas de homard (TORT-3) ainsi qu'un standard maison (plasma de brebis lyophilisé (OEP)). Ces standards seront analysés par 4 laboratoires de recherche diffèrent

regroupant l'ENS de Lyon, l'Institut Max Planck, Allemagne (contact : Klervia Jaouen), l'Université de Bruxelles, Belgique (Laboratoire G-Time ; contact : Nadine Mattielli) et l'Université de British Columbia, Canada (contacts : Dominique Weis et Amini, M.A. Marghaleray). Pour cette inter-calibration, nous nous sommes principalement concentrés sur cinq éléments chimiques (Cu, Zn, Fe, Mg et Ca). Pour chaque élément, les concentrations et les compositions isotopiques sont déterminées indépendamment par chaque laboratoire, chacun ayant recours à des méthodes d'attaque, de séparation sur colonne et de mesures différentes. A Bruxelles, le protocole analytique repose par exemple sur la calcination des échantillons dans un four à moufle Lenton (2h à 350ºC, 12h à 450ºC et 2h de refroidissement) suivi par une attaque en HNO_3 concentré sans H_2O_2. La séparation des ions se fait ensuite sur des colonnes Bio-rad remplies avec 2 mL de résine anionique AG1-x8 (100-200 Mesh), un protocole différent de celui que j'ai utilisé à Lyon (cf II.2.1.b et II.2.2.b). La grande majorité des analyses étant toujours en cours dans les laboratoires partenaires, je ne présenterai ici qu'une partie des résultats, notamment ceux en Cu et en Zn que j'ai mesuré à Lyon (cette étude) et ceux actuellement obtenus par Nadine Mattielli à Bruxelles. Toutes ces données sont regroupées dans l'annexe 3 et illustrées dans les figures ci-dessous.

La Figure 17 montre les compositions isotopiques et les concentrations en Cu et Zn des 9 standards biologiques mesurés plusieurs fois à Lyon.

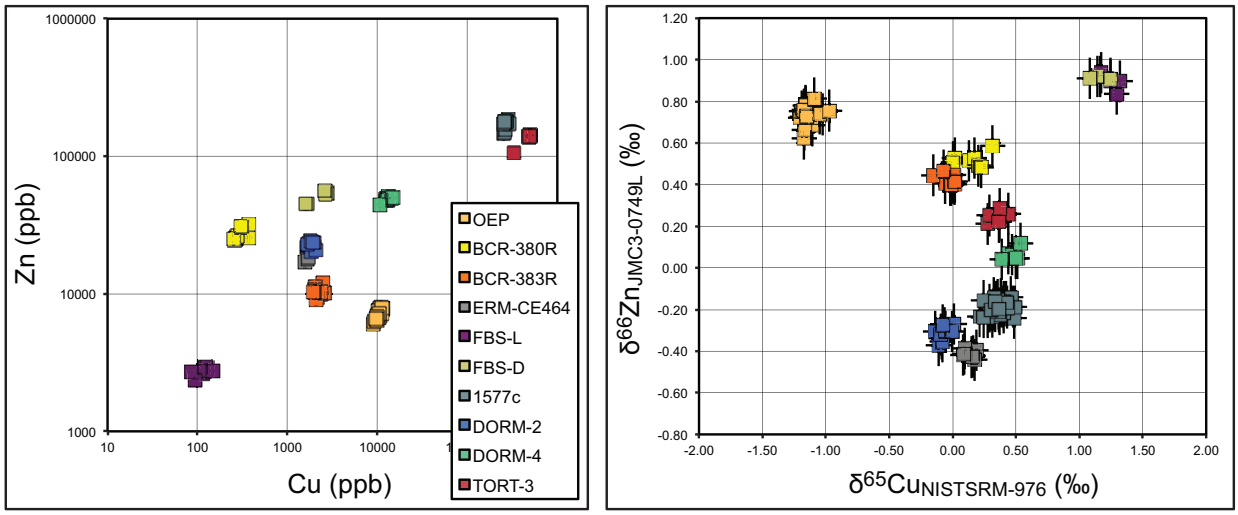

Figure 17 : Concentrations et compositions isotopiques en cuivre (Cu) et en zinc (Zn) (données de Lyon uniquement) mesurées dans 8 standards internationaux et un standard maison (OEP). Les barres d'erreurs représentent une incertitude à ± 2sd. Les concentrations en Cu et Zn sont représentées sur des échelles logarithmiques du fait de la grande dispersion au sein de tous les échantillons. OEP : plasma de brebis, BCR-380R :lait en poudre, BCR-383R :haricots verts, ERM-CE464 :thon, FBS-L/D : serum de bœuf liquide/lyophilisé, 1577c :foie de bœuf, DORM-2/4 :protéines de poissons et TORT-3 : hépatopancréas de homard.

La gamme de variabilité entre les standards est importante et fluctue en moyenne entre -1.14 ‰ (OEP) et +1.21 ‰ (FBS) pour δ^{65}Cu, -0.42 ‰ (ERM-CE464) et +0.91 ‰ (FBS) pour δ^{66}Zn, ~500 000 (TORT-3) et ~115 ppb (FBS-L) pour [Cu] et ~170 000 (1577c) et ~2600 ppb (FBS-L) pour [Zn].

Chaque standard possède sa propre signature chimique et isotopique (Figure 17). Les résultats, bien que préliminaires, indiquent que les concentrations et les compositions isotopiques en Zn et Cu des standards testés et mesurés à Lyon sont généralement reproductibles (Figures 17 et 18). En moyenne, la précision et la justesse des analyses sont de l'ordre de celles communément obtenues pour des échantillons biologiques (*i.e.* en moyenne ±10-15% pour les concentrations et ±0.1‰ pour les compositions isotopiques, cf Annexe 3). Pour les concentrations, l'incertitude de mesure est néanmoins quelque peu élevée pour certains échantillons et semble directement reliée à la qualité de l'attaque. Un échantillon mal attaqué (attaque incomplète *i.e.* < 5 heures) tel que DORM4-6 et TORT3-6 aura une concentration en Cu (DORM4-6 = 10.77 ppm, TORT3-6 = 331.05 ppm) et en Zn (DORM4-6 = 44.56 ppm, TORT3-6 = 105.92 ppm) inferieure à la valeur moyenne attendue (Cu_{DORM4} = 13.39 ± 1.82 ppm (2sd, n=7), Zn_{DORM4} = 49.28 ± 2.32 ppm (2sd, n=7) et Cu_{TORT3} = 492.26 ± 14.75 ppm (2sd, n=6), Zn_{TORT3} = 140.29 ± 4.90 ppm (2sd, n=6)), pouvant affecter la précisons de la mesure.

En plus d'être en moyennes reproductibles, ces valeurs sont en accord avec les valeurs de références certifiées et/ou celles obtenues dans les autres laboratoires. Concernant les concentrations en Cu et Zn, seuls quatre échantillons sont à ce jour certifiés (*i.e.* 1577c, DORM-2, DORM-4 et TORT-3). A l'exception des concentrations en Cu mesurées dans DORM-2 (Cu = 1.85 ± 0.24 ppm (2sd, n=10)) et DORM-4 (Cu = 13.39 ± 1.82 ppm (2sd, n=7)) qui se trouvent légèrement inférieures aux valeurs de références reportées par le NRC (National Research Council Canada) (*i.e.* Cu_{DORM-2} = 2.34 ± 0.16 ppm (2sd) et Cu_{DORM-4} = 15.70 ± 0.46 ppm (2sd)), bien que néanmoins proches de celles mesurées par dilution isotopique par Park et al.(2011) (*i.e.* Cu_{DORM-2} = 2.08 ± 0.21 ppm (2sd)), toutes les autres valeurs sont en accord avec les valeurs certifiées (cf Annexe 3). Par exemple, pour les échantillons TORT-3 et 1577c on a : Cu_{TORT-3} = 492 ± 15 ppm (2sd, n=6) , Zn_{TORT-3} = 140 ± 5 ppm (2sd, n=6) et Cu_{1577c} = 265 ± 22 ppm (2sd, n=19), Zn_{1577c} = 169 ± 23 ppm (2sd, n=19), des valeurs en accord avec celles publiées par le NRC (Cu_{TORT-3} = 497 ± 22 ppm (2sd), Zn_{TORT-3} = 136 ± 6 ppm (2sd)) et NIST (National Institute of Standards and Technology) (Cu_{1577c} = 272.5 ± 4.6 ppm (2sd), Zn_{1577c}= 181.1 ± 1.0 ppm (2sd)) respectivement (cf Annexe 3). Pour les compositions isotopiques en Zn, Jaouen et al.(2016) ont récemment publié une valeur de -0.13 ± 0.02 ‰ (2sd, n=4) pour l'échantillon 1577c, en accord avec les données

présentées dans cette étude (-0.19 ± 0.07 ‰ (2sd, n=51) pour Lyon et -0.15 ± 0.06 ‰ (2sd, n=3) pour Bruxelles). Les données obtenues à l'ENS de Lyon pour les échantillons BCR-380R, FBS, DORM-4 et TORT-3 sont également en accord avec celles mesurées à Bruxelles (Figure 18), des résultats appuyant la précision, la justesse et la reproductibilité des données isotopiques en Zn.

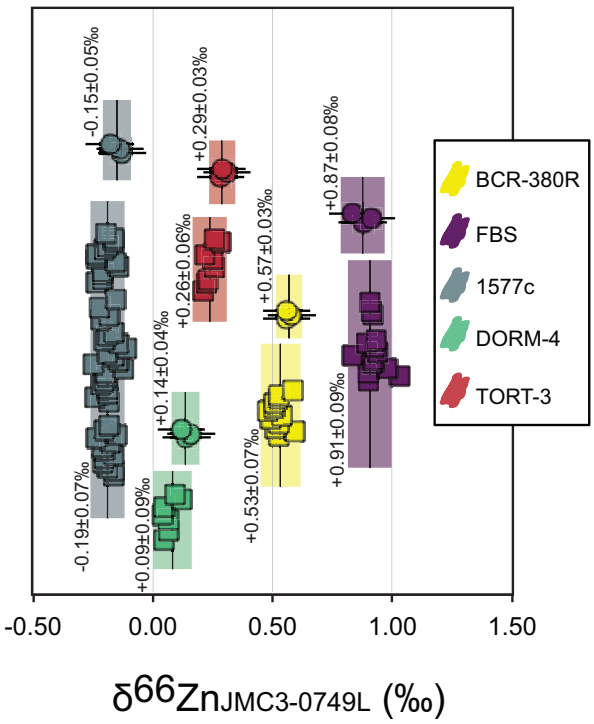

Figure 18 : Composition isotopique en zinc mesurées à Lyon (carrés : cette étude) et Bruxelles (ronds : Nadine Mattielli). Les barres d'erreurs représentent une incertitude à ± 2sd. Seuls les standards mesurés à la fois à Lyon et à Bruxelles sont illustrés. Les barres verticales et les champs colorés représentent les valeurs moyennes et leur incertitude associée.

A l'inverse, pour les compositions isotopiques en Cu, aucune valeur certifiée n'a encore été reportée et/ou publiée par un autre laboratoire, ne nous permettant pas d'évaluer la justesse de nos résultats. Bien que les compositions isotopiques en Cu obtenues s'avèrent être en moyenne reproductibles pour la majorité des échantillons (Figure 17), certaines sont néanmoins entachées de plus grandes incertitudes (Figure 19). C'est le cas par exemple des échantillons BCR®380R (Whole milk, δ^{65}Cu = 0.14 ± 0.21 (2sd, n=8) ‰) et FBS (Fetal Bovine Serum, δ^{65}Cu = 1.21 ± 0.16 (2sd, n=8) ‰) dont la précision reportée sur les δ^{65}Cu avoisine les ± 0.2 ‰ (2sd) tandis qu'elle se rapproche des ± 0.1 ‰ (2sd) pour des échantillons mieux contraints comme le 1577c (δ^{65}Cu = 0.37 ± 0.14 (2sd, n=43) ‰) et le pancréas de homard (TORT-3) (δ^{65}Cu= 0.35 ± 0.12 (2sd, n=9) ‰) (cf. Figure 19).

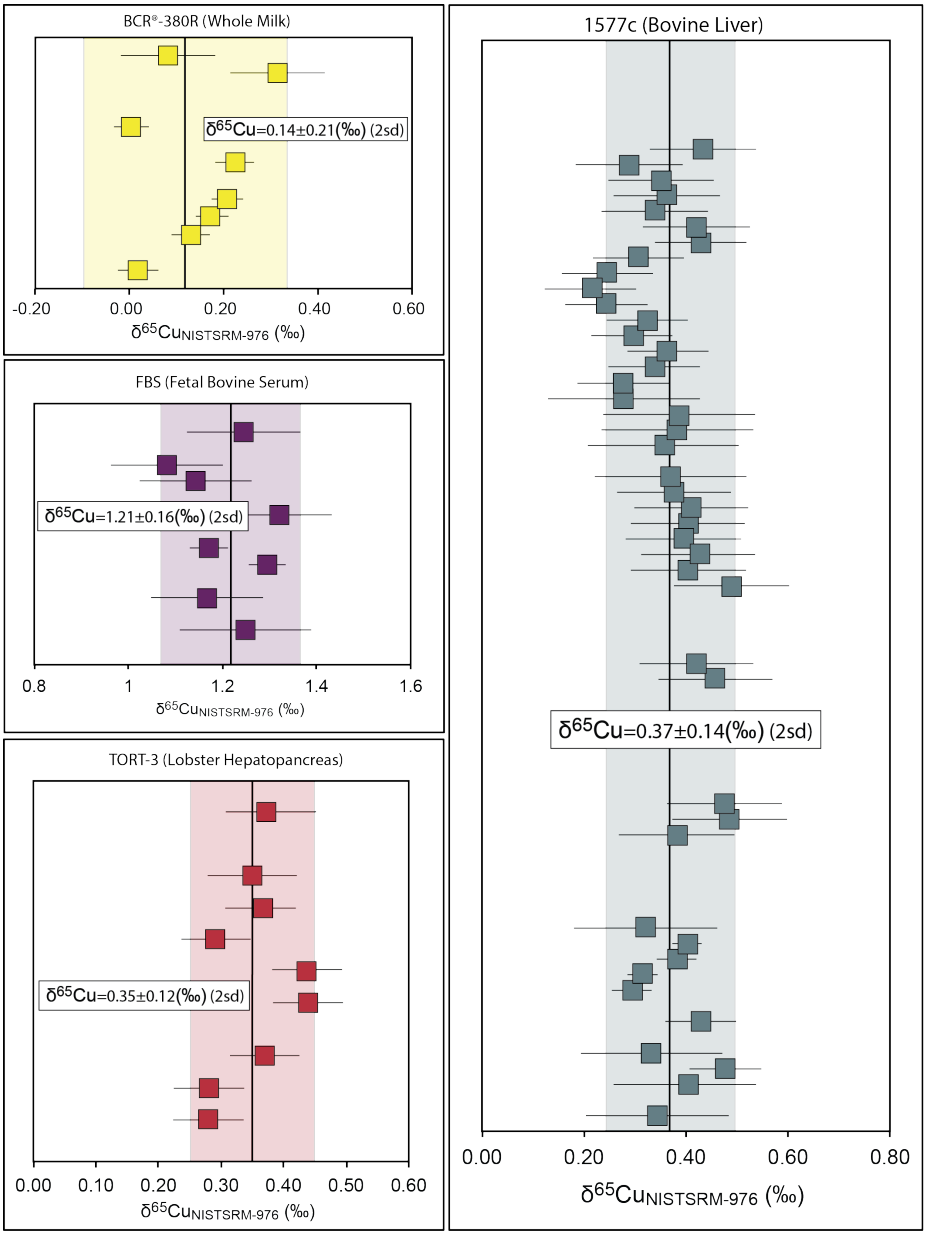

Figure 19 : Compositions isotopiques en cuivre (Cu) (données de Lyon uniquement) mesurées dans quatre standards biologiques. Les barres d'erreurs représentent une incertitude à ± 2sd. Les barres verticales et les champs colorés représentent les valeurs moyennes et leur incertitude associée.

Cette différence pourrait s'expliquer par des dissemblances relatives entre la charge matricielle (Matrice) et la quantité de Cu présente dans l'échantillon, puisque les échantillons entachés de larges incertitudes comme BCR®380R (Whole milk) et FBS (Fetal Bovine Serum) ont en moyenne un rapport Cu/Matrice plus bas ($<3.10^{-5}$) que les échantillons mieux contraints comme 1577c et TORT-3 (Cu/Matrice $>8.10^{-3}$) (Figure 20). Ce problème n'affecte pas ou peu les rapport isotopiques en Zn probablement car les quantités de Zn présentent dans les échantillons sont plus élevées que celles en Cu (Figure 17). En moyenne le rapport Zn/Matrice avoisine les $1,5.10^{-3}$ (cf Annexe 3).

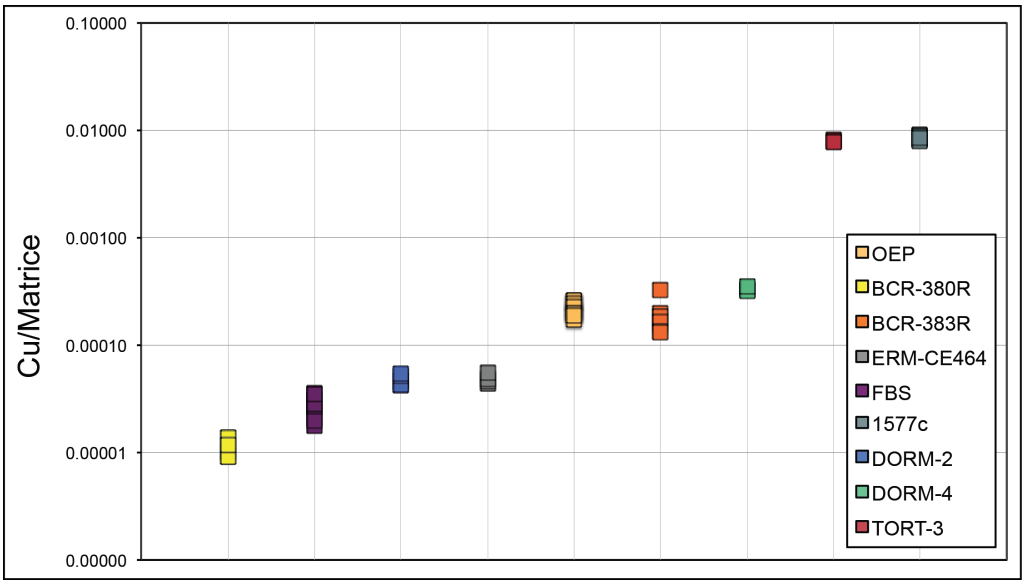

Figure 20 : Proportion relative de cuivre par rapport à la charge matricielle présente initialement dans l'échantillon. La charge matricielle (Matrice) est définie comme étant la somme de tous les éléments majeurs dont les concertations sont supérieures à 200 ppm, à savoir Ca, K, Na, P, S et Mg. Les rapports Cu/Matrice étant très variables entre les différents échantillons, une échelle logarithmique a été utilisée afin de pouvoir représenter toutes les valeurs.

Un échantillon ayant une charge matricielle importante est, par définition, plus difficile a attaqué et présente un risque élevé de mauvaise séparation du Cu lors de la séparation sur colonnes échangeuse d'ions. Le mode d'attaque est donc un paramètre déterminant dans la précision de la mesure des rapports isotopiques. Afin de diminuer l'erreur de mesure sur les échantillons à forte charge matricielle, nous envisageons de réaliser plusieurs tests de dissolution telles qu'une simple et/ou une double attaque en $HNO_{3,\ conc}$ + H_2O_2 30% suivie ou non par un passage aux ultraviolets (UVs) pendant environ 24h (ENS Lyon) ou une attaque simple en $HNO_{3,\ conc}$ précédée par une étape de calcination faite dans des creusets en verre a ~400ºC (Laboratoire G-Time, Bruxelles).

L'effet de la lyophilisation sur les compositions isotopiques a également été évalué et quantifié afin de s'assurer qu'une lyophilisation incomplète ne soit pas à l'origine d'un biais analytique. Seule le FBS initialement sous forme liquide a pu être testé. Bien que de larges variations soient observées à la fois pour $\delta^{65}Cu$ et $\delta^{66}Zn$, aucune distinction significative n'est visible entre l'échantillon liquide ($\delta^{65}Cu$= 1.24 ± 0.14 (2sd, n=5) ‰ et $\delta^{66}Zn$= 0.92 ± 0.10 (2sd, n=11) ‰) et lyophilisé (solide) ($\delta^{65}Cu$ = 1.16 ± 0.16 (2sd, n=3) ‰ et $\delta^{66}Zn$ = 0.91 ± 0.01 (2sd, n=3) ‰) (Figure 21).

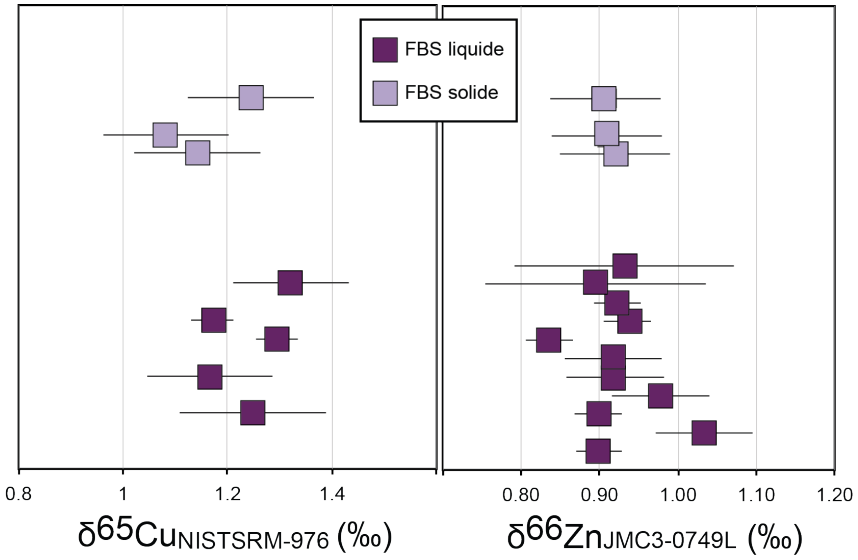

Figure 21 : Effet de la lyophilisation sur les compositions isotopiques en cuivre et en zinc. FBS= Fetal Bovine Serum. Les barres d'erreurs représentent une incertitude à ± 2sd.

Pour conclure, les premiers résultats de cette étude comparative sont encourageants bien qu'à ce jour plusieurs analyses soient encore en cours et certaines données demandent d'être vérifiées. Les compositions isotopiques en Cu et en Zn de ces standards internationaux permettront à terme de fournir une base de données de référence sur huit standards biologiques et un standard maison pour l'ensemble de la communauté scientifique.

II.4.3. Evaluation des principales sources de contamination externe

Outre les différents contrôles effectués ci-dessus, la qualité d'une mesure isotopique, et plus précisément sa justesse, repose également sur la connaissance et la limitation de toutes contaminations externes. Dans les année 1980, Hoffman et al. (1988) fut l'un des premiers à montrer que la plupart des contaminations exogènes provenaient des ustensiles de chimie quotidiennement utilisés comme les embouts de pipettes, les bouteilles en polyéthylène, les spatules en plastique et les gants de protection. Afin d'approfondir ces études préliminaires, nous avons analysé l'ensemble des tubes de stockage et de prélèvement utilisés dans cette étude ainsi qu'une quinzaine de gants de différentes matières (latex, nitrile, vinyle et néoprène).

II.4.3.a. Les tubes de prélèvement et stockage

Les quantités (ng) d'une dizaine d'éléments chimiques relâchés par différents tubes ainsi qu'une pipette compte-goutte utilisée pour conserver et prélever les liquides céphalo-

rachidiens (LCRs) et les organes de souris ont été déterminées. Les tubes testés comprennent (1) des tubes utilisés pour prélever les LCRs (LCR-A : tube en polypropylène, Sarstedt, 10mL, 92x15.3mm, et LCR-B : tube en polypropylène, Sarstedt, 5mL, 57x15.3mm), (2) des tubes dans lesquels sont stockés les LCRs (LCR-C: micro-tube conique à jupe en polypropylène, Sarstedt, 1.5mL), (3) des tubes dans lesquels sont conservés l'ensemble des organes de souris analysés dans cette étude (TA : cryotube en polypropylène, Thermo Scientific™ Nalgene™, 1.5mL, PP threaded, w/silicone gasket, bouchon HDPE), et (4) des tubes utilisés pour mesurer les concentrations en éléments traces (LCR-D: tube en polypropylène, Dutscher, 10 mL). Enfin, les pipettes compte-gouttes (LCR-E) sont des pipettes en plastique PVC (Thermo ScientificTM, Sterilin™ Plastic Transfer Pipettes) (cf Figure 22).

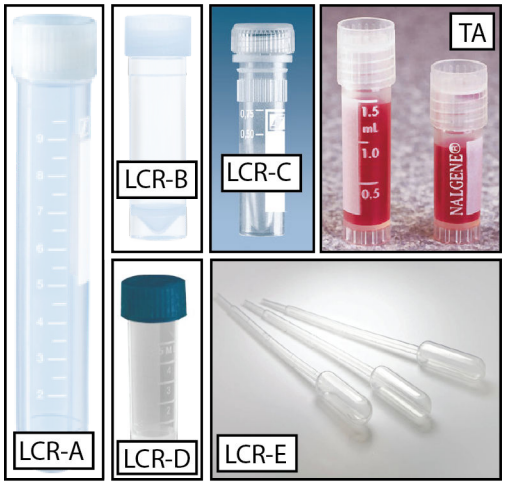

Figure 22 : Ensemble des tubes de stockage, de prélèvement et des pipettes compte-gouttes analysés dans le but contrôler l'impact contaminant sur les échantillons

La procédure analytique consiste à remplir tous les tubes avec 2mL d'HNO_3 0.5N + 2µg/L d'Indium puis de les stocker au réfrigérateur pendant environ 3 semaines. Seul les tubes LCR-D sont remplis avec 5mL d'HNO_3 0.5N + 2µg/L d'Indium afin d'augmenter la surface de contact entre la paroi du tube et l'acide et de reproduire les conditions de mesures (~ 5mL de solution) sur l'iCap-Q. Pour la pipette compte-goutte, un bécher savillex® en téflon a été remplie avec 2mL d'HNO_3 0.5N + 2µg/L d'In. Ce volume de solution a ensuite été prélevé avec la pipette puis relâché dans le bécher ; une procédure qui a été répétée 5 fois de suite. Il est important de noter que ces tests de contamination ont été réalisés en salle blanche sous hotte à flux laminaire avec des acides extra-purs doublements distillés pour éviter d'éventuelles contaminations supplémentaires. Les concentrations sont ensuite mesurées sur Q-ICP-MS (Thermo iCap-Q) à l'ENS de Lyon basé sur le protocole détaillé dans le chapitre II (cf II.3.1.b).

Les résultats présentés dans la Figure 23 montrent que les quantités d'éléments traces relâchées par les tubes et les pipettes sont négligeables devant celles initialement présentes dans ces échantillons (quantité tubes/quantité échantillon <<0.1).

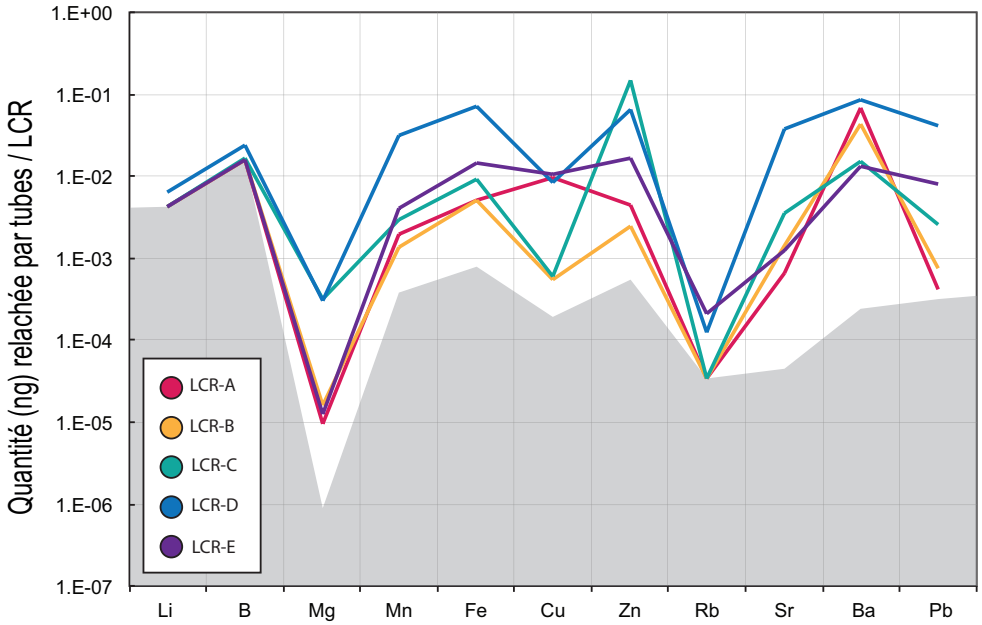

Figure 23 : Quantités (ng) relâchées par les tubes de prélèvement, de stockage et les pipettes utilisées pour conserver et manipuler les échantillons après 3 semaines en contact avec de l'acide HNO3 0.5N + 2µg/L d'In. Pour les tubes de stockages (LCR-A, LCR-B et LCR-C), les quantités sont normalisées à celles présentes dans un échantillon totale de taille moyenne (~2 mL) afin d'évaluer la contamination pendant le stockage/prélèvement. Pour le tube LCR-D, la normalisation a été faite par rapport à la quantité présente dans la solution fille mesurée sur l'iCap-Q (soit ~1/10 de la quantité initialement présente dans l'échantillon) afin d'évaluer la contamination possible pendant la mesure sur l'iCap-Q. La normalisation est faite par rapport aux LCRs car ces derniers sont les échantillons les moins concentrés et par conséquent les plus facilement contaminables. Seul les éléments significativement abondants dans les LCRs sont représentés. La limite de détection (champ grisé) est définie comme trois fois la moyenne des blancs (i.e. solution d'HNO_3 0.5N + 2µg/L In).

De façon similaire, les quantités relâchées par les tubes TA et TB sont en moyenne <0.1 ng même après deux mois de conservation pour les tubes TB au réfrigérateur. Pour ces deux tubes, seule les concentrations en cuivre et en zinc ont été mesurées, c'est pourquoi ils ne sont pas représentés sur le diagramme ci-dessous.

Par ailleurs, seules les quantités d'éléments traces ont été quantifiées du fait de leur faible teneur initialement présente dans les échantillons à l'inverse des éléments majeurs (e.g. Ca, K, Na, P et S) dont les concentrations sont bien plus importantes et donc moins soumises aux contaminations.

Au vue de ces résultats et en supposant qu'il est fortement probable que les quantités relâchées par les tubes en contact avec de l'acide, même faiblement dilué, soit plus importantes que celles relâchées lorsque le tube est en contact avec un échantillon, on peut conclure que tous les tubes/pipettes utilisés dans cette étude qu'ils soient en polypropylène ou en PVC ne sont pas des agents de contamination potentiels et, ne peuvent en aucun cas

biaiser nos mesures élémentaires et isotopiques faites sur les liquides céphalo-rachidiens (LCRs). Une conclusion que l'on peut étendre à l'ensemble des échantillons analysés dans cette étude étant donné que les LCRs sont les échantillons ayant le plus de risque d'être contaminés du fait de leur très faible teneur en élément chimique.

II.4.3.b. Les gants de protection

L'étude de Friel et al.(1996) a révélé de façon quantitative que les gants de protection utilisé en biologie et en chimie étaient fortement concentrés en éléments chimiques et donc potentiellement très contaminant pour les mesures d'éléments traces et la détermination de compositions isotopiques. Friel et al. (1996) ont reporté les concentrations de 25 éléments dans 2 types de gants (latex et vinyle) dont les marques ne sont quasiment plus commercialisées aujourd'hui. Dans le manuscrit qui suit, nous avons réévalué le potentiel contaminant de gants couramment utilisés en salle blanche de nos jours. Nous avons déterminé les concentrations de plus de 60 éléments chimiques ainsi que les compositions isotopiques en Zn de 15 gants différents provenant d'Europe et des Etats-Unis. Cela nous a permis de mettre en évidence le potentiel très contaminant des gants envers les échantillons biologiques et géologiques, notamment les gants en nitrile, latex et néoprène pour le Zn. Nous avons également quantifié le biais pouvant être engendré par une contamination des gants sur les concentrations en éléments traces et la composition isotopique en Zn de différents échantillons (cf. article ci-dessous).

ARTICLE

Nitrile, latex, neoprene and vinyl gloves: A primary source of contamination for trace element and Zn isotopic analyses in geological and biological samples

*Marion Garçon, **Lucie Sauzéat**, Richard W. Carlson, Steven B. Shirey, Mélanie Simon, Vincent Balter and Maud Boyet*

(Published in GEOSTANDARDS and GEOANALYTICAL RESEARCH)

GEOSTANDARDS and GEOANALYTICAL RESEARCH

Nitrile, Latex, Neoprene and Vinyl Gloves: A Primary Source of Contamination for Trace Element and Zn Isotopic Analyses in Geological and Biological Samples

Marion **Garçon** (1, 2, 4)*, Lucie **Sauzéat** (3), Richard W. **Carlson** (2), Steven B. **Shirey** (2), Mélanie **Simon** (3), Vincent **Balter** (3) and Maud **Boyet** (1)

(1) Laboratoire Magmas et Volcans, Université Blaise Pascal, UMR CNRS 6524, Campus Universitaire des Cézeaux, 6 avenue Blaise Pascal, Aubière Cedex, 63178, France
(2) Department of Terrestrial Magnetism, Carnegie Institution for Science, 5241 Broad Branch Road, NW, Washington, DC, 20015, USA
(3) UMR 5276, Laboratoire de Géologie de Lyon, Ecole Normale Supérieure de Lyon, CNRS, Université de Lyon 1, Lyon, BP 7000, France
(4) Present address: Department of Earth Sciences, Institute of Geochemistry and Petrology, ETH Zürich, Clausiustrasse 25, Zürich, 8092, Switzerland
* Corresponding author. e-mail: marion.garcon@erdw.ethz.ch

Exogenic contamination is of primary concern for geochemical and biological clean laboratories working with sample sizes at the nanogram or even subpicogram level. Here, we determined sixty trace elements in fifteen different types of gloves from major suppliers world-wide to evaluate whether gloves could be potential sources of contamination for routine trace element and isotope measurements. We found that all gloves contain some trace elements that can be easily mobilised in significant amounts. In weak acid at room temperature, the tested gloves released up to 17 mg of Zn, more than 1 µg of Mg, Ti, Mn, Fe, Rb, Sr, Zr, Sn, Hf and Pb and between 100 and 1000 ng of Li, Sc, V, Cr, Ni, Cu, Ga, As, Se, Y, Ag, Ba, La, Ce, Nd, Tl and Th. Vinyl gloves released lower quantities of biologically and geologically important elements, with the exception of In and Sn. Isotopic analyses indicate that all gloves share roughly the same Zn isotopic composition (average δ^{66}Zn = +0.10 ± 0.32‰ (2*s*)). A single contact between glove and labware releases an average of ~ 6 ng of Zn and hence can significantly shift δ^{66}Zn above the precision level when the amount of Zn determined is below 500 ng.

Keywords: gloves, contamination, zinc, isotopic compositions, trace elements.

Received 21 Sep 16 – Accepted 02 Dec 16

Trace element contents and Zn isotopic compositions are used in various research fields such as Earth and planetary sciences, biology and, more recently, medicine. The level of precision and sensitivity of such measurements have significantly increased through time mainly due to technological improvements in mass spectrometry. To date, routine analyses of Zn isotopic compositions and trace element contents reach an average precision of ± 0.1‰ (2*s*) and ± 5% (2*s*), respectively, with sample sizes as low as the nanogram to the low picogram range. To get accurate results, following the best analytical procedures is necessary, in particular control of exogenic contamination during sample preparation and analysis. In this context, most geochemical and biological clean laboratories carefully acid-wash all pipette tips, tubes and other labware, and use ultra-pure water and acids that they distil themselves. While several precautions, such as measuring laboratory blanks in reagents, are taken to evaluate contamination levels, less attention has been given to less direct sources of surface contamination as well as their potential impact on measurement quality. Three decades ago, Hoffmann (1988) mentioned that the sources of contamination were often where one least expects to find them, for example in labware such as gloves, pipette tips, laboratory wipes, polyethylene bottles and spoons, an assumption that was confirmed 12 years later by Friel *et al.* (1996). Friel *et al.* (1996) found that gloves were highly enriched in several elements such as Zn, Fe and Se and recommended wearing vinyl gloves that were acid-washed before use for routine trace element work. In their study, Friel

doi: 10.1111/ggr.12161

et al. (1996) report only approximately twenty-five trace elements in brands of latex and vinyl gloves that are mostly not used anymore in clean laboratories. The glove market has indeed significantly evolved and diversified through the past two decades. Several new types of gloves, made for example of nitrile or neoprene, are now commonly used in biological and geochemical laboratories world-wide. In addition, the scientific community has been interested in studying an increasing diversity of chemical and isotopic compositions highlighting the need to review and re-assess the risk of contamination associated with the use of recent laboratory gloves on a wide range of trace and minor elements.

In this paper, we quantitatively evaluate the risk of contamination caused by gloves on sixty trace elements commonly measured in Earth and planetary sciences, biology and medicine. We tested fifteen different types of gloves made of vinyl, neoprene, nitrile or latex from different suppliers such as Kimberley-Clark®, Ansell® or Medline®. Since Zn is by far the most enriched trace element in gloves (Friel *et al.* 1996), we also determined their Zn isotopic compositions (henceforth referred as δ^{66}Zn) to see whether glove contamination could significantly shift Zn isotopic compositions of geological and biological samples. The aims of the study were thus multiple: (a) to determine whether the gloves currently used in clean laboratories are still a major source of contamination for trace element and isotopic work; (b) which gloves offer lower levels of contamination; (c) to quantify the amount of each element that can be released from gloves into samples during preparation and analytical processes and pinpoint which elements are most susceptible to contamination; and (d) to quantify the effect of glove contamination on Zn isotopic compositions of geological and biological samples.

Tested gloves and analytical methods

Tested gloves

The gloves tested in this study are among the most often used in geochemical and biological clean laboratories. These include nitrile, vinyl, neoprene and latex powder-free gloves from nine main suppliers world-wide: Kimberley Clark®, Ansell®, Polysem Medical®, LCH medical®, Microflex®, Showa®, Clean-Dex®, Jet® and Medline®. Further details on the models, colours, packaging and reference numbers of the tested gloves are provided in Table 1. To avoid sample bias and allow a direct comparison between all analyses, we tested M size (7.5″–8.5″) gloves only. All gloves were taken from unopened boxes to avoid external contamination. Complete duplicates were analysed for three gloves (a vinyl, a nitrile and a neoprene glove) to assess the repeatability of the results and the measurement precision.

Materials and analytical conditions

All tests were performed in a clean laboratory below laminar flow clean hoods using ultra-pure water at 18.2 MΩ cm resistivity and acids that were distilled to ensure low trace element contents. Polypropylene tubes and pipette tips used all through the analytical procedure were not acid-washed before use to avoid any contamination by gloves worn during cleaning procedure. However, blanks were systematically run to quantify detection limits and

Table 1.
Description of the tested gloves

Sample name	Type	Supplier	Model	Colour	Packaging	Reference number
G1	Vinyl	Polysem *Medical*	Tactilis	Translucent	Cardboard box	GVB1200/PM
G2	Nitrile	Kimberley-Clark	KleenGuard G10	Blue	Cardboard box	57372
G3	Nitrile	Kimberley-Clark	KimTech Science Sterling Nitrile-XTRA	Grey	Cardboard box	98343
G4	Latex	Kimberley-Clark	KimTech Science Satin Plus	Pale yellow	Cardboard box	SP2330E
G5	Neoprene	Ansell	NeoTouch®	Green	Cardboard box	25–101
G6	Nitrile	Ansell	TouchNTuff®	Dark green	Cardboard box	92–605
G7	PFE Latex	Kimberley-Clark	KimTech Science	Pale yellow	Cardboard box	E330
G8	Vinyl	LCH medical	Sensinyl Free	Translucent	Cardboard box	VNX-02
G9	Nitrile	Microflex	Class 10 – Controlled environments	White	Plastic bag	CE4-313
G10	Nitrile	SHOWA	Nitrile N-DEX Ultimate	Light Blue	Plastic bag	9905PF
G11	Nitrile	Clean-Dex Best	Class 100 cleanrooms	White	Plastic bag	C9905PFM
G12	Nitrile	Kimberley-Clark	Nitrile G5 - KimTech Pure	White	Plastic bag	56865
G13	Vinyl	Jet	Non powdered natural vinyl gloves	Translucent	Cardboard box	07GV0708U
G14	Vinyl	Ansell	Synsation™ PF	Translucent	Cardboard box	4001OM
G15	Nitrile	Medline Industries Inc.	Sensicare® Ice	Dark blue	Cardboard box	486802

integrate potential contamination from the material and/or the acids used to perform the experiments. Blank measurements thus eliminated the possibility that pipette tips, polypropylene tubes and reagents used in the analyses contributed to the results on for the gloves.

Experiments on gloves

We used two different techniques to test the potential contamination by gloves during analytical preparation and analyses of geological or biological samples. They are both schematically illustrated in Figure 1. The first test (Test A) consisted of soaking the gloves at room temperature for 40 h in 20 ml of 0.4 mol l^{-1} HNO_3 + 0.05 mol l^{-1} HF and then analysing the content of the soaking solutions to see which chemical elements were preferentially released in solutions. The test was done in weak acid to mimic the effects of leaching by acid fumes that may occur when handling samples and labware in the laboratory. The leaching acid also corresponds to that in which samples are commonly diluted and then introduced into an ICP-MS for trace element determination (e.g., see Chauvel *et al.* 2011). The small amount of HF ensures the stability of the solution by preventing the precipitation of high field-strength elements such as Zr. The duration of the test was chosen arbitrarily and likely does not correspond to the complete leaching of the gloves. The detailed procedure consisted of putting each of the tested gloves in a 50-ml polypropylene vial being careful not to cross-contaminate the different vials in between each tested glove. We then added 20 ml of 0.4 mol l^{-1} HNO_3 + 0.05 mol l^{-1} HF in each vial and made sure that the whole gloves were soaked in the acid for 40 h. The soaking solutions were pipetted out the vials and analysed on the mass spectrometer following the method described below.

The second test (Test B) aimed to evaluate how easily gloves could release trace and minor elements just through contact with disposable labware (*cf.* Figure 1). For this test, we put 3 ml of 0.4 mol l^{-1} HNO_3 in a 15-ml polypropylene tube, touched the extremity of a 1-ml pipette tip with a dry glove for a second, washed the pipette tip with the solution into the tube and analysed the latter solution for trace element concentrations. In parallel, we also rubbed each glove along the interior of another 15-ml polypropylene tube for a second, added 3 ml of 0.4 mol l^{-1} HNO_3, swished the acid around and then determined the trace element content of the solution. The acid used in Test B was different from that used in Test A for a technical reason. To reach higher sensitivity and improve detection limits, we measured the solutions from Test B with a different instrument that was not conditioned to analyse solutions with HF even in small amounts. Therefore, Test B was performed using 0.4 mol l^{-1} HNO_3 only.

Analyses for trace element contents

Trace element concentrations were measured in solutions from Test A using the quadrupole ICP-MS Agilent 7500 at the Laboratoire Magmas et Volcans (LMV) in Clermont-Ferrand, France. Solutions from Test B were measured using the quadrupole ICP-MS Thermo iCap-Q at the Ecole Normale Supérieure (ENS) of Lyon, an instrument with lower detection limits. Most elements were measured in 'no gas mode' except Mg, Sc, Ti, V, Cr, Mn, Fe, Co, Ni, Cu, Zn, Ga, Ge, As and Se that were determined in 'He mode' using a collision cell to minimise spectral interferences caused by polyatomic ions. Concentrations were calibrated using repeated measurements of solutions containing sixty trace elements mixed to concentrations of 0.02, 0.1, 0.5, 1, 2 and 60 ng ml^{-1}. These solutions were also used to monitor and

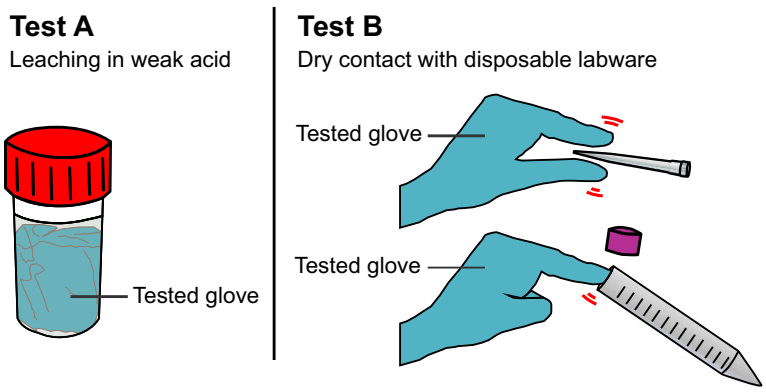

Figure 1. Illustration showing how tests A and B were performed. [Colour figure can be viewed at wileyonlinelibrary.com]

correct the instrumental drift over one analytical sequence. Solutions from Test A had to be diluted by factors of 50 or even 500 to precisely measure Zn mass fractions and avoid detector saturation. For each test, detection limits (DL) were calculated following IUPAC guidelines for each element *i* as $DL_i = x_{bi} + k\ s_{bi}$ where $k = 3$ (95% confidence level), and x_{bi} and s_{bi} are, respectively, the mean and standard deviation of the number of counts measured in blanks (i.e., acids stored and handled with the same material used to test the gloves). The measurement precision of tests A and B was estimated using complete duplicates (see online supporting information Appendices S1 and S2). Duplicated analyses are graphically represented in Appendix S3 where one can see that Test A produces repeatable results that clearly differentiate the tested gloves. The repeatability is poorer when the concentrations are low, hence closer to detection limits (*cf.* G1 and G1 Dup in Appendices S1 and S3). The repeatability of Test B is not as good as for Test A probably because the duration and surface of contact between glove and labware were variable from one tested glove to another.

Analyses for Zn isotopic compositions

Zinc isotopic compositions were measured in the soaking solutions from Test A at the ENS of Lyon, France, following the procedure described by Maréchal *et al.* (1999). The solutions were generally not purified by ion-exchange chromatography before measurement because Zn was a hundred to a million times more concentrated than any other potential interfering element in the solutions. In a recent paper, Chen *et al.* (2016) indicate that small amounts of Ni and Ti residues could produce isobaric interferences and shift the measured $\delta^{66}Zn$ values by more than 0.07‰ if the Ni/Zn and Ti/Zn ratios were higher than 0.001 and 0.01, respectively. The Ni/Zn and Ti/Zn ratios of the soaking solutions are either close to these values or significantly lower (see Appendices S1 and S4). However, to ensure that the matrix of the solutions did not induce interferences and/or that Cu from the gloves did not influence the mass bias correction based on Cu doping, three vinyl gloves (plus two duplicates) with relatively high Cu/Zn, Ni/Zn and Ti/Zn ratios and one nitrile glove were processed through column chemistry. For these samples, Zn was purified on quartz columns filled with 1.8 ml of Bio-Rad AGMP-1 (100–200 mesh) anion-exchange resin by eluting 10 ml of HNO_3 0.5 mol l^{-1} (see Maréchal *et al.* 1999 for more details). The comparison of Zn isotopic compositions measured with and without purification by ion-exchange chromatography is discussed in the results section.

On the day of the analyses, an aliquot of each solution from Test A was evaporated to dryness and dissolved in a Cu-doped solution (Cu NIST SRM 976, National Institute of Standards and Technology, Gaithersburg, MD, USA) to reach a Zn concentration of about 300 ng ml^{-1}, which is similar within 10% to the concentration of the standard solution that was run between each sample. Zinc isotopic compositions, expressed as follows:

$$\delta^{66}Zn_{sample} = \left[\frac{(^{66}Zn/^{64}Zn)_{sample}}{(^{66}Zn/^{64}Zn)_{standard}} - 1\right] * 1000 \quad (1)$$

were measured on a Nu Plasma (Nu 500) MC-ICP-MS in wet plasma conditions to avoid potential isotopic bias induced by the desolvation system on Zn isotopic ratios (Jaouen *et al.* 2013b). Instrumental mass fractionation was corrected with an exponential law using the isotopic composition of Cu that was introduced as dopant in the analysed samples as recommended by Maréchal *et al.* (1999). $\delta^{66}Zn$ were calculated by standard bracketing using Zn JMC 3-0749L (also called JMC-Lyon; Johnson Matthey, Royston, UK) as reference standard. The latter was repeatedly measured in between each sample to correct for the instrumental drift throughout the measurement sequence.

The accuracy of Zn isotopic compositions was assessed based on the analyses of an in-house standard solution (sheep plasma; SHP) at the beginning of each measurement

Figure 2. Amount of trace and minor elements released by gloves when soaked in 20 ml of 0.4 mol l^{-1} HNO_3 + 0.05 mol l^{-1} HF for 40 h (results of Test A) normalised to the amount of elements present in (a) 1 mg of basalt BHVO-2, (b) 1 mg of chondrite, (c) 1 g of natural river water SLRS-4 and (d) 30 mg of bovine serum NIST SRM 1598. Enrichment factors were calculated relative to the preferred values compiled by GeoReM for reference materials BHVO-2, SLRS-4 and NIST SRM 1598. Reference values were taken from Palme and O'Neill (2014) for CI chondrites. For panels (c) and (d), only a few elements are shown because the concentrations of other elements in SLRS-4 and NIST SRM 1598 are not available in the literature. The grey field represents values below the detection limits defined following IUPAC guidelines as the average number of counts measured in blanks plus three times the standard deviation (see section Analyses for trace element contents for more details). When the amount of element detected in a solution was below the detection limit (< DL in Appendix S1), it is represented as equal to the detection limit. [Colour figure can be viewed at wileyonlinelibrary.com]

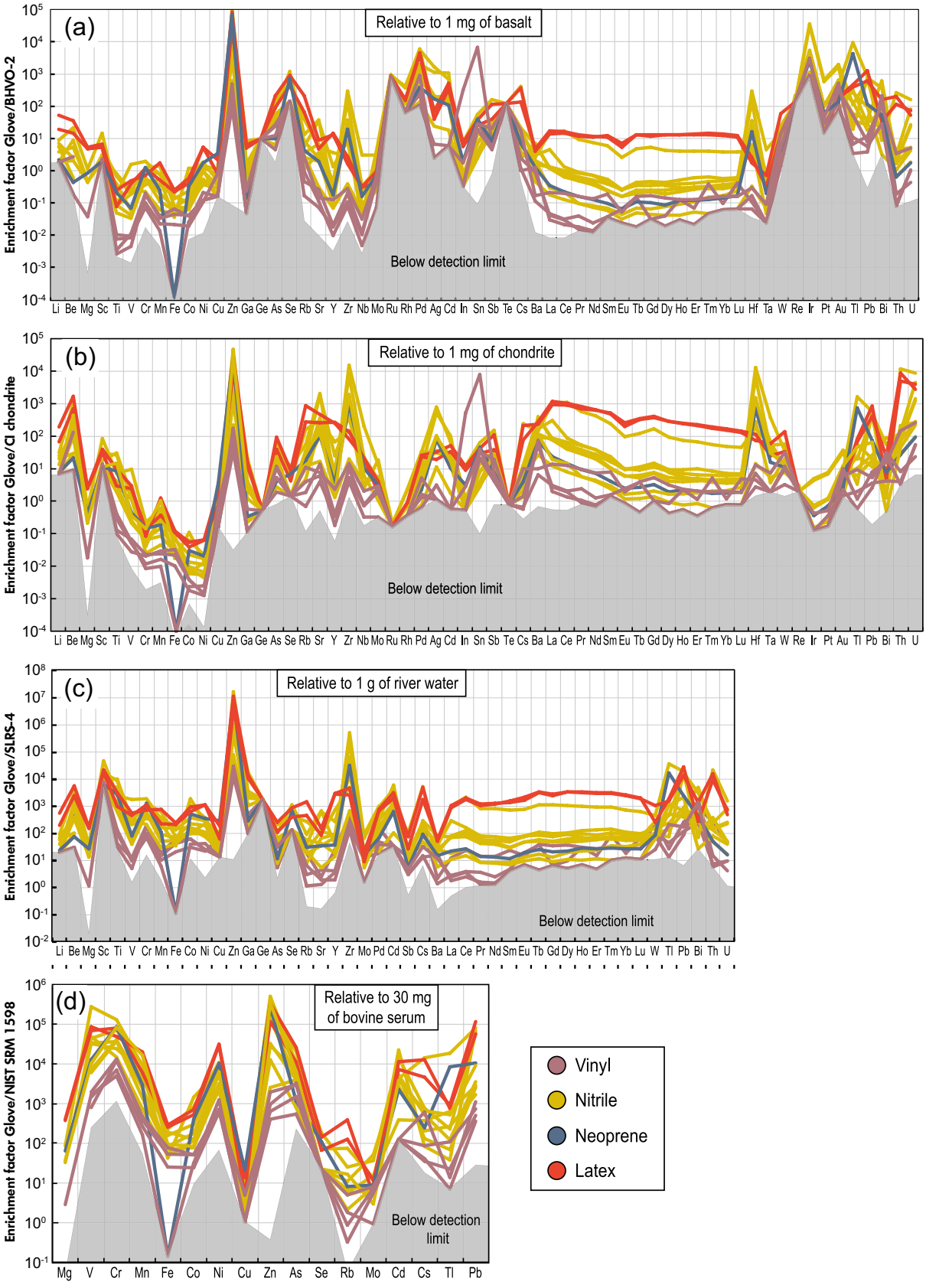

sequence. The average δ^{66}Zn measured for the in-house standard solution was +0.75 ± 0.12 (2*s*, *n* = 2), which is in good agreement with our reference in-house value of +0.73 ± 0.08 (2*s*, *n* = 8). Based on repeated measurements of standard Zn JMC 3-0749L, re-run samples and complete duplicate analyses, we estimate the precision of our measurements at ± 0.12‰ (2*s*). The long-term precision (duration = 18 months) based on the repeated measurements of Zn JMC 3-0749L alone is better than ± 0.06‰ (2*s*, *n* = 140).

Results

The amount of each element released by gloves in the soaking solutions of Test A is reported in Appendix S1 and shown normalised to geological and biological reference materials in Figure 2. The first important result is that all soaking solutions contained amounts of almost all elements determined that were well above detection limits. The exceptions are elements such as Ge, Te or Re (Appendix S1, Figure 2). Gloves are thus highly enriched in leachable trace elements, especially in Zn for which the amounts released in solutions are very large, between 11 µg and 17 mg (Figure 3). Large amounts (> 1 µg) were also measured for Mg, Ti, Mn, Fe, Rb, Sr, Zr, Sn, Hf and Pb. Nitrile, neoprene and latex gloves released the highest amounts of elements into solution. Latex gloves released the most rare earth elements (REE). Vinyl gloves generally released much lower amounts of trace elements, except G1 for In and Sn. Neoprene gloves released intermediate amounts of leachable elements. No systematic variation was noticed as a function of the packaging or the colour of the gloves.

Results from Test B are summarised in Appendix S2 and shown in Figure 4. The amounts of elements released by gloves when touching a pipette tip were generally higher than when touching the interior of a polypropylene tube (Figure 4). We think these features are directly related to the way the tests were performed, mostly the fact that the surface of contact between glove and pipette tip was probably larger than for the tube. In any case, results of Test B show that surface contaminants on the gloves are easily transferable from glove to labware and then to solutions by simple and quick contact. The most abundant transferable elements include Zn (up to 40 ng), Mg (up to ~ 20 ng), Fe (up to ~ 17 ng), Ba (up to ~ 4 ng) and all REEs (e.g., up to ~ 10 ng for Ce and 17 ng for Nd). Amounts of Ti, Cr, Mn, Fe, Ni, Cu, Ga, Ge, As, Se, Sn, Sr and Pb > 0.1 ng were also detected for some tests. Vinyl gloves generally released lower amounts of potentially contaminant elements than all other gloves, except Sn. Note that most measurements are below detection limits (Appendix S2). This does not mean that the risk of contamination is negligible since detection limits were often > 0.1 ng or even > 1 ng for some elements and highly variable from one element to another.

The Zn isotopic compositions of the five soaking solutions analysed with and without separation by ion-exchange chromatography are compared in Appendix S4. No large difference was observed with and without purification although the two solutions with the highest Cu/Zn ratios (i.e., Cu/Zn ~ 0.002 for G8 and 0.006 for G14; *cf.* Appendix S4) have δ^{66}Zn values that do not totally overlap within measurement precision. Since these variations remain small and within the range of values measured for the other tested gloves, we conclude that not performing ion-exchange purification of the soaking solutions makes only a very minor difference in Zn isotopic composition and its omission probably has no effect at all when Cu/Zn is < 0.002. Note that high Ti/Zn and Ni/Zn ratios (*cf.* G1 and G1 Dup, Appendix S4) did not bias δ^{66}Zn beyond measurement precision.

The Zn isotopic compositions of all the soaking solutions of Test A are reported in Table 2 and shown in Figure 5. For the four samples (plus two duplicates) processed through column chemistry, we reported the compositions measured after purification by ion-exchange chromatography in Table 2 (see Table caption for more details). The measured isotopic compositions span a relatively small range of values with -0.20‰ < δ^{66}Zn < +0.34‰. The average isotopic composition of the tested gloves yielded δ^{66}Zn = +0.10 ± 0.32‰ (2*s*). The most negative values were measured in nitrile and latex gloves, while the most positive were measured in vinyl gloves. Within the measurement precision, there was, however, no significant difference of Zn isotopic composition between vinyl, nitrile, neoprene and latex gloves or as a function of the glove colour.

Discussion

Gloves as potential sources of contamination

Trace element contamination by gloves is of significant concern for all laboratories dealing with analyses at the nanogram to picogram levels. The potential for contamination is a function of the abundance of the element in the sample to be analysed relative to the amount of that element contributed by the glove. To take this effect into account when discussing the results, we normalised the amount of each element released by gloves into the soaking solutions (results from Test A) to the amount of that element present in 1 mg of BHVO-2 (basalt), 1 mg of CI chondrite (meteorite), 1 g of SLRS-4 (natural river water) or 30 mg of NIST SRM

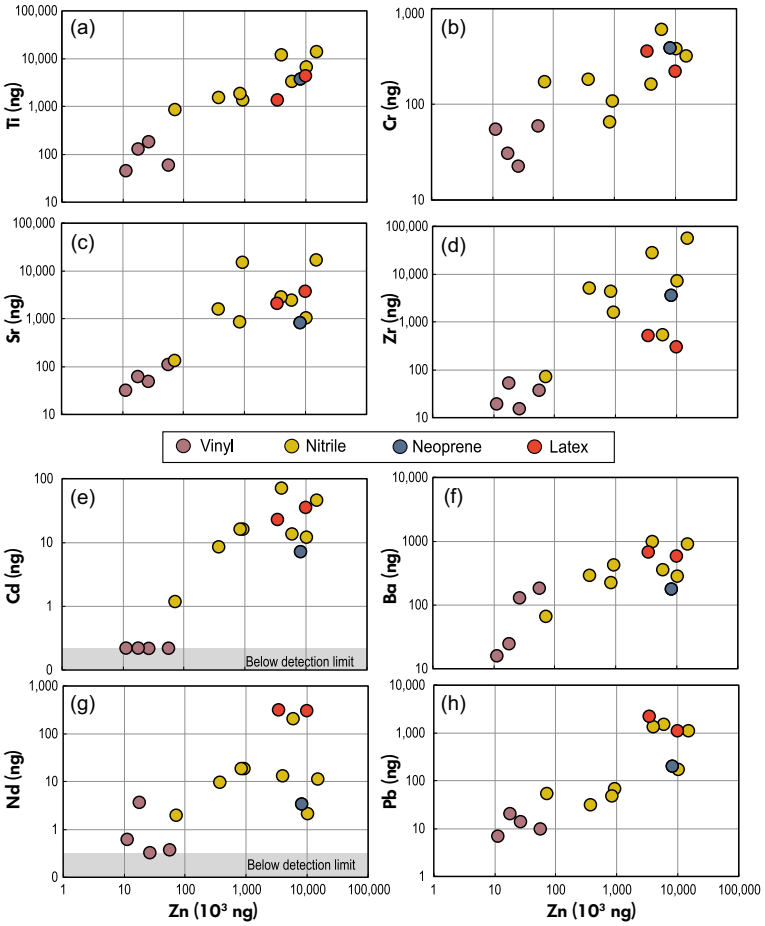

Figure 3. Binary plots showing the amount of chemical elements released by gloves when soaked in 20 ml of 0.4 mol l^{-1} HNO_3 + 0.05 mol l^{-1} HF for 40 h (results of Test A). The grey field represents values below detection limits defined following IUPAC guidelines as the average number of counts measured in blanks plus three times the standard deviation (see section Analyses for trace element content for more details). When the amount of element detected in a solution was below the detection limit (< DL in Appendix S1), it is represented as equal to the detection limit: this is the case of some vinyl glove in panels (e) and (g). [Colour figure can be viewed at wileyonlinelibrary.com]

1598 (bovine serum). These amounts correspond to the approximate amounts of geological and biological test portions usually run on ICP-MS for routine trace element determinations. The normalised amounts are shown in Figure 2a–d. In Figure 3, we report the amounts of selected elements leached from the gloves in binary plots as a function of the Zn released from the same glove. The results of Test A (Figures 2 and 3) demonstrate that gloves currently used in clean laboratories are important sources of contamination for both geological and biological samples. For example, the amount of many elements leached from the gloves is comparable and often higher than the amount of those elements present in 1 mg of geological reference material BHVO-2 (basalt) (Figure 2a). In particular, the glove leaches contain up to 100000 times more Zn; 1000 times more Se, Ru, Ag, Cd, Sn, Ir, Au, Tl, Pb; 100 times more As, Rb, Zr, Pd, In, Sb, Te, Cs, Hf, Re, Pt, Bi, Th, U; and ten times more Li, Be, Sc, Sr, Y, REE and W than in a typically sized analytical aliquot of the geological reference material. Compared with materials with lower trace element concentrations such as chondrite or river water (Figures 2b, c), enrichment factors reach higher values, for example more than 1000 for Be, Sc, Ti, V, Cr, Co, Ni, Zn, Se, Rb, Sr, Y, Zr, Cd, Sn, Cs, REE, Hf, Tl, Pb, Bi, Th and U. The situation is even worse for biological samples because their trace element contents are usually much lower than in geological samples. Figure 2d shows that the gloves can release up to 100000 times the amounts of V, Cr, Zn and Pb present in 30 mg of biological reference material NIST SRM 1598 (i.e., bovine serum); 10000 times the amounts of Mn, Ni, As, Cd, Cs and Tl; 1000 times the

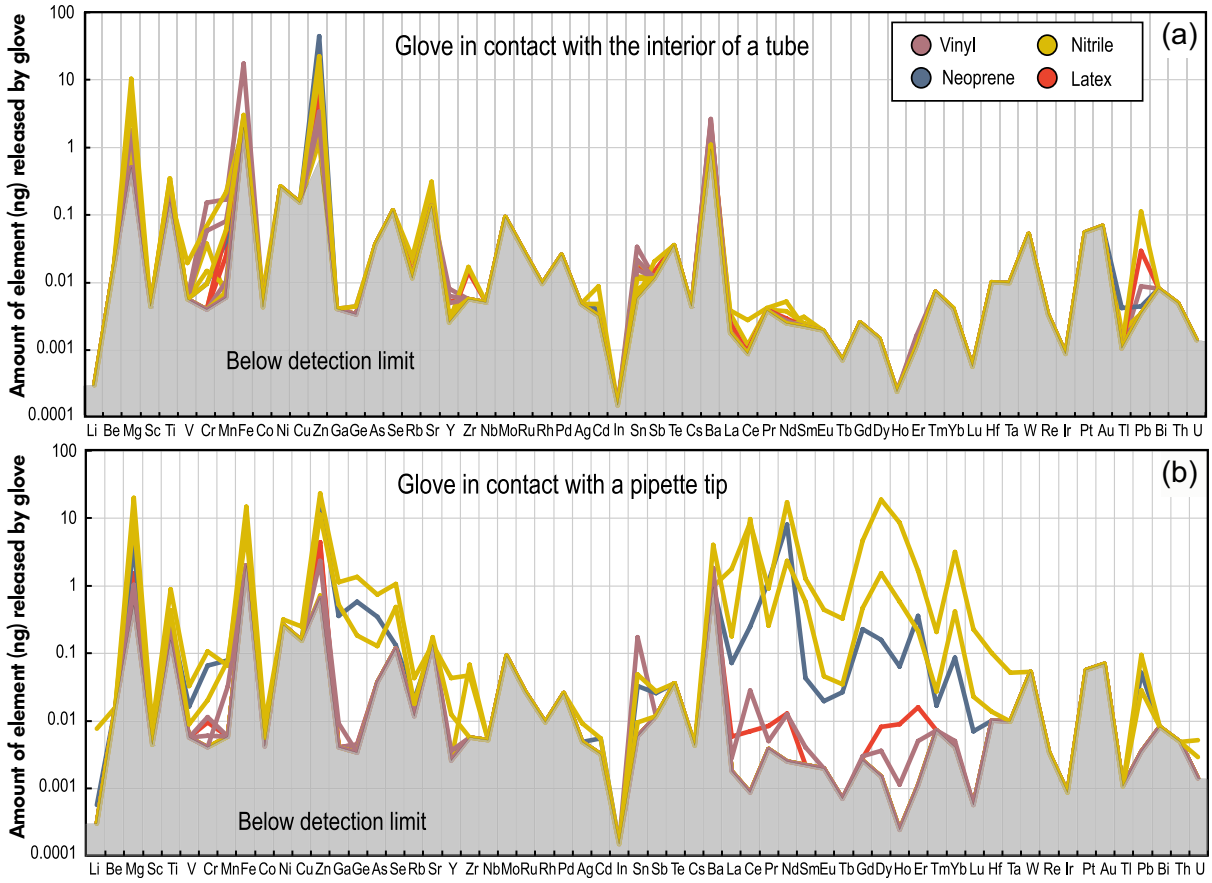

Figure 4. Amount of trace and minor elements (ng) released by gloves by short contact with (a) the interior of a polypropylene tube and (b) a 1-ml pipette tip (results of Test B). The grey field represents values below detection limits defined following IUPAC guidelines as the average number of counts measured in blanks plus three times the standard deviation (see section Analyses for trace element content for more details). When the amount of element detected in a solution was below the detection limit (< DL in Appendix S2), it is represented as equal to the detection limit in the two panels. [Colour figure can be viewed at wileyonlinelibrary.com]

amount of Co; 100 times the amounts of Mg, Fe, Se and Rb; and up to ten times the amounts of Cu and Mo. Whatever the chosen reference, the results of Test A indicate that almost all elements are present at higher levels in the glove leaches than in the samples themselves, which constitutes a tremendous potential for contamination. This conclusion is supported by the results of our second test (Test B) aiming to quantify the amount of trace elements released by gloves by a single contact with either a dry pipette tip that is then used to pipette the sample or the interior of a polypropylene tube in which the sample is stored (Appendix S2 and Figure 4). This test demonstrates that high amounts (between 1 and ~ 40 ng) of Mg, Fe, Zn, Ba, La, Ce, Nd, Sm, Gd, Dy, Ho, Er, Yb and non-negligible amounts (between 0.1 and 1 ng) of Ti, Cr, Mn, Cu, Ga, Ge, As, Se, Sn, Eu, Tb, Tm, Lu and Pb can be transferred from the glove to the sample by a single contact with labware. The contamination can, however, reach much higher values if repeated contacts between labware and glove occur during sample preparation and analysis. Surprisingly, the neoprene glove G5 and the nitrile gloves G10 and G15 released comparable amounts of REEs in the solutions of Test A and Test B although the two experiments were very different in design and duration. During Test A, we noted that the soaking solutions of G5 and G10 were cloudy, possibly indicating the presence of small particles in suspension. The surface of gloves G5, G10 and G15 is also rougher and more granular than the other gloves, which may be related to the easier release of particles from their surface by single dry contact. Whatever the case, Test B represents only one possible scenario of contamination in the laboratory. The behaviour of wet gloves or gloves exposed to acid fumes was not tested and could be very different. Careful handling of the samples is thus crucial to reduce the risk of contamination. Contamination of

Table 2.
Zinc isotopic composition ($\delta^{66}Zn$) of gloves

Sample Name	$^{66}Zn/^{64}Zn$	2SE	$\delta^{66}Zn$ (‰) JMC 3-0749L
G1[a]	0.562961	1.30E-05	0.34
G1 dup[a]	0.562900	1.09E-05	0.23
G2[a]	0.562738	1.02E-05	-0.05
G2[a] bis	0.562751	9.92E-06	-0.04
G3	0.562811	5.84E-06	0.17
G3 dup	0.562789	4.75E-06	0.14
G4	0.562727	8.20E-06	0.00
G5	0.562869	8.99E-06	0.19
G5 bis	0.562868	8.24E-06	0.20
G6	0.562735	1.50E-05	0.02
G7	0.562652	6.35E-06	-0.14
G8[a]	0.563036	4.71E-06	0.26
G8 dup[a]	0.562943	7.26E-06	0.07
G9	0.563050	4.42E-06	0.24
G9 bis	0.563046	4.80E-06	0.25
G10	0.563036	4.66E-06	0.18
G10 bis	0.563049	4.77E-06	0.23
G11	0.562807	4.60E-06	-0.20
G12	0.563034	5.75E-06	0.19
G12 bis	0.563039	5.03E-06	0.24
G13	0.562959	5.82E-06	0.04
G13 bis	0.562954	5.52E-06	0.03
G14[a]	0.562973	6.67E-06	0.12
G15	0.562895	9.60E-06	-0.13
G15 bis	0.562880	9.00E-06	-0.16

[a] Samples processed on column chemistry. bis stands for re-run analyses. dup stands for complete duplicate analyses. 2SE are in-run errors.

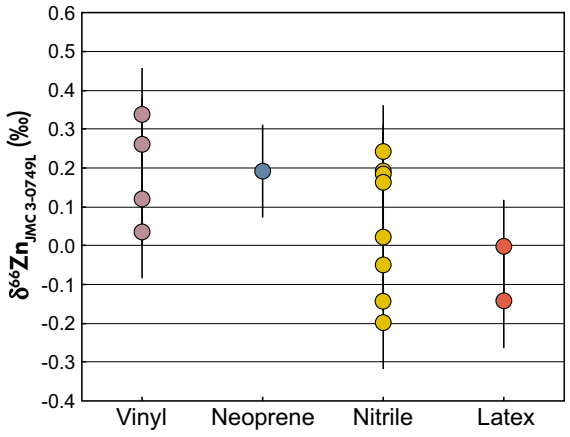

Figure 5. Zinc isotopic compositions ($\delta^{66}Zn$) of the tested gloves. Error bars are fixed at ± 0.12‰ based on complete duplicate analyses. [Colour figure can be viewed at wileyonlinelibrary.com]

labware by gloves when acid-washing pipette tips, beakers and polypropylene tubes is, in particular, a serious concern. The operation requires several handlings with gloves that may contaminate the labware rather than clean it. We thus suggest the use of plastic tongs at every step of the acid-washing procedure to avoid direct contact between gloves and labware, and subsequent contamination of the samples.

The two tests show that all gloves contain high amounts of trace and minor elements, which is a potentially serious source of contamination for trace element and isotopic analyses. However, the amount of elements released depends on the material from which the glove is made. Except for In and Sn, nitrile, latex and neoprene gloves generally contain higher amounts of leachable elements than vinyl gloves, on average between 10 and 100 times more Mg, Ti, V, Cr, Mn, Co, Ni, Zn, Se, Rb, Sr, Y, Zr, Nb, Rh, Cd, Cs, Ba, LREE, Hf, Pt, Tl, Pb and U (Figures 2 and 3). Similarly, results from Test B (Figure 4) show that vinyl gloves generally release less Zn and other elements (below detection limits), with the exception of Sn and Fe, by single contact with labware. The adequacy of each type of glove for handling a particular type of chemical needs to be established by rigorous testing and should not be presumed without such testing. However, the wearer needs to keep in mind that the risk of sample contamination is higher for most elements when using gloves made of nitrile, latex or neoprene to acid-wash labware and to prepare and analyse geological and biological samples.

Why are the gloves so enriched in trace elements?

The high Zn content in rubber gloves (i.e., neoprene, latex and nitrile) is very likely explained by manufacturing processes and the use of activators and accelerators such as Zn oxide and Zn organic carbamates or thiazoles (Nieuwenhuizen 2001). These catalysts are used to 'cure' the rubber (i.e., sulfur vulcanisation), an industrial process that allows the cross-linking of rubber macromolecules to confer strength, elasticity and good aging properties to the gloves. Even if most suppliers ensure low levels of accelerators in the finished products, the certificates of analysis that we were able to consult for some of the tested gloves (nitrile and latex) indicate Zn mass fractions between 2 and 60 $\mu g\ g^{-1}$, which is still extremely high if the gloves are used for trace element or isotopic work. Since other trace elements are generally positively correlated with Zn (Figure 3), we suspect that they derive from the Zn catalysts used to cure the rubber. Note that the data are more scattered for Zr-Hf and REEs (Figures 3d, g), which could be related to the type of Zn catalyst. Trace elements are probably present in different proportions in Zn oxides and Zn complexes (carbamates and thiazoles). The type of Zn catalysts added to rubber mixtures depends on industrial processes and is highly variable from one glove to another. According to the information available on the websites of some of the glove

manufacturers, two nitrile gloves from the same brand can be made from rubber treated with Zn oxides or Zn complexes or a combination of both. Unfortunately, the exact recipe used by glove manufacturers is not available for each tested glove making it difficult to establish a direct relationship between the type of Zn catalyst used and the trace element budget of the finished product.

For vinyl gloves, the lower but still significant mass fractions of Zn cannot be accounted for the use of Zn activators and accelerators for sulfur vulcanisation since this process is used for rubber only, not for plastic such as vinyl (i.e., PVC). The presence of Ca-Zn stabilisers is, however, clearly mentioned in the composition of all tested vinyl gloves. Such stabilisers are used to prevent the degradation of PVC when heated to soften during the extrusion or moulding processes (Balköse *et al.* 2001, Fang *et al.* 2009). Ca-Zn stabilisers are very likely the sources of most trace and minor elements released by vinyl gloves.

For both plastic and rubber gloves, zinc and associated trace elements are additives entering directly in the composition of the gloves. They are not carried in a coating or disseminated at the surface of the gloves, except possibly REEs for the neoprene glove G5 and the nitrile gloves G10 and G15. Prewashing the gloves under water or acid-washing them before use as recommended by Friel *et al.* (1996) might slightly reduce the risk of contamination, but is probably not enough to totally rule out the risk of contamination. In our opinion, the most efficient way to minimise the contamination is to avoid as much as possible the contact between gloves and labware during washing, preparation and analyses.

Effect of glove contamination on Zn isotopic compositions

Zinc is clearly the most abundant leachable element in all types of glove, which means that glove contamination is a serious concern for the measurement of the Zn concentrations in biological and geological samples. But, what about zinc isotopic compositions? Zinc isotopic compositions have been used to understand both Earth and planetary processes, including the formation of the Solar System (Bridgestock *et al.* 2014), the origin of the Moon (Paniello *et al.* 2012), magmatic differentiation processes occurring in the bulk silicate Earth (Chen *et al.* 2013), as well as biological processes (Pichat *et al.* 2003, Cloquet *et al.* 2008, Moynier *et al.* 2009, Aucour *et al.* 2015), metabolic and pathological reactions in humans and mammals (Ohno *et al.* 2005, Stenberg *et al.* 2005, Büchl *et al.* 2008, Balter *et al.* 2010, Moynier *et al.* 2013), dietary habits (Van Heghe *et al.* 2012, Jaouen *et al.* 2013b, Costas-Rodríguez *et al.* 2014) and as markers of gender and age (Jaouen *et al.* 2013a). More recently, the use of this analytical tool is also increasing in the disease-related research field where stable isotopes are used as new biomarkers of diverse pathologies such as breast cancer (Larner *et al.* 2015). In these studies, the relevance of the results and the associated interpretations are based on highly precise isotopic ratios by MC-ICP-MS because the range of isotopic variation in geological samples and, in particular, in biological samples is relatively small, a few per mil at most. To date, the measurement precision on $\delta^{66}Zn$ measured by MC-ICP-MS can be lower than ± 0.1‰ (2*s*) when performed under optimal analytical conditions (i.e., high sensitivity, stable plasma, elevated Zn content in samples).

To quantify the impact of glove contamination on Zn isotopic compositions, we calculated the Zn isotopic composition of a binary mixture of few nanograms of Zn from gloves and the rest from geological or biological samples that have different Zn isotopic compositions (Figure 6). We re-wrote the classical mixing equation to express the Zn isotopic composition of a binary mixture as a function of the amount of Zn present in the two end-members:

$$\left(\frac{^{66}Zn}{^{64}Zn}\right)_{mixture} = \frac{mZn_{glove}}{mZn_{glove} + mZn_{sample}} \left(\frac{^{66}Zn}{^{64}Zn}\right)_{glove} + \frac{mZn_{sample}}{mZn_{glove} + mZn_{sample}} \left(\frac{^{66}Zn}{^{64}Zn}\right)_{sample} \quad (2)$$

where mZn_{glove} and mZn_{sample} are the amount of Zn (generally in ng) from the glove and the sample, respectively. For the glove end-member, we used the average Zn isotopic composition of all gloves [$\delta^{66}Zn$ = +0.10 ± 0.32‰ (2*s*); Table 2] and the average amount of Zn released in Test B for both pipette tips and tubes [=6.0 ± 19.3 ng (2*s*); Appendix S2]. Note that 6.0 ng is a minimum since the average amount of Zn released by one contact with glove was calculated taking analyses below detection limit equal to zero ng in Appendix S2. Then, we considered three different scenarios to account for different degrees of contamination: (a) glove in contact with labware once during acid-washing, sample preparation and analysis such as mZn_{glove} = 6.0 ng; (b) glove in contact with labware twice such as mZn_{glove} = 2*6.0 ng; and (c) glove in contact with labware three times such as mZn_{glove} = 3*6.0 ng. For each scenario, we calculated the effect of contamination on Zn isotopic compositions as a function of the amount of Zn processed through chemistry and determined by MC-ICP-MS (i.e., 30 ng < mZn_{sample} < 500 ng, *cf.* Figure 6).

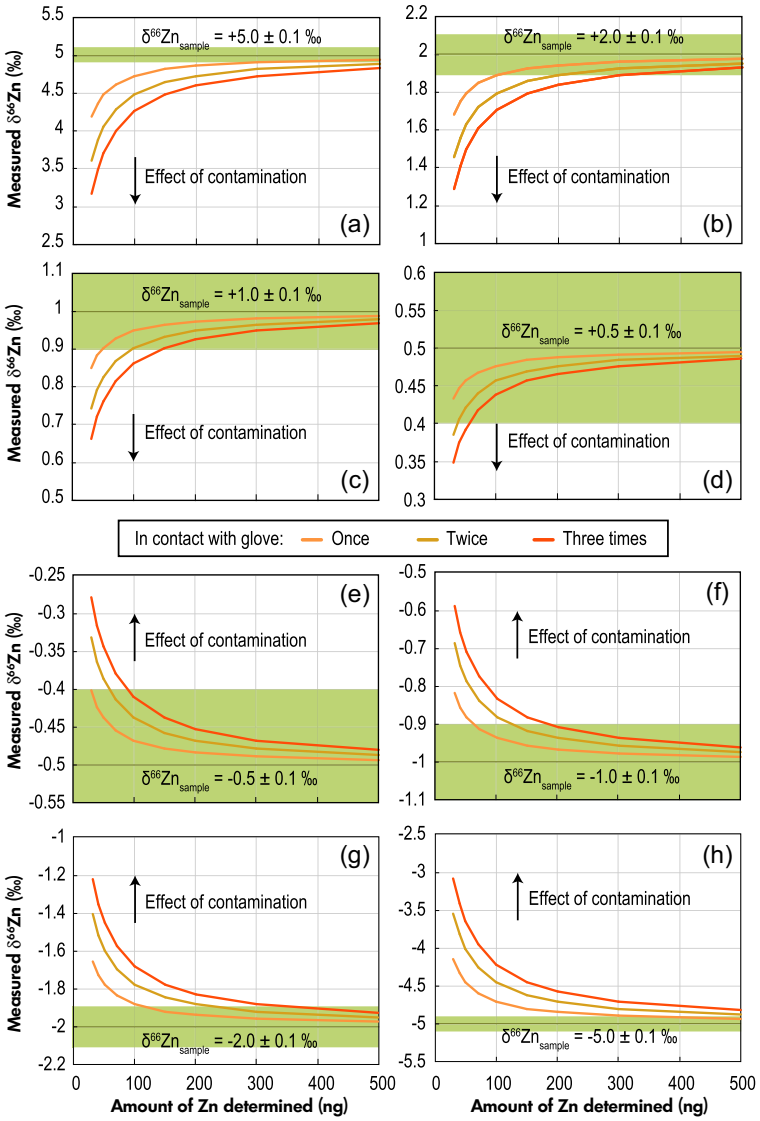

Figure 6. Effect of contamination by gloves on Zn isotopic compositions as a function on the amount of Zn processed through chemistry and determined by mass spectrometry. For this calculation, we used the average δ^{66}Zn of all tested gloves (δ^{66}Zn = +0.10‰) and assumed that the amount of Zn released by gloves for one contact was equal to 6.0 ng (average amount of Zn released in Test B), 2*6.0 ng for two contacts and 3*6.0 ng for three contacts. The green field shows the isotopic composition of the sample and its measurement precision that is fixed at ± 0.1‰ (2s) for this figure. More information about the calculation can be found in the main text. [Colour figure can be viewed at wileyonlinelibrary.com]

Geological samples: In terrestrial and extra-terrestrial samples, the range of variability of Zn isotopic compositions can be quite large. Extreme δ^{66}Zn values of -7.4‰ and +6.4‰ have been reported by Moynier *et al.* (2011) and Herzog *et al.* (2009) in meteorites (EL6 chondrites) and lunar soils, respectively. Gloves have an average δ^{66}Zn of ~ 0‰. As expected, Figure 6 shows that the larger the difference is between δ^{66}Zn of glove and sample, the greater is the effect of contamination. For extreme sample compositions of -5‰ and +5‰, one contact between glove and labware during washing, preparation or analysis is enough to shift the measured isotopic compositions beyond their uncertainties (i.e., ± 0.1‰, 2*s*) given typical amounts of Zn processed through chemistry and subsequently determined by MC-ICP-MS (Figure 6a, h). For low amounts of Zn determined (< 50 ng), shifts in δ^{66}Zn due to contact with gloves can reach ± 0.5‰ (one contact) and almost ± 2‰ in the worst scenario (i.e., three contacts).

In geological materials, most δ^{66}Zn values, however, cluster between -1‰ and +1‰ (see e.g., the values reported by Chen *et al.* (2016) for seventeen whole-rock reference materials). For these more typical Zn isotopic compositions (*cf.* Figure 6c–f), the effect of glove contamination is less important though shifts of more than ± 0.1‰ can occur if less than 200 ng is processed through chemistry and three contacts between glove and labware occur during the analytical procedure. Taking into account the whole range of possible isotopic compositions for terrestrial and extra-terrestrial samples, we thus recommend that a minimum of 500 ng of Zn be processed through chemistry and determined. Extreme precaution when acid-washing labware, preparing and analysing samples is, however, required since any contact with glove would shift extreme Zn isotopic compositions beyond the precision level taken here at ± 0.1‰. If duplicate analyses allow for a better measurement precision on δ^{66}Zn values, for example down to 0.03‰ (2*s*) as reported by Chen *et al.* (2016), then higher amounts of Zn should be analysed to make sure the effect of glove contamination remains negligible.

Biological samples: The range of δ^{66}Zn measured in biological samples varies between -1‰ and +2‰ (e.g., Moynier *et al.* 2009, Balter *et al.* 2010, Jaouen *et al.* 2013a, b, Larner *et al.* 2015). To our knowledge, no extreme values outside this range have been reported so far. Biological samples such as body fluids are often not very concentrated in Zn, for example no more than a few μg g^{-1} in urine (Balter *et al.* 2010) and few hundred ng g^{-1} in cerebro-spinal fluids. Moreover, the amount of sample available for research purposes is restricted to extremely low quantities; hence, the total amount of Zn available for isotopic compositions in a biological sample sometimes does not exceed 50 ng. Figure 6 shows that for such low amounts of Zn, one contact between glove and labware could significantly shift the measured Zn isotopic composition beyond the measurement uncertainties (i.e., > ± 0.1‰, *cf.* Figure 6c–f). For instance, for a typical δ^{66}Zn of +1‰ (Figure 6c), one contact with a glove can bias δ^{66}Zn by ~ 0.1‰ and three contacts by more than 0.3‰ if the amount of Zn determined is below 50 ng. The effect of contamination becomes negligible, that is within the measurement precision of ± 0.1‰, when the amount of Zn processed through chemistry and subsequently determined is higher than 300 ng. We thus recommend that, whenever possible, measurements of Zn isotopic compositions in biological samples be done on amounts > 300 ng. In the case where the measurement precision is estimated to be better than ± 0.1‰, the amount of Zn analysed should be increased accordingly.

Conclusions

The new generation of mass spectrometers and the curiosity of scientists to analyse an increasing number of elements with high precision and sensitivity require increasingly low procedural blanks and control on potential exogenic contamination during sample preparation and analysis. The results of this study clearly show that gloves are a primary and important source of contamination in clean laboratories for both trace element and isotope studies. Of the sixty elements measured in nitrile, latex, neoprene and vinyl gloves, very few appear to be safe from potential contamination. Soaking of gloves in weak acid (0.4 mol l^{-1} HNO_3 + 0.05 mol l^{-1} HF) at room temperature for several hours released significant amounts of trace elements, up to 17 mg of Zn, 200 μg of Mg and 10–60 μg of Ti, Fe, Sr and Zr. Compared with vinyl gloves, nitrile, latex and neoprene gloves are much more enriched in leachable elements, with the exception of In and Sn.

The tests also indicate that most elements are easily transferred from the gloves to the sample by simple contact of a pipette tip or the interior of a polypropylene tube. Acid-washing labware is in particular a potential major source of contamination since it requires several handlings with gloves.

Zinc has by far the highest risk of being contaminated by gloves. A single dry contact between labware and gloves releases an average of 6.0 ± 19.3 (2*s*) ng of Zn into the samples. Such contamination has variable effects on the Zn isotopic composition of the sample depending on the amount of Zn processed through chemistry and the difference between the Zn isotopic composition of the studied sample and that of the glove. All tested gloves shared roughly the same δ^{66}Zn (average δ^{66}Zn = +0.10 ± 0.32‰ (2*s*)). The lower the amount of Zn processed through chemistry, and the higher the difference between δ^{66}Zn of the sample and the glove, the greater is the effect of contamination. Whatever the amount of Zn determined (from 30 to 500 ng), a single contact between glove and labware is enough to bias the composition of a sample with extreme δ^{66}Zn of -5 or +5‰ beyond the measurement precision taken at ± 0.1‰ here. A bias as large as ± 1.5‰ can be reached for samples with extreme δ^{66}Zn of -5 or +5‰ if the amount of Zn deterrmined is low (< 50 ng), and labware is touched repeatedly during washing, preparation or analysis. For typical δ^{66}Zn values between -1‰ and +2‰, a minimum of 300 ng of Zn should be analysed to limit the potential bias due to glove contamination below 0.1‰.

We recommend the following best practices to keep glove-derived contamination in control: (a) recognise that

gloves can be a significant source of laboratory contamination, (b) carry out every step of washing procedures with clean tongs to minimise contact between gloves and labware, (c) take extreme precautions when handling samples for trace element and Zn isotopic compositions with any type of glove, (d) monitor and minimise glove contamination using Zn contents in blanks even if Zn is not in the analysis protocol and (e), for Zn isotopic compositions, measure whole procedural blanks routinely (i.e., in every batch of samples) and calculate the effect of contamination on each sample using Equation (2). If the isotopic bias exceeds the measurement precision, reject the data.

Acknowledgements

We would like to thank C. Chauvel and M. Horan for providing some of the tested gloves; C. Bosq for ensuring optimal working conditions in the clean laboratory; and T. Mock, P. Télouk and J-L. Piro for their assistance with the mass spectrometers. We acknowledge two anonymous reviewers for their constructive comments on the first version of the manuscript. This study was financed by the Carnegie Institution for Science, the French Government Laboratory of Excellence initiative no. ANR-10-LABX-0006, the Région Auvergne and the European Regional Development Fund. This is Laboratory of Excellence ClerVolc contribution number 225.

References

Aucour A.-M., Bedell J.-P., Queyron M., Magnin V., Testemale D. and Sarret G. (2015)
Dynamics of Zn in an urban wetland soil–plant system: Coupling isotopic and EXAFS approaches. **Geochimica et Cosmochimica Acta**, **160**, 55–69.

Balköse D., Gökçel H.İ. and Göktepe S.E. (2001)
Synergism of Ca/Zn soaps in poly (vinyl chloride) thermal stability. **European Polymer Journal**, **37**, 1191–1197.

Balter V., Zazzo A., Moloney A.P., Moynier F., Schmidt O., Monahan F.J. and Albarède F. (2010)
Bodily variability of zinc natural isotope abundances in sheep. **Rapid Communications in Mass Spectrometry**, **24**, 605–612.

Bridgestock L.J., Williams H., Rehkämper M., Larner F., Giscard M.D., Hammond S., Coles B., Andreasen R., Wood B.J., Theis K.J., Smith C.L., Benedix G.K. and Schönbächler M. (2014)
Unlocking the zinc isotope systematics of iron meteorites. **Earth and Planetary Science Letters**, **400**, 153–164.

Büchl A., Hawkesworth C.J., Ragnarsdottir K.V. and Brown D.R. (2008)
Re-partitioning of Cu and Zn isotopes by modified protein expression. **Geochemical Transactions**, **9**, 11.

Chauvel C., Bureau S. and Poggi C. (2011)
Comprehensive chemical and isotopic analyses of basalt and sediment reference materials. **Geostandards and Geoanalytical Research**, **35**, 125–143.

Chen H., Savage P.S., Teng F.-Z., Helz R.T. and Moynier F. (2013)
Zinc isotope fractionation during magmatic differentiation and the isotopic composition of the bulk Earth. **Earth and Planetary Science Letters**, **369–370**, 34–42.

Chen S., Liu Y., Hu J., Zhang Z., Hou Z., Huang F. and Yu H. (2016)
Zinc isotopic compositions of NIST SRM 683 and whole-rock reference materials. **Geostandards and Geoanalytical Research**, **40**, 417–432.

Cloquet C., Carignan J., Lehmann M.F. and Vanhaecke F. (2008)
Variation in the isotopic composition of zinc in the natural environment and the use of zinc isotopes in biogeosciences: A review. **Analytical and Bioanalytical Chemistry**, **390**, 451–463.

Costas-Rodríguez M., Van Heghe L. and Vanhaecke F. (2014)
Evidence for a possible dietary effect on the isotopic composition of Zn in blood via isotopic analysis of food products by multi-collector ICP-mass spectrometry. **Metallomics**, **6**, 139–146.

Fang L., Song Y., Zhu X. and Zheng Q. (2009)
Influence of lanthanum stearate as a co-stabilizer on stabilization efficiency of calcium/zinc stabilizers to polyvinyl chloride. **Polymer Degradation and Stability**, **94**, 845–850.

Friel J.K., Mercer C., Andrews W.L. and Simmons B.R. (1996)
Laboratory gloves as a source of trace element contamination. **Biological Trace Element Research**, **54**, 135–142.

Herzog G.F., Moynier F., Albarède F. and Berezhnoy A.A. (2009)
Isotopic and elemental abundances of copper and zinc in lunar samples, Zagami, Pele's hairs, and a terrestrial basalt. **Geochimica et Cosmochimica Acta**, **73**, 5884–5904.

Hoffmann J. (1988)
Experience with the sources of contamination when preparing samples for the analysis of trace elements. **Fresenius Zeitschrift für Analytische Chemie**, **331**, 220–222.

Jaouen K., Gibert M., Lamboux A., Télouk P., Fourel F., Albarède F., Alekseev A.N., Crubézy E. and Balter V. (2013a)
Is aging recorded in blood Cu and Zn isotope compositions? **Metallomics**, **5**, 1016–1024.

references

Jaouen K., Pons M.-L. and Balter V. (2013b)
Iron, copper and zinc isotopic fractionation up mammal trophic chains. Earth and Planetary Science Letters, 374, 164–172.

Larner F., Woodley L.N., Shousha S., Moyes A., Humphreys-Williams E., Strekopytov S., Halliday A.N., Rehkämper M. and Coombes R.C. (2015)
Zinc isotopic compositions of breast cancer tissue. Metallomics, 7, 112–117.

Maréchal C.N., Télouk P. and Albarède F. (1999)
Precise analysis of copper and zinc isotopic compositions by plasma-source mass spectrometry. Chemical Geology, 156, 251–273.

Moynier F., Pichat S., Pons M.-L., Fike D., Balter V. and Albarède F. (2009)
Isotopic fractionation and transport mechanisms of Zn in plants. Chemical Geology, 267, 125–130.

Moynier F., Paniello R.C., Gounelle M., Albarède F., Beck P., Podosek F. and Zanda B. (2011)
Nature of volatile depletion and genetic relationships in enstatite chondrites and aubrites inferred from Zn isotopes. Geochimica et Cosmochimica Acta, 75, 297–307.

Moynier F., Fujii T., Shaw A.S. and Le Borgne M. (2013)
Heterogeneous distribution of natural zinc isotopes in mice. Metallomics, 5, 693.

Nieuwenhuizen P.J. (2001)
Zinc accelerator complexes: Versatile homogeneous catalysts in sulfur vulcanization. Applied Catalysis A: General, 207, 55–68.

Ohno T., Shinohara A., Chiba M. and Hirata T. (2005)
Precise Zn isotopic ratio measurements of human red blood cell and hair samples by multiple collector ICP-mass spectrometry. Analytical Sciences, 21, 425–428.

Palme H. and O'Neill H.St.C. (2014)
Cosmochemical estimates of mantle composition. In: Holland H.D. and Turekian K.K. (eds), Treatise on Geochemistry (2nd edition), vol. 3. Elsevier (Pergamon), 1–39.

Paniello R.C., Day J.M.D. and Moynier F. (2012)
Zinc isotopic evidence for the origin of the Moon. Nature, 490, 376–379.

Pichat S., Douchet C. and Albarède F. (2003)
Zinc isotope variations in deep-sea carbonates from the eastern equatorial Pacific over the last 175 ka. Earth and Planetary Science Letters, 210, 167–178.

Stenberg A., Malinovsky D., Öhlander B., Andrén H., Forsling W., Engström L.-M., Wahlin A., Engström E., Rodushkin I. and Baxter D.C. (2005)
Measurement of iron and zinc isotopes in human whole blood: Preliminary application to the study of HFE genotypes. Journal of Trace Elements in Medicine and Biology, 19, 55–60.

Van Heghe L., Engström E., Rodushkin I., Cloquet C. and Vanhaecke F. (2012)
Isotopic analysis of the metabolically relevant transition metals Cu, Fe and Zn in human blood from vegetarians and omnivores using multi-collector ICP-mass spectrometry. Journal of Analytical Atomic Spectrometry, 27, 1327.

Supporting information

The following supporting information may be found in the online version of this article:

Appendix S1. Results of Test A (gloves).

Appendix S2. Results of Test B (tube or pipette).

Appendix S3. Comparison of duplicate analyses (Test A).

Appendix S4. Comparison of zinc isotopic compositions.

This material is available as part of the online article from: http://onlinelibrary.wiley.com/doi/10.1111/ggr.12161/abstract (This link will take you to the article abstract).

Appendix S1.

Amount of trace elements (ng) released by gloves soaked in 20 ml of 0.4 mol l^{-1} HNO_3 + 0.05 mol l^{-1} HF for 40 hours (results of Test A)

	G1	G1 Dup	G2	G3	G3 Dup	G4	G5	G5 Dup	G6	G7	G8	G9	G10	G11	G12	G13	G14	G15	***Detection limit***
Type	Vinyl		Nitrile	Nitrile		Latex	Neoprene		Nitrile	PFE Latex	Vinyl	Nitrile	Nitrile	Nitrile	Nitrile	Vinyl	Vinyl	Nitrile	
Li	<DL	<DL	47	19.7	18.6	102	11.8	13.1	<DL	284	<DL	37	30.2	<DL	<DL	<DL	<DL	<DL	*9.89*
Be	<DL	<DL	23.4	5.86	5.94	15.8	0.484	0.482	2.28	38.4	<DL	2.74	0.674	0.546	0.66	<DL	3.06	9.8	*0.201*
Mg	1762	1138	54520	20300	20380	235020	40140	43340	21840	249640	*Not measured*	*Not measured*	*Not measured*	*Not measured*	*Not measured*	*Not measured*	*Not measured*	*21520*	*30.4*
Sc	82.6	82.8	514	109	108	191	<DL	<DL	<DL	238	<DL	177	<DL	<DL	<DL	<DL	<DL	<DL	*67.9*
Ti	184	166	3320	13900	17440	1372	3820	3480	1396	4480	45.2	12160	1850	874	1546	59.6	132	6840	*37.0*
V	3.2	2.58	536	86.2	87.2	134	24.2	26	64.2	166	1.53	65.8	97.8	11.7	14	3.7	2.8	19.8	*0.473*
Cr	22.6	11.4	604	322	248	362	392	416	109	224	55.2	163	66.2	173	183	59.8	31	382	*5.05*
Mn	19.1	14.4	1086	1176	1176	720	362	430	778	2480	56.6	516	88.2	165	290	46.6	31.4	2020	*6.16*
Fe	<DL	<DL	18160	12700	14660	20500	<DL	<DL	3340	22840	6160	15000	3740	5420	6720	4160	1950	7520	*10.8*
Co	1.22	0.858	32.8	11.6	11.7	20.2	15.9	17.2	58	28.2	1.96	4.94	4.54	3.04	6.9	1.99	0.93	3.24	*0.351*
Ni	27.4	11.9	244	186	182	694	226	234	160	714	15.7	72	47.8	59.8	124	15.4	13.7	141	*1.47*
Cu	<DL	<DL	69	152	132	109	482	538	103	310	23.6	<DL	40.2	79.4	48	<DL	110	<DL	*22.4*
Zn	26480	13320	5960660	14926600	17275740	3397960	8118300	8409500	935080	9898660	11200	3955600	829520	71160	369860	55640	17700	10159800	*9.72*
Ga	<DL	<DL	204	40.8	45	119	3.34	3.96	2.22	157	1.19	30.2	23.6	2.76	12	<DL	5.62	22	*1.1*
Ge	<DL	<DL	<DL	<DL	<DL	<DL	<DL	<DL	<DL	<DL	<DL	<DL	<DL	<DL	<DL	<DL	<DL	<DL	*17.2*
As	21	18.2	134	67.4	68	71.8	7.42	8.32	25.2	166	3.46	29	41.4	25	5	19.1	9.64	42.4	*1.43*
Se	<DL	<DL	94.4	246	268	87.2	144	174	<DL	184	<DL	<DL	<DL	<DL	<DL	<DL	<DL	<DL	*29.2*
Rb	9.32	6.92	392	132	138	666	42.8	55.2	57.8	2120	1.65	35.8	26.4	29.4	11	4.44	25.8	85.8	*0.28*
Sr	48.6	26.6	2480	16880	18980	2080	836	980	15240	3760	32	2860	860	134	1598	111	61.2	1040	*4.08*
Y	0.268	0.172	102	5.52	5.02	408	5.06	5.54	37.4	374	0.504	12	9.5	1.95	12.4	0.58	3.52	2.54	*0.0885*
Zr	15.1	16.7	554	57320	63300	528	3600	4060	1590	304	19.6	28100	4340	73.8	5200	37	53	7220	*4.96*
Nb	0.0932	0.0638	6.38	60	67	6.1	3.04	3.9	0.726	6.16	0.206	6.58	4.6	1.08	4.34	0.22	0.6	1.75	*0.0516*
Mo	<DL	<DL	4.66	13.1	12.7	4.04	3.1	3.64	18.1	1.78	1.97	3.24	2.62	5.54	2.8	2.54	2.86	1.03	*0.316*
Ru	<DL	<DL	<DL	0.135	<DL	<DL	<DL	<DL	0.143	0.122	<DL	<DL	<DL	<DL	<DL	<DL	<DL	<DL	*0.115*
Rh	<DL	<DL	0.0948	0.318	0.34	0.121	<DL	<DL	0.296	0.122	<DL	0.122	<DL	<DL	0.051	<DL	<DL	<DL	*0.0488*
Pd	0.768	<DL	5.98	18.5	20.6	13.3	1.29	1.54	19.4	14.7	0.938	6.58	2.46	0.442	3.98	<DL	2.98	2.2	*0.354*
Ag	<DL	<DL	7.48	163	181	3.94	16.5	19.4	6.22	6.84	<DL	112	17.9	2.32	21.6	0.638	<DL	20.4	*0.233*
Cd	<DL	<DL	13.6	45.6	46.2	23	7.24	8.44	16.2	35.6	<DL	70.4	16.1	1.2	8.54	<DL	<DL	12.1	*0.388*
In	41.4	28	0.98	0.0938	0.0938	0.718	0.248	1.23	0.058	0.954	<DL	<DL	<DL	<DL	<DL	<DL	0.23	<DL	*0.0428*
Sn	13280	8980	106	24.2	23.8	48.8	76.2	380	13.8	70.6	66.6	32.6	4.56	13.1	5.18	35.4	54	6.64	*0.163*
Sb	1	0.718	23	2.2	2.02	5.7	1.18	2.42	2.76	16.4	0.682	4.42	3.1	5.56	2.08	0.63	2.86	4.24	*0.116*
Te	<DL	<DL	<DL	<DL	<DL	<DL	<DL	<DL	<DL	<DL	<DL	<DL	<DL	<DL	<DL	<DL	<DL	<DL	*1.85*
Cs	0.272	0.189	46.4	2.4	2.6	14.9	0.774	0.96	1.63	41.4	0.126	0.26	0.414	1.18	0.654	0.109	1.95	2.1	*0.0543*
Ba	131	86.6	362	904	874	684	178	234	428	590	16.2	1000	228	67.2	296	183	24.4	284	*1.74*
La	0.682	4.02	266	20.8	19.1	294	5.88	6.22	76.8	236	0.758	19.2	21.6	2.98	19.3	0.49	3.38	4.82	*0.137*
Ce	1.23	11.8	708	28	25.8	664	9	9.04	55.6	588	1.3	34	41.8	5.06	25.6	0.848	7.92	9.2	*0.336*
Pr	0.0862	<DL	54.8	3.14	2.9	78.8	0.906	1.06	5.14	68	0.232	3.7	5.02	0.544	2.78	0.103	0.944	0.548	*0.0774*
Nd	<DL	<DL	206	11.3	10.3	320	3.44	3.84	18.8	306	0.616	13.5	18.8	1.97	9.7	0.368	3.66	2.12	*0.328*
Sm	<DL	<DL	39	1.67	1.68	75.8	0.646	0.684	2.8	83	0.248	2.54	3.66	0.376	1.57	<DL	1.25	0.464	*0.228*
Eu	<DL	<DL	5.82	0.362	0.326	12.3	0.149	0.183	0.572	16	0.148	0.6	0.59	0.07	0.35	<DL	0.116	0.0968	*0.0527*
Tb	<DL	<DL	4.7	0.202	0.194	13	0.105	0.094	0.412	13.5	0.151	0.352	0.438	0.0478	0.242	<DL	0.156	0.0692	*0.0175*
Gd	<DL	<DL	36	1.53	1.45	79	0.682	0.77	3.18	87.6	0.216	2.38	3.14	0.294	1.64	<DL	1.12	0.434	*0.21*
Dy	<DL	<DL	24.4	1.09	1.01	75.6	0.504	0.604	2.44	75.4	0.22	2.12	2.02	0.244	1.42	<DL	0.832	0.432	*0.112*
Ho	<DL	<DL	4.38	0.23	0.208	14.5	0.129	0.123	0.548	14	0.133	0.422	0.314	0.0446	0.29	<DL	0.135	0.096	*0.0313*
Er	<DL	<DL	11.5	0.724	0.69	39.2	0.336	0.388	1.67	36.4	0.194	1.11	0.792	0.142	0.854	<DL	0.344	0.3	*0.0582*
Tm	<DL	<DL	1.46	0.114	0.106	5.18	0.0458	0.0608	0.228	4.68	0.138	0.167	0.101	<DL	0.12	<DL	0.0508	0.0542	*0.0166*
Yb	<DL	<DL	8.38	0.72	0.714	29.8	0.312	0.326	1.25	27	0.204	1.04	0.616	<DL	0.802	<DL	0.342	0.372	*0.136*
Lu	<DL	<DL	1.15	0.128	0.131	3.72	0.0488	0.0528	0.179	3.36	0.123	0.164	0.096	<DL	0.123	<DL	0.0474	0.0686	*0.0198*
Hf	0.3	0.388	19.2	1458	1532	12.4	78.4	90.4	30.4	8.14	0.496	688	96.8	1.58	109	0.774	1.41	172	*0.163*
Ta	<DL	<DL	0.836	5.72	5.88	0.392	0.246	0.268	0.0574	0.912	<DL	0.628	0.724	0.0844	1.04	<DL	0.114	0.476	*0.0299*
W	0.316	0.154	5.7	3.5	3.48	3.28	1.07	1.79	1.95	13.6	0.986	1.12	1.28	0.762	0.968	1.15	3.12	1.32	*0.141*
Re	<DL	<DL	<DL	<DL	<DL	<DL	<DL	<DL	<DL	<DL	<DL	<DL	<DL	0.125	0.0908	<DL	<DL	<DL	*0.081*
Ir	<DL	<DL	<DL	2.38	2.82	<DL	0.17	0.185	0.0726	<DL	<DL	2.08	0.302	<DL	0.354	<DL	0.204	0.346	*0.0591*
Pt	<DL	<DL	<DL	7.34	8.42	<DL	0.672	0.74	0.228	<DL	0.338	6.64	1.09	<DL	1.15	<DL	0.482	1.14	*0.157*
Au	0.91	0.308	1.34	5.74	5.7	0.56	0.39	0.416	1.04	0.518	0.342	4.88	1.54	<DL	1.03	<DL	1.5	1.84	*0.224*
Tl	1.33	0.886	240	2.88	3.02	11.8	107	134	1.5	9.72	<DL	0.478	0.868	7.88	3.38	0.28	0.168	6.66	*0.0849*
Pb	14.2	8.36	1552	1128	1064	2280	202	244	69.2	1118	6.86	1356	48.2	54.6	31.8	9.72	21	177	*0.516*
Bi	2.72	3.08	0.141	0.588	0.28	0.542	0.86	0.862	10.1	2.66	3.56	6.26	0.214	1.12	0.508	0.474	1.77	<DL	*0.0538*
Th	<DL	<DL	370	2.66	2.14	156	0.84	1.02	2.46	270	0.248	4.16	6.52	0.836	2.22	0.122	4.54	1.4	*0.0995*
U	0.458	0.302	73.2	12.1	12.9	33	0.77	0.912	10.6	23.4	0.195	37.6	2.24	0.798	2.4	0.44	2.18	1.85	*0.0531*

"Dup" stands for complete duplicate (i.e., glove from another unopened box). "<DL" means below detection limits defined following IUPAC guidelines as the average number of counts measured in blanks plus 3 times the standard deviation (see text for more details).

Appendix S2.
Amount of element (ng) released when glove is in contact with tube or pipette tip (results of Test B)

Glove	G1	G1	G1	G1	G2	G2	G3	G3	G3	G3	G4	G4	G5	G5	G5	G5	G6	G6	G7	G7	G8	G8	G9	G9	G10	G10	G11	G11	G12	G12	G13	G13	G14	G14	G15	G15	Detection limit
Type	Vinyl				Nitrile		Nitrile				Latex		Neoprene				Nitrile		Latex		Vinyl		Nitrile		Nitrile		Nitrile		Nitrile		Vinyl		Vinyl		Nitrile		
In contact with	Tube	Tube Dup	Pipette tip	Pipette tip Dup	Tube	Pipette tip	Tube	Tube Dup	Pipette tip	Pipette tip Dup	Tube	Pipette tip	Tube	Tube Dup	Pipette tip	Pipette tip Dup	Tube	Pipette tip	Tube	Pipette tip	Tube	Pipette tip	Tube	Pipette tip	Tube	Pipette tip	Tube	Pipette tip	Tube	Pipette tip	Tube	Pipette tip	Tube	Pipette tip	Tube	Pipette tip	
Li	<DL	<DL	<DL	<DL	<DL	<DL	<DL	<DL	<DL	<DL	<DL	<DL	<DL	<DL	0.00054854	0.000803469	<DL	<DL	<DL	<DL	<DL	<DL	<DL	<DL	<DL	0.00743	<DL	<DL	<DL	<DL	<DL	<DL	<DL	<DL	<DL	<DL	0.000292
Be	<DL	<DL	<DL	<DL	<DL	<DL	<DL	<DL	<DL	<DL	<DL	<DL	<DL	<DL	<DL	<DL	<DL	<DL	<DL	<DL	<DL	<DL	<DL	<DL	<DL	<DL	<DL	<DL	<DL	<DL	<DL	<DL	<DL	<DL	<DL	<DL	0.0155
Mg	1.58	0.54	<DL	<DL	1.72	<DL	0.583	<DL	<DL	2.93	0.673	1.49	1.63	<DL	4.02	10.5	0.865	0.775	1.49	<DL	0.514	<DL	<DL	<DL	10.1	19.6	<DL	<DL	0.929	<DL	1.74	0.993	<DL	<DL	4.4	9.33	0.497
Sc	<DL	<DL	<DL	<DL	<DL	<DL	<DL	<DL	<DL	<DL	<DL	<DL	<DL	<DL	<DL	<DL	<DL	<DL	<DL	<DL	<DL	<DL	<DL	<DL	<DL	0.00814	<DL	<DL	<DL	<DL	<DL	<DL	<DL	<DL	<DL	<DL	0.00431
Ti	0.258	0.247	<DL	<DL	0.236	<DL	0.18	0.18	<DL	0.236	0.157	<DL	<DL	0.213	0.292	0.74	0.157	<DL	0.303	<DL	0.191	<DL	0.292	<DL	0.191	0.852	0.337	<DL	0.191	<DL	0.281	0.247	0.191	<DL	0.337	0.415	0.154
V	<DL	<DL	<DL	<DL	<DL	<DL	<DL	<DL	<DL	0.012	<DL	<DL	<DL	<DL	0.0161	0.0192	<DL	<DL	<DL	<DL	<DL	<DL	<DL	<DL	0.0189	0.0319	<DL	<DL	<DL	<DL	<DL	<DL	<DL	<DL	<DL	0.00879	0.00554
Cr	0.149	<DL	<DL	<DL	<DL	<DL	0.0363	0.0497	<DL	0.0059	<DL	0.00927	0.00927	<DL	0.0649	0.0143	0.0143	<DL	<DL	<DL	<DL	0.011	<DL	<DL	0.0666	0.104	<DL	<DL	<DL	<DL	0.0565	<DL	<DL	0.0059	0.00927	0.0194	0.0039
Mn	0.165	<DL	<DL	<DL	0.0544	<DL	<DL	0.0445	<DL	<DL	0.024	<DL	0.0397	<DL	0.0764	0.0804	0.00858	<DL	0.0559	<DL	0.01	<DL	<DL	<DL	0.212	0.0639	<DL	<DL	0.00711	<DL	0.0786	0.0317	<DL	<DL	0.0577	0.0768	0.00576
Fe	17.1	<DL	<DL	<DL	<DL	<DL	<DL	3.88	<DL	3.81	<DL	<DL	<DL	<DL	<DL	7.01	<DL	<DL	<DL	<DL	<DL	<DL	<DL	<DL	<DL	14.4	<DL	<DL	<DL	<DL	2.72	<DL	<DL	<DL	3	6.18	1.96
Co	0.00512	<DL	<DL	<DL	<DL	<DL	<DL	<DL	<DL	0.00468	<DL	<DL	<DL	<DL	0.00688	0.00589	<DL	<DL	<DL	<DL	<DL	<DL	<DL	<DL	0.00699	0.0093	<DL	<DL	<DL	<DL	<DL	<DL	<DL	<DL	<DL	0.00556	0.00413
Ni	<DL	<DL	<DL	<DL	<DL	<DL	<DL	<DL	<DL	<DL	<DL	<DL	<DL	<DL	<DL	<DL	<DL	<DL	<DL	<DL	<DL	<DL	<DL	<DL	<DL	0.305	<DL	<DL	<DL	<DL	<DL	<DL	<DL	<DL	<DL	<DL	0.258
Cu	<DL	<DL	<DL	<DL	<DL	<DL	<DL	<DL	<DL	<DL	<DL	<DL	<DL	<DL	<DL	<DL	<DL	<DL	<DL	<DL	<DL	<DL	<DL	<DL	<DL	0.245	<DL	<DL	<DL	<DL	<DL	<DL	<DL	<DL	<DL	<DL	0.148
Zn	2.37	2.26	<DL	<DL	5.38	0.696	2.46	3.18	<DL	1.01	3.55	4.3	43.8	4.14	19	11.7	1.19	<DL	7.37	3.84	1.84	<DL	1.92	<DL	12.8	22.7	2.37	<DL	2.15	<DL	3.34	2.3	2.34	<DL	22.3	11	0.64
Ga	<DL	<DL	<DL	<DL	0.00405	<DL	<DL	<DL	<DL	0.0669	<DL	<DL	<DL	<DL	0.349	0.432	<DL	<DL	0.00405	<DL	<DL	<DL	<DL	<DL	<DL	1.11	<DL	<DL	<DL	<DL	<DL	0.00884	<DL	<DL	<DL	0.509	0.004
Ge	0.00434	<DL	<DL	<DL	<DL	<DL	<DL	<DL	<DL	0.0532	<DL	<DL	<DL	<DL	0.57	0.268	<DL	<DL	<DL	0.00434	<DL	0.00434	<DL	<DL	<DL	1.32	<DL	<DL	<DL	<DL	<DL	<DL	<DL	0.00434	0.181	0.00331
As	<DL	<DL	<DL	<DL	<DL	<DL	<DL	<DL	<DL	0.058	<DL	<DL	<DL	<DL	0.335	0.18	<DL	<DL	<DL	<DL	<DL	<DL	<DL	<DL	<DL	0.727	<DL	<DL	<DL	<DL	<DL	<DL	<DL	<DL	<DL	0.123	0.0355
Se	<DL	<DL	<DL	<DL	<DL	<DL	<DL	<DL	<DL	0.146	<DL	<DL	<DL	<DL	0.129	0.215	<DL	<DL	<DL	<DL	<DL	<DL	<DL	<DL	<DL	1.05	<DL	<DL	<DL	<DL	<DL	<DL	<DL	<DL	<DL	0.471	0.113
Rb	<DL	<DL	<DL	<DL	0.019	<DL	0.0116	<DL	<DL	<DL	0.0127	0.0116	<DL	<DL	0.0205	0.0142	<DL	<DL	<DL	<DL	<DL	<DL	<DL	<DL	0.023	0.0421	<DL	<DL	<DL	<DL	<DL	<DL	<DL	<DL	<DL	0.0174	0.0113
Sr	<DL	<DL	<DL	<DL	<DL	<DL	<DL	<DL	<DL	<DL	<DL	<DL	<DL	<DL	<DL	<DL	0.194	<DL	<DL	<DL	<DL	<DL	<DL	<DL	0.305	<DL	<DL	<DL	<DL	<DL	0.134	<DL	<DL	<DL	<DL	0.169	0.132
Y	0.00794	0.00326	<DL	<DL	0.0049	<DL	<DL	<DL	<DL	<DL	<DL	<DL	<DL	0.00303	0.00303	0.00872	<DL	<DL	0.00506	<DL	0.00287	<DL	<DL	<DL	<DL	0.0416	0.0028	<DL	<DL	<DL	0.00623	0.0035	0.00482	<DL	0.00334	0.012	0.0025
Zr	<DL	<DL	<DL	<DL	<DL	<DL	<DL	<DL	<DL	<DL	<DL	<DL	<DL	<DL	<DL	<DL	<DL	<DL	0.0665	<DL	<DL	<DL	<DL	<DL	0.0165	0.0458	<DL	<DL	<DL	<DL	<DL	<DL	<DL	<DL	<DL	<DL	0.00553
Nb	<DL	<DL	<DL	<DL	<DL	<DL	<DL	<DL	<DL	<DL	<DL	<DL	<DL	<DL	<DL	<DL	<DL	<DL	<DL	<DL	<DL	<DL	<DL	<DL	<DL	<DL	<DL	<DL	<DL	<DL	<DL	<DL	<DL	<DL	<DL	<DL	0.00498
Mo	<DL	<DL	<DL	<DL	<DL	<DL	<DL	<DL	<DL	<DL	<DL	<DL	<DL	<DL	<DL	<DL	<DL	<DL	<DL	<DL	<DL	<DL	<DL	<DL	<DL	<DL	<DL	<DL	<DL	<DL	<DL	<DL	<DL	<DL	<DL	<DL	0.0899
Ru	<DL	<DL	<DL	<DL	<DL	<DL	<DL	<DL	<DL	<DL	<DL	<DL	<DL	<DL	<DL	<DL	<DL	<DL	<DL	<DL	<DL	<DL	<DL	<DL	<DL	<DL	<DL	<DL	<DL	<DL	<DL	<DL	<DL	<DL	<DL	<DL	0.0269
Rh	<DL	<DL	<DL	<DL	<DL	<DL	<DL	<DL	<DL	<DL	<DL	<DL	<DL	<DL	<DL	<DL	<DL	<DL	<DL	<DL	<DL	<DL	<DL	<DL	<DL	<DL	<DL	<DL	<DL	<DL	<DL	<DL	<DL	<DL	<DL	<DL	0.00917
Pd	<DL	<DL	<DL	<DL	<DL	<DL	<DL	<DL	<DL	<DL	<DL	<DL	<DL	<DL	<DL	<DL	<DL	<DL	<DL	<DL	<DL	<DL	<DL	<DL	<DL	<DL	<DL	<DL	<DL	<DL	<DL	<DL	<DL	<DL	<DL	<DL	0.0247
Ag	<DL	<DL	<DL	<DL	<DL	<DL	<DL	<DL	<DL	<DL	<DL	<DL	<DL	<DL	<DL	<DL	<DL	<DL	<DL	<DL	<DL	<DL	<DL	<DL	<DL	0.00889	<DL	<DL	<DL	<DL	<DL	<DL	<DL	<DL	<DL	<DL	0.0047
Cd	<DL	<DL	<DL	<DL	<DL	<DL	0.00382	<DL	<DL	0.00382	<DL	<DL	0.00382	<DL	0.00543	<DL	0.00864	<DL	<DL	<DL	<DL	<DL	<DL	<DL	0.00462	0.00543	<DL	<DL	<DL	<DL	<DL	<DL	<DL	<DL	<DL	<DL	0.00307
In	<DL	<DL	<DL	<DL	<DL	<DL	<DL	<DL	<DL	<DL	<DL	<DL	<DL	<DL	<DL	<DL	<DL	<DL	<DL	<DL	<DL	<DL	<DL	<DL	<DL	<DL	<DL	<DL	<DL	<DL	<DL	<DL	<DL	<DL	<DL	<DL	0.000146
Sn	0.033	0.117	0.168	0.0408	0.0119	<DL	<DL	0.00962	<DL	<DL	<DL	<DL	<DL	<DL	0.0319	0.0379	<DL	<DL	0.0162	<DL	<DL	<DL	<DL	<DL	<DL	0.0479	0.00762	<DL	0.0208	<DL	0.0213	<DL	0.0153	<DL	0.0108	0.00933	0.00562
Sb	<DL	<DL	<DL	<DL	0.0116	<DL	<DL	<DL	<DL	<DL	<DL	<DL	<DL	<DL	0.0252	0.0122	<DL	<DL	0.0146	<DL	<DL	<DL	<DL	<DL	0.0199	0.0263	<DL	<DL	<DL	<DL	<DL	<DL	<DL	0.0199	<DL	<DL	0.0113
Te	<DL	<DL	<DL	<DL	<DL	<DL	<DL	<DL	<DL	<DL	<DL	<DL	<DL	<DL	<DL	<DL	<DL	<DL	<DL	<DL	<DL	<DL	<DL	<DL	<DL	<DL	<DL	<DL	<DL	<DL	<DL	<DL	<DL	<DL	<DL	<DL	0.0345
Cs	<DL	<DL	<DL	<DL	<DL	<DL	<DL	<DL	<DL	<DL	<DL	<DL	<DL	<DL	<DL	<DL	<DL	<DL	<DL	<DL	<DL	<DL	<DL	<DL	<DL	<DL	<DL	<DL	<DL	<DL	<DL	<DL	<DL	<DL	<DL	<DL	0.00425
Ba	2.48	1.3	<DL	<DL	1.89	<DL	<DL	<DL	<DL	<DL	1.01	<DL	<DL	<DL	<DL	2.63	<DL	<DL	2.2	<DL	1.33	<DL	<DL	<DL	1.19	<DL	1.28	<DL	1.05	<DL	2.56	1.77	1.57	<DL	1.08	3.94	0.941
La	0.00196	<DL	<DL	<DL	0.00337	<DL	<DL	0.00185	<DL	0.0702	<DL	0.00571	<DL	<DL	0.0697	0.075	<DL	<DL	0.00249	<DL	<DL	<DL	<DL	<DL	0.00378	1.71	0.00185	<DL	<DL	<DL	0.00179	0.00278	<DL	<DL	<DL	0.175	0.00173
Ce	<DL	<DL	<DL	<DL	0.00114	<DL	<DL	<DL	<DL	0.768	0.00093703	0.00685	<DL	<DL	0.245	6.31	<DL	<DL	<DL	<DL	<DL	<DL	<DL	<DL	0.00272	8.37	<DL	<DL	<DL	<DL	<DL	0.0277	<DL	<DL	<DL	9.34	0.000846
Pr	<DL	<DL	<DL	<DL	0.00388	<DL	<DL	<DL	<DL	0.0472	<DL	0.00824	<DL	<DL	1.15	0.348	<DL	<DL	0.00388	<DL	<DL	<DL	<DL	<DL	0.00412	0.888	<DL	<DL	<DL	<DL	<DL	0.00488	<DL	<DL	<DL	0.252	0.00377
Nd	<DL	<DL	<DL	<DL	0.00361	<DL	<DL	<DL	<DL	0.525	<DL	0.0123	<DL	<DL	7.81	3.16	<DL	<DL	0.00287	<DL	<DL	<DL	<DL	<DL	0.00509	17	<DL	<DL	<DL	<DL	<DL	0.012	0.00262	<DL	<DL	2.26	0.0024
Sm	0.00244	<DL	<DL	<DL	0.00244	<DL	0.00304	<DL	<DL	0.0831	<DL	<DL	<DL	<DL	0.0417	0.228	<DL	<DL	<DL	<DL	<DL	<DL	<DL	<DL	<DL	1.24	<DL	<DL	0.00244	<DL	<DL	0.00394	<DL	<DL	<DL	0.565	0.00219
Eu	<DL	<DL	<DL	<DL	<DL	<DL	<DL	<DL	<DL	0.0175	<DL	<DL	<DL	<DL	0.0189	0.102	<DL	<DL	<DL	<DL	<DL	<DL	<DL	<DL	<DL	0.436	<DL	<DL	<DL	<DL	<DL	<DL	<DL	<DL	<DL	0.0439	0.0019
Tb	<DL	<DL	<DL	<DL	<DL	<DL	<DL	<DL	<DL	0.0111	<DL	<DL	<DL	<DL	0.0257	0.0211	<DL	<DL	<DL	<DL	<DL	<DL	<DL	<DL	<DL	0.32	<DL	<DL	<DL	<DL	<DL	<DL	<DL	<DL	<DL	0.0343	0.000681
Gd	<DL	<DL	<DL	<DL	<DL	<DL	<DL	<DL	<DL	0.211	<DL	0.00271	<DL	<DL	0.221	0.246	<DL	<DL	<DL	<DL	<DL	<DL	<DL	<DL	<DL	4.59	<DL	<DL	<DL	<DL	<DL	0.00288	<DL	<DL	<DL	0.463	0.00248
Dy	<DL	<DL	<DL	<DL	<DL	<DL	<DL	<DL	<DL	0.845	<DL	0.00791	<DL	<DL	0.153	0.79	<DL	<DL	<DL	<DL	<DL	<DL	<DL	<DL	<DL	18.1	<DL	<DL	<DL	<DL	<DL	0.00352	<DL	<DL	<DL	1.49	0.00144
Ho	<DL	<DL	<DL	<DL	<DL	<DL	<DL	<DL	<DL	0.0857	<DL	0.00879	<DL	<DL	0.0628	0.0586	<DL	<DL	<DL	<DL	<DL	<DL	<DL	<DL	<DL	8.24	<DL	<DL	<DL	<DL	<DL	0.0011	<DL	<DL	<DL	0.569	0.000237
Er	0.00155	<DL	<DL	<DL	<DL	<DL	<DL	<DL	<DL	0.0666	<DL	0.0152	<DL	<DL	0.345	0.143	<DL	<DL	<DL	<DL	<DL	<DL	<DL	<DL	<DL	1.62	<DL	<DL	0.00119	<DL	0.00143	0.00486	<DL	<DL	<DL	0.211	0.00108
Tm	<DL	<DL	<DL	<DL	<DL	<DL	<DL	<DL	<DL	0.0142	<DL	<DL	<DL	<DL	0.0162	0.0147	<DL	<DL	<DL	<DL	<DL	<DL	<DL	<DL	<DL	0.204	<DL	<DL	<DL	<DL	<DL	<DL	<DL	<DL	<DL	0.0268	0.00701
Yb	0.00393	<DL	<DL	<DL	<DL	<DL	<DL	<DL	<DL	0.0737	0.00393	0.00443	<DL	<DL	0.083	0.0797	<DL	<DL	<DL	<DL	<DL	<DL	<DL	<DL	<DL	3.07	0.00409	<DL	<DL	<DL	0.00393	0.00493	0.00409	<DL	0.00409	0.401	0.00391
Lu	<DL	<DL	<DL	<DL	<DL	<DL	<DL	<DL	<DL	0.0269	<DL	<DL	<DL	<DL	0.00682	0.00891	<DL	<DL	<DL	<DL	<DL	<DL	<DL	<DL	<DL	0.219	<DL	<DL	<DL	<DL	<DL	<DL	<DL	<DL	<DL	0.0219	0.000553
Hf	<DL	<DL	<DL	<DL	<DL	<DL	<DL	<DL	<DL	0.0113	<DL	<DL	<DL	<DL	<DL	0.0111	<DL	<DL	<DL	<DL	<DL	<DL	<DL	<DL	<DL	0.099	<DL	<DL	<DL	<DL	<DL	<DL	<DL	<DL	<DL	0.0133	0.00981
Ta	<DL	<DL	<DL	<DL	<DL	<DL	<DL	<DL	<DL	<DL	<DL	<DL	<DL	<DL	<DL	<DL	<DL	<DL	<DL	<DL	<DL	<DL	<DL	<DL	<DL	0.0495	<DL	<DL	<DL	<DL	<DL	<DL	<DL	<DL	<DL	<DL	0.00963
W	<DL	<DL	<DL	<DL	<DL	<DL	<DL	<DL	<DL	<DL	<DL	<DL	<DL	<DL	<DL	<DL	<DL	<DL	<DL	<DL	<DL	<DL	<DL	<DL	<DL	<DL	<DL	<DL	<DL	<DL	<DL	<DL	<DL	<DL	<DL	<DL	0.051
Re	<DL	<DL	<DL	<DL	<DL	<DL	<DL	<DL	<DL	<DL	<DL	<DL	<DL	<DL	<DL	<DL	<DL	<DL	<DL	<DL	<DL	<DL	<DL	<DL	<DL	0.00327	<DL	<DL	<DL	<DL	<DL	<DL	<DL	<DL	<DL	<DL	0.00325
Ir	<DL	<DL	<DL	<DL	<DL	<DL	<DL	<DL	<DL	<DL	<DL	<DL	<DL	<DL	<DL	<DL	<DL	<DL	<DL	<DL	<DL	<DL	<DL	<DL	<DL	<DL	<DL	<DL	<DL	<DL	<DL	<DL	<DL	<DL	<DL	<DL	0.000842
Pt	<DL	<DL	<DL	<DL	<DL	<DL	<DL	<DL	<DL	<DL	<DL	<DL	<DL	<DL	<DL	<DL	<DL	<DL	<DL	<DL	<DL	<DL	<DL	<DL	<DL	<DL	<DL	<DL	<DL	<DL	<DL	<DL	<DL	<DL	<DL	<DL	0.0544
Au	<DL	<DL	<DL	<DL	<DL	<DL	<DL	<DL	<DL	<DL	<DL	<DL	<DL	<DL	<DL	<DL	<DL	<DL	<DL	<DL	<DL	<DL	<DL	<DL	<DL	<DL	<DL	<DL	<DL	<DL	<DL	<DL	<DL	<DL	<DL	<DL	0.0671
Tl	<DL	<DL	<DL	<DL	0.00183	<DL	<DL	<DL	<DL	<DL	<DL	<DL	<DL	<DL	0.00407	<DL	<DL	<DL	<DL	<DL	<DL	<DL	<DL	<DL	<DL	<DL	<DL	<DL	<DL	<DL	<DL	<DL	<DL	<DL	<DL	<DL	0.00103
Pb	0.00864	0.00682	<DL	<DL	<DL	<DL	<DL	<DL	<DL	<DL	<DL	<DL	<DL	0.00434	0.05	0.0243	<DL	<DL	0.029	<DL	<DL	<DL	<DL	<DL	0.111	0.0923	<DL	<DL	<DL	<DL	<DL	<DL	<DL	<DL	<DL	0.0278	0.0034
Bi	<DL	<DL	<DL	<DL	<DL	<DL	<DL	<DL	<DL	<DL	<DL	<DL	<DL	<DL	<DL	<DL	<DL	<DL	<DL	<DL	<DL	<DL	<DL	<DL	<DL	<DL	<DL	<DL	<DL	<DL	<DL	<DL	<DL	<DL	<DL	<DL	0.00793
Th	<DL	<DL	<DL	<DL	<DL	<DL	<DL	<DL	<DL	<DL	<DL	<DL	<DL	<DL	<DL	<DL	<DL	<DL	<DL	<DL	<DL	<DL	<DL	<DL	<DL	<DL	<DL	<DL	<DL	<DL	<DL	<DL	<DL	<DL	<DL	<DL	0.0048
U	<DL	<DL	<DL	<DL	<DL	<DL	<DL	<DL	<DL	<DL	<DL	<DL	<DL	<DL	<DL	<DL	<DL	<DL	<DL	<DL	<DL	<DL	<DL	<DL	<DL	0.00505	<DL	<DL	<DL	<DL	<DL	<DL	<DL	<DL	<DL	0.00283	0.00137

"Dup" stands for complete duplicate (i.e., glove from another unopened box). "<DL" means below detection limits. The detection limit is defined following IUPAC guidelines as the average number of counts measured in blanks plus 3 times the standard deviation (see text for

Appendix C: Comparison of duplicate analyses (results from Test A)

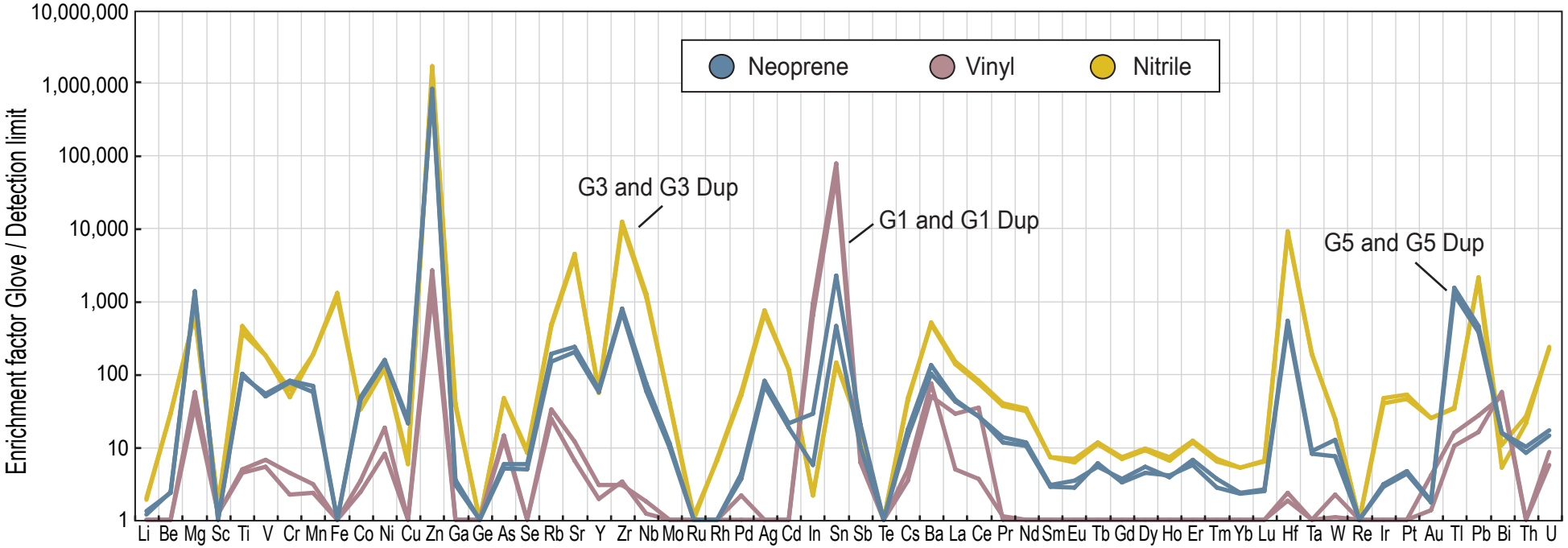

Figure caption: “Dup” stands for complete duplicate analyses (glove from another unopened box)

Appendix S4.

Comparison of zinc isotopic compositions measured with and without purification by ion-exchange chromatography

Sample Name	Type of glove	Ni/Zn	Cu/Zn	Ti/Zn	δ^{66}Zn (‰)Zn $_{JMC\ 3\text{-}0749L}$ without purification	δ^{66}Zn (‰)Zn $_{JMC\ 3\text{-}0749L}$ with previous purification
G1	Vinyl	0.001	< 0.0008	0.007	0.17	0.34
G1 Dup	Vinyl	0.001	< 0.0016	0.012	0.36	0.23
G2	Nitrile	0.00004	0.00001	0.001	0.16	-0.05
G8	Vinyl	0.001	0.002	0.004	-0.01	0.26
G8 dup	Vinyl				-0.14	0.07
G14	Vinyl	0.001	0.006	0.007	-0.19	0.12

Table caption: The Ni/Zn, Cu/Zn and Ti/Zn ratios in the soaking solutions were calculated using data from Appendix S1. Note that trace element mass fractions were not determined in the soaking solution G8 Dup, hence the Ni/Zn, Cu/Zn and Ti/Zn ratios could not be calculated.

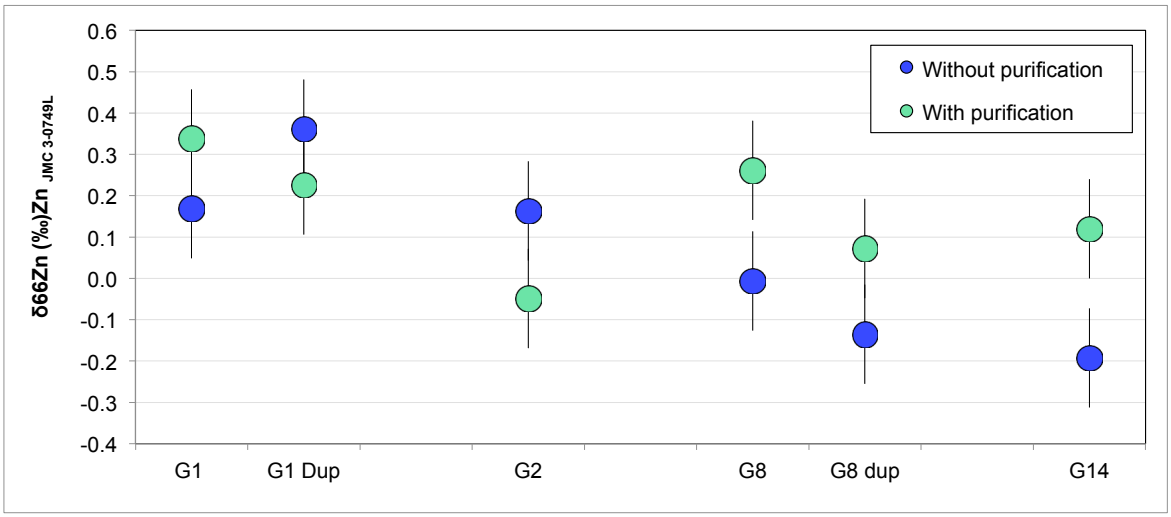

Figure caption: Error bars are fixed at ± 0.12‰ (2*s*) to reflect our measurement precision

NOUVELLES PERSPECTIVES CHIMIQUES ET ISOTOPIQUES DU VIEILLISSEMENT

CHAPITRE III

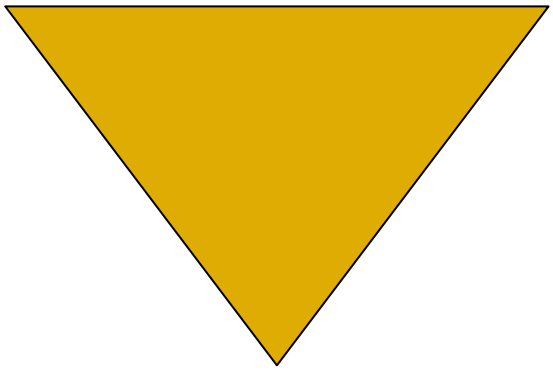

Comment vieillit-on ? Pourquoi avec l'âge, certaines personnes développent préférentiellement des maladies et d'autres non ? Est-il utopique de penser qu'un jour nous pourrons contrôler le vieillissement dans le but d'améliorer la qualité de vies des personnes âgées ? Un ensemble de questions qui reste à ce jour énigmatiques s'expliquant par notre manque de connaissance concernant le vieillissement.

Dans ce chapitre divisé en deux grandes parties, nous avons tenté de mieux comprendre ce processus complexe en adoptant une nouvelle approche basée sur l'étude des éléments chimiques. Dans un premier temps, nous avons analysé les concentrations chimiques de 15 éléments (traces et majeurs) ainsi que les compositions isotopiques en cuivre ($\delta^{65}Cu$) et en zinc ($\delta^{66}Zn$) dans (1) des organes de souris (C57BL/6J) (partie I) et (2) des nématodes (vers *C.elegans*) (partie II), le but étant de quantifier l'amplitude des variations chimiques en fonction l'âge à différentes échelles, de l'organe à l'organisme. Pour les nématodes, des courbes de longévité (*i.e.* lifespan) ont, en plus, été réalisées dans des conditions chimiques spécifiques afin d'évaluer l'impact de telles fluctuations sur le vieillissement.

III.1. Contraintes apportées par le modèle murin (souris C57BL/6J)

ARTICLE

"Isotopic metallome evolution during ageing"

***Lucie Sauzéat**, Pooja Jha, Johan Auwerx, Vincent Balter*

(in preparation)

III.2. Contraintes apportées par le modèle de vers (*C.elegans*)

III.2.1. Variations chimiques et isotopiques: de nouveaux outils pour quantifier le vieillissement

ARTICLE

"Metallome evolution in ageing *C. elegans* and a copper stable isotope perspective"

***Lucie Sauzéat**, Anne Laurençon, Vincent Balter*

(Published in Metallomics)

III.2.2. Peut-on accroitre la longévité des vers en modulant leur rapport isotopique en deutérium ?

III.1. Contraintes apportées par le modèle murin (souris C57BL/6J)

Au cours des dix dernières années, le nombre d'études reportant des dysfonctionnements chimiques avec l'âge n'a cessé d'augmenter (Fu et al., 2015; Giacconi et al., 2016; Malavolta et al., 2010; 2015; Mezzetti et al., 1998; Rembach et al., 2014) et depuis peu, des dérèglements isotopiques ont également été observés chez l'Homme (Jaouen et al., 2013) et la souris (Moynier et al., 2017). Cependant, la majorité de ces études sont réalisées sur des réservoirs (e.g. sérum/sang) restreints et/ou se limitent à un seul voire deux éléments chimiques, affectant notre capacité à comprendre l'ensemble des processus participant aux dérèglements chimiques au cours du vieillissement. L'objectif du manuscrit présenté ci-dessous est de diversifier le type d'échantillon mais aussi d 'augmenter le nombre d'éléments chimiques analysés afin d'avoir une vision plus complète du vieillissement. Pour cela, 5 organes de souris isogéniques (*i.e.* génétiquement identique) comprenant des foies, des cœurs, des reins, des muscles (quadriceps) et des cerveaux ont été analysés. Afin de quantifier le rôle des différents organes dans le vieillissement, nous avons choisi d'utiliser des outils statistiques (analyse en composantes principales, ACP) pour modéliser leur évolution chimique et isotopique au cours du temps. Le lien existant entre les variations chimiques et la dérégulation de certaines voies métaboliques et physiologiques avec l'âge est discuté dans ce premier manuscrit.

ARTICLE

"Isotopic metallome evolution during ageing"

***Lucie Sauzéat**, Pooja Jha, Johan Auwerx, Vincent Balter*

(in preparation)

NB: For ease of reading, the figures and tables are directly integrated in the main text and the manuscript takes the form of an article

Isotopic metallome evolution during ageing

(in preparation)

Lucie Sauzéat[1], Pooja Jha[2], Johan Auwerx[2], V. Balter[1*]

[1]*UMR 5276, Laboratoire de Géologie de Lyon, Ecole Normale Supérieure de Lyon, BP 7000 Lyon, France*

[2]*Laboratory for Integrative and Systems Physiology, Ecole Polytechnique Fédérale de Lausanne, Lausanne, Switzerland*

*correspondence: Vincent.balter@ens-lyon.fr

Chemical deregulations including metal concentrations[1] and isotopic compositions[2] are significantly deregulated over time, having thus the potential for capturing specificity of ageing. The way and extent they are related to ageing deteriorations are however poorly understood. Here we show that systematic changes in Cu composition and particularly isotopic ratio in the body is related to fundamental deregulations accounting for ageing progression. We found that δ^{65}Cu decreases in liver over time, associated with a concomitant increase of the Cu content in brain. These chemical variations are associated with physiological and metabolic deregulations such as blood-brain barrier impairment as well as altered glycogen and fatty acid metabolism. Altogether, these results show that Cu isotopic composition is a new relevant signature of physiological and metabolic activity change over time.

Ageing is characterized by a progressive functional decline resulting from physiological[3] and metabolic[4] deleterious changes, increasing vulnerability to death. Individual biomarkers may assist identifying these age-related deregulations and subsequently develop prevention strategies that promote healthy lifespan. However, due to the multi-causal nature of ageing including increase in oxidative stress[5], cellular senescence[3], genomic instability and DNA damages[6], loss of proteostasis[7], telomere attrition[8], mitochondrial dysfunction[9] and impaired glycogen metabolism[10], no convincing measurements have proven to be relevant yet, showing that biological markers may likely not be sufficient to determine the biological age. Conversely, chemical deregulations including elemental concentrations and isotopic compositions may offer more relevant information. Over time, significant variations have been observed in yeast[11], worms[12], mice[1] and humans[2,13]. In addition, it has recently been demonstrated that several age-related biological deteriorations like reactive oxygen species (ROS) could be suppressed by heavy hydrogen isotope supplementation [11] supporting the importance of chemical dyshomeostasis on ageing. The present work investigates age-related chemical deregulations and particularly isotopic variations as a new reliable marker of ageing and shed lights on key features of ageing. In contrast to the previous studies focusing mainly on single specific element

within limited reservoirs, this work includes the concentrations of 15 chemical elements as well as Cu and Zn isotopic compositions measured in five distinct organs including brain, liver, muscle, heart and kidney.

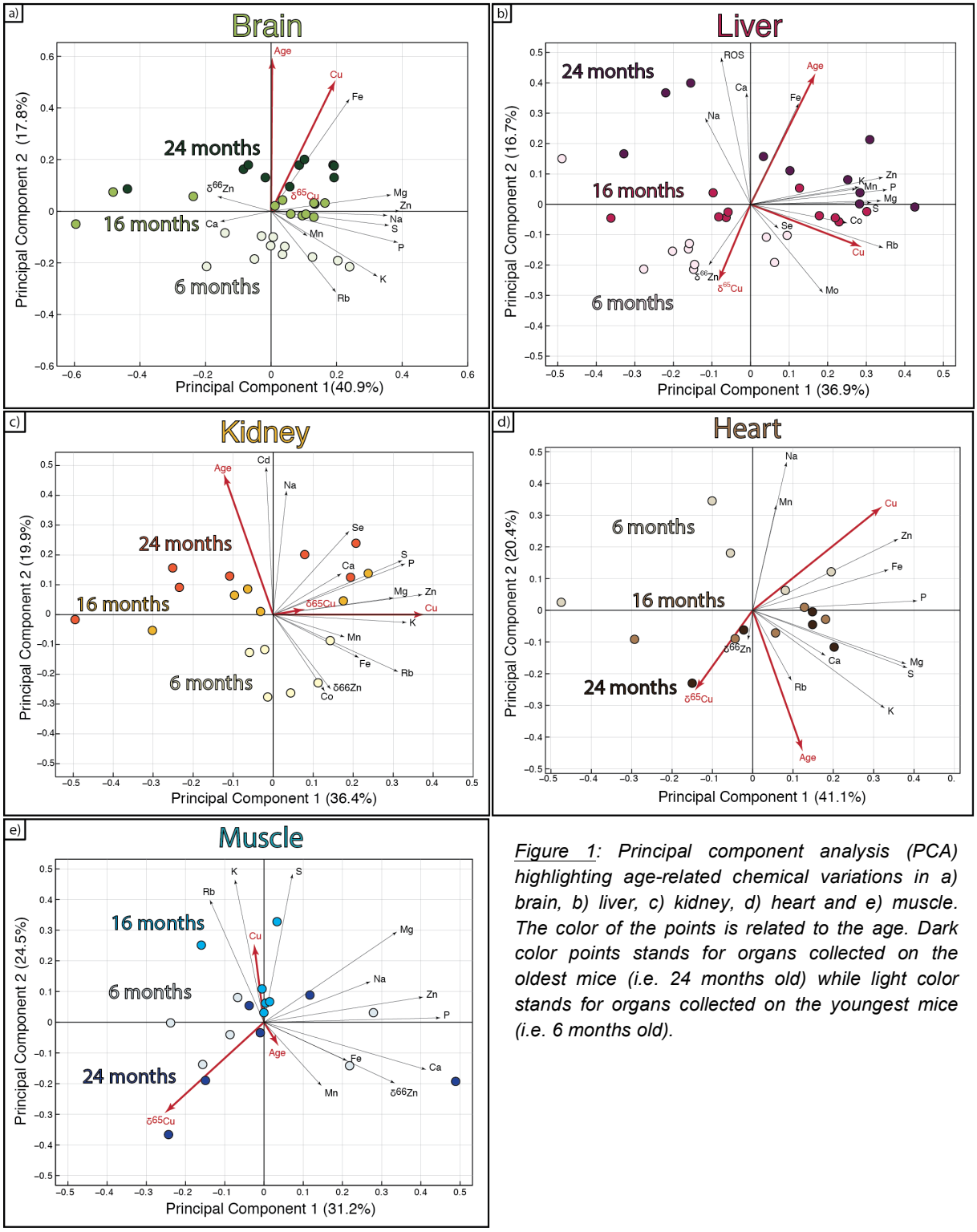

Figure 1: Principal component analysis (PCA) highlighting age-related chemical variations in a) brain, b) liver, c) kidney, d) heart and e) muscle. The color of the points is related to the age. Dark color points stands for organs collected on the oldest mice (i.e. 24 months old) while light color stands for organs collected on the youngest mice (i.e. 6 months old).

The highest chemical variability is observed among the organs regardless of the age (Fig.S1). For example, muscles are enriched in magnesium (Mg) and calcium (Ca), two metals required for muscle contraction regulation[14,15]. Similarly, brains are enriched in Ca and have elevated amount of phosphorus (P) that guarantee proper brain functions as well as cognitive growth and development[16]. Inversely, iron (Fe) is more concentrated in liver—the main Fe storage organ[17] and heart, where it is required to prevent deleterious cardiac effects[18]. Likewise, isotopic compositions differ, the highest copper and zinc isotopic ratio was observed in kidneys ($\delta^{65}Cu$ = +1.32 ± 0.09 (1sd) ‰, $\delta^{66}Zn$ = +0.29 ± 0.05 (1sd) ‰) (Fig.S2), which is consistent with previous observations reported in mice[19,20]. This specific chemical pattern demonstrates that all the organs are chemically distinct, a speciation highly required to sustain vital functions in the body.

During ageing, most of these chemical parameters are significantly affected, as illustrated by the age-related variations observed along the y principal component axis (Fig.1), the more significant fluctuations being found in brain (Fig.1a), liver (Fig.1b) and kidney (Fig.1c) compared to heart and muscle (Fig.1d and Fig.1e). This is for example illustrated by the increase of the copper content in brain (Fig.2a), an observation in line with previous studies such as Fu et al.[1]. However, we demonstrate that not only brain but also all the other organs are affected with specific chemical variations comprising trace and major elemental concentrations and Cu-Zn isotopic compositions (Fig.2). Focusing specifically on copper, in addition to the rise of Cu observed in brain with age (Fig. 1a and Fig.2b), we also note a tendency toward enrichment in ^{63}Cu (*i.e.* $\delta^{65}Cu$ diminution) in livers (Fig.1a and Fig.2b) that tend to be roughly consistent with the $\delta^{65}Cu$ decrease reported by Jaouen et al.[2] in human blood. In contrast, Cu content remains relatively stable in liver over time, like $\delta^{65}Cu$ in brains (Fig.2b). For heart, muscle and particularly kidney, no significant copper variations are noted with age (Fig.2b). Altogether, these results highlight an extremely complex chemical pattern developing progressively with age, a pattern much more complex that may have been previously suggested[21].

One way to comprehend the origination of these copper variations is to understand how organs interact with one another over time, a method poorly investigated in the past due to limited elemental and reservoir specificity of the studies. Liver is the main organ controlling the copper distribution in the body[22]. At early-age, brain is isolated from the rest of the body by the blood-brain barrier (BBB) implying that Cu exchanges are restricted to liver, kidney, heart and muscle *i.e.* the three main organs requiring copper for their functioning[22]. Using an isotopic mixing performed over a closed system and steady state conditions (*i.e.* input and output fluxes between the organs are the same), we demonstrate that, in the first period of the life (*i.e.* 6 months), the Cu composition of the liver depends on that of the kidney, heart and muscle in well-defined proportions. Respectively, 35±5%, 28±5% and 37±10% of the Cu composition of liver is controlled by muscle, kidney and heart (Fig.2a). These relatively similar contributions reveal a stable copper homeostasis that supports a well-regulated system characteristic of equilibrium stage at young age. In contrast, with time, the system is progressively deregulated as illustrated by the $\delta^{65}Cu$ decrease in livers from +0.27 ± 0.15 (1sd) ‰ to +0.03 ± 0.12 (1sd) ‰ (Fig.2b). At first sight, this may result from disturbed Cu fluxes exchanged

between liver (*i.e.* the central organ) and the three main surrounded organs (*i.e.* heart, kidney and muscle). In such case, we should however expect to observe chemical variations in kidney, heart and muscle, which is not the case (Fig.2b).

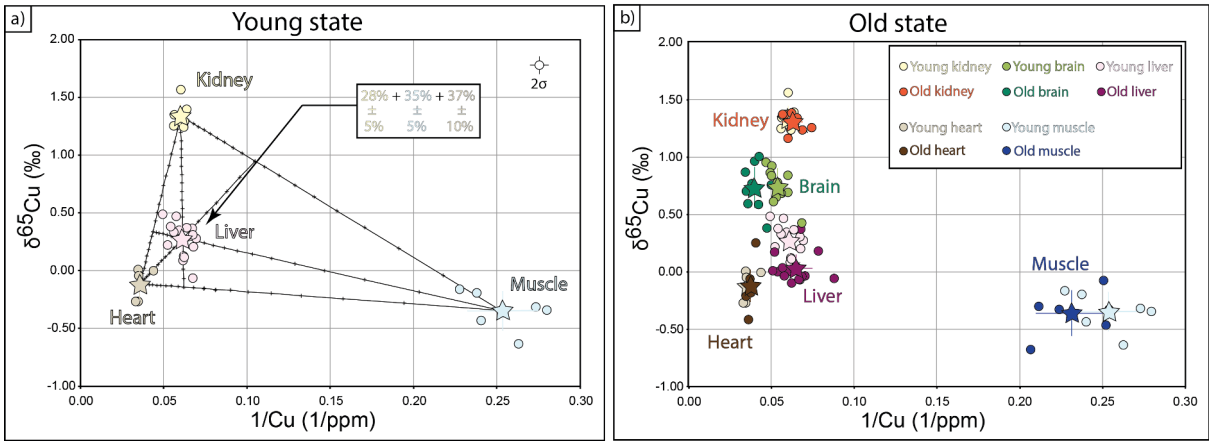

Figure 2: a) Copper isotopic mixing between liver, muscle (i.e. quadriceps), kidney and heart at early-age (i.e. 6months). Equations used for isotopic mixing are from Langmuir et al.[33]. Ticks on the mixing lines correspond to 5% increments. Analytical errors are 2σ. b) δ^{65}Cu *versus Cu diagram highlighting Cu deregulation over time in liver and brain.*

By contrast, Cu content increases significantly in brain from 18.57 ± 1.93 (1sd) ppm to 25.08 ± 2.86 (1sd) ppm although its copper isotopic composition remains relatively constant ($\delta^{65}Cu_{young}$ = 0.75 ± 0.16 (1sd) ‰ and $\delta^{65}Cu_{old}$ = 0.73 ± 0.18 (1sd) ‰) (Fig.2b). Cu liver fluctuation is thus likely related to brain temporal deregulations. In terms of physiological processes, it may include intestinal absorption impairment and the breaking of the blood-brain barrier (BBB) (Fig.S3). Although the timing remain elusive, the BBB is significantly affected over time[23], facilitating Cu chemical fluxes toward brain with age. In parallel, with age, organisms have reduced dietary intake resulting into lower Cu intake [24], a phenomenon increasing intestinal copper absorption[25]. To counterbalance the excess of copper ingested over time, we can suggest that, instead of accommodating the excess Cu by itself that will deregulate the whole-body metallome, liver will export Cu and preferentially the heavier ^{65}Cu isotope towards the brain resulting in Cu increases and stable δ^{65}Cu in brain associated with constant Cu and δ^{65}Cu decrease in liver (Fig.2b). Decrease in Cu isotopic composition in liver can also result from preferentially light copper isotope (^{63}Cu) intake (Fig.S3). Elderly have reduced dietary intake[24], which may favor a ^{63}Cu-diet selection based on the results of Jaouen et al.[26] reporting a diet effect on δ^{65}Cu. Impaired hepatic proteins regulating intracellular Cu intake and/or excretion may also result from decrease δ^{65}Cu in liver (Fig.S3). Although no isotopic data exist for biliary excretion, it has been shown that this excretory flux was affected over time[27] likely resulting form ATP7B impairment, the main cuproprotein regulating Cu biliary excretion[22]. Because impaired binding of Cu to specific proteins[28] and deficient Cu transporters[29] can fractionate copper isotopes, enrichment in ^{63}Cu over ^{65}Cu in livers may result from membrane proteins impairment and preferential heavy ^{65}Cu biliary excretion. Another explanation could be the abnormal formation of reactive oxygen species (ROS). In

excess, cuprous (Cu^{+}) copper ions can be oxidized to cupric (Cu^{2+}) and induce the formation of highly reactive oxygen species (ROS) such as hydroxyl radicals (•OH) via the Haber-Weiss reaction[30]. In parallel, one important parameter controlling Cu isotope fractionation is redox variation state. Reduced Cu^{+} compounds are expected to favor light isotopes relative to Cu^{2+}. Therefore, the progressive hepatic accumulation of ROS over time[5] should contribute to a Cu isotope fractionation favoring light ^{63}Cu over heavy ^{65}Cu, leading ultimately to a decrease of the $\delta^{65}Cu$ value in liver. Although all these physiological processes are likely occurring simultaneously and further studies are required to precisely say where the Cu dyshomeostasis originate from, these results highly support a link between ageing and physiological impairments over time demonstrating that chemical variations are relevant parameters helpful to constrain the cumulated physiological deregulation.

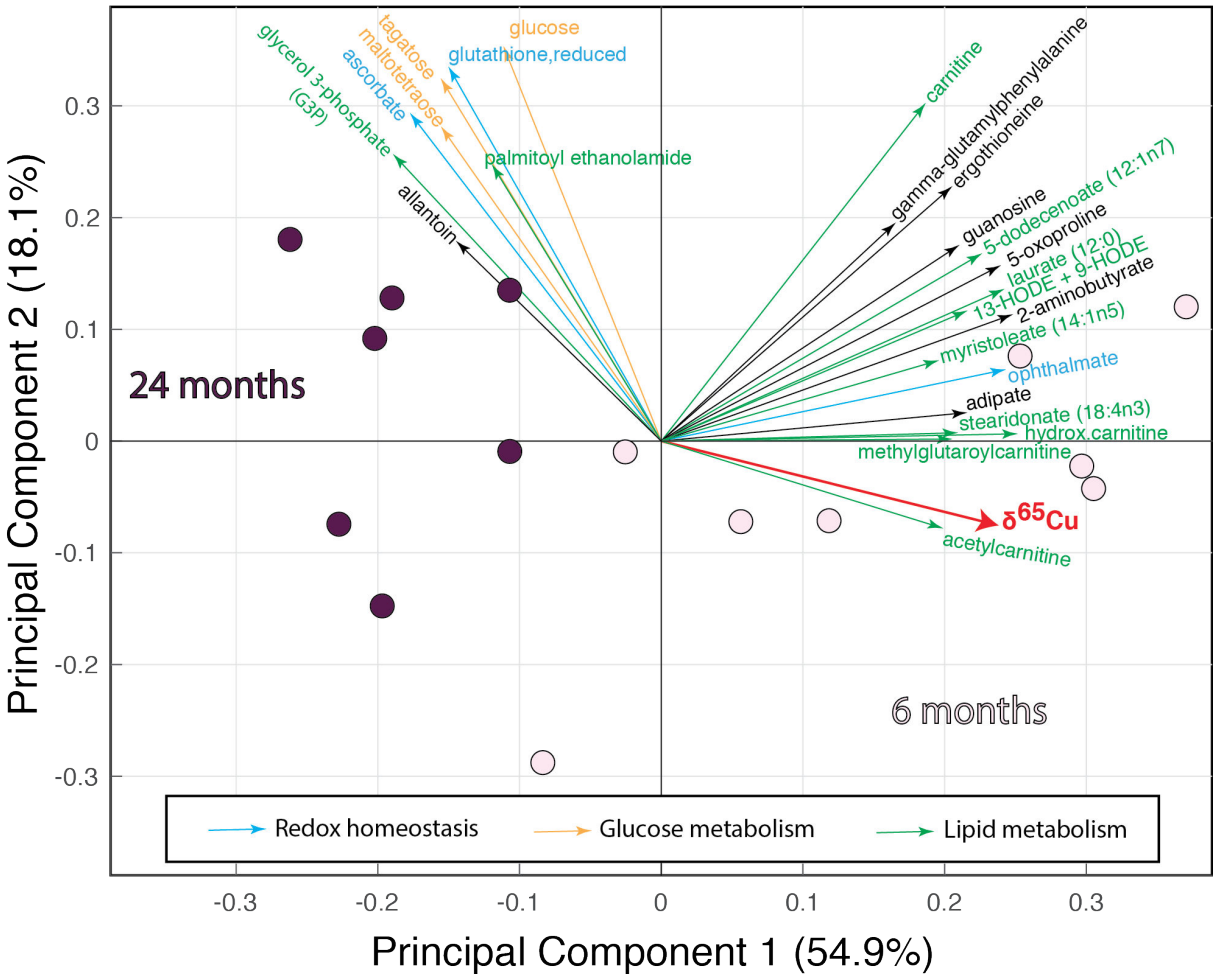

Figure 3: Principal component analysis (PCA) highlighting correlation between metabolites involved in redox homeostasis (blue), glucose metabolism (orange) and lipid metabolism (green) and $\delta^{65}Cu$ deregulation over time in liver.

Furthermore, as illustrated in liver, chemical variations are also associated with change in metabolomic homeostasis with age (Fig.3). This is particularly true regarding $\delta^{65}Cu$, whose age-specific decrease is related to various metabolites changes involved in several pathways including

glucose and lipid metabolism as well as redox homeostasis. $\delta^{65}Cu$ is for example anti-correlated with the accumulation of glycogen intermediates including glucose and maltotetraose, both reflecting altered glycogen metabolism[4] (Fig.3). Correlations are also predominantly observed with fatty acid metabolites (e.g. acetylcarnitine, laurate, methylglutaroylcarnitine) that tend to be higher in young mice as well as with redox dyshomeostasis metabolites (e.g. glutathione reduced, ascorbate) (Fig.3). Since ageing is associated with changes in these three pathways[4], these results demonstrate that $\delta^{65}Cu$ may bring relevant information regarding the cumulated metabolomic signature.

Altogether, our results demonstrate that chemical parameters and particularly copper isotopic composition appear as a new promising tool that may provide promising insights on the temporal evolution of the biological ageing. In perspective, we speculate our assay to be a new opportunity to establish prevention strategies aiming for example to maintain stable metallome homeostasis over time within the organs that will help promoting healthy lifespan. We also anticipate our study should be extended to other isotopes that may further improve our understanding about other physiological and metabolomics deregulations likely contributing to ageing.

References

1. Fu, S., Jiang, W. & Zheng, W. Age-dependent increase of brain copper levels and expressions of copper regulatory proteins in the subventricular zone and choroid plexus. *Front. Mol. Neurosci.* **8,** 966 (2015).
2. Jaouen, K. *et al.* Is aging recorded in blood Cu and Zn isotope compositions? *Metallomics* **5,** 1016–1024 (2013).
3. Baker, D. J. *et al.* Naturally occurring $p16^{Ink4a}$-positive cells shorten healthy lifespan. *Nature* **000,** 1–20 (2016).
4. Houtkooper, R. H. *et al.* The metabolic footprint of aging in mice. *Sci Rep* **1,** 1–10 (2011).
5. Finkel, T. & Holbrook, N. J. Oxidants, oxidative stress and the biology of ageing. *Nature* **408,** 1–9 (2000).
6. White, R. R. *et al.* Controlled induction of DNA double-strand breaks in the mouse liver induces features of tissue ageing. *Nature Communications* **6,** 1–11 (2015).
7. Kaushik, S. & Cuervo, A. M. Proteostasis and aging. *Nature Medicine* **21,** 1406–1415 (2015).
8. Blasco, M. A. Telomere length, stem cells and aging. *Nat Chem Biol* **3,** 640–649 (2007).
9. Lee, S. S. *et al.* A systematic RNAi screen identifies a critical role for mitochondria in C. elegans longevity. *Nat Genet* **33,** 40–48 (2003).
10. Gusarov, I. *et al.* Glycogen controls Caenorhabditis elegans lifespan and resistance to oxidative stress. *Nature Communications* **8,** 1–12 (2017).
11. Li, X. & Snyder, M. P. Yeast longevity promoted by reversing aging-associateddecline in heavy isotope content. *Npj Aging And Mechanisms Of Disease* **2,** 1–10 (2016).
12. Klang, I. M. *et al.* Iron promotes protein insolubility and aging in C. elegans. *Aging-Us* **6,** 975–991 (2014).
13. Rembach, A. *et al.* Decreased serum zinc is an effect of ageing and not Alzheimer's disease. *Metallomics* **6,** 1216–1219 (2014).
14. Gröber, U., Schmidt, J. & Kisters, K. Magnesium in Prevention and Therapy. *Nutrients* **7,** 8199–8226 (2015).
15. Cheng, A. J. & Westerblad, H. Mechanical isolation, and measurement of force and myoplasmic free $[Ca^{2+}]$ in fully intact single skeletal muscle fibers. *Nature Publishing Group* **12,** 1763–1776 (2017).

16. Hidalgo, C. & Núñez, M. T. Calcium, iron and neuronal function. *TBMB* **59,** 280–285 (2007).
17. Anderson, G. J. & Frazer, D. M. Hepatic Iron Metabolism. *Seminars in liver disease* **25,** 420–432 (2005).
18. Haehling, von, S., Jankowska, E. A., van Veldhuisen, D. J., Ponikowski, P. & Anker, S. D. Iron deficiency and cardiovascular disease. *Nature Publishing Group* 1–11 (2015). doi:10.1038/nrcardio.2015.109
19. Moynier, F., Fujii, T., Shaw, A. S. & Le Borgne, M. Heterogeneous distribution of natural zinc isotopes in mice. *Metallomics* **5,** 693 (2013).
20. Balter, V. *et al.* Contrasting Cu, Fe, and Zn isotopic patterns in organs and body fluids of mice and sheep, with emphasis on cellular fractionation. *Metallomics* **5,** 1470 (2013).
21. Malavolta, M. *et al.* Plasma copper/zinc ratio: an inflammatory/nutritional biomarker as predictor of all-cause mortality in elderly population. *Biogerontology* **11,** 309–319 (2010).
22. Kim, B.-E., Nevitt, T. & Thiele, D. J. Mechanisms for copper acquisition, distribution and regulation. *Nat Chem Biol* **4,** 176–185 (2008).
23. Montagne, A. *et al.* Blood-Brain Barrier Breakdown in the Aging Human Hippocampus. *Neuron* **85,** 296–302 (2015).
24. Ma, J. & Betts, N. M. Zinc and Copper Intakes and Their Major Food Sources for Older Adults in the 1994–96 Continuing Survey of Food Intakes by Individuals (CSFII). *Journal of Nutrition* **130,** 2838–2843 (2000).
25. Wapnir, R. A. Copper absorption and bioavailability. *The American Journal of Clinical Nutrition* **67,** 1054S–1060S (1998).
26. Jaouen, K. *et al.* Iron, copper and zinc isotopic fractionation up mammal trophic chains. *Earth and Planetary Science Letters* **374,** 1016–1024 (2013).
27. Suzuki, M. & Aoki, T. Impaired Hepatic Copper Homeostasis in Long- Evans Cinnamon Rats: Reduced Biliary Excretion of Copper. *Pediatric Research* **35,** 598–601 (1994).
28. Tennant, A., Rauk, A. & Wieser, M. E. Computational modelling of the redistribution of copper isotopes by proteins in the liver†. *Metallomics* 1–11 (2017). doi:10.1039/C7MT00248C
29. Cadiou, J.-L. *et al.* Copper transporters are responsiblefor copper isotopic fractionation ineukaryotic cells. *Sci Rep* 1–10 (2017). doi:10.1038/srep44533
30. Bremner, I. Manifestations of copper excess. *American Journal of Clinical Nutrition* 1069S–1073S (1998).
31. Garçon, M. *et al.* Nitrile, Latex, Neoprene and Vinyl Gloves: A Primary Source of Contamination for Trace Element and Zn Isotopic Analyses in Geological and Biological Samples. *Geostandards and Geoanalytical Research* **41,** 367–380 (2017).
32. Maréchal, C. N., Telouk, P. & Albarede, F. Precise analysis of copper and zinc isotopic compositions by plasma-source mass spectrometry. *Chemical Geology* **156,** 251–273 (1999).
33. Langmuir, C. H., Vocke, R. D., Jr, Hanson, G. N. & Hart, S. R. A general mixing equation with applications to Icelandic basalts. *Earth and Planetary Science Letters* **37,** 380–392 (1978).
34. Jaouen, K., Beasley, M., Schoeninger, M., Hublin, J.-J. & Richards, M. P. Zinc isotope ratios of bones and teeth as new dietary indicators: results from a modern food web (Koobi Fora, Kenya). *Nature Publishing Group* 1–8 (2016). doi:10.1038/srep26281

Acknowledgements The authors thank Philippe Télouk and E. Albalat for assistance during isotopic measurements and help in the clean laboratory. We thank the Foundation Bullukian and the Foundation Mérieux for financial support of the V.B laboratory. The research in the J.A. laboratory is supported by the EPFL, NIH (R01AG043930), Systems X (SySX.ch 2013/153), Velux Stiftung (1019), and the Swiss National Science Foundation (31003A-140780).

Author Contributions V. Balter and J. Auwerx designed the study, L. Sauzéat and P. Jha carried out the analysis and L. Sauzéat wrote the manuscript on V. Balter, J. Auwerx and P.Jha's recommendations. All authors discussed the results.

Author Information Reprints and permissions information is available at www.nature.com/reprints. The authors declare no competing financial interests. Readers are welcome to comment on the online version of this article at www.nature.com/nature. Correspondence and requests for materials should be addressed to V. Balter (Vincent.balter@ens-lyon.fr) for chemical and isotopic data and to J. Auwerx for biology assays (johan.auwerx@epfl.ch).

METHODS

Chemical assays

Mice organs were collected from male C57BL/6J mice (Janvier, St Berthevin, France) at three different time-points in their life *i.e.* 6months (mature adult), 16months (middle age) and 24 months (old). All mice were fed with a standard chow diet (i.e. #2018, containing 18% protein, 50% carbohydrate and 6.0% fat; Harlan Laboratories, Madison, WI, USA) at the Laboratory of Integrative Systems Physiology (LIPS) at EPFL (Ecole Polytechnique Fédérale de Lausanne). An optic ICP-AES, (iCap 6000 Radial) and a quadrupole ICP-MS (Thermo iCap-Q) were used for the measurement of major and trace element concentrations respectively following the procedure described by Garçon et al.[31]. Cu and Zn isotopic compositions were measured on a MC-ICP-MS (Nu 500) following the procedure provided by Maréchal et al.[32]. Concentrations and isotopic compositions were all measured at the Ecole Normale Supérieure (ENS) of Lyon and all data are summarized in Supplementary Table 1. Accuracy and reproducibility were monitored by complete duplicate analyses, replication of an in-house (OEP) and certified standard (1577c) as well as re-run analyses over the course of an analytical session. Given our long-term reproducibility on the in-house/certified standards and duplicates analyses (Supp. Table 2), the analytical uncertainty adopted in this study for trace and major concentrations is on average better than 10% (2sd) and of ±0.12 ‰ (2sd) for isotopic ratios. The method is fully described in the Supplementary Information.

Metabolomics data of young (*i.e.* 6months) and old (*i.e*. 24months) liver used in this study derived from Houtkooper et al.[4]. All data are summarized in Supplementary Table 3.

SUPPLEMENTARY INFORMATION

SAMPLES AND METHODS

Samples

In this study, we analyzed chemical parameters of several organs (i.e. livers, brains, hearts, muscles (i.e. quadriceps) and kidneys) from male C57BL/6J mice (Janvier, St Berthevin, France) collected at three different time-points in their life i.e. 6months (mature adult), 16months (middle age) and 24 months (old). All mice were fed with a standard chow diet (i.e. #2018, containing 18% protein, 50% carbohydrate and 6.0% fat; Harlan Laboratories, Madison, WI, USA) at the Laboratory of Integrative

Systems Physiology (LIPS) at EPFL (Ecole Polytechnique Fédérale de Lausanne). The organs were collected and frozen in liquid nitrogen (N_2) to promote their conservation before chemical and metabolomics analyses.

Methods

All the chemical analyses were carried out in a clean laboratory below laminar flow clean hoods using ultra-pure water at 18.2 MΩ.cm and acids that were doubly distilled to ensure low trace element contents and avoid any exogenous contaminations. Blanks were also run to quantify and integrate potential contamination from the material and/or acids used to perform experiments.

Analyses of major and trace element concentrations

The samples were crushed under liquid N_2, freeze-dried, weighted and then dissolved in a concentrated HNO_3-H_2O_2 30% mixture in Savillex beakers for about 72h at 120ºC. Once dissolved, major (Ca, K, Na, P, S and Mg) and trace elements (Mn, Co, Cu, Zn, Fe, Se, Rb, Mo and Cd) were measured using the ICP-AES, iCAP 6000 Radial and the quadrupole ICP-MS Thermo iCap-Q respectively at the Ecole Normale Supérieure (ENS) of Lyon. All the data are summarized in the Supplementary Table 1. The concentrations were calculated using calibration curves determined based on multi-elemental solutions (SP-33MS for trace element and in-house solution made from mono-elemental solutions for major element) following the procedure detailed in Garçon et al.[31]. Both, accuracy and reproducibility were monitored by complete duplicate analyses, replication of an in-house (sheep plasma; OEP) and certified standards (bovine liver;1577c) as well as re-run analyses over the course of an analytical session. Given our long-term reproducibility on the in-house/certified standards and duplicates analyses, the 2 sigma analytical uncertainty adopted in this study for both trace and major concentrations is on average better than 10% (*cf* Supp. Table 1 and Supp. Table 2).

Analyses of copper and zinc isotopic compositions

Copper and zinc isotopic compositions are provided in the Supplementary Table 1. They were measured at the Ecole Normale Supérieure (ENS) of Lyon following the procedure described by Maréchal et al.[32]. Briefly, before each isotopic measurement, the sample solutions were purified by ion-exchange chromatography using quartz columns filled with 1.8mL of Bio-Rad AGMP-1 (100-200 mesh) anion-exchange resin. Both copper and zinc were successively eluted with 20mL of HCl 7N + 0.001% H_2O_2 and 10mL of HNO_3 0.5 $mol.L^{-1}$ respectively. The whole procedure blanks were less than 1ng for Cu and 11ng for Zn, which represents, on average less than 1% of the Cu and Zn isolated from the samples. On the day of the analyses, Zn and Cu purified solutions, previously evaporated to dryness, were dissolved in a Cu (Cu SRM 976, National Institute of Standards and Technology, Gaithersburg, MD, USA) or Zn-doped solution (Zn JMC 3-0749L, Johnson Matthey Royston, UK) respectively to reach a Zn or Cu sample concentration of about 300 ppb, which is similar to the concentration of the standard solution that was run between each sample.

Both copper and zinc isotopic compositions, expressed as $\delta^{65}Cu_{sample} = \left[\frac{\left({}^{65}Cu/_{63}Cu\right)_{sample}}{\left({}^{65}Cu/_{63}Cu\right)_{standard}} - 1\right] * 1000$ and $\delta^{66}Zn_{sample} = \left[\frac{\left({}^{66}Zn/_{64}Zn\right)_{sample}}{\left({}^{66}Zn/_{64}Zn\right)_{standard}} - 1\right] * 1000 \text{ in } ‰$ respectively were then measured on a Nu Plasma (Nu 500) MC-ICP-MS in wet plasma conditions. Zn JMC 3-0749L (also called JMC-Lyon; Johnson Matthey, Royston, UK) and Cu SRM 976 were used as reference standards for $\delta^{66}Zn$ and $\delta^{65}Cu$ respectively. Instrumental mass fractionation was corrected with an exponential law using an elemental-doping method and instrumental drift over time was controlled with standard sample bracketing as recommended by Maréchal et al.[32].

The accuracy of isotopic compositions was assessed by the analysis of in-house and commercial standard solutions (*i.e.* sheep plasma; OEP and bovine liver; 1577c) during each analytical sequence. For zinc, the average $\delta^{66}Zn$ measured for the two standard solutions is +0.76 ± 0.08 ‰ (2s, n = 3) for OEP and -0.18 ± 0.05 ‰ (2s, n = 4) for 1577c which is in good agreement with our best estimate values ($\delta^{66}Zn_{OEP}$ = 0.73 ± 0.09 ‰ (2s, n = 35) and $\delta^{66}Zn_{1577c}$ = -0.19 ± 0.06 ‰ (2s, n = 45) and previous published results ($\delta^{66}Zn_{1577c}$ = -0.13 ± 0.02 ‰ (2s, n = 4) [34]). For copper, we measured $\delta^{65}Cu_{OEP}$ = -1.10 ± 0.15 ‰ (2s, n = 3) and $\delta^{65}Cu_{1577c}$ = +0.43 ± 0.04 ‰ (2s, n = 4) which is also in good agreement with previous estimated values ($\delta^{65}Cu_{OEP}$ = -1.14 ± 0.13 ‰ (2s, n = 35) and $\delta^{65}Cu_{1577c}$ = +0.37 ± 0.14 ‰ (2s, n = 45) (*cf* Supplementary Table 2).

Based on re-run samples, complete duplicate analyses and standard measurements, we estimate the precision of our measurements at ± 0.12 ‰ (2s). The long-term precision based on the repeated measurements of standard Zn JMC 3-0749L and Cu SRM 976 alone is however better than ± 0.06 ‰ (2s, n = 140).

Principal component analysis (PCA)

Principal component analysis is a multivariate method used to highlight strong patterns in a dataset. In this study, this technique was performed using several parameters including chemical concentrations of major and trace elements and copper and zinc isotopic compositions as well as metabolomics data measured in liver. PCA allows reducing the number of preliminary variables to few linear combinations of the data called principal components (PCs). This procedure (i.e. conversion of raw data to PCs) relies on an orthogonal transformation. In more details, the process of PCA consists of (1) Create a matrix containing all the raw data (i.e. elemental concentrations and isotopic compositions of all the samples). Note that samples for which a measure was missing were excluded. (2) Determine the covariance matrix and (3) Calculate the eigenvectors and the eigenvalues of this covariance matrix to determine the principal components (PCs) (PC1 and PC2 correspond to the eigenvectors with the largest eigenvalues). All these steps were implemented in MATLAB™.

SUPPLEMENTARY FIGURES

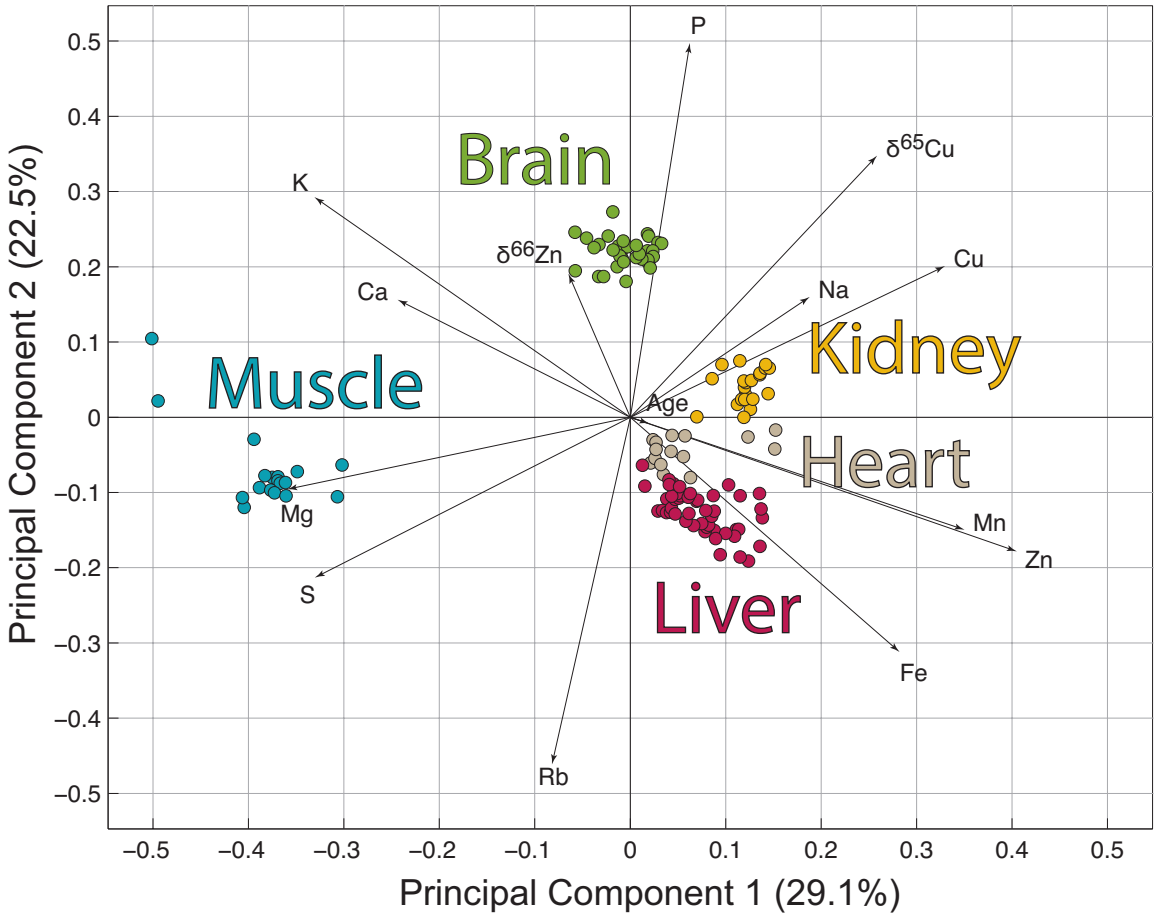

Figure S1: Principal component analysis (PCA).
PCA distinguishes mice organs regardless of the age based on their intrinsic elemental concentrations and Cu-Zn isotopic composition.

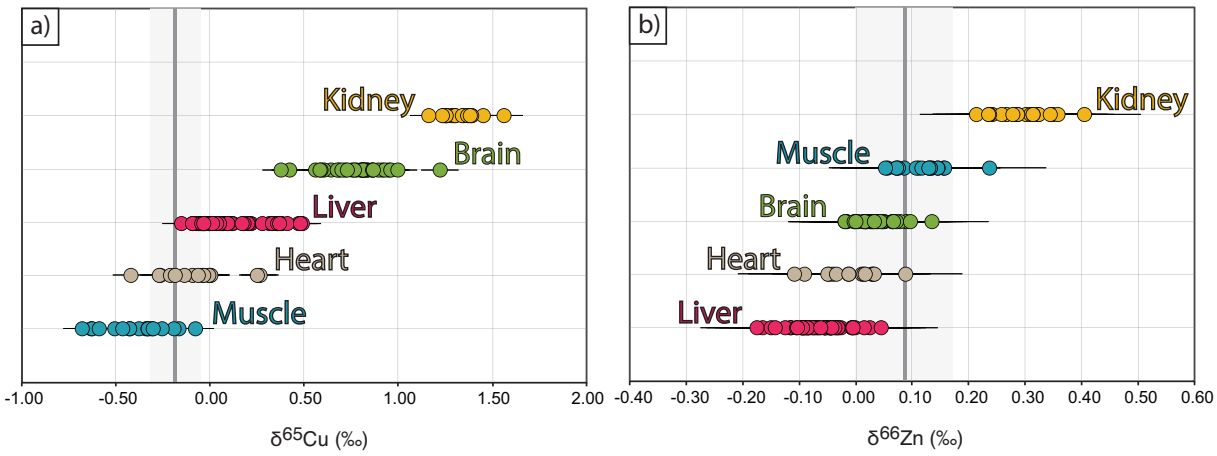

Figure S2: a) Copper and b) zinc isotopic compositions measured in kidneys, brains, livers, hearts and quadriceps muscles of mice. The grey area represents the value measured in food diet.

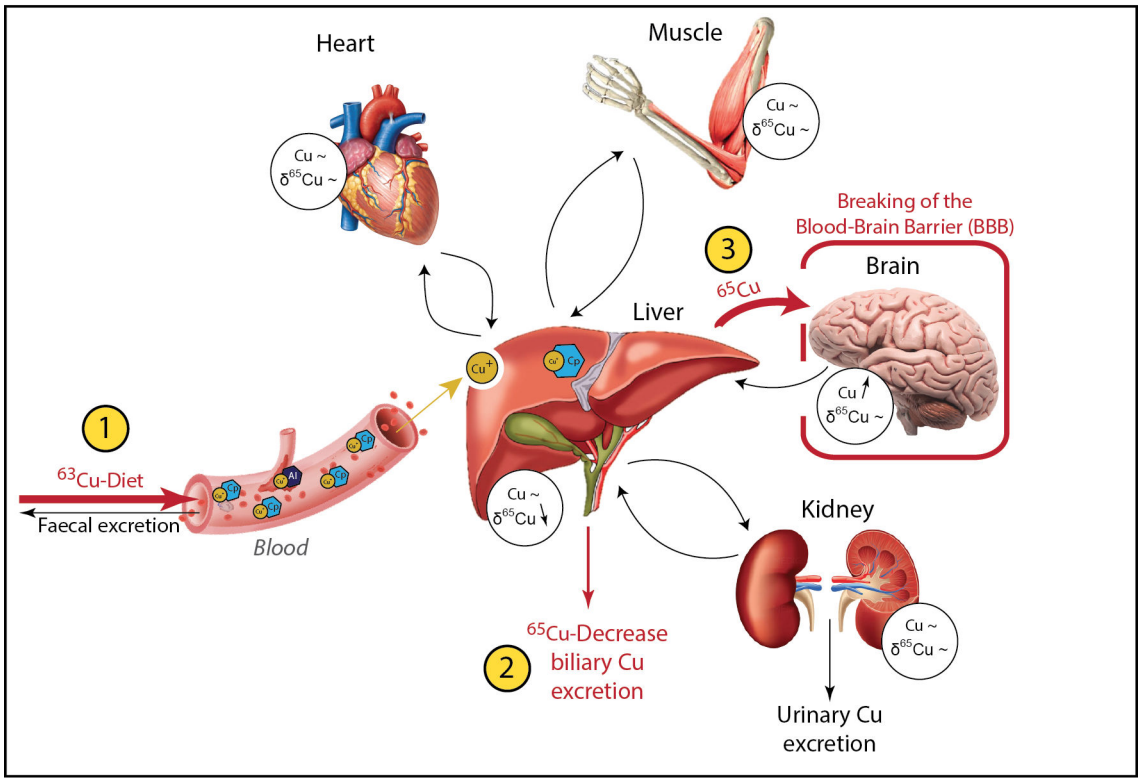

Figure S3: Schematic diagram illustrating mechanistic processes accounting for $\delta^{65}Cu$ decrease in livers associated with Cu increase in brain over time. Hypotheses include impaired Blood-Brain barrier (BBB), affected Cu dietary intake and Cu biliary excretion.

SUPPLEMENTARY TABLES

NB: With regard to confidentiality, the supplementary data are not provided in this manuscript

Table S1: Elementary concentrations (ppm) and Cu-Zn isotopic compositions of mice organs including liver (L), brain (B), heart (H), quadriceps muscles (M) and kidney (K).
"dup" stands for complete dissolution duplicate and "bis" for re-run analysis. "<LD" and "n/a" stands for below limit of detection (defined by IUPAC) and not measured data respectively.

Table S2: Elementary concentrations (ppm) and Cu-Zn isotopic compositions of in-house (OEP) and certified (1577c) reference materials.
"n/a" stands for not measured data. OEP (ewe plasma) is an in-house standard. 15577c is an international bovine liver standard from NIST (National Institute of Standards and Technology).
** long-term in-lab average*
*** Reference values form NIST*

Table S3: Metabolomics data measured in young (i.e. 6months) and old (i.e. 24months) liver of mice. Data are from Houtkooper et al.[4]

III.2. Contraintes apportées par le modèle de vers (*C.elegans*)

III.2.1. Variations chimiques et isotopiques: de nouveaux outils pour quantifier le vieillissement

Dans le manuscrit précédent, nous avons démontré que la majorité des organes de souris étaient affectés par des dérèglements chimiques et isotopiques et que ces variations, bien qu'elles soient spécifiques à chaque organe, sont dépendantes les unes des autres et sont reliées à des dysfonctionnements physiologiques et métaboliques au cours du temps. Par la suite, nous avons cherché à savoir si ces variations pouvaient également apporter des informations pour (1) prédire l'évolution temporelle et la vitesse de développement du vieillissement, et (2) pour contrôler voire 'renverser' la progression de ce processus afin d'optimiser la qualité de vie des personnes âgées.

Pour répondre à ces questions, nous nous sommes intéressés dans le manuscrit ci-dessous à 4 lignées de nématodes (*C.elegans*) génétiquement modifiés comprenant : (1) un vers sauvage, c'est à dire un vers génétiquement non modifié (N2), (2) une espèce longévive (e1370), (3) une espèce à courte durée de vie (mu86) et (4) un double-mutant (CF1588) ayant une durée de vie similaire à celle du vers sauvage. En travaillant avec des modèles animaux génétiquement modifiés au sein d'un laboratoire de biologie, plusieurs paramètres indépendants du vieillissement peuvent cependant affecter de façon significative les variations chimiques et donc biaiser les interprétations finales. C'est par exemple le cas de la contamination externe pouvant être induite pendant la phase de récolte des nématodes. De manière générale, les animaux sont collectés avec une solution tampon à pH neutre (M9) puis lavés avec de l'eau ultra-pure déionisée (voir chapitre II.1.1.b pour plus de détails). La figure 4 montre qu'un mauvais lavage (*i.e.* un seul lavage en eau) peut entrainer une contamination non négligeable pour certains éléments traces comme le cuivre ($[Cu]_{1\ lavage}$ = 6.48 ± 1.54 (1sd, n=9) ppm versus $[Cu]_{3\ lavages}$= 3.30 ± 0.77 (1sd, n=18) ppm) et le manganèse ($[Mn]_{1\ lavage}$= 40.88 ± 19.85 (1sd, n=9) ppm versus $[Mn]_{3\ lavages}$= 19.16 ± 5.75 (1sd, n=18) ppm) s'expliquant par des traces résiduelles de M9 dans l'échantillon final. L'analyse des concentrations en éléments traces et majeurs de la solution tampon M9 indique que si 1mL de cette solution reste dans le culot du tube contenant l'échantillon, cela peut quasiment doubler la concentration en cuivre finale mesurée, par exemple de ~3ppm à ~6ppm (Figure 5). Dans cette étude, tous les nématodes ont donc été lavés au minimum trois fois avec de l'eau ultra-pure dé-ionisée afin de limiter les contaminations au M9.

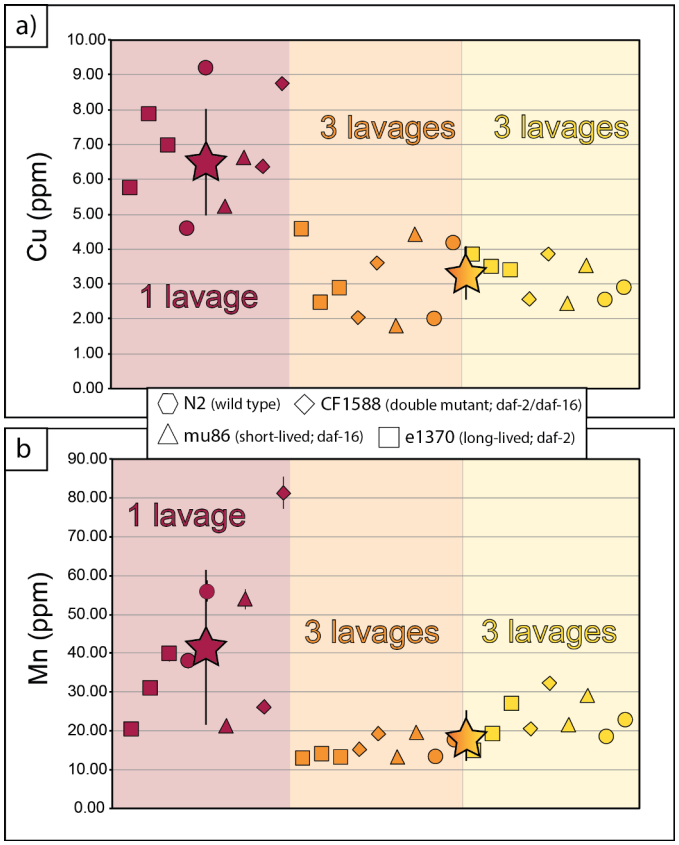

Figure 4 : Effet de la contamination externe sur les concentrations en cuivre (Cu) et en manganèse (Mn) dans différentes lignées de nématodes C.elegans (N2, CF1588, e1370 et mu86). 'Lavage' signifie lavage à l'eau ultra-pure déionisée. Les étoiles représentent les valeurs moyennes pour chaque batch attachées de leur incertitudes (1sd) respectives. Chaque couleur représente un test différent.

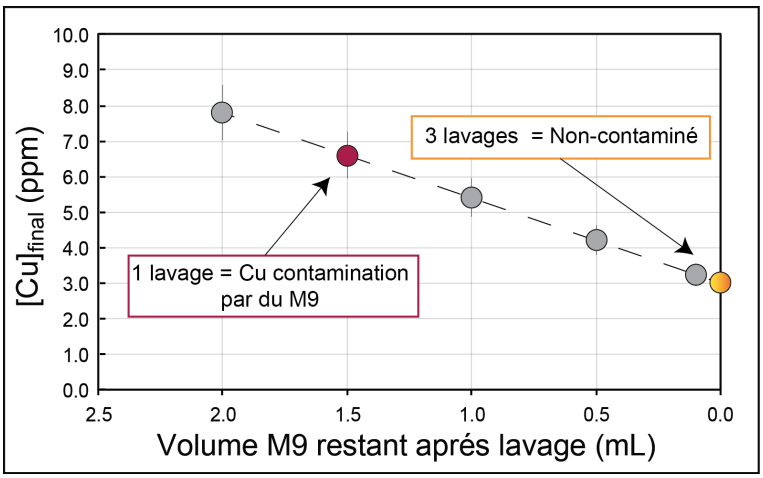

Figure 5 : Modélisation représentant l'impact d'une contamination par du M9 (solution tampon utilisée pour collecter les vers) sur les concentrations en cuivre. Les points rouge et jaune représentent les concentrations en cuivre mesurées dans des vers après avoir été récoltés avec du M9 puis lavés avec 1 lavage et 3 lavages en eau respectivement. En supposant que l'écart de concentrations entre 1 et 3 lavages résulte uniquement de traces résiduelles de M9, il est possible de déterminer le pouvoir contaminant du M9. La formule est la suivante: $m_{Cu1lavage} = m_{Cu3lavage} + m_{CuM9}$. Connaissant la concentration en M9, il est possible de quantifier le volume de M9 expliquant l'écart de concentrations entre les deux échantillons.

Des variations chimiques peuvent également être induites par des manipulations génétiques telles que les mutations. Par définition une mutation vise à sur ou sous-exprimer un gène codant pour une protéine. Les métaux étant bien souvent des cofacteurs de ces protéines, le dérèglement biologique induit par la mutation peut entrainer de facto des variations chimiques plus ou moins importantes. Avant de s'intéresser aux variations chimiques liées au vieillissement, il nous a donc fallu identifier et différencier les éléments chimiques dont les variations étaient spécifiques au processus de mutation de celles spécifiques au vieillissement. Cet aspect est discuté en détail dans la première partie du manuscrit présenté ci-dessous. Cela nous a ensuite permis de centrer notre étude sur des éléments spécifiques ne variant qu'avec l'âge, comme par exemple le cuivre, afin d'identifier de nouveaux outils permettant de quantifier l'évolution du vieillissement et de prédire la qualité de vie des organismes vieillissant.

ARTICLE

"Metallome evolution in ageing *C. elegans* and a copper stable isotope perspective"

Lucie Sauzéat*, Anne Laurençon, Vincent Balter*

(Published in Metallomics)

Metallomics

PAPER

Cite this: *Metallomics*, 2018, **10**, 496

Metallome evolution in ageing *C. elegans* and a copper stable isotope perspective†

Lucie Sauzéat, *[a] Anne Laurençon[b] and Vincent Balter [a]

Received 20th November 2017,
Accepted 15th February 2018

DOI: 10.1039/c7mt00318h

rsc.li/metallomics

Ageing is accompanied by important chemical deregulations resulting in bodily metal imbalances. The way and extent to which these deregulations are associated with ageing processes are however poorly understood and their use as potential biomarkers of ageing has not been investigated. In this study, we report whole-body elementary concentrations and copper and zinc isotopic compositions of *Caenorhabditis elegans* in ageing wild type (*i.e.* 'normal'-lived) and mutant (*i.e.* short and long-lived) strains. We show that the strains are characterized by different levels of mutation-related variations such as in phosphorus and magnesium as well as in zinc isotopic composition. During ageing, strains are affected by elemental age-related variations, such as an increase in calcium and iron concentrations and a decrease in the copper isotopic composition and concentration for long-lived mutants. The deregulated metabolism of copper seems to be connected to ageing probably in association with the production of reactive oxygen species. We emphasize that the copper stable isotope composition could serve as a biomarker of normal or accelerated ageing in the future.

Significance to metallomics

Here we report a comprehensive set of metal concentrations and Cu–Zn isotopic compositions of wild type and mutant worms analyzed at different stages of their life. We identified two types of chemical variations: one related to the age, highlighting a critical role of metal deregulations in ageing, and the other specific to mutations. Focusing on age-specific elements, in particular copper, we show that long-lived animals are characterized by distinct early-age variations compared to control worms. Although these results need to be verified by further studies, the present study suggests that copper isotopic compositions could be used in the future to predict lifespan and detect premature ageing conditions.

1. Introduction

By 2050, the number of elderly people over 65 is expected to triple to about 1.5 billion representing 16 percent of the world's population.[1] This rapid increase in life expectancy will encompass dramatic changes such as the development of severe pathological disorders[2] and neurodegenerative diseases[3] making ageing one of the most prominent risk factors for death in the old population. To date, the identification and measurement of biomarkers of ageing have been a major subject of research because biomarkers can shed light on some ageing processes but most importantly, because biomarkers could be potentially useful to detect abnormal and/or premature ageing conditions.[4]

In accordance with the heterogeneity of all the pathways involved in ageing, many biomarkers, being chemical or biological, have already been proposed. These include for example proteostasis impairment,[5] an increase in advanced glycation end products[6] related to glycogen metabolism deregulation (*i.e.* high glucose diet),[7,8] oxidative stress increase[9] and mitochondrial dysfunction,[10] as well as markers linked to DNA processes like DNA methylation,[11,12] telomere shortening[13] or DNA damage accumulation.[14] Predicting biological age is nonetheless a difficult task, and we know that we still do not have a good single index of prediction in humans[15] meaning that we are probably missing a key factor that would work from simple to more complex organisms.

Over the last few decades, the number of studies focusing on age-related changes of the concentrations of major and trace elements has continuously increased supporting the idea that ageing is associated with important elemental deregulations. These elemental deregulations have been observed at the scale of the whole body of the *C. elegans* worm,[16] in various organs in murine models[17–19] and in human blood.[20–23] More recently,

[a] *Université de Lyon, ENS de Lyon, CNRS, LGL-TPE, 69007 Lyon, France. E-mail: lucie.sauzeat@ens-lyon.fr*
[b] *UMR 5534, Institut de Génomique Fonctionelle de Lyon (IGFL), CNRS, Université Claude Bernard (Lyon 1), Ecole normale supérieure de Lyon, France*

† Electronic supplementary information (ESI) available. See DOI: 10.1039/c7mt00318h

studies on the worm model have suggested that lifespan could be dependent on metal deregulations. This relies on the observation that high levels of metal exposure including aluminum, iron, copper, zinc, manganese, lead, calcium and cadmium significantly decrease the mean lifespan with a concomitant impairment of several pathological functions such as reproduction, brood size, development and locomotion behavior.[24–26] Conversely, metal binding interventions allowing stopping metal accumulation usually extend the normal lifespan.[16,27,28] All these results are clearly substantial pieces of evidence of the contribution of metallome dyshomeostasis to the ageing process to some extent, although the exact mechanistic links by which they are related to each other remain poorly understood.

Stable isotopic compositions may offer a more comprehensive view and additional means to constrain the metallome evolution during ageing. In two pilot studies, the copper and zinc isotope compositions, δ^{65}Cu and δ^{66}Zn, respectively, were measured for the first time in various organs of sheep raised experimentally with a controlled diet.[29,30] The key observation was that the δ^{66}Zn and δ^{65}Cu values in feces were slightly different from that of the diet, the Zn and Cu isotope compositions in feces being ^{66}Zn-depleted and ^{65}Cu-enriched, respectively. Therefore, mass conservation requires that organisms balance these disequilibria by accumulating a ^{66}Zn-enriched and a ^{65}Cu-depleted component, suggesting that δ^{65}Cu and δ^{66}Zn could be potential biomarkers of ageing. Challenging this hypothesis, Jaouen *et al.*[31] measured the copper and zinc isotope compositions in the blood of volunteers from a remote Yakut population, and found that the δ^{65}Cu and δ^{66}Zn values, respectively, decrease and increase with age, in accordance with previous assumptions. Therefore, although metal concentrations can provide relevant information regarding biological changes over time, additional measurements of isotopic compositions may offer a more comprehensive view of ageing than concentrations alone. Indeed, one advantage of using isotope composition over concentration for a given metal is that the isotopic fractionation, *i.e.* the variation of the isotopic ratio, is independent of the amount of the metal. Thus, isotopic ratios are potentially more reliable biomarkers than concentrations.

In this regard, we report the concentrations of 13 elements as well as the Cu and Zn isotopic compositions during the ageing of wild type and mutant (*i.e. daf-16* short-lived, *daf-2* long-lived and double mutant) *Caenorhabditis elegans* nematodes. We describe the evolution of the metallome of the different strains in terms of mutation-related and age-related variations, discuss the deregulation of the Cu metabolism in relation to the production of reactive oxygen species, and finally propose that the δ^{65}Cu value could be a potential future biomarker of ageing.

2. Materials and methods

2.1. *C. elegans* strains and worms development assay

Four different strains of worms including a wild-type (Bristol N2), a long-lived mutant of the insulin/IGF-1 receptor *daf-2* (*e1370*), a short-lived mutant of the FOXO transcription factor *daf-16*, (*mu86*) and the double mutant for both alleles of CF1588 were used. All the strains were provided by the Caenorhabditis Genetics Center (CGC, University of Minnesota) and were maintained at 20 °C and fed with *E. coli* strain OP50 on nematode growth media (NGM) agar plates as previously described.[32] Bacteria were cultivated within a nutrient-rich microbial growth medium (*i.e.* LB broth-Lennox) containing peptides, amino acids and carbohydrates in a low-salt formulation.

For chemical measurements, synchronized populations of L4 larval stage were placed on 85 mm NGM plates previously seeded with OP50 bacteria and supplemented with 3.95 mg L^{-1} FluoroUracil (FU; Sigma F6627). FU addition was used to prevent egg hatching and young larvae development on plates. Animals were transferred to fresh NGM plates every 5 days to avoid starvation. They were collected before visible age-related declines at three different time points (2 and 10 days for all genotypes as well as 17 days only for the long-lived animals) defined as the period with 100% survival and maximum mobility capacities. This step was carried out under a microbiological safety workbench to ensure sterile conditions and minimize external contaminations. Briefly, worms are collected using a pH-neutral M9 buffer (22 mM KH_2PO_4, 42 mM Na_2HPO_4, 86 mM NaCl, 1 mM $MgSO_4$) followed by 3 rinses with ultra-pure water before being transferred into 2 mL sterilized Eppendorf tubes and frozen at −80 °C for optimized conservation.

2.2. Analyses of concentrations and Cu–Zn isotopic compositions

The Cu and Zn isotopic compositions of worms cannot be determined on a single animal because worms are small (~1 mm). On average, between 10 000 and 30 000 worms are needed per strain and per assay to obtain the minimum amount of Zn and Cu required for precise isotopic measurements. For example, 10 000 worms correspond to about 500 ng of Zn but only 25 ng of Cu. This means that Cu isotopic analyses are highly challenging and require an uncommon and large amount of worms. In addition, since no more than 1000 worms can be deposited per plate, at least 10 plates per condition are necessary. This gives a total of 150 plates for only one assay when including the transfer plates (1 strain collected at 3 timepoints *i.e.* 30 plates + 30 transfer plates and 3 strains collected at 2 different timepoints *i.e.* 60 plates + 30 transfer plates) and 150 additional plates for a single duplicate *i.e.* up to 450 plates for 2 duplicates. Furthermore, keeping the worms alive necessitates a transfer to fresh NGM plates every 5 days, which is time consuming when working with hundreds of plates. Each data point thus represents an important amount of worms and time making the analytical analyses highly difficult and also our capacity to obtain many duplicates as usually carried out in biological studies.

Before each analytical measurement, all samples were first freeze-dried during 48 hours, weighed and then dissolved in a mixture of $HNO_3{\cdot}15N/H_2O_2$ 30% on a hot plate at 130 °C. All the steps of the chemical procedure were carried out in a clean laboratory below laminar flow clean hoods and acids that were doubly distilled to avoid external contaminations. After complete dissolution, major and trace element concentrations as

well as Cu–Zn isotopic compositions were measured at the Ecole normale supérieure (ENS) of Lyon following the procedure described by Maréchal *et al.*[33] and Garçon *et al.*;[34] only brief synopses are provided here.

The concentrations of titanium (Ti), manganese (Mn), iron (Fe), copper (Cu), zinc (Zn), strontium (Sr) and cadmium (Cd) were measured on a quadrupole ICP-MS Thermo iCap-Q and the concentrations of magnesium (Mg), calcium (Ca), potassium (K), sodium (Na), phosphorus (P) and sulfur (S) were measured on an ICP-AES (iCAP 6000 Radial) at the Ecole normale supérieure of Lyon. Indium (In) and scandium (Sc) were used as internal standards on ICP-MS and ICP-AES, respectively, to correct instrumental biases. The validity and reproducibility of major and trace element concentrations are estimated to be better than 10% (2sd) based on the analyses of re-run analysis, complete duplicates and repeated measurements of international (*i.e.* bovine liver, 1577c) and in-house (*i.e.* owe plasma, OEP) reference materials as unknown samples (see Table S1 in the ESI† for the details).

Once elementary concentrations were measured, copper and zinc were isolated using ion chromatography based on the procedure previously detailed by Maréchal *et al.*[33] Briefly, Cu and Zn were purified using quartz columns filled with 1.8 mL of Bio-Rad AG MP-1 (100–200 mesh) anion exchange resin. After removing the matrix phase with 10 mL of 7 N HCl + 0.001% H_2O_2, Cu was first eluted with 20 mL of the same solution, followed by Zn with 10 mL of a 0.5 N HNO_3 solution. Total procedural blanks were less than 4 ng for Zn and lower than 0.4 ng for Cu which represents 1/125 and 1/62 of the amount of element isolated from the samples for Zn and Cu, respectively ($\sim$500 ng for Zn and $\sim$25 ng for Cu).

Isotopic compositions were measured on a Nu Plasma (Nu 500) MC-ICP-MS under wet plasma conditions. On the day of the analyses, Zn and Cu purified solutions were diluted in a Cu (Cu SRM 976, National Institute of Standards and Technology, Gaithersburg, MD, USA) and Zn-doped solution (Zn JMC 3-0749L, Johnson Matthey Royston, UK) respectively to match the concentration of the standard mixture run between the samples (between 75 and 300 μg L^{-1} depending on the sample). The delta values (expressed in ‰) are reported relative to the isotopic solution reference material NIST SRM 976 for Cu and JMC 3-0749L for Zn and are referred to as:

$$\delta^{65}Cu_{sample} = \left[\frac{\left(^{65}Cu/^{63}Cu\right)_{sample}}{\left(^{65}Cu/^{63}Cu\right)_{standard}} - 1 \right] \times 1000$$

and

$$\delta^{66}Zn_{sample} = \left[\frac{\left(^{66}Zn/^{64}Zn\right)_{sample}}{\left(^{66}Zn/^{64}Zn\right)_{standard}} - 1 \right] \times 1000$$

Instrumental mass fractionation was corrected with an exponential law using an elemental-doping method and instrumental drift over time was controlled with standard sample bracketing as recommended by Maréchal *et al.*[33]

The long-term precision of our results is assessed by repeated analyses of the pure Cu SRM 976 and Zn JMC 3-0749L standard solutions run every two samples and the accuracy is assessed by the analysis of in-house and international reference materials. The reproducibility (2sd) of the Cu SRM 976 and Zn JMC 3-0749L standards was better than 0.1‰ (n = 50) for both $^{65}Cu/^{63}Cu$ and $^{66}Zn/^{64}Zn$ ratios. Our results for the reference standards are 0.16‰ (2sd, n = 9) for OEP and 0.09‰ (2sd, n = 5) for 1577c for $^{65}Cu/^{63}Cu$ ($\delta^{65}Cu_{OEP} = -1.11 \pm 0.16$ (2sd, n = 9), $\delta^{65}Cu_{1577c} = +0.35 \pm 0.09$ (2sd, n = 5)) and better than 0.1‰ for OEP and 1577c for $^{66}Zn/^{64}Zn$ ratios ($\delta^{66}Zn_{OEP} = +0.73 \pm 0.04$ (2sd, n = 3), $\delta^{66}Zn_{1577c} = -0.19 \pm 0.09$ (2sd, n = 6)). All these values are in good agreement with our previous laboratory measurements *i.e.* $\delta^{65}Cu_{OEPref} = -1.15 \pm 0.20$ (2sd, n = 35), $\delta^{65}Cu_{1577cref} = +0.37 \pm 0.14$ (2sd, n = 45) and $\delta^{66}Zn_{OEPref} = +0.73 \pm 0.09$ (2sd, n = 35), $\delta^{66}Zn_{1577cref} = -0.16 \pm 0.15$ (2sd, n = 45) as well as with previous published results ($\delta^{66}Zn_{1577c} = -0.13 \pm 0.02$ (2sd, n = 4)[35]). Given our long-term precision and the accuracy obtained on reference material measurements, the 2sd analytical uncertainty adopted in this study for the Cu and Zn isotopic compositions is ± 0.1‰.

3. Results

Major and trace element concentrations as well as Cu and Zn isotopic compositions ($\delta^{65}Cu$ and $\delta^{66}Zn$, respectively) measured in the four different strains are all reported in Table S1 in the ESI† and shown in Fig. 1. To evaluate the whole pattern of variations, we used a principal component analysis (PCA). Briefly, this statistical technique performs a linear transformation to find a system for the complete dataset with new variables called principal components (PCs). The main result is that all the animals are affected by distinct and specific chemical variations that are either age-related (variations along the x principal component axis; 46.7%) or mutation-related (variations along the y principal component axis; 32.2%).

Along the x principal component axis, the 2 day old animals are less enriched in Cd, Mn, Ca, Sr, Fe, Ti and Cu and have a higher amount of $\delta^{65}Cu$ compared to the 10 day old animals (Fig. 1, 2a and b). An illustration is given in Fig. 2a for Fe showing that concentrations are roughly similar ($\sim$100 ppm) in all the strains at 2 days, and then increase by a factor of 2 at 10 days. This holds for Ca too, which is concentrated by at most a factor of 3 between 2 and 10 days in the N2 strain (Fig. 2b). For all these elements, the major source of variation is age whatever the strain considered is.

Along the y principal component axis, the wild type strains are more concentrated in P, Mg, S, Na and K than the short-lived and the double mutants that are in turn more enriched in these elements than the long-lived worms. An example is given in Fig. 2c for P. The highest P content is observed in the wild type nematodes (23721 ± 3779 (2sd, n = 3) ppm) while the lowest concentrations are measured in the long-lived *daf-2* (e1370) mutants (17573 ± 3214 (2sd, n = 3) ppm). However, for a given strain, subtle variations with age can be observed and, as in the

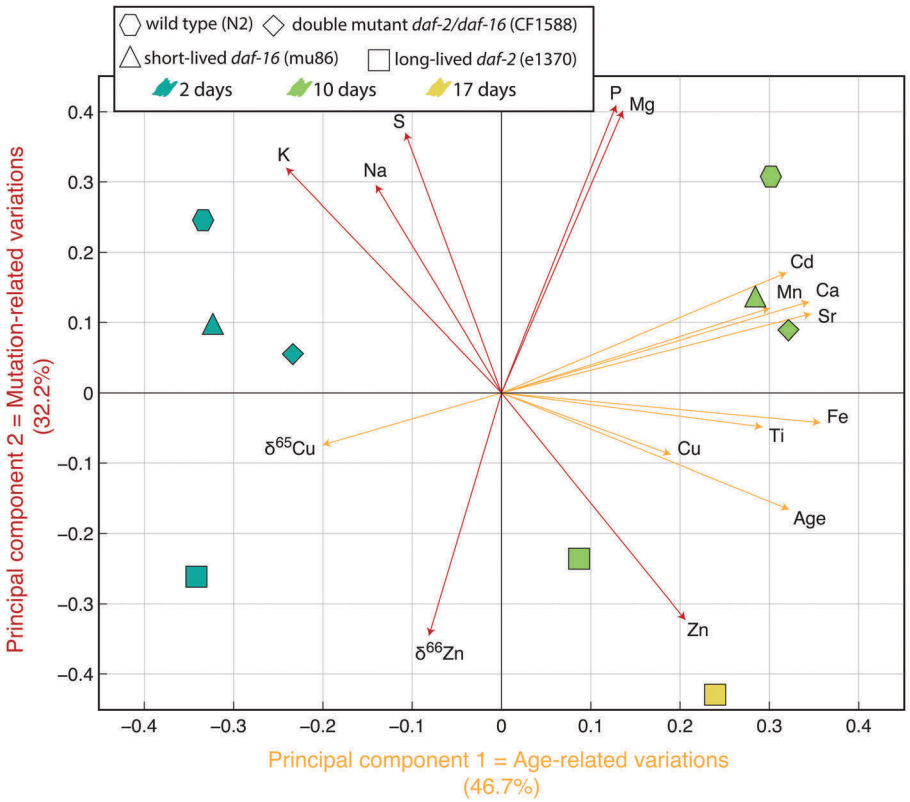

Fig. 1 Principal component analysis (PCA) diagram. PCA is a multivariate method used to highlight strong patterns in a dataset. In this study, this technique was used to classify four different *C. elegans* nematode strains based on several parameters including the chemical concentrations of about 15 elements and copper and zinc isotopic compositions that were normalized to their standard deviation. In more detail, the process of PCA consisted of (1) creating a matrix containing all the raw data (*i.e.* elemental concentrations and isotopic compositions of all the samples). Note that samples for which a measure was missing were excluded. (2) Determining the covariance matrix and (3) calculating the eigen-vectors and the eigen-values of this covariance matrix to determine the principal components (PCs) (PC1 and PC2 correspond to the eigen-vectors with the largest eigenvalues). All these steps were implemented in MATLAB™. PC1 and PC2 explain ~80% of the total variance in chemical composition. Orange and red arrows are graphic representations of loading factors for PC1 and PC2 respectively. Each point is an average of three different complete duplicate analyses (n = 3) except for Cu, Mn and δ^{65}Cu (n = 2). The PCA allows for the classification of chemical variations observed in mutant worms over time into two different groups: (1) the elements related to the age progression (principal component 1, PC1) *i.e.* Cd, Mn, Ca, Sr, Fe, Ti, Cu and δ^{65}Cu and (2) the elements related to the mutation process (principal component 2, PC2) *i.e.* K, Na, S, P, Mg, Zn and δ^{66}Zn.

case of purely age-related variations, trace element concentrations generally increase between 2 and 10 days (Fig. 2c). The type of mutation drives the Zn isotope composition (Fig. 2d), long-lived mutants *daf-2* (e1370) having the highest δ^{66}Zn values ($\delta^{66}Zn_{e1370} = -0.19‰ \pm 0.08$ (2sd, n = 3)), and N2 wild types the lowest δ^{66}Zn values ($\delta^{66}Zn_{N2} = -0.36‰ \pm 0.28$ (2sd, n = 3)). The influence of ageing on the Zn isotope composition is very weak (Fig. 2d).

Focusing on the Cu isotopic composition and concentration, distinct temporal variations are observed between long-lived animals and all the other strains (Fig. 3). Between 2 and 10 days, the δ^{65}Cu value remains constant in the wild type, short-lived and double mutant worms while it decreases in the long-lived mutant from -0.25 ± 0.69 (2sd, n = 2) ‰ to -0.85 ± 0.06 (2sd, n = 2) ‰ reaching -1.08 ± 0.76 (2sd, n = 2) ‰ at 17 days (Fig. 3a). Similarly, the Cu concentration decreases in the long-lived worms from 4.22 ± 1.01 (2sd, n = 2) ppm to 3.00 ± 1.46 (2sd, n = 2) ppm between 2 and 10 days and then tends to stabilize at 17 days (3.15 ± 0.75 (2sd, n = 2) ppm) while it increases in all the other strains from ~2.25 to ~3.75 ppm (Fig. 3b).

Despite the large uncertainties likely resulting from the variability between batches of animals of the same age and the great difficulty to obtain many duplicates as usually carried out in biological studies (see details in Section 2.2.), these preliminary results tend to demonstrate that long-lived animals are chemically different from the other strains. In the future, increasing the number of duplicates would undoubtedly improve the data precision and probably help to strengthen this interpretation.

4. Discussion

4.1. Age *versus* mutation-related chemical variations

The present results show that all the 10 day old worms are enriched in Cd, Mn, Ca, Sr, Fe, Ti and Cu and have lower amounts of δ^{65}Cu compared to the 2 day old worms (Fig. 1, 2a and b). The metal accumulation over time is in agreement with

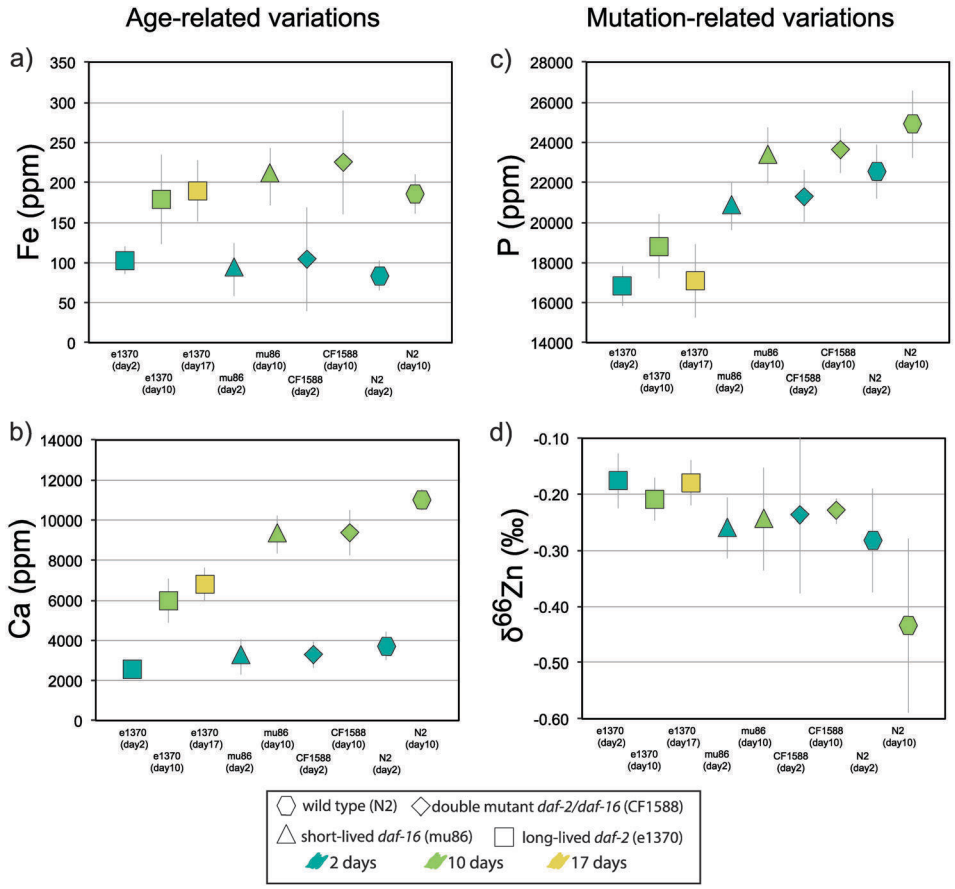

Fig. 2 Distinction between age and mutation-related variations. (a) Iron (Fe) and (b) calcium (Ca) fluctuations over time reflect age-related variations while (c) phosphorus (P) and (d) zinc isotopic compositions (δ^{66}Zn) reflect mutation-related variations. Blue, green and yellow points represent animals collected at 2, 10 and 17 days old respectively. For each value analytical error bars represent 1sd obtained on the average of three different complete duplicate analyses (n = 3).

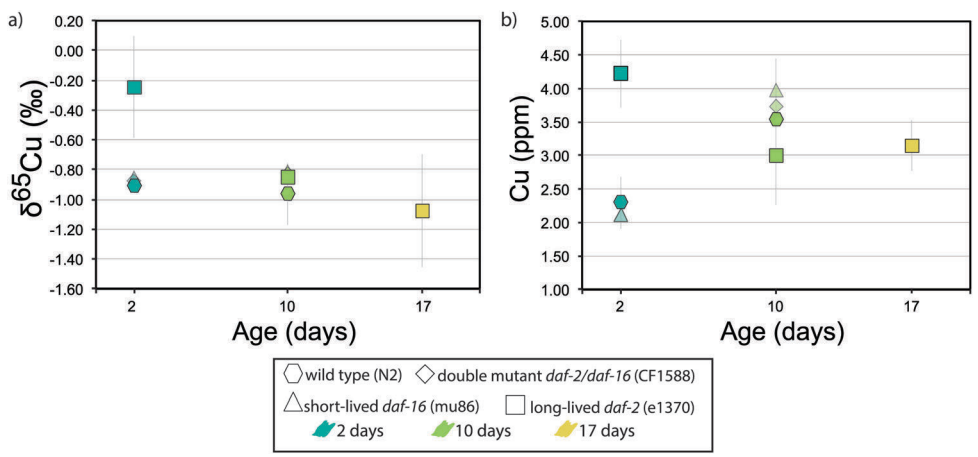

Fig. 3 (a) δ^{65}Cu and (b) Cu fluctuations over time in four *C. elegans* nematode strains including (1) wild-type (N2), (2) short-lived mutants of the DAF-16 FOXO transcription factor: *daf-16*(mu86), (3) long-lived mutants of the insulin/IGF1 receptor: *daf-2*(e1370) and (4) double mutants for both *daf-2* and *daf-16* alleles: CF1588. Reverse early-age chemical fluctuations are observed between wild type (N2) and long-lived (e1370) worms. Each value is an average of two different complete duplicate analyses (n = 2). Analytical error bars are 1sd for long-lived (e1370) and wild type (N2) nematodes. Note that for the δ^{65}Cu diagram, short-lived (mu86) and double mutants (CF1588) are hidden beneath the wild type (N2) at 2 days and the long-lived (e1370) at 10 days. Similarly for the copper concentration at 2 days, the double mutant (CF1588) is hidden beneath the wild-type (N2).

a previous study[16] reporting an increase of Ca, Cu, Fe and Mn levels as a function of age in worms. Similar results have also been reported for mammals (*i.e.* mice and bovines)[17,19,36] and humans[22,37] for which increases of copper and iron have been

observed in organs and plasma, respectively, supporting a critical role of metal accumulation in ageing.

Regarding isotopic ratios, the decrease of the δ^{65}Cu values with lifespan is in line with the results reported by Jaouen *et al.*[31] who measured a decrease of the blood δ^{65}Cu value during ageing in a remote Yakut population. Similarly, the constant δ^{66}Zn value observed over time (Fig. 2d) is consistent with the results of Moynier *et al.*[38,39] who reported a constant δ^{66}Zn value in serum and red blood cells of mice between 9 and 12 months. However, the study of Jaouen *et al.*[31] reports a small increase of the blood δ^{66}Zn value during ageing that is not observed consistently in the present dataset (Fig. 1 and 2d). This is probably because our study includes genetically modified organisms with specific mutations that have a stronger influence on the Zn isotopic composition. As shown in Fig. 2d, the long-lived *daf-2* mutants present a higher isotopic ratio than those of the control mutants, while variations linked to age are rather low.

Genetic mutations affect gene-specific signaling pathways in which trace elements can be involved as co-factors, leading to a potentially important variation of elemental concentrations. The *daf-2* mutation triggers for example inappropriate activation of the downstream DAF-16 transcription factor (*i.e.* a FOXO-family)[40,41] that regulates the expression of several metal detoxification genes including *mtl-1* (metallothionein homologue gene)[42] and *sod-3* (superoxide dismutase gene)[43] *i.e.* two genes encoding the metallothionein and the superoxide dismutase metal-binding proteins, respectively. By chelating, sequestering and then excreting free metal ions out of the cells, these proteins in association with other larger metal-binding proteins prevent metal accumulation and play a major role in metal detoxification; a process referred to as a metal stress response. Consequently, the *daf-2* mutants, which possess an extended lifespan, have a higher metal stress response[42,44,45] that may account for the lower metal content such as K, Na and Mg compared to wild type worms (Fig. 1). While we have not tested these mutants, we can however cite the studies of Davis *et al.*[46] and Roh *et al.*[47] which demonstrated that *cdf-2* and *ttm-1* loss-of-function mutant nematodes displayed reduced Zn content compared to wild type animals. Taken together, these results demonstrate that for a given strain, elemental burden is characteristic of a time-point in the lifespan of *C. elegans*.

4.2. The case of Cu in ageing

The early-age temporal evolution of Cu concentration and isotopic composition is different between long-lived worms and all the other strains (Fig. 3). Between 2 and 10 days, the δ^{65}Cu value tends to remain relatively constant in the wild type, short-lived and double mutant worms while it slightly decreases in the long-lived mutant from -0.25 ± 0.69 (2sd, $n = 2$) ‰ to -0.85 ± 0.06 (2sd, $n = 2$) ‰ reaching -1.08 ± 0.76 (2sd, $n = 2$) ‰ at 17 days (Fig. 3a). Similarly, the Cu concentration tends to decline in the long-lived mutants from 4.22 ± 1.01 (2sd, $n = 2$) ppm to 3.00 ± 1.46 (2sd, $n = 2$) ppm between 2 and 10 days and then tends to stabilize at 17 days (3.15 ± 0.75 (2sd, $n = 2$) ppm) while it increases in the wild type, the double mutant and the short-lived worms from $\sim$2.25 to $\sim$3.75 ppm (Fig. 3b). Despite large uncertainties likely resulting from the variability between the animals of the same age, these results demonstrate for the first time that long-lived mutants slightly differ in their early life from the other strains. Increasing the number of duplicates, which is not straightforward regarding the difficulties represented by precise elemental and isotopic measurements on worm samples, would contribute to improve the data precision and thus help to strengthen this interpretation. The differences observed between the long-lived mutants and all the other strains are not linked to genetic background but rather reflect specific lifespan and probably healthspan. Previous studies indeed showed that long-lived worms have a lifespan but also healthspan which is twice longer than those of wild type, double mutant as well as short-lived worms.[40,48] The long-lived animals can live up to 60 days with approximately 20 days in good health conditions while the maximal lifespan of the three other strains does not exceed 20 to 25 days with less than 8 average days in good health conditions.[48]

Given these preliminary results, although further studies are requested to improve the data precision and strengthen our interpretation, we emphasize that the early-age kinetic of the burden of some metals, especially Cu, may be a reliable marker of ageing and can help to distinguish animals with extended lifespans. This assumption is supported by similar evolution of the concentrations of other metals such as Fe and Ca. These metals accumulate in the body during ageing, but the rate of accumulation is higher in short-lived, double mutants and wild type worms compared with in long-lived mutants (Fig. 2a and b). For instance, while the Ca concentration tends to triple between 2 days and 10 days in the short-lived, double mutant and the wild-type strains, it only doubles in the long-lived mutant between 2 days and 17 days (Fig. 2b).

Interpreting the Cu isotopic data is difficult given that the use of stable isotope for metallomic studies is still in its infancy. We can however propose a mechanistic explanation to account for the observed Cu isotope fractionation during ageing.

In excess and in an environment favorable for oxidation, cuprous (Cu^{+}) copper ions can be oxidized to cupric (Cu^{2+}) favoring the formation of highly reactive oxygen species (ROS) such as hydroxyl radicals ($^{\bullet}OH$) *via* the Haber–Weiss reaction[49,50] (Fig. 4). Once produced, ROS damage proteins, lipids and DNA[51,52] and consequently accelerate ageing onset and progression. In parallel, reduced Cu^{+} compounds are expected to favor light isotopes relative to Cu^{2+}. Therefore, the formation of ROS should preferentially be associated with the oxidation of $^{63}Cu^{+}$ into $^{63}Cu^{2+}$ contributing to a Cu isotope fractionation favoring light ^{63}Cu over heavy ^{65}Cu; the latter being not involved in ROS production is preferentially excreted leading ultimately to a decrease of the δ^{65}Cu value over time (Fig. 4).

However, this hypothesis does not clarify all the observations made in the present study. For instance, the absence of any decrease in the δ^{65}Cu value is puzzling, in spite of a significant Cu concentration increase, for the short-lived, double mutants and wild type worms. The diminution of the Cu content between 2 and 10 days observed in the long-lived worms (Fig. 3b) probably tends to limit the abnormal generation of ROS resulting in the

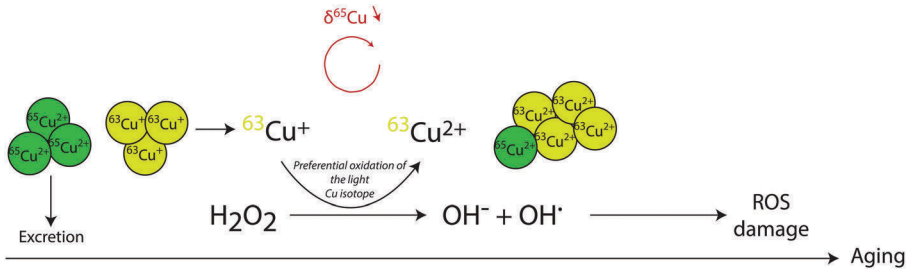

Fig. 4 Conceptual model explaining the temporal diminution of the copper isotopic composition ($\delta^{65}Cu$) with ageing. ROS stands for reactive oxygen species. OH^- (hydroxyl ion) and $OH^\bullet$ (hydroxyl radical) are two different types of ROS.

extension of lifespan. If correct, it would suggest that Cu accumulation over time could be a key factor accounting for ROS-induced damages and ageing acceleration. Although these assumptions need to be verified by further experiments including for example the measurement of ROS and lipid peroxidation changes in *C. elegans* exposed to Cu overload, mitigating these chemical processes, notably through chelation, could eventually improve healthy lifespan.

5. Conclusions

Important elemental and isotopic variations were measured in genetically controlled *C. elegans* strains during ageing supporting a critical role for metal deregulations in ageing. Strains are also affected by mutation-related variations suggesting that caution should be taken when comparing the metallome of different genetically modified *C. elegans*. This caution should apply to other genetically engineered organisms, such as the fruit fly and even the rodent models. Focusing on age-related variations, Cu concentration and isotopic composition differences were observed between long-lived strains and their controls. Altogether, these results demonstrate that the simultaneous measurement of elemental concentration and isotopic composition may offer a more comprehensive view on ageing than the elemental concentrations alone and that these chemical parameters can be used to predict *C. elegans* lifespan and detect accelerated ageing.

Conflicts of interest

There are no conflicts to declare.

Acknowledgements

We gratefully acknowledge Philippe Gillet of the Ecole Polytechnique Fédérale de Lausanne (EPFL) and the CNRS "mission pour l'interdisciplinarité" for their financial support. We are thankful to Mélanie Simon for her help in the clean laboratory and assistance during isotopic measurements. We also greatly thank Eleni Panagiotidou for the technical help as well as Florence Solari (Claude Bernard University Lyon 1, Villeurbanne), Alexia Buis and Anne-Laure Bulteau (Institut Génomique Fonctionelle de Lyon; IGFL) for their constructive comments and valuable advice on the *C. elegans* assay development.

References

1 World Health Organization, *Global Health and Aging*, 2011.
2 G. A. Roth, M. H. Forouzanfar, A. E. Moran, R. Barber, G. Nguyen, V. L. Feigin, M. Naghavi, G. A. Mensah and C. J. L. Murray, *N. Engl. J. Med.*, 2015, **372**, 1333–1341.
3 H. W. Querfurth and F. M. LaFerla, *N. Engl. J. Med.*, 2010, **362**, 329–344.
4 X. Xia, W. Chen, J. McDermott and J.-D. J. Han, *F1000Research*, 2017, **6**, 860.
5 W. A. Sands, M. M. Page and C. Selman, *J. Physiol.*, 2017, **595**, 6383–6390.
6 P. Gkogkolou and M. Böhm, *Derm.-Endocrinol.*, 2012, **4**, 259–270.
7 I. Gusarov, B. Pani, L. Gautier, O. Smolentseva, S. Eremina, I. Shamovsky, O. Katkova-Zhukotskaya, A. Mironov and E. Nudler, *Nat. Commun.*, 2017, **8**, 1–12.
8 A. Schlotterer, G. Kukudov, F. Bozorgmehr, H. Hutter, X. Du, D. Oikonomou, Y. Ibrahim, F. Pfisterer, N. Rabbani, P. Thornalley, A. Sayed, T. Fleming, P. Humpert, V. Schwenger, M. Zeier, A. Hamann, D. Stern, M. Brownlee, A. Bierhaus, P. Nawroth and M. Morcos, *Diabetes*, 2009, **58**, 2450–2456.
9 K. C. Kregel and H. J. Zhang, *Am. J. Physiol.*, 2006, **292**, R18–R36.
10 S. S. Lee, R. Y. N. Lee, A. G. Fraser, R. S. Kamath, J. Ahringer and G. Ruvkun, *Nat. Genet.*, 2003, **33**, 40–48.
11 P. Sen, P. P. Shah, R. Nativio and S. L. Berger, *Cell*, 2016, **166**, 822–839.
12 S. Horvath, *Genome Biol.*, 2013, **14**, 1–19.
13 H. Jiang, Z. Ju and K. L. Rudolph, *Z. Gerontol.*, 2007, **40**, 314–324.
14 R. R. White, B. Milholland, A. de Bruin, S. Curran, R.-M. Laberge, H. van Steeg, J. Campisi, A. Y. Maslov and J. Vijg, *Nat. Commun.*, 2015, **6**, 1–11.
15 D. W. Belsky, T. E. Moffitt, A. A. Cohen, D. L. Corcoran, M. E. Levine, J. Prinz, J. Schaefer, K. Sugden, B. Williams, R. Poulton and A. Caspi, *bioRxiv*, 2017, 1–26.
16 I. M. Klang, B. Schilling, D. J. Sorensen, A. K. Sahu, P. Kapahi, J. K. Andersen, P. Swoboda, D. W. Killilea, B. W. Gibson and G. J. Lithgow, *Aging*, 2014, **6**, 975–991.
17 A. Morita, M. Kimura and Y. Itokawa, *Biol. Trace Elem. Res.*, 1994, **42**, 165–177.
18 L.-M. Wang, J. S. Becker, Q. Wu, M. F. Oliveira, F. A. Bozza, A. L. Schwager, J. M. Hoffman and K. A. Morton, *Metallomics*, 2010, **2**, 348.

19 S. Fu, W. Jiang and W. Zheng, *Front. Mol. Neurosci.*, 2015, **8**, 966.

20 A. Mezzetti, S. D. Pierdomenico, F. Costantini, F. Romano, D. De Cesare, F. Cuccurullo, T. Imbastaro, G. Riario-Sforza, F. Di Giacomo, G. Zuliani and R. Fellin, *Free Radicals Biol. Med.*, 1998, **25**, 676–681.

21 A. Rembach, D. J. Hare, J. D. Doecke, S. C. Burnham, I. Volitakis, C. J. Fowler, R. A. Cherny, C. McLean, R. Grimm, R. Martins, D. Ames, C. L. Masters, A. I. Bush and B. R. Roberts, *Metallomics*, 2014, **6**, 1216–1219.

22 M. Malavolta, F. Piacenza, A. Basso, R. Giacconi, L. Costarelli and E. Mocchegiani, *Mech. Ageing Dev.*, 2015, 1–8.

23 R. Giacconi, L. Costarelli, F. Piacenza, A. Basso, L. Rink, E. Mariani, T. Fulop, G. Dedoussis, G. Herbein, M. Provinciali, J. Jajte, I. Lengyel, E. Mocchegiani and M. Malavolta, *Eur. J. Nutr.*, 2016, 1–10.

24 H. Harada, M. Kurauchi, R. Hayashi and T. Eki, *Ecotoxicol. Environ. Saf.*, 2007, **66**, 378–383.

25 Y. Zhang, B. Ye and D. Wang, *Arch. Environ. Contam. Toxicol.*, 2010, **59**, 129–136.

26 P. Chen, E. J. Martinez-Finley, J. Bornhorst, S. Chakraborty and M. Aschner, *Front. Aging Neurosci.*, 2013, **5**, 1–11.

27 J. M. Harrington, W. A. Boyd, M. V. Smith, J. R. Rice, J. H. Freedman and A. L. Crumbliss, *Toxicology*, 2012, **129**, 49–56.

28 J. Kumar, T. Barhydt, A. Awasthi, G. J. Lithgow, D. W. Killilea and P. Kapahi, *PLoS One*, 2016, **11**, 1–21.

29 V. Balter, A. Zazzo, A. P. Moloney, F. Moynier, O. Schmidt, F. J. Monahan and F. Albarède, *Rapid Commun. Mass Spectrom.*, 2010, **24**, 605–612.

30 V. Balter, A. Lamboux, A. Zazzo, P. Telouk, Y. Leverrier, J. Marvel, A. P. Moloney, F. J. Monahan, O. Schmidt and F. Albarède, *Metallomics*, 2013, **5**, 1470.

31 K. Jaouen, M. Gibert, A. Lamboux, P. Telouk, F. Fourel, F. Albarède, A. N. Alekseev, E. Crubézy and V. Balter, *Metallomics*, 2013, **5**, 1016–1024.

32 S. Brenner, *Genetics*, 1974, **77**, 71–94.

33 C. N. Maréchal, P. Telouk and F. Albarede, *Chem. Geol.*, 1999, **156**, 251–273.

34 M. Garçon, L. Sauzéat, R. W. Carlson, S. B. Shirey, M. Simon, V. Balter and M. Boyet, *Geostand. Geoanal. Res.*, 2017, **41**, 367–380.

35 K. Jaouen, M. Beasley, M. Schoeninger, J.-J. Hublin and M. P. Richards, *Zinc isotope ratios of bones and teeth as new dietary indicators: results from a modern food web (Koobi Fora, Kenya)*, Nature Publishing Group, 2016, pp. 1–8.

36 P. Zatta, D. Drago, P. Zambenedetti, S. Bolognin, E. Nogara, A. Peruffo and B. Cozzi, *J. Chem. Neuroanat.*, 2008, **36**, 1–5.

37 M. Malavolta, R. Giacconi, F. Piacenza, L. Santarelli, C. Cipriano, L. Costarelli, S. Tesei, S. Pierpaoli, A. Basso, R. Galeazzi, F. Lattanzio and E. Mocchegiani, *Biogerontology*, 2010, **11**, 309–319.

38 F. Moynier, J. Foriel, A. S. Shaw and M. Le Borgne, *Geochem. Persp. Let.*, 2017, 142–150.

39 F. Moynier, T. Fujii, A. S. Shaw and M. Le Borgne, *Metallomics*, 2013, **5**, 693.

40 C. Kenyon, J. Chang, E. Gensch, A. Rudner and R. Tabtiang, *Nature*, 1993, **4**, 366–461.

41 C. Kenyon, *Cell*, 2005, **120**, 449–460.

42 D. Barsyte, D. A. Lovejoy and G. J. Lithgow, *FASEB J.*, 2001, **15**, 627–634.

43 Y. Honda and S. Honda, *FASEB J.*, 1999, **13**, 1385–1393.

44 C. T. Murphy, S. A. McCarroll, C. I. Bargmann, A. Fraser, R. S. Kamath, J. Ahringer and H. L. C. Kenyon, *Nature*, 2003, **424**, 277–284.

45 K. I. Zhou, Z. Pincus and F. J. Slack, *Aging*, 2011, **3**, 1–21.

46 D. E. Davis, H. C. Roh, K. Deshmukh, J. J. Bruinsma, D. L. Schneider, J. Guthrie, J. D. Robertson and K. Kornfeld, *Genetics*, 2009, **182**, 1015–1033.

47 H. C. Roh, S. Collier, K. Deshmukh, J. Guthrie, J. D. Robertson and K. Kornfeld, *PLoS Genet.*, 2013, **9**, e1003522.

48 J.-H. Hahm, S. Kim, R. DiLoreto, C. Shi, S.-J. V. Lee, C. T. Murphy and H. G. Nam, *Nat. Commun.*, 2015, **6**, 1–7.

49 I. Bremner, *Am. J. Clin. Nutr.*, 1998, 1069S–1073S.

50 J. P. Kehrer, *Toxicology*, 2000, **149**, 43–50.

51 L. M. Gaetke and C. K. Chow, *Toxicology*, 2003, **189**, 147–163.

52 E. Matuszewska, J. Kwiatkowska, D. Kuczynska-Wisnik and E. Laskowska, *Microbiology*, 2008, **154**, 1739–1747.

III.2.2. Peut-on accroitre la longévité des vers en modulant leur rapport isotopique en deutérium ?

Dans les deux manuscrits présentés ci-dessus, il a été montré que le vieillissement s'accompagnait d'importants dérèglements chimiques et isotopiques visibles à l'échelle de l'organe et de l'organisme. Ces variations étant spécifiques du vieillissement et apparaissant relativement tôt sur l'échelle d'une vie (voir manuscrit ci-dessus), il est possible qu'elles contribuent à son développement. Réguler ces variations élémentaires et isotopiques pourrait donc constituer un nouveau traitement thérapeutique permettant d'optimiser les conditions de vies des personnes âgées. Cette méthode est par ailleurs déjà utilisée pour retarder l'avancée de certaines pathologies comme la maladie d'Alzheimer (Bush and Tanzi, 2008; Nuttall and Oteiza, 2014) et la maladie de Wilson (Hedera, 2017; Rodriguez-Castro et al., 2015), où des chélateurs (*i.e.* protéines liant les métaux comme le Clioquinol pour le Zn ou la D-penicillamine pour le Cu) sont administrés aux patients pour réduire leur niveau de métaux. Depuis peu, cette technique s'est également vue généralisée au processus de vieillissement (Kumar et al., 2016; Li and Snyder, 2016a; 2016b). Cependant, ces études restent encore rares et restreintes à certains organismes limitant notre compréhension globale du rôle de la modulation chimique et isotopique vis à vis du vieillissement.

Concernant les modulations isotopiques, Demidov et al.(2007) et Shchepinov et al.(2010) ont démontré pour la première fois à travers des modèles cellulaires que des protéines enrichies en isotope lourd du carbone (^{13}C) et en deutérium (D *i.e.* isotope lourd de l'hydrogène) étaient moins affectées par l'action destructive des radicaux libres (ROS), suggérant qu'un enrichissement en isotopes lourds pourrait permettre d'améliorer la qualité de vie des personnes âgées. En 2016, les études de Li and Snyder (Li and Snyder, 2016b; 2016a) confirment cette hypothèse et montrent que la supplémentation de deutérium supprime la formation de ROS et permet d'augmenter la durée de vie de levures de plus de 85% ($D \geq 50\%$). Cependant, si ces résultats sont en accord avec ceux de Vasdev et al.(1990); Kushner et al.(1999); Hammel et al.(2013) et Andreyev et al.(2015) montrant que l'ajout de deutérium optimise les conditions de vies de cellules, drosophiles, algues et rongeurs; ils s'avèrent cependant être contradictoire avec les études de Taylor (1934) et Lewis (1934). En 1934, ces premières études visant à quantifier l'impact des variations isotopiques sur l'organisme montrent en effet que l'ajout de deutérium n'a pas d'effet significatif (Lewis, 1934) voire même, à des effets négatifs sur la respiration et le vieillissement cellulaire (Taylor and Harvey, 1934). Par ailleurs, un autre désaccord intervient sur la dose de deutérium à injecter. Alors que Li and Snyder (Li and Snyder, 2016b; 2016a) démontrent que plus la dose est importante, plus la réponse est optimale; Hammel et

al.(2013) parlent de seuil critique à ne pas dépasser; au delà de 22.5% de deutérium, ce dernier peut s'avérer toxique et la durée de vie des drosophiles s'en voit réduite. Au vu de ces résultats, il est évident que le lien de cause à effet reliant modulation isotopique et longévité est complexe.

Afin d'éclaircir ces points de désaccords et d'apporter davantage d'informations permettant de mieux comprendre le rôle d'un enrichissement isotopique, nous avons dans un premier temps chercher à identifier l'origine des divergences observées pour le deutérium, le but étant par la suite de tester d'autres systèmes isotopiques comme celui du cuivre. Pour cela, des souches 'wild-type N2', c'est à dire n'ayant subit aucune modification génétique, ont été maintenues à 20ºC et synchronisées au stade L1 (voir figure 2 du chapitre II pour plus de détails). Les jeunes vers ont ensuite été déposés sur des boites de pétries contenant un milieu gélosé à base d'agar-agar (NGM) sur lequel a été ajouté une couche de bactéries vivantes (HT115) s'étant préalablement développées dans un milieu de croissance enrichie ou non en deutérium et dont les concentrations varient entre 0% et 100% (0%, 20%,50% et 100%).

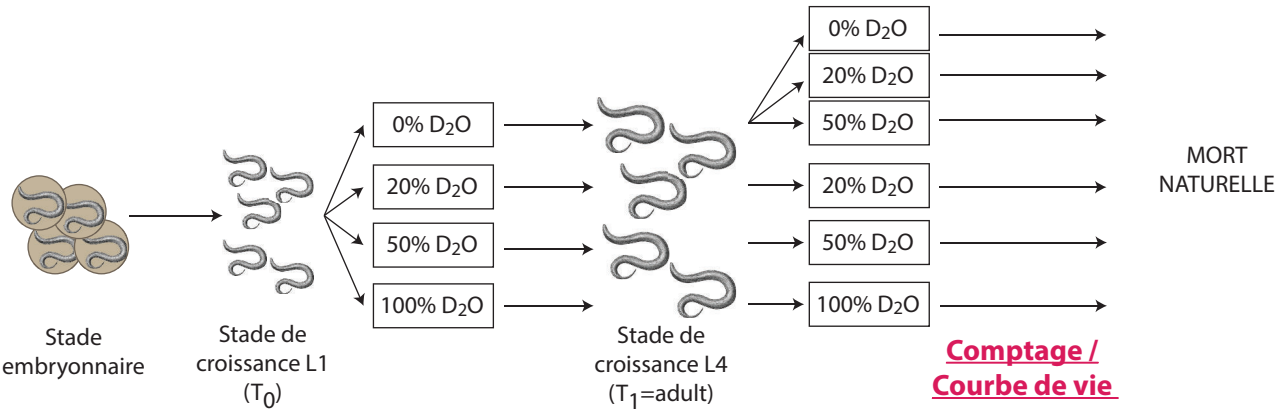

Figure 6: Organigramme résumant toutes les étapes successives du tracer des courbes de vies permettant de quantifier l'effet d'une exposition précoce et/ou tardive au deutérium sur des vers (C.elegans, N2). D_2O = eau enrichie en deutérium

Au stade de croissance L4 (~ âge adulte), les vers sont ensuite transférés sur de nouvelles boites (20 vers par boites / 5 boites par condition) présentant les mêmes ou différentes conditions (*i.e.* 0%, 20%, 50% et 100% de deutérium) sur lesquelles ils évoluent librement jusqu'à leur mort (Figure 6). En comptant le nombre de vers décédés par jour, il est possible de tracer des courbes de vie (*i.e.* lifespan) et ainsi de quantifier l'impact d'une exposition précoce et/ou tardive au deutérium sur la durée de vie et le vieillissement des vers.

Afin de vérifier la reproductibilité de nos résultats, nous avons dupliqués nos analyses. Autrement dit, trois expériences similaires ont été réalisées à des intervalles de temps réguliers (Batch 1 : Mi-Mai/début Juin, Batch 2 : début Juin/début Juillet et Batch 3 : Fin Juillet/mi-août). Tous les résultats relatifs aux courbes de vies sont résumés dans la Table 1 et présentés sur la figure 7 ci-dessous.

Mean/Median Lifespan

Name	No. of subjects	Restricted mean			Age in days at % mortality					
		Days	Std. error	95% C.I.	25%	50%	75%	90%	100%	95% Median C.I.
G0 A0 B1	120	15.38	0.36	14.67 ~ 16.08	13	15	18	22	26	13.0 ~ 13.0
G0 A20 B1	100	15.52	0.37	14.80 ~ 16.24	13	15	18	20	26	13.0 ~ 13.0
G0 A50 B1	80	14.95	0.44	14.09 ~ 15.82	13	15	18	20	26	- ~ -
G0 A0 B2	79	20.16	0.52	19.14 ~ 21.19	15	20	25	27	29	18.0 ~ 20.0
G0 A20 B2	100	19.68	0.50	18.71 ~ 20.66	15	20	22	25	32	18.0 ~ 20.0
G0 A50 B2	80	20.61	0.45	19.72 ~ 21.49	18	22	25	27	30	20.0 ~ 20.0
G0 A0 B2 bis	80	19.45	0.50	18.48 ~ 20.43	15	18	22	25	30	18.0 ~ 20.0
G20 A20 B2	119	18.44	0.40	17.66 ~ 19.22	14	18	22	25	28	15.0 ~ 18.0
G50 A50 B2	80	19.40	0.50	18.41 ~ 20.38	15	18	22	25	32	18.0 ~ 20.0
G0 A0 B3	119	19.06	0.48	18.12 ~ 20.00	15	19	24	26	31	17.0 ~ 17.0
G0 A50 B3	119	18.72	0.48	17.78 ~ 19.66	15	17	24	26	31	17.0 ~ 17.0
G20 A20 B3	105	18.00	0.47	17.08 ~ 18.92	15	17	24	26	31	17.0 ~ 17.0
G50 A50-100 B3	78	21.62	0.65	20.35 ~ 22.88	15	24	26	29	31	17.0 ~ 24.0
G100 A100 B3	61	18.74	0.64	17.49 ~ 19.98	15	19	24	26	29	17.0 ~ 17.0

Table 1: Résultats relatifs aux courbes de vie obtenus pour des vers 'wild-type' N2 (C.elegans) ayant été soumis à différente concentration de deutérium (i.e. 0,20,50 et 100%) pendant leur période de croissance (G) et/ou la phase adulte (A). La durée de vie moyenne (restricted mean) et l'âge relatif à différents taux de mortalité (Age in days at % mortality) ainsi que leur incertitude respective ont été calculé avec le logiciel OASIS (Online Application for the Survival analysIS of lifespan assays ; http://sbi.postech.ac.kr/oasis/surv/).
Pour le nom des échantillons : A= adulte (stade L4) et G=croissance (stade L1). 0, 20, 50 et 100 représentent les différents pourcentage de deutérium auxquels ont été exposés les vers. Par exemple, A0G0 est un vers ayant été exposé à des doses nulles de deutérium à l'âge enfant et adulte tandis que A20G20 est un vers ayant été exposé à des concentrations en deutérium de 20% a l'âge enfant et adulte. B1, B2 et B3 signifie Batch 1, 2 et 3 correspondant à 3 expériences distinctes menées à intervalles de temps réguliers.

Comme nous pouvons le voir sur la Figure 7, pour des conditions identiques, le batch 2 et 3 donnent des résultats relativement similaires en terme de pourcentage de survie au cours du temps (Figure 7a) et de durée de vie moyenne (Figure 7b). Cependant, le batch 1 est différent (Figure 7 et 8a). Pour le batch 1, la durée de vie moyenne estimée pour un vers n'ayant jamais été exposé au deutérium (G0A0) est de 15.38 ± 0.36 jours (1sd) dans le batch 1 et, en moyenne, de 19.81 ± 0.50 jours (1sd, n=2) dans le batch 2 (Figure 8). Idem pour des vers exposés à l'âge adulte (stade L4) à des concentrations plus élevées (G0A20 et G0A50) : pour des concentrations de 20 et 50%, les durées de vie moyennes dans le batch 1 sont de 15.52 ± 0.37 jours (1sd) et 14.95 ± 0.44 jours (1sd) tandis qu'elles sont de 19.68 ± 0.50 jours (1sd) et 20.61 ± 0.45 jours (1sd) dans le batch 2 respectivement (Figure 8a).

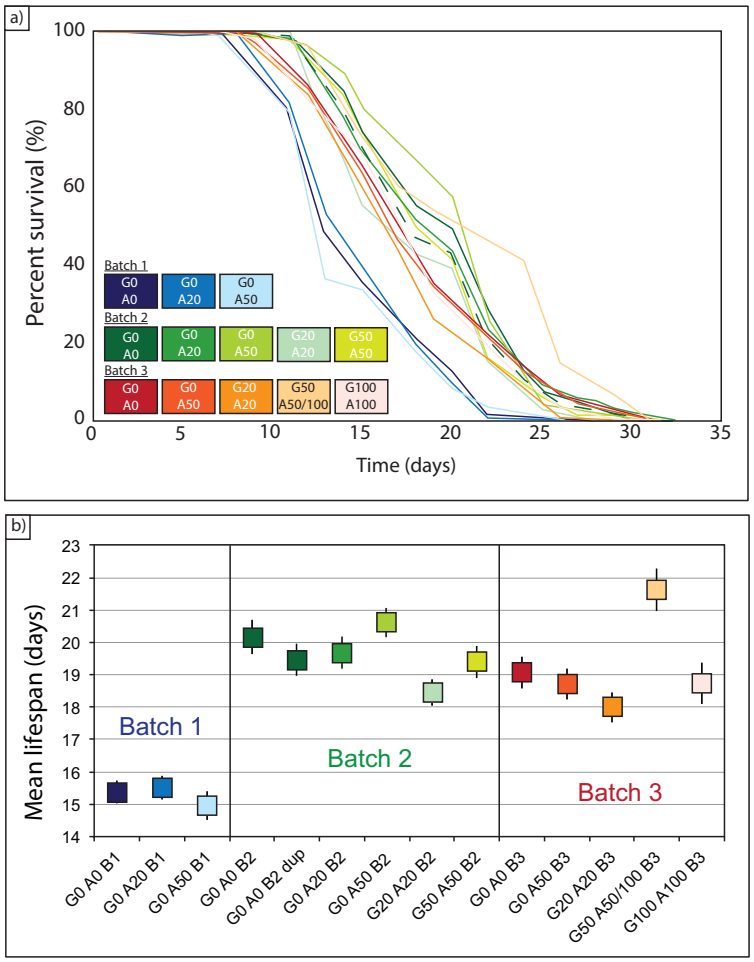

Figure 7: (a) Courbe de vie (lifespan) i.e. pourcentage de survie au cours du temps et (b) durée de vie moyenne chez des vers 'wild-type' N2 (C.elegans) ayant été soumis à différentes concentrations de deutérium (i.e. 0, 20, 50 et 100%) pendant leur période de croissance (G) et/ou phase adulte (A). Par exemple, A20G20 est un vers ayant été exposé à des concentrations en deutérium de 20% à l'âge enfant et adulte.

Les vers étant thermosensibles (Xiao et al., 2013), ces différences pourraient s'expliquer par des écarts de températures au moment des expériences puisque la salle de manipulation n'est pas contrôlée en température et est donc assujettie aux changements climatiques extérieurs. D'après les relevés Météo France de Lyon, nous notons une différence de température extérieure de l'ordre de 4ºC entre l'étude du batch 1 et celle du batch 2 (Figure 8b). Le batch 1 a été étudié entre le 11/05/2017 et le 06/06/2017 avec une température extérieure moyenne de 19ºC alors que la température était de 23ºC pour le batch 2 étudié du 06/06/2017 au 03/07/2017. La baisse des températures à donc dans notre cas eu un effet néfaste sur la durée de vie des vers. Néanmoins, bien que la température soit un facteur important, il est important de noter que d'autres paramètres peuvent entrainer des divergences similaires. On compte par exemple la 'souplesse' du manipulateur, la température de l'incubateur et la nature des réactifs tel que la javel utilisée pour synchroniser

les vers (Lithgow et al., 2017). Dans notre étude, tous ces paramètres sont cependant restés constants supportant le fait que seule la différence de température extérieure pourrait être à l'origine des écarts observés.

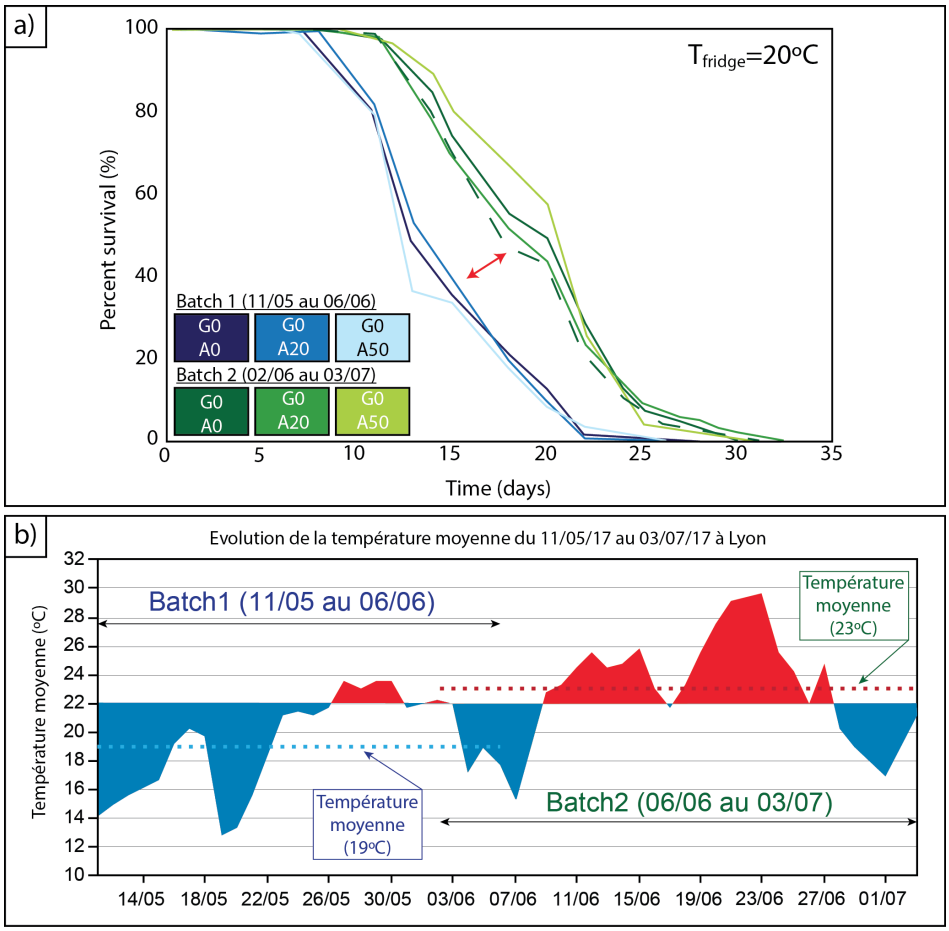

Figure 8 : (a) Pourcentage de survie en fonction du temps et (b) Evolution des températures à Lyon entre le 11/05/2017 et le 03/07/2017 réalisée d'après les données de MétéoFrance. 0,20 et 50 représente les concentrations deutérium auxquelles sont exposés les vers (C.elegans N2) pendant leur phase de croissance (G) et/ou adulte (A). La courbe en pointillée représente une analyse dupliquée.

Au delà des variabilités potentiellement liées à la température, aucune différence significative n'est visible entre les vers exposés ou non au deutérium; un résultat avéré dans les 3 batchs quelque soit la concentration en deutérium et/ou la période d'exposition (*i.e.* précoce, G ou adulte, A) (Figure 9).

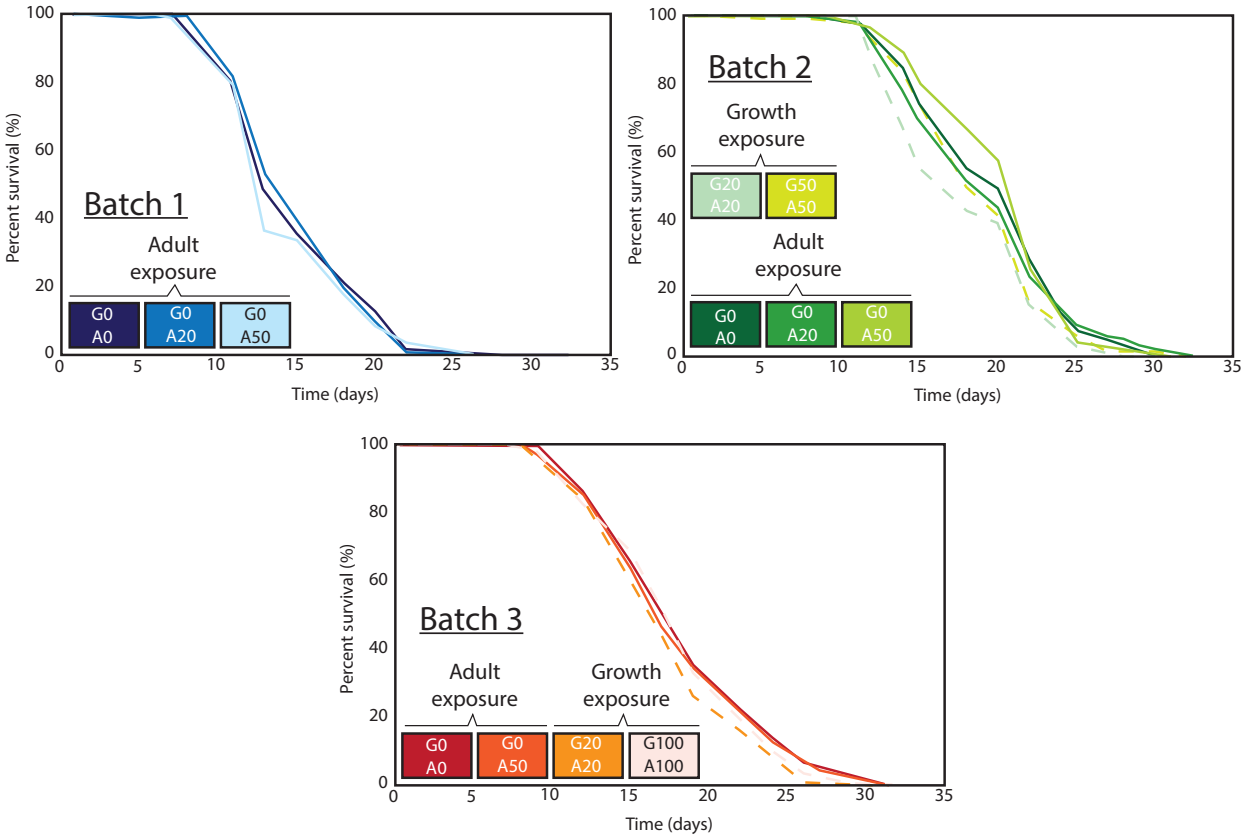

Figure 9 : Effet du deutérium sur la longévité. Les courbes de vie ont été réalisées sur des vers 'wild-type' N2 (C.elegans) soumis à différentes concentrations de deutérium (i.e. 0,20,50 et 100%) pendant leur période de croissance (G) et/ou phase adulte (A). Batch 1, 2 et 3 correspondent à 3 expériences similaires reproduites à différentes périodes de temps (Batch 1 : Mi-Mai/début Juin, Batch 2 : début Juin/début Juillet et Batch 3 : Fin Juillet/mi-août).

L'ajout de deutérium en quantité plus ou moins importante n'a donc aucun effet significatif sur la durée de vie des nématodes. Bien que ces résultats viennent contredire les observations faites par Hammel et al.(2013) et Li et Snyder (2016b; 2016a), il est important de noter que cette étude se focalise sur des vers, tandis que les deux études précédentes ont analysé des drosophiles et des levures, respectivement. Il est donc envisageable que l'effet du deutérium sur la longévité soit dépendant de l'organisme dans lequel il est administré ; une hypothèse qui devra par la suite être vérifiée.

Une seule exception a néanmoins été observée dans cette étude faisant suite à une erreur de manipulation. N'ayant plus assez de boites en conditions D_2O 50%, des vers ayant préalablement grandi du stade de croissance (G) à celui de jeune adulte (A) sur de telles conditions ont été transvasés en plein milieu de leur vie adulte sur des boites de concentrations plus élevées (100%). A l'inverse des expériences précédentes où le changement de conditions se faisait toujours entre la période de croissance et l'âge adulte, il

intervient ici de façon plus soudaine au cours de l'âge adulte. Une différence qui semble avoir des répercussions majeurs sur l'augmentation de la durée de vie (p=0.0004) (Figure 10).

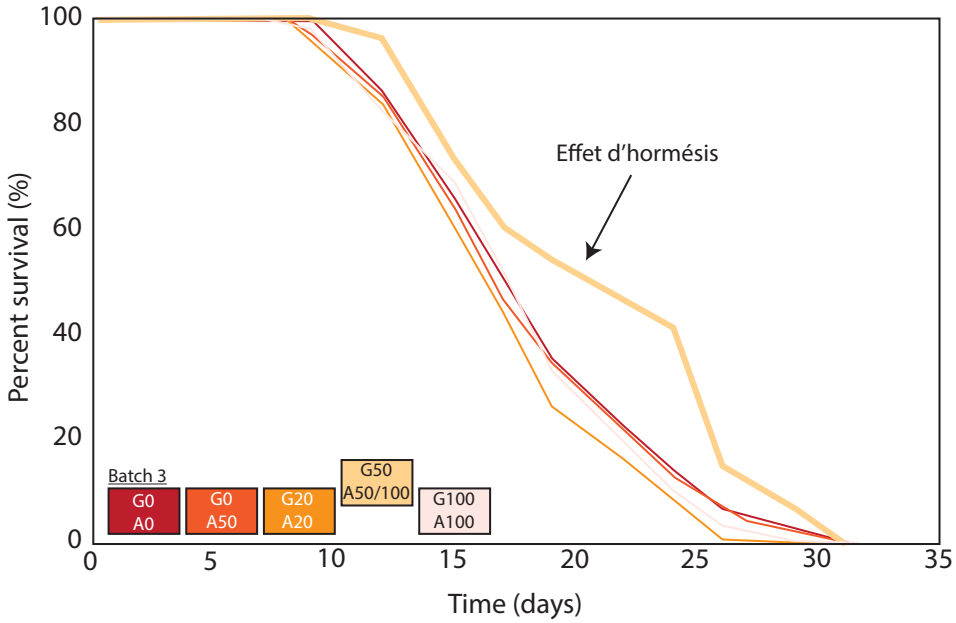

Figure 10: Effet d'hormésis sur la longévité. Les courbes de vie ont été réalisées sur des vers 'wild-type' N2 (C.elegans) soumis à différentes concentrations de deutérium (i.e. 0, 20, 50 et 100%) pendant leur période de croissance (G) et/ou phase adulte (A).

Cela pourrait s'expliquer par ce que l'on appelle un effet d'hormésis ou effet bénéfique des faibles doses. Cet effet protecteur fait suite à une réponse de stimulation positive de l'organisme face à l'exposition précoce à faible dose d'agents hormétiques (substances nocives). Il a par exemple été mis en évidence chez l'animal par Duport (2003), ce dernier ayant montré que des souris exposés à de faibles doses de rayonnements ionisants avait moins de risque de développer un cancer. Dans notre cas, il semblerait donc que ce soit la capacité adaptative de l'organisme plus que la simple administration d'isotopes lourds qui contrôlerait la longévité. Cependant, si cette hypothèse est vrai, comment expliquer que des vers ayant grandi sur de faibles doses de D_2O et ayant subi un changement de conditions entre l'âge enfant et l'âge adulte (stade L4) ne soit pas aussi marqués par une augmentation de leur durée de vie ? L'augmentation de la dose de D_2O en fin de phase de croissance (stade L4) est-elle trop rapide ? Au stade L4, l'organisme vient tout juste de terminer sa phase de croissance. Il est donc possible que l'organisme, encore quelque peu juvénile, ne soit pas prêt à affronter des doses élevées de D_2O, entrainent ainsi un effet néfaste. Afin d'éclaircir ce point, des études supplémentaires visant a reproduire ces conditions sont alors nécessaires.

Au vu des résultats précédemment obtenus sur les compositions isotopiques en cuivre (*i.e.* $\delta^{65}Cu$ qui diminue chez les vers vivant le plus longtemps en bonne santé, daf-2/e1370), nous voudrions voir si cette conclusion est spécifique au deutérium ou si elle peut être généralisée à d'autres systèmes isotopiques comme le cuivre. Autrement dit, moduler la composition isotopique en Cu des vers a t-elle un effet bénéfique sur leur durée et leur qualité de vie ? Pour répondre à cette question, nous envisageons donc de refaire ces expériences en remplaçant le deutérium par un spike de cuivre préférentiellement enrichi en isotope léger (^{63}Cu).

APPORT DES COMPOSITIONS ISOTOPIQUES EN CUIVRE POUR L'ÉTUDE DE LA SCLÉROSE LATÉRALE AMYOTROPHIQUE (SLA)

CHAPITRE IV

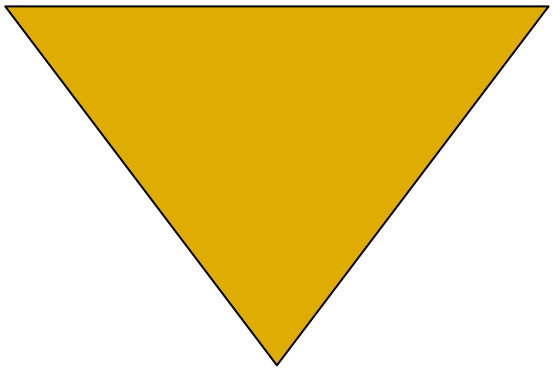

CHAPITRE IV: APPORT DES COMPOSITIONS ISOTOPIQUES EN CUIVRE POUR L'ÉTUDE DE LA SCLÉROSE LATÉRALE AMYOTROPHIQUE (SLA)

Ce chapitre, divisé en deux grandes parties a pour objectif d'évaluer l'importance des variations chimiques et isotopiques pouvant être associées à la sclérose latérale amyotrophique (SLA) afin (1) d'identifier de nouveaux marqueurs biologiques spécifique à cette maladie et (2) de mieux comprendre les mécanismes physiopathologiques en étant à l'origine. Pour cela, une dizaine d'éléments chimiques (traces et majeurs) ainsi que les compositions isotopiques en cuivre ($\delta^{65}Cu$) et en zinc ($\delta^{66}Zn$) ont été mesurées dans des liquides céphalo-rachidiens (LCRs) de personnes saines (*i.e.* sans pathologies neurodégénératives) et atteintes de SLA mais également dans des modèles de cellules humaines (neuroblastes et cellules de reins). Afin de contrôler la spécificité de ces variations chimiques, l'analyse des LCRs a également été réalisée sur des patients atteints de la maladie d'Alzheimer.

La première partie de ce chapitre, sous forme de manuscrit, documente les systématiques chimiques et isotopiques dans les liquides céphalo-rachidiens tandis que la deuxième partie vise à mieux contraindre les processus à l'origine de ces variations grâce à l'étude de modèles cellulaires humain.

IV.1. Analyses des liquides céphalo-rachidiens

ARTICLE

"Isotopic evidence for disrupted copper metabolism in cerebrospinal fluids of ALS patients"

***Lucie Sauzéat**, Emilien Bernard, Armand Perret-Liaudet, Isabelle Quadrio, Alain Vighetto, Pierre Krolak-Salmon, Emmanuel Broussolle, Pascal Leblanc, Vincent Balter*

(submitted to PNAS)

IV.2. Analyses de cellules humaines

IV.1. Analyses des liquides céphalo-rachidiens

Le manuscrit présenté ci-dessous propose d'étudier et d'évaluer le potentiel des variations chimiques et isotopiques des liquides céphalo-rachidiens (LCRs) comme nouveaux marqueurs de la sclérose latérale amyotrophique (SLA).

ARTICLE

"Isotopic evidence for disrupted copper metabolism in cerebrospinal fluids of ALS patients"

Lucie Sauzéat, *Emilien Bernard, Armand Perret-Liaudet, Isabelle Quadrio, Alain Vighetto, Pierre Krolak-Salmon, Emmanuel Broussolle, Pascal Leblanc, Vincent Balter*

(submitted to PNAS)

NB: For ease of reading, the figures and tables are directly integrated in the main text

Isotopic evidence for disrupted copper metabolism in cerebrospinal fluids of ALS patients

(submitted to PNAS)

Lucie Sauzéat[1], Emilien Bernard[2], Armand Perret-Liaudet[3,4], Isabelle Quadrio[3,4], Alain Vighetto[5], Pierre Krolak-Salmon[6], Emmanuel Broussolle[7], Pascal Leblanc[8], Vincent Balter[1]

[1]*UMR 5276, Laboratoire de Géologie de Lyon, Ecole Normale Supérieure de Lyon, BP 7000 Lyon, France*
[2]*Hospices Civils de Lyon, Hôpital Neurologique Pierre Wertheimer, Centre de ressources et de compétence SLA de Lyon, Service de Neurologie C, Bron, France*
[3]*Univ Lyon, University of Lyon 1, CNRS UMR5292, INSERM U1028, BioRan, Lyon, France*
[4]*Hospices Civils de Lyon, Neurobiology Laboratory, Biochemistry and Molecular Biology Department, Lyon, France*
[5]*Service Neurocognition et Neuroophtalmologie, hôpital neurologique, 59 boulevard Pinel 69677 Bron cedex, Université Lyon 1, Hospices Civils de Lyon, Centre de Recherche en Neurosciences de Lyon, équipe IMPACT, Lyon, France*
[6]*Centre Mémoire Ressources Recherche de Lyon, Hospices Civils de Lyon, Hôpital des Charpennes, Villeurbanne, France*
[7]*Univ Lyon, Faculté de Médecine Lyon Sud Charles Mérieux; Institut des Sciences Cognitives Marc Jeannerod, CNRS, UMR 5229; Hospices Civils de Lyon, Hôpital Neurologique Pierre Wertheimer, Centre de ressources et de compétence SLA de Lyon, Service de Neurologie C, Lyon, France*
[8]*Institut NeuroMyoGène, CNRS UMR5310, INSERM U1217, Faculté de Médecine Rockefeller, 8 avenue Rockefeller, Université Claude Bernard Lyon I,* 69373 Lyon Cedex 08, France

*correspondence: lucie.sauzeat@ens-lyon.fr

Significance statement

Establishing diagnosis and providing treatment to prevent Amyotrophic Lateral Sclerosis (ALS) remain a challenge because reliable markers are lacking and the fundamental cause is unknown. Breakdown in metal homeostasis is thought to be a key factor in neurodegenerative diseases. Metal concentrations in cerebrospinal fluids (CSFs) are however highly variable and usually failed to be reliable markers of ALS. In this study, we demonstrate for the first time that CSFs of ALS patients have heavier copper isotopic composition compared to age-matched controls and Alzheimer's disease patients. Although further studies are needed, these promising results demonstrate that Cu isotopes may offer a more comprehensive view on ALS and help providing a more valuable ALS-specific diagnosis.

[Abstract]

So far, our knowledge and consequently our capacity to treat the Amyotrophic Lateral Sclerosis (ALS) are limited, notably because of the lack of valuable biomarkers. The dyshomeostasis of redox-active metals, frequently linked to the generation of reactive oxygen species, is thought to be a key feature of neurodegenerative diseases. The concentration of redox-active metals in cerebrospinal fluids (CSFs) is however most of the time subject to high variability and usually gives conflicting results, questioning their reliability as potential biomarkers. Conversely, stable isotopic compositions may offer an innovative means to circumvent this problem. Here, to address and clarify these points, we measured the concentrations of 12 elements and, for the first time, the copper (redox sensitive) and zinc (redox insensitive) isotopic compositions in human CSFs of 31 ALS patients, 11 age-matched controls (CTRL) and 14 Alzheimer's disease (AD) subjects. We first confirm that metal concentrations, being redox-active or not, weakly discriminate ALS patients from the two other groups. We then report for the first time that, in contrast to indistinguishable zinc isotopic compositions, ALS patients have significantly heavier copper isotopic compositions than CTRL and AD subjects. This result unambiguously demonstrates that the Cu metabolism is disturbed in ALS. We suggest that Cu isotopic variations likely result from progressive physiological deteriorations including abnormal protein aggregation in the brain parenchyma and emphasize that copper isotopes may provide valuable ALS-specific diagnosis and could help unraveling the molecular mechanisms at work.

Keywords: Amyotrophic lateral sclerosis, cerebrospinal fluid, copper, isotopes, mass spectrometry

Amyotrophic Lateral Sclerosis (ALS) is one of the most harmful neurodegenerative diseases characterized by the progressive deterioration of the upper and lower motor neurons, leading to muscle weakness and atrophy, severe paralysis and finally death within 3-5 years after symptom onset (1). Affecting over 400,000 people world-wide and with a predicted increase of 69% expected between 2015 and 2040 (2), this disease will rapidly represent a significant burden for future generations. Currently, although genetic factors have been identified to play a role in familial ALS (3), representing only 10% of the reported cases, the leading mechanisms accounting for motor neuron degeneration in sporadic ALS (*i.e.* 90% of ALS cases) remains unknown. In addition, because of the complexity of the pathology, reliable markers (4) and efficient treatments are still missing (5). The clinical diagnosis of ALS is classically evaluated by using the revised El Escorial and the Awaji criteria (6) and the

ALSFRS-R scale (ALS functional rating scale instrument) is used for monitoring the progression of disability in ALS patients (7). Recently, biological cerebrospinal fluid (CSF) markers including neurotrophic and inflammatory protein changes such as neurofilament light chain (NfL) (8) and chemokines (9) have been identified. However, most of them are not usually diagnosed until the disease has progressed and may not be specific of ALS. Concentration of NfLs in CSF have also been reported to be elevated in other neurological disorders such as Alzheimer (10) and Parkinson disease (11). Robust and specific ALS markers are still therefore scarce.

Like for other neurodegenerative diseases, the progression of ALS is associated with the production of free radicals such as reactive oxygen species (ROS) (12) *i.e.* highly toxic species (13), the production of which necessitates the presence of free, redox-active metals such as copper (Cu) (14). Conversely, these metals can also be catalytic cofactors of several enzymes, like Cu/Zn superoxide dismutase (SOD1), involved in free radical detoxification by catalyzing highly toxic products (*i.e.* superoxide) to less dangerous species such as dioxygen and hydrogen peroxide (15). Redox-active metals like Cu play thus a pivotal role in both the pro- and anti-oxidant homeostasis and it is expected that dysregulation affecting these pathways will be characterized by significant elemental impairment. In a mouse model of familial ALS (*i.e.* 10% of ALS cases) which are caused by genetic mutations (3, 16), 20% of which affecting the gene coding for the SOD1 Cu-binding protein (17), Cu has for example been observed to accumulate in the spinal cord (18, 19). Metal dysregulations have also been observed for other redox-active metals in CSFs of ALS including iron (20), manganese (21) and selenium (22). Zinc (Zn), which is not redox-active but binds to SOD1, has also been reported to be dysregulated in CSFs of ALS patients (23). However, comparing the published results generally leads to equivocal conclusions about the usefulness of metal concentrations in CSFs to study and diagnose ALS.

Contrary to concentrations, stable isotope compositions may offer a more comprehensive view on biological reactions and neurological disease progression. This is due to two main reasons. First, isotope compositions are measured with a precision of about two orders of magnitude better than concentrations. Second, the intensity of enrichment or depletion of a metal in a given compartment is hardly predictable while isotopic fractionation, *i.e.* the variation of the natural abundances of stable isotopes ratios between coexisting compartments, can usually be quantitatively predicted by *ab initio* calculations (24). In blood and/or bones, Cu isotope compositions ($\delta^{65}Cu$) exhibit for example significant differences between men and women (25, 26) as well as during ageing (27) and menopause transition (28, 29). In addition, the $\delta^{65}Cu$ value varies in pathological conditions, such as liver cirrhosis (30) and cancer (31-33). Regarding neurodegenerative disorders, although Cu isotope

compositions seem to be insensitive to the $SOD1^{G93A}$ mutation in the brain of mouse model (34), they are highly responsive in those of prion protein knockout (PrP-KO) mice (35, 36). Zn isotope compositions ($\delta^{66}Zn$) were also scrutinized in mouse models of neurodegenerative diseases. In PrP-KO mice, the brain $\delta^{66}Zn$ values were heavier than in wild-type controls (35), a pattern also observed in mutant mouse (APPswe/PSEN1dE9) developing Alzheimer's-like disease (37).

In the present work, to further explore the potential of elemental concentrations and for the first time the use of isotopic compositions for clinical studies of ALS, we measured the concentration of 12 major and trace elements and the Cu and Zn isotopic compositions in the CSFs of ALS patients (n=31), age-matched controls (CTRL, n=11) and Alzheimer's disease patients (AD, n=14).

Results

Major and trace element concentrations as well as Cu and Zn isotopic compositions measured in CSFs of ALS, CTRL and AD subjects are all reported in Table S1. Both accuracy and reproducibility of the major *i.e.* magnesium (Mg), sodium (Na), phosphorous (P), sulfur (S), potassium (K), calcium (Ca), and trace element, *i.e.* iron (Fe), manganese (Mn), rubidium (Rb), strontium (Sr), Cu and Zn concentrations as well as Cu and Zn isotopic compositions were monitored by replication of in-house (*i.e.* sheep plasma, OEP and fetal bovine serum, FBS) and international (*i.e.* bovine liver, 1577c and fish protein, DORM-2) reference materials. The concentrations and isotopic compositions obtained for the reference standards (see Table S2) are in agreement with the reference values, and reproducibility is, on average, better than 10% (2sd) for the concentrations and do not exceed 0.07‰ for Cu-Zn isotopic compositions (Table S2).

To evaluate the whole pattern of variations, we used a principal component analysis (PCA) *i.e.* a mathematical algorithm that reduces the dimensionality of the data to highlight the most important variation in the data set (38). The most noticeable feature is the chemical distinction between CSFs of ALS patients and CTRL as illustrated by the y principal component axis (Figure S1). ALS subjects have for example significant lower Fe (Wilcoxon-Mann-Whitney, $p_{value}= 2.426.10^{-3}$) and Mn (Wilcoxon-Mann-Whitney, $p_{value}= 2.206.10^{-3}$) (Figure S2a and S2b) and higher Rb (Wilcoxon-Mann-Whitney, $p_{value}= 1.003.10^{-2}$). Conversely, concentrations of Zn (Wilcoxon-Mann-Whitney, $p_{value}= 0.0715$) and Cu (Wilcoxon-Mann-Whitney, $p_{value}= 0.1610$) do not exhibit any systematics (Figure S2c and S2d), an observation that holds also for other trace and major elements such as Sr, S, P or Na (Table S1). Although these results are in line with a couple of studies such as

Ostachowicz et al.(39), Kanias and Kapaki (40) and Kapaki et al.(41), opposite or equivocal results have also been reported for Fe (20, 23), Mn (20, 21, 23, 40, 41) and Zn (20, 23, 42, 43) (Figure S2a, S2b and S2c). Altogether, these results demonstrate that the observed variations of metal concentrations in CSFs do not exhibit well-defined systematics, therefore questioning their reliability as potential diagnostic or prognostic biomarker of ALS.

Regarding the Cu and Zn isotopic compositions, Cu isotopic ratios in ALS (median $\delta^{65}Cu_{ALS}$ = 0.01 ‰, 25th percentile = -0.10‰; 75th percentile = 0.18‰) are significantly heavier (Wilcoxon-Mann-Whitney, p_{value}= 0.0146) than CTRL (median $\delta^{65}Cu_{CTRL}$ = -0.20‰, 25th percentile = -0.26‰; 75th percentile = -0.02‰) (Figure 1a). By contrast, no significant difference is observed between Zn isotopic compositions of ALS (median $\delta^{66}Zn_{ALS}$ = 0.15 ‰, 25th percentile = 0.07‰; 75th percentile = 0.20‰) and CTRL (median $\delta^{66}Zn_{CTRL}$ = 0.19 ‰, 25th percentile = 0.15‰; 75th percentile = 0.23‰) (Wilcoxon-Mann-Whitney, p_{value}= 0.1764) (Figure 1b).

Similar observations can be made when comparing the $\delta^{65}Cu$ value of ALS and AD patients (median $\delta^{65}Cu_{AD}$ = -0.06 ‰, 25th percentile = -0.23‰; 75th percentile = 0.01‰), the latters being chemically indistinguishable from CTRL (Wilcoxon-Mann-Whitney, p_{value}= 0.6638) (Figure 1a). However, compared to ALS patients, AD subjects tend to have a slightly lower $\delta^{66}Zn$ value (median $\delta^{66}Zn$ = 0.10 ‰, 25th percentile = -0.01‰; 75th percentile = 0.15‰) than CTRL subjects (Wilcoxon-Mann-Whitney, p_{value}= 0.0426).

Biological (gender and age at sample collection) and clinical (localization of first symptoms, Awaji criteria, ALSFRS-R score, delay between sampling date and first visible symptoms) parameters are given in Table S3. Focusing on the ALS and CTRL groups, neither clinical parameters, nor biological parameters show significant association with elemental concentrations and Cu-Zn isotopic compositions as shown for example by the similar $\delta^{65}Cu$ values between male and female subjects in the ALS group (median $\delta^{65}Cu_{ALS\text{-}female}$ = -0.02 ‰, 25th percentile = -0.16‰; 75th percentile = 0.07‰ and median $\delta^{65}Cu_{ALS\text{-}male}$ = +0.01 ‰, 25th percentile = -0.10‰; 75th percentile = 0.20‰) (Wilcoxon-Mann-Whitney, p_{value}= 0.2721) (Table S1).

Discussion

Disruption of the homeostasis of metals such as Cu and Zn are thought to be a key feature of neurodegenerative diseases, including ALS (44). Inappropriately redistributed in the brain and spinal cord (45, 46), they notably tend to accumulate in misfolded protein aggregates as shown for example in amyloid-β (Aβ) plaques within AD brain (47). Assessing

the spatial and temporal metallome evolution may therefore provide valuable information regarding the etiology and the potential diagnosis of neurodegenerative diseases.

In ALS, misfolded proteins aggregate including TAR-DNA binding protein 43 (TDP-43) (48), Fused in sarcoma (FUS) (49), and SOD1 (50) have been reported in the brain. Described as the main pathological hallmark of ALS, these proteins, like Aβ, may also concentrate metals. The local accumulation is likely to deplete the surrounding environment *i.e.* the CSF, as we observed for Fe (Figure S2a) and Mn (Figure S2b). However, this does not seem to be a robust picture because no clear pattern in trace element concentrations is observed as shown by the large discrepancies reported by different studies (Figure S2 and reference therein), therefore questioning their reliability as potential diagnostic or prognostic biomarker of ALS. The natural wide range of metal concentrations in human fluids (*e.g.* (51)), is likely to erase case patients and control subjects differences. A more robust pattern of variations of metal concentrations is probably specific to each patient and would thus be accessible through analysis of cohorts. In addition, two practical explanations can be put forward to explain the scattering of the results. First, the use of inappropriate control subjects with unmatched age class such as spouses or friends of ALS patients (20) can likely introduce biases. Second, collection, storage and preparation of CSFs can be sensitive to trace elements contamination (52, 53). CSFs are made of 99% water and have very low metal contents; hence the risk of contamination is high. In this study, we ensure absence of external contamination by quantifying the chemical content that may be released by sampling and storage tubes as well as dropper-type pipettes used to collect and conserve the CSFs respectively. A complete description of the procedure is given in supplementary information (Supplementary Information SI 1). We also ensured low acid blanks before and after each column chemistry and, we only used vinyl gloves as suggested by Garçon et al.(52).

One advantage of using isotopic composition over concentration for a given element is that the isotopic fractionation is not dependent of the amount of the element. Isotopic compositions are thus potentially more reliable biomarkers than concentrations. In this study, we found for the first time that CSFs of ALS patients have significantly heavier Cu isotopic composition compared to age-matched controls (Wilcoxon-Mann-Whitney, p_{value}= 0.0146) and tend also to distinguish from AD subjects by slightly heavier δ^{65}Cu (Wilcoxon-Mann-Whitney, p_{value}= 0.0510) (Figure 1a), while no distinction is observed for Cu concentration (Figure S2d and Table S1). Using receiver operating characteristic (ROC) analysis, we determined a δ^{65}Cu cut-off value of -0.05‰ with a sensitivity and a specificity of 73% and 65% respectively, and an area under the curve of 0.7570 (Figure S3). Although further additional studies are undoubtedly needed to improve the present results achieved by the ROC test, the latters still remain meaningful (AUC>0.7 *i.e.* correct-trial) showing that the CSF

$\delta^{65}Cu$ value is likely a promising performance indicator of ALS, a result furthermore supported by the ALS specificity of this marker as illustrated by the absence of significant $\delta^{65}Cu$ difference between AD and control subjects (Wilcoxon-Mann-Whitney, p_{value}= 0.6638) (Figure 1a).

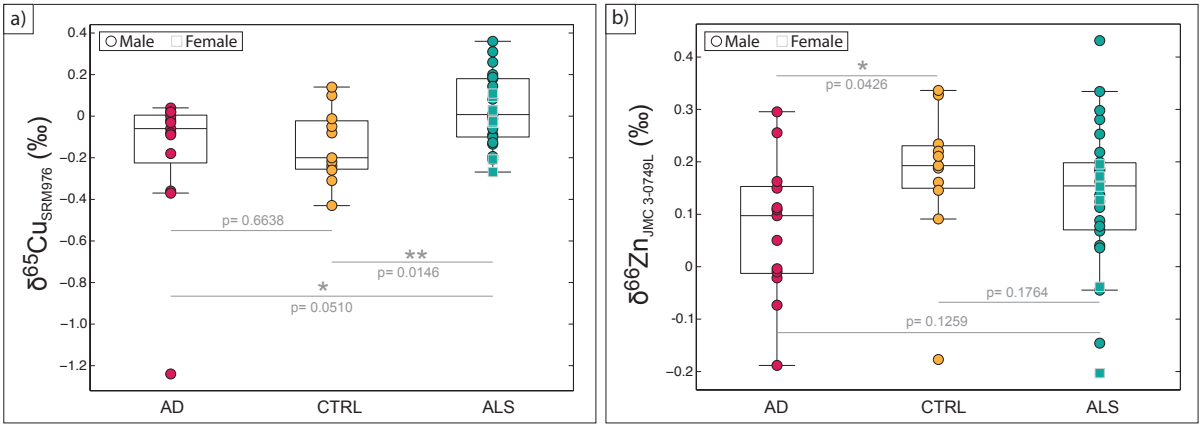

Figure 1: a) Copper ($\delta^{65}Cu$) and b) zinc ($\delta^{66}Zn$) isotopic compositions measured in cerebrospinal fluid (CSF) of control (CTRL, yellow dots), Alzheimer's disease (AD, pink dots) and Amyotrophic Lateral Sclerosis subjects (ALS, green dots). Circles and squares points are for male and female subjects respectively. For each boxplot, the central mark is the median, the edges of the box are the first (*i.e.* 25th percentiles) and the third quartile (*i.e.* 75th percentiles) respectively and the points outside the boxes extend to the most extreme data points (*i.e.* not considered outliers). Significance level (*i.e.* p_{value}) was determined using non-parametric 'two-sided', Wilcoxon-Mann-Whitney U-tests. ** stands for $p_{value} < 0.005$ and * for $p_{value} < 0.05$.

However, before reliably asserting that the $\delta^{65}Cu$ value in CSFs could be used as a robust ALS marker, further work is warranted and this requires elucidating the mechanisms accounting for Cu isotopic variations in CSFs. Recently, Moynier et al.(37) showed that AD mice brain have higher $\delta^{66}Zn$ value than wild type mice and suggested that this isotopic enrichment may result from the formation of Aβ plaques in the brain parenchyma binding preferentially the heavier Zn isotopes. Given these observations, the Cu isotopic variation observed in CSFs could similarly result from impaired Cu binding sites and subsequent mislocalization within abnormal misfolded proteins, including the Cu-binding protein SOD1 (17) as well as the TDP-43 and/or FUS proteins (48) aggregating in the ALS brain. Because TDP-43 and FUS are not Cu-binding proteins, the way and extent they may affect Cu isotopes in CSF is likely indirect, an observation supported by the results of Pokrishevsky et al.(49, 54) reporting that TDP-43 and FUS aggregation can trigger the initiation and the cell-to-cell propagation of the Cu-binding protein SOD1. Following the hypothesis of Moynier et al.(37), if the accumulation of a metal in the protein aggregates of the brain is associated with an isotopic fractionation, this must be balanced in the CSF, brain and CSF being two complementary reservoirs. As a first step approach, we can test whether this assumption

resists to mass balance equations imposed by mass conservation laws, by using a simple two-reservoirs (*i.e.* CSF and protein aggregates) model (Figure 2).

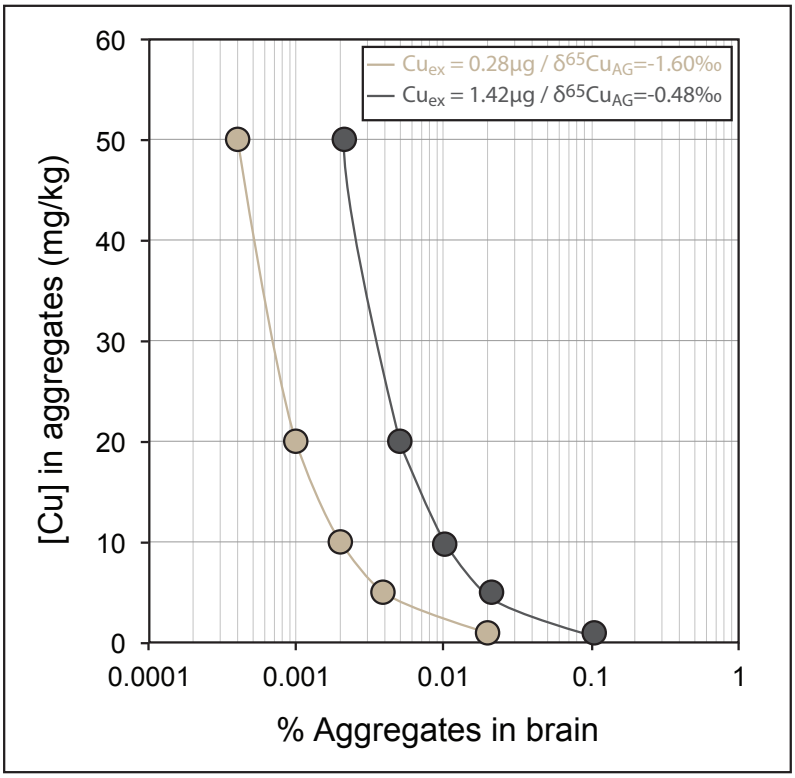

Figure 2: Two-reservoirs mass balance showing the proportion of brain aggregates accounting for the observed increase of the $\delta^{65}Cu$ value in CSFs of ALS patients. The proportions are calculated for different Cu concentrations in the aggregates using a Cu isotopic mixing (the full set of calculation is provided in Supplementary Information SI 2). The two mixing lines correspond to different Cu content exchanged (Cu_{ex}) between CSF and aggregates.

All the details of the calculation can be found in the Supplementary Information SI 2. In this model, initial state (*i.e.* healthy condition) corresponds to a brain with no aggregate and a corresponding $\delta^{65}Cu$ value equal to that measured in CSFs of the CTRL group. The mass of Cu exchanged from CSF to aggregates corresponds to the mass difference between CSFs of CTRL and ALS (*i.e.* 0.28 µg). With a final $\delta^{65}Cu_{CSF\text{-}EF}$ of +0.01‰ (*i.e.* ALS conditions, 25th percentile = -0.10‰, 75th percentile = +0.18‰) and an initial $\delta^{65}Cu_{CSF\text{-}EI}$ of -0.20‰ (*i.e.* CTRL conditions, 25th percentile = -0.26‰, 75th percentile = -0.02‰) and assuming a Cu concentration in aggregates comparable to that of the normal human brain, *i.e.* ranging between 1 and 50 mg/kg (55-58), the results of the mass balance indicate that the observed $\delta^{65}Cu$ value in CSF of ALS patients may results from the formation of aggregates having a $\delta^{65}Cu$ value of -1.60 ± 1.51 ‰ and whose the proportion range from 0.0004 % to 0.02 % of the mass of the brain (Figure 2). Increasing the Cu concentration in aggregates leads to even smaller fraction of newly formed aggregates (Figure 2). To test the sensitivity of the mass

balance, we calculate that for a Cu amount exchanged between CSF and aggregates being 5 times higher (*i.e.* 1.42 µg), 0.002 % to 0.1 % of aggregates are formed with a δ^{65}Cu value of -0.48 ± 0.39 ‰ (Figure 2). Altogether, these results show that minute proportions of aggregates formation associated with relevant Cu isotopic fractionation can likely explain the observed differences between the CSFs δ^{65}Cu values of CTRL and ALS. Whatever the proportion of formed aggregates, the increase of the δ^{65}Cu value of ALS CSFs implies for mass balance requirement that ^{63}Cu preferentially accumulates in aggregates (Figure 3). Measuring the Cu isotopic composition of aggregates and normal adjacent areas in autopsies of brain of ALS patients, and/or in brains of ALS animal model like the SOD1^{G93A} mice, can be the aim of future experiments to challenge this hypothesis.

Another assumption that could explain the observed Cu isotopic rise in the CSFs of ALS patients may imply the impairment of the blood-brain barrier (BBB) and/or of the Cu reductase/transporter. In a majority of neurological disorders, the BBB is damaged (59, 60) becoming more permeable. This could likely favor the incorporation of ^{65}Cu in the brain (Figure 3), a process that does not occur under normal conditions.

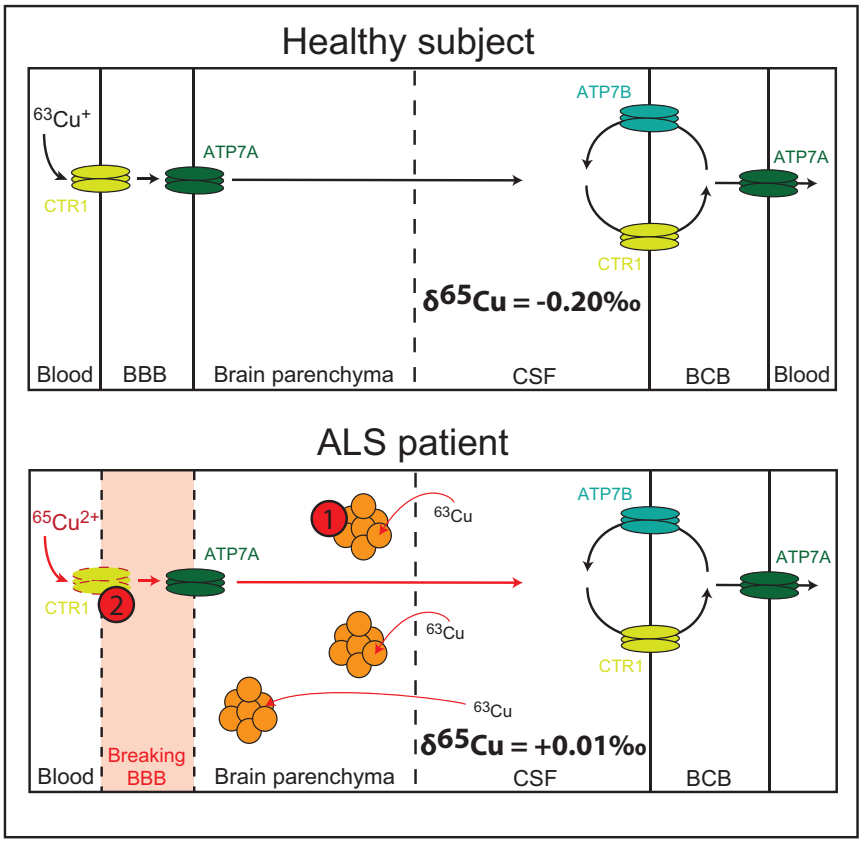

Figure 3: Schematic diagram illustrating plausible mechanisms suggested in this study to account for the rise of the δ^{65}Cu value in the CSFs of ALS patients. This includes (1) abnormal protein aggregation in the brain parenchyma incorporating preferentially ^{63}Cu over ^{65}Cu isotope and (2) the breaking of the BBB associated with the impairment of Cu transporter/reductase favoring preferential ^{65}Cu uptake. The diagram is modified from Scheiber et al.(67). BBB stands for blood-brain barrier, CSF is for cerebrospinal fluid, BCB designed blood-cerebrospinal fluid. CTR1, ATP7A/B are copper transporters.

When the BBB is intact, Cu is reduced by a STEAP2 or DCYTB reductase before being incorporated in the brain through the CTR1 transporter (44). Because reduced Cu^{+} compounds are expected to favor light isotopes over Cu^{2+}, ^{63}Cu would be preferentially incorporated into the brain during healthy conditions, as previously suggested for any other type of cells (61). Conversely, Cadiou et al.(62) recently demonstrated that Cu isotopic fractionation is regulated by membrane importers and/or reductase activity and showed that cells with impaired reductase have heavier $\delta^{65}Cu$ value. Given these results, impaired BBB could probably favor the incorporation of more heavy ^{65}Cu isotope than in healthy conditions leading to the observed increase of the $\delta^{65}Cu$ value in CSFs of ALS patients compared to CTRL (Figure 3). All the present suggested hypotheses likely accounting for the $\delta^{65}Cu$ increase observed in ALS CSFs are schematically summarized in Figure 3. Although all these assumptions need to be verified by further experiments, the $\delta^{65}Cu$ ALS-specific increase observed in CSF seems to reflect physiological deregulations that could account for ALS onset and progression.

To conclude, these results, *i.e.* the first to report Cu and Zn isotopic compositions in CSF of ALS, AD and CTRL subjects, demonstrate that Cu isotopic measurements in CSF may offer a more comprehensive view of the ALS metallome than elemental concentrations alone and may likely reinforce its diagnosis. Similarly, the lighter $\delta^{66}Zn$ value observed in the CSF of AD patients compared to that of CTRL subjects (Wilcoxon-Mann-Whitney, p_{value}= 0.0426) (Figure 1b) may also offer promising information regarding Zn dyshomeostasis in AD. Increasing the number of Cu and Zn isotopic measurements in CSFs of ALS and AD respectively as well as in other neurodegenerative pathologies, such as Parkinson or Huntington diseases would undoubtedly challenge the proposition that CSF $\delta^{65}Cu$ and $\delta^{66}Zn$ values are future highly promising biomarker of neurodegenerative diseases.

Materials and Methods

Subjects and samples

In this study, all subjects were hospitalized in the Department of Neurology for diagnosis purposes, which included cerebrospinal fluid (CSF) analyses among other tests. All patients signed informed consent about the potential use of their CSF for further research purposes and an ethical approval was also delivered by the local Ethics committee of the Hospices Civils de Lyon (date of delivery: 7th October, 2016). We investigated the CSF of 31 ALS patients diagnosed using the Awaji criteria (6). They were compared to a group of 25 patients suffering from neurocognitive complaint referred to expert memory clinic linked to Lyon

Center for Memory Resources and Research. These 25 patients underwent lumbar puncture using a standard procedure (63) in the context of clinical diagnosis of neurodegenerative diseases. Cerebrospinal fluid biomarker for AD pathology (*i.e* total and phosphorylated TAU proteins and Amyloid beta 1-42 peptide) were performed blind to the clinical diagnosis in the Neurochemistry Unit of Lyon University Hospital using commercially available enzyme-linked immunosorbent assays (INNOTEST hTau-Ag, INNOTEST phosphorylated-Tau181, and INNOTEST Aβ1-42; Fujirebio Europe) according to the manufacturer's instructions. The Neurochemistry Unit participated in the Alzheimer Association Quality Control Program for these biomarkers. Diagnoses were finally proposed in the framework of multidisciplinary consultation taking into account medical history, caregivers interviews, neurologic examination, neuropsychological evaluation, brain imaging and results of cerebrospinal fluid biomarker for AD pathology. AD diagnostic was excluded in 11 of these 25 patients who were finally classified as suffering mainly from psychiatric conditions and were then considered as controls for this study. The remaining 14 patients met the diagnostic criteria of Alzheimer 's disease according to McKhann et al.(64).

Both male and female from different ages ranging from 34 to 86 years old were studied. To avoid any sample bias, we also considered diverse ALS cases *i.e.* characterized by different onset brain location (bulbar, lower and upper limbs), distinct value of Awaji criteria and ALSFRS as well as variable time of symptom onset (6 to 36 months). All the details are summarized in Table S3.

Major and trace element concentrations

All chemical analyses were carried out in clean laminar flow hoods using double-distilled acids to avoid any exogenous contaminations. Samples were first weighted and then dissolved in a mixture of 15N HNO_3 and H_2O_2 (30%) in Savillex® beakers at 120°C for about 72h. When dissolved, major and trace element concentrations were measured in a small aliquot on an ICP-AES (iCAP 6000 Radial) and a quadrupole ICP-MS Thermo iCap-Q respectively at the Ecole Normale Supérieure (ENS) of Lyon following the method described in Garçon et al.(52). Trace and major element concentrations are reported in ng/mL and µg/mL respectively in Table S1. Briefly, the concentrations were calculated using calibration curves based on multi-elemental solutions. These solutions were also used to monitor and correct the instrumental drift over the analytical session. The precision of the results was assessed by complete duplicate and re-run analyses (referred as "dup" and "bis" samples respectively in Table S1) and accuracy and reproducibility were monitored by replication of certified reference materials (1577c, DORM2) and an in-house standards (OEP, FBS)

measured as unknown samples (Table S2). The results are generally reproducible and consistent within 10% (2sd) of published data (see Table S2). Based on the analysis of reference standards and duplicates analyses, we therefore estimate that the measurement precision is, on average, better than 10% for both major and trace elements.

Copper and zinc isotopic compositions

Samples were purified by ion-exchange chromatography using quartz columns filled with 1.8mL of Bio-Rad AGMP-1 (100-200 mesh) anion-exchange resin. Copper and zinc were successively eluted with 20mL of HCl 7N + 0.001% H_2O_2 and 10mL of HNO_3 0.5N respectively following the procedure described by Marechal et al.(65). The total procedural blanks were on average 0.4 ng for Cu (n=7) and 3.0 ng for Zn (n=7), which is below the amount of element isolated from the sample and available for isotopic measurement (*i.e.* average Cu_{CSFs} and Zn_{CSFs} of 20 ng). Although Zn blank amount was lower than the one in the samples, the relative difference was pretty small compared to copper. Therefore, to ensure the quality of our Zn isotopic data, we quantified the impact of this exogenous contamination using the mixing equation provided by Garçon et al.(52). Tubes and pipettes used to collect and store the CSFs cannot release significant amount that may account for exogenous contamination (*cf* Supplementary Information SI 1). Conversely, gloves contain high Zn content that may be easily mobilized during sample preparation (52). Assuming thus that the main source of contamination are the gloves, with $\delta^{66}Zn_{gloves}$ = 0.10 ± 0.32 ‰ (2sd), we show that for Zn = 20 ng (*i.e.* the content available for isotopic measurement), no significant shift can be induced beyond the measurement uncertainties (*i.e.* ±0.07 ‰, 2sd) (Figure S4).

Copper and zinc isotopic compositions are measured by multi-collector inductively coupled plasma mass spectrometry (MC-ICP-MS, Nu500) in wet plasma conditions following the procedure described by Maréchal et al.(65). On the day of the analyses, Zn and Cu purified solutions are diluted in a Cu (Cu SRM 976, National Institute of Standards and Technology, Gaithersburg, MD, USA) or Zn-doped solution (Zn JMC 3-0749L, Johnson Matthey Royston, UK) respectively to match the concentration of the standard mixture run between the samples (between 75 and 300 µg.L^{-1} depending on the sample). The delta values (expressed in ‰) are reported relative to the isotopic solution reference material NIST SRM 976 for Cu and JMC 3-0749L for Zn and are referred as:

$$\delta^{65}Cu_{sample} = \left[\frac{\left({}^{65}Cu/_{63}Cu\right)_{sample}}{\left({}^{65}Cu/_{63}Cu\right)_{standard}} - 1\right] * 1000 \quad \text{and} \quad \delta^{66}Zn_{sample} = \left[\frac{\left({}^{66}Zn/_{64}Zn\right)_{sample}}{\left({}^{66}Zn/_{64}Zn\right)_{standard}} - 1\right] * 1000$$

Instrumental mass fractionation and temporal drift is corrected with an exponential law using

the elemental-doping method and standard-sample bracketing respectively as recommended by Maréchal et al.(65). The precision and the accuracy of Cu and Zn isotopic ratios were assessed by repeated measurements of re-run and duplicate samples and by reference materials (1577c, bovine liver) and in-house standard solutions (OEP, sheep plasma) respectively. The average $\delta^{66}Zn$ of reference materials 1577c and OEP were -0.19 ± 0.04 (2sd, n=4) and +0.64 ± 0.06 (2sd, n=2), respectively, which is in good agreement with our in-house previous average values: $\delta^{66}Zn_{1577c}$ = -0.19 ± 0.05 (2sd, n=13) and $\delta^{66}Zn_{OEP}$ = +0.72 ± 0.08 (2sd, n=15) as well as with previous published result ($\delta^{66}Zn_{1577c}$ = -0.13 ± 0.02 (2sd, n=4)(66)) (Table S2). For $\delta^{65}Cu$, we measured +0.35 ± 0.07 (2sd, n=4) for 1577c and -1.16 ± 0.03 (2sd, n=3) which is also in agreement with our in-house reference values: $\delta^{65}Cu_{1577c}$ = +0.37 ± 0.12 (2sd, n=10) and $\delta^{65}Cu_{OEP}$ = -1.14 ± 0.09 (2sd, n=20) (Table S2). Based on these results, we estimate the 2sd analytical uncertainty of our isotopic measurements at ± 0.07. Note that the long-term precision based on the repeated measurements of the pure Zn JMC 3-0749L and Cu SRM 976 solutions run every two samples are very similar to these values (± 0.05 ‰ (2s, n = 140)).

Statistical analyses

Principal component analysis (PCA)

PCA is a mathematical algorithm that reduces the dimensionality of the data to highlight the most important variation in the data set (38). In this study, this multivariate technique was used to classify ALS (amyotrophic lateral sclerosis) patients from AD (Alzheimer) and age-matched controls (CTRL) based on several parameters including the chemical concentrations of 12 major and trace elements and copper and zinc isotopic compositions. PCA allows reducing the number of preliminary variables to few linear combinations of the data called principal components (PCs). This procedure (*i.e.* conversion of raw data to PCs) relies on an orthogonal transformation. In more details, the process of PCA consists of (1) Create a matrix containing all the raw data (*i.e.* elemental concentrations and isotopic compositions of all the samples). All samples for which a measure was missing were excluded. (2) Determine the covariance matrix and (3) Calculate the eigenvectors and the eigenvalues of this covariance matrix to determine the principal components (PCs) (PC1 and PC2 correspond to the eigenvectors with the largest eigenvalues). All these steps were implemented in MATLAB™.

Boxplot

In the present study, all the boxplot diagrams were implemented in MATLAB™ and significance level was determined using a non-parametric 'two-sided', Wilcoxon-Mann-

Whitney U-test. For each boxplot, the central mark is the median, the edges of the box are the first (*i.e.* 25th percentiles) and third quartiles (*i.e.* 75th percentiles) respectively and the whiskers extend to the most extreme data points (*i.e.* not considered outliers).

ROC

Receiver Operating Curve (ROC) was used to evaluate the reliability of $\delta^{65}Cu$ as a potential ALS diagnostic test in the aim to confirm the presence of ALS disease but also to rule out the presence of this pathology in healthy subjects. In this study, the ROC test was implemented in MATLAB^{TM} and four distinctive parameters were obtained: (1) the cut-off value *i.e.* the threshold value discriminating ALS form CTRL subjects, (2) the true positive rate (*i.e.* sensitivity) corresponding to the probability that a result will be higher the cut-off value when the ALS disease is present, (3) the false positive rate (*i.e.* 1-specificity) defined as the probability that a result will be lower the cut-off value when the ALS disease is not present and (4) The area under the curve (AUC) and (4). Optimal performance test correspond to a sensitivity and specificity of 100% and an AUC of 1.

Acknowledgements

We thank P. Télouk for his assistance during isotopic measurements as well as E. Albalat and A. Lamboux for their help in the clean laboratory. Thanks also to the clinicians Dr Anne Nove-Josserand and Dr Dominique Minier, the chiefs of the Division of Neurology at Hospital North of Villefranche sur Saône and at William Morey Hospital in Chalon sur Saône respectively. We are grateful to Fondation Bullukian and Fondation Mérieux as well as the Ecole Polytechnique Fédérale of Lausanne (EPFL) for their financial support

References

1. Narasimhan SD (2015) A Brief History of ALS. *Cell* 161(2):181–183.
2. Arthur KC, et al. (2016) Projected increase in amyotrophic lateral sclerosis from 2015 to 2040. *Nature Communications* 7:1–6.
3. Taylor JP, Brown RH, Cleveland DW (2016) Decoding ALS: from genes to mechanism. *Nature* 539(7628):197–206.
4. Savage N (2017) Calculating disease. *Nature* 550:S115.
5. Scott A (2017) On the treatment trail for ALS. *Nature* 550:S120.
6. Costa J, Swash M, de Carvalho M (2012) Awaji Criteria for the Diagnosis of Amyotrophic Lateral Sclerosis. *Arch Neurol* 69(11):1410.
7. Cedarbaum JM, et al. (1999) The ALSFRS-R: a revised ALS functional rating scale that incorporates assessments of respiratory function. *Journal of the Neurological Sciences* 169(1999):13–21.
8. Lu CH, et al. (2015) Neurofilament light chain: A prognostic biomarker in amyotrophic lateral sclerosis. *Neurology* 84(22):2247–2257.
9. Lind A-L, et al. (2016) A Multiplex Protein Panel Applied to Cerebrospinal Fluid Reveals Three New Biomarker Candidates in ALS but None in Neuropathic Pain Patients. *PLoS ONE*:1–17.
10. Zetterberg H, et al. (2016) Association of Cerebrospinal Fluid Neurofilament Light Concentration With Alzheimer Disease Progression. *JAMA Neurol* 73(1):60.
11. Bäckström DC, et al. (2015) Cerebrospinal Fluid patterns and the risk of future dementia in early, incident Parkinson disease. *JAMA Neurol* 72:1175–1182.

12. Barnham KJ, Masters CL, Bush AI (2004) Neurodegenerative diseases and oxidative stress. *Nat Rev Drug Discov* 3(3):205–214.
13. Finkel T, Holbrook NJ (2000) Oxidants, oxidative stress and the biology of ageing. *Nature* 408:1–9.
14. Gaetke LM, Chow CK (2003) Copper toxicity, oxidative stress, and antioxidant nutrients. *Toxicology* 189(1-2):147–163.
15. Valentine JS, Doucette PA, Zittin Potter S (2005) Copper-Zinc superoxide dismutase and amyotrophic lateral sclerosis. *Annu Rev Biochem* 74(1):563–593.
16. Dolgin E (2017) The hexanucleotide hex. *Nature* 550:S108.
17. Rosen DR, et al. (1993) Mutations in Cu/Zn superoxide dismutase gene are associated with familial amyotrophic lateral sclerosis. *Nature* 362:59–62.
18. Tokuda E, Okawa E, Watanabe S, Ono S-I, Marklund SL (2013) Dysregulation of intracellular copper homeostasis is common to transgenic mice expressing human mutant superoxide dismutase-1s regardless of their copper-binding abilities. *Neurobiology of Disease* 54(C):308–319.
19. Tokuda E, Okawa E, Ono S-I (2009) Dysregulation of intracellular copper trafficking pathway in a mouse model of mutant copper/zinc superoxide dismutase-linked familial amyotrophic lateral sclerosis. *Journal of Neurochemistry* 111(1):181–191.
20. Roos PM, Vesterberg O, Syversen T, Flaten TP, Nordberg M (2013) Metal Concentrations in Cerebrospinal Fluid and Blood Plasma from Patients with Amyotrophic Lateral Sclerosis. *Biological Trace Element Research* 151(2):159–170.
21. Roos PM, et al. (2012) Manganese in cerebrospinal fluid and blood plasma of patients with amyotrophic lateral sclerosis. *Exp Biol Med (Maywood)* 237(7):803–810.
22. Vinceti M, et al. (2013) NeuroToxicologyCerebrospinal fluid of newly diagnosed amyotrophic lateral sclerosis patients exhibits abnormal levels of selenium species including elevated selenite. *Neurotoxicology* 38:25–32.
23. Hozumi I, et al. (2011) Patterns of levels of biological metals in CSF differ among neurodegenerative diseases. *Journal of the Neurological Sciences* 303(1-2):95–99.
24. Albarède F, et al. (2016) Medical applications of Cu, Zn, and S isotope effects. *Metallomics* 8:1056–1070.
25. Albarède F, Telouk P, Lamboux A, Jaouen K, Balter V (2011) Isotopic evidence of unaccounted for Fe and Cu erythropoietic pathways. *Metallomics* 3(9):926.
26. Jaouen K, et al. (2012) Fe and Cu stable isotopes in archeological human bones and their relationship to sex. *Am J Phys Anthropol* 148(3):334–340.
27. Jaouen K, et al. (2013) Is aging recorded in blood Cu and Zn isotope compositions? *Metallomics* 5(8):1016–1024.
28. Jaouen K, Balter V (2014) Menopause effect on blood Fe and Cu isotope compositions. *Am J Phys Anthropol* 153(2):280–285.
29. Van Heghe L, Deltombe O, Delanghe J, Depypere H, Vanhaecke F (2014) The influence of menstrual blood loss and age on the isotopic composition of Cu, Fe and Zn in human whole blood. *J Anal At Spectrom* 29(3):478–482.
30. Costas-Rodríguez M, et al. (2015) Isotopic analysis of Cu in blood serum by multi- collector ICP-mass spectrometry: a new approach for the diagnosis and prognosis of liver cirrhosis?†. *Metallomics* 7:491–498.
31. Balter V, et al. (2015) Natural variations of copper and sulfur stable isotopes in blood of hepatocellular carcinoma patients. *Proceedings of the National Academy of Sciences* 112(4):982–985.
32. Bondanese VP, et al. (2016) Hypoxia induces copper stable isotope fractionation in hepatocellular carcinoma, in a HIF-independent manner†. *Metallomics*:1–8.
33. Telouk P, et al. (2015) Copper isotope effect in serum of cancer patients. A pilot study. *Metallomics* 7:299–308.
34. Enge TG, Ecroyd H, Jolley DF, Yerbury JJ, Dosseto A (2017) Longitudinal assessment of metal concentrations and copper isotope ratios in the G93A SOD1 mouse model of amyotrophic lateral sclerosis. *Metallomics* 9(2):161–174.
35. Büchl A, Hawkesworth CJ, Ragnarsdottir KV, Brown DR (2008) Re-partitioning of Cu and Zn isotopes by modified protein expression. *Geochem Trans* 9(1):11.
36. Miller KA, et al. (2016) The expression levels of cellular prion protein affect copper isotopic shifts in the organs of mice. *J Anal At Spectrom* 00:1–8.

37. Moynier F, Foriel J, Shaw AS, Le Borgne M (2017) Distribution of Zn isotopes during Alzheimer's disease. *Geochem Persp Let*:142–150.
38. Ringnér M (2008) What is principal component analysis? *Nature Biotechnology* 26:1–2.
39. Ostachowicz B, et al. (2006) Analysis of some chosen elements of cerebrospinal fluid and serum in amyotrophic lateral sclerosis patients by total reflection X-ray fluorescence. *Spectrochimica Acta Part B: Atomic Spectroscopy* 61(10-11):1210–1213.
40. Kanias GD, Kapaki E (1997) Trace Elements, Age, and Sex in Amyotrophic Lateral Sclerosis Disease. *Biological Trace Element Research* 56:187–201.
41. Kapaki E, et al. (1997) Essential trace element alterations in amyotrophic lateral sclerosis. *Journal of Neurological Sciences* 147:171–175.
42. Ihara Y, Nobukuni K, Takata H, Hayabara T (2013) Oxidative stress and metal content in blood and cerebrospinal fluid of amyotrophic lateral sclerosis patients with and without a Cu, Zn-superoxide dismutase mutation. *Neurological Research* 27(1):105–108.
43. Kapaki E, Segditsa J, Zournas C, Xenos D, Papageorgiou C (1989) Determination of cerebrospinal fluid and serum lead levels in patients with amyotrophic lateral sclerosis and other neurological diseases. *Experientia* 45:1108–1110.
44. Gil-Bea F, Aldanondo G, Lasa-Fernandez H, Lopez de Munain A, Vallejo-Illarramendi A (2017) Insights into mechanisms of copper dyshomeostasis in amyotrophic lateral sclerosis. *Expert Reviews in Molecular Medicine* 19:1–14.
45. Lelie HL, et al. (2011) Copper and Zinc Metallation Status of Copper-Zinc Superoxide Dismutase from Amyotrophic Lateral Sclerosis Transgenic Mice. *J Biol Chem* 286(4):2795–2806.
46. Dang T, et al. (2014) Increased metal content in the TDP-43A315T transgenic mouse model of frontotemporal lobar degeneration and amyotrophic lateral sclerosis. *Frontiers in Aging Neuroscience* 6:1–8.
47. Pithadia A, Lim MH (2012) Metal-associated amyloid-β in Alzheimer's disease. *Current Opinion in Chemical Biology* 16(1-2):67–73.
48. Kabashi E, et al. (2008) TARDBP mutations in individuals with sporadic and familial amyotrophic lateral sclerosis. *Nat Genet* 40(5):572–574.
49. Pokrishevsky E, et al. (2012) Aberrant Localization of FUS and TDP43 Is Associated with Misfolding of SOD1 in Amyotrophic Lateral Sclerosis. *PLoS ONE* 7(4):1–9.
50. Steinacker P, et al. (2014) Protease-resistant SOD1 aggregates in amyotrophic lateral sclerosis demonstrated by paraffin-embedded tissue (PET) blot. *acta neuropathol commun* 2(1):101.
51. Iyengar V, Wolttiez J (1988) Trace elements in Human clinical specimens: Evaluation of literature daat to identify reference values. *Clinical chemistry*:474–481.
52. Garçon M, et al. (2017) Nitrile, Latex, Neoprene and Vinyl Gloves: A Primary Source of Contamination for Trace Element and Zn Isotopic Analyses in Geological and Biological Samples. *Geostandards and Geoanalytical Research* 41(3):367–380.
53. Perret-Liaudet A, Pelpel M, Tholance Y (2012) Risk of Alzheimer's disease biological misdiagnosis linked to cerebrospinal collection tubes. *Journal of Alzheimer's Disease* 31:13–20.
54. Pokrishevsky E, Grad LI, Cashman NR (2016) TDP-43 or FUS-induced misfolded human wild-type SOD1 can propagate intercellularly in a prion- like fashion. *Sci Rep*:1–10.
55. Bodansky M (1921) The zinc and copper content of the human brain. *JBiolChem* 48:361–364.
56. Bonilla E, et al. (1984) Copper distribution in the normal human brain. *Neurochemical Research* 9:1–6.
57. House E, Esiri M, Forster G, Ince PG, Exley C (2012) Aluminium, iron and copper in human brain tissues donated to the medical research council's cognitive function and ageing study. *Metallomics* 4(1):56–65.
58. Harrison WW, Netsky MG, Brown MD (1968) Trace elements in human brain: Copper, zinc, iron and magnesium. *Clinica Chimica Acta* 21:55–60.
59. Nicaise C, et al. (2009) Impaired blood–brain and blood–spinal cord barriers in mutant SOD1-linked ALS rat. *Brain Research* 1301(C):152–162.
60. Garbuzova-Davis S, et al. (2007) Evidence of Compromised Blood-Spinal Cord Barrier in Early and Late Symptomatic SOD1 Mice Modeling ALS. *PLoS ONE* 2(11):e1205.
61. Balter V, et al. (2013) Contrasting Cu, Fe, and Zn isotopic patterns in organs and body fluids of mice and sheep, with emphasis on cellular fractionation. *Metallomics* 5(11):1470.

62. Cadiou J-L, et al. (2017) Copper transporters are responsiblefor copper isotopic fractionation ineukaryotic cells. *Sci Rep*:1–10.
63. del Campo M, et al. (2012) Recommendations to standardize preanalytical confounding factors in Alzheimer's and Parkinson's disease cerebrospinal fluid biomarkers: an update. *Biomarkers Med* 6(4):419–430.
64. McKhann GM, et al. (2011) The diagnosis of dementia due to Alzheimer's disease: Recommendations from the National Institute on Aging-Alzheimer's Association workgroups on diagnostic guidelines for Alzheimer's disease. *Alzheimer's & Dementia* 7(3):263–269.
65. Maréchal CN, Telouk P, Albarede F (1999) Precise analysis of copper and zinc isotopic compositions by plasma-source mass spectrometry. *Chemical Geology* 156(1-4):251–273.
66. Jaouen K, Beasley M, Schoeninger M, Hublin J-J, Richards MP (2016) Zinc isotope ratios of bones and teeth as new dietary indicators: results from a modern food web (Koobi Fora, Kenya). *Nature Publishing Group*:1–8.
67. Scheiber IF, Mercer JFB, Dringen R (2014) Metabolism and functions of copper in brain. *Progress in Neurobiology* 116:33–57.
68. Kapaki E, Segditsa C, Papageorgiou C (1989) Zinc, copper and magnesium concentration in serum and CSF of patients with neurological disorders. *Acat Neurol Scand* 79:373–378.

SUPPLEMENTARY INFORMATION

All the Supplementary Information are presented thereafter and include:

2 Supplementary Files:

- SI 1
- SI 2

4 Supplementray Figures :

- Figure S1
- Figure S2
- Figure S3
- Figure S4

3 Supplementary Tables:

- Table S1
- Table S2
- Table S3

Supplementary Information SI 1

Effect of exogenous contamination induced by tubes and pipettes on major and trace element concentrations measured in CSFs.

Cerebrospinal fluids (CSFs) are made of 99% water and have low amount of major and trace elements. To ensure absence of cerebrospinal fluids (CSFs) external contamination during sample collection and/or storage, we quantify the content of the most contaminable trace elements (*i.e.* Mn, Fe, Cu, Zn, Rb and Sr as well as Mg) that may be released by tubes and pipettes being directly in contact with the samples. This includes sampling (CSF-A: polypropylene, Sarstedt, 10mL, 92x15.3mm and CSF-B: polypropylene, Sarstedt, 5mL, 57x15.3mm) and storage tubes (CSF-C: polypropylene, Sarstedt, 1.5mL) as well as dropper-type pipette.

The detailed procedure consist of putting 2mL of HNO_3 0.5N + 2ppb indium (In) in the tubes, before storing them 3 weeks in a fridge. The volume of 2mL corresponds to the average volume of CSFs analyzed in this study. The duration of the test correspond to the approximate period for which CSF samples were stored in the tubes. To assess the amount of trace elements released by dropper-type pipette, we used a slightly different technique. For this test, we pour 2mL of HNO_3 0.5N + 2ppb indium (In) in clean savillex® beaker and washed the pipette three times with the solution. An aliquot of each solution is then analyzed on the Thermo iCap-Q mass spectrometer following the method described in the main text (see Materials and Methods section).

For all the elements measured in this study, the amount released by tubes and pipette that have been in contact with low concentrated HNO3 acid is always lower (<0.01) than the quantity present in the CSF samples (see figure below).

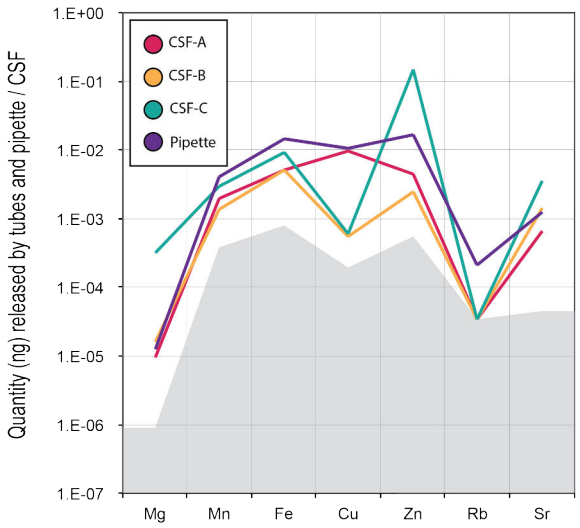

Supplementary Figure SI 1: *Amount of trace element released by sampling and storage tubes as well as dropper-like pipette normalized to the amount of elements initially present in 2mL of cerebrospinal fluids (CSFs) (i.e. the average volume analyzed in this study). The grey field represents values below the limit of detection (DL) defined following IUPAC guideline (i.e. $DL_i=xb_i + k*sb_i$ where k=3, xb_i and sb_i are respectively the mean and the standard deviation of the number of counts measured in blanks). When the amount detected in the solution was lower the limit of detection, data were represented as equal to the detection limit.*

Only one exception is noted for the amount of Zn released by the dropper-type pipette, but this amount remains relatively low (<0.1) compared to the amount initially present in the

samples. Although we used low concentrated acid solutions, it is important to note that chemical elements are more easily released in acidic solution than when they are in contact with non-acidic CSF samples. Therefore, our study likely provides maximized results being ten times higher that the real amounts released by tubes and pipettes when they are only filled with CSFs.

Altogether, these results show that storage and sampling tubes and dropper-type pipettes cannot induce significant exogenous contamination and bias the Mg and trace element concentrations including Fe, Cu, Zn, Mn, Rb and Sr measured in CSFs. Similar conclusion can also be drawn for Ca, K, Na, P and S, the latters being initially more concentrated in CSFs compared to the trace elements.

Supplementary Information SI 2
Detailed equations of the simple two-reservoirs (CSF and protein aggregates) mass balance model

To test the assumption that Cu isotopic variation observed in ALS cerebrospinal fluids (CFSs) may result from misfolded protein aggregation in the brain parenchyma associated with a Cu accumulation, we used a steady-state mass balance. Assuming a simple two reservoirs model composed of cerebrospinal fluids (CSF) and protein aggregates (AG), with a copper content incorporated in aggregates coming mainly from cerebrospinal fluids, the total mass (TOT) of ^{65}Cu and ^{63}Cu in the system (*i.e.* AG + CSF) can be described as:

$m^{65}Cu_{TOT} = m^{65}Cu_{AG} + m^{65}Cu_{CSF}$
$m^{63}Cu_{TOT} = m^{63}Cu_{AG} + m^{63}Cu_{CSF}$

Re-writing the classical mixing equation to express the Cu isotopic composition of a binary mixture as a function of the Cu amount present in the two end-members leads to:

$$(\delta^{65}Cu)_{TOT} = \frac{m^{65}Cu_{AG}}{m^{65}Cu_{AG} + m^{65}Cu_{CSF}} * (\delta^{65}Cu)_{AG} + \frac{m^{65}Cu_{CSF}}{m^{65}Cu_{AG} + m^{65}Cu_{CSF}} * (\delta^{65}Cu)_{CSF}$$ (Equation 1)

as $m\,Cu_{AG} = m^{65}Cu_{AG} * \left(1 + \frac{m^{65}Cu_{AG}}{m^{63}Cu_{AG}}\right)$ $with$ $1 + \frac{m^{65}Cu_{AG}}{m^{63}Cu_{AG}} \approx 1$

therefore $m\,Cu_{AG} \approx m^{65}Cu_{AG}$ $and\ likewise$ $mCu_{CSF} \approx m^{65}Cu_{CSF}$

Equation 1 becomes:

$$\left(\delta^{65}Cu\right)_{TOT} = \frac{m\,Cu_{AG}}{m\,Cu_{AG} + m\,Cu_{CSF}} * \left(\delta^{65}Cu\right)_{AG} + \frac{m\,Cu_{CSF}}{m\,Cu_{AG} + m\,Cu_{CSF}} * \left(\delta^{65}Cu\right)_{CSF}$$ (Equation 2)

At initial state (EI *i.e.* healthy condition), there are no aggregates in the brain (*i.e.* mCu_{AG} = 0), therefore:

$$\left(\delta^{65}Cu\right)_{TOT_{EI}} = \left(\delta^{65}Cu\right)_{CSF_{EI}}$$ (Equation 3)

with $\left(\delta^{65}Cu\right)_{CSF_{EI}}$ the value measured in the control group (*i.e.* -0.20 ‰, 25th percentile = -0.26‰, 75th percentile = -0.02‰)

At final state (EF *i.e.* ALS disease), aggregates have been formed, so we have (Equation 4):

$$\left(\delta^{65}Cu\right)_{TOT_{EF}} = \frac{m\,Cu_{AG_{EF}}}{m\,Cu_{AG_{EF}} + m\,Cu_{CSF_{EF}}} * \left(\delta^{65}Cu\right)_{AG_{EF}} + \frac{m\,Cu_{CSF_{EF}}}{m\,Cu_{AG_{EF}} + m\,Cu_{CSF_{EF}}} * \left(\delta^{65}Cu\right)_{CSF_{EF}}$$

In this equation $\left(\delta^{65}Cu\right)_{CSF_{EF}}$ $and\ m\ Cu_{CSF_{EF}}$ correspond to the value measured in the ALS group (*i.e.* $\delta^{65}Cu_{CSF\,EF}$ = +0.01‰, (25th percentile = -0.10‰, 75th percentile = +0.18‰) and $m\ Cu_{CSF_{EF}} = 1.9\mu g$). $m\ Cu_{AG_{EF}}$ is the amount of copper incorporated in the aggregates determined as the mass difference measured between CSF of controls and ALS subjects (*i.e.* $m\ Cu_{AG_{EF}} = 0.28\mu g$).

Then, mass conservation implies that $(\delta^{65}Cu)_{TOT_{EI}} = (\delta^{65}Cu)_{TOT_{EF}}$

Rearranging the equations 3 and 4 finally gives:

$$\delta^{65}Cu_{AG} = \frac{\delta^{65}Cu_{CSF_{EI}} - \left(\frac{m\ Cu_{CSF_{EF}}}{m\ Cu_{CSF_{EF}} + m\ Cu_{AG_{EF}}} * \delta^{65}Cu_{CSF_{EF}}\right)}{\frac{m\ Cu_{AG_{EF}}}{m\ Cu_{CSF_{EF}} + m\ Cu_{AG_{EF}}}}$$ (Equation 5)

Using this equation, we can calculate the copper isotopic composition that should have the aggregates to account for the $\delta^{65}Cu$ measured in CSF for a $m\ Cu_{CSF_{EF}}$ of 0.28µg. For the sake of sensitivity purposes, we also performed the calculation with a Cu amount exchanged between CSF and AG being 5 times higher (*i.e.* 1.42 µg).
Assuming a Cu concentration in the aggregates similar to the brain *i.e.* ranging between 1 and 50mg/kg (1-4), and a volume of CSF of 150mL (5) we can calculate the whole mass of these aggregates and determined the relative proportion they represent compared to the whole brain (m=1400g).

For a $m\ Cu_{AG_{EF}}$ of 0.28µg, we obtained a $\delta^{65}Cu_{AG}$ in the aggregates of -1.60 ± 1.51 ‰ with a proportion ranging between 0.0004% ($[Cu]_{AG}$=50mg/kg) and 0.02% ($[Cu]_{AG}$=1mg/kg) of the mass of the brain. For a $m\ Cu_{AG_{EF}}$ = 1.42µg, we obtained a $\delta^{65}Cu_{AG}$ in the aggregates of -0.48 ± 0.39 ‰ with proportion ranging between 0.002% ($[Cu]_{AG}$=50mg/kg) and 0.1% ($[Cu]_{AG}$=1mg/kg).

References:

1. Bodansky M (1921) The zinc and copper content of the human brain. *JBiolChem* 48:361–364.

2. Bonilla E, et al. (1984) Copper distribution in the normal human brain. *Neurochemical Research* 9:1–6.

3. Harrison WW, Netsky MG, Brown MD (1968) Trace elements in human brain: Copper, zinc, iron and magnesium. *Clinica Chimica Acta* 21:55–60.

4. House E, Esiri M, Forster G, Ince PG, Exley C (2012) Aluminium, iron and copper in human brain tissues donated to the medical research council's cognitive function and ageing study. *Metallomics* 4(1):56–65.

5. Sakka L, Coll G, Chazal J (2011) Anatomy and physiology of cerebrospinal fluid. *European Annals of Otorhinolaryngology, Head and Neck diseases* 128(6):309–316.

Supplementary Figures

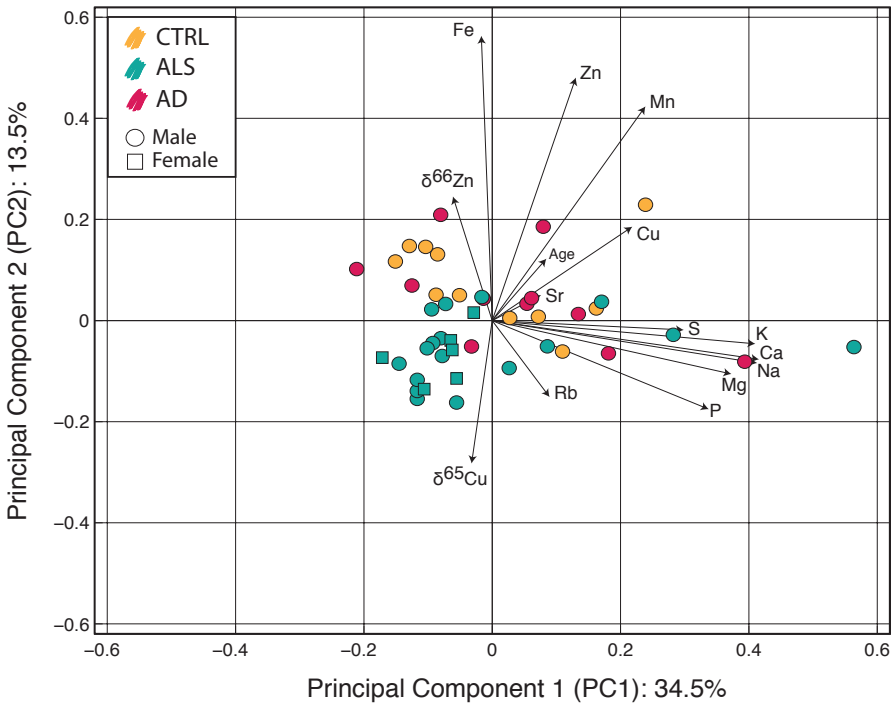

Figure S1: Principal component analysis (PCA)
The PCA allows the distinction of amyotrophic lateral sclerosis (ALS) patients (green points) with control (yellow points) and Alzheimer subjects (pink points). In this figure, concentrations and isotopic compositions are normalized to their standard deviation. The two principal components (PC1 and PC2) are represented and explain ~ 50% of the total variance in chemical composition. For each component, black straight lines show the loading factors (*i.e.* the weight of each variable on the principal components). Circles and squares points stand for male and female subjects respectively. No significant variation is observed between the male and the female subjects within the ALS group.

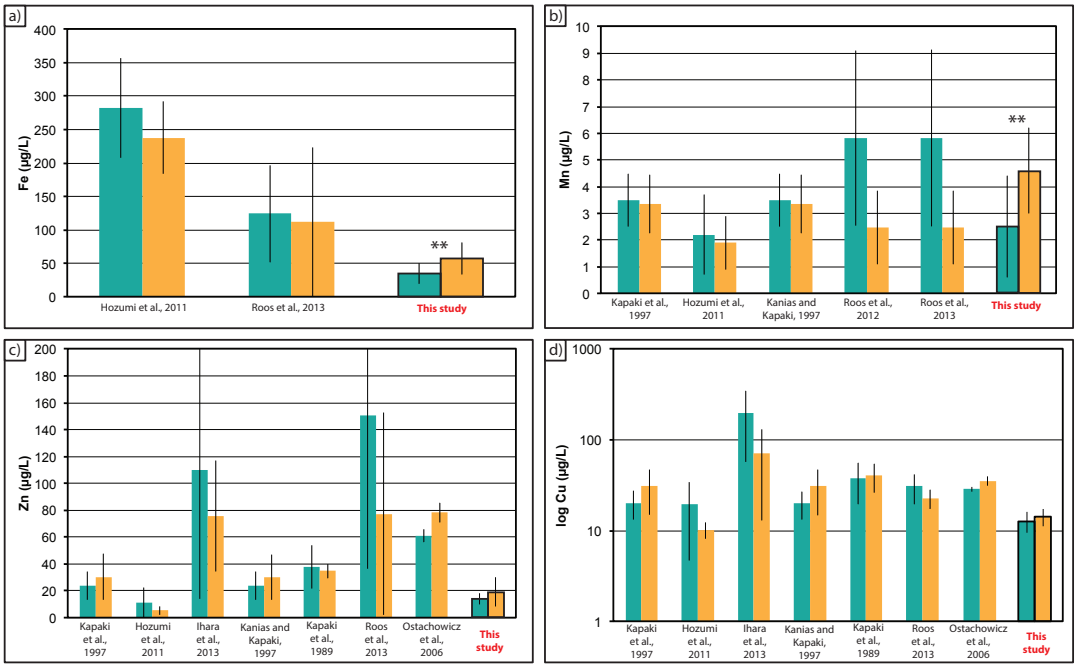

Figure S2: Compilation of a) Fe, b) Mn, c) Zn and d) Cu concentrations of cerebrospinal fluids (CSFs) in both control (yellow points) and amyotrophic lateral sclerosis subjects (green points). Regarding the literature data, Fe concentrations are from Hozumi et al.(23) and Roos et al.(20), Mn concentrations derived from Kapaki et al.(41); Hozumi et al.(23); Kanias and Kapaki (40); Roos et al.(20, 21) and Zn and Cu concentrations are from Kapaki et al.(41); Hozumi et al.(23); Ihara et al.(42); Kanias and Kapaki (40); Kapaki et al.(68); Roos et al.(20) and Ostachowicz et al.(39). Error bars represent 2sd. Cu diagram is represented with a logarithm scale. ** stands for Wilcoxon-Mann-Whitney, p_{value} <0.005.

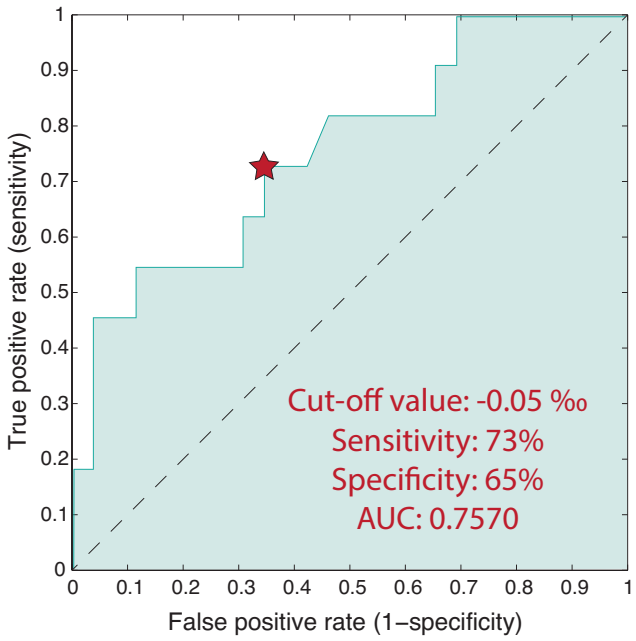

Figure S3: Receiver Operating Curve (ROC)
ROC was used to quantify the accuracy of $\delta^{65}Cu$ as performance indicator of ALS patients from control subjects. The test was performed using copper isotopic compositions of amyotrophic lateral sclerosis (ALS) and control groups. Effective measures of accuracy are (1) the area under the curve (AUC) of 0.7570, (2) the sensitivity of 73% and (3) the specificity of 65%. The cut-off value (*i.e.* the critical value below which we can exclude the presence of ALS disease) is defined at -0.05‰.

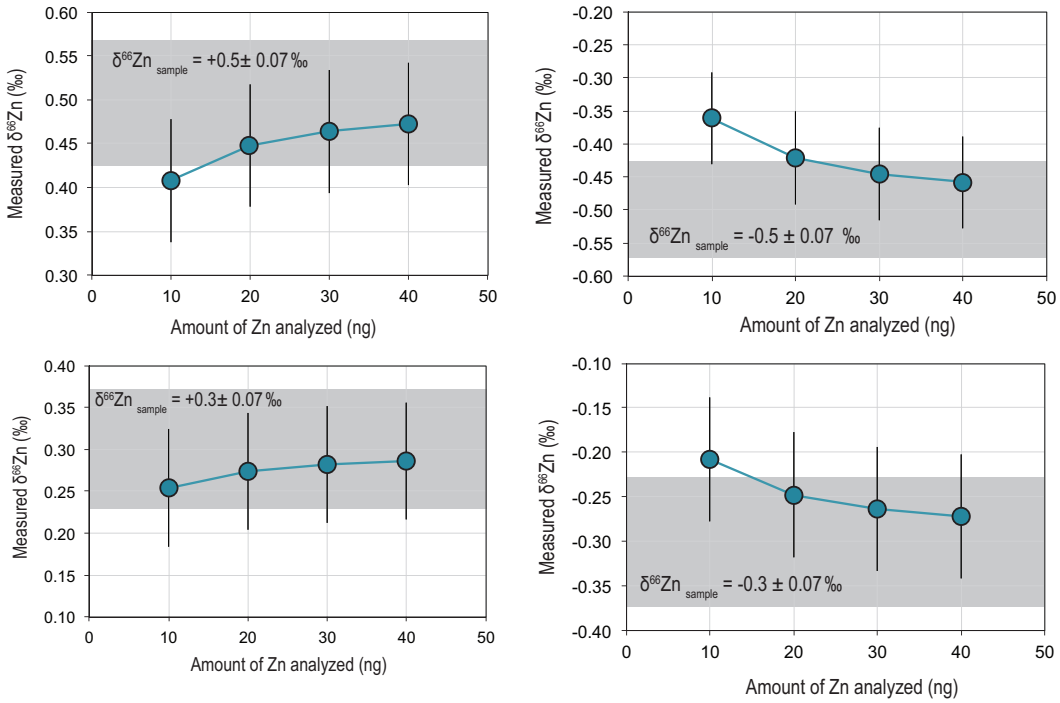

Figure S4: Quantification of exogenous contamination on Zn isotopic compositions as a function of the amount of Zn available in CSF samples and measured by mass spectrometry. For this calculation, we used the mixing equation provided by Garçon et al.(52). We assumed that the main source of contamination is the gloves releasing an average amount of 3ng and having an average $\delta^{66}Zn$ of +0.10 ± 0.32 ‰ (52). The grey fields show several isotopic compositions (maximum and minimum value) of the sample and its measurement precision that is fixed at ± 0.07‰ (2sd). For more details on the mixing calculation please report to Garçon et al.(52).

Table S1: Trace and major element concentrations and Cu and Zn isotopic compositions measured in cerebrospinal fluids

NB: With regard to confidentiality issues concerning the publication of the present work, these data are not provided in this manuscript

DATA NOT PROVIDED IN THIS MANUSCRIPT

Table S2: Major and trace element concentrations (ppm) and Cu-Zn isotopic compositions (‰) of in-house and certified standards measured in this study

Table S2: Major and trace element concentrations (ppm) and Cu-Zn isotopic compositions (‰) of in-house and certified standards measured in this study

Sample Name	Mn	Fe	Cu	Zn	Rb	Sr	Ca	K	Na	P	S	Mg	$\delta^{65}Cu_{NIST\,SRM\,976}$	$\delta^{66}Zn_{NRC\,a\,3249}$
OEP-1	n/a	21.71	10.85	8.06	1.17	2.06	1090.2	2545.9	45857.1	1230.8	11721.8	260.2	-1.17	0.62
OEP-2	n/a	21.50	10.31	7.66	1.06	1.86	883.0	2076.8	36813.7	1045.9	9924.8	252.1	-1.17	0.66
OEP-3	n/a	18.50	10.22	7.55	1.05	1.77	833.2	2110.3	33845.8	1045.8	9883.2	240.7	-1.14	n/a
OEP-4	n/a	18.23	10.31	7.13	1.00	1.75	862.3	2121.7	37097.9	1155.5	10290.8	255.1	n/a	n/a
Average	*n/a*	*19.99*	*10.42*	*7.60*	*1.07*	*1.86*	*917.2*	*2213.7*	*38403.6*	*1119.5*	*10455.2*	*252.0*	*-1.16*	*0.64*
2sd	*n/a*	*3.75*	*0.57*	*0.76*	*0.14*	*0.28*	*234.3*	*444.6*	*10364.1*	*180.9*	*1728.1*	*16.5*	*0.03*	*0.06*
In-house reference value; ±2σ (n)		**18.64 ± 7.04 (14)**	**10.54 ± 1.42 (19)**	**7.24 ± 1.23 (19)**	**1.04 ± 0.18 (17)**	**1.83 ± 0.24 (17)**	**868.1 ± 152.4 (16)**	**1981.7 ± 428.2 (16)**	**34208.7 ± 8598.4 (16)**	**1063.8 ± 159.2 (16)**	**9734.8 ± 1522.9 (16)**	**274.6 ± 68.5 (16)**	**-1.14 ± 0.05 (20)**	**+0.72 ± 0.08 (15)**
FBS	0.06	1.75	0.09	2.37	1.62	0.14	113.4	423.1	2760.9	86.9	434.7	24.6	n/a	n/a
In-house reference value; ±2σ (n)	**0.07 ± 0.02 (5)**	**1.87 ± 1.21 (9)**	**0.11 ± 0.04 (9)**	**2.64 ± 0.47 (11)**	**1.56 ± 0.26 (7)**	**0.16 ± 0.03 (7)**	**131.9 ± 26.0 (10)**	**436.1 ± 55.7 (10)**	**3021.3 ± 565.9 (10)**	**102.2 ± 16.9 (10)**	**494.6 ± 122.4 (10)**	**29.4 ± 7.8 (10)**	**n/a**	**n/a**
1577C-1	12.12	196.38	265.85	179.37	33.09	<LD	213.3	11033.3	2105.0	11066.7	7546.7	638.3	0.34	-0.16
1577C-2	12.14	198.76	260.86	177.90	32.91	<LD	181.4	10517.1	1947.1	10775.7	7424.3	610.0	0.40	-0.19
1577C-3	11.32	190.45	253.34	171.47	32.23	<LD	180.5	10280.5	1908.5	10611.0	7363.4	597.6	0.33	-0.20
1577C-4	11.51	192.85	253.05	171.23	32.15	<LD	198.7	10471.8	1882.1	10743.6	7341.0	607.7	0.32	-0.20
Average	*11.77*	*194.61*	*258.27*	*174.99*	*32.59*	*n/a*	*193.5*	*10575.7*	*1960.7*	*10799.2*	*7418.8*	*613.4*	*0.35*	*-0.19*
2sd	*0.84*	*7.37*	*12.42*	*8.50*	*0.94*	*n/a*	*31.3*	*643.7*	*199.7*	*384.0*	*184.4*	*35.0*	*0.07*	*0.04*
Certified Reference value*; ±2σ	**10.46 ± 0.47**	**197.94 ± 0.65**	**272.50 ± 4.6**	**181.10 ± 1.00**	**35.30 ± 1.10**		**131.0 ± 10.0**	**10230.0 ±640.0**	**2033.0 ± 64.0**	**11750.0 ± 270.0**	**7490.0 ± 340.0**	**620.0 ± 42.0**	**+0.37±0.12 (n=10)** *(in house reference value)*	**-0.19±0.05 (n=13)** *(in-house reference value)* **-0.13±0.02 (n=4)** *(Jouvin et al., 2016)*
DORM2	3.61	131.34	2.00	23.58	5.86	2.38	501.5	15910.4	4810.9	9129.4	7674.1	998.3	n/a	n/a
Certified Reference value; ±2σ	**3.66 ± 0.34 *** **	**142.00 ± 10.00 *** **	**2.34 ± 0.16 *** **	**25.60 ± 2.30 *** **	**5.63 ± 1.04** *(in house reference value, n=10)*	**1.66 ± 0.06 ****	**388.0 ± 149.9 ****	**13573.8 ± 2524.7 ****	**4925.1 ± 702.9****	**8406.3 ± 3809.1 ****	**7957.0 ± 272.0 ****	**1024.0 ± 85.0 ****	**n/a**	**n/a**

Footnote:
OEP (sheep plasma) and FBS (Fetal bovine serum) are in-house standards and 1577c (bovine liver) and DORM2 (fish protein) are certified standards
* Reference values from NIST (National Institute of Standards and Technology)
** Preferred values from GeoREM
*** Certified values form NRC (National Council of Canada)

Table S3: General information and patients' clinical records

Sample Name	Gender	Age (years) at sample collection	Localization of first symptoms *	Awaji criteria	ALSFRS-R **	Time (months) between sampling date and first symptoms
ALS1	Male	45	MI	definite	44	7
ALS2	Male	62	MS	definite	39	6
ALS4	Male	81	MS	definite	40	6
ALS5	Male	46	bulb	definite	40	12
ALS6	Male	34	MS	definite	42	12
ALS7	Male	65	bulb	definite	44	12
ALS8	Male	86	MI	possible	37	6
ALS9	Male	68	MI	definite	45	12
ALS10	Male	73	MS	definite	37	6
ALS11	Male	64	MS	probable	28	6
ALS12	Male	60	MS	definite	33	6
ALS13	Male	60	bulb	definite	34	6
ALS14	Male	57	MI	definite	32	24
ALS 15	Male	49	bulb	definite	41	6
ALS 16	Male	50	MS	probable	39	12
ALS 17	Male	69	MI	probable	45	36
ALS 18	Male	60	bulb	definite	39	24
ALS 19	Male	49	bulb	definite	39	12
ALS 20	Male	75	MI	probable	35	12
ALS 21	Male	70	MS	definite	23	24
ALS 22	Male	76	bulb	definite	42	12
ALS 23	Male	54	bulb	definite	43	7
ALS 24	Male	44	MI	probable	46	24
ALS 25	Female	71	MS	probable	43	4
ALS 26	Female	64	bulb	definite	40	6
ALS 27	Female	63	bulb	definite	40	24
ALS 28	Female	67	MI	definite	40	5
ALS 29	Female	69	MI	probable	34	6
ALS 30	Female	64	MI	probable	40	9
ALS 31	Female	45	MS	definite	41	24
ALS 32	Female	43	MI	probable	42	6
CTRL2	Male	49				
CTRL3	Male	62				
CTRL4	Male	69				
CTRL5	Male	48				
CTRL6	Male	46				
CTRL7	Male	67			n/a	
CTRL8	Male	60				
CTRL9	Male	44				
CTRL10	Male	70				
CTRL11	Male	58				
CTRL 12	Male	79				
AD4	Male	75				
AD5	Male	78				
AD6	Male	68				
AD7	Male	68				
AD8	Male	78				
AD9	Male	63				
AD10	Male	70			n/a	
AD11	Male	59				
AD12	Male	63				
AD13	Male	71				
AD14	Male	73				
AD15	Male	73				
AD16	Male	79				
AD17	Male	78				

Footnote:
"n/a" stands for unspecified value
CTRL stands for control subjects, ALS and AD are for Amyotrophic lateral sclerosis and Alzheimer patients respectively

*Site at onset: - MI=lower limbs
- MS=upper limbs
- bulb=bulbar

**ALSFRS-R stands for the revised version of the Amyotrophic Lateral Sclerosis Rating scale

IV.2. Analyses de cellules humaines

Nous avons précédemment montré que la composition isotopique en cuivre ($\delta^{65}Cu$) des liquides céphalo-rachidiens apparaissait comme un marqueur de diagnostic potentiel de la sclérose latérale amyotrophique (SLA) ; les personnes malades ayant un ratio isotopique ($\delta^{65}Cu$) plus élevé que les personnes en bonne santé. Comme il l'a été suggéré dans le manuscrit ci-dessus, ces variations isotopiques pourrait être reliées à l'agrégation de protéines mal conformées dans le cerveau. Pour éclaircir ce point et tenter d'identifier la cause de cette pathologie, nous avons analysé la composition isotopique en cuivre de plusieurs modèles cellulaires dans lesquelles ont été transfectés des gènes codant pour une protéine viable ou mal-conformée appelée TDP-43 (TAR DNA-binding protein 43). L'étude préférentielle de cette protéine repose sur le fait que: (1) tous les patients atteints de SLA présentent des agrégats cytoplasmique de TDP-43 dans leurs cellules neuronales (Chen-Plotkin et al., 2010; Dang et al., 2014; Kasai et al., 2009; Nonaka et al., 2013; Noto et al., 2011; Smethurst et al., 2015) et (2) l'agrégation de protéine mal-conformée similaire à la TDP-43 a été montré comme étant à l'origine d'importantes variations chimiques et isotopiques (Büchl et al., 2008; Miller et al., 2016) pouvant s'expliquer par l'accumulation préférentielle des métaux au sein des ces agrégats (Kepp, 2017; Pithadia and Lim, 2012; Sastre et al., 2015); deux points laissant penser que l'accumulation cytoplasmique de TDP-43 dans le cerveau et le dérèglement isotopique en cuivre précédemment observé dans les LCRs pourraient être reliés.

L'ensemble des manipulations génétiques a été réalisé par Pascal Leblanc au LBMC (Laboratoire de Biologie et Modélisation de la Cellule). Brièvement, des cellules humaines de reins (293T) et des neurones (SHSY5Y) ont été transfectées (*i.e.* transfert de gènes) avec des gènes codant pour la protéine TDP-43 sauvage (*i.e.* non mutée) (WT) ou mutée. Les protéines mutées résultent de 6 mutations distinctes: (1) Q331K (331), G298S (298) et G294A (284), trois mutations localisées dans le domaine terminal (glycine rich C terminal), (2) NLS (78-84) (D) et NLS (78-84 et 187-192) (DD), deux mutations localisées dans le domaine 'NLS' et (3) la suppression du domaine 'NLS' (CTF) (Figure 6). Toutes les cellules expriment donc après transfert, leur propre TDP-43 endogène ainsi qu'une TDP-43 externe qui est soit 'normale' (*i.e.* gène codant non muté) soit mal conformée (cf Table 3 du Chapitre II pour plus de détails). Pour les cellules de reins, un gène codant pour une protéine fluorescente (GFP) a également été transférée dans les cellules afin de pouvoir mettre en évidence la présence de TDP-43 (le gène étant accolé à celui codant la protéine TDP-43). L'ensemble des résultats isotopiques obtenus sur les cellules est résumé dans la Table 3.

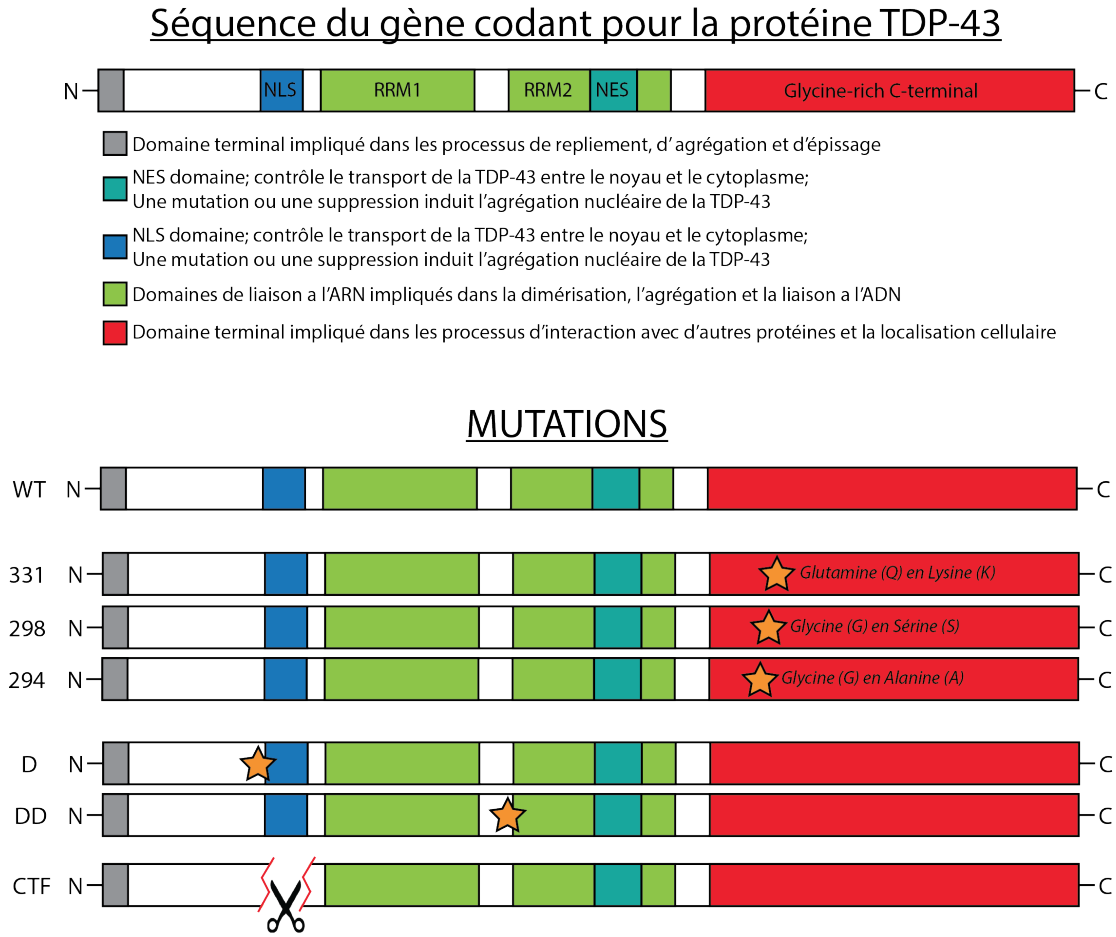

Figure 6: Mutations génétiques réalisées sur les gènes codant pour la protéine TDP-43 (TAR DNA-binding protein 43). Les étoiles indiquent la localisation des mutations et le ciseau symbolise une coupure du brin d'ADN. Ces gènes sont ensuite transfectés dans des cellules humaines. Modifié d'après Smethurst et al. (2015)

	Nom de l'échantillon	Proportion d'agrégats cytoplasmique	$\delta^{65}Cu_{NIST976}$ (‰)	1SD	Nombre de duplicats (n)
Cellule de rein	WT	+	0.87	0.30	3
	GFP -1	-	1.13	0.12	1
	T -1	-	1.17	0.12	1
	CTF -1	++++	1.15	0.12	1
	331 -1	+	1.13	0.12	1
	298 -1	+	0.87	0.17	3
	294 -1	+	1.10	0.12	1
	D -1	++	0.94	0.06	3
	DD -1	+++	0.77	0.19	4
Neuroblaste	S-400 -1	-	0.30	0.47	3
	S-wt -1	++/+	0.39	0.19	3
	D -1	++/+	0.26	0.27	2
	298 -1	++/+	0.60	0.14	3

Table 3: Composition isotopique en cuivre ($\delta^{65}Cu$) mesurée dans des cellules de reins et neuronales (i.e. neuroblastes) ayant été transfectées. L'ensemble des informations relatives aux mutations et au transfert se trouve résumé dans la Table 3 du Chapitre II.

Comme illustré sur la figure 7, aucune distinction significative ; que ce soit dans les cellules de reins (Figure 7a) ou les neuroblastes (Figure 7b) n'est visible entre les cellules présentant des agrégats cytoplasmiques de TDP-43 en grande (CTF, DD) ou moyenne quantité (331, 298, 294 et D) et celles n'ayant pas d'agrégats (T et S-400) voire très peu (WT et S-WT) (Figure 7). Ni l'ajout de GFP, ni le processus de transfert génétique ont un impact sur le rapport isotopique en cuivre ; les cellules non transfectées (T et S-400) et/ou transfectées avec de la GFP ont des rapports isotopiques identiques aux cellules transfectées avec un gène non-muté codant pour une TDP-43 normale (WT et S-wt). De même, les cellules exprimant la TDP-43 normale (WT et S-wt) ont des compositions isotopiques semblables aux incertitudes de mesures près, à celles exprimant la TDP-43 mal conformée (CTF, 331, 298,294, D et DD).

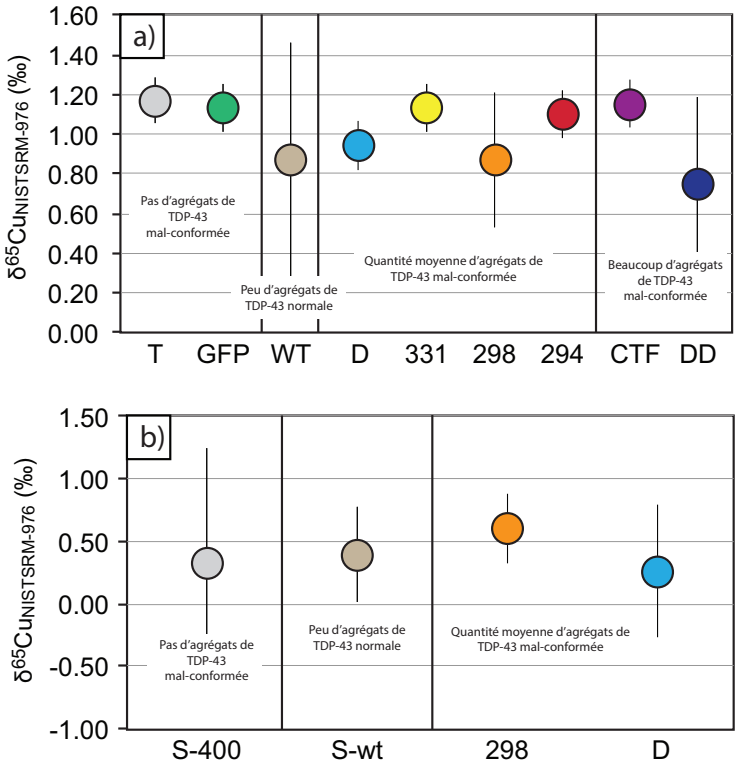

Figure 7: Composition isotopique en cuivre mesurée dans des cellules de reins (a) et des cellules neuronales (b) après avoir été transféctées par des gènes mutés (CTF, 331, 298, 294, D et DD) et non mutés (WT) codant pour la protéine TDP-43 (TAR DNA-binding protein 43). T et S-400 correspondent à des cellules non transfectées. GFP est une cellule dans laquelle seulement le tag pour la GFP (green fluorescent protein) a été transféré. Les barres d'erreurs représentent 2sd.

A première vue, ces résultats pourraient donc laisser penser que l'augmentation du rapport isotopique en Cu chez les personnes atteintes de SLA discuté dans l'article précédent (IV.1) n'est probablement pas relié à l'agrégation de protéines mal-conformées dans le cerveau. Cependant, nous nous sommes focalisés uniquement sur la protéine TDP-

43. Or, il se peut que le dérèglement isotopique en Cu ne soit pas spécifique de cette protéine mais d'une autre. En effet, bien que la protéine TDP-43 s'agrège dans le cerveau des personnes malades, d'autres protéines similaires comme la Cu-Zn superoxide dismutase (SOD1) et la FUS (RNA-binding protein fused in sarcoma) ont également été identifiées (Bourassa et al., 2014; Pokrishevsky et al., 2012; Valentine et al., 2005). La protéine Cu-Zn SOD1 est impliquée dans le renforcement du système de défense antioxydant et s'avère être plus spécifique du cuivre et du zinc que ne l'est la TDP-43 (Valentine et al., 2005). Il est donc possible que les variations isotopiques en cuivre observées dans les LCRs soient préférentiellement reliées à l'agrégation de cette protéine, bien que l'accumulation de TDP-43 semble tout de même avoir un rôle à jouer. Les études de Pokrishevsky et al.(2012; 2016) ont en effet démontré que l'agrégation de TDP-43 pouvait engendrer la mal-conformation et la propagation de la protéine SOD1, démontrant que l'effet potentiel de SOD1 sur les compositions isotopiques en cuivre dépendrait indirectement de l'agrégation de la TDP-43. Néanmoins, si l'agrégation de la protéine SOD1 contrôle les rapports isotopiques en Cu des LCRs, la teneur en cuivre (Cu) et en zinc (Zn) contenue dans les sites actifs de cette protéine étant similaire, nous devrions nous attendre à des dérèglement isotopiques similaires pour ces deux éléments chimiques. Or, aucune variation significative n'est observée entre les rapports isotopiques en zinc ($\delta^{66}Zn$) des LCRs de patients sains et atteints de SLA (Wilcoxon-Mann-Whitney, p_{value} = 0.1764) (Figure 8).

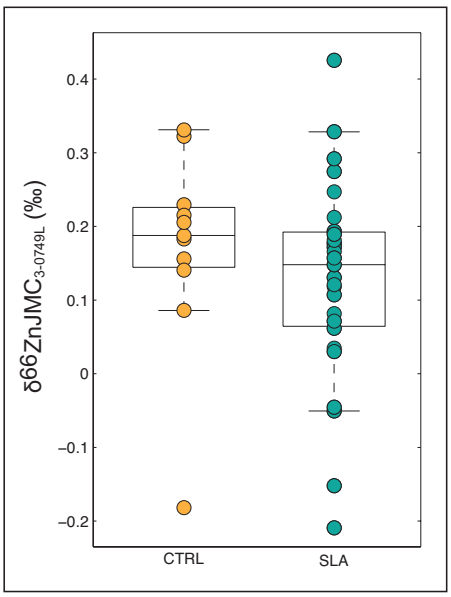

Figure 8 : Diagramme de boîtes à moustache montrant les compositions isotopiques en zinc ($\delta^{66}Zn$) dans les liquides céphalorachidiens (LCRs) de patients sains (CTRL, points jaunes) et atteints de sclérose latérale amyotrophique (SLA, points verts). Pour chaque boîte, la ligne horizontale centrale représente la valeur médiane, les bords sont les 1er et 3ème quartiles. Les points hors des boites sont des cas extrêmes non considérés dans le calcul statistique. Le seuil de signification a été estimé grâce à un test non-paramétrique dit de Wilcoxon-Mann-Whitney U-test réalisé sous MATLAB^{TM}. La p-value, non significative, est de 0.1764.

L'état d'oxydation du Cu et du Zn pourrait également jouer un rôle dans le dérèglement isotopique. Le zinc n'a qu'un seul état d'oxydation (Zn^{2+}) qui lui confère une stabilité réactive dans un milieu gouverné par les processus d'oxydo-réduction. À l'inverse, le cuivre peut être présent sous deux formes distinctes: Cu^{2+} et Cu^{+}. La protéine SOD1 étant une enzyme de détoxification dont la réaction catalytique (e.g. transformation de l'espèce réactive O_2^- en oxygène O_2) nécessite des changements d'état d'oxydation de ses cofacteurs métalliques (Valentine et al., 2005), l'absence de variation isotopique en Zn pourrait donc s'expliquer par son nombre d'oxydation limité.

Pour conclure, l'ensemble des résultats obtenus sur les cellules ne sont actuellement pas concluants pour confirmer l'existence d'un lien fort entre l'accroissement du rapport isotopique en Cu dans les LCRs de patients malades et l'accumulation progressive de la protéine TDP-43 mal-conformées dans le cerveau. Néanmoins, cela ne permet pas d'exclure que le dérèglement isotopique en Cu est relié à l'accumulation d'agrégats protéiques car, il se peut que ce processus soit spécifique d'une autre protéine. Des analyses supplémentaires sont alors nécessaires, notamment sur les protéines SOD1 et FUS, pour complémenter et valider ces premiers résultats préliminaires.

CONCLUSION ET PERSPECTIVES

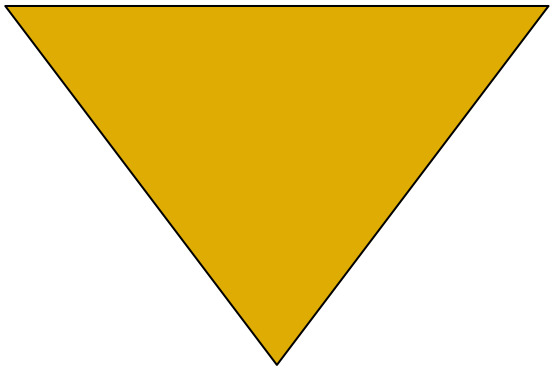

L'ensemble des résultats présentés dans cette étude nous permet dans un premier temps de porter un regard nouveau sur notre compréhension globale du vieillissement. Ce processus biologique complexe est caractérisé par l'affaiblissement progressif de nos capacités physiques. La plupart des personnes subit un déclin modéré de nombreuses fonctions tandis que d'autres maintiennent ces fonctions tout au long leur vie ('Super Seniors'). Ces divergences peuvent en partie être expliquées par la génétique et/ou des facteurs environnementaux mais pas seulement. Au cours des 30 dernières années, un certain nombres d'études ont cherché à démontrer le danger que pourraient représenter les dérèglements chimiques, et depuis peu isotopiques, pour l'organisme au cours du temps, mais ses études sont bien souvent restées focalisé sur un nombre limités d'éléments chimiques au sein de réservoirs restreints (e.g. sang, cerveau). Dans cette étude, nous avons analysé les concentrations de plus de 15 éléments chimiques ainsi que les compositions isotopiques en cuivre et en zinc de plusieurs organes de souris (foie, muscle, cœur, cerveau et rein) au cours du temps ce qui nous a tout d'abord permis de confirmer l'importance des dérèglements chimiques et isotopiques dans le vieillissement. Ainsi, en démontrant que ces variations chimiques pouvaient se généraliser à l'ensemble de l'organisme et non pas seulement à des réservoirs spécifiques, nous avons soulevé un point de complexité montrant que, certes les dérèglements chimiques et isotopiques font bel et bien parti du vieillissement mais que le lien existant entre ces deux processus s'avère probablement bien plus complexe qu'il n'en a l'air. Cette vision plus globale à l'échelle de l'organisme, nous permet in fine d'approfondir notre compréhension du vieillissement. En comparant les variations inter- et intra-organe, nos résultats indiquent que les variations temporelles observées, bien que spécifiques d'un organe donné, sont interconnectées les unes aux autres et qu'elles témoignent d'importants dysfonctionnements physiologiques et métaboliques au sein de l'organisme avec l'âge. A l'échelle de l'organisme, l'analyse des compositions isotopiques en Cu nous ont par exemple permis de mettre en évidence des dysfonctionnements physiologiques majeurs qui pourrait inclure une défaillance de la barrière hémato-encéphalique (BBB), une détérioration progressive des voies d'excrétion biliaire ou encore, des troubles reliés à l'absorption intestinale avec le temps. A l'échelle interne de l'organe, les variations isotopiques corrèlent également avec plusieurs dérèglements biologiques liés notamment à des paramètres métaboliques comme par exemple un dysfonctionnement du métabolisme du glucose et des lipides ou de l'homéostasie des voies de détoxification. Ces premiers résultats démontrent ainsi que les paramètres chimiques et isotopiques sont potentiellement d'excellents marqueurs de l'âge physiologique et métabolique et laissent suggérer que leurs fluctuations pourraient être utilisées pour dépister un vieillissement prématuré.

Pour tester cette hypothèse et aller plus loin dans l'interprétation, nous avons quantifier

l'amplitude de tels dérèglements chez un autre organisme : le vers (*C.elegans*) et ce, dans différentes souches génétiquement modifiées. Nous avons dans un premier temps montré qu'ils existaient deux types de variations, la première, reliée principalement aux mutations et relativement indépendante de l'âge et la seconde, liée au vieillissement. Cela nous a permis de montrer que l'utilisation d'organismes génétiquement modifiés, visant à mieux comprendre le lien de cause à effet reliant variations chimiques et vieillissement doit se faire avec précaution.

En comparant uniquement les variations reliées à l'âge au sein des différentes souches, nous avons démontré qu'un animal vivant plus longtemps en bonne santé (daf-2, e1370) avait une signature chimique et isotopique distincte d'un animal à plus courte durée de vie, à savoir une diminution de sa composition isotopique et de sa concentration en cuivre entre 2 et 10 jours. Ces variations sont visibles relativement tôt sur l'échelle de vie (~1/10 de temps de vie du vers). Un suivi constant et temporel dès le plus jeune âge laisse alors entrevoir la possibilité d'anticiper un vieillissement précoce et ainsi d'optimiser les conditions de vies des organismes vieillissants.

Au delà du processus de vieillissement généralisé chez tous les êtres vivants, ce travail s'est également intéressé à l'étude d'une maladie neurodégénérative rare, la sclérose latérale amyotrophique (SLA) ou maladie de Charcot. Cette pathologie qui touche à l'heure actuelle plus de 220 000 personnes dans le monde et qui devrait en toucher plus de 376 000 en 2040, soit une hausse d'environ 70% en 25 ans, représente un enjeu médical important. De cause inconnue, sans outil de diagnostique fiable et en l'absence de traitements, cette maladie aujourd'hui incurable entraîne la mort rapide des personnes qui en sont atteintes ; un sujet porteur de SLA a généralement une durée de vie maximale de 5 ans.

A travers cette étude nous avons donc tenté d'apporter des informations novatrices et complémentaires susceptibles de nous aider à mieux comprendre et diagnostiquer cette pathologie. Grâce à l'analyse élémentaire et isotopique de liquides céphalo-rachidiens (LCRs) de personnes humaines, nous avons démontré que les patients touchés par la SLA se distinguaient des patients sains (*i.e.* sans pathologie neurodégénérative) et/ou atteints d'autres pathologies présentant également une dégénérescence neuronale comme la maladie d'Alzheimer. Les patients atteints de SLA ont notamment des rapports isotopiques en cuivre ($\delta^{65}Cu$) plus élevés que les personnes saines et atteintes de la maladie d'Alzheimer et ce, de façon significative. Ces résultats montrent donc que les rapports isotopiques en Cu apparaissent être de nouveaux outils de diagnostic spécifique de la SLA et offrent de nouveaux espoirs à la médecine actuelle en laissant entrevoir de nouvelles pistes d'étude pour déceler d'autres maladies rares comme la maladie de Creutzfeldt Jacob ou la maladie du Prion. Un fait d'autant plus important qu'il est possible que ces

dérèglements isotopiques en cuivre interviennent relativement tôt chez l'Homme. Si tel est le cas, cela augmenterait de façon considérable la possibilité d'une prise en charge précoce du patient, ce qui permettrait in fine de casser l'évolution naturelle de la maladie et la stabiliser. Notons qu'à ce jour les seuls outils de diagnostique existant ne permettent pas de détecter la maladie avant qu'elle ne se soit réellement développée.

Concernant la cause de ces dérèglements isotopiques, ils pourraient être directement reliés à la formation et à l'accumulation progressive d'agrégats protéiques mal-conformés dans le cerveau dont la proportion varieraient entre 0.0004% et 0.1%. Les premiers tests réalisés sur des modèles cellulaires démontrent par ailleurs que ce phénomène semblerait spécifique d'une protéine autre que la TDP-43, une protéine communément suggérée comme étant impliquée dans le développement pathologique de la SLA. En effet, nos résultats démontrent que des cellules portant un gène muté codant pour la protéine TDP-43 mal-conformée induisant des agrégats cytoplasmiques ne présentent pas de différences isotopiques significatives par rapport à des cellules contrôles (*i.e.* sans agrégats cytoplasmique).

En perspective de ces travaux, il conviendrait tout d'abord d'approfondir nos résultats concernant le vieillissement au sens large. Nous avons démontré le potentiel prometteur des paramètres chimiques et isotopiques en tant que marqueur de l'âge métabolique et physiologique pour prédire l'évolution du vieillissement. L'un des points clés qui reste à élucider est de comprendre si les dysfonctionnements chimiques sont la cause ou la conséquence des dysfonctionnements biologiques, autrement dit lequel des deux entraine l'autre. Est-il possible d'envisager que les dérèglements chimiques observés soient la cause primaire du vieillissement ? Les résultats obtenus sur les vers ont montré qu'un organisme avec une espérance de vie en bonne santé élevée se distinguait part une diminution de sa concentration et de sa composition isotopique en cuivre dès son plus jeune âge. Reproduire ces fluctuations sur un organisme 'contrôle' en utilisant par exemple des chélateurs spécifiques du cuivre et/ou l'ajout de cuivre léger dans le milieu bactérien faisant office de nourriture permettrait de clarifier et de quantifier le rôle qu'occupent les dysfonctionnements métallomiques dans le vieillissement. Il adviendrait également de tester d'autres systématiques isotopiques comme par exemple celle du sélénium (Se). Impliqué dans la production de sélénoprotéines telle que la glutathione peroxidase (Gpx) qui catalyse la glutathione (protéine antioxydante), le sélénium intervient dans la détoxification des radicaux libres (Prabhakar et al., 2005) et pourrait ainsi favoriser le ralentissement du vieillissement et l'apparition de maladies. Le sélénium semble également optimiser les capacités physiques (motricité) et neuronales des vers (Heath et al., 2010). Evaluer le fractionnement isotopique en Se, en plus de celui du Cu, pourrait donc apporter des informations supplémentaires

concernant le dérèglement d'autres voies biochimiques potentiellement impliquées dans le vieillissement.

En ce qui concerne la SLA, il adviendrait dans un premier temps de confirmer la divergence isotopique observée sur un plus grand nombre de sujets. Cela permettrait d'avoir une meilleur idée de l'amplitude des variations et ainsi d'optimiser la fiabilité du diagnostic reposant sur les isotopes du cuivre.

Par la suite, il serait également intéressant de préciser la cause des dérèglements chimiques et isotopiques observés chez les patients atteints de SLA afin de vérifier les différentes hypothèses avancées dans cette étude. Nous avons suggéré que l'enrichissement en isotope lourd du cuivre (^{65}Cu) dans les liquides céphalo-rachidiens (LCRs) des malades pouvait résulter de l'accumulation progressive de protéines mal conformées dans le cerveau. Les résultats des tests que nous avons réalisé sur des modèles cellulaires impliquant la TDP-43 ne montrent cependant aucune variation isotopique significative laissant suggérer que les variations isotopiques en Cu dans les LCRs de patients atteints de SLA seraient préférentiellement reliées à l'agrégation d'une autre protéine. Pour vérifier cette hypothèse, il serait intéressant de reproduire le test avec d'autres protéines plus spécifique du cuivre comme par exemple la Cu-Zn SOD1, une protéine également présente dans le cerveau des personnes atteintes de SLA. Outre l'accumulation de protéines, d'autres paramètres comme le changement d'état redox, des modifications dans le transport et l'absorption transmembranaire du cuivre favorisant son incorporation dans le cerveau ainsi que la façon dont il se fixe (*i.e.* ligand) et s'intègre dans les organelles intracellulaires pourraient également affecter les rapports isotopiques et reste aussi d'autres hypothèses à tester.

Par ailleurs, la connaissance de l'échelle de temps à laquelle débutent et se développent ces dérèglements isotopiques pourrait améliorer le diagnostique de la maladie. Des tests sur des organismes modèles tels que des souris porteuses de SLA (e.g. G93A SOD1) sur lesquelles un suivi isotopique temporel serait réalisé permettrait d'optimiser nos capacités à déceler l'âge des premiers dérèglements isotopiques. Par la suite, nous pourrions également envisager de renverser les variations observées dans les LCRs en administrant une dose de cuivre léger (*i.e.* spike de ^{63}Cu) à des souris dans le but de voir si la maladie se stabilise ou régresse. Un résultat positif laisserait entrevoir des perspectives en terme de traitements thérapeutiques. Outre la SLA, d'autres pathologies neurodégénératives comme la maladie du Prion ou celle de Creutzfeldt Jacob restent à ce jour mal comprises et, au vu de nos résultats, l'analyse chimique et isotopique de LCRs permettrait peut-être d'apporter de nouveaux outils de diagnostique ainsi que des informations complémentaires sur la cause et l'évolution de ces maladies.

BIBLIOGRAPHIE

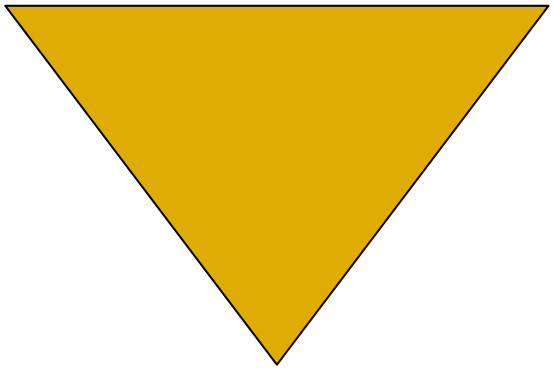

Ahuja, A., Dev, K., Tanwar, R.S., Selwal, K.K., Tyagi, P.K., 2015. Copper mediated neurological disorder: Visions into amyotrophic lateral sclerosis, Alzheimer and Menkes disease. Journal of Trace Elements in Medicine and Biology 29, 11–23. doi:10.1016/j.jtemb.2014.05.003

Albarède, F., Philippe, T., Balter, V., Bondanese, V.P., Albalat, E., Oger, P., Bonaventura, P., Miossec, P., Fujii, T., 2016. Medical applications of Cu, Zn, and S isotope effects. Metallomics 8, 1056–1070. doi:10.1039/c5mt00316d

Anderson, C.P., Leibold, E.A., 2014. Mechanisms of iron metabolism in Caenorhabditis elegans. Frontiers in Pharmacology/Drug Metabolism and Transport 5, 1–8. doi:10.3389/fphar.2014.00113/abstract

Andreux, P.A., Williams, E.G., Koutnikova, H., Houtkooper, R.H., Champy, M.-F., Henry, H., Schoonjans, K., Williams, R.W., Auwerx, J., 2012. Systems Genetics of Metabolism: The Use of the BXD Murine Reference Panel for Multiscalar Integration of Traits. Cell 150, 1287–1299. doi:10.1016/j.cell.2012.08.012

Andreyev, A.Y., Tsui, H.S., Milne, G.L., Shmanai, V.V., Bekish, A.V., Fomich, M.A., Pham, M.N., Nong, Y., Murphy, A.N., Clarke, C.F., Shchepinov, M.S., 2015. Isotope-reinforced polyunsaturated fatty acids protect mitochondria from oxidative stress. Free Radical Biology and Medicine 82, 63–72. doi:10.1016/j.freeradbiomed.2014.12.023

Angelova, M., Asenova, S., Koleva-Kolarova, R., 2011. Copper in the Human Organism. Trakia Journal of Sciences 9, 88–98.

Anoshkina, Y., guez, M.C.-R.X., Speeckaert, M., Van Biesen, W., Delanghe, J., Vanhaecke, F., 2017. Iron isotopic composition of blood serum in anemia of chronic kidney disease†. Metallomics 9, 517–524. doi:10.1039/C7MT00021A

Aramendía, M., Rello, L., Council, R., Vanhaecke, F., 2013. Isotopic analysis of Cu in serum samples for diagnosis of Wilson's disease: a pilot study. J. Anal. At. Spectrom. 28, 675. doi:10.1042/cs0410189

Arantes-Oliveira, N., Berman, J.R., Kenyon, C., 2003. Healthy Animals with Extreme Longevity. Science 302, 1–2.

Aschner, M., Palinski, C., Sperling, M., Karst, U., Schwerdtle, T., Bornhorst, J., 2017. Imaging metals in Caenorhabditis elegans. Metallomics 9, 357–364. doi:10.1039/C6MT00265J

Au, C., Benedetto, A., Anderson, J., Labrousse, A., Erikson, K., Ewbank, J.J., Aschner, M., 2009. SMF-1, SMF-2 and SMF-3 DMT1 Orthologues Regulate and Are Regulated Differentially by Manganese Levels in C. elegans. PLoS ONE 4, e7792. doi:10.1371/journal.pone.0007792.g010

Auld, D.S., 2001. Zinc coordination sphere in biochemical zinc sites. BioMetals 14, 271–313.

Azhdarzadeh, M., Noroozian, M., Aghaverdi, H., Akbari, S.M., Baum, L., Mahmoudi, M., 2013. Serum Multivalent Cationic Pattern: Speculation on the Efficient Approach for Detection of Alzheimer's Disease. Sci Rep 3, 61. doi:10.1192/bjp.123.4.467

Bakan, R., 1979. The role of zinc in anorexia nervosa: etiology and treatment. Medical Hypotheses 5, 731–736.

Balter, V., Lamboux, A., Zazzo, A., Telouk, P., Leverrier, Y., Marvel, J., Moloney, A.P., Monahan, F.J., Schmidt, O., Albarède, F., 2013. Contrasting Cu, Fe, and Zn isotopic patterns in organs and body fluids of mice and sheep, with emphasis on cellular fractionation. Metallomics 5, 1470. doi:10.1007/s00018-002-8454-2

Balter, V., Nogueira da Costa, A., Bondanese, V.P., Jaouen, K., Lamboux, A., Sangrajrang, S., Vincent, N., Fourel, F., Telouk, P., Gigou, M., Lécuyer, C., Srivatanakul, P., Bréchot, C., Albarède, F., Hainaut, P., 2015. Natural variations of copper and sulfur stable

isotopes in blood of hepatocellular carcinoma patients. Proceedings of the National Academy of Sciences 112, 982–985. doi:10.1016/S0009-2541(98)00191-0

Banci, L., Bertini, I., Cantini, F., Ciofi-Baffoni, S., 2010. Cellular copper distribution: a mechanistic systems biology approach. Cell. Mol. Life Sci. 67, 2563–2589. doi:10.1016/0304-4157(95)00017-8

Bandmann, O., Weiss, K.H., Kaler, S.G., 2015. Wilson's disease and other neurological copper disorders. The Lancet Neurology 14, 103–113. doi:10.1016/S1474-4422(14)70190-5

Barnham, K.J., Bush, A.I., 2008. Metals in Alzheimer"s and Parkinson"s Diseases. Current Opinion in Chemical Biology 12, 222–228. doi:10.1016/j.cbpa.2008.02.019

Barnham, K.J., Masters, C.L., Bush, A.I., 2004. Neurodegenerative diseases and oxidative stress. Nat Rev Drug Discov 3, 205–214. doi:10.1038/nrd1330

Beach, S.R.H., Dogan, M.V., Lei, M.-K., Cutrona, C.E., Gerrard, M., Gibbons, F.X., Simons, R.L., Brody, G.H., Philibert, R.A., 2015. Methylomic Aging as a Window onto the Influence of Lifestyle: Tobacco and Alcohol Use Alter the Rate of Biological Aging. J Am Geriatr Soc 63, 2519–2525. doi:10.1186/gb-2014-15-2-r24

Bede, P., Iyer, P.M., Finegan, E., Omer, T., Hardiman, O., 2017. Virtual brain biopsies in amyotrophic lateral sclerosis: Diagnostic classification based on in vivo pathological patterns 1–6. doi:10.1016/j.nicl.2017.06.010

Bedlack, R., 2017. Untangling the ALS X-Files. Nature 550, S122.

Bellot, G.L., Wang, X., 2013. Extra-Telomeric Effects of Telomerase (hTERT) in Cell Death. Intech Open science 1–18. doi:10.5772/48583

Beto, J.A., 2015. The Role of Calcium in Human Aging. Clin Nutr Res 4, 1. doi:10.7762/cnr.2015.4.1.1

Betteridge, D.J., 2000. What is oxidative stress? Metabolism 49, 3–8.

Bharathi, Indi, S.S., Rao, K.S.J., 2007. Copper- and iron-induced differential fibril formation in α-synuclein: TEM study. Neuroscience Letters 424, 78–82. doi:10.1016/j.neulet.2007.06.052

Birmingham, C.L., Gritzner, S., 2006. How does zinc supplementation benefit anorexia nervosa? Eating Weight Disorder 11, 109–111.

Bonaventura, P., Benedetti, G., Albarède, F., Miossec, P., 2014. Zinc and its role in immunity and inflammation. Autoimmunity Reviews 1–9. doi:10.1016/j.autrev.2014.11.008

Bondanese, V.P., Lamboux, A., Simon, M., Lafont, J., Albalat, E., Pichat, S., Vanacker, J.-M., Telouk, P., Balter, V., Oger, P., Albarède, F., 2016. Hypoxia induces copper stable isotope fractionation in hepatocellular carcinoma, in a HIF-independent manner†. Metallomics 1–8. doi:10.1039/C6MT00102E

Bourassa, M.W., Brown, H.H., Borchelt, D.R., Vogt, S., Miller, L.M., 2014. Metal-deficient aggregates and diminished copper found in cells expressing SOD1 mutations that cause ALS. Frontiers in Aging Neuroscience 6, 1–6. doi:10.3389/fnagi.2014.00110/abstract

Brady, D.C., Crowe, M.S., Turski, M.L., Hobbs, G.A., Yao, X., Chaikuad, A., Knapp, S., Xiao, K., Campbell, S.L., Thiele, D.J., Counter, C.M., 2014. Copper is required for oncogenic BRAF signalling and tumorigenesis. Nature 509, 492–496. doi:10.1038/nature13180

Brown, C., 2017. A tangled web. Nature 550, S109.

Bucossi, S., Ventriglia, M., Panetta, V., Salustri, C., Pasqualetti, P., Mariani, S., Siotto, M., Rossini, P.M., Squitti, R., 2011. Copper in Alzheimer's Disease:A Meta-Analysis of Serum, Plasma, and Cerebrospinal Fluid Studies. Journal of Alzheimer's Disease 24, 175–185. doi:10.3233/JAD-2010-101473

Bush, A.I., 2000. Metals and neuroscience. Current Opinion in Chemical Biology 4, 184–191.

Bush, A.I., Tanzi, R.E., 2008. Therapeutics for Alzheimer's Disease Based on the Metal Hypothesis. Neurotherapeutics 5, 421–432.

Büchl, A., Hawkesworth, C.J., Ragnarsdottir, K.V., Brown, D.R., 2008. Re-partitioning of Cu and Zn isotopes by modified protein expression. Geochem Trans 9, 11. doi:10.1186/1467-4866-9-11

Cabrera, Á.J.R., 2015. Zinc, aging, and immunosenescence: an overview. Pathobiology of Aging & Age-related Diseases 5, 25592. doi:10.1007/s10522-010-9276-5

Cai, C., Lin, P., Zhu, H., Ko, J.-K., Hwang, M., Tan, T., Pan, Z., Korichneva, I., Ma, J., 2015. Zinc Binding to MG53 Protein Facilitates Repair of Injury to Cell Membranes. J. Biol. Chem. 290, 13830–13839. doi:10.1038/nature11834

Calafato, S., Swain, S., Hughes, S., Kille, P., Stürzenbaum, S.R., 2008. Knock down of Caenorhabditis elegans cutc-1 Exacerbates the Sensitivity Toward High Levels of Copper. Toxicology 106, 384–391. doi:10.1093/toxsci/kfn180

Cawthon, R.M., Smith, K.R., O'Brien, E., Sivatchenko, A., Kerber, R.A., 2003. Association between telomere length in blood and mortality in people aged 60 years or older. The Lancet 361, 393–395.

Cedarbaum, J.M., Stambler, N., Malta, E., Fuller, C., Hilt, D., Thurmond, B., Nakanishi, A., 1999. The ALSFRS-R: a revised ALS functional rating scale that incorporates assessments of respiratory function. Journal of the Neurological Sciences 169, 13–21.

Chakraborty, S., Chen, P., Bornhorst, J., Schwerdtle, T., Schumacher, F., Kleuser, B., Bowman, A.B., Aschner, M., 2015. Loss of pdr-1/parkin influences Mn homeostasis through altered ferroportin expression in C. elegans. Metallomics 7, 847–856. doi:10.1039/C5MT00052A

Chamel, G., Gourlan, A.T., Telouk, P., Sayag, D., Milliard, V., Loiseau, C., Simon, M., Buff, S., Ponce, F., 2016. Retrospective evaluation of blood copper stable isotopes ratio 65Cu/ 63Cu as a biomarker of cancer in dogs. Vet Comp Oncol 21, 274. doi:10.1002/jtra.10033

Chasapis, C.T., Loutsidou, A.C., Spiliopoulou, C.A., Stefanidou, M.E., 2012. Zinc and human health: an update. Arch Toxicol 86, 521–534. doi:10.3233/JAD-2010-1363

Chen, P., Martinez-Finley, E.J., Bornhorst, J., Chakraborty, S., Aschner, M., 2013. Metal-induced neurodegeneration in C. elegans. Frontiers in Aging Neuroscience 5. doi:10.3389/fnagi.2013.00018

Chen, S., Liu, Y., Hu, J., Zhang, Z., Hou, Z., Huang, F., Yu, H., 2016. Zinc Isotopic Compositions of NIST SRM 683 and Whole-Rock Reference Materials. Geostandards and Geoanalytical Research 40, 417–432. doi:10.1111/j.1751-908X.2015.00377.x

Chen, X., Shang, H.-F., 2015. New developments and future opportunities in biomarkers for amyotrophic lateral sclerosis 1–8. doi:10.1186/s40035-015-0040-2

Chen-Plotkin, A.S., Lee, V.M.Y., Trojanowski, J.Q., 2010. TAR DNA-binding protein 43 in neurodegenerative disease. Nat Rev Neurol 6, 211–220. doi:10.1212/WNL.45.4.788

Chun, H., Sharma, A.K., Lee, J., Chan, J., Jia, S., Kim, B.-E., 2017. The Intestinal Copper Exporter CUA-1 Is Required for Systemic Copper Homeostasis in Caenorhabditis elegans. J. Biol. Chem. 292, 1–14. doi:10.1093/nar/gkt376

Cirulli, E.T., Lasseigne, B.N., Petrovski, S., Peter C Sapp, P.A.D., Leblond, C.S., Couthouis, J., Lu, Y.-F., Wang, Q., Krueger, B.J., Ren, Z., Keebler, J., Han, Y., Levy, S.E., Boone, B.E., Wimbish, J.R., Waite, L.L., Angela L Jones, J.P.C., Day-Williams, A.G., Staropoli, J.F., Xin, W.W., Chesi, A., Raphael, A.R., McKenna-Yasek, D., Janet Cady, J.M.B.V. de J., Kenna,

K.P., Smith, B.N., Simon Topp, J.M., Gkazi, A., Consortium, F.S., Al-Chalabi, A., van den Berg, L.H., Veldink, J., Silani, V., Ticozzi, N., Shaw, C.E., Baloh, R.H., Appel, S., Ericka Simpson, C.L.-T., Pulst, S.M., Gibson, S., Trojanowski, J.Q., Elman, L., McCluskey, L., Grossman, M., Neil A Shneider, W.K.C., Ravits, J.M., Glass, J.D., Sims, K.B., Van Deerlin, V.M., Maniatis, T., Sebastian D Hayes, Ordureau, A., Swarup, S., Landers, J., Baas, F., Allen, A.S., Bedlack, R.S., Harper, J.W., Gitler, A.D., Rouleau, G.A., Brown, R., Harms, M.B., Cooper, G.M., Harris, T., Myers, R.M., Goldstein, D.B., 2015. Exome sequencing in amyotrophic lateral sclerosis identifies risk genes and pathways. Science 347, 1–7.

Collins, J.F., Prohaska, J.R., Knutson, M.D., 2010. Metabolic crossroads of iron and copper. Nutrition Reviews 68, 133–147. doi:10.1111/j.1753-4887.2010.00271.x

Conradi, S., Ronnevi, L.-O., Vesterberg, O., 1976. Abnormal Tissue Distribution of Lead in Amyotrophic Lateral Sclerosis. Journal of the Neurological Sciences 29, 259–265.

Costas-Rodríguez, M., Anoshkina, Y., Lauwens, S., Van Vlierberghe, H., Delanghe, J., Vanhaecke, F., 2015. Isotopic analysis of Cu in blood serum by multi- collector ICP-mass spectrometry: a new approach for the diagnosis and prognosis of liver cirrhosis?†. Metallomics 7, 491–498. doi:10.1039/C4MT00319E

Costas-Rodríguez, M., Delanghe, J., Vanhaecke, F., 2016. Trends in Analytical Chemistry 1–12. doi:10.1016/j.trac.2015.10.008

Costas-Rodríguez, M., Van Heghe, L., Vanhaecke, F., 2014. Evidence for a possible dietary effect on the isotopic composition of Zn in blood via isotopic analysis of food products by multi-collector ICP-mass spectrometry. Metallomics 6, 139–146. doi:10.1039/C3MT00244F

Coudray, C., Feillet-Coudray, C., Rambeau, M., Tressol, J.C., Gueux, E., Mazur, A., Rayssiguier, Y., 2006. The effect of aging on intestinal absorption and status of calcium, magnesium, zinc, and copper in rats: A stable isotope study. Journal of Trace Elements in Medicine and Biology 20, 73–81. doi:10.1016/j.jtemb.2005.10.007

Damkier, H.H., Brown, P.D., Praetorius, J., 2013. Cerebrospinal Fluid Secretion by the Choroid Plexus. Physiological Reviews 93, 1847–1892. doi:10.1152/physrev.00004.2013

Dang, T., Lim, N., Grubman, A., Li, Q.-X., Volitakis, I., White, A.R., Crouch, P., 2014. Increased metal content in the TDP-43A315T transgenic mouse model of frontotemporal lobar degeneration and amyotrophic lateral sclerosis. Frontiers in Aging Neuroscience 6, 1–8. doi:10.3389/fnagi.2014.00015

Day, J.G.A.S.G., 2007. Cryopreservation and Freeze-Drying Protocols, Humana Press. ed. Methods in Molecular Biology™.

Demidov, V.V., 2007. Heavy isotopes to avert ageing? Trends in Biotechnology 25, 371–375. doi:10.1016/j.tibtech.2007.07.007

Dolgin, E., 2017. The hexanucleotide hex. Nature 550, S108.

Duport, P., 2003. A database of cancer induction by low-dose radiationin mammals: overview and initial observations. Int. J. of Low Radiation 1, 120–131.

Eide, D.J., 2006. Zinc transporters and the cellular trafficking of zinc. Biochimica et Biophysica Acta (BBA) - Molecular Cell Research 1763, 711–722. doi:10.1016/j.bbamcr.2006.03.005

Faris, J.P., Buchanan, R.F., Commission, U.S.A.E., Laboratory, A.N., 1964. Anion exchange characteristics of the elements in nitric acid and nitrate solutions and application in trace element analysis. UNT Digital Library.

Finkel, T., Holbrook, N.J., 2000. Oxidants, oxidative stress and the biology of ageing. Nature 408, 1–9.

Fong, L., Tan, K., Tran, C., Cool, J., Scherer, M.A., Elovaris, R., Coyle, P., Foster, B.K., Rofe, A.M., Xian, C.J., 2009. Interaction of dietary zinc and intracellular binding protein metallothionein in postnatal bone growth. Bone 44, 1151–1162. doi:10.1016/j.bone.2009.02.011

Foster, D., Wastney, M., Henkin, R., 1984. Zinc metabolism in Humans: A kinetic Model. Mathematical Biosciences 72, 359–372.

Friel, J.K., Mercer, C., Andrews, W.L., Simmons, B.R., 1996. Laboratory gloves as a source of trace element contamination. Biological Trace Element Research 54, 135–142. doi:10.1007/BF02786260

Fu, S., Jiang, W., Zheng, W., 2015. Age-dependent increase of brain copper levels and expressions of copper regulatory proteins in the subventricular zone and choroid plexus. Front. Mol. Neurosci. 8, 966. doi:10.1016/s0006-8993(99)01558-9

Fukai, T., Ushio-Fukai, M., 2011. Superoxide Dismutases: Role in Redox Signaling, Vascular Function, and Diseases. Antioxidants & Redox Signaling 15, 1583–1606. doi:10.1089/ars.2011.3999

Fulop, T., Larbi, A., Witkowski, J.M., McElhaney, J., Loeb, M., Mitnitski, A., Pawelec, G., 2010. Aging, frailty and age-related diseases. Biogerontology 11, 547–563. doi:10.1093/geronb/gbp102

Gabriel Nowak, Siwek, M., Dudek, D., Zieba, A., Pilc, A., 2003. Effect of zinc supplementation on antidepressant therapy in umipolar depression: A preliminary placebo-controlled study. Polish Journal of Pharmacology 55, 1143–1147.

Gaetke, L.M., Chow, C.K., 2003. Copper toxicity, oxidative stress, and antioxidant nutrients. Toxicology 189, 147–163. doi:10.1016/S0300-483X(03)00159-8

Garçon, M., Sauzéat, L., Carlson, R.W., Shirey, S.B., Simon, M., Balter, V., Boyet, M., 2017. Nitrile, Latex, Neoprene and Vinyl Gloves: A Primary Source of Contamination for Trace Element and Zn Isotopic Analyses in Geological and Biological Samples. Geostandards and Geoanalytical Research 41, 367–380. doi:10.1039/c2ja30070b

Giacconi, R., Costarelli, L., Piacenza, F., Basso, A., Rink, L., Mariani, E., Fulop, T., Dedoussis, G., Herbein, G., Provinciali, M., Jajte, J., Lengyel, I., Mocchegiani, E., Malavolta, M., 2016. Main biomarkers associated with age-related plasma zinc decrease and copper/zinc ratio in healthy elderly from ZincAge study. European Journal of Nutrition 1–10. doi:10.1007/s00394-016-1281-2

Gil-Bea, F., Aldanondo, G., Lasa-Fernandez, H., Lopez de Munain, A., Vallejo-Illarramendi, A., 2017. Insights into mechanisms of copper dyshomeostasis in amyotrophic lateral sclerosis. Expert Reviews in Molecular Medicine 19, 1–14. doi:10.1017/erm.2017.9

Gkogkolou, P., Böhm, M., 2012. Advanced glycation end products. Dermato-Endocrinology 4, 259–270. doi:10.3109/09546634.2010.521812

Gower-Winter, S.D., Levenson, C.W., 2012. Zinc in the central nervous system: From molecules to behavior. BioFactors 38, 186–193. doi:10.1016/j.ejpn.2008.08.007

Gropper, S.S., Smith, J.L., 2012. Advanced Nutrition and Human Metabolism 6th Edition. Wadsworth Publishing; 6 edition.

Guarente, L., 2005. Calorie restriction and SIR2 genes—Towards a mechanism. Mechanisms of Ageing and Development 126, 923–928. doi:10.1016/j.mad.2005.03.013

Gupte, A., Mumper, R.J., 2009. Elevated copper and oxidative stress in cancer cells as a target for cancer treatment. Cancer Treatment Reviews 35, 32–46. doi:10.1016/j.ctrv.2008.07.004

Gusarov, I., Pani, B., Gautier, L., Smolentseva, O., Eremina, S., Shamovsky, I., Katkova-Zhukotskaya, O., Mironov, A., Nudler, E., 2017. Glycogen controls Caenorhabditis

elegans lifespan and resistance to oxidative stress. Nature Communications 8, 1–12. doi:10.1038/ncomms15868

Haase, H., Rink, L., 2009. The immune system and the impact of zinc during aging. Immun Ageing 6, 9. doi:10.1186/1742-4933-6-9

Hainaut, P., Rolley, N., Davies, M., Milner, J., 1995. Modulation by copper of p53 conformation and sequance-specific DNA binding: role for Cu(II)/Cu(I) redox mechanism. Oncogene 10, 27–32.

Hammel, S.C., East, K., Shaka, A.J., Rose, M.R., Shahrestani, P., 2013. Brief Early-Life Non-Specific Incorporation of Deuterium Extends Mean Life Span in Drosophila melanogasterWithout Affecting Fecundity. Rejuvenation Research 16, 98–104. doi:10.1089/rej.2012.1368

Heath, J.C., Banna, K.M., Reed, M.N., Pesek, E.F., Cole, N., Li, J., Newland, M.C., 2010. NeuroToxicologyDietary selenium protects against selected signs of aging and methylmercury exposure. Neurotoxicology 31, 169–179. doi:10.1016/j.neuro.2010.01.003

Hedera, P., 2017. Update on the clinical management of Wilson's disease. TACG Volume 10, 9–19. doi:10.2147/TACG.S79121

Heilbronn, L.K., de Jonge, L., Frisard, M.I., DeLany, J.P., Larson-Meyer, D.E., Rood, J., Nguyen, T., Martin, C.K., Volaufova, J., Most, M.M., Greenway, F.L., Smith, S.R., Deutsch, W.A., Williamson, D.A., Ravussin, E., Pennington CALERIE Team, F.T., 2006. Effect of 6-Month Calorie Restriction on Biomarkers of Longevity, Metabolic Adaptation, and Oxidative Stress in Overweight Individuals. JAMA 295, 1539. doi:10.1001/jama.295.13.1539

Hellman, N.E., Gitlin, J.D., 2002. Ceruloplasmin metabolism and function. Annu. Rev. Nutr. 22, 439–458. doi:10.1146/annurev.nutr.22.012502.114457

Hoffmann, J., 1988. Experience with the sources of contamination when preparing samples for the analysis of trace elements. Fresenius' Zeitschrift für analytische Chemie 331, 220–222. doi:10.1007/BF01105172

Horvath, S., 2013. DNA methylation age of human tissues and cell types. Genome Biology 14. doi:10.1186/gb-2013-14-10-r115

Hotz, K., Krayenbuehl, P.-A., Walczyk, T., 2012. Mobilization of storage iron is reflected in the iron isotopic composition of blood in humans. J Biol Inorg Chem 17, 301–309. doi:10.1017/S0029665199000634

Houthoofd, K., Vanfleteren, J.R., 2006. The longevity effect of dietary restriction in Caenorhabditis elegans. Experimental Gerontology 41, 1026–1031. doi:10.1016/j.exger.2006.05.007

Houtkooper, R.H., Argmann, C., Houten, S.M., Cantó, C., Jeninga, E.H., Andreux, P.A., Thomas, C., Doenlen, R., Schoonjans, K., Auwerx, J., 2011. The metabolic footprint of aging in mice. Sci Rep 1, 1–10. doi:10.1038/srep00134

Hozumi, I., Hasegawa, T., Honda, A., Ozawa, K., Hayashi, Y., Hashimoto, K., Yamada, M., Koumura, A., Sakurai, T., Kimura, A., Tanaka, Y., Satoh, M., Inuzuka, T., 2011. Patterns of levels of biological metals in CSF differ among neurodegenerative diseases. Journal of the Neurological Sciences 303, 95–99. doi:10.1016/j.jns.2011.01.003

Huang, X., Cuajungco, M.P., Atwood, C.S., Moir, R.D., Tanzi, R.E., Bush, A.I., 2000. Alzheimer's Disease, β-Amyloid Protein and Zinc. Journal of Nutrition 130, 1488S–1492S.

Hulme, S.E., Whitesides, G.M., 2011. Chemistry and the Worm: Caenorhabditis elegans as a Platform for Integrating Chemical and Biological Research. Angew. Chem. Int. Ed. 50, 4774–4807. doi:10.1002/biot.201000183

Ibrahim, N.L., 2013. Study of Serum Copper and Iron in Children with Chronic Liver Diseases. Anat Physiol 04. doi:10.4172/2161-0940.1000130

Institute of Medicine, 2002. Dietary Reference Intakes for Vitamin A, Vitamin K, Arsenic, Boron, Chromium, Copper, Iodine, Iron, Manganese, Molybdenum, Nickel, Silicon, Vanadium, and Zinc. National Academies Press.

Ishida, S., Andreux, P., Poitry-Yamatec, C., Auwerx, J., Hanahan, D., 2013. Bioavailable copper modulates oxidative phosphorylation and growth of tumors. PNAS 110, 19507–19512. doi:10.1073/pnas.1318431110/-/DCSupplemental

Ishida, S., McCormick, F., Smith-McCune, K., Hanahan, D., 2010. Enhancing Tumor-Specific Uptake of the Anticancer Drug Cisplatin with a Copper Chelator. Cancer Cell 17, 574–583. doi:10.1016/j.ccr.2010.04.011

Iwata, S., Ostermeier, C., Ludwig, B., Michel, H., 1995. Structure at 2.8 A resolution of cytochrome c oxidase from Paracoccus denitrificans. Nature 376, 660–669.

Jaouen, K., Balter, V., 2014. Menopause effect on blood Fe and Cu isotope compositions. Am. J. Phys. Anthropol. 153, 280–285. doi:10.1002/ajpa.22430

Jaouen, K., Balter, V., Herrscher, E., Lamboux, A., Telouk, P., Albarède, F., 2012. Fe and Cu stable isotopes in archeological human bones and their relationship to sex. Am. J. Phys. Anthropol. 148, 334–340. doi:10.1002/ajpa.22053

Jaouen, K., Beasley, M., Schoeninger, M., Hublin, J.-J., Richards, M.P., 2016a. Zinc isotope ratios of bones and teeth as new dietary indicators: results from a modern food web (Koobi Fora, Kenya). Nature Publishing Group 1–8. doi:10.1038/srep26281

Jaouen, K., Gibert, M., Lamboux, A., Telouk, P., Fourel, F., Albarède, F., Alekseev, A.N., Crubézy, E., Balter, V., 2013a. Is aging recorded in blood Cu and Zn isotope compositions? Metallomics 5, 1016–1024. doi:10.2307/2844097

Jaouen, K., Gibert, M., Lamboux, A., Telouk, P., Fourel, F., Albarède, F., Alekseev, A.N., Crubézy, E., Balter, V., 2013b. Iron, copper and zinc isotopic fractionation up mammal trophic chains. Earth and Planetary Science Letters 374, 1016–1024. doi:10.1016/j.epsl.2013.05.037

Jaouen, K., Herrscher, E., Balter, V., 2016b. Copper and zinc isotope ratios in human bone and enamel. Am. J. Phys. Anthropol. 162, 491–500. doi:10.1016/j.gca.2005.02.031

Jaouen, K., Szpak, P., Richards, M.P., 2016c. Zinc Isotope Ratios as Indicators of Diet and Trophic Level in Arctic Marine Mammals 1–13. doi:10.1371/journal.pone.0152299

Jia, K., 2004. The TOR pathway interacts with the insulin signaling pathway to regulate C. elegans larval development, metabolism and life span. Development 131, 3897–3906. doi:10.1242/dev.01255

Jiang, H., Ju, Z., Rudolph, K.L., 2007. Telomere shortening and ageing. Zeitschrift für Gerontologie und Geriatrie 40, 314–324. doi:10.1128/MCB.10.2.518

Jones, C.E., Abdelraheim, S.R., Brown, D.R., Viles, J.H., 2004. Preferential Cu 2+ Coordination by His 96 and His 111 Induces β-Sheet Formation in the Unstructured Amyloidogenic Region of the Prion Protein. J. Biol. Chem. 279, 32018–32027. doi:10.1002/cbic.200300786

Kaler, S.G., 2011. ATP7A-related copper transport diseases—emerging concepts and future trends. Nat Rev Neurol 7, 15–29. doi:10.1016/j.mcn.2008.09.008

Kambe, T., Tsuji, T., Hashimoto, A., Itsumura, N., 2015. The Physiological, Biochemical, and Molecular Roles of Zinc Transporters in Zinc Homeostasis and Metabolism. Physiological Reviews 95, 749–784. doi:10.1152/physrev.00035.2014

Kasai, T., Tokuda, T., Ishigami, N., Sasayama, H., Foulds, P., Mitchell, D.J., Mann, D.M.A., Allsop, D., Nakagawa, M., 2009. Increased TDP-43 protein in cerebrospinal Xuid of patients with amyotrophic lateral sclerosis. Acta Neuropathol 117, 55–62.

doi:10.1007/s00401-008-0456-1
Kenyon, C., 2005. The Plasticity of Aging: Insights from Long-Lived Mutants. Cell 120, 449–460. doi:10.1016/j.cell.2005.02.002
Kenyon, C., Chang, J., Gensch, E., Rudner, A., Tabtiang, R., 1993. A C. elegans mutant that lives twice as long as wild type. Nature 4, 366–461. doi:10.1038/366461a0
Kepp, K.P., 2017. Alzheimer's disease: How metal ions define b-amyloid function. Coordination Chemistry Reviews 1–33. doi:10.1016/j.ccr.2017.05.007
Kim, B.-E., Nevitt, T., Thiele, D.J., 2008. Mechanisms for copper acquisition, distribution and regulation. Nat Chem Biol 4, 176–185. doi:10.1126/science.291.5505.881
Klang, I.M., Schilling, B., Sorensen, D.J., Sahu, A.K., Kapahi, P., Andersen, J.K., Swoboda, P., Killilea, D.W., Gibson, B.W., Lithgow, G.J., 2014. Iron promotes protein insolubility and aging in C. elegans. Aging-Us 6, 975–991.
Kowald, G., Stürzenbaum, S., Blindauer, C., 2016. Earthworm Lumbricus rubellus MT-2: Metal Binding and Protein Folding of a True Cadmium-MT. IJMS 17, 65. doi:10.1126/science.286.5446.1888
Kraus, K., Nelson, F., 1958. Metal separations by anion exchange. Symposium on Ion Exchange and Chromatography in Analytical Chemistry, American Society for Testing Materials.
Krayenbuehl, P.-A., Walczyk, T., Schoenberg, R., Blanckenburg, von, F., Schulthess, G., 2005. Hereditary hemochromatosis is reflected in the iron isotope composition of Blood. Blood 105, 3812–3816.
Kregel, K.C., Zhang, H.J., 2006. An integrated view of oxidative stress in aging: basic mechanisms, functional effects, and pathological considerations. AJP: Regulatory, Integrative and Comparative Physiology 292, R18–R36. doi:10.1152/ajpregu.00327.2006
Kroemer, G., 2015. Autophagy: a druggable process that is deregulated in aging and human disease. J. Clin. Invest. 125, 1–4. doi:10.1172/JCI78652
Kuhle, J., Lindberg, R.L.P., Regeniter, A., Mehling, M., Steck, A.J., Kappos, L., Czaplinski, A., 2009. Increased levels of inflammatory chemokines in amyotrophic lateral sclerosis. European Journal of Neurology 16, 771–774. doi:10.1212/WNL.62.10.1758
Kumar, J., Barhydt, T., Awasthi, A., Lithgow, G.J., Killilea, D.W., Kapahi, P., 2016. Zinc Levels Modulate Lifespan throughMultiple Longevity Pathways inCaenorhabditis elegans. PLoS ONE 11, 1–21. doi:10.1371/journal.pone.0153513
Kushner, D.J., Baker, A., Dunstall, T.G., 1999. Pharmacological uses and perspectives of heavy water and deuterated compounds. Can J Physiol Pharmacol. 77, 79–88.
Lai, C.-H., Chou, C.-Y., Chang, L.-Y., Liu, C.-S., Lin, W.-C., 2000. Identification of Novel Human Genes Evolutionarily Conserved in Caenorhabditis elegans by Comparative Proteomics. Genome Research 10, 703–713.
Lakowski, B., Hekimi, S., 1998. The genetics of caloric restriction in Caenorhabditis elegans. Genetics 95, 13091–13096.
Lang, P.O., Govind, S., Aspinall, R., 2012. L'immunosénescence. NPG Neurologie - Psychiatrie - Gériatrie 12, 171–181. doi:10.1016/j.npg.2012.04.005
Lansdown, A.B.G., Mirastschijski, U., Stubbs, N., Scanlon, E., Ågren, M.S., 2007. Zinc in wound healing: Theoretical, experimental, and clinical aspects. Wound Repair Regen 15, 2–16. doi:10.1016/S0140-6736(80)91722-5
Larner, F., 2015. Can we use high precision metal isotope analysis to improve our understanding of cancer? Anal Bioanal Chem 408, 345–349. doi:10.1039/C5JA00209E
Larner, F., Sampson, B., Rehkämper, M., Weiss, D.J., Dainty, J.R., O'Riordan, S., Panetta, T.,

Bain, P.G., 2013. High precision isotope measurements reveal poor control of copper metabolism in Parkinsonism. Metallomics 5, 125. doi:10.1007/BF00441163

Larner, F., Woodley, L.N., Shousha, S., Moyes, A., Humphreys-Williams, E., Strekopytov, S., Halliday, A.N., mper, M.R.X., Coombes, R.C., 2015. Zinc isotopic compositions of breast cancer tissue†. Metallomics 7, 112–117. doi:10.1039/C4MT00260A

Lauwens, S., Costas-Rodríguez, M., Van Vlierberghe, H., Vanhaecke, F., 2016. Cu isotopic signature in bloodserum of liver transplant patients:a follow-up study. Sci Rep 1–9. doi:10.1038/srep30683

Lee, S.S., Lee, R.Y.N., Fraser, A.G., Kamath, R.S., Ahringer, J., Ruvkun, G., 2003. A systematic RNAi screen identifies a critical role for mitochondria in C. elegans longevity. Nat Genet 33, 40–48. doi:10.1016/S0047-6374(01)00331-1

Leonov, A., Feldman, R., Piano, A., Arlia-Ciommo, A., Lutchman, V., Ahmadi, M., Elsaser, S., Fakim, H., HeshmatiMoghaddam, M., Hussain, A., Orfali, S., Rajen, H., Roofigari-Esfahani, N., Rosanelli, L., Titorenko, V.I., 2017. Caloric restriction extends yeast chronological lifespan via a mechanism linking cellular aging to cell cycle regulation, maintenance of a quiescent state, entry into a non-quiescent state and survival in the non-quiescent state. Oncotarget 8, 69328–69350.

Lewis, G.N., 1934. The Biology of Heavy Water. Science 79, 151–153.

Li, D.-W., Liu, M., Cui, B., Fang, J., Guan, Y.-Z., Ding, Q., Li, X., Cui, L., 2017. The Awaji criteria increases the diagnostic sensitivity of the revised El Escorial criteria for amyotrophic lateral sclerosis diagnosis in a Chinese population 1–8. doi:10.1371/journal.pone.0171522

Li, X., Snyder, M.P., 2016a. Can heavy isotopes increase lifespan? Studies of relative abundance in various organisms reveal chemical perspectives on aging. BioEssays 38, 1093–1101. doi:10.1093/nar/gkt1103

Li, X., Snyder, M.P., 2016b. Yeast longevity promoted by reversing aging-associateddecline in heavy isotope content. Npj Aging And Mechanisms Of Disease 2, 1–10. doi:10.1038/npjamd.2016.4

Lind, A.-L., Wu, D., Freyhult, E., Bodolea, C., Ekegren, T., Larssson, A., Gustafsson, M.G., Katilla, L., Bergquist, J., Gordh, T., Landegren, U., Kamali-Moghaddam, M., 2016. A Multiplex Protein Panel Applied to Cerebrospinal Fluid Reveals Three New Biomarker Candidates in ALS but None in Neuropathic Pain Patients. PLoS ONE 1–17. doi:10.1371/journal.pone.0149821

Lithgow, G.J., Driscoll, M., Phillips, P., 2017. A long journey toreproducible results. Nature 548, 387–388.

Lobo, L., Costas-Rodríguez, M., de Vicente, J.C., Pereiro, R., Vanhaecke, F., Sanz-Medel, A., 2017. Elemental and isotopic analysis of oral squamous cell carcinoma tissues using sector-field and multi-collector ICP-mass spectrometry 1–6. doi:10.1016/j.talanta.2016.12.007

Lu, C.H., Macdonald-Wallis, C., Gray, E., Pearce, N., Petzold, A., Norgren, N., Giovannoni, G., Fratta, P., Sidle, K., Fish, M., Orrell, R., Howard, R., Talbot, K., Greensmith, L., Kuhle, J., Turner, M.R., Malaspina, A., 2015. Neurofilament light chain: A prognostic biomarker in amyotrophic lateral sclerosis. Neurology 84, 2247–2257.

Luevano-Contreras, C., Chapman-Novakofski, K., 2010. Dietary Advanced Glycation End Products and Aging. Nutrients 2, 1247–1265. doi:10.1196/annals.1433.040

Madej, D., Borowska, K., Bylinowska, J., Szybalska, A., Pietruszka, B., 2013. Dietary intakes of iron and zinc assessed in a selected group of the elderly: Are they adequate? 1–8.

Maegawa, S., Lu, Y., Tahara, T., Lee, J.T., Madzo, J., Liang, S., Jelinek, J., Colman, R.J., Issa, J.-

P.J., 2017. Caloric restriction delays age-related methylation drift. Nature Communications 1–11. doi:10.1038/s41467-017-00607-3

Malavolta, M., Giacconi, R., Piacenza, F., Santarelli, L., Cipriano, C., Costarelli, L., Tesei, S., Pierpaoli, S., Basso, A., Galeazzi, R., Lattanzio, F., Mocchegiani, E., 2010. Plasma copper/zinc ratio: an inflammatory/nutritional biomarker as predictor of all-cause mortality in elderly population. Biogerontology 11, 309–319. doi:10.1093/gerona/61.10.1070

Malavolta, M., Piacenza, F., Basso, A., Giacconi, R., Costarelli, L., Mocchegiani, E., 2015. Serum copper to zinc ratio: Relationship with aging and health status. Mechanisms of Ageing and Development 1–8. doi:10.1016/j.mad.2015.01.004

Manzl, C., Enrich, J., Ebner, H., Dallinger, R., Krumschnabel, G., 2004. Copper-induced formation of reactive oxygen species causes cell death and disruption of calcium homeostasis in trout hepatocytes. Toxicology 196, 57–64. doi:10.1016/j.tox.2003.11.001

Maréchal, C., Albarede, F., 2002. Ion-exchange fractionation of copper and zinc isotopes. Geochimica et Cosmochimica Acta 66, 1499–1509. doi:10.1016/S0016-7037(01)00815-8

Maréchal, C.N., Telouk, P., Albarede, F., 1999. Precise analysis of copper and zinc isotopic compositions by plasma-source mass spectrometry. Chemical Geology 156, 251–273.

Martinez-Finley, E.J., Aschner, M., 2011. Revelations from the Nematode Caenorhabditis eleganson the Complex Interplay of Metal Toxicological Mechanisms. Journal of Toxicology 2011, 1–10. doi:10.1128/MCB.5.6.1268

Masoro, E.J., 2005. Overview of caloric restriction and ageing. Mechanisms of Ageing and Development 126, 913–922. doi:10.1016/j.mad.2005.03.012

Maynard, C.J., Bush, A.I., Masters, C.L., Cappai, R., Li, Q.-X., 2005. Metals and Amyloid-β In Alzheimer's Disease. Int. J. Exp. Path 86, 147–159.

McCay, C.M., Crowell, M.F., Maynard, L.A., 1935. The effect of retarded growth upon the lenght of life span and upon the ultimate body size. J Nutr. 10, 63–79.

McClain, C.J., Stuart, M.A., Vivian, B., McClain, M., Talwalker, R., Snelling, L., Humphries, L., 1992. Zinc status before and after zinc supplementation of eating disorder patients. Journal of the American College of Nutrition 11, 694–700. doi:10.1016/S0022-3476(80)80198-3

McCord, M.C., Aizenman, E., 2014. The role of intracellular zinc release in aging, oxidative stress, and Alzheimer's disease 1–16. doi:10.3389/fnagi.2014.00077/abstract

McDonald, R.B., Ramsey, J.J., 2010. Honoring Clive McCay and 75 Years of Calorie Restriction Research. Journal of Nutrition 140, 1205–1210. doi:10.3945/jn.110.122804

Meissner, C., Ritz-Timme, S., 2010. Molecular pathology and age estimation. Forensic Science International 203, 34–43. doi:10.1016/j.forsciint.2010.07.010

Mezzetti, A., Pierdomenico, S.D., Costantini, F., Romano, F., De Cesare, D., Cuccurullo, F., Imbastaro, T., Riario-Sforza, G., Di Giacomo, F., Zuliani, G., Fellin, R., 1998. Copper/zinc ratio and systemic oxidant load: Effect of aging and aging-related degenerative diseases. Free Radical Biology and Medicine 25, 676–681.

Michan, S., Sinclair, D., 2007. Sirtuins in mammals: insights into their biological function. Biochem. J. 404, 1–13. doi:10.1042/BJ20070140

Milanino, R., Cassini, A., Conforti, A., Franco, L., Marrella, M., Moretti, U., Velo, G.P., 1986. Copper and zinc status during acute inflammation: studies on blood, liver and

kidneys metal levels in normal and inflamed rats. Agents and Actions 19, 215–223.
Miller, K.A., Keenan, C.M., Martin, G.R., Jirik, F.R., Sharkey, K.A., Wieser, M.E., 2016. The expression levels of cellular prion protein affect copper isotopic shifts in the organs of mice. J. Anal. At. Spectrom. 00, 1–8. doi:10.1039/C6JA00195E
Mocchegiani, E., Costarelli, L., Giacconi, R., Piacenza, F., Basso, A., Malavolta, M., 2012. Micronutrient (Zn, Cu, Fe)–gene interactions in ageing and inflammatory age-related diseases: Implications for treatments. Ageing Research Reviews 11, 297–319. doi:10.1016/j.arr.2012.01.004
Morita, A., Kimura, M., Itokawa, Y., 1994. The Effect of Aging on the Mineral Status of Female Mice. Biological Trace Element Research 42, 165–177.
Moynier, F., Albarede, F., Herzog, G.F., 2006. Isotopic composition of zinc, copper, and iron in lunar samples. Geochimica et Cosmochimica Acta 70, 6103–6117. doi:10.1016/j.gca.2006.02.030
Moynier, F., Foriel, J., Shaw, A.S., Le Borgne, M., 2017. Distribution of Zn isotopes during Alzheimer's disease. Geochem. Persp. Let. 142–150. doi:10.7185/geochemlet.1717
Muradian, K., Schachtschabel, D.O., 2001. The role of apoptosis in aging and age-related disease: update. Zeitschrift für Gerontologie und Geriatrie 34, 441–446.
Murakami, M., Hirano, T., 2008. Intracellular zinc homeostasis and zinc signaling. Cancer Science 99, 1515–1522. doi:10.1002/1097-0142
Narasimhan, S.D., 2015. A Brief History of ALS. Cell 161, 181–183. doi:10.1016/j.cell.2015.03.044
National Research Council, 1989. Recommended Dietary Allowances: 10th Edition. The National Academies Press, Washington, DC. doi:10.17226/1349
Nonaka, T., Masuda-Suzukake, M., Arai, T., Hasegawa, Y., Akatsu, H., Obi, T., Yoshida, M., Murayama, S., Mann, D.M.A., Akiyama, H., Hasegawa, M., 2013. Prion-like Properties of Pathological TDP-43 Aggregates from Diseased Brains. CellReports 4, 124–134. doi:10.1016/j.celrep.2013.06.007
Noto, Y.-I., Shibuya, K., Sato, Y., Kanai, K., Misawa, S., Sawai, S., Mori, M., Uchiyama, T., Isose, S., Nasu, S., Sekiguchi, Y., Fujimaki, Y., Kasai, T., Tokuda, T., Nakagawa, M., Kuwabara, S., 2011. Elevated CSF TDP-43 levels in amyotrophic lateral sclerosis: Specificity, sensitivity, and a possible prognostic value. Amyotrophic Lateral Sclerosis 12, 140–143. doi:10.3109/17482968.2010.541263
Nuttall, J.R., Oteiza, P.I., 2014. Zinc and the aging brain. Genes Nutr 9, 1631. doi:10.1016/j.ejphar.2004.02.045
O'Sullivan, R.J., Karlseder, J., 2010. Telomeres: protecting chromosomes against genome instability. Nat. Rev. Mol. Cell. Biol 11, 171–181. doi:10.1038/nrm2848
Okusa, M.D., Crystal, L.J.T., 1994. Clinical Manifestations and Mangement of Acute Lithium Intoxication. The American Journal of Medicine 97, 383–389.
Osredkar, J., Sustar, N., 2011. Copper and Zinc, Biological Role and Significance of Copper/Zinc Imbalance. J Clin Toxicol s3. doi:10.4172/2161-0495.S3-001
Ostachowicz, B., Lankosz, M., Tomik, B., Adamek, D., Wobrauschek, P., Streli, C., Kregsamer, P., 2006. Analysis of some chosen elements of cerebrospinal fluid and serum in amyotrophic lateral sclerosis patients by total reflection X-ray fluorescence. Spectrochimica Acta Part B: Atomic Spectroscopy 61, 1210–1213. doi:10.1016/j.sab.2006.08.008
Paglia, G., Miedico, O., Cristofano, A., Vitale, M., Angiolillo, A., Chiaravalle, A.E., Corso, G., Di Costanzo, A., 2016. Distinctive Pattern of SerumElements During the Progression ofAlzheimer's Disease. Sci Rep 1–12. doi:10.1038/srep22769
Pall, H.S., Blake, D.R., Lunec, J., Gutteridge, J.M., Hall, M., 1987. Raised cerebrospinal-fluid

copper concentration in parkinson disease. The Lancet 330, 238–241.
Park, K., Min, H., Yim, Y.-H., Yim, Y.-L., Hwang, E.-J., Cho, K., 2011. Instrumental neutron activation analysis (INAA) and isotope dilution-inductively coupled plasma mass spectrometry (ID-ICP/MS) for certification of multielements in a tuna fish candidate certified reference material. Journal of Food Composition and Analysis 24, 1064–1068. doi:10.1016/j.jfca.2011.01.009
Parker, S.J., Meyerowitz, J., James, J.L., Liddell, J.R., Nonaka, T., Hasegawa, M., Kanninen, K.M., Lim, S., Paterson, B.M., Donnelly, P.S., Crouch, P.J., White, A.R., 2012. Inhibition of TDP-43 Accumulation by Bis(thiosemicarbazonato)-Copper Complexes. PLoS ONE 7, e42277. doi:10.1371/journal.pone.0042277.s002
Partridge, L., Piper, M.D.W., Mair, W., 2005. Dietary restriction in Drosophila. Mechanisms of Ageing and Development 126, 938–950. doi:10.1016/j.mad.2005.03.023
Pauze, D.K., MDa, Brooks, D.E., 2007. Lithium Toxicity From an Internet Dietary Supplement. Toxicology Observations 3, 61–62.
Pithadia, A., Lim, M.H., 2012. Metal-associated amyloid-β in Alzheimer's disease. Current Opinion in Chemical Biology 16, 67–73. doi:10.1016/j.cbpa.2012.01.016
Pokrishevsky, E., Grad, L.I., Cashman, N.R., 2016. TDP-43 or FUS-induced misfolded human wild-type SOD1 can propagate intercellularly in a prion- like fashion. Sci Rep 1–10. doi:10.1038/srep22155
Pokrishevsky, E., Grad, L.I., Yousefi, M., Wang, J., Mackenzie, I.R., Cashman, N.R., 2012. Aberrant Localization of FUS and TDP43 Is Associated with Misfolding of SOD1 in Amyotrophic Lateral Sclerosis. PLoS ONE 7, 1–9. doi:10.1371/journal.pone.0035050
Prabhakar, R., Vreven, T., Morokuma, K., Musaev, D.G., 2005. Elucidation of the Mechanism of Selenoprotein Glutathione Peroxidase (GPx)-Catalyzed Hydrogen Peroxide Reduction by Two Glutathione Molecules: A Density Functional Study †. Biochemistry 44, 11864–11871. doi:10.1021/bi050815q
Prasad, A.S., 1995. Zinc: an overview. Nutrition 11, 93–99.
Qiu, C., Kivipelto, M., Strauss, E.V., 2009. Epidemiology of Alzheimer's disease:occurrence, determinants, and strategiestoward intervention. Dialogues in Clinical Neuroscience 11, 111–128.
Querfurth, H.W., LaFerla, F.M., 2010. Alzheimer's Disease. N Engl J Med 362, 329–344. doi:10.1056/NEJMra0909142
Rahelić, D., Kujundžić, M., Romić, Ž., Brkić, K., Petrovečki, M., 2006. Serum Concentration of Zinc, Copper, Manganese and Magnesium in Patients with Liver Cirrhosis. Coll. Antropol. 30, 523–528.
Ramsey, J.J., Harper, M.E., Weindruch, R., 2000. Restriction of energy intake, energy expenditure, and aging. Free Radical Biology and Medicine 29, 946–968.
Reitz, C., 2012. Alzheimer's Disease and the Amyloid Cascade Hypothesis: A Critical Review. International Journal of Alzheimer's disease 2012, 1–11. doi:10.1155/2012/369808
Rembach, A., Hare, D.J., Doecke, J.D., Burnham, S.C., Volitakis, I., Fowler, C.J., Cherny, R.A., McLean, C., Grimm, R., Martins, R., Ames, D., Masters, C.L., Bush, A.I., Roberts, B.R., 2014. Decreased serum zinc is an effect of ageing and not Alzheimer's disease. Metallomics 6, 1216–1219. doi:10.1016/j.jsb.2005.09.004
Rodriguez-Castro, K.I., Hevia-Urrutia, F.J., Sturniolo, G.C., 2015. Wilson's disease: A review of what we have learned. WJH 7, 2859–2870. doi:10.4254/wjh.v7.i29.2859
Roh, H.C., Collier, S., Deshmukh, K., Guthrie, J., Robertson, J.D., Kornfeld, K., 2013. ttm-1 Encodes CDF Transporters That Excrete Zinc from Intestinal Cells of C. elegans and

Act in a Parallel Negative Feedback Circuit That Promotes Homeostasis. PLoS Genet 9, e1003522. doi:10.1371/journal.pgen.1003522.s004

Roh, H.C., Collier, S., Guthrie, J., Robertson, J.D., Kornfeld, K., 2012. Lysosome-Related Organelles in Intestinal Cells Are a Zinc Storage Site in C. elegans. Cell Metabolism 15, 88–99. doi:10.1016/j.cmet.2011.12.003

Roohani, N., Hurrell, R., Kelishadi, R., Schulin, R., 2013. Zinc and its importance for human health: An integrative review. J Res Med Sci 18, 144–157.

Roos, P.M., Lierhagen, S., Flaten, T.P., Syversen, T., Vesterberg, O., Nordberg, M., 2012. Manganese in cerebrospinal fluid and blood plasma of patients with amyotrophic lateral sclerosis. Exp Biol Med (Maywood) 237, 803–810. doi:10.1016/0022-510X(83)90012-6

Roos, P.M., Vesterberg, O., Syversen, T., Flaten, T.P., Nordberg, M., 2013. Metal Concentrations in Cerebrospinal Fluid and Blood Plasma from Patients with Amyotrophic Lateral Sclerosis. Biological Trace Element Research 151, 159–170. doi:10.1093/toxsci/kfq266

Roth, G.A., Forouzanfar, M.H., Moran, A.E., Barber, R., Nguyen, G., Feigin, V.L., Naghavi, M., Mensah, G.A., Murray, C.J.L., 2015. Demographic and Epidemiologic Drivers of Global Cardiovascular Mortality. N Engl J Med 372, 1333–1341. doi:10.1056/NEJMoa1406656

Roux, M., Dosseto, A., 2017. From direct to indirect lithium targets: a comprehensive review of omics data. Metallomics 9, 1326–1351. doi:10.1039/C7MT00203C

Ryu, D., Mouchiroud, L., Andreux, P., Katsyuba, E., Moullan, N., Nicolet-dit-Felix, A., Williams, E.G., Jha, P., Sasso, Lo, G., Huzard, D., Aebischer, P., Sandi, C., Rinsch, C., Auwerx, J., 2016. Urolithin A induces mitophagy and prolongs lifespan in. Nature Medicine 22, 879–888. doi:10.1038/nm.4132

Safai-Kutti, S., 1990. Oral zinc supplementation in Anorexia Nervosa. Acta Psychiatr Scand 82, 14–17.

Sakka, L., Coll, G., Chazal, J., 2011. Anatomy and physiology of cerebrospinal fluid. European Annals of Otorhinolaryngology, Head and Neck diseases 128, 309–316. doi:10.1016/j.anorl.2011.03.002

Sands, W.A., Page, M.M., Selman, C., 2017. Proteostasis and ageing: insights from long-lived mutant mice. J Physiol 595, 6383–6390. doi:10.1016/j.yjmcc.2015.07.027

Sanuade, O.A., Anarfi, J.K., Aikins, A.D.-G., Koram, K.A., 2014. Patterns of cardiovascular disease mortality in Ghana. A 5-year review of autopsy cases at KorleBu Teaching Hospital. Ethnicity & Disease 24, 55–59.

Sastre, M., Ritchie, C.W., Hajji, N., 2015. Metal Ions in Alzheimer's Disease Brain. JSM Alzheimer's Dis Related Dementia 2, 1–6.

Savage, N., 2017. Calculating disease. Nature 550, S115.

Schauble, E., 2004. Applying Stable Isotope Fractionation Theory to New Systems. Reviews in Mineralogy and Geochemistry 55, 65–111.

Scheiber, I.F., Dringen, R., 2013. Astrocyte functions in the copper homeostasis of the brain. Neurochemistry International 62, 556–565. doi:10.1016/j.neuint.2012.08.017

Scheiber, I.F., Mercer, J.F.B., Dringen, R., 2014. Metabolism and functions of copper in brain. Progress in Neurobiology 116, 33–57. doi:10.1016/j.pneurobio.2014.01.002

Schlotterer, A., Kukudov, G., Bozorgmehr, F., Hutter, H., Du, X., Oikonomou, D., Ibrahim, Y., Pfisterer, F., Rabbani, N., Thornalley, P., Sayed, A., Fleming, T., Humpert, P., Schwenger, V., Zeier, M., Hamann, A., Stern, D., Brownlee, M., Bierhaus, A., Nawroth, P., Morcos, M., 2009. C. elegans as Model for the Study of High Glucose- Mediated Life Span Reduction. Diabetes 58, 2450–2456. doi:10.2337/db09-0567

Scott, A., 2017. On the treatment trail for ALS. Nature 550, S120.
Shaye, D.D., Greenwald, I., 2011. OrthoList: A Compendium of C. elegans Genes with Human Orthologs. PLoS ONE 6, 1–12.
Shchepinov, M.S., Pestov, N.B., 2010. Isotope effect, essential diet components, and prospects of aging retardation. Russ J Gen Chem 80, 1514–1522. doi:10.1134/S1070363210070480
Siggs, O.M., Cruite, J.T., Du, X., Rutschmann, S., Masliah, E., Beutler, B., Oldstone, M.B.A., 2012. Disruption of copper homeostasis due to a mutation of Atp7a delays the onset of prion disease. Proceedings of the National Academy of Sciences 109, 13733–13738. doi:10.1038/nmeth0410-248
Singh, G.K., Siahpush, M., 2006. Widening socioeconomic inequalities in US life expectancy, 1980–2000. International Journal of Epidemiology 35, 969–979. doi:10.1093/ije/dyl083
Smart, T.G., Hosie, A.M., Miller, P.S., 2004. Zn2+ Ions: Modulators of Excitatory and Inhibitory Synaptic Activity. Neuroscientist 10, 432–442. doi:10.1038/634
Smethurst, P., Sidle, K.C.L., Hardy, J., 2015. Review: Prion-like mechanisms of transactive response DNA binding protein of 43 kDa (TDP-43) in amyotrophic lateral sclerosis (ALS). Neuropathol Appl Neurobiol 41, 578–597. doi:10.1016/j.celrep.2014.05.033
Sohal, R.S., Weindruch, R., 1996. Oxidative Stress, Caloric Restriction, and Aging. Science 273, 59–63.
Solomons, N.W., 2013. Update on Zinc Biology. Ann Nutr Metab 62, 8–17. doi:10.1159/000348547
Sossi, P.A., Halverson, G.P., Nebel, O., Eggins, S.M., 2014. Combined Separation of Cu, Fe and Zn from Rock Matrices and Improved Analytical Protocols for Stable Isotope Determination. Geostandards and Geoanalytical Research 39, 129–149. doi:10.1111/j.1751-908X.2014.00298.x
Squitti, R., Siotto, M., Polimanti, R., 2014. Low-copper diet as a preventive strategy for Alzheimer's disease. Neurobiology of Aging 35, S40–S50. doi:10.1016/j.neurobiolaging.2014.02.031
Stadtman, E.R., 2004. Role of Oxidant Species in Aging. Current Medicinal Chemistry 11, 1105–1112.
Stenberg, A., Malinovsky, D., Öhlander, B., Andrén, H., Forsling, W., Engström, L.-M., Wahlin, A., Engström, E., Rodushkin, I., Baxter, D.C., 2005. Measurement of iron and zinc isotopes in human whole blood: Preliminary application to the study of HFE genotypes. Journal of Trace Elements in Medicine and Biology 19, 55–60. doi:10.1016/j.jtemb.2005.07.004
Stitt, A.W., 2001. Advanced glycation: an important pathological event in diabetic and age related ocular disease. Br. J. Ophtalmol. 85, 746–753.
Strozyk, D., Launer, L.J., Adlard, P.A., Cherny, R.A., Tsatsanis, A., Volitakis, I., Blennow, K., Petrovitch, H., White, L.R., Bush, A.I., 2009. Zinc and copper modulate Alzheimer Aβ levels in human cerebrospinal fluid. Neurobiology of Aging 30, 1069–1077. doi:10.1016/j.neurobiolaging.2007.10.012
Su, J.C., Birmingham, C.L., 2001. Zinc supplementation in the treatment of anorexia nervosa. Review Article 20–22.
Sullivan, J., Blotcky, A., Jetton, M., Hahn, H., Burch, R., 1979. Serum Levels of Selenium, Calcium, CopperMagnesium, Manganese and Zinc in Various Human Diseases. Journal of Nutrition 109, 1432–1437.
Sun, J., Tower, J., 1999. FLP Recombinase-Mediated Induction of Cu/Zn-SuperoxideDismutase Transgene Expression Can Extend the LifeSpan of Adult

Drosophila melanogaster Flies. Molecular and Cellular Biology 19, 216–228.
Sunyecz, J.A., 2008. The use of calcium and vitamin D in the management of osteoporosis. Ther Clin Risk Manag 4, 827–836.
Tacail, T., Thivichon-Prince, B., Martin, J.E., Charles, C., Viriot, L., Balter, V., 2017. Assessing human weaning practices with calcium isotopes in tooth enamel. Proceedings of the National Academy of Sciences 114, 6268–6273. doi:10.1007/978-3-540-68953-9_5
Tarasiuk, J., Kułakowska, A., Drozdowski, W., Kornhuber, J., Lewczuk, P., 2012. CSF markers in amyotrophic lateral sclerosis. J Neural Transm 119, 747–757. doi:10.1016/j.jns.2006.06.027
Taylor, G.W., Harvey, E.N., 1934. Respiration of Yeast in Water Containing Deuterium Oxide. Exp Biol Med (Maywood) 31, 954–957. doi:10.3181/00379727-31-7390C
Taylor, J.P., Brown, R.H., Cleveland, D.W., 2016. Decoding ALS: from genes to mechanism. Nature 539, 197–206. doi:10.1038/nn.4000
Telouk, P., Puisieux, A., Fujii, T., Balter, V., Bondanese, V.P., Morel, A.-P., Clapisson, G., Lamboux, A., Albarède, F., 2015. Copper isotope effect in serum of cancer patients. A pilot study. Metallomics 7, 299–308. doi:10.1039/C4MT00269E
Ticozzi, N., Tiloca, C., Mencacci, N.E., Morelli, C., Doretti, A., Rusconi, D., Colombrita, C., Sangalli, D., Verde, F., Finelli, P., Messina, S., Ratti, A., Silani, V., 2012. Oligoclonal bands in the cerebrospinal fluid of amyotrophic lateral sclerosis patients with disease-associated mutations. J Neurol 260, 85–92. doi:10.1172/JCI9369
Tomás-Loba, A., Bernardes de Jesus, B., Mato, J.M., Blasco, M.A., 2013. A metabolic signature predicts biological age in mice. Aging Cell 12, 93–101. doi:10.1111/acel.12025
Tosato, M., Zamboni, V., Ferrini, A., Cesari, M., 2007. The aging process and potential interventions to extend life expectancy. Clinical Interventions in Aging 2, 401–412.
Turnlund, J.R., 1998. Human whole-body copper metabolism. The American Journal of Clinical Nutrition 67, 960S–964S.
Turnlund, J.R., Durkin, N., Costa, F., Margen, S., 1986. Stable Isotope Studies of Zinc-Absorption and Retention in Young and Elderly Men. Journal of Nutrition 116, 1239–1247.
Turnlund, J.R., King, J.C., Keyes, W.R., Gong, B., Michel, M.C., 1984. A Stable Isotope Study of Zinc Absorption in Young Men: Effects of Phytate and A-Cellulose. The American Journal of Clinical Nutrition 40, 1071–1077.
Turski, M.L., Thiele, D.J., 2009. New Roles for Copper Metabolism in Cell Proliferation, Signaling, and Disease. J. Biol. Chem. 284, 717–721. doi:10.1038/ng0596-43
Valentine, J.S., Doucette, P.A., Zittin Potter, S., 2005. Copper-Zinc superoxide dismutase and amyotrophic lateral sclerosis. Annu. Rev. Biochem. 74, 563–593. doi:10.1146/annurev.biochem.72.121801.161647
Vallee, B., Falchuk, K., 1993. The Biochemical Basis of Zinc Physiology. Physiological Reviews 73, 1–40.
Van Heghe, L., Delanghe, J., Van Vlierberghe, H., Vanhaecke, F., 2013. The relationship between the iron isotopic composition of human whole blood and iron status parameters. Metallomics 5, 1503. doi:10.1007/s00775-012-0943-7
Van Heghe, L., Deltombe, O., Delanghe, J., Depypere, H., Vanhaecke, F., 2014. The influence of menstrual blood loss and age on the isotopic composition of Cu, Fe and Zn in human whole blood. J. Anal. At. Spectrom. 29, 478–482. doi:10.1002/jcla.20012
Van Heghe, L., Engström, E., Rodushkin, I., Cloquet, C., Vanhaecke, F., 2012. Isotopic

analysis of the metabolically relevant transition metals Cu, Fe and Zn in human blood from vegetarians and omnivores using multi-collector ICP-mass spectrometry. J. Anal. At. Spectrom. 27, 1327. doi:10.1016/S1387-3806(03)00078-2

Vasdev, S., Prabhakaran, V., Sampson, C.A., 1990. Deuterium oxide normalizes blood pressure and vascular calcium uptake in dahl salt-Sensitive hypertensive rats. Hypertension 15, 183–189.

Vestergaard, P., Licht, R.W., 2001. 50 Years with Lithium Treatment in Affective Disorders: Present Problems and Priorities 2, 18–26.

Vinceti, M., Filippini, T., Mandrioli, J., Violi, F., Bargellini, A., Weuve, J., Fini, N., Grill, P., Michalke, B., 2017. Lead, cadmium and mercury in cerebrospinal fluid and risk of amyotrophic lateral sclerosis: A case-control study. J Trace Elem Med Biol 43, 121–125. doi:10.1016/j.jtemb.2016.12.012

Walczyk, T., Blanckenburg, von, F., 2002. Natural iron isotope variations in human blood. Science 295, 2065–2066.

Wang, L.-M., Becker, J.S., Wu, Q., Oliveira, M.F., Bozza, F.A., Schwager, A.L., Hoffman, J.M., Morton, K.A., 2010. Bioimaging of copper alterations in the aging mouse brain by autoradiography, laser ablation inductively coupled plasma mass spectrometry and immunohistochemistry. Metallomics 2, 348. doi:10.1016/S0065-1281(81)80003-7

Whittle, N., Lubec, G., Singewald, N., 2009. Zinc deficiency induces enhanced depression-like behaviour and altered limbic activation reversed by antidepressant treatment in mice. Amino Acids 36, 147–158. doi:10.1211/0022357021778835

Wiedau-Pazos, M., Goto, J.J., Rabizadeh, S., Gralla, E.B., Roe, J.A., Lee, M.K., Valentine, J.S., Bredesen, D.E., 1996. Altered Reactivity of Superoxide Dismutase in Familial Amyotrophic Lateral Sclerosis. Science 271, 515–518. doi:10.1126/science.271.5248.515

World Health Organization (Ed.), 2011. Global Health and Aging.

Wu, Y., Wu, M., Zhang, Y., Li, W., Gao, Y., Li, Z., Wang, Z., Lubec, G., Zhang, C., 2012. Lyophilization is suitable for storage and shipment of fresh tissue samples without altering RNA and protein levels stored at room temperature. Amino Acids 43, 1383–1388. doi:10.1007/s00726-011-1212-8

Xiao, R., Zhang, B., Dong, Y., Gong, J., Xu, T., Liu, J., Xu, X.Z.S., 2013. A Genetic Program Promotes C. elegans Longevity at Cold Temperatures via a Thermosensitive TRP Channel. Cell 152, 806–817. doi:10.1016/j.cell.2013.01.020

Zatta, P., Drago, D., Zambenedetti, P., Bolognin, S., Nogara, E., Peruffo, A., Cozzi, B., 2008. Accumulation of copper and other metal ions, and metallothionein I/II expression in the bovine brain as a function of aging. Journal of Chemical Neuroanatomy 36, 1–5. doi:10.1016/j.jchemneu.2008.02.008

Zetterberg, H., Skillbäck, T., Mattsson, N., Trojanowski, J.Q., Portelius, E., Shaw, L.M., Weiner, M.W., Blennow, K., for the Alzheimer's Disease Neuroimaging Initiative, 2016. Association of Cerebrospinal Fluid Neurofilament Light Concentration With Alzheimer Disease Progression. JAMA Neurol 73, 60. doi:10.1001/jamaneurol.2015.3037

Zhang, J.-H., Zhang, Y., Herman, B., 2003. Caspases, apoptosis and aging. Ageing Research Reviews 2, 357–366. doi:10.1016/S1568-1637(03)00026-6

ANNEXES

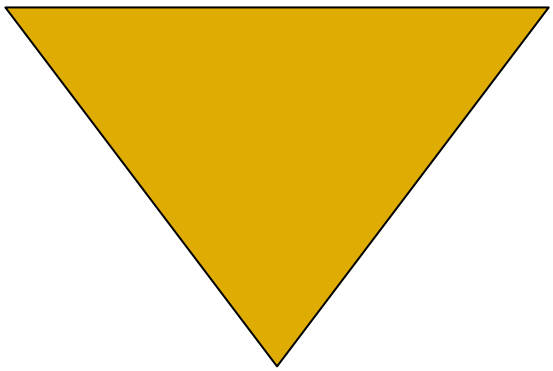

Annexe 1 : Études supplémentaires réalisées pendant ma thèse et articles associés

Au cours de ma thèse, en plus des travaux menés sur le vieillissement et les maladies neurodégénératives, j'ai également contribué à divers projets de recherche, notamment sur l'avenir des coraux face au réchauffement climatique en collaboration avec Christine Ferrier-Pagès du Centre Scientifique de Monaco. Pour ce projet, j'ai réalisé l'ensemble des analyses isotopiques (Cu-Zn) et élémentaires (majeurs et traces) sur des coraux et des algues symbiotiques (40 échantillons) et participé à l'interprétation des résultats dans le but de mieux contraindre les réponses chimiques et isotopiques associées au blanchiment des coraux induit par un stress thermique (*i.e.* changement climatique) et nutritif. Cette étude a abouti à la rédaction d'un manuscrit publié dans le journal « Global Change Biology » et présenté ci-dessous.

ARTICLE

Coral bleaching is linked to the capacity of the animal host to supply essential metals to the symbionts

Christine Ferrier-Pagès, ***Lucie Sauzéat****, Vincent Balter*

(Published in Global Change Biology)

Received: 1 December 2017 | Revised: 7 March 2018 | Accepted: 7 March 2018

DOI: 10.1111/gcb.14141

PRIMARY RESEARCH ARTICLE

WILEY Global Change Biology

Coral bleaching is linked to the capacity of the animal host to supply essential metals to the symbionts

Christine Ferrier-Pagès[1] | Lucie Sauzéat[2] | Vincent Balter[2]

[1]Centre Scientifique de Monaco, Equipe Ecophysiologie corallienne, Monaco, Monaco

[2]CNRS UMR 5276 "Laboratoire de Géologie de Lyon", Ecole Normale Supérieure de Lyon, Lyon Cedex 07, France

Correspondence
Christine Ferrier-Pagès, Centre Scientifique de Monaco, Monaco, Monaco.
Email: ferrier@centrescientifique.mc

Abstract

Massive coral bleaching events result in extensive coral loss throughout the world. These events are mainly caused by seawater warming, but are exacerbated by the subsequent decrease in nutrient availability in surface waters. It has therefore been shown that nitrogen, phosphorus or iron limitation contribute to the underlying conditions by which thermal stress induces coral bleaching. Generally, information on the trophic ecology of trace elements (micronutrients) in corals, and on how they modulate the coral response to thermal stress is lacking. Here, we demonstrate for the first time that heterotrophic feeding (i.e. the capture of zooplankton prey by the coral host) and thermal stress induce significant changes in micro element concentrations and isotopic signatures of the scleractinian coral *Stylophora pistillata*. The results obtained first reveal that coral symbionts are the major sink for the heterotrophically acquired micronutrients and accumulate manganese, magnesium and iron from the food. These metals are involved in photosynthesis and antioxidant protection. In addition, we show that fed corals can maintain high micronutrient concentrations in the host tissue during thermal stress and do not bleach, whereas unfed corals experience a significant decrease in copper, zinc, boron, calcium and magnesium in the host tissue and bleach. In addition, the significant increase in δ^{65}Cu and δ^{66}Zn signature of symbionts and host tissue at high temperature suggests that these isotopic compositions are good proxy for stress in corals. Overall, present findings highlight a new way in which coral heterotrophy and micronutrient availability contribute to coral resistance to global warming and bleaching.

KEYWORDS
copper isotope, coral bleaching, essential metals, global warming, heterotrophy, zinc isotope

1 | INTRODUCTION

Mutualistic nutritional symbioses between animals and microorganisms are widespread in aquatic and terrestrial ecosystems, because they convey ecological advantages to the partners by allowing them to exploit a large panel of food sources (Douglas, 1998; Saffo, 1992; Venn, Loram, & Douglas, 2008). For example cyanobacteria in symbiosis with lichens, or bacteria associated to insects, supply their host with essential amino acids (Douglas, 1998; Usher, Bergman, & Raven, 2007). Prominent and widely recognized nutritional symbioses in the marine environment are those formed between dinoflagellate algae and sea anemones, jellyfish, sponges, clams or corals (Muscatine & Porter, 1977; Norton, Shepherd, Long, & Fitt, 1992). In particular, the association between corals and dinoflagellates of the genus *Symbiodinium* is at the basis of tropical reef ecosystems, which are as biodiverse as the rain forest, gathering more than 25% of all known marine species (Moberg & Folke, 1999).

Dinoflagellates in symbiosis with corals transform inorganic into organic nutrients via photosynthesis and translocate most of their photosynthates to the animal host for its own nutritional needs

(Muscatine, Falkowski, Porter, & Dubinsky, 1984; Tremblay, Grover, Maguer, Legendre, & Ferrier-Pagès, 2012). In turn, the host provides shelter to the dinoflagellates, but also nutrients from its metabolic waste products and/or its heterotrophic nutrition, i.e. the capture of zooplankton prey (Tremblay, Maguer, Grover, & Ferrier-Pagès, 2015; Yellowlees, Rees, & Leggat, 2008). Since photosynthates cover almost 100% of the energetic needs of the symbiotic association in optimal living conditions, most studies until now have focused on better understanding the many services provided by dinoflagellates to corals under varying environmental conditions (reviewed in Davy, Allemand, & Weis, 2012; Tremblay, Grover, Maguer, Hoogenboom, & Ferrier-Pagès, 2014). The contrary, i.e. the amount and nature of heterotrophic nutrients translocated from the host to the symbionts have been very poorly studied (Hughes, Grottoli, Pease, & Matsui, 2010; Piniak, Lipschultz, & McClelland, 2003; Tremblay et al., 2015). Heterotrophy can, however, maintain the growth and metabolism of both symbionts and hosts whenever conditions are not favourable to autotrophy, such as in low-light environments (Anthony, 2000), or during seawater warming, which leads to oxidative stress, symbiont expulsion (bleaching) and nutritional starvation (Ferrier-Pagès, Rottier, Beraud, & Levy, 2010; Grottoli, Rodrigues, & Palardy, 2006). The processes by which heterotrophy sustains coral metabolism during bleaching are not all known, except that particle capture is a major source of macronutrients (carbon, nitrogen and phosphorus), which enter into the composition of energetic reserves (Grottoli et al., 2006; Hughes & Grottoli, 2013). In addition, heterotrophy promotes the re-establishment of photosynthate translocation after heat stress, suggesting that the symbionts are one of the main beneficiaries of this nutrient source (Tremblay, Gori, Maguer, Hoogenboom, & Ferrier-Pagès, 2016). Recently, genomic analyses also showed, in corals fed with zooplankton, an up-regulation of genes involved in the antioxidant response (Levy et al., 2016). Such response may be mediated through the heterotrophic supply of micronutrients (trace metals), which are constituents of antioxidant enzymes (Richier, Furla, Plantivaux, Merle, & Allemand, 2005), or which enter into the composition of photosynthetic pigments of the coral symbionts and are essential during bleaching (Shick et al., 2011).

Although the acquisition and allocation of autotrophic and heterotrophic macronutrients in corals start to be well studied via the use of stable isotope ratios such as $^{13}C/^{12}C$ and $^{15}N/^{14}N$ (Hughes et al., 2010; Tremblay et al., 2015), the trophic ecology of trace elements remains almost unknown, both under normal growth conditions and during thermal stress. To date, the wide majority of studies have focused on metal and trace element concentrations in coral skeletons to follow pollution events (Barnes, Taylor, & Lough, 1995; Bastidas & Garcıa, 1999; David, 2003; Fallon, White, & McCulloch, 2002). Those performed at the tissue level showed that algal symbionts actively take up and accumulate trace elements dissolved in seawater (Ferrier-Pagès et al., 2005; Harland & Nganro, 1990; Reichelt-Brushett & McOrist, 2003), suggesting that coral bleaching may result in micronutrient limitation through symbiont loss. However, the changes in micronutrient concentrations or isotopic signature of symbionts and host tissue with feeding and environmental stress are still unknown. As shown in other organisms such as mice and humans, isotopic signature of copper and zinc can be significantly affected by pathological conditions (e.g. Balter et al., 2015) as well as by dietary conditions (e.g. Costas-Rodríguez, Van Heghe, & Vanhaecke, 2014; Jaouen, Pons, & Balter, 2013; Jaouen, Szpak, & Richards, 2016). This suggests that a change from autotrophic to heterotrophic feeding caused by bleaching conditions could also be marked by isotopic deregulations. In this study, we have investigated the trophic ecology of trace elements in the scleractinian coral *Stylophora pistillata* as well as the changes in the isotopic signature of copper and zinc under normal and thermal stress conditions. The first aim was to assess whether heterotrophy brings essential micronutrients to the symbiotic association, and contributes, by this process, to increase the resistance of corals to thermal-stress induced bleaching. The second aim was to evaluate whether heterotrophy, and/or thermal stress, can be traced through a change in the isotopic signature of copper and zinc. Investigating those aspects allows for a better understanding of the processes leading to coral bleaching. The results will show whether bleaching is exacerbated by the lack of trace elements in coral tissue and whether zooplankton capture can supply these micronutrients to corals.

2 | MATERIALS AND METHODS

2.1 | Maintenance of coral colonies

Five colonies of the scleractinian coral *Stylophora pistillata* (Esper 1797), originating from the Red Sea (Aqaba, Jordan), were used to generate 40 large nubbins of ca. 10 cm long (8 nubbins from each of the five colonies). Nubbins were then equally divided into four treatments and two 20 L aquaria per treatment (8 aquaria in total). During the first 5 weeks, four aquaria were fed during 2 hr and three times a week with 4,000 *artemia salina* nauplii, whereas the other four aquaria were kept unfed. All aquaria were maintained in an open flow system, with a water renewal rate of 10 L/hr and at a constant temperature of 25°C ± 0.5°C. Light was provided by hydrargyrum quartz iodide (HQI) lights at a photosynthetic active radiation level (PAR) of 200 μmol m^{-2} s^{-1} (measured using a spherical quantum sensor; LiCor LI-193, Lincoln, NE, USA), with a 12 hr:12 hr dark:light cycle. After these first 5 weeks, and for each feeding conditions, two aquaria were kept at 25°C while temperature was slowly raised (1°C every 2 days) in the two other aquaria to reach 30°C. Temperature and trophic conditions were maintained for three additional weeks prior measurements of trace metal concentrations and symbiont density were performed as described below.

2.2 | Treatments

Five nubbins in each condition were sampled for the determination of the symbiont density. Coral tissue was extracted from the skeleton using an air pick and homogenized with a Potter tissue grinder.

The symbiont density was quantified with three sub-samples of 100 μl using a Z1 Coulter Particle Counter (Beckman Coulter). The five remaining nubbins in each condition were sampled, rinsed using artificial seawater (ASW) made with ultrapure sodium chloride (NaCl) (Trace Select for trace analysis ≥99.999%, Sigma Aldrich). They were then individually placed in 50 ml beakers (precombusted at 480°C for 4 hr in a ThermolyneH 62700 oven and rinsed with ASW) containing 5 ml of ASW. For each sample, tissue was completely removed from the skeleton with an air pick and homogenized with a Potter tissue grinder (treated as beakers). The homogenate was divided into a host and a symbiont fraction. For the host fraction, the homogenate was centrifuged (Biofuge 17RS Heraeus) at 3,000 *g* for 10 min to pellet most of the symbionts. The supernatant was re-centrifuged twice to eliminate the remaining symbionts, then flash frozen with liquid nitrogen, and freeze-dried using a Heto (model CT 60) drier. For the symbiont fraction, the pellet was washed several times in ASW, flashed frozen and freeze-dried.

2.3 | Analyses of trace and major element concentrations

All chemical analyses were carried out in clean laminar flow hoods using double-distilled acids to avoid any exogenous contaminations. Freeze-dried coral and symbiont samples were dissolved in a concentrated HNO_3-H_2O_2 mixture, in Savillex beakers, at 120°C for at least 72 hr. Major and trace element concentrations were first measured in a small aliquot on an ICP-AES (iCAP 6000 Radial) and a quadrupole ICP-MS Thermo iCap-Q, respectively, at the Ecole Normale Supérieure (ENS) of Lyon following the method described in Garçon et al. (2017). Oxide interference and analytical drift were corrected using indium (In) and scandium (Sc) addition as internal standards for trace and major elements respectively (Sigma Aldrich, France). In-house (sheep plasma, OEP) and international standards (bovine liver, 1577c, Sigma Aldrich) as well as complete duplicate and re-run analyses were measured to ensure the validity and assess the precision of our results. Metal concentrations are all reported in μg/g (ppm) dry weight.

2.4 | Analyses of copper and zinc isotopic compositions

Copper and zinc isotopic compositions were then measured following the procedure described by Maréchal, Télouk, and Albarède (1999). Briefly, before each isotopic measurement, samples were purified by ion-exchange chromatography using quartz columns filled with 1.8 ml of Bio-Rad AGMP-1 (100–200 mesh) anion-exchange resin. Copper was first eluted with 20 ml of HCl (7 mol/L) + 0.001% H_2O_2 followed by zinc with 10 ml of HNO_3 (0.5 mol/L). The purification step helps removing elements (e.g. Ni, Ti, Al or Ba), which may interfere with copper and zinc during the instrumental measurement (Chen et al., 2016; Sossi, Halverson, Nebel, & Eggins, 2014). Indeed, it has been shown that small amounts of Ni and Ti residues, for example can produce isobaric interferences and shift the measured $\delta^{66}Zn$ values by more than 0.07‰ if the Ni/Zn and Ti/Zn ratios are higher than 0.001 and 0.01 respectively (Chen et al., 2016).

On the day of the analyses, an aliquot of the Zn and Cu purified solutions, previously evaporated to dryness, are dissolved in a Cu (Cu SRM 976, National Institute of Standards and Technology, Gaithersburg, MD, USA) or Zn-doped solution (Zn JMC 3-0749L, Johnson Matthey Royston, UK), respectively, to reach sample concentration of about 300 μg/L that is similar to the concentration of the standard solution that was run between each sample. Both copper and zinc isotopic compositions, expressed as

$$\delta^{65}Cu_{sample}\,(\text{in}\,‰) = \left[\frac{\left(^{65}Cu/^{63}Cu\right)_{sample}}{\left(^{65}Cu/^{63}Cu\right)_{standard}} - 1\right] * 1,000$$

$$\delta^{66}Zn_{sample}\,(\text{in}\,‰) = \left[\frac{\left(^{66}Zn/^{64}Zn\right)_{sample}}{\left(^{66}Zn/^{64}Zn\right)_{standard}} - 1\right] * 1,000$$

were measured on a Nu Plasma (Nu 500) MC-ICP-MS in wet plasma conditions. Instrumental mass fractionation was corrected with an exponential law using an elemental-doping method as recommended by Maréchal et al. (1999). $\delta^{66}Zn$ and $\delta^{65}Cu$ were then calculated by standard bracketing using Zn JMC 3-0749L (Johnson Matthey Royston, UK) and Cu SRM 976 (NIST, Gaithersburg, MD, USA) as reference standards. Note that these standards were repeatedly measured between each sample to correct for the instrumental drift throughout the analytical sequence; a method called standard bracketing. The accuracy of the isotopic compositions was assessed based on the analyses of an in-house (sheep plasma; OEP) and international (bovine liver, 1577c, Sigma Aldrich, France) standard solution at the beginning and during the analytical sequence. The average $\delta^{66}Zn$ measured for the in-house standard solution was +0.75‰ ± 0.07 and −1.19‰ ± 0.07 for $\delta^{65}Cu$ which is in good agreement with our previous reference in-house values ($\delta^{65}Cu$ = −1.15‰ ± 0.20 (standard deviation (*SD*), *n* = 35) and $\delta^{66}Zn$ = +0.73‰ ± 0.09 (*SD*, *n* = 20). Our results for the international standard (1577c) are also in good agreements with previous results: $\delta^{66}Zn_{this\ study}$ = −0.20‰ ± 0.06 (*SD*, *n* = 10) compared to $\delta^{66}Zn_{1577c}$ = −0.16‰ ± 0.15 (*SD*, *n* = 45) and $\delta^{65}Cu_{this\ study}$ = +0.30‰ ± 0.13 (*SD*, *n* = 10) compared to $\delta^{65}Cu_{1577c}$ = +0.37‰ ± 0.14 (*SD*, *n* = 43). On the basis of re-run samples and complete duplicate analyses, we estimate the precision of our measurements at ± 0.1 (*SD*) for both $\delta^{65}Cu$ and $\delta^{66}Zn$. The long-term precision based on the repeated measurements of standard Zn JMC 3-0749L and Cu SRM 976 alone is similar (±0.07‰ (*SD*, *n* = 480)).

2.5 | Statistics

A correlation-based principal component analysis (PCA) was used to quantify the effect of thermal stress and heterotrophic feeding on the chemical composition of symbionts and host tissue of colonies of *Sylophora pistillata*. The method consists in identifying new variables called principal components (PCs), which are linear combination of the original variables and along which data variation is maximal. For each principal component (PC), linear regressions, using standard

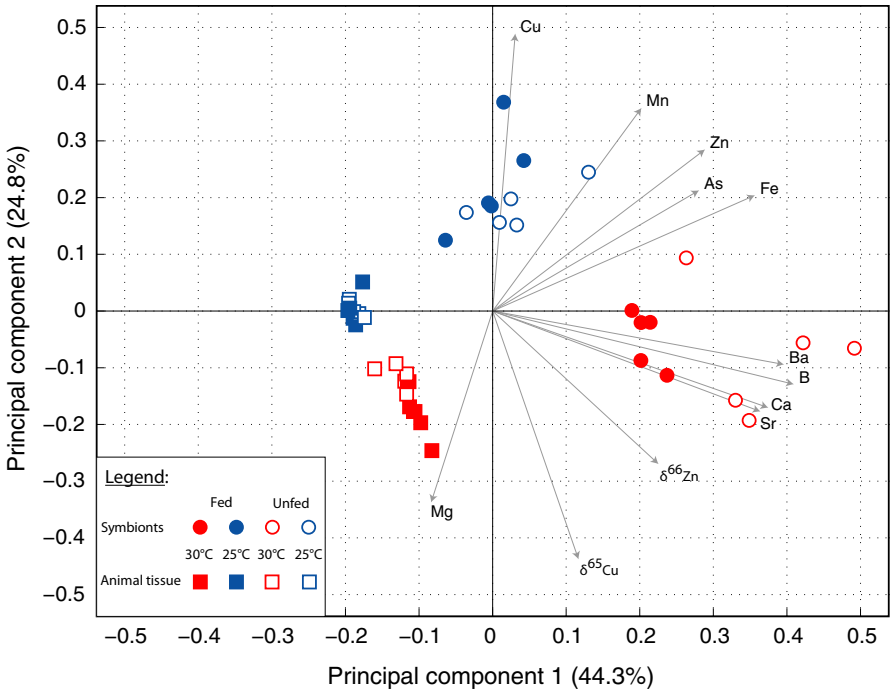

FIGURE 1 Principal Component Analysis (PCA) taking into account all data (micronutrient concentrations in symbionts and host tissue, as well as the isotopic signature of zinc and copper in each compartments, $n = 5$ samples for each condition) at 25°C (normal growth temperature) and 30°C (stress)

least-squares techniques, were thus used to estimate the relationship between parameters. In this study, the variables include the chemical concentrations of the trace elements measured in host tissue and symbionts (manganese, iron, magnesium, zinc, strontium, arsenic, barium, calcium, boron and copper), as well as copper (δ^{65}Cu) and zinc (δ^{66}Zn) isotopic compositions. All data were log transformed and normalized, and samples with incomplete data were excluded. PCA was implemented in MATLAB™.

2.5.1 | Statistical analyses

All parameters were expressed as mean ± standard deviation (*SD*) of five measurements. Statistical analyses were performed using SYSTAT 13 software (Systat Software, Chicago, IL, USA). Data were checked for normality using the Kolmogorov–Smirnov test with Lilliefors correction and for homoscedasticity using Levene test. Data were transformed with a natural logarithm transformation when required (i.e. Fe, Sr, Ca and B in symbionts; Fe, Mg, Zn, Ba, Ca and B in coral host). Factorial ANOVA with two factors (feeding an temperature) were performed and when there were significant differences between treatments, analyses were followed by a posteriori testing (Tukey's test). Differences between factors were considered significant for p-values <.05.

3 | RESULTS

The PCA yielded two principal components (PC1 and PC2) that explain ca. 70% of the total variance (Figure 1). In this figure, grey arrows graphically represent the loading factors (i.e. weight of each variable on PC1 and PC2, and Table S1). The first component (PC1), which explains 44% of the total variance, is defined by positive correlations with several trace elements such as iron (Fe), barium (Ba) or boron (B). This principal component demonstrates that symbionts contained higher micronutrient concentrations (μg/g dry weight) than the animal tissue, suggesting that nutrients were not distributed equally in these two compartments. Principal component 2 (PC2) explains 25% of the total variance and is defined by relatively high weights from Cu, but negative correlation with magnesium (Mg), δ^{65}Cu and δ^{66}Zn. This principal component separates both symbionts and animal tissues maintained at 25 and 30°C, showing that thermal stress was associated with variation in both their micronutrient content and isotopic composition. As demonstrated by the PCA and the results summarized in Table 1, for both temperatures investigated (25 and 30°C), and in all feeding conditions, symbionts presented higher concentrations (μg/g dry weight) than the animal tissue, except for Mg, whose concentration tended to be slightly higher in the host tissue (Figure 1).

The two factors ANOVA (Table 2) shows significant effect of both feeding and temperature, alone or in combination, on the micronutrient concentrations of symbionts and animal tissue. At the normal growth temperature (25°C), symbionts of fed colonies presented higher concentrations of Mg (post hoc, p-value = .002), Fe (p-value = .003) and Mn (p-value <.001), but lower concentrations of strontium (Sr), and arsenic (As) (p-value = .01 and .004 respectively) than symbionts of unfed colonies (Table S2). Inversely, there was no significant difference in micronutrient concentrations between fed and unfed coral tissue at 25°C (Table S3, post hoc, p value >.1). Host tissue of fed corals had, however, a higher δ^{65}Cu signature (−0.42‰ ± 0.12, ANOVA, p value = .0455) than the host tissue of unfed corals (−0.67‰ ± 0.05 respectively) (Figure 2).

Thermal stress (30°C) induced a significant bleaching in unfed colonies (t-test, p-value = .0016), with a 50% reduction in symbiont

TABLE 1 Micronutrient concentrations (μg/g dry weight) in symbionts and host tissue of fed and unfed *S. pistillata* maintained under normal (25°C) and thermal stress (30°C) conditions

	Higher concentrations in fed symbionts at 25°C			Lower concentrations in fed symbionts at 25°C								
	Mn	Fe	Mg	Zn	Sr	As	Ba	Ca	B	Cu	δ^{65}Cu (‰)	δ^{66}Zn (‰)
Symbionts 25°C												
Fed	6.12*	81.73	659.15	156.61*	160.35*	4.48	0.59*	12.02*	12.86*	14.02*	−0.70*	0.36*
SD	1.22	13.89	168.28	23.70	64.89	0.86	0.17	4.72	2.27	3.13	0.18	0.04
Symbionts 25°C												
Unfed	0.22*	45.83*	275.15*	198.14*	358.77*	10.77	1.22*	23.39*	16.24*	16.76*	−0.75*	0.46
SD	0.25	4.89	58.82	31.84	94.19	4.07	0.61	8.55	4.79	1.38	0.09	0.03
Symbionts 30°C												
Fed	1.19*	83.61	810.45	209.40*	1,992*	5.99	2.98*	96,242*	60.01*	3.56*	0.25*	0.56*
SD	0.33	35.15	132.33	20.13	840.41	1.17	1.18	73,835	8.28	0.93	0.11	0.03
Symbionts 30°C												
Unfed	2.32*	100.84*	864.49*	111.33*	3,984*	6.48	4.89*	116,904*	59.53*	3.57*	0.22*	0.54
SD	1.52	57.38	360.29	72.34	1,975	3.91	2.16	65,108	25.66	1.40	0.09	0.05
Host 25°C												
Fed	0.07*	4.22*	924.45*	11.87*	8.02*	1.83*	0.04	0.73*	3.02*	6.59	−0.42*	0.35*
SD	0.07	0.74	178.86	2.46	0.67	0.28	0.01	0.05	1.25	7.52	0.12	0.02
Host 25°C												
Unfed	0.04	3.63	881.99	13.14*	9.24*	1.74*	0.09	0.80*	2.62*	3.55*	−0.67*	0.56
SD	0.08	0.44	273.63	1.68	3.59	0.27	0.10	0.25	1.07	0.19	0.05	0.02
Host 30°C												
Fed	0.35*	11.11*	5,670*	31.24*	46.62*	3.32*	0.19	3,581*	16.63*	1.36	0.38*	0.56*
SD	0.10	2.44	2,002	3.37	8.49	1.36	0.18	583.86	4.53	0.30	0.18	0.02
Host 30°C												
Unfed	0.10	4.45	1,360	6.28*	27.06*	3.21*	0.04	1,393*	5.84*	0.63*	0.31*	0.52
SD	0.03	2.06	461.09	0.74	3.51	1.29	0.01	446.35	1.79	0.31	0.12	0.08

Data are mean and standard deviation (*SD*) of five samples per condition.
*Represents significant differences in micronutrient concentrations between the two temperature conditions for both symbionts and host under fed or unfed conditions.

density (Figure 2). On the contrary, it had no effect on the symbiont density of fed colonies, which also presented two times more symbionts (Figure 2). Thermal stress significantly changed the micronutrient concentrations (Tables 1, 2 and S2, S3) of the symbiotic association. There was a significant increase of Sr, Ca, Zn and B concentrations in both symbionts and host of fed and unfed colonies (Tables 1 and 2). High temperature also significantly increased Mg concentrations in fed host tissue and unfed symbionts, Ba in fed and unfed symbionts, as well as Mn in the host tissue of fed corals (Tables 2, S2, S3). On the contrary, the Cu content of fed and unfed colonies was significantly decreased (Table 2). Finally, thermal stress significantly increased the δ^{65}Cu and δ^{66}Zn values of both host and symbionts, independently of the feeding status (Figure 2).

The binary plot of Figure 3a shows that there was an overall increase in both the δ^{65}Cu and δ^{66}Zn values with thermal stress in corals and symbionts. The other binary plots performed with micronutrient concentrations (Figure 3b–f) exhibit two thermal stress patterns on fed and unfed coral colonies: data corresponding to fed and unfed host or fed and unfed symbionts are tightly clustered at 25°C, suggesting that at this temperature there is no effect of the dietary regime. The same pattern is observed for all symbionts at 30°C, suggesting that they obtain the same amount of micronutrients from their respective fed and unfed hosts. On the contrary, micronutrient concentrations in the host show a distillation process at 30°C, associated to a depletion in unfed hosts compared to fed ones (red arrows bleaching, Figure 3b–f). The amplitude by which hosts are depleted increases as the micronutrient concentrations decrease.

4 | DISCUSSION

Understanding the nutritional requirements of scleractinian corals is critical to assess their health status and predict how reefs will change in response to rising seawater temperatures (Connolly, Lopez-Yglesias, & Anthony, 2012; Ferrier-Pagès et al., 2010). The main finding of this study is that heterotrophic feeding brings

TABLE 2 Results of the two factors ANOVA testing the effects of temperature and feeding on the nutrient concentrations and isotopic signatures

	Symbionts			Tissue		
	df	*p*	*F*	*df*	*p*	*f*
Manganese (Mn)						
Feeding	1	**.0010**	17.27	1	**.0010**	16.04
Temperature	1	**.0273**	6.07	1	**.0002**	22.89
Feeding × temperature	1	**<.001**	61.84	1	**.0075**	9.36
Error	14					
Iron (Fe)						
Feeding	1	**.0467**	4.65	1	**.0004**	20
Temperature	1	**.0004**	19.61	1	**.0003**	21.75
Feeding × temperature	1	**<.0001**	65.32	1	**.0044**	10.95
Error	16			16		
Magnesium (Mg)						
Feeding	1	.3671	0.86	1	**.0014**	14.84
Temperature	1	**<.0001**	48	1	**<.0001**	43.72
Feeding × temperature	1	**<.0001**	28.43	1	**.0039**	11.38
Error	16			16		
Zinc (Zn)						
Feeding	1	.0419	4.89	1	**<.0001**	45.67
Temperature	1	.2934	1.18	1	.4327	0.64
Feeding × temperature	1	**<.0001**	30.4	1	**<.0001**	38.65
Error	16			16		
Strontium (Sr)						
Feeding	1	**.0105**	8.39	1	**.0005**	18.89
Temperature	1	**<.0001**	90.03	1	**<.0001**	119.91
Feeding × temperature	1	.3487	0.93	1	**.0002**	22.85
Error	16			16		
Arsenic (As)						
Feeding	1	**.0048**	10.7	1	.5212	0.43
Temperature	1	.6682	0.17	1	**.0008**	18.83
Feeding × temperature	1	.1279	2.58	1	.6728	0.19
Error	16			16		
Barium (Ba)						
Feeding	1	**.0021**	13.49	1	.5284	0.18
Temperature	1	**<.0001**	52.96	1	.2393	0.34
Feeding × temperature	1	**.0438**	4.79	1	**.0357**	5.66
Error	16			16		
Calcium (Ca)						
Feeding	1	**.0223**	7.02	1	**.0075**	8.75
Temperature	1	**<.0001**	744.93	1	**<.0001**	650.5
Feeding × temperature	1	.82	0.05	1	**.0035**	12.11
Error	11			16		
Boron (B)						
Feeding	1	**.0052**	10.43	1	**.0042**	11.15
Temperature	1	**<.0001**	132.15	1	**<.0001**	56.67
Feeding × temperature	1	**.0294**	5.71	1	**.0275**	5.89

(Continues)

TABLE 2 (Continued)

	Symbionts			Tissue		
	df	*p*	*F*	*df*	*p*	*f*
Error	16			16		
Copper (Cu)						
Feeding	1	**.0336**	5.4	1	.2796	1.25
Temperature	1	**<.0001**	222.68	1	**.0286**	5.78
Feeding × temperature	1	.141	2.4	1	.5027	0.47
Error	16			16		
δ^{65}Cu						
Feeding	1	.8399	0.04	1	**.0455**	4.7
Temperature	1	**<.0001**	72.23	1	**<.0001**	44.26
Feeding × temperature	1	.8398	0.04	1	.3745	0.83
Error	16			16		
δ^{66}Zn						
Feeding	1	.6455	0.22	1	.5186	0.44
Temperature	1	**<.0001**	33.11	1	**<.0001**	103.31
Feeding × temperature	1	.1159	2.76	1	**.0331**	5.44
Error	16			16		

Analyses were performed with five replicates per condition. Significant differences are in bold.

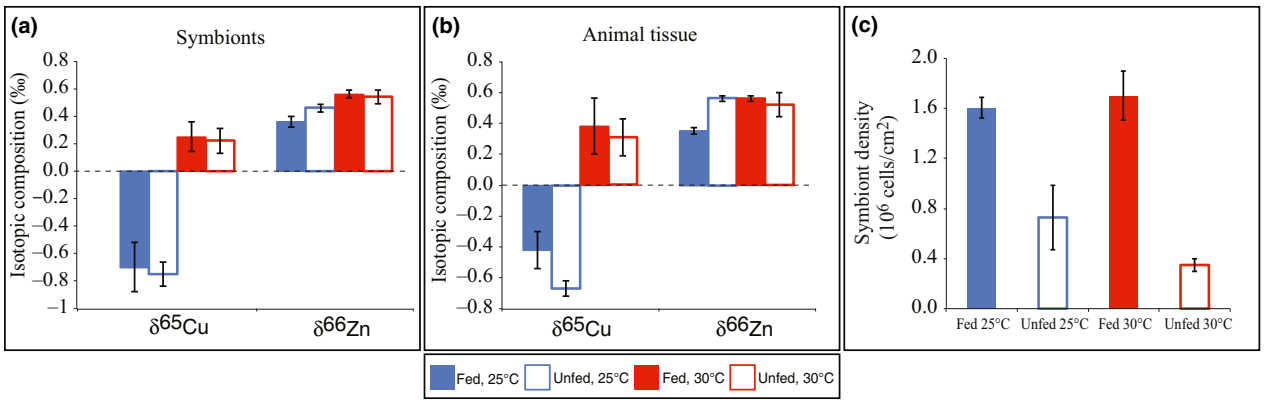

FIGURE 2 Isotopic signature of copper (δ^{65}Cu) and zinc (δ^{66}Zn) in (a) symbionts and (b) host tissue of colonies maintained fed and unfed at 25°C or 30°C; (c) Symbiont density (10^6 cell/cm^2) (data are mean and standard deviation of 5 samples per experimental conditions)

essential micronutrients to corals, which are mainly accumulated in the symbionts, and help avoid thermal stress damages and subsequent bleaching. During thermal stress, symbionts retain micronutrients at the expense of the coral host, thus being more parasites than symbionts. We also demonstrate a significant disruption in the Ca, Mg, Sr and B homeostasis in coral tissue during thermal stress, as well as a significant increase in the δ^{65}Cu and δ^{66}Zn values of coral host and symbionts. These isotopic compositions thus constitute good proxies for thermal stress in corals.

4.1 | Effect of the dietary regime at 25°C

Symbionts were the main sink for micronutrients within the symbiotic association (Figure 1), although these nutrients were provided to corals as particulate organic food, first digested by the animal. This observation is contrary to the usual view that symbionts are the main food suppliers of the symbiotic association, and provides one of the rare evidence of inverse nutrient translocation, from the animal host to the symbionts (Piniak et al., 2003; Tremblay et al., 2015). Although the above studies showed that symbionts profited from heterotrophic macronutrients (carbon, nitrogen) entering the symbiotic association, the transfer was restricted to less than 20% of the total gain, against 100% in this study.

Plankton feeding significantly increased, in symbiont cells, the concentrations of three main micronutrients, namely Mn, Fe and Mg (Table 1). Among other functions, Mn, Fe and Mg are all involved in the composition of antioxidant enzymes (Krueger et al., 2015). These enzymes, such as catalases, peroxidases and Fe/Mn or Mn-superoxide dismutases (SOD), are present in *Symbiodinium* (Lin et al., 2015; Zhang, Zhuang, Gill, & Lin, 2013), and are used to scavenge reactive

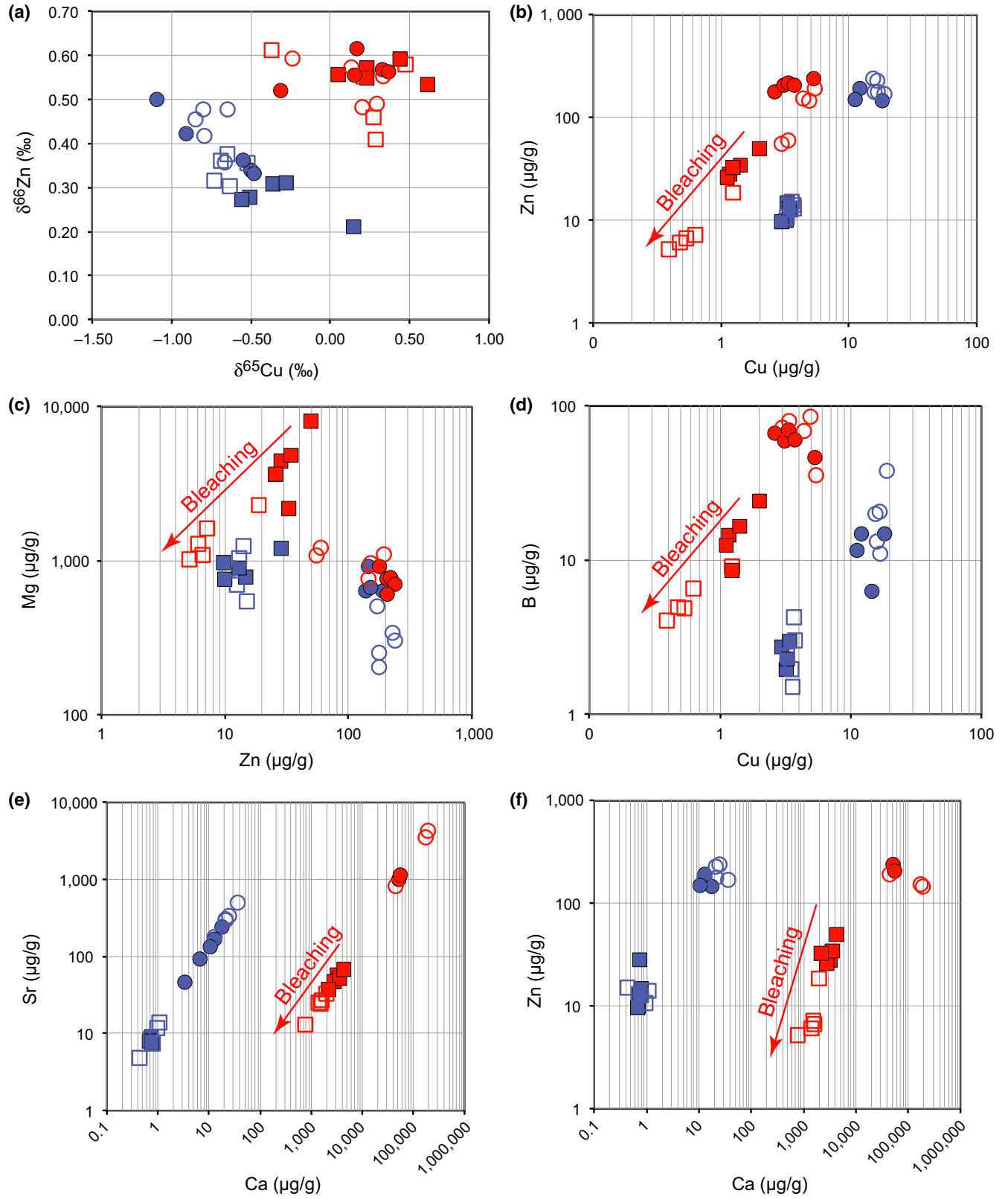

FIGURE 3 Relationship between the δ^{65}Cu and δ^{66}Zn values, or between the concentration (µg/g) in Cu and Zn, Mg and Zn, B and Cu, Ba and Ca, Zn and Ca (n = 5 samples for each experimental condition). Open circles and squares represent unfed symbionts and host tissue at 25°C (blue) or 30°C (red) respectively. Filled circles and squares represent fed symbionts and host tissue at 25°C (blue) or 30°C (red) respectively. The arrow indicates the direction of the distillation process during bleaching

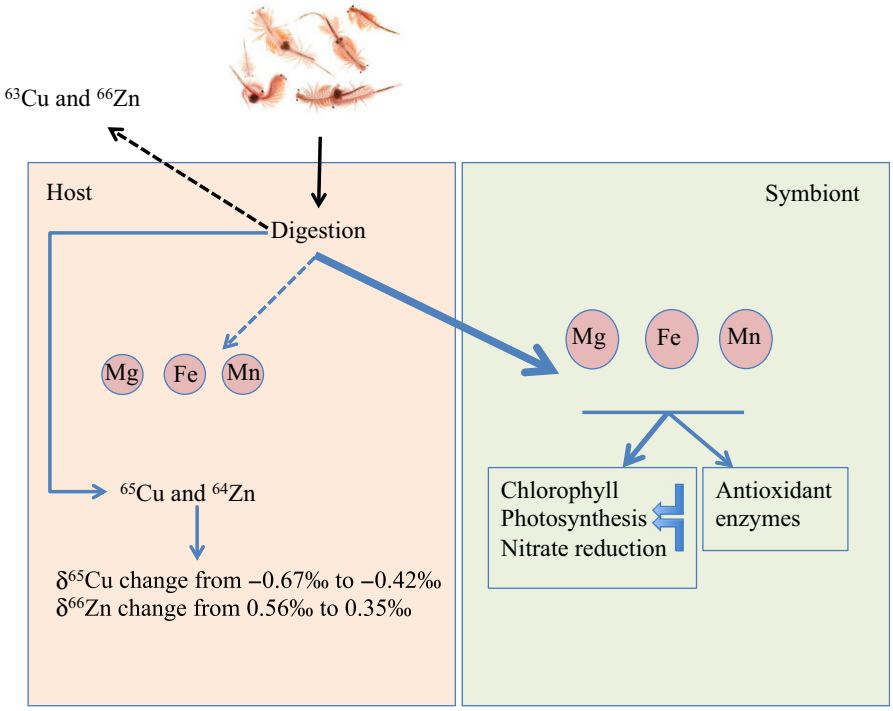

FIGURE 4 Heterotrophic supply of micronutrients within the coral-dinoflagellate association. Zooplankton predation increases the amount of Mg, Mn and Fe in symbionts. These metals are involved in photosynthesis processes, in nitrate reduction and in the structure of antioxidant enzymes. Prey digestion preferentially releases light copper isotope (i.e. ^{63}Cu) and inversely heavy zinc isotope (^{66}Zn), increasing the δ^{65}Cu signature and decreasing the δ^{66}Zn signature of coral tissue. Blue arrows: positive effect

oxygen species (ROS) continuously produced through photosynthesis and over-produced during thermal stress (Weis, 2008). Mn and Fe also play a major role in photosynthesis, nitrate reduction, as well as in chlorophyll and amino acid synthesis (Twining & Baines, 2013). This involvement of Fe and Mn in photosynthetic processes is one of the explanations why symbiont density, chlorophyll content, and photosynthetic rates are significantly enhanced in heterotrophically fed coral colonies compared to unfed ones, both in normal growth and stress conditions (this study and reviewed in Houlbrèque & Ferrier-Pagès, 2009). On the contrary, a lack of Fe during thermal stress increases the bleaching susceptibility of corals (Shick et al., 2011). Overall, these results highlight the importance of Fe and other key micronutrient availability for coral photosynthesis and health. Whereas concentrations of Fe, Mn, Mg were enhanced in fed symbionts under normal growth conditions, concentrations of Ca and Sr, which are main components of coral skeletons, were significantly decreased (Table 1). Such changes may be linked to a higher translocation of these elements to the skeleton, since fed corals present higher calcification rates than unfed corals (Houlbrèque & Ferrier-Pagès, 2009). The schematic diagram of Figure 4 summarizes the findings observed in this study and the potential role of metals in symbionts, under normal growth conditions of *S. pistillata*.

The δ^{65}Cu and δ^{66}Zn values were significantly different between fed and unfed hosts and symbionts (Figure 2), suggesting, for the first time, that corals fractionate Cu and Zn isotopes depending on their dietary regime. The higher δ^{65}Cu values in fed colonies is linked to the consumption of Cu in the form of particulate organic matter, whereas unfed colonies only rely on the uptake of dissolved inorganic Cu by the symbionts. The δ^{65}Cu signature in fed corals indeed follows the rule that organic matter is enriched in the heavier Cu isotope compared to dissolved inorganic Cu (Petit et al., 2013). The lower δ^{66}Zn signature of fed compared to unfed colonies is also in agreement with the observation that carnivores are slightly ^{66}Zn-depleted relative to herbivores (Jaouen et al., 2016). Overall, the significant effect of feeding on the δ^{66}Zn and δ^{65}Cu signatures demonstrates that metal isotopes represent useful proxies to trace nutrient flows within a symbiotic association, although they have poorly been studied in marine food webs in general (Jaouen et al., 2016).

4.2 | Effect of thermal stress

After 3 weeks of thermal stress, which induced bleaching in unfed corals (Figure 2), significant changes occurred in micronutrient concentrations and Cu-Zn isotopic compositions of symbionts and host tissue under both fed and unfed conditions. We observed a clear increase in the δ^{65}Cu and δ^{66}Zn values of both hosts and symbionts (Figure 3a). Such isotopic variations can be related to an increase in reactive oxygen species (ROS) generated by thermal stress in coral tissue (Cunning & Baker, 2013). As light isotopes create weaker links with molecules compared to heavy isotopes (Schauble, 2004), these bonds are more easily disrupted by ROS (Demidov, 2007; Shchepinov & Pestov, 2010). Light isotopes will thus preferentially be released in the medium. Although this assumption still needs to be verified, we can already suggest that δ^{65}Cu and δ^{66}Zn signatures represent good proxies for thermal stress in corals. In addition, the correlation which existed between δ^{65}Cu and δ^{66}Zn at 25°C was lost at 30°C (Figure 3), suggesting that animals and symbionts were not in equilibrium any more at 30°C.

For all corals, thermal stress also induced a very large increase of the Mg, Sr, Ca and B concentrations compared to normal growth conditions, in particular in symbionts of unfed colonies. Although

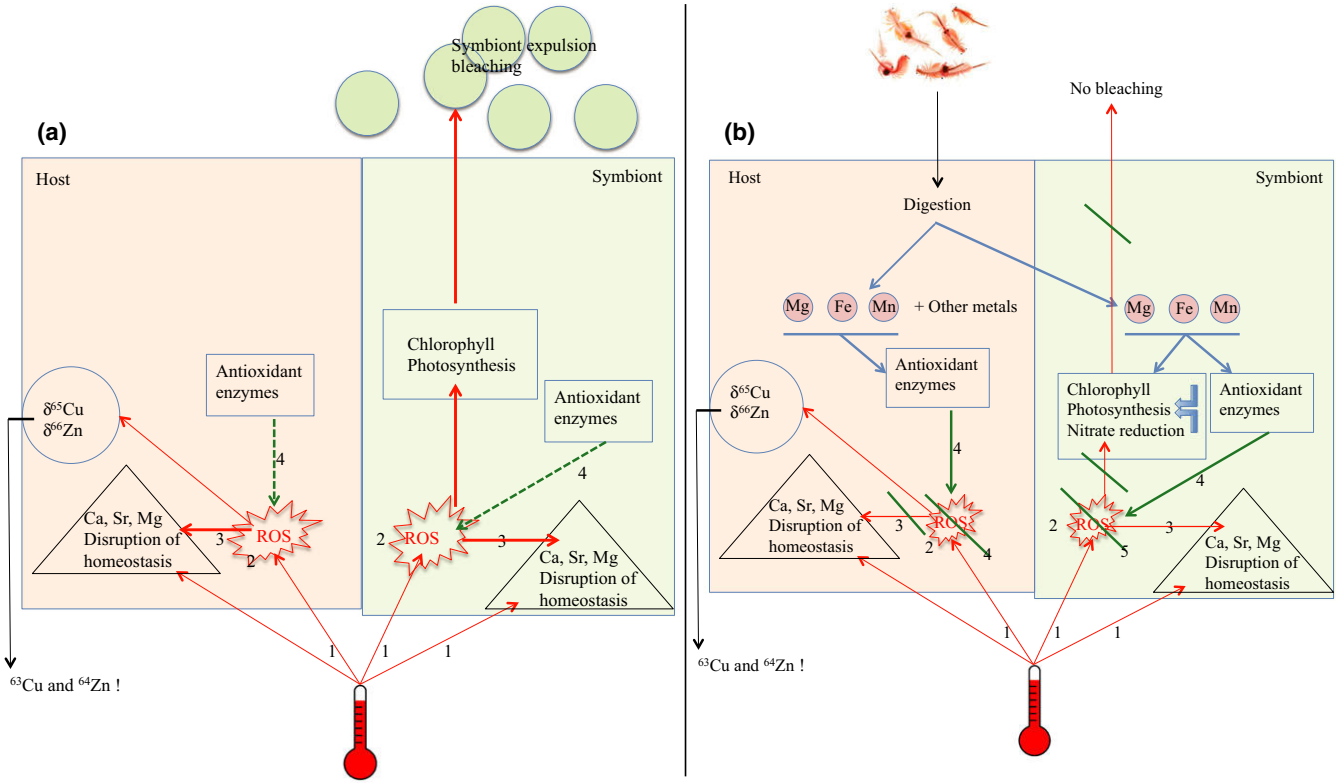

FIGURE 5 Schematic diagram summarizing the effect of thermal stress on micronutrient concentrations in unfed (a) and fed (b) corals. Thermal stress (1) increases ROS (reactive oxygen species) in coral tissue (2), and induces the disruption of Ca, Sr, Mg and B homeostasis (3). In unfed corals (a), micronutrient concentrations and antioxidant enzymes are not produced in sufficient amount to significantly reduce ROS (4). Photosynthesis is impaired and symbionts are expulsed (bleaching). In fed corals (b), feeding increases the amount of micronutrients in host tissue and symbionts. Antioxidant enzymes are produced in sufficient amount to significantly reduce ROS (4). Photosynthesis is not impaired and symbionts are not expulsed (no bleaching). Red arrows: negative effect, green arrows: positive effect

such changes have never been investigated in corals, an increase in intracellular Ca concentration has been monitored in insects (Teets, Yi, Lee, & Denlinger, 2013), chicken lymphocytes (Han et al., 2010) or terrestrial plants (Zhu, 2001) during thermal stress, whereas an increase in Mg was observed in the shrimp *Crangon crangon* (Sartoris & Pörtner, 1997). Genomic studies, which have investigated the molecular basis of cnidarian bleaching, also suggested that Ca homeostasis was disrupted in heat-stressed corals (DeSalvo et al., 2008; Levy et al., 2016; Rodriguez-Lanetty, Harii, & Hoegh-Guldberg, 2009). Finally, Dishon et al. (2015) demonstrated a decline of $\delta^{11}B$ as a result of coral bleaching, likely due, according to our results, to the observed large increase in B concentration, which should have changed the intracellular pH. All these micronutrients play important cellular roles. Ca is an intracellular messenger, whereas Mg has a protective role against oxidative damage (Freedman et al., 1992; Sartoris & Pörtner, 1997), which suggests that the significant Mg increase in coral cells followed the temperature-induced ROS production (Weis, 2008). Finally, B is needed, among others, for membrane structural integrity and carbohydrate metabolism (reviewed in Pilbeam & Kirkby, 1983), two important processes in corals.

Despite the large internal changes induced by thermal stress, mixotrophic corals (fed with artemia) did not bleach while autotrophic corals did. The lack of bleaching, as well as the maintenance of high rates of photosynthesis and calcification in mixotrophic corals have been observed several times in previous studies (Borell & Bischof, 2008; Connolly et al., 2012; Ferrier-Pagès et al., 2010). The binary plots of micronutrient concentrations in fed and unfed coral colonies (Figure 3b–f) highlight a new mechanism by which heterotrophy sustains coral metabolism during thermal stress, e.g. via the supply of essential micronutrients to the host and symbionts. These plots show similar micronutrient concentrations in symbionts of both fed and unfed colonies during thermal stress. In other words, symbionts sequestered the same amount of nutrients irrespective of the feeding status of their host. As micronutrients are mostly translocated from the host to the symbionts, this led to two different conditions in host tissue depending on the feeding status of the colonies. In fed corals, heterotrophy supplied enough micronutrients to the host to sustain symbiont's needs and no bleaching is observed. In unfed corals, symbiont repletion lead to a significant depletion of micronutrients in host tissue (Figure 3b–f), and a cost for the symbiotic association, which underwent bleaching and nutrient starvation. The amplitude by which hosts were depleted increased as the micronutrient concentrations decreased. These results thus demonstrate the significant effect of feeding in providing essential trace and major elements to the animals during thermal stress. The significant bleaching in unfed colonies further suggests

that, contrary to fed corals, micronutrient concentrations in unfed host tissue were not sufficient to sustain high densities of symbionts. Finally, they also suggest that thermal stress has promoted symbiont parasitism in unfed corals. A similar selfish behaviour of symbionts during thermal stress has very recently been observed for macronutrients (Baker, Freeman, Wong, Fogel, & Knowlton, 2018). Figure 5 summarizes the findings and hypotheses on the role of metals in coral bleaching.

In summary, our results indicate that the δ^{65}Cu and δ^{66}Zn values represent good proxies for stress in corals. They also show that heterotrophy and thermal stress induce significant changes in micronutrient concentrations and isotopic signatures of the scleractinian coral *Stylophora pistillata*. The results obtained first reveal that symbionts are the major sink for trace elements in the symbiotic association, and accumulate Mn, Mg and Fe from the heterotrophic feeding of the host. They also demonstrate that bleaching is exacerbated by the shortage of trace elements in coral tissue (especially Cu, Zn, B, Mg, Ca) and that heterotrophic feeding can supply these essential metals to corals. Such results thus highlight a new way by which heterotrophy contributes to coral resistance to bleaching, and have major implications for the resilience of coral reefs under threat of global change.

ACKNOWLEDGEMENTS

The authors thank Cecile Rottier and Magali Boussion for help in coral extraction. We also thank two reviewers, and Prof. Oren Levy, for their helpful comments, which have greatly improved the manuscript. This work is part of RTPI Nutress (Réseau Thématique Pluridisciplinaire International sur l'Ecophysiologie de la Nutrition).

ORCID

Christine Ferrier-Pagès http://orcid.org/0000-0002-0357-4486

REFERENCES

Anthony, K. R. N. (2000). Enhanced particle-feeding capacity of corals on turbid reefs (Great Barrier Reef, Australia). *Coral Reefs*, *19*(1), 59–67. https://doi.org/10.1007/s003380050227

Baker, D. M., Freeman, C. J., Wong, J. C. Y., Fogel, M. L., Knowlton, N. (2018). Climate change promotes parasitism in a coral symbiosis. *The ISME Journal*, *12* (3), 921–930. https://doi.org/10.1038/s41396-018-0046-8

Balter, V., da Costa, A. N., Bondanese, V. P., Jaouen, K., Lamboux, A., Sangrajrang, S., … Heynaud, P. (2015). Natural variations of copper and sulfur stable isotopes in blood of hepatocellular carcinoma patients. *Proceedings of the National Academy of Sciences*, *112*(4), 982–985. https://doi.org/10.1073/pnas.1415151112

Barnes, D. J., Taylor, R. B., & Lough, J. M. (1995). On the inclusion of trace materials into massive coral skeletons. Part II: Distortions in skeletal records of annual climate cycles due to growth processes. *Journal of Experimental Marine Biology and Ecology*, *194*(2), 251–275. https://doi.org/10.1016/0022-0981(95)00091-7

Bastidas, C., & Garcıa, E. (1999). Metal content on the reef coral *Porites astreoides*: An evaluation of river influence and 35 years of chronology. *Marine Pollution Bulletin*, *38*(10), 899–907. https://doi.org/10.1016/S0025-326X(99)00089-2

Borell, E. M., & Bischof, K. (2008). Feeding sustains photosynthetic quantum yield of a scleractinian coral during thermal stress. *Oecologia*, *157*(4), 593. https://doi.org/10.1007/s00442-008-1102-2

Chen, S., Liu, Y., Hu, J., Zhang, Z., Hou, Z., Huang, F., & Yu, H. (2016). Zinc isotopic compositions of NIST SRM 683 and Whole-Rock reference materials. *Geostandards and Geoanalytical Research*, *40*(3), 417–432. https://doi.org/10.1111/j.1751-908X.2015.00377.x

Connolly, S. R., Lopez-Yglesias, M. A., & Anthony, K. R. (2012). Food availability promotes rapid recovery from thermal stress in a scleractinian coral. *Coral Reefs*, *31*(4), 951–960. https://doi.org/10.1007/s00338-012-0925-9

Costas-Rodríguez, M., Van Heghe, L., & Vanhaecke, F. (2014). Evidence for a possible dietary effect on the isotopic composition of Zn in blood via isotopic analysis of food products by multi-collector ICP-mass spectrometry. *Metallomics*, *6*, 139–146. https://doi.org/10.1039/C3MT00244F

Cunning, R., & Baker, A. C. (2013). Excess algal symbionts increase the susceptibility of reef corals to bleaching. *Nature Climate Change*, *3*(3), 259–262. https://doi.org/10.1038/nclimate1711

David, C. P. (2003). Heavy metal concentrations in growth bands of corals: A record of mine tailings input through time (Marinduque Island, Philippines). *Marine Pollution Bulletin*, *46*(2), 187–196. https://doi.org/10.1016/S0025-326X(02)00315-6

Davy, S. K., Allemand, D., & Weis, V. M. (2012). Cell biology of cnidarian-dinoflagellate symbiosis. *Microbiology and Molecular Biology Reviews*, *76*(2), 229–261. https://doi.org/10.1128/MMBR.05014-11

Demidov, V. V. (2007). Heavy isotopes to avert ageing? *Trends in Biotechnology*, *25*(9), 371–375. https://doi.org/10.1016/j.tibtech.2007.07.007

DeSalvo, M. K., Voolstra, C. R., Sunagawa, S., Schwarz, J. A., Stillman, J. H., Coffroth, M. A., … Medina, M. (2008). Differential gene expression during thermal stress and bleaching in the Caribbean coral *Montastraea faveolata*. *Molecular Ecology*, *17*(17), 3952–3971. https://doi.org/10.1111/j.1365-294X.2008.03879.x

Dishon, G., Fisch, J., Horn, I., Kaczmarek, K., Bijma, J., Gruber, D. F., … Tchernov, D. (2015). A novel paleo-bleaching proxy using boron isotopes and high-resolution laser ablation to reconstruct coral bleaching events. *Biogeosciences*, *12*(19), 5677–5687. https://doi.org/10.5194/bg-12-5677-2015

Douglas, A. E. (1998). Nutritional interactions in insect-microbial symbioses: Aphids and their symbiotic bacteria Buchnera. *Annual Review of Entomology*, *43*(1), 17–37. https://doi.org/10.1146/annurev.ento.43.1.17

Fallon, S. J., White, J. C., & McCulloch, M. T. (2002). Porites corals as recorders of mining and environmental impacts: Misima Island, Papua New Guinea. *Geochimica et Cosmochimica Acta*, *66*(1), 45–62. https://doi.org/10.1016/S0016-7037(01)00715-3

Ferrier-Pagès, C., Houlbrèque, F., Wyse, E., Richard, C., Allemand, D., & Boisson, F. (2005). Bioaccumulation of zinc in the scleractinian coral *Stylophora pistillata*. *Coral Reefs*, *24*(4), 636–645. https://doi.org/10.1007/s00338-005-0045-x

Ferrier-Pagès, C., Rottier, C., Beraud, E., & Levy, O. (2010). Experimental assessment of the feeding effort of three scleractinian coral species during a thermal stress: Effect on the rates of photosynthesis. *Journal of Experimental Marine Biology and Ecology*, *390*(2), 118–124. https://doi.org/10.1016/j.jembe.2010.05.007

Freedman, A. M., Mak, I. T., Stafford, R. E., Dickens, B. F., Cassidy, M. M., Muesing, R. A., & Weglicki, W. B. (1992). Erythrocytes from magnesium-deficient hamsters display an enhanced susceptibility to oxidative stress. *American Journal of Physiology*, *262*, C1371–C1375. https://doi.org/10.1152/ajpcell.1992.262.6.C1371

Garçon, M., Sauzéat, L., Carlson, R. W., Shirey, S. B., Simon, M., Balter, V., & Boyet, M. (2017). Nitrile, latex, neoprene and vinyl gloves: A primary source of contamination for trace element and zn isotopic analyses in geological and biological samples. *Geostandards and Geoanalytical Research*, *41*(3), 367–380.

Grottoli, A. G., Rodrigues, L. J., & Palardy, J. E. (2006). Heterotrophic plasticity and resilience in bleached corals. *Nature*, *440*(7088), 1186–1189. https://doi.org/10.1038/nature04565

Han, A. Y., Zhang, M. H., Zuo, X. L., Zheng, S. S., Zhao, C. F., Feng, J. H., & Cheng, C. (2010). Effect of acute heat stress on calcium concentration, proliferation, cell cycle, and interleukin-2 production in splenic lymphocytes from broiler chickens. *Poultry Science*, *89*(10), 2063–2070. https://doi.org/10.3382/ps.2010-00715

Harland, A. D., & Nganro, N. R. (1990). Copper uptake by the sea anemone *Anemonia viridis* and the role of zooxanthellae in metal regulation. *Marine Biology*, *104*(2), 297–301. https://doi.org/10.1007/BF01313271

Houlbrèque, F., & Ferrier-Pagès, C. (2009). Heterotrophy in tropical scleractinian corals. *Biological Reviews*, *84*(1), 1–17. https://doi.org/10.1111/j.1469-185X.2008.00058.x

Hughes, A. D., & Grottoli, A. G. (2013). Heterotrophic compensation: A possible mechanism for resilience of coral reefs to global warming or a sign of prolonged stress? *PLoS ONE*, *8*(11), e81172. https://doi.org/10.1371/journal.pone.0081172

Hughes, A. D., Grottoli, A. G., Pease, T. K., & Matsui, Y. (2010). Acquisition and assimilation of carbon in non-bleached and bleached corals. *Marine Ecology Progress Series*, *420*, 91–101. https://doi.org/10.3354/meps08866

Jaouen, K., Pons, M. L., & Balter, V. (2013). Iron, copper and zinc isotopic fractionation up mammal trophic chains. *Earth and Planetary Science Letters*, *374*, 164–172. https://doi.org/10.1016/j.epsl.2013.05.037

Jaouen, K., Szpak, P., & Richards, M. P. (2016). Zinc isotope ratios as indicators of diet and trophic level in arctic marine mammals. *PLoS ONE*, *11*(3), e0152299. https://doi.org/10.1371/journal.pone.0152299

Krueger, T., Fisher, P. L., Becker, S., Pontasch, S., Dove, S., Hoegh-Guldberg, O., … Davy, S. K. (2015). Transcriptomic characterization of the enzymatic antioxidants FeSOD, MnSOD, APX and KatG in the dinoflagellate genus *Symbiodinium*. *BMC Evolutionary Biology*, *15*(1), 48. https://doi.org/10.1186/s12862-015-0326-0

Levy, O., Karako-Lampert, S., Ben-Asher, H. W., Zoccola, D., Pagès, G., & Ferrier-Pagès, C. (2016). Molecular assessment of the effect of light and heterotrophy in the scleractinian coral *Stylophora pistillata*. *Proceedings Royal Society B*, *283*, 20153025. https://doi.org/10.1098/rspb.2015.3025

Lin, S., Cheng, S., Song, B., Zhong, X., Lin, X., Li, W., … Cai, M. (2015). The *Symbiodinium* Kawaguti genome illuminates dinoflagellate gene expression and coral symbiosis. *Science*, *350*, 691–694. https://doi.org/10.1126/science.aad0408

Maréchal, C. N., Télouk, P., & Albarède, F. (1999). Precise analysis of copper and zinc isotopic compositions by plasma-source mass spectrometry. *Chemical Geology*, *156*(1), 251–273. https://doi.org/10.1016/S0009-2541(98)00191-0

Moberg, F., & Folke, C. (1999). Ecological goods and services of coral reef ecosystems. *Ecological Economics*, *29*(2), 215–233. https://doi.org/10.1016/S0921-8009(99)00009-9

Muscatine, L., Falkowski, P. G., Porter, J. W., & Dubinsky, Z. (1984). Fate of photosynthetic fixed carbon in light-and shade-adapted colonies of the symbiotic coral *Stylophora pistillata*. *Proceedings of the Royal Society of London B: Biological Sciences*, *222*(1227), 181–202. https://doi.org/10.1098/rspb.1984.0058

Muscatine, L., & Porter, J. W. (1977). Reef corals: Mutualistic symbioses adapted to nutrient-poor environments. *BioScience*, *27*(7), 454–460. https://doi.org/10.2307/1297526

Norton, J. H., Shepherd, M. A., Long, H. M., & Fitt, W. K. (1992). The zooxanthellal tubular system in the giant clam. *The Biological Bulletin*, *183*(3), 503–506. https://doi.org/10.2307/1542028

Petit, J. C., Schäfer, J., Coynel, A., Blanc, G., Deycard, V. N., Derriennic, H., … Mattielli, N. (2013). Anthropogenic sources and biogeochemical reactivity of particulate and dissolved Cu isotopes in the turbidity gradient of the Garonne River (France). *Chemical Geology*, *359*, 125–135. https://doi.org/10.1016/j.chemgeo.2013.09.019

Pilbeam, D. J., & Kirkby, E. A. (1983). The physiological role of boron in plants. *Journal of Plant Nutrition*, *6*(7), 563–582. https://doi.org/10.1080/01904168309363126

Piniak, G. A., Lipschultz, F., & McClelland, J. (2003). Assimilation and partitioning of prey nitrogen within two anthozoans and their endosymbiotic zooxanthellae. *Marine Ecology Progress Series*, *262*, 125–136. https://doi.org/10.3354/meps262125

Reichelt-Brushett, A. J., & McOrist, G. (2003). Trace metals in the living and nonliving components of scleractinian corals. *Marine Pollution Bulletin*, *46*(12), 1573–1582. https://doi.org/10.1016/S0025-326X(03)00323-0

Richier, S., Furla, P., Plantivaux, A., Merle, P. L., & Allemand, D. (2005). Symbiosis-induced adaptation to oxidative stress. *Journal of Experimental Biology*, *208*(2), 277–285. https://doi.org/10.1242/jeb.01368

Rodriguez-Lanetty, M., Harii, S., & Hoegh-Guldberg, O. (2009). Early molecular responses of coral larvae to hyperthermal stress. *Molecular Ecology*, *18*(24), 5101–5114. https://doi.org/10.1111/j.1365-294X.2009.04419.x

Saffo, M. B. (1992). Coming to terms with a field: Words and concepts in symbiosis. *Symbiosis*, *14*(1–3), 17–31.

Sartoris, F. J., & Pörtner, H. O. (1997). Increased concentrations of haemolymph Mg2 + protect intracellular pH and ATP levels during temperature stress and anoxia in the common shrimp. *Journal of Experimental Biology*, *200*, 785–792.

Schauble, E. A. (2004). Applying stable isotope fractionation theory to new systems. *Reviews in Mineralogy and Geochemistry*, *55*(1), 65–111. https://doi.org/10.2138/gsrmg.55.1.65

Shchepinov, M. S., & Pestov, N. B. (2010). Isotope effect, essential diet components and prospects of aging retardation. *Russian Journal of General Chemistry*, *80* (7), 1514–1522. https://doi.org/10.1134/S1070363210070480

Shick, J. M., Iglic, K., Wells, M. L., Trick, C. G., Doyle, J., & Dunlap, W. C. (2011). Responses to iron limitation in two colonies of *Stylophora pistillata* exposed to high temperature: Implications for coral bleaching. *Limnology and Oceanography*, *56*(3), 813–828. https://doi.org/10.4319/lo.2011.56.3.0813

Sossi, P. A., Halverson, G. P., Nebel, O., & Eggins, S. M. (2014). Combined separation of Cu, Fe and Zn from rock matrices and improved analytical protocols for stable isotope determination. *Geostandards and Geoanalytical Research*, *39*(2), 129–149.

Teets, N. M., Yi, S. X., Lee, R. E., & Denlinger, D. L. (2013). Calcium signaling mediates cold sensing in insect tissues. *Proceedings of the National Academy of Sciences*, *110*(22), 9154–9159. https://doi.org/10.1073/pnas.1306705110

Tremblay, P., Gori, A., Maguer, J. F., Hoogenboom, M., & Ferrier-Pagès, C. (2016). Heterotrophy promotes the re-establishment of photosynthate translocation in a symbiotic coral after heat stress. *Scientific Reports*, *6*, 38112. https://doi.org/10.1038/srep38112

Tremblay, P., Grover, R., Maguer, J. F., Hoogenboom, M., & Ferrier-Pagès, C. (2014). Carbon translocation from symbiont to host depends on irradiance and food availability in the tropical coral Stylophora pistillata. *Coral Reefs*, *33*(1), 1–13. https://doi.org/10.1007/s00338-013-1100-7

Tremblay, P., Grover, R., Maguer, J. F., Legendre, L., & Ferrier-Pagès, C. (2012). Autotrophic carbon budget in coral tissue: A new 13C-based model of photosynthate translocation. *Journal of Experimental Biology*, *215*(8), 1384–1393. https://doi.org/10.1242/jeb.065201

Tremblay, P., Maguer, J. F., Grover, R., & Ferrier-Pagès, C. (2015). Trophic dynamics of scleractinian corals: Stable isotope evidence. *Journal of Experimental Biology*, *218*(8), 1223–1234. https://doi.org/10.1242/jeb.115303

Twining, B. S., & Baines, S. B. (2013). The trace metal composition of marine phytoplankton. *Annual Review of Marine Science*, *5*, 191–215. https://doi.org/10.1146/annurev-marine-121211-172322

Usher, K. M., Bergman, B., & Raven, J. A. (2007). Exploring cyanobacterial mutualisms. *Annual Review of Ecology, Evolution, and Systematics*, *38*, 255–273. https://doi.org/10.1146/annurev.ecolsys.38.091206.095641

Venn, A. A., Loram, J. E., & Douglas, A. E. (2008). Photosynthetic symbioses in animals. *Journal of Experimental Botany*, *59*(5), 1069–1080. https://doi.org/10.1093/jxb/erm328

Weis, V. M. (2008). Cellular mechanisms of Cnidarian bleaching: Stress causes the collapse of symbiosis. *Journal of Experimental Biology*, *211* (19), 3059–3066. https://doi.org/10.1242/jeb.009597

Yellowlees, D., Rees, T. A. V., & Leggat, W. (2008). Metabolic interactions between algal symbionts and invertebrate hosts. *Plant, Cell & Environment*, *31*(5), 679–694. https://doi.org/10.1111/j.1365-3040.2008.01802.x

Zhang, H., Zhuang, Y., Gill, J., & Lin, S. (2013). Proof that dinoflagellate spliced leader (DinoSL) is a useful hook for fishing dinoflagellate transcripts from mixed microbial samples: *Symbiodinium* kawagutii as a case study. *Protist*, *164*(4), 510–527. https://doi.org/10.1016/j.protis.2013.04.002

Zhu, J. K. (2001). Cell signaling under salt, water and cold stresses. *Current Opinion in Plant Biology*, *4*(5), 401–440. https://doi.org/10.1016/S1369-5266(00)00192-8

SUPPORTING INFORMATION

Additional Supporting Information may be found online in the supporting information tab for this article.

How to cite this article: Ferrier-Pagès C, Sauzéat L, Balter V. Coral bleaching is linked to the capacity of the animal host to supply essential metals to the symbionts. *Glob Change Biol*. 2018;00:1–13. https://doi.org/10.1111/gcb.14141

Par ailleurs, j'ai eu l'occasion de finaliser un projet de recherche en Archéologie commencé au cours d'un stage à Grenoble avec Catherine Chauvel (CNRS ISTerre, Grenoble) en 2014 et au cours duquel j'avais mesuré les compositions isotopiques en plomb (Pb) et en strontium (Sr) d'herminettes (outils archéologiques Polynésiens) pour caractériser les échanges inter- et intra-îles en Polynésie à l'époque du Moyen Âge (entre 600 et 1800 AD). Ces résultats ont mené à la publication d'un article scientifique en 2017 dans 'Journal of Archaeological Science'; article pour lequel j'ai contribué à l'écriture, l'interprétation des données et l'élaboration des figures.

ARTICLE

Combined geochemical and geochronological analyses of stone artefacts provide unambiguous evidence of intra- and inter-island interactions in Polynesia

*Hermann A., **Sauzéat L.**, Guillou H., Maury R.C., Chauvel C., Liorzou C., Conte E.*

(Published in Journal of Archaeological Science)

Pour citer ce papier: Hermann A., **Sauzéat L.**, Guillou H., Maury R.C., Chauvel C., Liorzou C., Conte E., 2017. *Combined geochemical and geochronological analyses of stone artefacts provide unambiguous evidence of intra- and inter-island interactions in Polynesia*. Journal of Archaeological Science: Reports 13, 75–87. doi:10.1016/j.jasrep.2017.03.024

Journal of Archaeological Science: Reports 13 (2017) 75–87

Contents lists available at ScienceDirect

Journal of Archaeological Science: Reports

journal homepage: www.elsevier.com/locate/jasrep

Combined geochemical and geochronological analyses of stone artefacts provide unambiguous evidence of intra- and inter-island interactions in Polynesia

Aymeric Hermann [a,b,*], Lucie Sauzéat [c], Hervé Guillou [d], René C. Maury [e], Catherine Chauvel [f], Céline Liorzou [g], Eric Conte [h,i]

[a] Department of Social Science, University of French Polynesia, 98702 Fa'a'ā, French Polynesia
[b] ArScAn, UMR 7041 (CNRS), Maison de l'Archéologie et de l'Ethnologie, 92023 Nanterre, France
[c] ISTerre, UMR 5275 (CNRS), Université Grenoble Alpes, 38000 Grenoble, France
[d] Laboratoire des Sciences du Climat et de L'Environnement, UMR8212, LSCE/IPSL, CEA-CNRS-UVSQ, Bat.12, Avenue de la Terrasse, 91198 Gif-Sur-Yvette, France
[e] Géosciences Océan, UMR 6538 (CNRS), Université de Bretagne Occidentale, 29280 Plouzané, France
[f] ISTerre, UMR 5275 (CNRS), Université Grenoble Alpes, 38000 Grenoble, France
[g] Géosciences Océan, UMR 6538 (CNRS), Université de Bretagne Occidentale, 29280 Plouzané, France
[h] CIRAP, University of French Polynesia, 98702 Fa'a'ā, French Polynesia
[i] UMR 7041 ArScAn, Maison de l'Archéologie et de l'Ethnologie, 92023 Nanterre, France

ARTICLE INFO

Article history:
Received 11 January 2017
Received in revised form 22 February 2017
Accepted 12 March 2017
Available online xxxx

Keywords:
Provenance studies
Geochemistry
Geochronology
Polynesia
Adzes
Voyaging

ABSTRACT

Stone tool geochemistry provides hard evidence for post-settlement voyaging and inter-island contacts in East Polynesia. This offers promising information on inter-community exchange networks that are not documented by ethnographic accounts. Drawing on "geochemical fingerprints", provenance studies have slowly integrated geological data in order to better constrain the origin of archaeological material. However, the occurrence of overlapping geochemical signatures within Polynesian islands can cause difficulties when attempting to differentiate sources. Identifying clear geochemical characteristics for each island is therefore critical for a comprehensive understanding of the interaction patterns in East Polynesian societies. In this paper, we combine major and trace element data with isotopes as well as ^{40}Ar-^{39}Ar ages to constrain the local procurement networks that were occurring on the island of Tupua'i (Austral-Cook chain). We also demonstrate that some Tupua'i archaeological material originated from Eiao Island (Marquesas chain) circa 2000 km north. This represents the first hard evidence for inter-island connections between the Austral and the Marquesas Archipelagos.

1. Introduction

The long-distance transfer of prestige goods was an important aspect of the mobility between Pacific islands societies before European contact (Green and Kirch, 1997; Weisler, 1997). Based on geochemical sourcing, it has been possible to identify exotic commodities in archaeological sites and therefore to document wide-scale inter-community interactions during and after the colonization period, in both the western Pacific and eastern Polynesia (see Hermann, 2015 for a review).

Geochemical analysis of stone artefacts has been increasingly used in the last 20 years in order to document inter-island and inter-archipelago transfers of stone tools in Central Eastern Polynesia (CEP), where long-distance interactions during the first few centuries after East Polynesian colonization have been widely documented (e.g. McAlister et al., 2014; Weisler and Kirch, 1996; Weisler, 1997, 1998, 2002; Weisler et al., 2016a). Ethnographic accounts do not provide information on long-distance exchange in East Polynesia because these interactions date from a remote period of history. Therefore, only a comprehensive and high-precision examination of stone artefacts involving all required geochemical and geochronological analysis can allow for a proper reconstruction of ancient interaction patterns in CEP.

Focusing on stone artefacts from several archaeological sites on Tupua'i Island (Austral-Cook chain), we present a detailed provenance

* Corresponding author at: BP 111-180, 98709 Mahina, Tahiti, French Polynesia.
E-mail address: aymeric.hermann@upf.pf (A. Hermann).

http://dx.doi.org/10.1016/j.jasrep.2017.03.024
2352-409X/

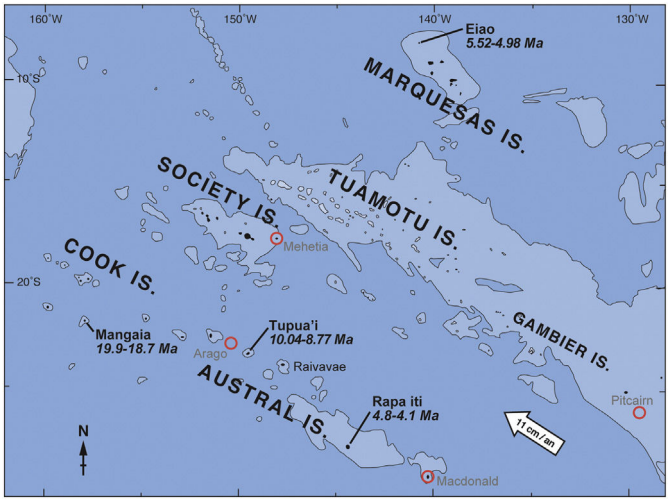

Fig. 1. Bathymetric map of Central Eastern Polynesia showing its linear island chains and the - 4000 m isobath. The names of the islands discussed in this paper (Tupua'i, Mangaia, Eiao, Rapa Iti) are in bold characters and their age spans in italics. Hotspot locations are shown as red empty circles. (For interpretation of the references to colour in this figure legend, the reader is referred to the web version of this article.)

analysis based on two specific aims: (1) documenting intra-island movement of raw material as a part of local procurement strategies and adze production processes, and (2) providing evidence for inter-island transfers of artefacts.

2. Geological setting and source discrimination in Polynesia

In CEP, provenance analyses of stone tools were first based on petrographic features (Weisler, 1993), then on major and trace element compositions (Mills et al., 2010; Kirch et al., 2012; Kahn et al., 2013; McAlister et al., 2014; Rolett et al., 2015; Walter and Sheppard, 1996; Weisler and Kirch, 1996; Weisler, 1998, 2002), and more recently on Sr, Nd and Pb isotopic ratios (Collerson and Weisler, 2007; Weisler et al., 2016a; Weisler and Woodhead, 1995; Woodhead and Weisler, 1997). Except for the above isotopic analyses, most sourcing studies have focused on quarry sites in order to trace the origin of archaeological artefacts. However, we argue here that provenance studies of stone artefacts must rely on the acquisition of wide and reliable geological data related to this specific geological setting, as most prehistoric quarries in Polynesian islands have yet to be identified. Further complicating matters, several Polynesian islands show similar geochemical characteristics, while others exhibit different but partly overlapping geochemical signatures (Chauvel et al., 1992; Chauvel et al., 2012; White and Duncan, 1996; Zindler and Hart, 1986). One must therefore examine the temporal and geochemical evolution of each island chain in order to constrain the origin of specific basaltic material.

The islands of CEP are distributed across four linear chains (Austral-Cook, Pitcairn-Gambier, Society and the Marquesas) spreading over a large part of the South Pacific Ocean due to the Pacific Plate motion towards the NW (Fig. 1). Corresponding hotspots are located underneath young volcanoes at the south-eastern tip of each archipelago. Over the last 20 years, a systematic program of detailed geological mapping, associating geochemical and age data, was conducted in French Polynesia by the National institute for geological survey (Bureau de Recherches Géologiques et Minières). This led to considerably better characterizations of intra- and inter-island petrologic, geochemical, and age variations in the Austral (Chauvel et al., 1997; Maury et al., 2013; Maury et al., 2014a), Gambier (Delavault et al., 2015), Society (Cordier et al., 2016; Guillou et al., 2005) and Marquesas Islands (Chauvel et al., 2012; Guillou et al., 2014; Maury et al., 2014b).

Major element compositions are variable both within a given island and between different islands. The total alkali/silica diagram (SiO_2 versus $K_2O + Na_2O$) provides a useful classification of igneous rocks, from mafic to felsic and from tholeiitic to silica-undersaturated, and these petrographic groups are often specific to volcanic edifices or periods of magma emplacement. TAS classification can be combined with TiO_2 versus MgO plots in order to identify geochemical variations within volcanic edifices, and therefore discriminate a number of localities as potential sources of rock supply.

Trace element variations can also be used to differentiate different geological units that share the same petrographic characteristics. As summarized by Dupuy et al. (1989), Polynesian lavas display selective enrichments in incompatible elements: alkali and alkali earth elements (K, Rb, Ba, Sr) as well as high field strength elements (Nb, Zr, Ti, Hf) and light rare earth elements (La, Ce, Nd). Consequently, trace element data combined with major element data can be used to assign artefacts to a geological source at a restricted geographical scale, typically within an island or a specific volcanic edifice.

Plume-related basalts have been documented as chemically and isotopically heterogeneous because of the dynamic evolution of the mantle over time (White and Duncan, 1996; Chauvel et al., 1992; Chauvel et al., 2012; Delavault et al., 2015). Four main geochemical mantle end-members, characterized by specific isotopic compositions, have been identified in CEP islands. The HIMU (High $^{238}U/^{204}Pb$) signature, characterized by low $^{87}Sr/^{86}Sr$ and very high $^{206}Pb/^{204}Pb$, is found in lavas from Ra'ivavae, Tupua'i, Rurutu and Mangaia. The EM (Enriched Mantle) signatures, defined by higher $^{87}Sr/^{86}Sr$ ratios and lower $^{143}Nd/^{144}Nd$, Nb/Th and Ta/La ratios (White and Duncan, 1996; Chauvel et al., 1992), are present in the source of Rarotonga and Pitcairn volcanics as EM1 (Enriched Mantle type I), while EM2 (Enriched Mantle type II) dominates that of most Society and Marquesas islands (Zindler and Hart, 1986; White and Duncan, 1996; Chauvel et al., 1992). Compared to EM2, EM1 shows even lower $^{87}Sr/^{86}Sr$ and $^{143}Nd/^{144}Nd$ ratios together with rather low $^{206}Pb/^{204}Pb$. The identification of such isotopic signatures provides obvious information for provenance analysis.

Moreover, most Polynesian archipelagos show correlations between island ages and corresponding distances to the presumed hotspot area located at the SE end of the volcanic chain (Delavault et al., 2015; Maury et al., 2013; Maury et al., 2014a, 2014b; Guillou et al., 2005; Guillou et al., 2014; Turner and Jarrard, 1982; Guillou et al., 1994). As a result, the general age progression along volcanic chains provides another variable that can be used for source discrimination. Hence our use of geochronological analyses to further constraint exotic sources and identifies the provenance of stone artefacts from archaeological contexts.

3. The study site: Tupua'i (Tubuai) island, Austral-Cook chain

Tupua'i (23°23′00″S, 149°27′00″W), together with Mangaia (Southern Cook chain), is well known for the unusual 'HIMU' isotopic signature of its lavas, which display very high $^{206}Pb/^{204}Pb$ ratios (Maury et al., 2013; Vidal et al., 1984). The island was mapped between 1989 and 1995 by the BRGM team (Maury et al., 1994; Maury et al., 2000; Maury et al., 2013). Three types of basalt rocks (alkali basalts, basanites and nephelinites) and three types of intermediate lavas (basanitic tephrites, tephrites and peralkaline phonolites) were emplaced between 10.04 and 8.77 Ma. Such a relatively high-resolution geological study allows us to postulate that local sources are well constrained on the island. Additionally, several quarry sites, including the Tanataetea site, have been identified as possible sources of fine-grained basalt procurement (Hermann et al., 2012; Hermann, 2013, Hermann et al., 2016).

The archaeological material examined in this paper consists of 48 samples, including 23 surface-collected artefacts from quarries and domestic or ceremonial sites, and 25 artefacts from the Atiahara site,

Table 1
- List, GPS location and description of archaeological samples collected in Tupua'i.

Sample no.	Sample type	Site, Provenience	Coordinates (UTM)	Alt.	Description
Tan3-005	Artefact	Tanataetea workshop	6 K 246605 7414013	49 m	Adze preform type 3A
Tan1-006	Artefact	Tanataetea quarry	6 K 246591 7413998	53 m	Natural prism
Taahuaia1-008	Artefact	Field Taahuaia	6 K 250777 7412610	5 m	Adze fragment distal
Tehauteuruura1-017	Artefact	Field Mataura	6 K 246806 7415934	4 m	Adze type 1A (12 cm)
Tiirua1-020	Artefact	Field Taahuaia	6 K 250840 7413757	4 m	Adze fragment distal (6 cm)
Teuo2-021	Artefact	Field Taahuaia	6 K 250641 7414663	5 m	Adze fragment type 1A distal (8 cm)
Teautara3-023	Artefact	Field Taahuaia	6 K 249593 7415533	4 m	Adze type 2C (5 cm)
At3-583-029	Artefact	Atiahara, Layer 3 (K5)	6 K 244479 7415453	–	Massive flake fragment
At3-814-031	Artefact	Atiahara, Layer 4 (Q5)	6 K 244479 7415453	–	Adze
At3-817-032	Artefact	Atiahara, Layer 4 (Q5)	6 K 244479 7415453	–	Prism
At3-1152-033	Artefact	Atiahara, Layer 4 (W3)	6 K 244479 7415453	–	Adze preform (fragment)
PaneeSouth-041	Geological	Dyke Panee south 1	6 K 246721 7412828	338 m	Dyke
PaneeSouth-042	Geological	Dyke Panee south 2	6 K 246735 7412845	344 m	Dyke
Taitaa1-050	Artefact	Taitaa summit 1	6 K 247725 7413705	418 m	Flakes
Taitaa2-051	Artefact	Taitaa summit 2	6 K 247643 7413485	416 m	Flakes
Pahatu2-053	Artefact	Petit Pahatu workshop 1	6 K 242813 7412629	35 m	Adze fragment (preform)
Pahatu8-059	Artefact	Petit Pahatu workshop 3	6 K 243032 7412771	13 m	Adze preforms, flakes
At3-381-060	Artefact	Atiahara, Layer 3 (H4)	6 K 244479 7415453	–	Adze preform
At3-259-061	Artefact	Atiahara, Layer 1/surf	6 K 244479 7415453	–	Adze preform
At3-53-062	Artefact	Atiahara, Layer 5 (N12)	6 K 244479 7415453	–	Adze preform
At3-104-063	Artefact	Atiahara, Layer 6 (N13)	6 K 244479 7415453	–	Flakes
At3-229-064	Artefact	Atiahara, Layer 7 (L14)	6 K 244479 7415453	–	Polished adze fragment
At3-317-065	Artefact	Atiahara, Layer 3 (B3)	6 K 244479 7415453	–	Adze fragment
At3-395-066	Artefact	Atiahara, Layer 4/5 (H2)	6 K 244479 7415453	–	Adze fragment
Tamatoa2-072	Artefact	Surface, Field Tamatoa 2	6 K 249306 7411711	10 m	Flakes
Tapapatauae1-074	Artefact	Motu Tapapatauae, shore	6 K 253781 7415930	−1 m	Flakes
At3-122-075	Artefact	Atiahara, Layer 5 (M13)	6 K 242774 7412337	–	Adze roughout
At3-1274-076	Artefact	Atiahara, Layer 4/5 (X2)	6 K 244479 7415453	–	Polished adze fragment
At3-852-077	Artefact	Atiahara, Layer 3 (F1)	6 K 244479 7415453	–	Adze preform
At3-1316-079	Artefact	Atiahara, Layer 4 (V1)	6 K 244479 7415453	–	Flake
At3-1075-082	Artefact	Atiahara, Layer 4/5 (Q3)	6 K 244479 7415453	–	Polished adze fragment
At3-369-083	Artefact	Atiahara, Layer 3 (J4)	6 K 244479 7415453	–	Adze preform (fragment)
At3-337-084	Artefact	Atiahara, Layer 3 (L10)	6 K 244479 7415453	–	Polished adze fragment
At3-217-085	Artefact	Atiahara, Layer 6 (L12)	6 K 244479 7415453	–	Adze roughout
At3-1996-089	Artefact	Atiahara, Layer 3 (K11)	6 K 244479 7415453	–	Adze preform (fragment)
At3-1996-090	Artefact	Atiahara4, surface	6 K 244479 7415453	–	Adze preform (fragment)
At3-1996-091	Artefact	Atiahara, Layer 3 (K13)	6 K 244479 7415453	–	Adze preform (fragment)
At3-1321-092	Artefact	Atiahara, Layer 5 (T1)	6 K 244479 7415453	–	Adze preform (fragment)
At3-1227-094	Artefact	Atiahara, Layer 4 (Y2)	6 K 244479 7415453	–	Adze preform (fragment)
Taahuaia4-095	Artefact	Field Taahuaia	6 K 250482 7412134	4 m	Adze preform (fragment)
Taahuaia5-096	Artefact	Dry riverbed Taahuaia	6 K 249991 7415499	3 m	Adze roughout (fragment)
Taahuaia6-097	Artefact	Field Taahuaia	6 K 250443 7412081	5 m	Flake
Taahuaia7-098	Artefact	Field Taahuaia	6 K 250840 7412876	6 m	Adze preform
Mon1-099	Artefact	Surface, chez Monette	6 K 246017 7414889	12 m	Adze preform
Vahineata1-100	Artefact	Vahineata,FieldTamatoa1	6 K 248878 7411067	14 m	Adze
Vahineata2-101	Artefact	Vahineata,FieldTamatoa2	6 K 248878 7411067	14 m	Adze
Reretii-102	Geological	Reretii	6 K 250252 7413593	60 m	Prism
At3-1996-107	Artefact	Atiahara, Layer 5 (O11)	6 K 244479 7415453	–	Dyke

located at the north coast of Tupua'i (Table 1, Fig. 2). This well-stratified site consists of a succession of 4 cultural layers and 3 sterile sand deposits of aeolian and marine origin. The cultural sequence corresponds to a succession of four domestic occupations that were dated between CE 1215 and 1390 based on radiocarbon dates on wood charcoal (Hermann et al., 2016). In total, the Atiahara assemblage includes 43 polished adzes, 75 preformed and recycled adzes, and more than 2600 flake wastes and flake tools distributed over a total excavated area of 216 m^2 (Hermann, 2013; Hermann et al., 2016). Based on macroscopic observation of artefacts, we consider that the 25 samples submitted for geochemical analyses represent the diversity of exploited raw material on the site.

4. Material and methods

Major and trace elements were measured by Inductively Coupled Plasma-Atomic Emission Spectrometry (ICP-AES) for 48 samples at PSO/IUEM (Plouzané, France): 25 from the Atiahara site, 16 from surface sites, and 7 from quarry sites and outcrops. The list and locations of the archaeological and geological samples are shown in Table 1. Eight samples were then selected for Sr and Pb isotopic analyses: 3 artefacts from deep layers of the Atiahara site (At3-229-064, At3-317-065 and At3-395-066), 2 geological samples from Tupua'i quarries (Tan1-006 and Pahatu8-059), and 3 geological samples from Mangaia (Cook Is.) collected by P.V. Kirch in the valleys of Mata'are, Veitatei and Keia (Table 1). Sr isotopes were analysed by Thermo Scientific Triton Mass Spectrometer (TIMS) at PSO/IUEM (Plouzané, France) and Pb isotopes were determined using a Nu Plasma Multicollector - Inductively Coupled Plasma Mass Spectrometer (MC-ICPMS) at the ENS Lyon (France). Finally, one Mata'are quarry sample from Mangaia and two adzes from Atiahara (At3-229-064 and At3-317-065) were dated by the 40Ar/39Ar method at LSCE. Further details on analytical procedures are described in Supplementary Data - Appendix A.

5. Results

5.1. Major and trace element analysis

Major and trace element data from artefacts, quarries, and geological outcrops in Tupua'i, with additional data from other islands of the Austral-Cook chain (Mangaia, Ra'ivavae, Rapa Iti) and the Marquesas

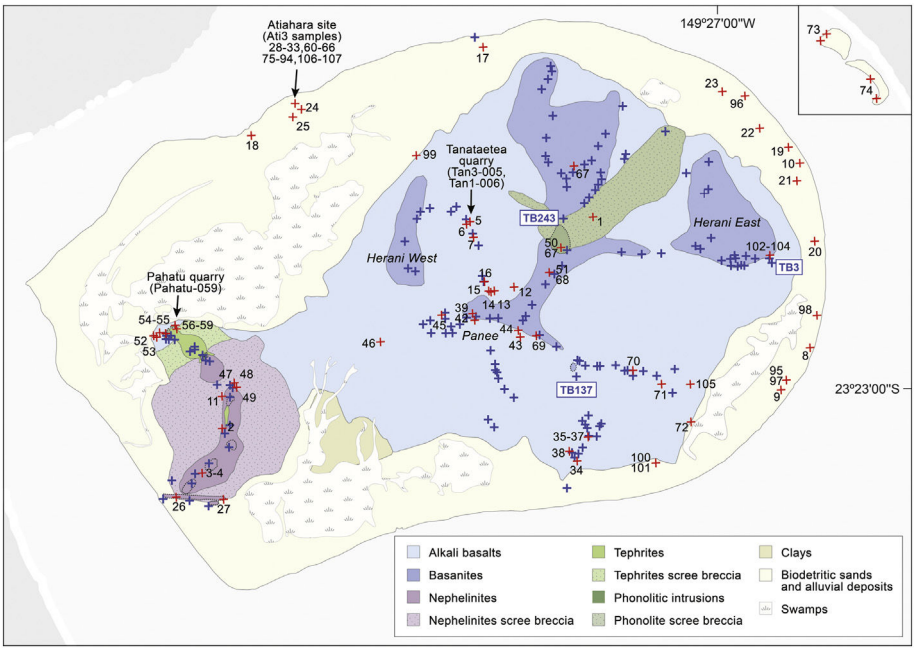

Fig. 2. Geological map of Tupua'i (modified from Maury et al. 2000) showing numbered archaeological samples (red crosses) collected by Hermann between 2010 and 2012, and geological samples (blue crosses) collected by BRGM between 1989 and 1995. (For interpretation of the references to colour in this figure legend, the reader is referred to the web version of this article.)

(Eiao) are shown in Tables 2 and 3. In Tupua'i, three types of basalt rocks (alkali basalts, basanites and nephelinites) and related intermediate lavas (tephrites) share the same silica-undersaturated and incompatible element-enriched signature typical of many Polynesian ocean island basalts (Dupuy et al., 1989). Their genesis is ascribed to low partial melting degrees of enriched mantle that decrease from alkali basalts to nephelinites (Caroff et al., 1997). Lavas from Tupua'i and the Mata'are quarry in Mangaia (Cook archipelago) display depletions in Rb, Ba, Th and K relative to Nb, La and Ce (Fig. 4c). This is considered characteristic of an HIMU affinity (Chauvel et al., 1992; Chauvel et al., 1997).

Almost all archaeological artefacts share the petrographic and geochemical features of Tupua'i lavas. The samples were clustered in 6 groups and associated with different possible sources based on petrographic groups and TiO_2-MgO plots (Fig. 3).

Clusters 1 and 2. match the fine-grained basanites found at the Tanataetea quarry and analysed as samples Tan3-005 and Tan1-006 (Tables 2 and 3; Fig. 4a and b).

Cluster 3. corresponds to a peculiar group of basanites that are petrographically characterized by the presence of recrystallized olivines and a dark green colour on polished surfaces. The source of this rock remains uncertain at this stage, as several lava flows in the Austral-Cook chain display the same trace element patterns, including RV-11, RV-27 and RV-35 on mount Rairua in Ra'ivavae (Maury et al., 2013), at Mata'are quarry in Mangaia, and TB-3 on Rereti'i ridge in Tupua'i (Tables 2 and 3; Fig. 4c). A rock sample from adze At3-229-064 was therefore selected for further isotopic analyses in order to constrain the geological origin of these artefacts.

Clusters 4 and 5. are tephritic rocks similar to those found in several locations on Herani volcano in Tupua'i, including geological samples TB-137 and TB-243 (Tables 2 and 3; Fig. 4d and e).

Cluster 6. corresponds to sample At3-317-065, which has been identified as an alkali basalt adze fragment (Table 2). This aphyric rock is very different from highly porphyritic alkali basalts from the oldest Tupua'i volcanic edifice and does not show the typical features of HIMU-derived Tupua'i lavas. Its major and trace element compositions are very similar to those of Eiao Island (Marquesas) artefacts and uppermost alkali basalts that derive from a dominantly EM2 mantle source and display relatively smooth enrichments in the most incompatible elements (Table 3; Fig. 4f; Caroff et al., 1995; Charleux et al., 2014).

5.2. Sr and Pb isotope analysis

The Sr and Pb isotopic compositions of the geological samples collected in Tupua'i quarry sites and of most artefacts except sample At3-317-065 show obvious similarities with previous data published for the island (Fig. 5, Chauvel et al., 1992; Maury et al., 2013; Schiano et al., 2001). Two of the adzes collected in the Atiahara site (At3-229-064 and At3-395-066, Table 4) show lead and strontium isotopic compositions consistent with Tupua'i lavas: an average of $^{87}Sr/^{86}Sr = 0.702804 \pm 0.000008$ (2σ) and $^{208}Pb/^{204}Pb = 40.1638 \pm 0.0020$ (2σ) for sample At3-229-064, and an average of $^{87}Sr/^{86}Sr = 0.702797 \pm 0.000008$ (2σ) and $^{208}Pb/^{204}Pb = 40.261498 \pm 0.0023$ (2σ) for sample At3-395-066. These values are very close to the average compositions of Tupua'i island: $^{87}Sr/^{86}Sr = 0.702840 \pm 0.000225$ (2σ) and $^{208}Pb/^{204}Pb = 40.2249 \pm 0.5828$ (2σ) (Fig. 5). In contrast, adze At3-317-065 shows a lesser radiogenic Pb composition, with an average of $^{208}Pb/^{204}Pb = 38.9991 \pm 0.0020$ (2σ) and is more radiogenic in Sr with an average of $^{87}Sr/^{86}Sr = 0.703922 \pm 0.000008$ (2σ) (Table 4, Fig. 5). Interestingly, this sample shares isotopic similarities with both Rapa Iti in the Australs and Eiao in the Marquesas (Table 4, Fig. 6). Therefore this sample was dated by the ^{40}Ar-^{39}Ar method to better constrain its origin.

5.3. Geochronology

^{40}Ar-^{39}Ar plateau ages, isochron ages, and total fusion ages are given in Table 5 and Appendix C. The isochron ages are considered more reliable than the plateau ages because the isochron approach makes no assumption regarding the trapped component, and it combines estimates

Table 2-
Major element oxide values (wt%) and trace element values (ppm) of Tupua'i artefacts

Sample	Location	Petrographic group	SiO_2	TiO_2	Al_2O_3	Fe_2O_3	MnO	MgO	CaO	Na_2O	K_2O	P_2O_5	LOI	Total
At3-583-029	Atiahara, layer 3 (K5)	Basanite	42.87	3.345	15.37	14.15	0.200	5.80	11.34	2.91	1.13	0.461	1.67	99.26
At3-583-029b	Atiahara, layer 3 (K5)	Basanite	41.92	3.382	14.74	14.25	0.200	5.89	11.44	2.73	0.95	0.436	3.44	99.38
At3-814-031	Atiahara, layer 4 (Q5)	Basanite	43.09	3.116	13.18	13.86	0.201	7.51	13.22	2.78	0.89	0.481	0.89	99.22
At3-817-032	Atiahara, layer 4 (Q5)	Basanite	44.51	2.670	11.89	12.82	0.201	8.73	13.75	2.00	0.65	0.345	1.47	99.03
At3-1152-033	Atiahara, layer 4 (W3)	Basanite	42.88	3.448	15.78	15.40	0.216	5.37	10.81	3.08	0.98	0.508	0.97	99.44
At3-381-060	Atiahara, layer 3 (H4)	Basanite	43.37	3.060	13.26	13.80	0.202	7.36	12.85	2.77	0.93	0.486	1.07	99.16
At3-381-060b	Atiahara, layer 3 (H4)	Basanite	43.18	3.053	13.11	13.60	0.197	7.31	12.37	2.79	0.93	0.475	1.07	98.10
At3-259-061	Atiahara, layer 1/surf	Basanite	42.86	3.464	15.83	15.45	0.217	5.36	11.01	3.13	1.06	0.506	0.50	99.38
At3-53-062	Atiahara, layer 5 (N12)	Tephrite	45.19	3.609	15.19	15.31	0.217	5.36	7.23	4.72	1.45	0.816	0.46	99.56
At3-104-063	Atiahara, layer 6 (N13)	Basanite	42.67	3.436	15.74	15.27	0.215	5.60	10.62	2.96	1.16	0.502	1.10	99.27
At3-229-064	Atiahara, layer 7 (L14)	Basanite	43.45	3.158	13.05	14.00	0.202	7.78	13.24	2.73	0.79	0.488	0.87	99.75
At3-317-065	Atiahara, layer 3 (B3)	Alkali basalt	47.12	3.85	14.92	13.67	0.168	6.93	9.18	3.27	1.01	0.51	−0.39	100.24
At3-395-066	Atiahara, layer 4/5 (H2)	Basanite	42.34	3.430	15.76	15.36	0.213	5.35	10.80	3.11	1.01	0.493	0.73	98.59
At3-122-075	Atiahara, layer 5 (M13)	Basanite	43.40	3.379	16.12	15.03	0.213	5.39	10.19	3.29	1.36	0.493	1.08	99.94
At3-1274-076	Atiahara, layer 4/5 (X2)	Basanite	43.49	3.564	16.05	15.60	0.218	5.41	10.60	3.64	1.16	0.488	−0.47	99.76
At3-852-077	Atiahara, layer 3 (F1)	Tephrite	45.76	2.574	15.36	14.09	0.243	3.36	7.23	6.44	2.00	1.798	0.22	99.08
At3-1316-079	Atiahara, layer 4 (V1)	Basanite	43.28	3.512	15.88	15.47	0.217	5.29	10.60	3.45	1.34	0.504	0.47	100.02
At3-1075-082	Atiahara, layer 4/5 (Q3)	Basanite	43.81	3.639	15.67	14.65	0.209	5.28	10.48	3.97	1.05	0.558	0.04	99.35
At3-369-083	Atiahara, layer 3 (J4)	Tephrite	45.03	2.900	15.11	14.74	0.240	4.08	7.81	5.38	1.88	1.914	0.89	99.97
At3-337-084	Atiahara, layer 3 (L10)	Basanite	43.35	3.282	12.82	14.08	0.202	7.93	13.61	2.66	0.64	0.448	0.43	99.46
At3-217-085	Atiahara, layer 6 (L12)	Basanite	43.45	3.177	15.89	14.80	0.227	5.45	10.97	3.77	1.30	0.604	0.49	100.13
At3-1996-089	Atiahara, layer 3 (K11)	Basanite	42.79	3.531	15.68	15.60	0.219	5.43	11.00	3.08	0.97	0.470	0.87	99.65
At3-1996-090	Atiahara4, surface	Tephrite	46.35	2.609	15.41	14.19	0.249	3.45	7.37	6.18	2.01	1.803	0.10	99.72
At3-1996-091	Atiahara, layer 3 (K13)	Basanite	43.14	4.122	15.26	14.10	0.197	4.61	10.86	2.69	1.86	0.581	3.13	100.55
At3-1321-092	Atiahara, layer 5 (T1)	Tephrite	45.57	2.746	17.09	13.21	0.243	3.85	9.80	4.85	1.51	0.744	0.99	100.60
At3-1227-094	Atiahara, layer 4 (Y2)	Basanite	42.99	3.501	15.84	15.33	0.217	5.59	10.50	3.30	0.98	0.494	1.11	99.86
At3-1996-107	Atiahara, layer 5 (O11)	Picrite	37.31	3.023	12.32	17.94	0.310	4.86	12.75	1.96	0.33	1.520	6.65	98.96
Taahuaia1-008	Field Taahuaia	Low silica basanite	41.86	3.452	14.03	14.59	0.198	6.04	12.34	4.04	1.33	0.800	2.24	100.92
Taahuaia1-008b	Field Taahuaia	Low silica basanite	40.79	3.384	13.81	14.03	0.189	5.95	11.87	3.98	1.31	0.771	2.24	98.32
Tehauteuruura1-017	Field Mataura	Low silica basanite	41.56	4.281	14.65	16.84	0.230	6.22	7.89	4.68	1.69	1.212	0.28	99.54
Tiirua1-020	Field Taahuaia	Tephrite	45.42	2.894	15.09	14.85	0.238	3.86	7.90	5.99	1.83	1.917	-0.25	99.74
Teuo2-021	Field Taahuaia	Tephrite	45.60	2.768	17.00	13.26	0.235	3.97	9.66	4.88	1.49	0.758	0.48	100.10
Teautara3-023	Field Taahuaia	Low silica basanite	41.47	4.138	15.01	14.91	0.215	6.06	11.05	4.21	1.43	0.651	0.51	99.65
Taitaa1-050	Taitaa-1	Low silica basanite	41.86	3.097	15.04	14.22	0.218	5.13	10.97	4.16	1.36	0.770	2.59	99.40
Taitaa2-051	Taitaa-2	Basanite	43.23	2.356	11.44	13.31	0.200	11.80	12.91	2.19	0.70	0.385	1.47	99.99
Tamatoa2-072	Field Tamatoa	Low silica basanite	42.25	3.469	16.04	14.15	0.233	5.26	10.08	4.36	1.40	0.640	0.77	98.64
Tapapatauae1-074	Motu Tapapatauae	Tephrite	45.23	2.709	17.10	12.99	0.232	3.95	9.25	4.96	1.50	0.754	0.42	99.10
Taahuaia4-095	Field Taahuaia	Tephrite	44.43	2.906	14.89	14.55	0.236	3.87	7.51	5.50	1.77	1.801	1.30	98.77
Taahuaia5-096	Dry riverbed Taahuaia	Tephrite	45.22	2.792	16.71	13.35	0.241	3.80	9.51	4.81	1.48	0.722	1.74	100.37
Taahuaia6-097	Field Taahuaia	Basanite	43.10	3.351	15.21	14.38	0.202	5.57	11.68	2.94	1.15	0.479	1.57	99.63
Taahuaia7-098	Field Taahuaia	Basanite	43.02	2.720	13.85	14.32	0.210	7.40	13.18	2.46	0.66	0.355	1.48	99.66
Mon1-099	Huahine, Monette's	Low silica basanite	41.46	4.358	14.50	16.77	0.234	5.98	7.76	4.93	1.68	1.190	0.40	99.26
Vahineata1-100	Field Tamatoa	Basanite	43.84	3.629	15.50	14.79	0.219	5.27	10.48	3.80	1.04	0.542	0.63	99.73
Vahineata2-101	Field Tamatoa	Basanite	43.67	3.553	15.04	14.79	0.211	5.27	10.98	3.54	1.02	0.550	2.01	100.62

of analytical precision and internal disturbance of the sample (scatter around the isochron).

The plateau age of the mildly altered Mata'are sample (Mangaia, Cook Is.), calculated from 7 steps out of 10 with 78.8% of the gas released, is 20.17 ± 0.63 Ma. This coincides with the isochron age of 20.03 ± 0.66 Ma that we retained to take into consideration the non-atmospheric value of the $^{40}Ar/^{36}Ar$ intercept, which may indicate subtle excess $^{40}Ar^*$ (Table 5). This data fits a previously measured K-Ar age for Mangaia, the oldest high island in the CEP (19.3 ± 0.6 Ma; Turner and Jarrard, 1982; Fig. 7).

The age spectra of adze At3-229-064 demonstrate an exponential decrease from high ages at low temperature steps to the age plateau, which correlates with an increase of the K/Ca ratio. The plateau age, calculated from 6 out of 10 steps (i.e. 60% of the gas released), is 10.32 ± 0.32 Ma; equivalent to the total fusion age (10.41 ± 0.30 Ma) and the isochron age of 10.30 ± 0.32 Ma. This age fits the previously known range of activity of Tupua'i (10.04–8.77 Ma by the unspiked K-Ar method; Maury et al., 2000; Fig. 7), further demonstrating the local origin of this artefact.

The plateau age of adze At3-317-065 is calculated from 10 out of 11 steps corresponding to the 81% of the gas released. This plateau age (5.61 ± 0.21 Ma) is equivalent to the isochron age (5.68 ± 0.24 Ma) and to the total fusion age (5.59 ± 0.21 Ma). Available K-Ar ages for Eiao Island (5.52–4.98 Ma; Guillou et al., 2014) fit that of Atiahara adze sample At3-317-065 (Fig. 7), while those of Rapa Iti lavas are younger (4.8–4.1 Ma; Maury et al., 2013). Furthermore, other contemporaneous volcanoes in the Gambier (6.26–5.66 Ma; Delavault et al., 2015; Guillou et al., 1994) and in Ra'ivavae of the Australs (10.6–5.4 Ma; Lassiter et al., 2003; Maury et al., 2013) have clearly different isotopic characteristics (Figs. 5 and 6). Therefore, this age result corroborates the geochemical evidence for an exotic origin of adze At3-317-065 from Eiao (Marquesas), circa 2000 km north of Tupua'i.

6. Discussion

6.1. Assessing geological provenances without ambiguity

Archaeometric studies of stone tool assemblages provide major insights for tracing patterns of mobility within and between Pacific islands. Previous work has shown that Sr, Nd and Pb isotopic data used together with major and trace element data permits assignment of artefacts to sources, because they provide additional constraints on their geochemical signatures (Collerson and Weisler, 2007; Hermann, 2013, 2016; Weisler et al., 2016a).

However, even the entire set of information available through rock chemistry (element and isotope analysis) can be insufficient to properly discriminate islands of origin. This is due to similar rock types arising across CEP islands, but also to trace element patterns and isotopic

Table 2
- cont.

Sample	Rb	Sr	Ba	Sc	V	Cr	Co	Ni	Y	Zr	Nb	La	Ce	Nd	Sm	Eu	Gd	Dy	Er	Yb	Th
At3-583-029	25	795	301	21	334	13	46	55	29	211	62	46	93	45	9.0	2.7	7.9	5.9	2.9	2.1	5.0
At3-583-029b	24	760	278	22	341	20	47	57	29	207	59	41	84	41	8.3	2.6	7.4	5.7	2.9	2.1	4.4
At3-814-031	21	641	296	31	319	153	49	104	29	209	64	49	95	45	8.9	2.6	7.6	5.7	2.8	2.0	5.2
At3-817-032	20	447	181	43	355	366	53	132	25	168	41	31	65	33	6.8	2.1	6.2	4.8	2.7	1.9	2.7
At3-1152-033	16	634	310	19	390	3	48	29	30	217	66	48	95	46	8.8	2.6	7.6	6.0	2.7	2.2	4.8
At3-381-060	31	607	302	32	315	151	50	103	29	218	69	50	98	46	9.1	2.6	7.8	5.6	2.7	2.0	5.7
At3-381-060b	28	622	301	31	317	154	50	103	28	218	67	51	97	46	8.9	2.6	7.6	5.8	2.6	2.1	5.8
At3-259-061	23	646	316	19	390	4	43	30	30	220	67	48	93	46	9.0	2.7	7.6	6.1	3.0	2.3	5.0
At3-53-062	32	1035	368	13	152	3	34	12	38	342	81	64	129	64	12.4	3.8	10.3	7.4	3.7	2.8	6.6
At3-104-063	25	638	307	18	379	3	47	30	29	215	66	48	93	46	9.2	2.7	7.9	6.0	3.2	2.2	4.7
At3-229-064	20	617	279	33	341	160	51	107	29	211	62	48	94	46	8.7	2.7	7.8	5.7	2.8	2.0	5.0
At3-317-065	26	603	187	22	307	71	47	115	36	284	27	26	61	40	9.3	3.0	9.4	7.3	3.7	2.4	2.4
At3-395-066	26	621	302	19	382	4	48	30	30	215	65	47	93	46	9.0	2.6	7.6	6.0	2.8	2.3	4.6
At3-122-075	34	681	335	18	370	3	46	28	31	230	74	51	101	48	9.2	2.8	7.8	6.1	2.8	2.4	5.9
At3-1274-076	24	664	314	19	397	3	49	29	30	218	66	48	97	47	9.2	2.8	7.7	5.9	2.8	2.3	5.2
At3-852-077	58	1564	586	7	71	2	24	3	49	545	125	115	236	106	19.4	5.5	14.6	9.6	4.2	3.3	11.7
At3-1316-079	32	635	314	19	388	3	49	31	31	220	68	49	98	47	8.8	2.7	7.9	6.0	2.9	2.3	5.5
At3-1075-082	25	779	367	19	332	12	46	42	32	235	78	57	113	53	10.6	3.1	8.8	6.5	3.0	2.3	6.3
At3-369-083	58	1470	521	8	104	3	28	6	47	485	112	106	221	102	18.7	5.4	14.3	9.3	4.2	3.1	10.4
At3-337-084	8	690	277	34	354	168	53	113	28	211	59	47	94	46	8.6	2.7	7.6	5.7	2.8	2.0	5.1
At3-217-085	38	772	390	16	325	7	47	46	32	250	85	62	121	56	10.5	3.1	8.5	6.3	3.0	2.4	7.0
At3-1996-089	20	628	298	19	400	21	49	30	30	216	64	47	93	46	8.9	2.7	7.6	6.0	3.1	2.3	4.9
At3-1996-090	59	1542	563	7	74	17	24	5	49	535	127	115	228	106	19.0	5.5	14.9	9.7	4.3	3.2	11.4
At3-1996-091	44	738	442	16	378	23	40	53	33	290	48	42	90	51	10.5	3.1	9.4	6.8	3.2	2.3	5.0
At3-1321-092	39	931	479	8	168	7	30	4	36	301	104	77	145	64	11.3	3.4	9.4	7.0	3.6	2.6	9.2
At3-1227-094	20	730	323	19	383	4	49	30	30	216	67	48	94	47	8.7	2.8	7.6	6.0	2.6	2.3	5.3
At3-1996-107	12	1244	504	9	142	6	51	167	56	561	213	170	320	134	23.4	6.7	17.8	11.7	4.9	3.4	20.6
Taahuaia1-008	47	1029	628	19	307	58	48	78	35	329	117	83	159	70	13.3	3.8	10.3	7.2	3.2	2.1	9.7
Taahuaia1-008b	44	1014	596	19	300	56	46	75	34	319	113	84	160	71	13.2	3.8	10.7	7.3	3.3	2.0	9.5
Tehauteuruura1-017	45	1044	407	14	209	9	46	40	39	395	98	75	153	74	13.9	4.2	11.7	7.9	3.8	2.8	7.2
Tiirua1-020	54	1468	540	8	112	3	28	6	46	489	115	105	214	99	18.1	5.3	14.8	9.4	4.2	3.2	10.1
Teuo2-021	43	910	483	9	176	3	31	2	36	305	103	77	146	64	11.7	3.4	9.6	6.9	3.4	2.7	8.7
Teautara3-023	41	883	486	17	373	4	48	51	33	261	94	65	126	61	11.8	3.4	9.9	6.6	3.0	2.2	7.1
Taitaa1-050	49	996	560	14	242	9	45	57	34	329	124	90	163	70	12.5	3.7	10.4	7.1	3.5	2.5	11.4
Taitaa2-051	24	507	245	34	304	666	59	303	24	172	54	41	81	39	7.41	2.3	6.4	4.9	2.6	1.8	4.2
Tamatoa2-072	35	879	457	13	292	3	39	13	33	256	91	66	128	59	11.5	3.3	9.3	6.7	3.1	2.4	7.0
Tapapatauae1-074	45	974	448	8	164	2	29	2	34	301	104	78	150	64	11.7	3.6	9.8	7.0	3.3	2.7	8.8
Taahuaia4-095	47	1407	527	8	100	13	29	8	47	485	114	102	206	98	17.9	5.2	13.8	9.2	4.1	3.1	10.1
Taahuaia5-096	40	901	468	9	178	14	31	12	36	304	103	75	142	64	11.5	3.4	9.4	6.9	3.4	2.6	8.7
Taahuaia6-097	24	663	309	21	334	18	48	56	30	219	64	46	91	45	8.5	2.7	7.6	6.0	2.9	2.2	5.2
Taahuaia7-098	13	563	262	33	377	45	53	82	27	170	54	41	79	39	7.5	2.2	6.2	5.1	3.0	2.1	4.6
Mon1-099	39	1057	397	14	212	25	48	45	40	408	100	75	152	76	13.8	4.1	11.1	7.9	3.9	2.7	7.6
Vahineata1-100	23	770	367	19	334	24	46	45	32	236	79	55	108	52	9.7	3.1	8.6	6.4	2.8	2.2	5.9
Vahineata2-101	24	791	372	18	325	24	46	44	32	239	81	56	109	53	10.5	3.2	9.3	6.7	3.0	2.2	6.1

compositions both overlapping between different islands, as we show for Eiao and Rapa iti, as well as for Mangaia and Tupua'i (Figs. 4, 5 and 6). In such cases, we argue that cross-referencing isotopic and geochronological data can provide enough proxies to unambiguously assign a source to a given artefact (Fig. 7). For instance, a strong HIMU geochemical signature and an age circa 20 Ma would readily identify any artefact or raw basalt as originating from Mangaia Island, because these two characteristics combined have no known equivalent in Polynesia. Associating ^{40}Ar-^{39}Ar (which can be performed on a 120 mg sample, see Supplementary Data - Appendix A) with major, trace elements and Sr, Nd, Pb isotopic analysis therefore proves to be the most accurate way to constrain stone artefact provenance in intraplate volcanic islands of the Pacific. Due to the time consuming irradiation of the samples by specific nuclear reactors (as described in Appendix A), Ar-Ar dating cannot be used routinely in provenance studies, but can be used to solve particular issues of source-assignment. For example, Ar-Ar dating would help separate possible Tupua'i-sourced artefacts from Mangaian ones in the Tangatatau site recently discussed by Weisler et al. (2016a).

6.2. Local procurement strategies and adze production process

Major and trace element data show a clear clustering of the geological samples collected in Tupua'i, which corresponds to the geochemical variability previously identified for the island (Maury et al., 1994; Maury et al. 2000; Maury et al., 2013). We identify several local procurement sources of basanite, tephrite and phonolite, including the previously undocumented Pahatu and Tanataetea quarries. Most of the artefacts collected in domestic contexts were made-up of basanites from the Tanataetea quarry and the Panee area, as well as of tephrites from the Herani volcano.

The distribution of flaked basalt boulders or dykes, adze preforms, and knapping wastes (flakes and discarded blanks) within the island suggests an organized form of adze production, in quarries and procurement areas on one hand, and in coastal settlements on the other. It has been shown that stone knapping activities involved both specialized craftsmen working in permanent workshops in the vicinity of fine-grained basalt quarries of Tanataetea and Pahatu (Fig. 2) and non-specialists within domestic contexts like the Atiahara site (Hermann, 2013, 2016, in press). Additionally, the Atiahara site assemblage shows uneven distribution of fine-grained basalt and difficult access to good-quality raw material, which can be interpreted as an aspect of the control by pre-European social elites over local valued resources.

6.3. Inter-archipelago transfers of artefacts: a Marquesas-Australs connection

Our identification of an Eiao adze (At3-317-065) within the Atiahara site in Tupua'i is the first hard evidence of a link between the Marquesas and the Austral Islands soon after the settlement of CEP by Polynesian

Table 3
- Major element oxide values (wt%) and trace element values (ppm) of related sources.

Sample*	Archipelago	Island	Location	Sample type	Petrographic group	SiO_2	TiO_2	Al_2O_3	Fe_2O_3	MnO	MgO	CaO	Na_2O	K_2O	P_2O_5	LOI	Total
Tan3-005	Austral-Cook	Tupua'i	Tanataetea workshop	Quarry	Basanite	43.71	3.496	15.86	15.75	0.220	5.42	11.18	3.29	1.18	0.505	0.41	101.02
Tan1-006	Austral-Cook	Tupua'i	Tanataetea quarry	Quarry	Basanite	43.93	3.529	15.86	15.92	0.230	5.74	10.89	3.33	0.99	0.529	0.59	101.55
Pahatu2-053	Austral-Cook	Tupua'i	Pahatu workshop 1	Quarry	Phonolite	57.37	0.024	18.58	5.38	0.247	0.09	0.85	8.72	4.70	0.051	2.41	98.43
Pahatu8-059	Austral-Cook	Tupua'i	Pahatu workshop 3	Quarry	Phonolite	59.20	0.040	18.47	5.99	0.302	0.08	1.08	8.63	4.36	0.045	2.33	100.53
PaneeSouth-041	Austral-Cook	Tupua'i	Panee south slope	Geological	Low silica basanite	41.76	3.123	14.92	14.42	0.215	5.38	11.11	5.09	1.40	0.780	1.17	99.37
PaneeSouth-041b	Austral-Cook	Tupua'i	Panee south slope	Geological	Low silica basanite	41.36	3.071	14.73	14.22	0.212	5.36	10.88	5.05	1.40	0.774	1.17	98.24
PaneeSouth-042	Austral-Cook	Tupua'i	Panee south slope	Geological	Low silica basanite	41.39	3.131	14.89	14.12	0.212	5.49	11.12	4.43	1.53	0.770	1.67	98.76
Reretii-102	Austral-Cook	Tupua'i	Herani cliff	Geological	Tephrite	45.23	2.745	16.93	13.16	0.237	3.83	9.58	4.83	1.49	0.748	1.10	99.89
TB-2	Austral-Cook	Tupua'i	Reretii	Geological	Basanite	44.00	2.880	12.32	13.86	0.200	8.56	12.55	1.66	0.40	0.490	3.13	100.05
TB-3	Austral-Cook	Tupua'i	Reretii	Geological	Basanite	43.40	3.110	13.80	14.45	0.203	7.37	12.00	2.77	1.02	0.510	1.47	100.10
TB-46	Austral-Cook	Tupua'i	Panee	Geological	Low silica basanite	41.65	3.070	14.98	14.78	0.230	5.44	11.13	4.29	1.36	0.850	1.41	99.19
TB-137	Austral-Cook	Tupua'i	Panee south ridge	Geological	Tephrite	45.75	2.700	17.30	13.21	0.250	3.75	9.43	4.85	1.55	n.a	1.18	99.97
TB-243	Austral-Cook	Tupua'i	Taitaa north ridge	Geological	Low silica basanite	41.10	3.480	15.35	14.90	0.230	6.03	11.34	3.95	1.25	0.650	1.36	99.64
Mata'are (a)	Austral-Cook	Mangaia	Mata'are	Geological	Basanite	44.029	3.353	15.11	14.38	0.195	5.583	11.40	3.16	0.83	0.450	1.36	99.85
Keia (a)	Austral-Cook	Mangaia	Keia	Geological	Basanite	45.570	1.807	16.93	11.58	0.202	2.360	7.64	3.28	1.84	0.840	7.18	99.23
Veitatei (a)	Austral-Cook	Mangaia	Veitatei	Geological	Basanite	44.814	3.274	13.39	12.92	0.196	5.370	10.84	2.75	1.06	0.45	4.34	99.41
92-32 (b)	Austral-Cook	Mangaia	Mata'are	Quarry	Basanite	44.87	3.288	14.45	13.16	0.186	5.93	12.21	3.01	0.82	0.437	n.a	98.36
92-20 (b)	Austral-Cook	Mangaia	Mata'are	Quarry	Basanite	45.20	3.349	15.21	13.09	0.197	5.89	11.66	3.44	0.84	0.456	n.a	99.33
92-4 (b)	Austral-Cook	Mangaia	Mata'are	Quarry	Basanite	45.08	3.344	15.04	13.17	0.200	5.87	11.60	3.28	0.82	0.454	n.a	98.86
2009-330-b (c)	Austral-Cook	Mangaia	Mata'are valley	Quarry	–	n.a	n.a	n.a	n.a	n.a	n.a	n.a	n.a	n.a	n.a	n.a	n.a
2009-331-b (c)	Austral-Cook	Mangaia	Mata'are valley	Geological	–	n.a	n.a	n.a	n.a	n.a	n.a	n.a	n.a	n.a	n.a	n.a	n.a
RV-11 (d)	Austral-Cook	Ra'ivavae	Rairua	Geological	Basanite	44.60	2.520	15.60	12.70	0.180	6.40	12.40	2.63	0.77	0.340	1.54	99.68
RV-27 (d)	Austral-Cook	Ra'ivavae	Rairua	Geological	Basanite	43.86	2.067	13.53	12.45	0.196	10.45	12.01	2.17	0.70	0.314	1.73	99.47
RV-35 (d)	Austral-Cook	Ra'ivavae	Rairua	Geological	Basanite	43.70	2.410	15.50	13.50	0.213	6.40	12.26	2.62	0.70	0.410	1.70	99.41
KC-05-11 (e)	Marquesas	Eiao	Surface	Artefact	Alkali basalt	47.83	3.96	15.44	n.a	0.170	6.41	9.22	3.33	1.05	0.54	n.a	87.95
2012-563 (f)	Marquesas	Eiao	Surface	Artefact	Alkali basalt	48.8	4.12	15.48	13.93	0.171	6.54	9.64	3.14	0.961	0.592	n.a	103.38
2012-573 (f)	Marquesas	Eiao	Surface	Artefact	Alkali basalt	46.45	3.89	14.71	13.20	0.162	6.34	9.11	3.02	1.01	0.54	n.a	98.44
198-39 (g)	Austral-Cook	Rapa iti	Surface	Geological	Alkali basalt	44.2	4.03	14	12.88	0.150	8.1	10.86	2.6	1.37	0.61	n.a	98.8
RPA-02 (h)	Austral-Cook	Rapa iti	Surface	Geological	Alkali basalt	44	3.58	11.69	13.55	0.160	13.1	9.95	2.46	1.07	0.59	0.5	100.65

* References: (a) This study (sampled by PV Kirch); (b) Weisler et al. (1994); (c) Weisler et al. (2016a); (d) Maury et al. (2013); (e) Collerson and Weisler (2007); (f) Weisler et al. (2016b); (g) Palacz and Saunders (1986); (h) Liotard (1988).

Table 3
- Cont.

Sample	Rb	Sr	Ba	Sc	V	Cr	Co	Ni	Y	Zr	Nb	La	Ce	Nd	Sm	Eu	Gd	Dy	Er	Yb	Th
Tan3-005	36	666	325	19	395	4	52	30	31	225	67	48	93	45	9.2	2.8	7.9	5.9	2.9	2.3	4.7
Tan1-006	27	675	337	19	392	3	52	30	31	223	67	48	97	46	8.9	2.7	8.1	6.0	2.8	2.3	5.0
Pahatu2-053	321	94	380	0.1	3	2	0	0	66	1588	395	275	470	131	18.1	3.8	12.7	10.4	6.2	6.1	41.4
Pahatu8-059	275	182	850	0.1	4	2	0.6	0.7	58	1391	373	268	444	128	18.2	3.8	12.4	9.8	5.6	5.4	34.7
PaneeSouth-041	49	856	533	14	248	10	45	55	36	330	120	91	169	72	12.6	3.7	10.6	7.3	3.3	2.5	11.1
PaneeSouth-041b	52	836	522	14	245	10	41	55	35	328	118	90	167	72	13.1	3.7	10.0	7.4	3.3	2.5	11.0
PaneeSouth-042	62	856	553	15	253	15	47	56	37	331	120	90	168	71	12.7	3.8	10.8	7.2	3.3	2.5	11.1
Reretii-102	40	890	461	8	172	7	31	3	36	301	105	76	145	64	11.3	3.4	9.1	7.1	3.7	2.6	9.0
TB-2	20	497	335	n.a	288	232	56	127	n.a	n.a	n.a	n.a	n.a	n.a	n.a	n.a	n.a	n.a	n.a	n.a	n.a
TB-3	28	694	340	n.a	318	162	55	127	n.a	n.a	n.a	n.a	n.a	n.a	n.a	n.a	n.a	n.a	n.a	n.a	n.a
TB-46	48	910	315	15	265	≤10	50	55	38	326	119	90	n.a	72	n.a	3.4	n.a	7.5	2.8	2.6	n.a
TB-137	n.a	n.a	n.a	n.a	n.a	n.a	n.a	n.a	29	283	96	71	n.a	60	n.a	3.4	n.a	6.5	1.9	1.5	n.a
TB-243	30	870	445	16	342	9	48	33	33	275	96	70	135	63	13.4	3.5	n.a	6.7	3.2	2.2	8.0
Mata'are (a)	20	555	249	25	331	30	47	49	30	218	53	39	83	43	8.5	2.6	7.9	6.0	2.8	2.2	4.0
Keia (a)	36	877	534	4	49	3	19	5	37	379	102	82	157	69	12.2	3.5	9.6	7.0	3.4	2.9	9.8
Veitatei (a)	23	463	287	31	335	492	74	344	28	218	59	43	90	46	9.6	2.7	8.0	5.7	2.3	1.9	4.8
92-32 (b)	n.a	n.a	n.a	n.a	n.a	n.a	n.a	n.a	n.a	n.a	n.a	n.a	n.a	n.a	n.a	n.a	n.a	n.a	n.a	n.a	n.a
92-20 (b)	n.a	n.a	n.a	n.a	n.a	n.a	n.a	n.a	n.a	n.a	n.a	n.a	n.a	n.a	n.a	n.a	n.a	n.a	n.a	n.a	n.a
92-4 (b)	n.a	n.a	n.a	n.a	n.a	n.a	n.a	n.a	n.a	n.a	n.a	n.a	n.a	n.a	n.a	n.a	n.a	n.a	n.a	n.a	n.a
2009-330-b (c)	35	698	337	20	304	29	42	61	28	228	59	47	97	45	8.9	2.7	8.0	6.0	2.8	2.2	5.1
2009-331-b (c)	18	560	247	26	325	28	48	44	28	221	55	38	82	41	8.4	2.8	7.8	6.0	2.8	2.3	4.1
RV-11 (d)	22	515	280	30	340	95	48	79	27	173	58	41	80	37	7.1	2.1	6.2	5.2	2.4	2.1	4.6
RV-27 (d)	10	457	265	33	282	461	55	197	23	146	57	41	76	34	6.3	1.9	5.4	4.4	2.1	1.9	4.8
RV-35 (d)	21	582	325	26	329	35	48	60	29	190	73	53	100	44	7.7	2.3	6.7	5.4	3.0	2.4	4.9
KC-05-11 (e)	9	421	133	31	324	193	43	77	31	256	24	20	49	33	8.5	2.8	8.5	6.8	3.1	2.4	1.9
2012-563 (f)	21	609	194	22	295	74	46	90	34	342	29	26	64	39	9.6	3.1	9.4	7.4	3.3	2.5	3.0
2012-573 (f)	32	612	196	22	309	81	45	94	33	342	29	26	63	39	9.5	3.1	9.4	7.3	3.3	2.5	2.9
198-39 (g)	28	795	403	n.a	n.a	325	n.a	169	24	278	57	40	96	46	9.8	3.2	n.a	n.a	n.a	1.8	4.7
RPA-02 (h)	22	670	296	23	225	391	71	253	24	260	50	33	77	39	7.6	2.5	n.a	n.a	n.a	1.4	4.1

Table 4-1
Sr and Pb isotopic ratios of artefacts and related sources (This study)

Archipelago	Island	Sample no.*	$^{87}Sr/^{86}Sr$	±2σ	$^{208}Pb/^{204}Pb$	±2σ
Austral	Tubuai	At3-229-064-P	0.702804	0.000008	40.127	0.002
Austral	Tubuai	At3-229-064-G	0.702803	0.000008	40.201	0.002
Austral	Tubuai	At3-317-065-P	0.703912	0.000008	38.996	0.002
Austral	Tubuai	At3-317-065-G	0.703932	0.000008	39.002	0.002
Austral	Tubuai	At3-395-066-P	0.702797	0.000008	40.261	0.002
Austral	Tubuai	Tan1-006-P	0.702803	0.000008	40.268	0.002
Austral	Tubuai	Tan1-006-G	0.702853	0.000008	40.281	0.001
Austral	Tubuai	Pahatu8-059-P	0.703496	0.000008	40.018	0.001
Cook	Mangaia	Mataare-G	0.702791	0.000008	40.443	0.002
Cook	Mangaia	Keia-G	0.702844	0.000006	40.544	0.001
Cook	Mangaia	Keia-G-Dup	0.702838	0.000006	40.539	0.003
Cook	Mangaia	Veitatei-G	0.703186	0.000006	40.571	0.002

* Footnote: P stands for analysis on powder sample, G for analysis on gravels and Dup for complete duplicate analysis.

Table 4-1
Cont.

Archipelago	Island	Sample no.*	$^{207}Pb/^{204}Pb$	±2σ	$^{206}Pb/^{204}Pb$	±2σ
Austral	Tubuai	At3-229-064-P	15.730549	0.0007	20.8499	0.0010
Austral	Tubuai	At3-229-064-G	15.72881	0.000943	20.9587	0.0009
Austral	Tubuai	At3-317-065-P	15.579801	0.000954	19.1880	0.0008
Austral	Tubuai	At3-317-065-G	15.579871	0.000763	19.1925	0.0009
Austral	Tubuai	At3-395-066-P	15.76081	0.000748	21.1367	0.0007
Austral	Tubuai	Tan1-006-P	15.761482	0.000696	21.1413	0.0009
Austral	Tubuai	Tan1-006-G	15.764295	0.000526	21.1408	0.0007
Austral	Tubuai	Pahatu8-059-P	15.673399	0.000433	20.5105	0.0005
Cook	Mangaia	Mataare-G	15.815252	0.000523	21.5235	0.0007
Cook	Mangaia	Keia-G	15.822993	0.000535	21.6029	0.0006
Cook	Mangaia	Keia-G-Dup	15.822861	0.00109	21.6029	0.0013
Cook	Mangaia	Veitatei-G	15.830421	0.000642	21.6500	0.0009

* Footnote: P stands for analysis on powder sample, G for analysis on gravels and Dup for complete duplicate analysis.

Table 4-2
Sr, Pb and Nd isotopic ratios of artefacts and related sources (Published data)

Archipelago	Island	Sample no.*	$^{87}Sr/^{86}Sr$	±2σ	$^{208}Pb/^{204}Pb$	±2σ
Austral	Tubuai	TBA 17 (a)	0.702761		40.229	
Austral	Tubuai	K109 (b)	0.7028		40.29	
Austral	Tubuai	TBA-11 (b)	0.703178		40.323	
Austral	Tubuai	K-109 (b)	0.702864		40.229	
Austral	Tubuai	TU 23 (c)	0.702832		40.306	
Austral	Raivavae	RV-11 (d)	0.702878		40.15634	
Austral	Raivavae	RV-27 (d)	0.702876		40.20646	
Austral	Raivavae	RV-35 (d)	0.702839		40.152211	
Marquesas	Eiao	2012-563 (e)	0.703935	0.000012	38.9699	0.0024
Marquesas	Eiao	2012-573 (e)	0.703922	0.000011	38.9648	0.0067
Marquesas	Eiao	D116.0 (f)	0.70378		38.998	
Marquesas	Eiao	D214.0 (f)	0.703743		38.999	
Marquesas	Eiao	KC-05-11 (g)	0.70394		40.156	
Austral	Rapa iti	198 [39] (f)	0.7038		39.054	
Austral	Rapa iti	RPA-02c (a)	0.703902		39.03	
Austral	Rapa iti	RA-31 (b)	0.704288		39.019	

* References: (a) Schiano et al. (2001); (b) Chauvel et al. 1992 (1992); (c) Vidal et al. (1984); (d) Maury et al. (2013); (e) Weisler et al. (2016b); (f) Duncan et al. (1986); (g) Collerson and Weisler (2007).

communities. This provides new insights into the potential scale of ancient long-distance interaction in the region.

This artefact was associated with the layer 3, which has been dated to the second half of the 14th century (1345–1395 cal. CE; Hermann et al., 2016). Nonetheless, this adze show obvious maintenance before it has been discarded and recycled as a wedging stone in the filling of a posthole. Thus, it is possible that this valuable object was acquired by Tupua'i people prior to this date and was then later transferred to the Atiahara residential area. In either case, the chronological context associated with the adze fits our current understanding that long-distance interactions were active in CEP at least until the 15th century CE.

7. Conclusion

Long-distance transfers of stone adzes in Central Polynesia were first interpreted in the terms of independent "interaction spheres" in CEP (Rolett, 2002; Weisler, 1998, 2002). To the contrary, our data and a number of more recent studies (Clark et al., 2014; Collerson and Weisler, 2007; McAlister et al., 2014; Weisler et al., 2016a) indicate that early inter-archipelago interactions extended beyond the limits of restricted regions.

Table 4-2
Cont.

Archipelago	Island	Sample no.*	$^{207}Pb/^{204}Pb$	±2σ	$^{206}Pb/^{204}Pb$	±2σ	$^{143}Nd/^{144}Nd$	±2σ
Austral	Tubuai	TBA 17 (a)	15.763		21.052		0.512875	
Austral	Tubuai	K109 (b)	15.76		21.14		0.512886	
Austral	Tubuai	TBA-11 (b)	15.749		21.039			
Austral	Tubuai	K-109 (b)	15.763		21.052			
Austral	Tubuai	TU 23 (c)	15.734		21.115		0.512891	
Austral	Raivavae	RV-11 (d)	15.726763		20.863603			
Austral	Raivavae	RV-27 (d)	15.728588		20.89702			
Austral	Raivavae	RV-35 (d)	15.724814		20.820474			
Marquesas	Eiao	2012-563 (e)	15.5791	0.001	19.1613	0.001	0.512935	0.000005
Marquesas	Eiao	2012-573 (e)	15.5797	0.0021	19.1499	0.0022	0.512942	0.000005
Marquesas	Eiao	D116.0 (f)	15.591		19.188			
Marquesas	Eiao	D214.0 (f)	15.576		19.195			
Marquesas	Eiao	KC-05-11 (g)	15.727		20.864			
Austral	Rapa iti	198 [39] (f)	15.706		19.327			
Austral	Rapa iti	RPA-02c (a)	15.58		19.07			
Austral	Rapa iti	RA-31 (b)	15.594		18.994			

* References: (a) Schiano et al. (2001); (b) Chauvel et al. (1992); (c) Vidal et al. (1984); (d) Maury et al. (2013); (e) Weisler et al. (2016b); (f) Duncan et al. (1986); (g) Collerson and Weisler (2007).

Table 5
Summary of $^{40}Ar/^{39}Ar$ data from incremental heating experiments.

Sample no. Experiment no.	wt. (mg)	K/Ca (total)	Total Fusion Age (Ma) ± 2 sigma	Age Spectrum*				Isochron Analysis*			
				Increments used (oC)	^{39}Ar (%)	Age ± 2 sigma (Ma)	MSWD	N	MSWD	$^{40}Ar/^{36}Ar$ ±2 sigma intercept	Age (Ma) ± 2 sigma
Mataare, groundmass FG-905 to FG-915	150	0.3	20.1 ± 0.62	749-1079	78.84	20.17 ± 0.63	1.65	7 of 10	1.64	304 ± 8.7	20.03 ± 0.66
At3-229-064, groundmass FG-916 to FG-925	150	0.4	10.41 ± 0.3	847-1149	60	10.32 ± 0.3	1.22	6 of 10	1.8	300.7 ± 8	10.32 ± 0.32
At3-317-065,groundmass FG-1197 to FG-1207	150	0.2	5.59 ± 0.21	595-1097	81	5.61 ± 0.21	1.16	10 of 11	1.14	293.8 ± 7.3	5.68 ± 0.24

* Footnote: Ages calculated relative to 1.193 Ma Alder Creek Rhyolite sanidine standard

Furthermore, we provide a clear chronological context for an adze imported from Eiao to Tupua'i. This directly corresponds to Weisler et al.'s (2016a) recent call for more stratigraphic sequences with imported material as necessary for better understanding the nature and the evolution of early inter-community interactions in CEP.

Additionally, our methods described here demonstrate that an integrated use of geological data in provenance studies help to unambiguously assign a source to a given artefact, and thus to refine current understanding of the spatial extent of adze production processes and inter-community exchange systems among Eastern Polynesian chiefdoms.

Acknowledgments

Archaeological fieldwork in Tupua'i and geochemical analysis formed part of A. Hermann's doctoral dissertation research and were carried out with financial support from the Université de Polynésie française and the Centre International de Recherche Archéologique en Polynésie. Special thanks to Prof. Manuel Moreira, and the Geochemistry and Cosmochemistry Laboratory at Institut de Physique du Globe de Paris for facilitating the preparation of archaeological samples. Additional thanks to Prof. Pat Kirch for providing the Mangaian samples and for his useful comments on an earlier version of this paper. A.H. and R.C.M. performed fieldwork in Tupua'i; A.H., L.S., H.G. and C.L. performed analytical research; A.H., L.S., H.G., R.C.M. and C.C. analysed data and wrote the paper. Finally, we wish to acknowledge the helpful comments by the two anonymous reviewers.

Appendix A. Supplementary data

Supplementary data to this article can be found online at http://dx.doi.org/10.1016/j.jasrep.2017.03.024.

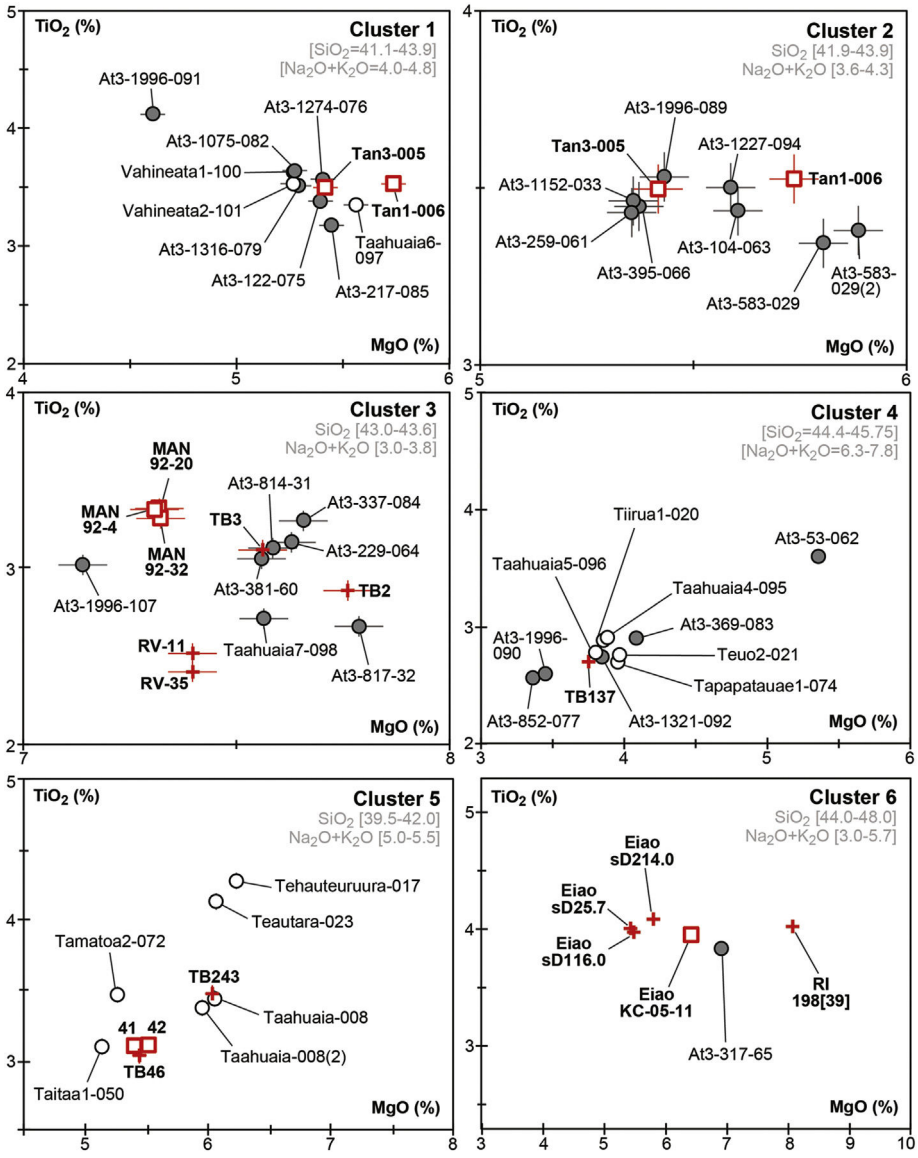

Fig. 3. Plots of TiO_2 versus MgO for the different clusters of Tupua'i stone artefacts and possible sources of procurement. Red crosses correspond to geological samples (TB = Tupua'i, RV = Raivavae, MAN = Mangaia, RI = Rapa Iti) and red squares to quarry sites samples. Circles correspond to archaeological artefacts (grey for the Atiahara site and white for surface finds in Tupua'i). Eiao sD samples are from Duncan et al. (1986), Eiao FC-05-11 is from Collerson and Weisler (2007). Rapa Iti sample is from Palacz and Saunders (1986). Ra'ivavae samples are from Maury et al. (2013). Error bars are indicated unless smaller than data points. (For interpretation of the references to colour in this figure legend, the reader is referred to the web version of this article.)

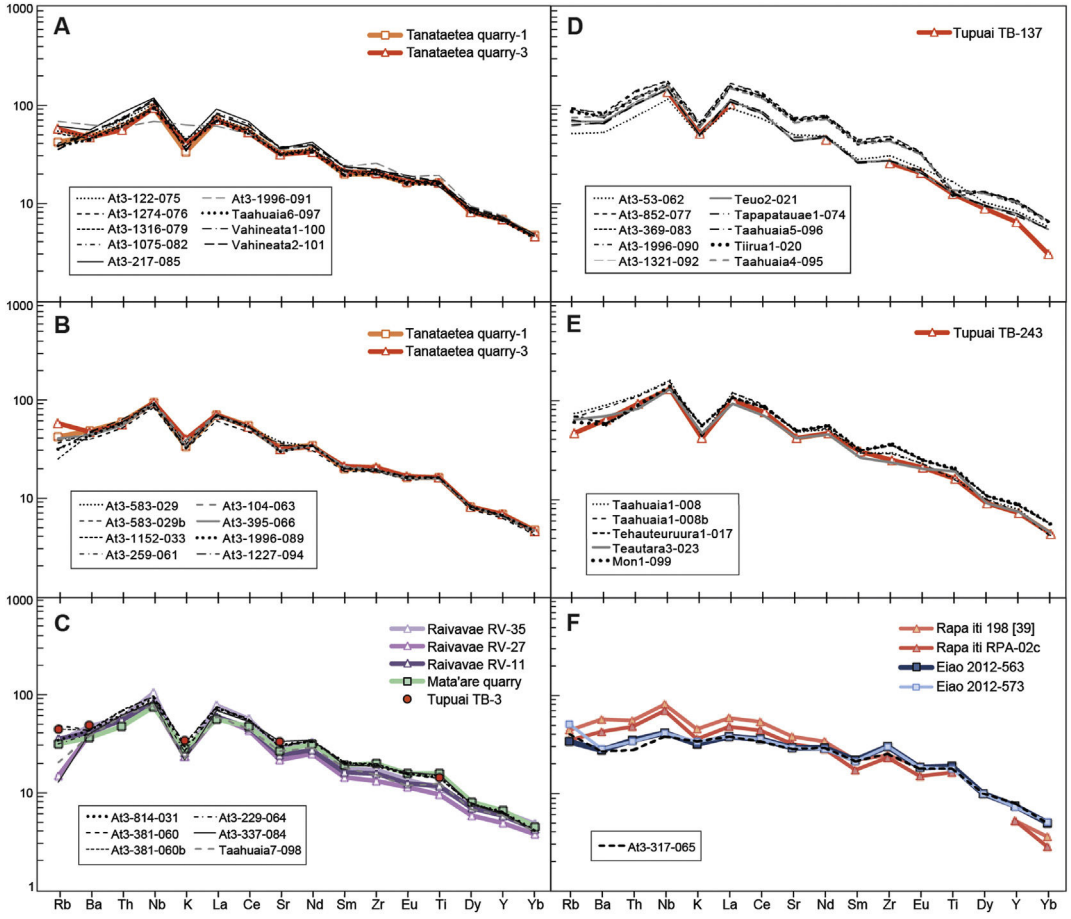

Fig. 4. Incompatible element patterns of selected artefacts from Atiahara site and of some of their potential sources. Eiao data are from Weisler and colleagues (2016). Patterns are normalized to the Primitive Mantle (Sun and McDonough 1989).

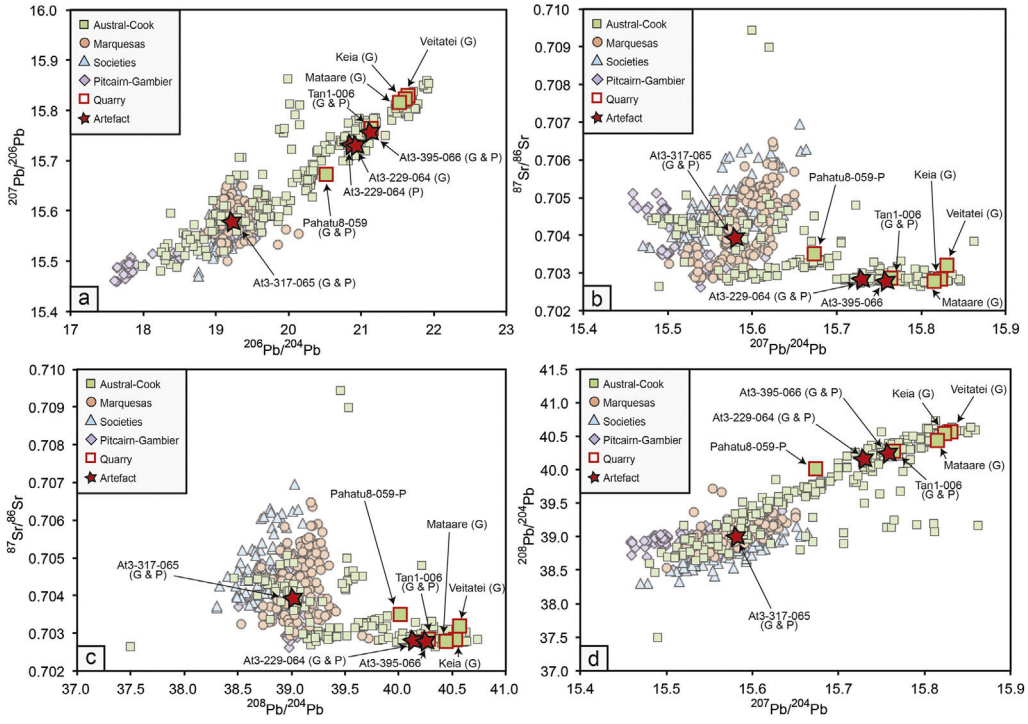

Fig. 5. Plots of Pb and Sr isotopic compositions for CEP islands. Stars and squares surrounded by red contours represent archaeological samples analyzed in this paper. Error bars (2σ) are smaller than data points. For each diagrams G stands for granulate and P for powder. Geological data is from the GEOROC database (http://georoc.mpchmainz.gwdg.de/georoc/). (For interpretation of the references to colour in this figure legend, the reader is referred to the web version of this article.)

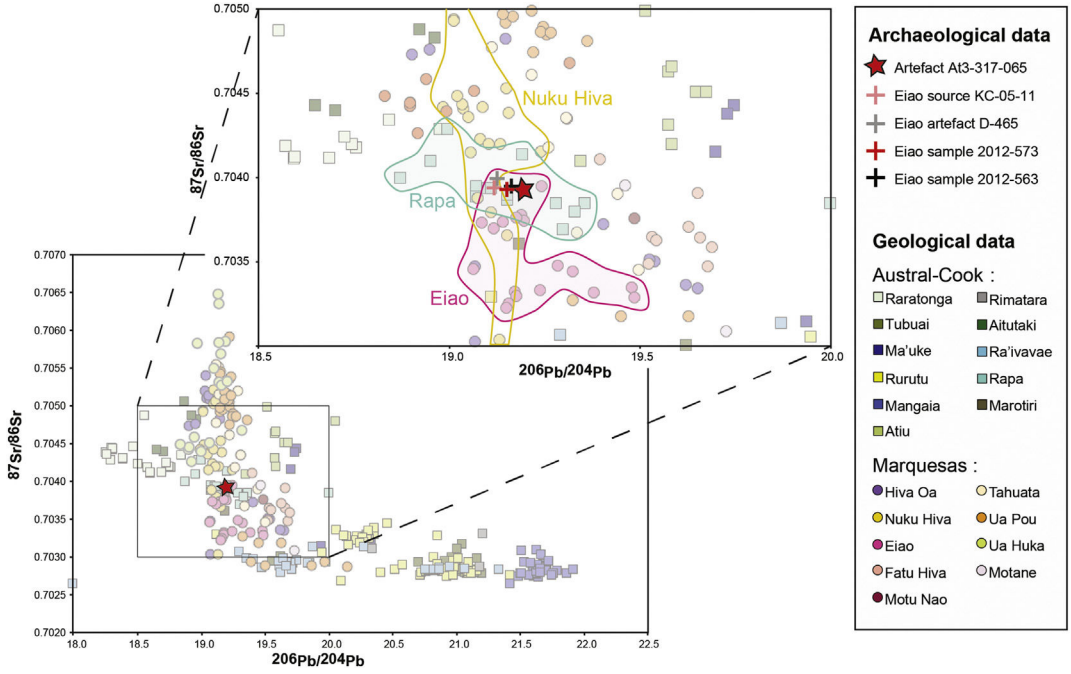

Fig. 6. Magnified plot of Pb and Sr isotopic compositions for CEP islands. Red star represents sample At3-317-065, red and black crosses represent Eiao data. Sample KC-05-11 is a flake originally collected by archaeologist R. Suggs on Eiao (Weisler, pers. com.), and sample D-465 is an Eiao adze found in Makatea: both analyses were published by Collerson and Weisler (2007). Samples 2012-563 and 2012-573 were collected by M. Charleux and published by Weisler and colleagues (2016). Error bars (2σ) are smaller than data points. Geological data is from the GEOROC database (http://georoc.mpchmainz.gwdg.de/georoc/). (For interpretation of the references to colour in this figure legend, the reader is referred to the web version of this article.)

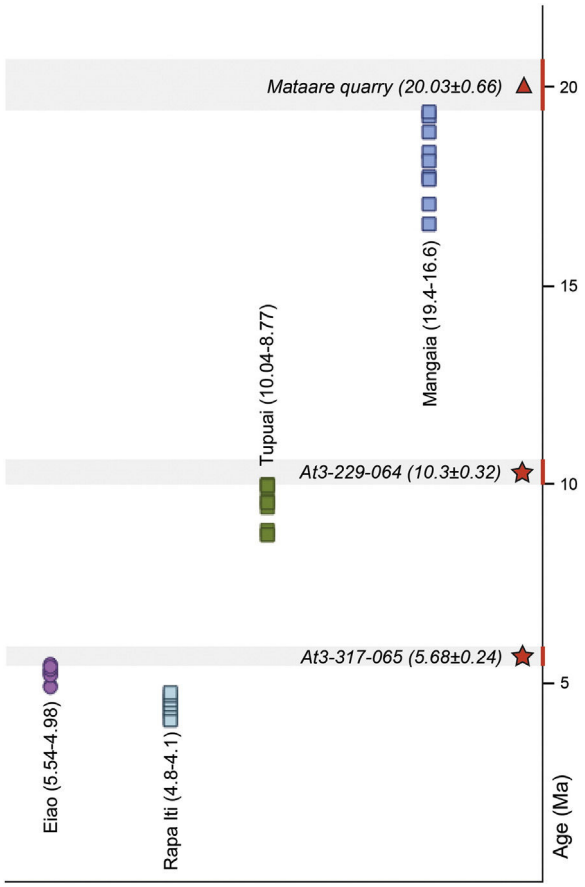

Fig. 7. Island ages and isochron dating of artefacts. Geochronological data are from Dalrymple et al. (1975), Turner and Jarrard (1982), Diraison (1991), Maury et al. (2000), Caroff et al. (1999).

References

Caroff, M., Maury, R.C., Vidal, Ph., Guille, G., Dupuy, C., Cotten, J., Guillou, H., Gillot, P.Y., 1995. Rapid temporal changes in Ocean Island basalt composition: evidence from a 800 m-deep drill hole in Eiao shield (Marquesas). J. Petrol. 36 (5):1333–1365. http://dx.doi.org/10.1093/petrology/36.5.1333.

Caroff, M., Maury, R.C., Guille, G., Cotten, J., 1997. Partial melting below Tubuai (Austral islands, French Polynesia). Contrib. Mineral. Petrol. 127:369–382. http://dx.doi.org/10.1007/s004100050286.

Caroff, M., Guillou, H., Lamiaux, M., Maury, R.C., Guille, G., Cotten, J., 1999. Assimilation of ocean crust by hawaiitic and mugearitic magmas: an example from Eiao (Marquesas). Lithos 46 (2):235–258. http://dx.doi.org/10.1016/S0024-4937(98)00068-1.

Charleux, M., McAlister, A., Mills, P.R., Lundblad, S.P., 2014. Non-destructive XRF analyses of fine-grained basalts from Eiao, Marquesas Islands. J. Pac. Archaeol. 5 (1), 75–89.

Chauvel, C., Hofmann, A.W., Vidal, P., 1992. HIMU-EM: the French Polynesian connection. Earth Planet. Sci. Lett. 110:99–119. http://dx.doi.org/10.1016/0012-821X(92)90042-T.

Chauvel, C., McDonough, W., Guille, G., Maury, R.C., Duncan, R., 1997. Contrasting old and young volcanism in Rurutu Island, Austral Chain. Chem. Geol. 139:125–143. http://dx.doi.org/10.1016/S0009-2541(97)00029-6.

Chauvel, C., Maury, R.C., Blais, S., Lewin, E., Guillou, H., Guille, G., Rossi, P., Gutscher, M.A., 2012. The size of plume heterogeneities constrained by Marquesas isotopic stripes. Geochem. Geophys. Geosyst.:13 http://dx.doi.org/10.1029/2012GC004123.

Clark, G.R., Reepmeyer, C., Melekiola, N., Woodhead, J., Dickinson, W.R., Martinsson-Wallin, H., 2014. Stone tools from the ancient Tongan state reveal prehistoric interaction centers in the Central Pacific. Proc. Natl. Acad. Sci. U. S. A. 111 (29): 10491–10496. http://dx.doi.org/10.1073/pnas.1406165111.

Collerson, K.D., Weisler, M.I., 2007. Stone adze compositions and the extent of ancient Polynesian voyaging and trade. Science 317 (5846):1907–1911. http://dx.doi.org/10.1126/science.1147013.

Cordier, C., Chauvel, C., Hémond, C., 2016. High-precision lead isotopes and stripy plumes: revisiting the society chain in French Polynesia. Geochim. Cosmochim. Acta 189: 236–250. http://dx.doi.org/10.1016/j.gca.2016.06.010.

Dalrymple, G.B., Jarrard, R.D., Clague, D.A., 1975. K-Ar ages of some volcanic rocks from the Cook and Austral Islands. Geol. Soc. Am. Bull. 86 (10):1463–1467. http://dx.doi.org/10.1130/0016-7606(1975)86<1463:KAOSVR>2.0.CO;2.

Delavault, H., Chauvel, C., Sobolev, A., Batanova, V., 2015. Combined petrological, geochemical and isotopic modeling of a plume source: example of Gambier Island, Pitcairn chain. Earth Planet. Sci. Lett. 426:25–35. http://dx.doi.org/10.1016/j.epsl.2015.06.013.

Diraison, C., 1991. Le volcanisme aérien des archipels polynésiens de la Société, des Marquises et des Australes-Cook. Téphrostratigraphie, datation isotopique et géochimie comparées. l'Université de Bretagne Occidentale, Brest PhD à. (413 p).

Duncan, R.A., McCulloch, M.T., Barsczus, H.G., Nelson, D.R., 1986. Plume versus lithospheric sources for melts at Ua Pou, Marquesas Islands. Nature 322, 534–538.

Dupuy, C., Barsczus, H.G., Dostal, J., Vidal, P., Liotard, J.M., 1989. Subducted and recycled lithosphere as the mantle source of ocean island basalts from southern Polynesia, central Pacific. Chem. Geol. 77:1–18. http://dx.doi.org/10.1016/0009-2541(89)90010-7.

Green, R.C., Kirch, P.V., 1997. Lapita exchange systems and their Polynesian transformations: seeking explanatory models. In: Weisler, M.I. (Ed.), Prehistoric Long-distance Interaction in Oceania: an Interdisciplinary Approach, Monograph 21. New Zealand Archaeological Association, Otago, New Zealand, pp. 19–37.

Guillou, H., Gillot, P.Y., Guille, G., 1994. Age (K-Ar) et position des îles Gambier dans l'alignement du point chaud de Pitcairn (Pacifique Sud). C. R. Acad. Sci. III 318, 635–641.

Guillou, H., Maury, R.C., Blais, S., Cotten, J., Legendre, C., Guille, G., Caroff, M., 2005. Age progression along the society hotspot chain (French Polynesia) based on new unspiked K-Ar ages. Bull. Soc. Geol. Fr. 176:135–150. http://dx.doi.org/10.2113/176.2.135.

Guillou, H., Maury, R.C., Guille, G., Chauvel, C., Rossi, Ph., Pallares, C., Legendre, C., Blais, S., Liorzou, C., Deroussi, S., 2014. Volcanic successions in Marquesas eruptive centers: a departure from the Hawaiian model. J. Volcanol. Geotherm. Res. 266:173–188. http://dx.doi.org/10.1016/j.jvolgeores.2013.12.003.

Hermann, A., 2013. Les industries lithiques pré-européennes de Polynésie centrale: savoir-faire et dynamiques techno-économiques. PhD dissertation. University of French Polynesia, Papeete, French Polynesia.

Hermann, A., 2015. Dynamique de peuplement et évolution des réseaux d'échange à longue distance en Océanie. Les systèmes de mobilité de la Préhistoire au Moyen Age. In: Naudinot, N., Meignen, L., Binder, D. (Eds.), XXXV International Meeting of Archaeology End History. APDCA, Antibes, pp. 109–125.

Hermann, A., 2016. Production et échange des lames d'herminette en pierre en Polynésie centrale: les dynamiques techno-économiques dans l'île de Tubuai (Archipel des Australes). La pratique de l'espace en Océanie: Découverte, appropriation et émergence des systèmes sociaux traditionnels. In: Valentin, F., Molle, G. (Eds.), Séance de la Société Préhistorique Française. INHA, Paris, pp. 205–221.

Hermann, A., Maury, R.C., Liorzou, C., 2012. Traçabilité des matières premières lithiques dans les assemblages archéologiques polynésiens: le cas de Tubuai (Archipel des Australes, Polynésie française). Géologues 173, 80–83.

Hermann, A., Bollt, R., Conte, E., 2016. The Atiahara site revisited: an early coastal settlement in Tubuai (Austral Islands, French Polynesia). Archaeol. Ocean. 51 (1):31–44. http://dx.doi.org/10.1002/arco.5070.

Kahn, J.G., Sinton, J., Mills, P.R., Lundblad, S.P., 2013. X-ray fluorescence analysis and intra-island exchange in the Society Island Archipelago (Central Eastern Polynesia). J. Archaeol. Sci. 40:1194–1202. http://dx.doi.org/10.1016/j.jas.2012.10.003.

Kirch, P.V., Mills, P.R., Lundblad, S.P., Sinton, J., Kahn, J.G., 2012. Interpolity exchange of basalt tools facilitated via elite control in Hawaiian archaic states. Proc. Natl. Acad. Sci. U. S. A. 109 (4):1056–1061. http://dx.doi.org/10.1073/pnas.1119009109.

Lassiter, J.C., Blichert-Toft, J., Hauri, E.H., Barsczus, H.G., 2003. Isotope and trace element variations in lavas from Raivavae and Rapa, Cook-Austral Islands: constraints on the nature of HIMU- and EM-mantle and the origin of mid-plate volcanism in French Polynesia. Chem. Geol. 202:115–138. http://dx.doi.org/10.1016/j.chemgeo.2003.08.002.

Liotard, J.M., 1988. Contribution au problème de l'origine des basaltes alcalins: fractionnement haute pression, caractérisation des zones sources, comparaison entre domaine océanique (Polynésie française) et domaine continental, Hoggar algérien, Massif central français. PhD dissertation. University of Montpellier 2.

Maury, R.C., El Azzouzi, M., Bellon, H., Liotard, J.M., Guille, G., Barsczus, H.G., Chauvel, C., Diraison, C., Dupuy, C., Vidal, Ph., Brousse, R., 1994. Géologie et pétrologie de l'île de Tubuai (Australes, Polynésie française). C. R. Acad. Sci. II 318, 1341–1347.

Maury, R.C., Guille, G., Guillou, H., Blais, S., Brousse, R., 2000. Notice explicative, Carte Géol France, feuille Rurutu et Tubuai, Polynésie française 1154. BRGM, Orléans (81 pp.).

Maury, R.C., Guille, G., Guillou, H., Chauvel, C., Rossi, Ph., Pallares, C., Legendre, C., 2013. Temporal evolution of a Polynesian hotspot: new evidence from Raivavae (Austral Islands, South Pacific Ocean). Bull. Soc. Geol. Fr. 184, 385–395.

Maury, R.C., Legendre, C., Chauvel, C., Guille, G., Blais, S., Guillou, H., Rossi, P., 2014a. Geology of the Austral Islands: an atypical hotspot chain. In: Meyer, J.Y., Claridge, E.M. (Eds.), Terrestrial Biodiversity Austral Islands, French Polynesia. MNHN, Paris, pp. 21–37.

Maury, R.C., Guille, G., Guillou, H., Chauvel, C., Legendre, C., Rossi, P., Blais, S., Pallares, C., Deroussi, S., Marabal, A.M., 2014b. Géologie des Marquises: des volcans boucliers intra-océaniques effondrés issus d'un point chaud atypique. Géol. Fr. 1, 111–135.

McAlister, A., Sheppard, P.J., Allen, M.S., 2014. The identification of a Marquesan Adze in the Cook Islands. J. Polyn. Soc. 122 (3), 257–274.

Mills, P.R., Lundblad, S.P., Field, J.S., Carpenter, A.B., McElroy, W.K., Rossi, P., 2010. Geochemical sourcing of basalt artefacts from Kaua'i, Hawaiian Islands. J. Archaeol. Sci. 37, 3385–3393.

Palacz, Z.A., Saunders, A.D., 1986. Coupled trace element and isotope enrichment in the Cook-Austral-Samoa islands, Southwest Pacific. Earth Planet. Sci. Lett. 79 (3–4), 270–280.

Rolett, B.V., 2002. Voyaging and interaction in ancient East Polynesia. Asian Perspect. 41 (2), 182–194.

Rolett, B.V., West, E., Sinton, J., Iovita, R., 2015. Ancient East Polynesian voyaging spheres: new evidence from the Vitaria Adze Quarry (Rurutu, Austral Islands). J. Archaeol. Sci. 53:459–471. http://dx.doi.org/10.1016/j.jas.2014.10.018.

Schiano, P., Burton, K.W., Dupré, B., Birck, J.L., Guille, G., Allègre, C.J., 2001. Correlated Os-Pb-Nd-Sr isotopes in the Austral-Cook chain basalts: the nature of mantle components in plume sources. Earth Planet. Sci. Lett. 186:527–537. http://dx.doi.org/10.1016/S0012-821X(01)00265-5.

Sun, S.S., McDonough, W.F., 1989. Chemical and isotopic systematics of oceanic basalts: implication for mantle composition and processes. Geological Society Special Publication, Vol. 42. In: Saunders, A.D., Norry, M.J. (Eds.), Magmatism in the Ocean Basins. Blackwell, London, pp. 313–345.

Turner, D.L., Jarrard, R.D., 1982. K/Ar dating of the Cook-Austral island chain: a test of the hot-spot hypothesis. J. Volcanol. Geotherm. Res. 12:187–220. http://dx.doi.org/10.1016/0377-0273(82)90027-0.

Vidal, P., Chauvel, C., Brousse, R., 1984. Large mantle heterogeneity beneath French Polynesia. Nature 307:536–538. http://dx.doi.org/10.1038/307536a0.

Walter, R.K., Sheppard, P.J., 1996. The Ngati Tiare adze cache: further evidence of prehistoric contact between west Polynesia and the southern Cook Islands. Archaeol. Ocean. 30:47–65. http://dx.doi.org/10.1002/j.1834-4453.1996.tb00344.x.

Weisler, M.I., 1993. Provenance studies of Polynesian basalt adze material: a review and suggestions for improving regional databases. Asian Perspect. 32, 61–83.

Weisler, M.I., 1997. Prehistoric long-distance Interaction in Oceania: an interdisciplinary approach. Monograph. 21. New Zealand Archaeological Association (238 pp).

Weisler, M.I., 1998. Hard evidence for prehistoric interaction in Polynesia. Curr. Anthropol. 39 (4):521–532. http://dx.doi.org/10.1086/204768.

Weisler, M.I., 2002. Centrality and the collapse of long-distance voyaging in East Polynesia. In: Glascock, M.D. (Ed.), Geochemical Evidence for Trade and Exchange. Bergin and Garvey, Westport, CT, pp. 257–273.

Weisler, M.I., Kirch, P.V., 1996. Interisland and interarchipelago transfer of stone tools in prehistoric Polynesia. Proc. Natl. Acad. Sci. U. S. A. 93 (4), 1381–1385.

Weisler, M.I., Woodhead, J.D., 1995. Basalt Pb isotope analysis and the prehistoric settlement of Polynesia. Proc. Natl. Acad. Sci. U. S. A. 92:1381–1385. http://dx.doi.org/10.1073/pnas.92.6.1881.

Weisler, M.I., Kirch, P.V., Endicott, J.M., 1994. The Mata'are basalt source: implications for prehistoric interaction studies in the Cook Islands. J. Polyn. Soc. 103 (2), 203–216.

Weisler, M.I., Bolhar, R., Ma, J., St Pierre, E., Sheppard, P., Walter, R.K., Feng, Y.X., Zhao, J.X., Kirch, P.V., 2016a. Cook Island artefact geochemistry demonstrates spatial and temporal extent of pre-European interarchipelago voyaging in East Polynesia. Proc. Natl. Acad. Sci. U. S. A. http://dx.doi.org/10.1073/pnas.1608130113.

Weisler, M., Bolhar, R., Charleux, M., Faith, J.T., Feng, Y.X., St Pierre, E., 2016b. Determining geochemical variability of fine-grained basalt sources/quarries for facilitating prehistoric interaction studies in Polynesia. Archaeol. Ocean. http://dx.doi.org/10.1002/arco.5088.

White, W.M., Duncan, R.A., 1996. Geochemistry and geochronology of the Society Islands: new evidence for deep mantle recycling. Geophys. Monogr. 95:183–206. http://dx.doi.org/10.1029/GM095p0183.

Woodhead, J.D., Weisler, M.I., 1997. Accurate sourcing of basalt artefacts by radiogenic isotope analysis. In: Weisler, M.I. (Ed.), Prehistoric Long-Distance Interaction in Oceania: An Interdisciplinary Approach, Monograph 21. New Zealand Archaeological Association, Otago, New Zealand, pp. 212–223.

Zindler, A., Hart, S.R., 1986. Chemical geodynamics. Earth Planet. Sci. 14:493–571. http://dx.doi.org/10.1146/annurev.ea.14.050186.002425.

Supplementary data

Appendix A: Analytical procedures

Major and trace element analysis

Major and trace elements were determined at the PSO/IUEM (Pôle Spectrométrie Océan, Institut Universitaire Européen de la Mer, Plouzané, France), following the analytical procedure of Cotten et al. (1995). Typically, 250 mg of rock power was dissolved in closed screw-top teflon vessels (Savillex) at about 90°C for one day using 3 ml of concentrated HF, and 1 ml of concentrated HNO_3. Next, 96 ml of H_3BO_3 aqueous solution (20 g/L H_3BO_3) were added to neutralize the excess HF. All reagents used are analytical grade.

Elements were measured by using a Horiba Jobin Yvon® Ultima 2 spectrometer. The boron included in the solution was used as an internal standard. Calibrations were made using international standard, ACE, ME, WSE, JB2. For major elements, relative standard deviation is ≤1% for SiO2 and ≤2% for the other major elements, for trace elements standard deviation is ≤5%.

Sr and Pb isotope analysis

Pb and Sr analytical procedures have been previously described by Chauvel et al. (2011). Hence, only a brief synopsis is provided here. Before isotopic analysis, each sample was hand-crushed in an agate mortar to obtain both powders (P) and granulates (G). Between 500 and 1000 mg of samples were then dissolved in a HF-HNO_3 mixture in Savillex beakers for two days on a hot plate at 130°C.

Pb was first isolated by chromatography using columns filled with anion AG1-X8 resin and dilute HBr and then eluted with HCl 6N. Isotopic ratios were determined using a Nu Plasma MC-ICP-MS at the ENS Lyon (France) using the thallium addition technique described by White et al. (2000) for mass bias correction. Analytical drift was corrected by standard bracketing using NBS 981 as reference material. Sr was purified using two successive columns filled with cationic resin AG50w-X8 and Sr-Spec resin and measured using a solid source Thermo Scientific Triton mass spectrometer (TIMS) at PSO/IUEM (Plouzané, France) in static mode.

The accuracy of Pb and Sr isotopic compositions was assessed by: (1) duplicate analysis, (2) re-run analyses (i.e. measuring several times the same sample either in powder and granulate forms), and (3) analyzing reference materials (NBS 981 for Pb and NBS 987 for Sr). Our results show that Sr and Pb isotopic compositions of powder samples are consistent with those of granulated samples within uncertainties and that duplicate measurements are analytically correct. The average of the measured values is $^{87}Sr/^{86}Sr = 0.710248 \pm 0.000008$ (2σ, n=3), versus 0.710262 ± 0.000011 (2σ, n=4) (Chauvel et al., 2011) for reference material NBS 987 and $^{208}Pb/^{204}Pb = 36.701 \pm 0.007$ (2σ, n=14), versus 36.722 ± 0.0044 (2σ, n=60) (Galer and Abouchami, 1998), $^{207}Pb/^{204}Pb = 15.4924 \pm 0.002$ (2σ, n=14), versus 15.4963 ± 0.0016 (2σ, n=60) (Galer and Abouchami, 1998) and $^{206}Pb/204Pb = 16.9415 \pm 0.0052$ (2σ, n=14), versus 16.9405 ± 0.0015 (2σ, n=60) (Galer and Abouchami, 1998) for NBS 981.

$^{40}Ar/^{39}Ar$ procedures

The samples were crushed and sieved to 0.250-0.125 mm size fractions, and ultrasonically washed in acetic acid (1N) during 45 minutes at a temperature of 60°C to remove unsuspected minute amounts of secondary mineral phases. Argon was measured on the microcrystalline groundmass, after removal of phenocrysts using heavy liquids and magnetic separations. This process removes at least some potential sources of systematic error due to the presence of excess ^{40}Ar in phenocrysts. Because of undesirable effects of the alteration on the radio-isotopic chronometer, the groundmass splits of the three samples were then carefully observed macroscopically and microscopically. No obvious signs of alteration were detected for samples At3-229-064 and At3-317-065, which are considered unaltered with respect to their loss on ignition (L.O.I.) values (Table S2). Some traces of oxidation, a sign of alteration, are observed within the groundmass of the Mata'are sample. They contribute to a L.O.I. value higher than 1% (i.e. 1.36%). Despite this moderate alteration we decided to process it, keeping in mind the possible effects of alteration on the isotopic measurements.

Irradiation procedures, extraction and gas clean-up, mass spectrometric measurements and blank corrections, are fully described in Guillou et al. (2011). The 120 mg samples were wrapped into 99.5% copper foil packets, loaded in aluminium disks and then irradiated 180 minutes (Irradiation # 75,91) in the β1 tube of the OSIRIS reactor (CEA Saclay, France). The samples received total neutron flux ranging from 1.2 10^{+14} to 2.7 10^{+14} n/cm-2. Neutron fluence (J) was monitored by co-irradiation of ACs (1.193 Ma, Nomade et al., 2005) placed in three positions around the aluminum disk. The J value for each sample was determined from 6 single crystal laser fusion analyses of ACs. The total decay constants of Min et al. (2000) and the $^{40}Ar/^{36}Ar$ atmospheric ratio at 298.56 (Lee et al., 2006) were applied to the flux and age calculations. J values vary by about 1.4% to 1.8% across each disk pit. Correction factors for interfering neutron reactions determined on pure compounds (K_2O, CaF_2) were: $(^{39}Ar/^{37}Ar)_{Ca}$ = 8.05 10-4, $(^{36}Ar/^{37}Ar)_{Ca}$ = 3.77 10-4, $(^{40}Ar/^{39}Ar)_{K}$ = 6.56 10-4; $(^{38}Ar/^{39}Ar)_{K}$ = 1.12 10-2.

After irradiations, pure groundmass aliquots were incrementally heated in 10 to 11 steps between 600º and 1200ºC using a metal resistance furnace. One step-heating experiment was conducted for each sample. Isotopic measurements were achieved using a high-sensitivity noble gas GV5400 instrument operated in ion counting mode. One analytical run consists of 20 peak scans of each argon isotope with integration times of 2 s (^{40}Ar, ^{39}Ar), 10 s (^{37}Ar, ^{38}Ar, baseline) and 20 s (^{36}Ar). This is first preceded by a peak centering routine on the five Ar isotopes, upon admission of the sample into the mass-spectrometer. Raw argon isotope abundances are regressed back to inlet time using GV software (NG v.2.90) based on linear or polynomial least-squares fit. The instrument was operated at a sensitivity of 8 x 10^{-3}A/Torr. The precision and accuracy of the mass discrimination correction was monitored by periodical measurements of air argon. This monitoring is performed using a dedicated air-calibration system featuring a 6 litres tank filled with purified atmospheric argon. This system allows for a 1 cc (e.g. 200 000 counts s-1 cps on ^{40}Ar) or multiple of 1cc atmospheric aliquots to be delivered into the mass spectrometer and permits a careful monitoring of the mass discrimination over a wide dynamic range with a precision better than 0.15% (2σ; standard deviation for multiples of experiments) for any given bean size measured. System blanks were measured prior to step-heating experiments at temperature between 600 and 1300°C. Blanks were between 2.0 10^{-16} and 7.8 10^{-16} mole of ^{40}Ar and between 1.0 10^{-18} and 3.0 10^{-18} mole of ^{36}Ar. These values are about 10 to 20 times smaller than the sample ^{36}Ar signals and about 20 to 140 times smaller than the sample ^{40}Ar signals. Secondary phases could not be entirely eliminated from the Mata'are groundmass sample. Most of the alteration products are preferentially outgassed during the pre-heating (around 500°c - 600°c) of the samples prior to the first step of the incremental heating experiments (Sharp and Renne, 2005). Alteration effects shaped symptomatically the age spectra (Fig. S5). During the two first low temperature steps (650°c - 700°c), argon is released from the less retentive sites (i.e., surface of the grain, secondary minerals formed by post magmatic alteration). As a consequence, these steps are characterized by high apparent ages coupled with increasing K/Ca ratios. They are eliminated from the age calculation as well as the highest temperature step. ^{40}Ar-^{39}Ar plateau ages, isochron regressions and probability of fit estimates were calculated using ArArCalc (Koppers, 2002) and following the criteria of Sharp and Renne (Sharp and Renne, 2005).

References

Cotten J, Le Dez A, Bau M, Caroff M, Maury RC, Dulski P, Fourcade S, Bohn M, Brousse R (1995) Origin of anomalous rare-earth element and yttrium enrichments in subaerially exposed basalts: Evidence from French Polynesia. Chem Geol 119: 115-138, doi: 10.1016/0009-2541(94)00102-E.

Chauvel C, Bureau S, Poggi C (2011) Comprehensive chemical and isotopic analyses of basalt and sediment reference materials. Geostand Geoanal Res 35(1): 125-143, doi: 10.1111/j.1751-908X.2010.00086.x.

Galer SJG, Abouchami W (1998) Practical application of lead triple spiking for correction of instrumental mass discrimination. Mineral Mag 62 A: 491-492.

Guillou H, Nomade S, Carracedo JC, Kissel C, Laj C, Wandres C (2011) Effectiveness of combined unspiked K–Ar and 40Ar/39Ar dating methods in the 14C age range. Quat Geochronol 6: 530-538, doi: 10.1016/j.quageo.2011.03.011.

Koppers AAP (2002) ArAr CALC software for 40Ar/39Ar age calculations. Comp and Geosci 28: 605-619.
Lee JY, Marti K, Severinghaus K, Kawamura K, Yoo HS, Lee JB, Kim JS (2006) A redetermination of the isotopic abundances of atmospheric Ar. Geochim Cosmochim Acta 70: 4507-4512, doi: 10.1016/j.gca.2006.06.1563.
Min KW, Mundil R, Renne PR, Ludwig KR (2000) A test for systematic errors in 40Ar/39Ar geochronology through comparison with U-Pb analysis of a 1.1 Ga rhyolite. Geochim Cosmochim Acta 64: 73–98, 10.1016/S0016-7037(99)00204-5.
Nomade S, Renne PR, Vogel N, Deino AL, Sharp WD, Becker TA, Jaouni AR, Mundil R (2005) Alder creek sanidine (ACs-2): a quaternary 40Ar/39Ar 40Ar/39Ar dating standard tied to the Cobb mountain geomagnetic event. Chem Geol 218: 315-338, doi: 10.1016/j.chemgeo.2005.01.005.
Sharp WD, Renne PR (2005) The 40Ar/39Ar dating of core recovered by the Hawaii scientific drilling project (phase 2), Hilo, Hawaii. Geochem Geophys Geosys 6(4), doi: 10.1029/2004GC000846.
White WM, Albarède F, Télouk P (2000) High-precision analysis of Pb isotope ratios by multi-collector ICP-MS. Chem Geol 167(3-4): 257-270, doi: 10.1016/S0009-2541(99)00182-5.

Appendix B: Photographs

Appendix B-1: The Tanataetea site. A. An open-air workshop outside quarry, and B. Detail on a remaining dyke seam (Tan-1-006) within the underground quarry.

Appendix B-2: Photographs of mentioned artifacts: A. At3-229-064, Polished adze collected in layer 7 of the Atiahara site; B. At3-317-65, Adze fragment (distal) collected in layer 3 of the Atiahara site; C. At3-395-066, Adze fragment (distal end) collected in layer 5 of the Atiahara site.

Appendix C: Geochronology of archaeological samples

Appendix C: Age spectra and isochrons depicting $^{40}Ar/^{39}Ar$ experimental results for Mata'are quarry, At3-229-064 and At3-317-065 samples. Black lines are $^{40}Ar/^{39}Ar$ ages. Red lines are K/Ca ratios. Uncertainties are ±2σ. Grey boxes are excluded steps in age plateau calculation. Black ellipses are included in isochron regression; grey ones are not. A complete set of $^{40}Ar/^{39}Ar$ measurements for all samples is given in Data Repository.

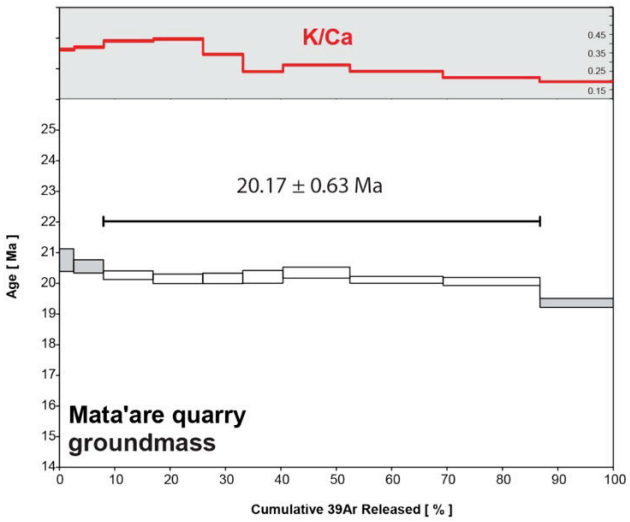

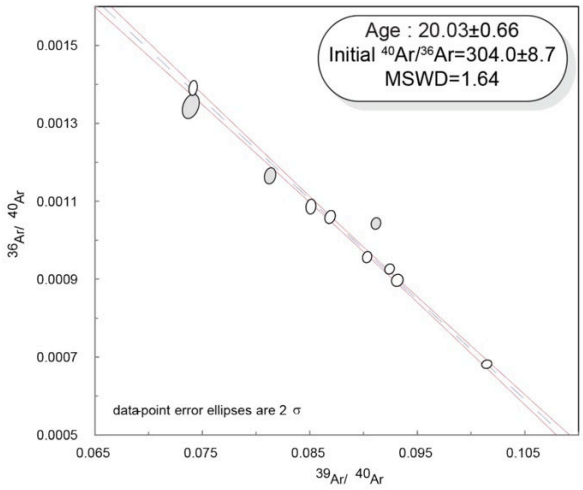

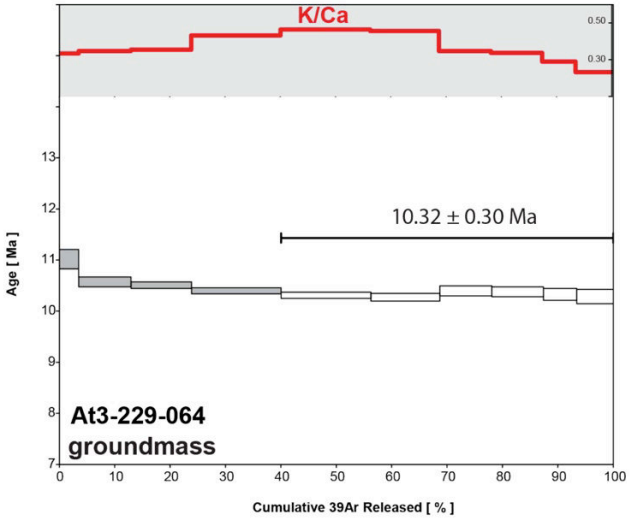

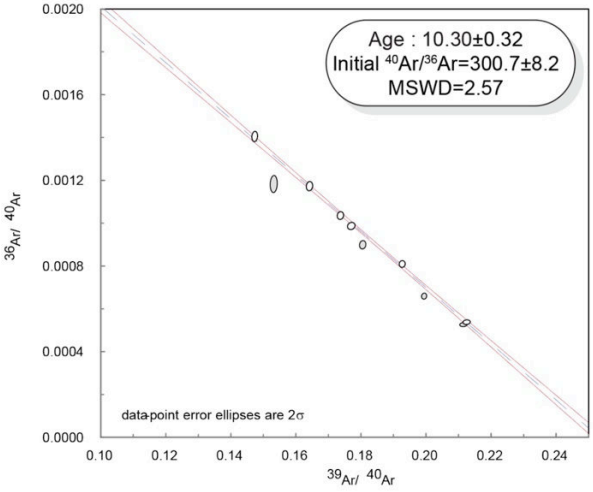

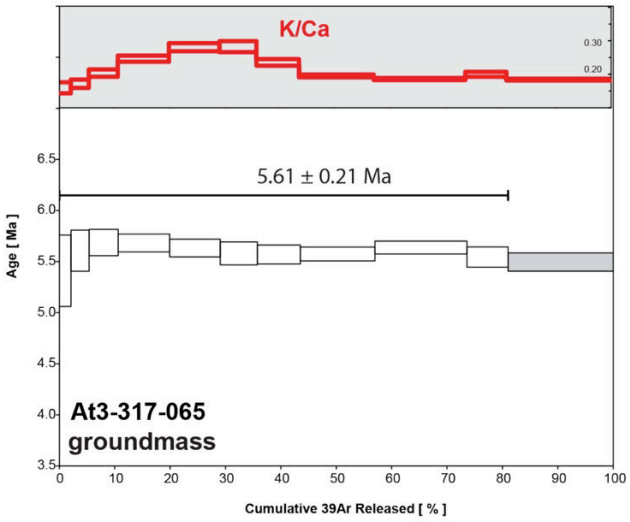

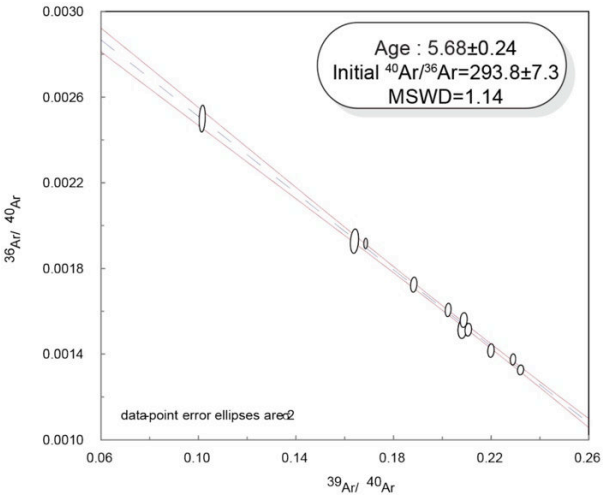

Annexe 2: Articles publiés avant ma thèse portant sur mes stages de Master 1 et 2

Mon projet de Master 2 a été mené aux Etats-Unis à l'université de Maryland sous la cotutelle de Roberta Rudnick (Professeur, UC Santa Barbara, USA) et Catherine Chauvel (Directeur de recherche, ISTerre, Grenoble). J'ai analysé les compositions isotopiques en lithium (Li) de loess (roches sédimentaires) dans le but d'apporter de plus amples informations concernant la composition de la croûte continentale et son degré d'altération actuel. Cela m'a amené à publier un article dans Earth and Planetary Science Letters (EPSL).

ARTICLE

New perspectives on the Li isotopic composition of the upper continental crust and its weathering signature

Sauzéat L., Rudnick R., Chauvel C., Garçon M., Tang M.

(Published in Earth and Planetary Science letters)

Pour citer ce papier *: **Sauzéat L.**, Rudnick R., Chauvel C., Garçon M., Tang M. New perspectives on the Li isotopic composition of the upper continental crust and its weathering signature; Earth and Planetary Science Letters (2015)*.

L'étude réalisée pendant mon Master 1 est également en lien avec la géologie mais porte sur la formation des kimberlites. Je l'ai réalisé sous la tutelle de Carole Cordier (Maître de conférences à ISTerre, Grenoble) et Nick Arndt (professeur émérite, ISTerre, Grenoble) à Grenoble. Brièvement, l'ensemble des données présentées dans ce manuscrit a été acquis avec une microsonde électronique JEOL JXA-8230 à Grenoble. Cela m'a permis d'établir des profiles chimiques montrant la distribution spatiale des éléments et ainsi de mieux comprendre le mode de formation des kimberlites. Cette étude a abouti à la publication d'un papier principal ayant suscité par la suite de nombreux commentaires nécessitant des réponses (2 papiers annexes).

ARTICLE PRINCIPAL

Metasomatism of the lithospheric mantle immediately precedes kimberlite eruption: new evidence from olivine composition and microstructures

*Cordier C., **Sauzéat L.**, Arndt N.T., Boullier A.-M., Batanova V., Barou F.*

(Published in Journal of Petrology)

Pour citer ce papier : *Cordier C., **Sauzéat L.**, Arndt N.T., Boullier A.-M., Batanova V., Barou F. Metasomatism of the lithospheric mantle immediately precedes kimberlite eruption: new evidence from olivine composition and microstructures; Journal of Petrology (2015)*

RÉPONSES À L'ARTICLE PRINCIPAL

- *Cordier C., **Sauzéat L.**, Arndt N.T., Boullier A.-M., Batanova V., Barou F. Quantitative modelling of the apparent decoupling of Mg# and Ni in kimberlitic olivine margins: a reply to the comment on Cordier et al. (2015) by Moore A.; Journal of Petrology (2017)*

- *Cordier C., **Sauzéat L.**, Arndt N.T., Boullier A.-M., Batanova V., Barou F. The Geochemical Complexity of Kimberlite Rocks and their Olivine Populations: a Reply to the Comment on Cordier et al. (2015) by Andrea Giuliani & Stephen F. Foley; Journal of Petrology (2016)*

Tous les articles, exceptés ceux faisant office de réponse à des articles précédents et pour lesquels je n'ai que très peu contribué, sont présentés ci-dessous.

Earth and Planetary Science Letters 428 (2015) 181–192

Contents lists available at ScienceDirect

Earth and Planetary Science Letters

www.elsevier.com/locate/epsl

New perspectives on the Li isotopic composition of the upper continental crust and its weathering signature

Lucie Sauzéat [a,b,*], Roberta L. Rudnick [a], Catherine Chauvel [b,c], Marion Garçon [d], Ming Tang [a]

[a] Department of Geology, University of Maryland, College Park, MD 20742, USA
[b] University of Grenoble Alpes, ISTerre, F-38041 Grenoble, France
[c] CNRS, ISTerre, F-38041 Grenoble, France
[d] Carnegie Institution of Washington, Department of Terrestrial Magnetism, Washington, DC 20015, USA

ARTICLE INFO

Article history:
Received 11 May 2015
Received in revised form 1 July 2015
Accepted 14 July 2015
Available online xxxx
Editor: M. Bickle

Keywords:
Li isotopes
loess
upper continental crust
chemical weathering

ABSTRACT

Lithium isotopes are increasingly used to trace both present-day and past weathering processes at the surface of the Earth, and could potentially be used to evaluate the average degree of past weathering recorded by the upper continental crust (UCC). Yet the previous estimate of average δ^7Li of the UCC has a rather large uncertainty, hindering the use of Li isotopes for this purpose. New δ^7Li for desert and periglacial loess deposits (windblown dust) from several parts of the world (Europe, Argentina, China and Tajikistan) demonstrate that the former are more homogeneous than the latter, and may therefore serve as excellent proxies of the average composition of large tracts of the UCC. The Li isotopic compositions and concentrations of desert loess samples are controlled by eolian sorting that can be quantified by a binary mixing between a weathered, fine-grained end-member, dominated by phyllosilicates and having low δ^7Li, and an unweathered, coarse-grained end-member, that is a mixture of quartz and plagioclase having higher δ^7Li. We use correlations between insoluble elements (REE, Nd/Hf and Fe_2O_3/SiO_2), Li concentrations (henceforth referred as [Li]), and δ^7Li to estimate a new, more precise, average Li isotopic composition and concentration for the UCC: $[Li] = 30.5 \pm 3.6 (2\sigma)$ ppm, and $\delta^7Li = +0.6 \pm 0.6 (2\sigma)$. The δ^7Li for desert loess deposits is anti-correlated with the chemical index of alteration (CIA). Using this relationship, along with our average δ^7Li, we infer that (1) the present-day CIA of the average UCC is $61^{+4}_{-2} (2\sigma)$, higher than the common reference value of 53, and (2) the average proportion of chemically weathered components is as high as $37^{+17}_{-10} (2\sigma)$% at the surface of the Earth.

1. Introduction

Weathering is an ubiquitous process that occurred in the past to form (meta-)sedimentary rocks ("past weathering") and still occurs at present to create sediments and soils ("present-day weathering"). It shapes the continental crust and modifies its chemical composition by producing detrital sediments and releasing ions into the hydrosphere over geological timescales (Taylor and McLennan, 1985; Rudnick, 1995; Lee et al., 2008; Liu and Rudnick, 2011). Chemical weathering also indirectly controls the evolution of climate because carbonates, precipitating with Ca released during weathering of the continental crust, sequester CO_2 (Gaillardet et al., 1999; Amiotte Suchet et al., 2003; Jin et al., 2014). Constraining the degree of weathering experienced by the uppermost part of the crust in the past is thus important in providing a framework that can be used to understand both the compositional evolution of the upper crust and climate variation through time.

It is now well established that lithium isotopes are fractionated by low-temperature processes due to preferential partitioning of ^{7}Li (the heavy isotope) into water while ^{6}Li (the light isotope) is incorporated into the weathered products of silicate rocks such as clays (e.g., Pistiner and Henderson, 2003; Vigier et al., 2008). Li isotopes are thus excellent tracers of fluid-rock reactions and have been used to trace weathering processes (Kısakürek et al., 2005, 2004; Liu et al., 2013; Millot et al., 2010; Rudnick et al., 2004), estimate the mass of continental crust lost by chemical weathering through geological times (i.e., Li dissolved in river water) (Liu and Rudnick, 2011) and constrain the present-day erosion cycle of mountain ranges (Dellinger et al., 2014). In addition, Li isotopes are not significantly fractionated by high-temperature

* Corresponding author at: University of Grenoble Alpes, ISTerre, F-38041 Grenoble, France.
E-mail address: lucie.sauzeat@ens-lyon.fr (L. Sauzéat).

http://dx.doi.org/10.1016/j.epsl.2015.07.032
0012-821X/

processes such as metamorphic dewatering (Qiu et al., 2011, 2009; Teng et al., 2007) or igneous differentiation (Teng et al., 2006; Tomascak et al., 1999), hence they are also useful proxies for studying crustal recycling in subduction zones (Elliott et al., 2006; Tang et al., 2014) or beyond (e.g., Vlastelic et al., 2011). Here, we propose to use Li isotopes to quantify the importance of chemical weathering experienced by the upper crust in the past.

To date, the published average lithium concentrations for the upper continental crust differ by more than 40%, ranging from 20 ppm (Taylor and McLennan, 1985) to more than 40 ppm (Teng et al., 2004; Hu and Gao, 2008). The average Li isotopic composition of the UCC (δ^7Li $= 0 \pm 4$ (2σ, Teng et al., 2004) is estimated to be lower than that of fresh, mantle-derived basalts, suggesting that the upper crust records a weathering signature, but the uncertainty on this value overlaps with that of the mantle (δ^7Li $\approx +4 \pm 2(2\sigma)$, average derived from Chan et al., 1992; Seitz et al., 2004, and Tomascak et al., 2008).

In this paper, we report [Li] and δ^7Li for loess deposits that sample vast regions of the UCC. The main advantage of using loesses instead of other sediments (e.g., shales, mudrocks, etc.) for this purpose is that loesses are deposits of eolian dust produced by mechanical erosion and mixing of silt derived from glacial outwash and/or desert environments (Pye, 1995); thus they generally experienced little chemical weathering during their formation. These two features allow loess deposits to be considered as proxies for the average UCC composition (Chauvel et al., 2014; Gallet et al., 1996, 1998; McLennan, 2001; Peucker Ehrenbrink and Jahn, 2001; Taylor et al., 1983).

2. Samples

Loess samples cover about 10% of the Earth's surface (Haase et al., 2007; Pécsi, 1990) and formed between the end of the Pliocene and the beginning of the Pleistocene, based on thermoluminescence dating (Liu, 1985). These Quaternary deposits can be divided into two distinct types: (1) periglacial loess, derived from glacial outwash and transported by winds over limited distances (Haase et al., 2007; Rousseau et al., 2014), and (2) desert loess, transported over longer distances, typically several hundreds of kilometers (Ding et al., 1999), from desert regions.

In this study, we analyzed previously well-characterized desert loesses from China (Jixian, Xifeng, Xining and Luochuan) (Gallet et al., 1996; Jahn et al., 2001), Tajikistan (Chashmanigar) (Ding et al., 2002; Yang et al., 2006) and Argentina (Buenos Aires) (Gallet et al., 1998), as well as periglacial loesses from Western Europe (France, England) and Spitsbergen (Gallet et al., 1998). A map showing the sample locations can be found in Chauvel et al. (2014). Mineralogy, provenance and grain-size distribution for these deposits have been reported in previous studies such as Jeong et al. (2008) and Bronger and Heinkele (1990) for the mineralogy of the Chinese loesses, Smith et al. (2003) and Zárate (2003) for the source location of the Argentinian loesses, and Ding and Ding (2003) for the grain-size distribution of loesses from Tajikistan.

3. Methods

3.1. Major, trace elements, and radiogenic isotopes

Trace element concentrations and Nd–Hf isotopes have been previously published for all the loess samples (Chauvel et al., 2014; Gallet et al., 1996). Major element concentrations are available in the literature for most of the samples (Gallet et al., 1998, 1996; Jahn et al., 2001), except for the Tajikistan loesses. We thus analyzed their major element contents in this study (see Supplementary Table A).

Major element data for the Tajikistan samples were determined using an ICP-AES (Varian 720 ES) at ISTerre (Grenoble) following the same procedure described in Chauvel et al. (2011); only a brief synopsis is provided here. About 50 mg of powder, hand-crushed in an agate mortar were dissolved in a HF-HNO_3 mixture in Savillex beakers for about 72 h at 90 °C. Boric acid was added to neutralize the HF and the resulting liquid was diluted with milliQ water. The concentrations are calculated using calibration curves based on diluted and doped (Al, Mg, Ca, Na, K and P) BCR-2 rock standard solutions.

Both accuracy and reproducibility of the major element contents of loesses from Tajikistan were monitored by replication of international rock standards. The concentrations obtained for the rock standards are in agreement with the reference values, and reproducibility is, on average, better than 5% (2σ) (see Supplementary Table B).

3.2. Lithium isotopic compositions

Lithium isotopic compositions were measured at the University of Maryland. For each sample, about 25 mg of rock powder was dissolved in a Savillex screw-top beaker in an HF–HNO_3 mixture following the procedure detailed by Teng et al. (2004). For samples containing organic matter, a second step of dissolution using a combination of HF–HNO_3–$HClO_4$ was employed to achieve a complete digestion. Separation of lithium was performed by chromatography on four successive columns following the ion resin techniques described by Moriguti and Nakamura (1998a). Lithium was purified using columns filled with 1 ml of Bio-Rad AG 50w-x12 (200–400 mesh) resin, first with an HCl solution, followed by an HCl-ethanol mixture. Lithium isotopic composition of the purified solutions (~50 ppb Li in 2% HNO_3) were measured on a Nu Plasma Multicollector Inductively Coupled Plasma Mass Spectrometry (MC-ICPMS) and calculated by standard bracketing using L-SVEC (Flesch et al., 1973) as the reference standard. Prior to each analysis, the Na/Li ratio of the solution was determined and samples with Na/Li ratio greater than 5 went through further purification by chromatography.

The accuracy of the Li isotopic composition is assessed based on the analysis of two rock reference materials (AGV-1 and G-2). Our measured values (Supplementary File A and Supplementary Table C) are within uncertainty of previously published results, with $\delta^7\text{Li}_{\text{AGV-1}} = +6.7 \pm 0.7$ (2σ, n = 3), versus +4.6 to +6.7 (Liu et al., 2013, 2010, 2015; Magna et al., 2004), and $\delta^7\text{Li}_{\text{G-2}} = +0.6 \pm 1.8$ (2σ, n = 3) versus −1.6 to +2.2; (James and Palmer, 2000; Liu et al., 2010; Pistiner and Henderson, 2003; Tang et al., 2014). The long-term precision of our results is assessed by repeated analyses of pure "in-house" Li standard solutions (UMD-1 and IRMM-016) performed over the course of our analyses. Our average δ^7Li results are $+54.9 \pm 0.5$ (2σ, n = 8) for UMD-1, and $+0.4 \pm 0.5$ (2σ, n = 8) for IRMM-016 (Supplementary File A and Supplementary Table C). Given our long-term reproducibility, the 2 sigma analytical uncertainty adopted in this study for the Li isotopic composition is ±1‰.

4. Results

New major element concentrations for the Tajikistan loesses and previously published data for all other samples are provided in Supplementary Table A. The reader is referred to the studies of Gallet et al. (1998, 1996) and Jahn et al. (2001) for a full description of major element concentrations in loess samples. Here, we briefly compare loess deposits as a function of their formation mechanism (i.e., periglacial vs. desert loesses) and as a function of their sampling locations. The first noticeable difference is

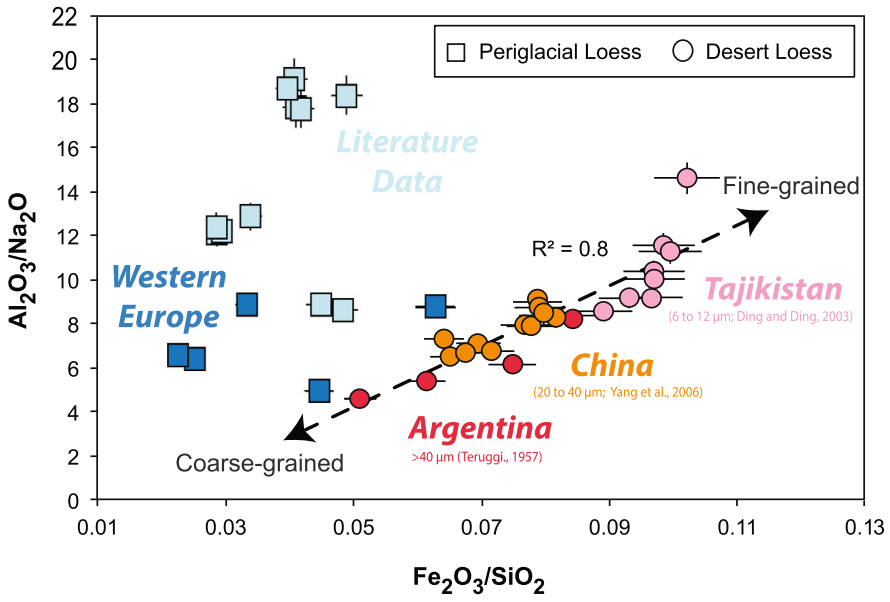

Fig. 1. Plot of grain-size proxies (Al_2O_3/Na_2O vs. Fe_2O_3/SiO_2) illustrating the differences between periglacial and desert loess samples. Periglacial loesses include data from this study, as well as literature data (light blue) from Teng et al. (2004). Fine-grained particles such as clays have high Al_2O_3/Na_2O and Fe_2O_3/SiO_2. Desert loesses plot on a well-defined mixing array, whereas periglacial loesses show greater scatter. Data for the Chinese loess come from Gallet et al. (1996) and Jahn et al. (2001) and from Gallet et al. (1998) for the Argentinian and Western Europe loess. The correlation coefficients R^2 are calculated for desert loesses only. Error bars represent 2σ. (For interpretation of the references to color in this figure legend, the reader is referred to the web version of this article.)

that periglacial samples have higher SiO_2 concentrations (average of $76 \pm 9(2\sigma)$ wt% vs. $57 \pm 12(2\sigma)$ wt% for desert loesses) and lower contents of all the other major elements compared to the desert loesses (see Supplementary Table A). Among desert loesses, samples from Tajikistan, China, and Argentina form three distinct groups. Loesses from Tajikistan are generally more concentrated in Fe_2O_3, CaO, Al_2O_3, MnO and MgO than Chinese loesses, which are themselves more enriched in these elements than Argentinian loesses. The only exception is the high Al_2O_3 contents of the Argentinian loesses (see Supplementary Table A). By contrast, loesses from Tajikistan are, on average, depleted in SiO_2, K_2O and Na_2O compared to Chinese loesses, which are themselves lower than the Argentian loesses. Some of these features are illustrated in Fig. 1 where we plot Al_2O_3/Na_2O vs. Fe_2O_3/SiO_2 showing that desert loesses follow a well-defined linear trend whereas periglacial loesses scatter, in part due to their low Fe_2O_3 and high SiO_2 contents that translates into low Fe_2O_3/SiO_2 ratios. Among desert loesses, Tajikistan samples have higher Al_2O_3/Na_2O and Fe_2O_3/SiO_2 ratios than Chinese samples while Argentinian samples are somewhat lower but more variable.

Lithium concentrations and isotopic compositions are reported in Table 1 for all loesses and are plotted in Figs. 2 and 3, respectively. As for major element concentrations, periglacial loesses differ from desert loesses in their Li compositions. Periglacial deposits show a wide range of δ^7Li values, between -2.9 and $+4.7$, with an average value of $+0.1 \pm 5.6(2\sigma)$ (Fig. 3). This variability is also seen in the Li concentrations, which range from 17 to 61 ppm, with an average of $40 \pm 39(2\sigma)$ ppm (Fig. 2). Such variability is comparable to that seen in periglacial loess deposits investigated by Teng et al. (2004) from New Zealand, Germany, and the midwestern USA (δ^7Li: -3.1 to $+4.8$; [Li]: 17 to 41 ppm). Desert loesses have less variable Li concentrations and isotopic compositions (on average $37 \pm 13(2\sigma)$ ppm and $+0.9 \pm 3.0(2\sigma)$ respectively; Fig. 2 and Fig. 3) and each locality also has distinct averages: the Tajiskistan samples have the highest [Li] and the lowest δ^7Li values ($[Li] = 41 \pm 15(2\sigma)$ ppm and $\delta^7Li = -0.3 \pm 1.2(2\sigma)$; Fig. 3), the Chinese samples are intermediate ($[Li] = 37 \pm 6(2\sigma)$ ppm and $\delta^7Li = +1.0 \pm 2.0(2\sigma)$; Fig. 3) while the Argentinian samples show the lowest [Li] but the heaviest Li isotopic composition ($[Li] = 30 \pm 9(2\sigma)$ ppm and $\delta^7Li = +2.7 \pm 3.5(2\sigma)$; Fig. 3).

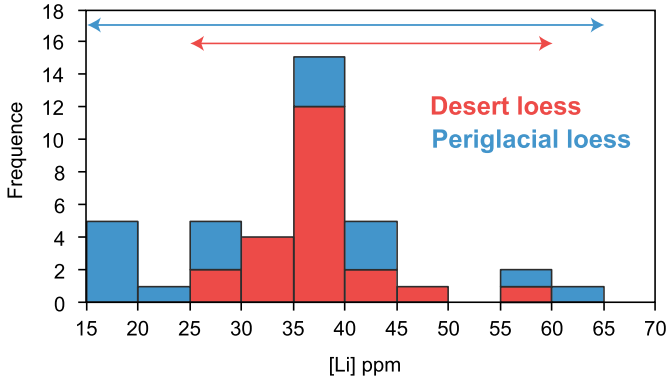

Fig. 2. Stacked histogram of [Li] in desert (red) and periglacial (blue) loess deposits. Periglacial loesses include data from this study, as well as data from Teng et al. (2004). Li concentrations for the samples analyzed in this study are from Chauvel et al. (2014). (For interpretation of the references to color in this figure legend, the reader is referred to the web version of this article.)

5. Discussion

5.1. Use of desert loess deposits to establish the Li isotopic composition of the upper continental crust (UCC)

Several studies have previously used loess deposits to estimate the average composition of the UCC (Taylor et al., 1983; Gallet et al., 1996, 1998; McLennan, 2001; Peucker Ehrenbrink and Jahn, 2001; Chauvel et al., 2014). Most of these studies focused on periglacial loesses. However, as can be seen in Figs. 1 to 3, the two types of loess do not carry the same information. Periglacial loess deposits appear to be enriched in quartz (as seen in their high SiO_2 and low Fe_2O_3/SiO_2, Fig. 1) and have a large range of Li concentrations and Li isotopic compositions (Figs. 2 and 3), while desert loess are more homogeneous. Such variability can result either from the presence of metamorphic and igneous rocks

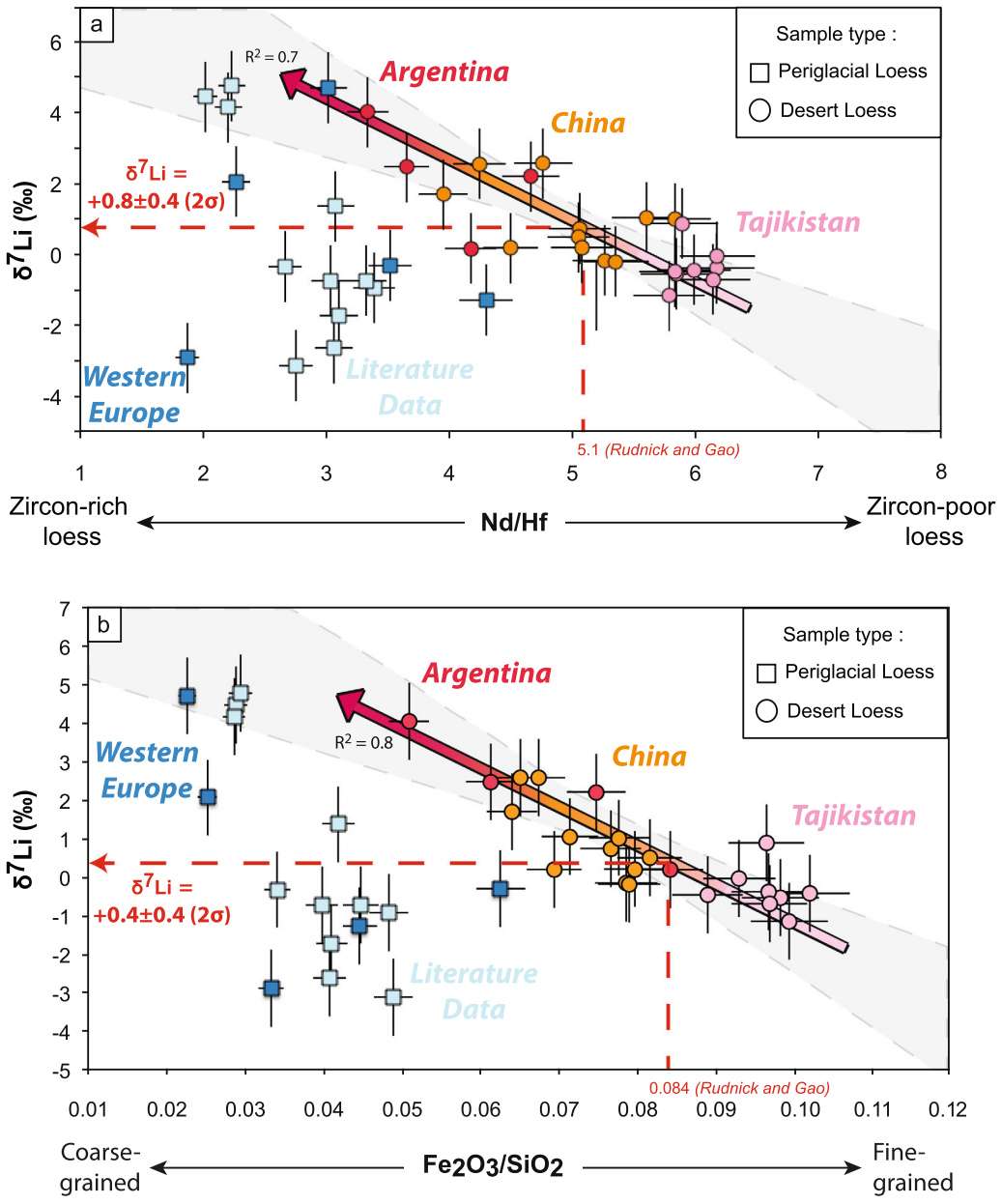

Fig. 3. Variations of a) δ^7Li versus Nd/Hf and b) δ^7Li versus Fe_2O_3/SiO_2 for all loess samples Dark blue data points are periglacial loess deposits from Western Europe analyzed in this study. Literature data (light blue) are from Teng et al. (2004) for periglacial loess deposits from New Zealand, Germany and the midwestern USA. Nd and Hf concentrations of desert loesses are from Chauvel et al. (2014). As Hf and SiO_2 are enriched in zircon and quartz respectively, the correlations observed for desert loesses reflect mixing between two grain-size end-members. The average Nd/Hf and Fe_2O_3/SiO_2 values for the upper continental crust are $5.1 \pm 2.1(2\sigma)$ and $0.084 \pm 0.02(2\sigma)$ respectively (Rudnick and Gao, 2014). For each correlation, the average δ^7Li of the UCC, together with its uncertainty, have been estimated using a weighted linear regression (York et al., 2004) to fit a straight line through the data, followed by a Monte-Carlo simulation to interpolate δ^7Li, taking into account the errors on the slopes and intercepts of the regression lines, as well as the uncertainties on the average Nd/Hf and Fe_2O_3/SiO_2 ratios of the UCC published by Rudnick and Gao (2014) (see Supplementary File B for more details). Gray field represents uncertainties on the linear regressions derived from Monte Carlo simulations. Error bars represent 2σ. (For interpretation of the references to color in this figure legend, the reader is referred to the web version of this article.)

fragments derived from the source (Swineford and Frye, 1955; Garçon et al., 2014); a "nugget effect" i.e. the over-concentration of heavy minerals associated to quartz grains or reflect the preservation of inherited isotopic variability from the source rocks due to short transport distances (Rousseau et al., 2014).

Although heavy minerals, mainly zircons, have been shown to significantly influence neodymium, hafnium and lead isotopic compositions of fine-grained sediments, including loesses (Garçon et al., 2014; Chauvel et al., 2014), such effects are unlikely to be responsible for the Li isotope variability we observe. Indeed, periglacial loesses are enriched in heavy minerals such as zircons (Chauvel et al., 2014; Taylor et al., 1983; Taylor and McLennan, 1985), as reflected by their very low Nd/Hf ratio (Fig. 3a), which is, on average, lower than 3.5 (Chauvel et al., 2014). Zircons control the Hf but not the Nd budget of sediments (Garçon et al., 2014), therefore, an excess of zircon in the sediments generates a low Nd/Hf ratio. Although zircons have variable Li contents (0.5 to 250 ppm) and Li isotopic compositions, ranging from −24 to +14 (Bouvier et al., 2012; Ushikubo et al., 2008), characteristics that could explain some of the Li variations seen in periglacial loesses, a mass balance calculation demonstrates that heterogeneous distribution of zircon cannot be the cause of the Li isotopic variability. Here we consider two extreme cases for Li in zircon ([Li] = 250 ppm; δ^7Li = −24 and [Li] = 250 ppm; δ^7Li = +14) and

Table 1
Li isotopic compositions and concentrations of loess samples.

Sample name	Location	Longitude	Latitude	δ^7Li* (‰)	[Li]** (ppm)
Western Europe (Periglacial loess)					
PR RT	Port Racine, Normandy, France	1°53′W	49°4′3N	2.1	17.9
SAB 1a <160 mm	Sables d'or, France	2°24′W	48°37′N	4.7	16.6
LO94	Spitsbergen (Svalbard)	20°43′E	77°40′N	−1.2	61.3
P2E1	Spitsbergen (Svalbard)			−0.3	59.9
SCIL	Scilly Island, England	6°20′W	49°55′N	−2.9	41.1
SCIL dup	Scilly Island, England			−1.5	
China (Desert loess)					
JX-4	Jixian	110°39′E	36°06′N	0.8	37.1
JX-6	Jixian			0.2	37.4
JX-10	Jixian			1.7	30.5
XF-10	Xifeng	107°42′E	35°45′N	0.5	40
XF-6	Xifeng			0.2	39.9
XN-2	Xining	101°48′E	36°36′N	1.1	37.5
XN-4	Xining			2.6	36.3
XN-10	Xining			2.6	38.1
L9	Luochuan	109°26′E	35°28′N	−0.1	37.9
L6	Luochuan			−0.2	no data
L2	Luochuan			1.1	no data
Tajikistan (Desert loess)					
TJK2772	Tajikistan	69°49′57″E	38°23′32″N	−1.1	44.3
TJK2773	Tajikistan			−0.5	43.0
TJK2930	Tajikistan			−0.4	35.6
TJK3012	Tajikistan			−0.4	46.7
TJK3070	Tajikistan			0.9	35.4
TJK3148	Tajikistan			−0.7	37.8
TJK3179	Tajikistan			−0.4	55.2
TJK3198	Tajikistan			0.0	32.5
Argentina (Desert loess)					
12–14	Argentina	59°22′W	34°38′S	2.5	26.3
24–26	Argentina			2.2	26.1
40RT	Argentina			0.2	36.7
LUJA	Argentina			4.1	30.6
LUJA dup	Argentina			4.6	

* $\delta^7\text{Li} = [(^7\text{Li}/^6\text{Li})_{sample}/(^7\text{Li}/^6\text{Li})_{L\text{-}SVEC} - 1)*1000$ in ‰. L-SVEC data comes from Flesch et al (1973).

** Li concentrations are from Chauvel et al. (2014). "dup" stands for complete duplicate analysis.

we calculate that the presence of ≤0.5% zircon by mass (the average proportion of zircons in periglacial loesses as suggested by Bronger, 2003 and Rousseau et al., 2007) can shift the Li isotopic composition by no more than 1‰. Therefore, the Li variations in periglacial loesses cannot be explained simply by an excess of zircons and a similar conclusion can probably be drawn for the other heavy minerals (e.g. epidote, goethite and hematite).

Thus, preservation of Li isotopic variability inherited form the source is likely responsible for the Li heterogeneity observed in periglacial loesses. Such results are consistent with the conclusions of Chauvel et al. (2014) who focused on trace elements and Nd–Hf isotopic characteristics of loess and concluded that periglacial loess samples, in addition to being extremely variable regarding their trace element patterns, are likely too heterogeneous to be useful in deriving upper crustal averages for Nd and Hf. We conclude that the same is likely true for determining the average Li composition of the UCC. By contrast, desert loesses are transported over greater distances (Ding et al., 1999), are less enriched in heavy minerals such as zircons (mostly Nd/Hf > 3.5, Chauvel et al., 2014; Fig. 3), and are well homogenized. As a consequence, their chemical composition is less biased, and they are better proxies for constraining the average composition of the UCC. We will thus only focus on the composition of the desert loesses in the following discussion.

5.2. Eolian mineralogical sorting controls Li within desert loess

It is essential to understand which processes control the variations of Li concentrations and isotopic compositions observed in the desert loess deposits and why each locality has a different average δ^7Li (Fig. 3). Because Li is a soluble element (Brenan et al., 1998) it is affected by weathering processes and Li concentration may vary due to post-depositional alteration. However, in desert loesses, positive correlations between Li contents and immobile elements such as the rare earth elements (REE) (Fig. 4) suggest that Li has not been significantly remobilized by post-depositional chemical weathering, which we refer to as present-day weathering, i.e., transformation into soils (Dellinger et al., 2014).

Another process that can lead to Li isotopic variability is source rock heterogeneity within the provenance (Dellinger et al., 2014; Qiu et al., 2009), i.e., mafic versus felsic or juvenile versus old crustal material. Based on the observation that Argentinian loesses are enriched in clasts of volcanic rocks (andesites, basalts, dacites, rhyolites) (Imbellone and Teruggi, 1993; Teruggi, 1957) and that young volcanogenic sediments tend to have higher δ^7Li (Bouman et al., 2004), one could link the observed variations in δ^7Li in desert loesses to the provenance of the dust. This assumption can be evaluated using source proxies that are not significantly affected by sedimentary processes, such as the ratio of insoluble elements Th/La (Plank, 2005) that traces the contribution of felsic and mafic materials, or the Nd isotopic composition (Goldstein et al., 1984) that is controlled by the proportion of young to old mantle-derived igneous rocks in the source region. If we consider the less evolved volcanic rocks (i.e., basalts) that should create the largest variability, we can see that the average Th/La ratio of desert loess samples of $0.37 \pm 0.04(2\sigma)$, including the Argentinian samples, is similar to that of the UCC (~0.34 after Rudnick and Gao, 2014) but sig-

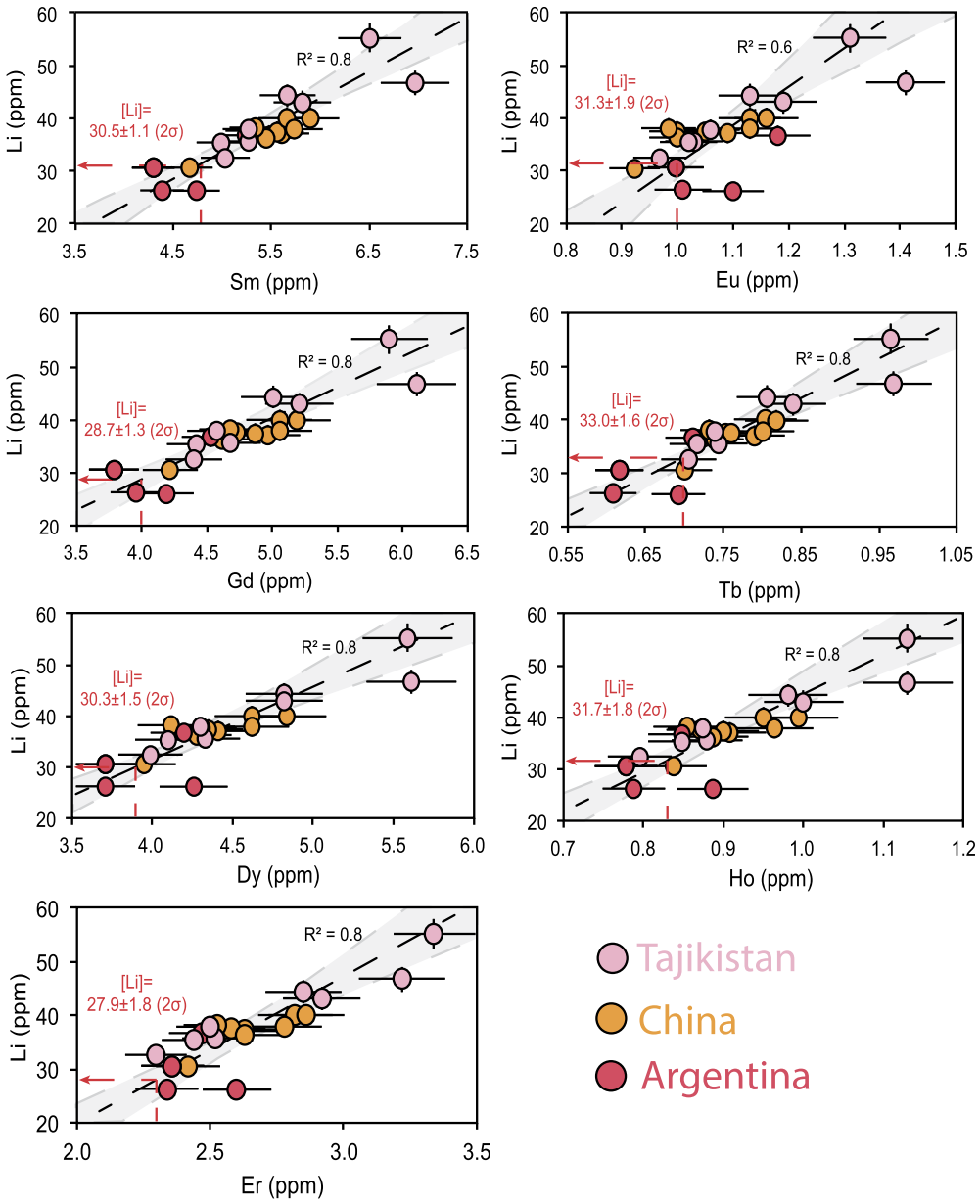

Fig. 4. [Li] versus rare earth elements (REE) in desert loess samples. For each correlation we used a weighted linear regression (York et al., 2004) followed by a Monte-Carlo simulation to interpolate [Li] and its uncertainty at the average REE concentration of the UCC published by Rudnick and Gao (2014). By averaging all of these values, we infer the average [Li] of the UCC (see Supplementary File B for more details). Gray field represents uncertainties on the linear regressions derived from Monte Carlo simulations. Errors bars represent 2σ uncertainty.

nificantly different from the range known for Andean arc basalts (Fig. 5a). This suggests that the presence of mafic components in the provenance, such as Andean basalts in the Argentinian loess samples, is probably minimal and has had no effect on the Li isotopic compositions, as shown by the absence of correlation between Th/La and δ^7Li (Fig. 5a). Even though the Argentinian loesses tend to have higher ε_{Nd} (~ -2), which is explained by the presence of juvenile material in their source (Chauvel et al., 2014; Gallet et al., 1998; Smith et al., 2003), the lack of correlation between the Nd and the Li isotopic compositions of our samples (Fig. 5b) suggests that the Li isotopic compositions and concentrations of desert loesses are not mainly controlled by source heterogeneity.

When sediments are transported by wind, the finest and lightest particles are preferentially transported over longer distances compared to coarse and dense particles that accumulate close to the source regions (Pye, 1995). This is manifest as differences in the average grain size (Yang and Ding, 2004), mineralogy (Eden et al., 1994; Yang et al., 2006), and chemical composition (Feng et al., 2009, 2010, 2011) as a function of distance from their source regions. This grain-size dependence of the chemical composition has also been observed in other types of sediments (Bouchez et al., 2011; Carpentier et al., 2014; Dellinger et al., 2014; Garçon et al., 2014, 2013; Garzanti et al., 2011). Indeed, as minerals have different chemical and isotopic compositions (Garçon et al., 2014, 2013, 2011), sediments with different grain-sizes, composed of different minerals in different proportions, will have different chemical compositions. For example, quartz is preferentially enriched in coarse-grained fractions (Garzanti et al., 2011, 2010), has very high δ^7Li of $\sim +30$ due to preferential enrichment of ^{7}Li in the 2- or 4-fold sites in quartz (Dennen, 1966; Maloney and Nabelek, 2008; Teng et al., 2006) and has relatively low [Li] of $\sim$10 ppm (Dennen, 1966; Garçon et al., 2014; Lynton et al., 2005; Monecke et al., 2000; Teng et al., 2006). By contrast, clay minerals

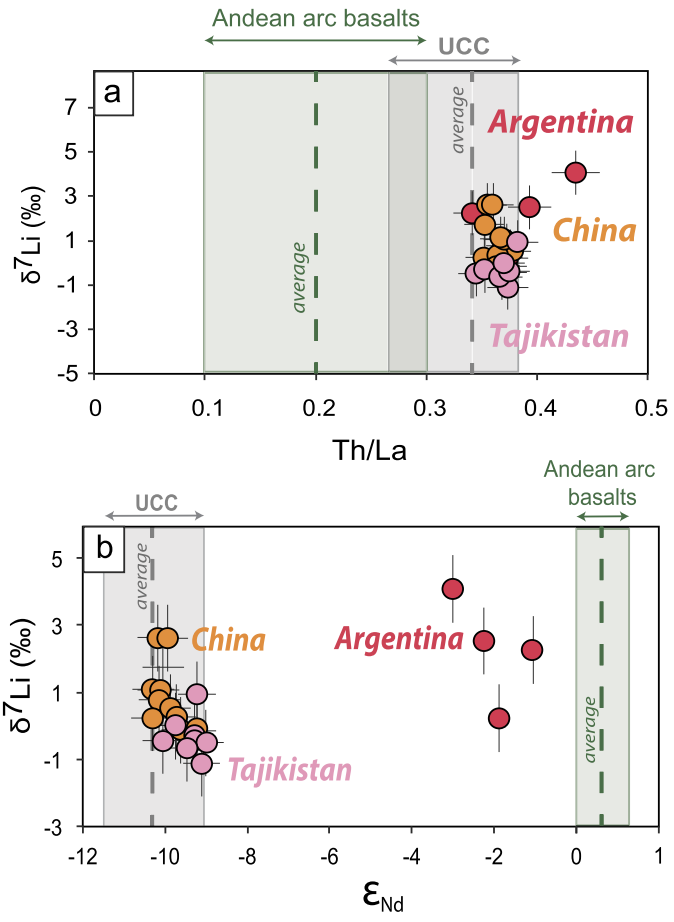

Fig. 5. a) δ^7Li versus Th/La and b) δ^7Li versus ε_{Nd} in desert loess samples. The range of Th/La ratio for the UCC is from Rudnick and Gao (2014) (excluding data from Eade and Fahrig (1973) due to XRF-determined La leading to anomalously high values). The average ε_{Nd} for the UCC is from Chauvel et al. (2014). Arrays represent the range of estimates for the UCC (gray) given by Rudnick and Gao (2014) for Th/La and by Chauvel et al. (2014) for ε_{Nd}. Data for Andean basalts (green) are from the GEOROC database. Error bars are 2σ. (For interpretation of the references to color in this figure legend, the reader is referred to the web version of this article.)

are enriched in the finest fractions (Garzanti et al., 2011, 2010) and have low δ^7Li of ~ -1 and high [Li] of ~63 ppm (Qiu et al., 2009; Romer et al., 2014; Tsai et al., 2014). Consequently, one could expect fine-grained sediments, preferentially enriched in clays, to have higher Li concentrations and lower δ^7Li than coarse-grained sediments that are preferentially enriched in quartz.

In desert loesses, the well-defined correlations between both [Li] and REE (Fig. 4), δ^7Li and Nd/Hf (Fig. 3a), δ^7Li and Fe_2O_3/SiO_2 (Fig. 3b), as well as between Al_2O_3/Na_2O and Fe_2O_3/SiO_2 (Fig. 1), suggest that the bulk composition and most Li variations are related to the sediment grain-size. Indeed, Fe_2O_3, Al_2O_3 and REE are preferentially enriched in the fine-grained fraction of the loesses because phyllosilicates (clays and micas) are rich in iron, aluminium and REE (Garçon et al., 2014; Taylor and McLennan, 1985). By contrast, Na_2O, SiO_2 and Hf are mostly hosted in plagioclase, quartz and zircons, respectively, three mineral phases that are abundant in the coarse fraction (Eden et al., 1994; Garzanti et al., 2011; Yang et al., 2006). As a consequence, Nd/Hf, Al_2O_3/Na_2O and Fe_2O_3/SiO_2 ratios are excellent proxies for grain-sizes and reflect transport-driven compositional changes. This observation is consistent with the average grain-size of the samples as determined by previous studies. The Tajikistan samples are the finest loess samples (6 to 12 μm, Ding and Ding, 2003; Fig. 1) and have the highest [Li] and the lowest δ^7Li values, while the Argentinian samples are the coarsest samples (>40 μm, Teruggi, 1957; Fig. 1) and have the lowest [Li] and the highest δ^7Li values.

The major minerals of desert loesses: quartz, plagioclase and phyllosilicates (Eden et al., 1994; Gallet et al., 1996; Jeong et al., 2008, 2011), can be mixed to produce the observed range of Li compositions (Fig. 6). Both Li concentrations and Li isotopic compositions are controlled by mineral sorting between a fine-grained end-member, enriched in phyllosilicates (clays and micas) – with a high [Li] and a low δ^7Li – and a coarse-grained end-member, enriched in quartz and plagioclase – with a low [Li] and a high δ^7Li (see caption of Fig. 6 for more details). Isotopic mixing calculations allow us to quantify the amount of unweathered, coarse-grained vs. weathered, fine-grained particles (Fig. 6). The results of the mixing calculations match the modal mineralogical proportions estimated from previous studies of the Chinese and Argentinian loess deposits (Camilión, 1993; Jeong et al., 2011, 2008; Teruggi, 1957) (Fig. 6). For example, the relative average proportions of phyllosilicates, quartz, and plagioclase given by our mixing calculations for the Argentinian loess are 40 wt.%, 36 wt.%, and 24 wt.% respectively, while the average modal proportions reported by Camilión (1993) and Teruggi (1957) are 40 wt.%, 33 wt.%, and 27 wt.% respectively. There are no estimated mineral proportions for the Tajikistan samples. Nevertheless, their average grain-size is smaller than the other loess deposits (<12 μm, Ding and Ding, 2003), which is consistent with the higher phyllosilicate proportion estimated from our isotopic mixing calculations (Fig. 6). Significant contributions from mafic minerals such as amphibole, which can contain appreciable Li (Marks et al., 2008), can be ruled out. Indeed, if we assume that our Li variations are partly controlled by mafic minerals (mainly amphibole), we cannot reproduce the Li variations observed in the desert loess deposits. Moreover, because the abundance of mafic minerals in desert loess samples is very low (proportions <4 wt.%, Eden et al., 1994; Jeong et al., 2008; Teruggi, 1957) relative to quartz, plagioclase and phyllosilicates, they cannot control the Li variations. Based on these observations, we conclude that the variations of δ^7Li and [Li] in desert loesses can be understood in terms of relatively simple mixing between minerals of different grain size fractions, as shown in Fig. 6.

5.3. A new estimate of the δ^7Li and [Li] in the average upper continental crust

Estimating the composition of the average UCC using sediments dates back to the work of Goldschmidt in the 1930s. This can be done either using an average composition of sediments, assuming that no processes had biased their composition compared to their source rocks, or using correlations observed in the concentrations of insoluble elements (McLennan, 2001). Because of the mineralogical sorting observed in our desert loess samples, it is not advisable to use their average composition as a representative value for the UCC and we focus here on the second method.

Fig. 4 shows well-defined correlations observed for desert loesses between Li and immobile elements, in this case, the REE. As REE are preferentially enriched in fine-grained sediments (Garçon et al., 2014; Taylor and McLennan, 1985), such trends reflect mixing lines between a fine-grained end-member (enriched in REE and Li) and a coarse-grained end-member (depleted in REE and Li). Using the correlations between Li and REE that are assumed to have the same behavior as Li during magmatic differentiation (i.e., Sm to Er) (Ryan and Langmuir, 1987), we estimate a new average Li concentration for the UCC (Fig. 4). For each of the seven correlations (i.e., Li vs. Sm, Li vs. Eu, Li vs. Gd, Li vs. Tb, Li vs. Dy, Li vs. Ho and Li vs. Er; Fig. 4), we start with the raw data and first run a Monte-Carlo routine to estimate the uncertainties on the slopes and intercepts of the linear regressions. For each individual data point, we thus randomly sample a value within the

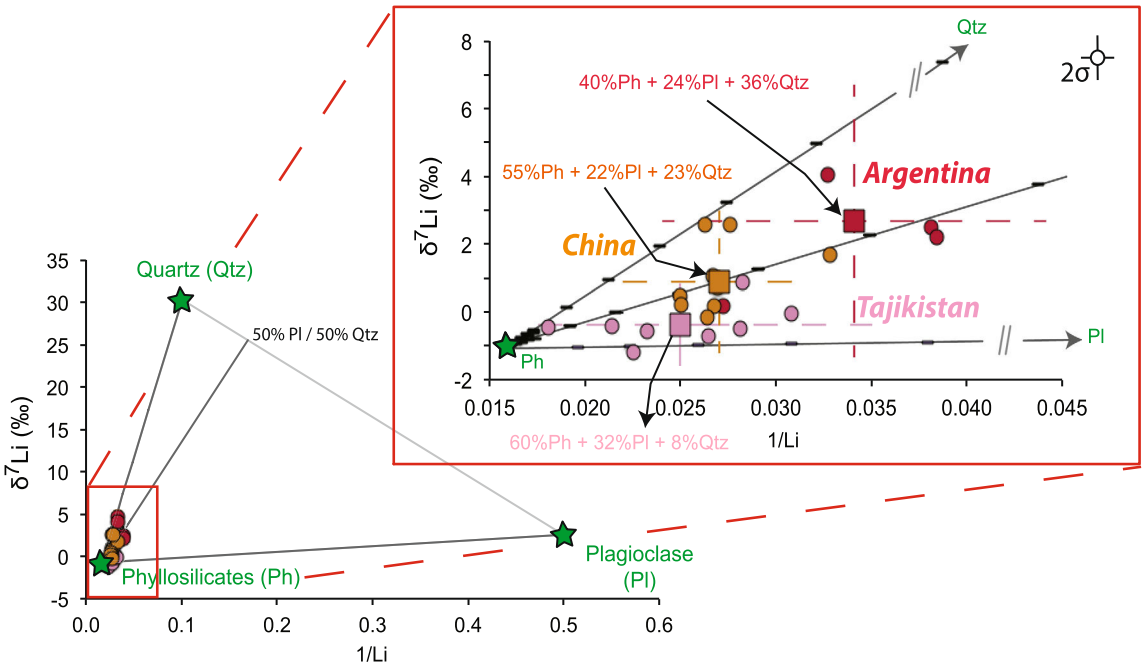

Fig. 6. Isotopic mixing between a fine-grained end-member enriched in phyllosilicates (Ph) and a coarse-grained end-member composed of a mixture of quartz (Qtz) and plagioclase (Pl). All the end-member values come from the literature. For phyllosilicates (mica, chlorite and clay minerals): [Li] ≈ 63 ppm and δ^7Li ≈ −1 (Bouman et al., 2004; Garçon et al., 2014; Tsai et al., 2014), for quartz: [Li] ≈ 10 ppm and δ^7Li ≈ +30 (Dennen, 1966; Garçon et al., 2014; Lynton et al., 2005; Monecke et al., 2000; Teng et al., 2006) and for plagioclase: [Li] ≈ 2 ppm and δ^7Li ≈ +2.5 (δ^7Li values from equilibrated plagioclase only; Bindeman and Bailey, 1999; Bindeman et al., 1999; Cabato et al., 2013; Teng et al., 2008). Equations used for isotopic mixing are from Langmuir et al. (1978). Ticks on the mixing lines correspond to 10% increments in the proportions of phyllosilicates, quartz and plagioclase. Analytical errors are 2σ.

uncertainty of the measured data point to generate a synthetic dataset. We then fit a straight line through all of the synthetic datasets using weighted linear regressions following the algorithm of York et al. (2004) that has been implemented in MATLAB™ by Thirumalai et al. (2011). Within this first Monte-Carlo routine, we perform a second Monte-Carlo simulation to interpolate [Li] at the REE concentrations published by Rudnick and Gao (2014) for the UCC, taking into account the uncertainties on the REE concentrations published by Rudnick and Gao (2014) (see Supplementary File B for more details). We then compile all the interpolated [Li] and calculate both the average and the standard deviation of the distribution. Using this method, we obtain an average Li concentration of 30.5 ± 3.6 (2σ) ppm for the UCC, in agreement with the previously published values of Teng et al. (2004; $35 \pm 11 (2\sigma)$ ppm) and Rudnick and Gao (2014; 24 ± 10 ppm) but with a significantly lower uncertainty. Our value is somewhat lower than the derived by Hu and Gao ($41 \pm 6 (2\sigma)$ ppm) on the basis of correlations between Li and In observed in various sediments and sedimentary rocks.

Following the same procedure (weighed linear regression followed by interpolation using Monte-Carlo simulations), we estimate the average δ^7Li of the UCC using the correlations between δ^7Li and two independent ratios of immobile elements that are not significantly affected by chemical weathering processes, namely, Nd/Hf (Fig. 3a) and Fe_2O_3/SiO_2 (Fig. 3b). These two ratios are good grain-size proxies (see previous section) and are relatively well known in the UCC ($Nd/Hf = 5.1 \pm 2.1 (2\sigma)$ and $Fe_2O_3/SiO_2 = 0.084 \pm 0.02 (2\sigma)$, Rudnick and Gao, 2014). Interpolating these values on the regression lines, we get two sets of values having consistent average Li isotopic compositions: $\delta^7Li = +0.8 \pm 0.4 (2\sigma)$ using the correlation between δ^7Li and Nd/Hf (Fig. 3a) and $\delta^7Li = +0.4 \pm 0.4 (2\sigma)$ using the correlation between δ^7Li and Fe_2O_3/SiO_2 (Fig. 3b). Combining these two sets of data, we obtain an average $\delta^7Li = +0.6 \pm 0.6 (2\sigma)$ (see Supplementary File B for more explanations). Here again, this new estimate is within the uncertainties of the previously published value of $0 \pm 4 (2\sigma)$ (Teng et al., 2004), but with a much smaller uncertainty.

5.4. Determining the average weathering signature of upper continental crust

Chemical weathering is an important process affecting the composition of the continental crust (Dellinger et al., 2014) because it involves the breakdown of rocks into secondary phases such as clays and hydroxides, and it releases soluble elements to the hydrosphere. It has been suggested that this process progressively modifies the chemical composition of the Earth's surface (Albarede, 1998; Lee et al., 2008; Liu and Rudnick, 2011; Rudnick, 1995) but the degree of weathering experienced in the past within the average UCC and quantified by the proportion of weathered sedimentary rocks exposed at the Earth's surface is still poorly known.

Silicate rock weathering is very important in the worldwide atmospheric CO_2 consumption occurring today (Amiotte Suchet et al., 2003; Dessert et al., 2003; Gaillardet et al., 1999; Jin et al., 2014). Hence, through the disintegration of pre-existing rocks, chemical weathering acts as sink for atmospheric CO_2, and so indirectly controls the evolution of our climate. Shales appear to have a significant influence on global CO_2 consumption, accounting for 40% of the total CO_2 consumed worldwide (Amiotte Suchet et al., 2003), but only a few studies have tried to quantify their abundances on continents and these studies show rather large discrepancies. Blatt and Jones (1975) estimate that 66% of the rocks exposed on the Earth's surface are sedimentary rocks, but estimates for the proportion of shales are less well known and differ widely between 13 and 34% (Amiotte Suchet et al., 2003; Condie, 1993; Gibbs and Klump, 1994; Meybeck, 1987). An isotopic approach could potentially provide a more robust estimate of the average degree of weathering experienced by the UCC, and help us to understand the processes controlling the compositional evolution of the upper crust.

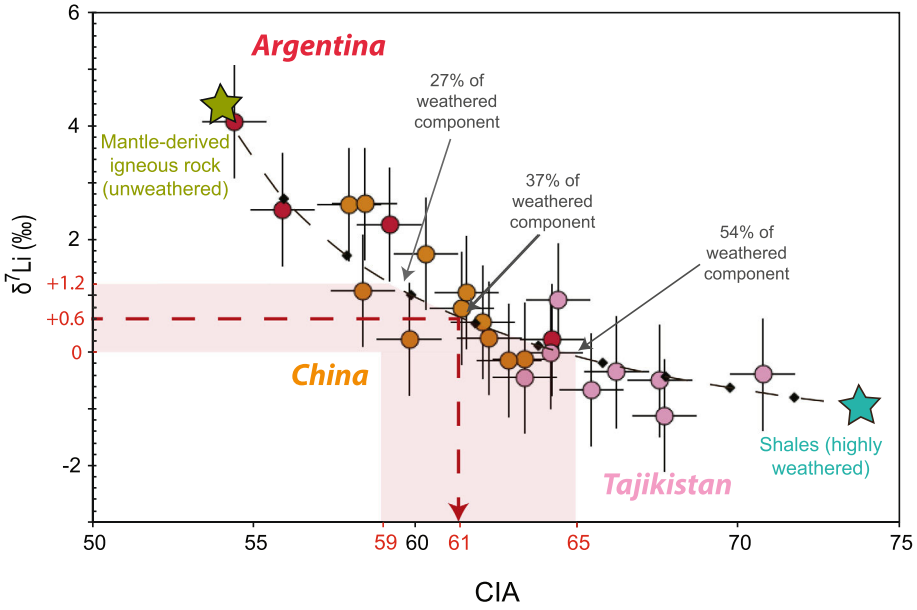

Fig. 7. δ^7Li versus CIA (Chemical Index of Alteration) in desert loess samples. CIA is the molar ratio $Al_2O_3/(Al_2O_3 + CaO^* + Na_2O + K_2O)$, where CaO* refers to Ca contained in silicates (McLennan, 1993; Nesbitt and Young, 1982). A correction is done to consider the presence of carbonates (calcite and dolomite) and phosphates (apatite). Correction for Ca in apatite is based on P_2O_5 concentration, while correction for Ca in carbonate is generally done on the basis of CO_2 concentrations. When such data are not available, reasonable CaO/Na_2O ratios in silicate can be assumed (i.e. $CaO/Na_2O < 1$) following the argument of McLennan (1993). CIA for the loess samples from China, and Argentina were calculated using the major element data of Gallet et al. (1996), Jahn et al. (2001) and Gallet et al. (1998). The black dotted line shows the binary mixing model between the highly weathered end-member (i.e., shales, blue star) and the unweathered igneous rocks (i.e., I-type granites without meta-sedimentary component in the source, green star). The equations used for the isotopic mixing are from Langmuir et al. (1978). Diamonds on the mixing line correspond to 10% increments in the proportion of weathered component. The pale red field represents 2σ uncertainty on the interpolated CIA. (For interpretation of the references to color in this figure legend, the reader is referred to the web version of this article.)

Fig. 7 shows how δ^7Li varies as a function of CIA (Chemical Index of Alteration) in the loess deposits. The CIA, calculated as the ratio of major elements ($Al_2O_3/[Al_2O_3 + CaO^* + Na_2O + K_2O]$, see caption of Fig. 7 for more details), measures the loss of mobile cations (Ca^{2+}, K^+ and Na^+) present in labile minerals (feldspars, pyroxenes, amphiboles) relative to the amount of Al^{3+} that is preserved in more stable minerals (i.e., clay) under surface conditions (Nesbitt and Young, 1982). Hence, the CIA is a good proxy for the intensity of chemical weathering: the higher the CIA, the greater the degree of weathering the sample has experienced in the past. In Fig. 7, we show that the range of δ^7Li and CIA values obtained for the desert loess deposits follow a binary isotopic mixing trend between unweathered, mantle-derived igneous rocks (i.e., I-type granites) with high δ^7Li and low CIA, and a weathered component (i.e., shales) with low δ^7Li and high CIA. The Li composition ($\delta^7Li = -0.9 \pm 4.7(2\sigma)$; $[Li] = 66 \pm 92(2\sigma)$ ppm) and CIA value ($CIA = 74 \pm 21(2\sigma)$) of the weathered end-member (shale) is compiled from several studies (Hu and Gao, 2008; Moriguti and Nakamura, 1998b; Qiu et al., 2009; Romer et al., 2014; Tang et al., 2014; Teng et al., 2004, and unpublished data of Su Li and others), while values for the unweathered end-member (Clarence River Supersuite I-type granite) come from Bryant et al. (2004) ($\delta^7Li = +4.3 \pm 4.1(2\sigma)$, $[Li] = 17 \pm 18(2\sigma)$ ppm and $CIA = 54 \pm 8(2\sigma)$). These granites differentiated from mantle-derived magma and have not incorporated any meta-sedimentary materials (Bryant et al., 2004), which is important as the unweathered end-member should not include weathered materials, which many other I-type granites do (Teng et al., 2004). Unfortunately, the compositions of the two end-members are not very well constrained (large uncertainties on the averages) and the large errors can have a non-negligible impact on our isotopic mixing calculation. However, the very good consistency observed between the isotopic modeling and our data suggests these average values of the two end-members are realistic.

The UCC is considered to have a granodioritic composition (Arndt, 2013; Eade and Fahrig, 1973; Rudnick and Gao, 2014; Taylor and McLennan, 1985) and juvenile crust should have the high δ^7Li and low CIA values shown in Fig. 7 for igneous rocks that are devoid of a sedimentary component in their source regions. As its composition is modified by chemical weathering, the Li isotopic composition of the UCC decreases, with a concomitant increase of its CIA, reaching, in extreme cases, the very low δ^7Li and high CIA values found in shales (Fig. 7). It is therefore reasonable to expect that the present-day UCC falls on a mixing line between an unweathered component (granites) and a weathered one (shales). Using our estimate for the average δ^7Li of upper crust and the results of the isotopic mixing, we derive the average CIA of present-day UCC to be between 59 and 65 with an average of 61 (Fig. 7). This new value differs from the average value given by Rudnick and Gao (2014) for the upper crust (CIA =53, calculated using the average major element concentrations), and which is derived from a compilation of several studies, mainly based on sampling widespread outcrop exposures. This discrepancy may reflect inadequate sampling methods, as a majority of these studies focused on a limited part of the world, e.g., North Craton China (Gao et al., 1998) and Canadian Precambrian shield (Eade and Fahrig, 1973; Shaw et al., 1976, 1967). The low CIA may thus reflect local composition where the proportion of weathered rocks is lower than the average UCC. Or, as these studies rely only on outcrops at the Earth's surface, the discrepancy can be explained by the presence of under-sampled sedimentary rocks that occur in fold belts and continental platforms, as previously suggested by Amiotte Suchet et al. (2003).

Our new CIA estimate is also significantly lower than the value estimated for Archean UCC (average CIA = 77) and for Paleoproterozoic UCC (average CIA = 67) as determined by Gaschnig et al. (2014) using ancient glacial diamictites. The higher CIA in the past has been interpreted as resulting from more intense weathering (Gaschnig et al., 2014). Condie (1993) reached a similar conclu-

sion on the basis of the depletion in Na, Ca and Sr in Archean shales, which he suggested reflected more intense chemical weathering during the Archean. Therefore, the difference between the present-day and ancient CIA of the UCC may reflect a change in the intensity of chemical weathering through time that modified the chemical composition of the UCC.

Another approach to quantify the importance of past chemical weathering is to determine the amount of weathered products produced by this process. Our novel isotopic approach shows that the chemical composition of the present upper continental crust, having a δ^7Li of $+0.6 \pm 0.6$ and a CIA of 61, can be explained by a mixture of $63^{+10}_{-17}(2\sigma)$% of unweathered igneous rocks (granites) and $37^{+17}_{-10}(2\sigma)$% of rocks produced by weathering (shales) (cf. Fig. 7). The inferred proportion of shales is slightly higher than previous estimates. Amiotte Suchet et al. (2003) have shown that ~25% shales present at the Earth's surface accounts for about 40% of the CO_2 drawdown in the atmosphere. With ~40% shales at the surface, as estimated here, almost 60% of the worldwide CO_2 could be consumed, highlighting how important weathering may be for the overall CO_2 budget of the Earth. This deserves more attention, particularly from a climate studies point of view. Thus, both means of estimating the average weathering signature of the UCC (average CIA and mixing of shales and granites) demonstrate that weathering has had a profound influence on the average composition of the UCC and, based on the relationship between weathering and CO_2 draw-down, the continental crust has, in turn, profoundly influenced climate.

6. Summary and conclusions

Based on analyses of global loess samples, periglacial loesses are too heterogeneous to be used as proxies to estimate the Li composition of the upper continental crust. Desert loess deposits appear to be more homogenous and thus more suitable to infer average Li values. The Li isotopic compositions and concentrations of desert loesses are controlled by mineralogical sorting and can be reproduced by mixing between a fine-grained, weathered end-member (i.e., phyllosilicates) and a coarse-grained, relatively unweathered end-member (i.e., a mixture of quartz and plagioclase). Using the correlations between Li and REE concentrations in the desert loesses we derive a new estimate for the average Li concentration of the upper crust: $30.5 \pm 3.6(2\sigma)$ ppm. Similarly, using correlations between δ^7Li and independent ratios of immobile elements, we estimate an average $\delta^7\text{Li} = +0.6 \pm 0.6(2\sigma)$ for the UCC. These results are similar to previous estimates, but are more precisely constrained, and show that the UCC carries a significantly more weathered signature than fresh mantle-derived rocks. Using an isotopic mixing approach we also quantify the cumulative importance of chemical weathering on the continents over Earth history. We estimate that $37^{+17}_{-10}(2\sigma)$% of the current upper crust is composed of highly weathered sediments (i.e., shales) that are the by-products of chemical weathering experienced in the past and that the UCC's present CIA is 61^{+4}_{-2}, 2σ, which is lower than what it was in the Paleoproterozoic and Archean periods, but higher than previous estimates of the UCC. Our results thus provide a framework from which to compare the UCC through time.

Acknowledgements

We thank S. Gallet and B.M. Jahn for providing the samples analyzed in this study. We also greatly thank S. Bureau for major element analyses, I.S. Puchtel for his help in the clean laboratory, as well as R.D. Ash for his assistance during isotopic measurements. Thanks also to X.-M. Liu and W.F. McDonough for constructive discussions and advices that helped improve the content of the manuscript. We thank reviewers Mathieu Dellinger and Edward Tipper for their comments that helped improve the manuscript and editor Mike Bickle for his pleasant comments and efficient editorial handling. This work was supported by NSF grant EAR 0948549 and General funds from INSU-CNRS, University of Grenoble and Rhône-Alpes Region.

Appendix A. Supplementary material

Supplementary material related to this article can be found online at http://dx.doi.org/10.1016/j.epsl.2015.07.032.

References

Albarede, F., 1998. The growth of continental crust. Tectonophysics 296, 1–14.
Amiotte Suchet, P., Probst, J.-L., Ludwig, W., 2003. Worldwide distribution of continental rock lithology: implications for the atmospheric/soil CO_2 uptake by continental weathering and alkalinity river transport to the oceans. Glob. Biogeochem. Cycles 17. http://dx.doi.org/10.1029/2002GB001891.
Arndt, N.T., 2013. Formation and evolution of the continental crust. Geochem. Persp 2 (3), 405–533. http://dx.doi.org/10.7185/geochempersp.2.3.
Bindeman, I.N., Bailey, J.C., 1999. Trace elements in anorthite megacrysts from the Kurile Island Arc: a window to across-arc geochemical variations in magma compositions. Earth Planet. Sci. Lett., 1–18.
Bindeman, I.N., Davis, A.M., Wickham, S.M., 1999. 400 my of basic magmatism in a single lithospheric block during cratonization: ion microprobe study of plagioclase megacrysts in mafic rocks from Transbaikalia, Russia. J. Petrol. 40, 807–830.
Blatt, H., Jones, R.L., 1975. Proportions of exposed igneous, metamorphic, and sedimentary rocks. Geology 86, 1085–1088.
Bouchez, J., Gaillardet, J., France-Lanord, C., Maurice, L., Dutra-Maia, P., 2011. Grain size control of river suspended sediment geochemistry: clues from Amazon River depth profiles. Geochem. Geophys. Geosyst. 12, Q03008.
Bouman, C., Elliott, T., Vroon, P.Z., 2004. Lithium inputs to subduction zones. Chem. Geol. 212, 59–79. http://dx.doi.org/10.1016/j.chemgeo.2004.08.004.
Bouvier, A.-S., Ushikubo, T., Kita, N.T., Cavosie, A.J., Kozdon, R., Valley, J.W., 2012. Li isotopes and trace elements as a petrogenetic tracer in zircon: insights from Archean TTGs and sanukitoids. Contrib. Mineral. Petrol. 163, 745–768. http://dx.doi.org/10.1007/s00410-011-0697-1.
Brenan, J.M., Ryerson, F.J., Shaw, H.F., 1998. The role of aqueous fluids in the slab-to-mantle transfer of boron, beryllium, and lithium during subduction: experiments and models. Geochim. Cosmochim. Acta 62, 3337–3347.
Bronger, A., 2003. Correlation of loess–paleosol sequences in East and Central Asia with SE Central Europe: towards a continental Quaternary pedostratigraphy and paleoclimatic history. Quat. Int. 106, 11–31.
Bronger, A., Heinkele, T., 1990. Mineralogical and clay mineralogical aspects of loess research. Quat. Int. 7, 37–51.
Bryant, C.J., Chappell, B.W., Bennett, V.C., McCulloch, M.T., 2004. Lithium isotopic compositions of the New England Batholith: correlations with inferred source rock compositions. Trans. R. Soc. Edinb. Earth Sci. 95, 199–214.
Cabato, J., Altherr, R., Ludwig, T., Meyer, H.-P., 2013. Li, Be, B concentrations and δ^7Li values in plagioclase phenocrysts of dacites from Nea Kameni (Santorini, Greece). Contrib. Mineral. Petrol. 165, 1135–1154. http://dx.doi.org/10.1007/s00410-013-0851-z.
Camilión, M.C., 1993. Clay mineral composition of Pampean loess (Argentina). Quat. Int. 17, 27–31.
Carpentier, M., Weis, D., Chauvel, C., 2014. Fractionation of Sr and Hf isotopes by mineral sorting in Cascadia Basin terrigenous sediments. Chem. Geol. 382, 67–82. http://dx.doi.org/10.1016/j.chemgeo.2014.05.028.
Chan, L.-H., Edmond, J.M., Thompson, G., Gillis, K., 1992. Lithium isotopic composition of submarine basalts – implications for the lithium cycle in the oceans. Earth Planet. Sci. Lett. 108, 151–160.
Chauvel, C., Bureau, S., Poggi, C., 2011. Comprehensive chemical and isotopic analyses of basalt and sediment reference materials. Geostand. Geoanal. Res. 35, 125–143. http://dx.doi.org/10.1111/j.1751-908X.2010.00086.x.
Chauvel, C., Garçon, M., Bureau, S., Besnault, A., Jahn, B.-M., Ding, Z., 2014. Constraints from loess on the Hf–Nd isotopic composition of the upper continental crust. Earth Planet. Sci. Lett. 388, 48–58. http://dx.doi.org/10.1016/j.epsl.2013.11.045.
Condie, K.C., 1993. Chemical composition and evolution of the upper continental crust: contrasting results from surface samples and shales. Chem. Geol. 104, 1–37.
Dellinger, M., Gaillardet, J., Bouchez, J., Calmels, D., Galy, V., Hilton, R.G., Louvat, P., France-Lanord, C., 2014. Lithium isotopes in large rivers reveal the cannibalistic nature of modern continental weathering and erosion. Earth Planet. Sci. Lett. 401, 359–372. http://dx.doi.org/10.1016/j.epsl.2014.05.061.
Dennen, W.H., 1966. Stoichiometric substitution in natural quartz. Geochim. Cosmochim. Acta 30, 1235–1241. http://dx.doi.org/10.1016/0016-7037(66)90122-0.

Dessert, C., Dupré, B., Gaillardet, J., François, L.M., Allègre, C.J., 2003. Basalt weathering laws and the impact of basalt weathering on the global carbon cycle. Chem. Geol. 202, 257–273. http://dx.doi.org/10.1016/j.chemgeo.2002.10.001.

Ding, F., Ding, Z., 2003. Chemical weathering history of the southern Tajikistan loess and paleoclimate implications. Sci. China, Ser. D 46, 1012–1021. http://dx.doi.org/10.1360/03yd0344.

Ding, Z., Sun, J., Rutter, N.W., Rokosh, D., Liu, T., 1999. Changes in sand content of loess deposits along a north–south transect of the Chinese Loess Plateau and the implications for desert variations. Quat. Res. 52, 56–62.

Ding, Z.L., Ranov, V., Yang, S.L., Finaev, A., Han, J.M., Wang, G.A., 2002. The loess record in southern Tajikistan and correlation with Chinese loess. Earth Planet. Sci. Lett. 200, 387–400.

Eade, K.E., Fahrig, W.F., 1973. Regional, lithological, and temporal variation in the abundances of some trace elements in the Canadian shield. Geological Survey of Canada. Paper. Dept. of Energy, Mines and Resources.

Eden, D.N., Qizhong, W., Hunt, J.L., Whitton, J.S., 1994. Mineralogical and geochemical trends across the Loess Plateau, North China. Catena 21, 73–90.

Elliott, T., Thomas, A., Jeffcoate, A., Niu, Y., 2006. Lithium isotope evidence for subduction-enriched mantle in the source of mid-ocean-ridge basalts. Nature 443, 565–568. http://dx.doi.org/10.1038/nature05144.

Feng, J.-L., Zhu, L.-P., Zhen, X.-L., Hu, Z.-G., 2009. Grain size effect on Sr and Nd isotopic compositions in eolian dust: implications for tracing dust provenance and Nd model age. Geochem. J. 43, 123–131.

Feng, J.L., Hu, Z.G., Cui, J.Y., Zhu, L.P., 2010. Distributions of lead isotopes with grain size in aeolian deposits. Terra Nova 22, 257–263. http://dx.doi.org/10.1111/j.1365-3121.2010.00941.x.

Feng, J.-L., Hu, Z.-G., Ju, J.-T., Zhu, L.-P., 2011. Variations in trace element (including rare earth element) concentrations with grain sizes in loess and their implications for tracing the provenance of eolian deposits. Quat. Int. 236, 116–126. http://dx.doi.org/10.1016/j.quaint.2010.04.024.

Flesch, G.D., Anderson Jr., A.R., Svec, H.J., 1973. A secondary isotopic standard for $^{6}Li/^{7}Li$ determinations. Int. J. Mass Spectrom. Ion Phys. 12, 265–272. http://dx.doi.org/10.1016/0020-7381(73)80043-9.

Gaillardet, J., Dupré, B., Louvat, P., Allegre, C.J., 1999. Global silicate weathering and CO_2 consumption rates deduced from the chemistry of large rivers. Chem. Geol. 159, 3–30.

Gallet, S., Jahn, B.-M., Torii, M., 1996. Geochemical characterization of the Luochuan loess-paleosol sequence, China, and paleoclimatic implications. Chem. Geol. 133, 67–88.

Gallet, S., Jahn, B.-M., Van Vliet Lanoë, B., Dia, A., Rossello, E., 1998. Loess geochemistry and its implications for particle origin and composition of the upper continental crust. Earth Planet. Sci. Lett. 156, 157–172.

Gao, S., Luo, T.-C., Zhang, B.-R., Zhang, H.-F., Han, Y.-W., Zhao, Z.-D., Hu, Y.-K., 1998. Chemical composition of the continental crust as revealed by studies in East China. Geochim. Cosmochim. Acta 62, 1959–1975.

Garçon, M., Chauvel, C., Bureau, S., 2011. Beach placer, a proxy for the average Nd and Hf isotopic composition of a continental area. Chem. Geol. 287, 182–192. http://dx.doi.org/10.1016/j.chemgeo.2011.06.007.

Garçon, M., Chauvel, C., France-Lanord, C., Huyghe, P., Lavé, J., 2013. Continental sedimentary processes decouple Nd and Hf isotopes. Geochim. Cosmochim. Acta 121, 177–195. http://dx.doi.org/10.1016/j.gca.2013.07.027.

Garçon, M., Chauvel, C., France-Lanord, C., Limonta, M., Garzanti, E., 2014. Which minerals control the Nd–Hf–Sr–Pb isotopic compositions of river sediments? Chem. Geol. 364, 42–55. http://dx.doi.org/10.1016/j.chemgeo.2013.11.018.

Garzanti, E., Andò, S., France-Lanord, C., Vezzoli, G., Censi, P., Galy, V., Najman, Y., 2010. Mineralogical and chemical variability of fluvial sediments 1. Bedload sand (Ganga-Brahmaputra, Bangladesh). Earth Planet. Sci. Lett. 299, 368–381. http://dx.doi.org/10.1016/j.epsl.2010.09.017.

Garzanti, E., Andò, S., France-Lanord, C., Censi, P., Vignola, P., Galy, V., Lupker, M., 2011. Mineralogical and chemical variability of fluvial sediments 2. Suspended-load silt (Ganga-Brahmaputra, Bangladesh). Earth Planet. Sci. Lett. 302, 107–120. http://dx.doi.org/10.1016/j.epsl.2010.11.043.

Gaschnig, R.M., Rudnick, R.L., McDonough, W.F., Kaufman, A.J., Hu, Z., Gao, S., 2014. Onset of oxidative weathering of continents recorded in the geochemistry of ancient glacial diamictites. Earth Planet. Sci. Lett. 408, 87–99. http://dx.doi.org/10.1016/j.epsl.2014.10.002.

Gibbs, M.T., Klump, L.R., 1994. Global chemical erosion during the last glacial maximum and the present: sensitivity to changes in lithology and hydrology. Paleoceanography 9, 529–543.

Goldstein, S.L., O'nions, R.K., Hamilton, P.J., 1984. A Sm–Nd isotopic study of atmospheric dusts and particulates from major river systems. Earth Planet. Sci. Lett. 70, 221–236.

Haase, D., Fink, J., Haase, G., Ruske, R., Pécsi, M., Richter, H., Altermann, M., Jäger, K.D., 2007. Loess in Europe—its spatial distribution based on a European Loess Map, scale 1:2,500,000. Quat. Sci. Rev. 26, 1301–1312. http://dx.doi.org/10.1016/j.quascirev.2007.02.003.

Hu, Z., Gao, S., 2008. Upper crustal abundances of trace elements: a revision and update. Chem. Geol. 253, 205–221. http://dx.doi.org/10.1016/j.chemgeo.2008.05.010.

Imbellone, P.A., Teruggi, M.E., 1993. Paleosols in loess deposits of the Argentine Pampas. Quat. Int. 17, 49–55.

Jahn, B.-M., Gallet, S., Han, J., 2001. Geochemistry of the Xining, Xifeng and Jixian sections, Loess Plateau of China: eolian dust provenance and paleosol evolution during the last 140 ka. Chem. Geol. 178, 71–94.

James, R.H., Palmer, M.R., 2000. The lithium isotope composition of international rock standards. Chem. Geol. 166, 319–326.

Jeong, G.Y., Hillier, S., Kemp, R.A., 2008. Quantitative bulk and single-particle mineralogy of a thick Chinese loess–paleosol section: implications for loess provenance and weathering. Quat. Sci. Rev. 27, 1271–1287. http://dx.doi.org/10.1016/j.quascirev.2008.02.006.

Jeong, G.Y., Hillier, S., Kemp, R.A., 2011. Changes in mineralogy of loess–paleosol sections across the Chinese Loess Plateau. Quat. Res. 75, 245–255. http://dx.doi.org/10.1016/j.yqres.2010.09.001.

Jin, L., Ogrinc, N., Yesavage, T., Hasenmueller, E.A., Ma, L., Sullivan, P.L., Kaye, J., Duffy, C., Brantley, S.L., 2014. The CO_2 consumption potential during gray shale weathering: insights from the evolution of carbon isotopes in the Susquehanna Shale Hills critical zone observatory. Geochim. Cosmochim. Acta 142, 260–280. http://dx.doi.org/10.1016/j.gca.2014.07.006.

Kısakürek, B., James, R.H., Harris, N.B.W., 2005. Li and $\delta^{7}Li$ in Himalayan rivers: proxies for silicate weathering? Earth Planet. Sci. Lett. 237, 387–401. http://dx.doi.org/10.1016/j.epsl.2005.07.019.

Kısakürek, B., Widdowson, M., James, R.H., 2004. Behaviour of Li isotopes during continental weathering: the Bidar laterite profile, India. Chem. Geol. 212, 27–44. http://dx.doi.org/10.1016/j.chemgeo.2004.08.027.

Langmuir, C.H., Vocke Jr, R.D., Hanson, G.N., Hart, S.R., 1978. A general mixing equation with applications to Icelandic basalts. Earth Planet. Sci. Lett. 37, 380–392.

Lee, C.-T.A., Morton, D.M., Little, M.G., Kistler, R., Horodyskyj, U.N., Leeman, W.P., Agranier, A., 2008. Regulating continent growth and composition by chemical weathering. Proc. Natl. Acad. Sci. USA 105, 4981–4986. http://dx.doi.org/10.1073/pna5.0711143105.

Liu, T.S., 1985. Loess and the Environment. China Ocean Press, Beijing.

Liu, X.-M., Rudnick, R.L., 2011. Constraints on continental crustal mass loss via chemical weathering using lithium and its isotopes. Proc. Natl. Acad. Sci. USA 108, 20873–20880. http://dx.doi.org/10.1073/pnas.1115671108.

Liu, X.-M., Rudnick, R.L., Hier-Majumder, S., Sirbescu, M.-L.C., 2010. Processes controlling lithium isotopic distribution in contact aureoles: a case study of the Florence County pegmatites, Wisconsin. Geochem. Geophys. Geosyst. 11. http://dx.doi.org/10.1029/2010GC003063.

Liu, X.-M., Rudnick, R.L., McDonough, W.F., Cummings, M.L., 2013. Influence of chemical weathering on the composition of the continental crust: insights from Li and Nd isotopesin bauxite profiles developed on Columbia River Basalts. Geochim. Cosmochim. Acta 115, 73–91. http://dx.doi.org/10.1016/j.gca.2013.03.043.

Liu, X.-M., Wanner, C., Rudnick, R.L., McDonough, W.F., 2015. Processes controlling $\delta^{7}Li$ in rivers illuminated by study of streams and groundwaters draining basalts. Earth Planet. Sci. Lett. 409, 212–224. http://dx.doi.org/10.1016/j.epsl.2014.10.032.

Lynton, S.J., Walker, R.J., Candela, P.A., 2005. Lithium isotopes in the system Qz–Ms-fluid: an experimental study. Geochim. Cosmochim. Acta 69, 3337–3347. http://dx.doi.org/10.1016/j.gca.2005.02.009.

Magna, T., Wiechert, U.H., Halliday, A.N., 2004. Low-blank isotope ratio measurement of small samples of lithium using multiple-collector ICPMS. Int. J. Mass Spectrom. 239, 67–76. http://dx.doi.org/10.1016/j.ijms.2004.09.008.

Maloney, J.S., Nabelek, P.I., 2008. Lithium and its isotopes in tourmaline as indicators of the crystallization process in the San Diego County pegmatites, California, USA. Eur. J. Mineral. 20, 905–916.

Marks, M.A., Rudnick, R.L., Ludwig, T., Marschall, H., Zack, T., Halama, R., McDonough, W.F., Rost, D., Wenzel, T., Vicenzi, E.P., 2008. Sodic pyroxene and sodic amphibole as potential reference materials for in situ lithium isotope determinations by SIMS. Geostand. Geoanal. Res. 32, 295–310.

McLennan, S.M., 1993. Weathering and global denudation. J. Geol. 101, 295–303.

McLennan, S.M., 2001. Relationships between the trace element composition of sedimentary rocks and upper continental crust. Geochem. Geophys. Geosyst. 2, 2000GC000109.

Meybeck, M., 1987. Global chemical weathering of surficial rocks estimated from river dissolved loads. Am. J. Sci. 287, 401–428.

Millot, R., Vigier, N., Gaillardet, J., 2010. Behaviour of lithium and its isotopes during weathering in the Mackenzie Basin, Canada. Geochim. Cosmochim. Acta 74, 3897–3912. http://dx.doi.org/10.1016/j.gca.2010.04.025.

Monecke, T., Bombach, G., Klemm, W., Kempe, U., Gotze, J., Wolf, D., 2000. Determination of trace elements in the quartz reference material UNS-SpS and in natural quartz samples by ICP-MS. Geostand. Newsl. 24, 73–81.

Moriguti, T., Nakamura, E., 1998a. High-yield lithium separation and the precise isotopic analysis for natural rock and aqueous samples. Chem. Geol. 145, 91–104.

Moriguti, T., Nakamura, E., 1998b. Across-arc variation of Li isotopes in lavas and implications for crust/mantle recycling at subduction zones. Earth Planet. Sci. Lett. 163, 167–174. http://dx.doi.org/10.1016/S0012-821X(98)00184-8.

Nesbitt, H.W., Young, G.M., 1982. Early proterozoic climates and plate motions inferred from major element chemistry of lutites. Nature 299, 715–717.

Peucker Ehrenbrink, B., Jahn, B.-M., 2001. Rhenium–osmium isotope systematics and platinum group element concentrations: loess and the upper continental crust. Geochem. Geophys. Geosyst. 2.

Pécsi, M., 1990. Loess is not just the accumulation of dust. Quat. Int. 7, 1–21.
Pistiner, J.S., Henderson, G.M., 2003. Lithium-isotope fractionation during continental weathering processes. Earth Planet. Sci. Lett. 214, 327–339. http://dx.doi.org/10.1016/S0012-821X(03)00348-0.
Plank, T., 2005. Constraints from thorium/lanthanum on sediment recycling at subduction zones and the evolution of the continents. J. Petrol. 46, 921–944. http://dx.doi.org/10.1093/petrology/egi005.
Pye, K., 1995. The nature, origin and accumulation of loess. Quat. Sci. Rev. 14, 653–667.
Qiu, L., Rudnick, R.L., McDonough, W.F., Merriman, R.J., 2009. Li in mudrocks from the British Caledonides: metamorphism and source influences. Geochim. Cosmochim. Acta 73, 7325–7340. http://dx.doi.org/10.1016/j.gca.2009.08.017.
Qiu, L., Rudnick, R.L., Ague, J.J., McDonough, W.F., 2011. A lithium isotopic study of sub-greenschist to greenschist facies metamorphism in an accretionary prism, New Zealand. Earth Planet. Sci. Lett. 301, 213–221. http://dx.doi.org/10.1016/j.epsl.2010.11.001.
Romer, R.L., Meixner, A., Hahne, K., 2014. Lithium and boron isotopic composition of sedimentary rocks – The role of source history and depositional environment: a 250 Ma record from the Cadomian orogeny to the Variscan orogeny. Gondwana Res. 26, 1093–1110. http://dx.doi.org/10.1016/j.gr.2013.08.015.
Rousseau, D.D., Derbyshire, E., Antoine, P., Hatté, C., 2007. Loess Records Europe. In: Encyclopedia of Quaternary Science, second edition. Elsevier, pp. 606–619.
Rousseau, D.-D., Chauvel, C., Sima, A., Hatté, C., Lagroix, F., Antoine, P., Balkanski, Y., Fuchs, M., Mellett, C., Kageyama, M., Ramstein, G., Lang, A., 2014. European glacial dust deposits: geochemical constraints on atmospheric dust cycle modeling. Geophys. Res. Lett. 41, 7666–7674. http://dx.doi.org/10.1002/(ISSN)1944-8007.
Rudnick, R.L., 1995. Making continental crust. Nature 378, 571–577.
Rudnick, R.L., Gao, S., 2014. 4.1 Composition of the Continental Crust, Treatise on Geochemistry, 2nd ed. Elsevier Ltd.
Rudnick, R.L., Tomascak, P.B., Njo, H.B., Gardner, L.R., 2004. Extreme lithium isotopic fractionation during continental weathering revealed in saprolites from South Carolina. Chem. Geol. 212, 45–57. http://dx.doi.org/10.1016/j.chemgeo.2004.08.008.
Ryan, J.G., Langmuir, C.H., 1987. The systematics of lithium abundances in young volcanic rocks. Geochim. Cosmochim. Acta 51, 1727–1741.
Seitz, H.-M., Brey, G.P., Lahaye, Y., Durali, S., Weyer, S., 2004. Lithium isotopic signatures of peridotite xenoliths and isotopic fractionation at high temperature between olivine and pyroxenes. Chem. Geol. 212, 163–177. http://dx.doi.org/10.1016/j.chemgeo.2004.08.009.
Shaw, D.M., Reilly, G.A., Muysson, J.R., Pattenden, G.E., Campbell, F.E., 1967. An estimate of the chemical composition of the Canadian Precambrian shield. Can. J. Earth Sci. 4, 829–853. http://dx.doi.org/10.1139/e67-058.
Shaw, D.M., Dostal, J., Keays, R.R., 1976. Additional estimates of continental surface Precambrian shield composition in Canada. Geochim. Cosmochim. Acta 40, 73–83.
Smith, J., Vance, D., Kemp, R.A., Archer, C., Toms, P., King, M., Zárate, M., 2003. Isotopic constraints on the source of Argentinian loess – with implications for atmospheric circulation and the provenance of Antarctic dust during recent glacial maxima. Earth Planet. Sci. Lett. 212, 181–196. http://dx.doi.org/10.1016/S0012-821X(03)00260-7.
Swineford, A., Frye, J.C., 1955. Petrographic comparison of some loess samples from western Europe with Kansas loess. J. Sediment. Res. 25.
Tang, M., Rudnick, R.L., Chauvel, C., 2014. Sedimentary input to the source of Lesser Antilles lavas: a Li perspective. Geochim. Cosmochim. Acta 144, 43–58. http://dx.doi.org/10.1016/j.gca.2014.09.003.
Taylor, S.R., McLennan, S.M., 1985. The continental crust: its composition and evolution. Blackwell Scientific Pub., Palo Alto, CA.
Taylor, S.R., McLennan, S.M., McCulloch, M.T., 1983. Geochemistry of Loess, Continental Crustal Composition and Crustal Model Ages. Geochim. Cosmochim. Acta 47, 1897–1905.
Teng, F.Z., McDonough, W.F., Rudnick, R.L., Dalpé, C., Tomascak, P.B., Chappell, B.W., Gao, S., 2004. Lithium isotopic composition and concentration of the upper continental crust. Geochim. Cosmochim. Acta 68, 4167–4178. http://dx.doi.org/10.1016/j.gca.2004.03.031.
Teng, F.Z., McDonough, W.F., Rudnick, R.L., Walker, R.J., Sirbescu, M.L.C., 2006. Lithium isotopic systematics of granites and pegmatites from the Black Hills, South Dakota. Am. Mineral. 91, 1488–1498. http://dx.doi.org/10.2138/am.2006.2083.
Teng, F.Z., McDonough, W.F., Rudnick, R.L., Wing, B., 2007. Limited lithium isotopic fractionation during progressive metamorphic dehydration in metapelites: a case study from the Onawa contact aureole, Maine. Chem. Geol. 239, 1–12. http://dx.doi.org/10.1016/j.chemgeo.2006.12.003.
Teng, F.-Z., Rudnick, R.L., McDonough, W.F., Gao, S., Tomascak, P.B., Liu, Y., 2008. Lithium isotopic composition and concentration of the deep continental crust. Chem. Geol. 255, 47–59. http://dx.doi.org/10.1016/j.chemgeo.2008.06.009.
Teruggi, M.E., 1957. The nature and origin of Argentine loess. J. Sediment. Res. 27.
Thirumalai, K., Singh, A., Ramesh, R., 2011. A MATLAB™ code to perform weighted linear regression with (correlated or uncorrelated) errors in bivariate data. J. Geol. Soc. India 77, 377–380.
Tomascak, P.B., Tera, F., Helz, R.T., Walker, R.J., 1999. The absence of lithium isotope fractionation during basalt differentiation: new measurements by multicollector sector ICP-MS. Geochim. Cosmochim. Acta 63, 907–910.
Tomascak, P.B., Langmuir, C.H., le Roux, P.J., Shirey, S.B., 2008. Lithium isotopes in global mid-ocean ridge basalts. Geochim. Cosmochim. Acta 72, 1626–1637. http://dx.doi.org/10.1016/j.gca.2007.12.021.
Tsai, P.-H., You, C.-F., Huang, K.-F., Chung, C.-H., Sun, Y.-B., 2014. Lithium distribution and isotopic fractionation during chemical weathering and soil formation in a loess profile. J. Asian Earth Sci. 87, 1–10. http://dx.doi.org/10.1016/j.jseaes.2014.02.001.
Ushikubo, T., Kita, N.T., Cavosie, A.J., Wilde, S.A., Rudnick, R.L., Valley, J.W., 2008. Lithium in Jack Hills zircons: evidence for extensive weathering of Earth's earliest crust. Earth Planet. Sci. Lett. 272, 666–676. http://dx.doi.org/10.1016/j.epsl.2008.05.032.
Vigier, N., Decarreau, A., Millot, R., Carignan, J., Petit, S., France-Lanord, C., 2008. Quantifying Li isotope fractionation during smectite formation and implications for the Li cycle. Geochim. Cosmochim. Acta 72, 780–792. http://dx.doi.org/10.1016/j.gca.2007.11.011.
Vlastélic, I., Staudacher, T., Bachèlery, P., Télouk, P., Neuville, D., Benbakkar, M., 2011. Lithium isotope fractionation during magma degassing: constraints from silicic differentiates and natural gas condensates from Piton de la Fournaise volcano (Réunion Island). Chem. Geol. 284, 26–34. http://dx.doi.org/10.1016/j.chemgeo.2011.02.002.
Yang, S.L., Ding, Z.L., 2004. Comparison of particle size characteristics of the Tertiary 'red clay' and Pleistocene loess in the Chinese Loess Plateau: implications for origin and sources of the "red clay". Sedimentology 51, 77–93. http://dx.doi.org/10.1046/j.1365-3091.2003.00612.x.
Yang, S., Ding, F., Ding, Z., 2006. Pleistocene chemical weathering history of Asian arid and semi-arid regions recorded in loess deposits of China and Tajikistan. Geochim. Cosmochim. Acta 70, 1695–1709. http://dx.doi.org/10.1016/j.gca.2005.12.012.
York, D., Evensen, N.M., Martínez, M.L., De Basabe Delgado, J., 2004. Unified equations for the slope, intercept, and standard errors of the best straight line. Am. J. Phys. 72, 367. http://dx.doi.org/10.1119/1.1632486.
Zárate, M., 2003. Loess of southern South America. Quat. Sci. Rev. 22, 1987–2006. http://dx.doi.org/10.1016/S0277-3791(03)00165-3.

JOURNAL OF PETROLOGY

Journal of Petrology, 2015, Vol. 56, No. 9, 1775–1796
doi: 10.1093/petrology/egv054
Original Article

OXFORD

Metasomatism of the Lithospheric Mantle Immediately Precedes Kimberlite Eruption: New Evidence from Olivine Composition and Microstructures

Carole Cordier[1,2]*, Lucie Sauzeat[1,2†], Nicholas T. Arndt[1,2], Anne-Marie Boullier[1,2], Valentina Batanova[1,2] and Fabrice Barou[3]

[1]Université Grenoble Alpes, ISTerre, F-38041 Grenoble, France, [2]CNRS, ISTerre, F-38041 Grenoble, France and [3]Université Montpellier 2, Géosciences Montpellier, Place Eugène Bataillon, 34095 Montpellier, cedex 05, France

*Corresponding author. E-mail: carole.cordier@ujf-grenoble.fr
[†]Present address: CNRS UMR 5276, Laboratoire de Géologie de Lyon, Ecole Normale Supérieure de Lyon, Université Lyon 1, 69634 Lyon, France.

Received July 30, 2014; Accepted August 27, 2015

ABSTRACT

Most kimberlites contain abundant dunitic nodules. These are centimetre-sized, rounded and multi-grained assemblages of xenocrystic olivine with a wide range of compositions (Fo83 to Fo94). The absence of orthopyroxene and other mantle minerals and the range of olivine compositions have been attributed to reaction between mantle peridotite and (proto)kimberlitic fluid or melt, but the timing of the reaction is a subject of debate. In a kimberlite from the Kangamiut region of Greenland, nodule cores are surrounded by fine-grained outer margins with near-constant Fo contents (~Fo88) but highly variable minor element contents (e.g. 500–2500 ppm Ni). These margins crystallized from the kimberlite melt and we show that their compositions can be explained by crystallization of olivine alone, if a high partition coefficient for Ni between melt and olivine ($D_{Ni} > 20$) is assumed. Orthopyroxene assimilation is not required, removing the constraint that its dissolution occurred during ascent of the kimberlite magma. Within some nodules, in addition to the usual core-to-margin gradients, we observe asymmetric compositional changes (variable Fo but near-constant minor element contents) across mobile grain boundaries. These changes document fluid percolation at the grain scale that occurred during dynamic recrystallization in the deforming lithospheric mantle. We note that chemical gradients associated with mobile grain boundaries are observed in olivines that cover the entire compositional range of the nodules, and propose that fluid-assisted dynamic recrystallization took place in dunite that was already compositionally heterogeneous. Reaction between peridotite and protokimberlitic melt or fluid and dissolution of orthopyroxene thus occurred within the lithospheric mantle, immediately (a few days) prior to the ascent of the kimberlite melt and the entrainment of the dunite nodules. We propose that the grain boundary zones probably mimic, at a fine scale, the fluid–peridotite interaction that caused, at a larger scale, orthopyroxene dissolution and formation of compositionally diverse olivine in kimberlites.

Key words: dunite; grain boundary migration; kimberlite; olivine xenocryst; metasomatism

INTRODUCTION

For decades the olivine grains in kimberlites have been classified into two populations on the basis of their grain size and morphology; each type has been ascribed a different origin (Skinner & Clement, 1979; Clement, 1982; Mitchell, 1986, 2008; Moore, 1988, 2012; Le Roex *et al.*, 2003; Kopylova *et al.*, 2007; Kamenetsky *et al.*, 2008; Brett *et al.*, 2009; Arndt *et al.*, 2010). Much of the discussion has focused on the relative proportion of xenocrysts—olivine from another source, typically the lithospheric mantle—and phenocrysts—cognate olivine that crystallized directly from the kimberlite magma. In earlier publications the cores of larger grains, particularly when anhedral or rounded, were regarded as xenocrysts whereas smaller sub- to euhedral grains were regarded as phenocrysts (e.g. Mitchell, 1986; Moore, 1988, 2012; Kamenetsky *et al.*, 2008). More recently, it was proposed that almost all of the olivine grains in kimberlites are xenocrysts and that cognate olivine is restricted to thin rims around anhedral olivine cores (Fedortchouk & Canil, 2004; Brett *et al.*, 2009; Arndt *et al.*, 2010; Pilbeam *et al.*, 2013).

Another issue that has elicited discussion is the fate of orthopyroxene, clinopyroxene and garnet, minerals that make up close to 50% of most deep-seated mantle peridotites, but are rare to absent in kimberlites. It is generally accepted that these minerals, especially orthopyroxene (Luth, 2009), are out of equilibrium with the proto-kimberlitic liquid, which most probably is a CO_2–H_2O-rich, silica-poor fluid, and that these minerals reacted with or dissolved in this liquid. The question is when this happened. Most researchers (Kamenetsky *et al.*, 2008; Brett *et al.*, 2009, 2015; Russell *et al.*, 2012; Pilbeam *et al.*, 2013; Kamenetsky & Yaxley, 2015) consider that this dissolution took place in the kimberlite en route to the surface. Arndt *et al.* (2010), however, proposed that the removal of mantle minerals other than olivine took place within the mantle lithosphere, producing dunites that subsequently were entrained into the kimberlite magma.

We present here a geochemical and microstructural study of olivine in a very well-preserved type-I kimberlite from the Kangamiut region in Greenland. We document in detail the variations in forsterite content as well as minor element contents in the olivine grains in this sample, in particular across the outer margins of grains and across internal grain boundaries in multigranular nodules. Combining microstructural evidence for dynamic recrystallization at mantle depths with evidence for chemical gradients across grain boundaries, we develop firm constraints on the timing and location of the processes that removed orthopyroxene, and clarify several important issues concerning the migration of kimberlitic magmas in the lithospheric mantle.

OLIVINE IN KIMBERLITES: LITERATURE REVIEW

Types of olivine grains

The eruptive facies in kimberlite pipes are breccias that contain abundant rock fragments. They are usually totally altered to secondary hydrous phases; however, some hypabyssal samples are well preserved. Fresh kimberlites contain abundant large grains of olivine that have been described using the terms listed in Table 1 and illustrated in Fig. 1. The large rounded grains that dominate the lithology of most samples are commonly referred to as 'macrocrysts' or 'megacrysts' (Clement, 1982; Mitchell, 1986), or more recently as 'olivine-I' (Kamenetsky *et al.*, 2008). These terms do not adequately depict their rounded form, nor do they accommodate their polycrystalline structure. For these reasons, we prefer to use the term 'nodule' (Arndt *et al.*, 2010). We emphasize that the objects described by this term are distinct from normal peridotite xenoliths; that is, fragments of mantle peridotite plucked from conduit walls and transported to the surface in the kimberlite magma. Whereas nodules in kimberlites are typically less than 1 cm across and almost always monomineralic, peridotite xenoliths are larger (2 cm or more) and mainly multimineralic; that is, they normally contain ortho- and clinopyroxene and an aluminous phase (garnet or spinel) in addition to olivine.

Olivine nodules in kimberlites are typically well rounded, with an average size <1 cm. Many are monogranular, but others are multigranular and consist of two of more large grains of anhedral olivine (Fig. 1). Many anhedral olivines exhibit abundant high-temperature and high-stress intracrystalline deformation features such as undulose extinction and subgrain dislocation walls (Boullier & Nicolas, 1975; Guéguen, 1977; Skinner, 1989; Arndt *et al.*, 2010). Some grains also show evidence for dynamic recrystallization at mantle depths with the development of small equigranular mosaic-textured and dislocation-rich grains (Arndt *et al.*, 2010). Little-deformed subhedral to euhedral crystals (tablets), which occur within many nodules, are thought to derive from deformed anhedral olivine by fluid-assisted static recrystallization (i.e. post-deformation annealing), during the first stage of upward migration of the kimberlite magma to the surface (Guéguen, 1977, 1979; Drury & van Roermund, 1988, 1989; Nermond, 1994). The size of single crystals in kimberlite nodules may reach 8–10 mm, greater than the typical grain size in peridotite xenoliths (<8 mm; Mercier & Nicolas, 1975).

The small, euhedral to rounded crystals in the kimberlite matrix have been called 'phenocrysts' by Clement (1982), 'olivine-II' by Kamenetsky *et al.* (2008) and 'matrix olivine' by Arndt *et al.* (2010). Some matrix olivine cores show dislocation microstructures similar to those in anhedral olivines, but others have an asymmetric, subhedral morphology very similar to that of tablets. Matrix grains are thus interpreted to result from disaggregation of larger xenocrystic nodules during kimberlite ascent (Brett *et al.*, 2009; Arndt *et al.*, 2010).

Olivine composition and nomenclature

A striking feature of the olivine grains in kimberlites is the wide range of core compositions from nodule to

Table 1: Nomenclature of olivine in kimberlites

Name	Components	Microstructures	Interpretation
Nodule (macrocrysts, olivine-I)* large, rounded, multi- or monomineralic	Anhedral, 1 to > 50 mm	Undulose extinction High dislocation density (walls + free dislocation)	Xenocrysts produced by metasomatism and deformation in the lithospheric mantle
	Mosaic-textured, <0·1 mm grains		Dynamically recrystallized grains
	Tablet, 0·3–1 mm	Low dislocation density	Static recrystallization during kimberlite ascent
Matrix olivine (phenocrysts, olivine-II)* small, euhedral to rounded in the kimberlite matrix	0·3–1 mm	High or low dislocation density	Disaggregated nodules (tablets or anhedral olivines)

*Terms used in the literature.

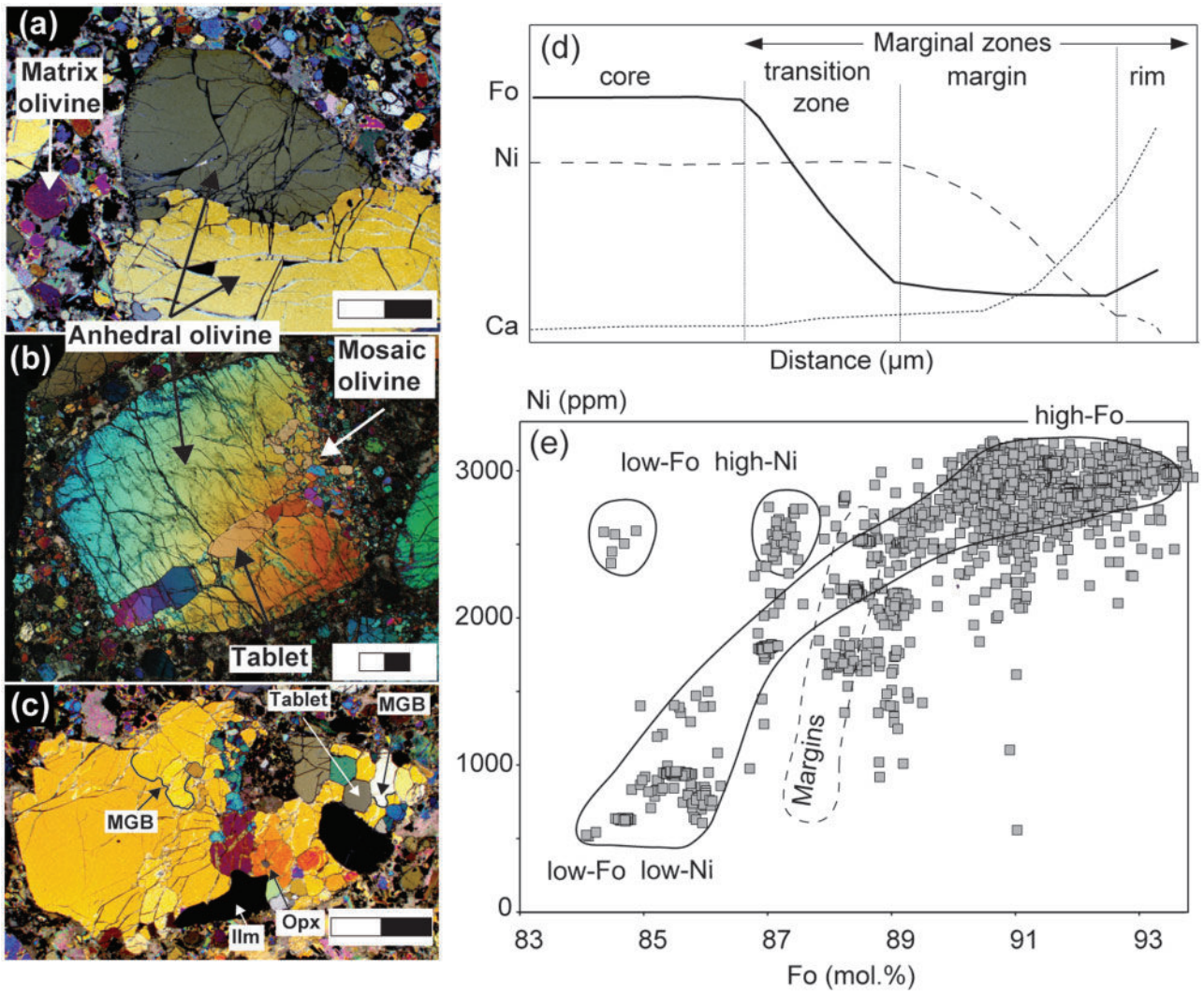

Fig. 1. Olivine nodules in sample NCR27 and olivine composition features in kimberlites. (a) Curvilinear contact between two anhedral olivine grains. (Note the subhedral matrix olivines.) (b) Multigranular nodule with tablets and mosaic-textured grains enclosed in anhedral olivine. (c) Mobile grain boundaries (MGB) in olivine nodule including ilmenite (Ilm) and rounded orthopyroxene (Opx) grains. Scale bar 1 mm. (d) Schematic diagram illustrating the compositional variations in the marginal zones of olivine grains and the terms used in this study to describe the zones. We prefer the terms 'transition zone' and 'rim' to the 'inner margin' and 'edge' of Pilbeam *et al.* (2013). (e) Ni vs Fo content in olivine cores in kimberlites from literature data (Kamenetsky *et al.*, 2008; Brett *et al.*, 2009; Arndt *et al.*, 2010; Pilbeam *et al.*, 2013). Cores with low Ni contents compared with the fields are probably mixed core–margin analyses.

nodule. As seen in Fig. 1e, the Fo content varies from Fo94 to Fo84. At the high-Fo end of this range (Fo>91, 'Type 1 olivines' of Pilbeam *et al.*, 2013) the Ni content is relatively constant and correlates only weakly with Fo content, defining a gentle positive slope in the Fo–Ni diagram. In contrast, at the low-Fo end, the Ni content varies widely to produce two distinct populations, one with low and the other with high Ni contents ('Type 2 and 3 olivines', respectively; Pilbeam *et al.*, 2013).

In the interior of nodules the Fo and minor element contents are remarkably uniform and only in thin and often discontinuous marginal zones does the composition vary significantly (Fig. 1). These marginal zones exhibit the complex compositional variation illustrated schematically in Fig. 1d (Pilbeam *et al.*, 2013). In a complete profile, the core is surrounded by (1) a transition zone (inner margin) in which the Fo content varies but the minor elements such as Ni, Mn and Ca remain almost constant, (2) a margin in which Fo remains almost constant but the minor elements change dramatically, and (3) an outer rim in which both Fo and minor elements vary. Marginal zones can show significant thickness variation within a grain or between grains and are often discontinuous or entirely absent. The variation of the margin thickness results from a combination of processes such as surface area activated growth, with small xenocrystic grains having thinner margins than larger ones (Brett *et al.*, 2009), and subsequent abrasion during upward transport of the kimberlite magma (Jones *et al.*, 2014; Brett *et al.*, 2015).

Even though their Ni and other minor element contents vary considerably, the margins have a restricted range of Fo contents (Fig. 1e). Margin olivine is interpreted to have crystallized directly from the kimberlite liquid, largely because of its enrichment in Ca (Brett *et al.*, 2009; Arndt *et al.*, 2010; Pilbeam *et al.*, 2013). When the Fo content of the core is higher than that of the marginal zones the zoning has been described in the literature as 'normal', and when it is lower the zoning has been said to be 'reverse' (Pilbeam *et al.*, 2013). If additional chemical zones are present, the zoning is 'complex'. These terms may be useful when describing zoned phenocrysts in volcanic rocks in which all zones crystallized from a melt, but we will argue below that the composition range of the cores was produced by a process that was largely independent of the margin crystallization. This being the case, using the terms 'normal', 'reverse' and 'complex' zoning is not appropriate. We will consequently describe the olivine grains based on their core composition, as illustrated in Fig. 1e.

PETROGRAPHY

Samples NCR27 and NCR29 were obtained from a Proterozoic kimberlite dike in the Kangamiut region of West Greenland. Their petrology and chemical composition have been reported by Arndt *et al.* (2006, 2010) and are briefly summarized below. The samples are very well-preserved hypabyssal type-I kimberlite. Sample NCR27 contains 60 vol. % of fresh olivine grains, mostly (~40%) as mono- or multigranular nodules up to 10 mm in size. Sample NCR29 contains far less olivine (25 vol. %), with only 5 vol. % as nodules. Anhedral olivines in the nodules display the high-temperature and high-stress deformation structures typical of nodules and xenoliths in kimberlites, including undulose extinction, close dislocation walls and small subgrains. Xenocrysts of minerals other than olivine are rare and limited to large ilmenite grains (<1 to 2 vol. %), and smaller amounts of phlogopite, serpentinized orthopyroxene, and garnet with kelyphitic rims. Orthopyroxene xenocrysts are rare and occur either dispersed within the matrix or in association with olivine in multigranular nodules. They are systematically rounded (Fig. 1c). The mesostasis is made up of small olivine crystals, phlogopite, Fe–Ti oxides, perovskite, monticellite, apatite and carbonate.

ANALYTICAL METHODS

Major element concentrations in samples NCR27 and NCR29 were measured by inductively coupled plasma atomic emission spectroscopy (ICP-AES) at the University Grenoble Alpes to determine their NiO contents, which were not analysed in the previous study (Arndt *et al.*, 2010). We followed the analytical procedure given by Chauvel *et al.* (2011), using 50 mg of rock powder. The international standard BCR-2 was used for calibration and four other standards (BEN, AGV-1, BHVO-2 and BR-24) were measured as unknown samples to check accuracy and reproducibility. Relative standard deviations are in most cases <1% for SiO_2 and <4% for other major elements.

Back-scattered electron (BSE) images and major and minor element concentrations in olivine were obtained at ISTerre, University Grenoble Alpes (France) using a JEOL JXA-8230 electron microprobe equipped with a single energy-dispersive spectrometer and five wavelength-dispersive spectrometers. Analytical conditions for quantitative analysis of olivine were 25 kV acceleration voltage, 900 nA beam current and electron beam 1 μm in nominal diameter. Raw data reduction was performed using the ZAF procedure. The selected counting time (60 s) allowed us to collect compositional profiles with high spatial resolution (steps of 2–5 μm) and low detection limits (less than 10 ppm for Al, Cr, Ca, Ni and Mn). The San Carlos olivine standard USNM 111312/444 and XEN internal standard were run three times for each 30–50 measurements. Relative standard deviation over 190 measurements is 0·05 wt % for SiO_2, 0·02% for Fo, and less than 0·7% for NiO, Cr_2O_3, CaO and MnO. A few profiles were measured with a longer counting time (720 s), to acquire trace element contents in representative olivine grains (Ti, P, Zn, detection limits lower than 5 ppm). All measurements were corrected for the deviation of the San Carlos standard from the reference values (Jarosewitch *et al.*, 1980). We disregarded analyses

with oxide sums in excess of 100 wt % or cation sums in excess of three, based on four oxygen atoms per formula unit. X-ray element maps were acquired using similar operating conditions (acceleration voltage 25 kV, beam current 900 nA) and dwell times of 100 and 500 ms.

Crystallographic orientations of olivine crystals within multigranular nodules were determined by indexation of electron-backscattered diffraction patterns using facilities at Géosciences Montpellier (CNRS-Université de Montpellier 2, France). Diffraction patterns were generated by interaction of an incident electron beam tilted at 70° with a carefully polished thin section placed in a horizontal holder, in a CamScan Crystal Probe X500 scanning electron microscope. CHANNEL + software (Oxford-HKL Technology) was used for crystallographic orientation indexing and acquisition. The orientation maps of multigranular nodules were obtained in automatic acquisition mode with a step size of 7 μm. Standard post-acquisition data treatment for olivine-rich rocks (Tommasi *et al.*, 2008) allowed the proportion of indexed points to be increased.

RESULTS

Bulk-rock composition

Samples NCR27 and NCR29 were re-analysed to obtain their Ni contents [Supplementary Data (SD) Electronic Appendix Table EA1; supplementary data are available for downloading at http://www.petrology.oxfordjournals.org]. The new analysis of the olivine-poor sample NCR29 is very similar to that reported by Arndt *et al.* (2010). In the nodule-rich sample NCR27, MgO contents are higher (+6 relative %) and Al_2O_3 and CaO are lower (–11·5 and –9 relative %, respectively) than in the previous analyses. However, all the concentrations obtained for NCR27 and NCR29 lie along linear trends in variation diagrams, suggesting that the divergence results from differences in olivine abundance in the analysed aliquots. NiO contents range from 0·10 wt % in NCR29 to 0·18 wt % in NCR27.

Microstructural evidence for grain boundary migration in multigranular nodules

In some multigranular nodules, the contacts between anhedral olivine grains have a distinctive form, being characterized by lobate, concave and convex portions as illustrated in Figs 1c and 2a. We studied the crystallographic orientation of the olivine grains adjacent to such 'bulging' grain boundaries in the multigranular nodule illustrated in Fig. 2. This nodule is 2 mm in diameter and composed of numerous small grains of olivine. Observations under crossed Nicols with an additional lambda plate (Fig. 2a) and a crystallographic orientation map and pole figures (Fig. 2b) demonstrate the presence of five interpenetrating olivine grains with complex shapes and different orientations as shown by their different colours. Two large grains (grains 1 and 2) make up most of the nodule, as shown in Fig. 2c. Misorientation relative to a reference point is less than 15° in these two grains. Bulging grain boundaries are systematically restricted to contacts between grains with different orientation (e.g. between grains 1 and 4, where the misorientation angle is ~20°, Fig. 2a and b).

The shape of the bulging contacts and their location between grains with different crystallographic orientations (Fig. 2b) indicate that these contacts result from grain boundary migration; that is, dynamic, stress-driven recrystallization caused by the difference of internal strain energy stored by dislocations. The migration produces characteristic lobate contacts that separate a concave, dislocation-poor advancing or growing grain from a convex, dislocation-rich retreating or consumed grain (Urai *et al.*, 1986; Drury & Urai, 1990). Such microstructures are described here for the first time in kimberlites; their occurrence provides important constraints on the origin of the nodules and supports the interpretation that they are fragments from deformed lithospheric mantle.

Migrating grain boundaries have been observed in other nodules including both high- and low-Fo types. As seen in Fig. 1c, the olivine tablets crosscut both the mosaic grains and the mobile grain boundaries and therefore postdate these textures.

These observations and interpretations indicate that the following sequence of events affected the olivine in the nodules: (1) generation of a range in olivine compositions; (2) deformation and grain boundary migration; (3) incorporation of dunitic fragments into the ascending kimberlitic magma; (4) growth of olivine tablets.

Core to margin gradients in olivine

The typical core to margin gradients observed in the olivines of sample NCR27 are illustrated by element versus Fo diagrams (Fig. 3) and by a set of chemical profiles (Fig. 4). Chemical analyses are given in SD Electronic Appendix Table EA2.

The margins range in thickness from 30 to 80 μm. They contain numerous fluid inclusions, but are devoid of mineral inclusions. We estimate the volumetric proportion of the margins in sample NCR27 at ~7 vol. % of the total olivine using a false colour image of an FeO microfluorescence map (see Arndt *et al.*, 2010) and ImageJ software (http://rsbweb.nih.gov/ij/).

The margins are characterized by near-constant Fo (Fo87·5 to Fo88·5) contents accompanied by large variations in minor element contents (Fig. 3a–c). In high-Fo grains, Ni contents drop dramatically from 2700 to 580 ppm, whereas Mn, Ca and Ti contents increase (SD Electronic Appendix Table EA2). In low-Fo, low-Ni grains the Fo content is higher in the margins than in the cores, as seen in Figs 3 and 4. In these grains, variations in minor element contents are irregular and not reproducible from one profile to another (Fig. 4c and i). In

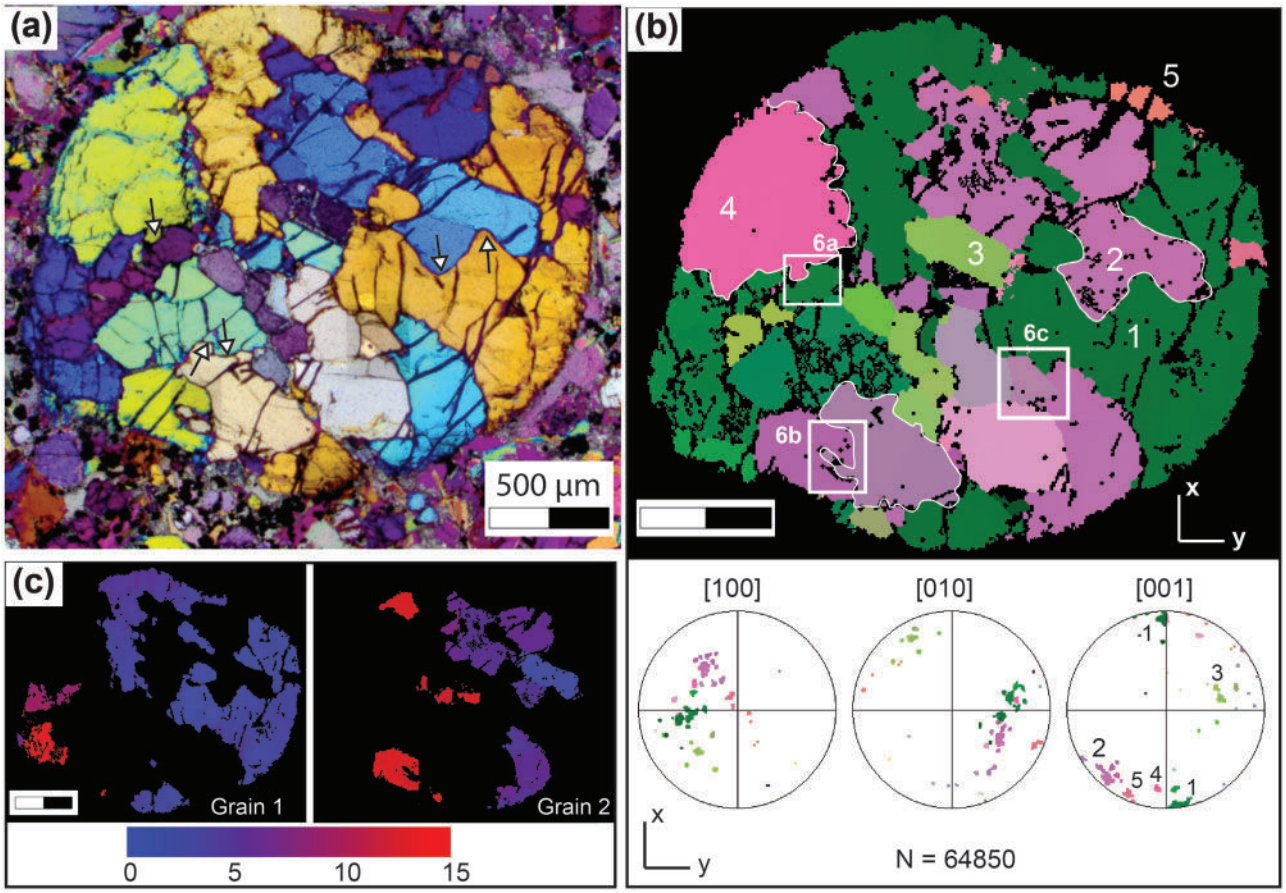

Fig. 2. Crystallographic orientation map of a multigranular nodule in NCR27 determined by electron-backscattered diffraction. (a) Photomicrograph under crossed Nicols with an additional lambda plate. The grains have five orientations corresponding to the different colours (blue, yellow, grey, green, purple). Mobile grain boundaries are arrowed. (b) Orientation map (upper part) and pole figures (lower part). Colours in stereograms (lower hemisphere) are similar to those of the map. N, number of indexed points. Squares show the areas whose compositions have been mapped (Fig. 6). (c) Misorientation maps (0–15°) showing the main two largest grains making up the nodule. Scale bar 500 μm.

particular, the Ni content sometimes increases at the transition between margin and rim (Fig. 4c).

The transition zones between cores and margins vary in thickness from 20 to 60 μm. Within these zones, the Fo content may increase or decrease whereas minor elements remain roughly constant. In high-Fo grains (Fig. 4a), the Fo content decreases sharply and steadily from core to margin. At the same time, Ni content decreases slightly, by less than 100 ppm, and Mn and Ca contents increase slightly, by less than 300 ppm. Transition zones around low-Fo cores are rare and thin (less than 20 μm), and they show a marked increase in Fo whereas Ni remains constant (Fig. 4c).

An important observation is that in minor element versus Fo diagrams (Fig. 3) the transition zones around high-Fo cores coincide with the trends defined by core compositions. For example, in the transition zones in Fig. 4a and b, the NiO content decreases only slightly as the Fo content changes from Fo91 to Fo88·5, reproducing part of the trend defined by high-Fo cores (Fig. 1).

We did not observe the outermost rims (5–10 μm) with extremely Mg-rich composition (Fo96) described from some other well-preserved kimberlites (Kamenetsky *et al.*, 2008; Brett *et al.*, 2009; Pilbeam *et al.*, 2013). However, in some cases, an incipient but sharp increase in Fo content (up to 89·5) associated with a small decrease in Ni (up to 500 ppm) and increase in Ca and Mn (up to 6000 ppm and 3000 ppm, respectively) is observed at the crystal edge (Fig. 4c and g).

Mobile grain boundaries and grain boundary zones

In sharp contrast to the remarkably uniform compositions in the interiors of most nodules, a few exceptional multigranular nodules, such as those illustrated in Figs 2 and 5, show large internal variations in Fo content. For example, the nodule in Fig. 5b contains numerous irregular zones adjacent to internal grain boundaries in which the Fo content is far lower than that of the core olivine. The distinctive features of these zones, which we will call 'grain boundary zones', are as follows: (1) they are adjacent to lobate (i.e. mobile) grain boundaries (Fig. 5); (2) the chemical gradients on opposing sides of the mobile grain boundaries are asymmetric, wide in the concave (growing) grain (up to

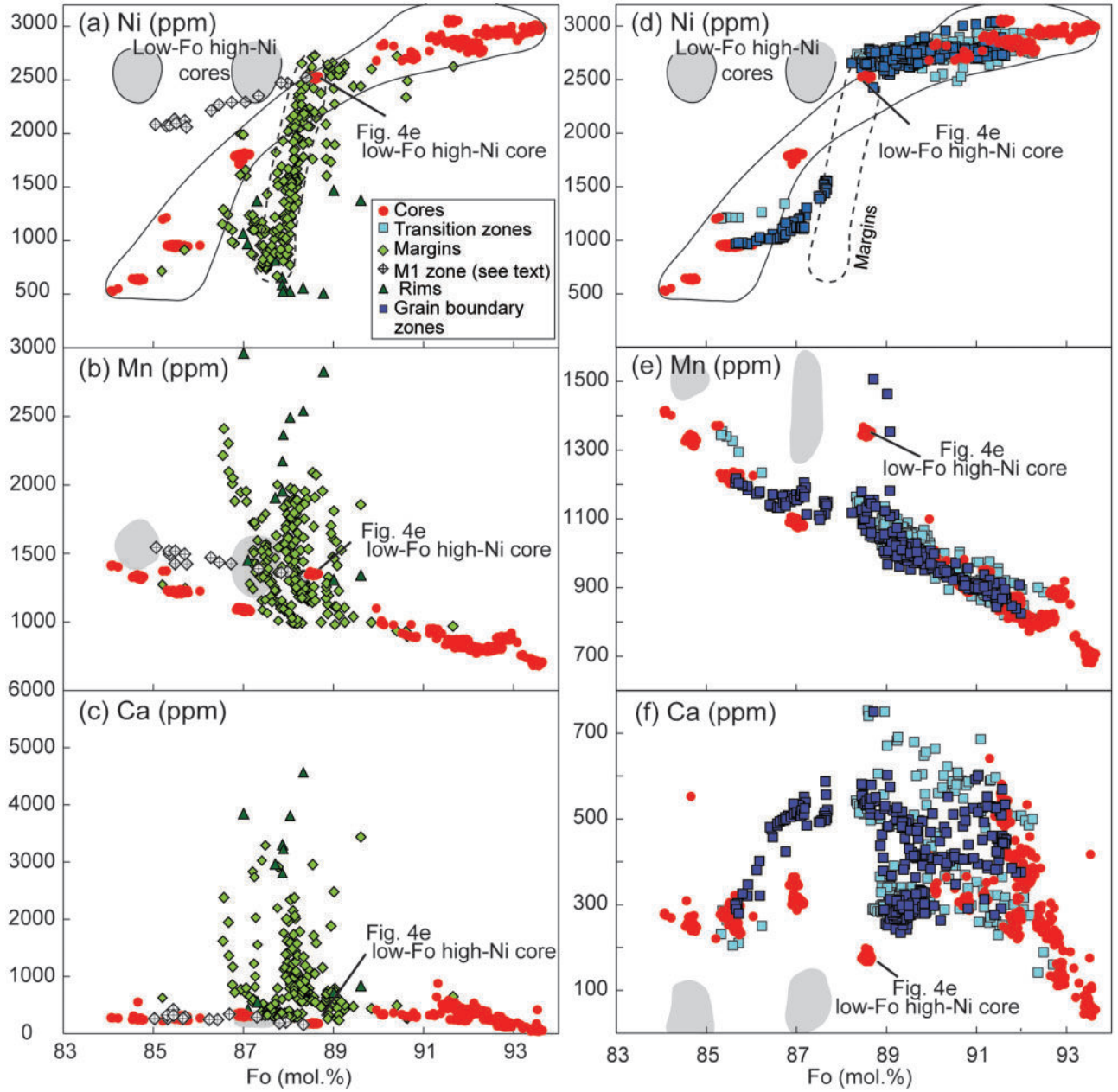

Fig. 3. Minor element (Ni, Mn, Ca) vs Fo variations. (a–c) Cores and margins; (d–f) cores, grain boundary zones and transition zones. Fields for low-Fo, high-Ni cores are after Pilbeam *et al.* (2013).

60 μm thick) but absent or very thin in the convex (consumed) grain; (3) the variations in Fo and minor elements are decoupled in the same way as in transition zones. The Fo content changes from uniform in the core to more variable in the grain boundary zone, whereas minor elements remain roughly constant and similar to those of the core.

In the high-Fo nodule in which we measured crystallographic orientations (Fig. 2), the Fo content of the growing grain decreases within the grain boundary zone from Fo92·7 (the core value) to Fo89, whereas minor elements remain constant (Figs 6 and 7a–d). Outwards, a zone with constant Fo and variable minor elements, like that observed in margins, lines the mobile grain boundary. Most notably, the Ca content increases dramatically, up to 3000 ppm (Fig. 7a). In the convex consumed grain, the core-to-margin transition is abrupt and marked by sharp jumps in Fo and minor element contents.

In the light of the above observations, we re-examine the intra-grain variations of the olivine composition in the large high-Fo (Fo93) multigranular nodule shown in Fig. 5b. This nodule is distinguished by numerous, large grain boundary zones, each of which displays distinctive chemical compositions and gradients. In chemical maps (Fig. 8), three zones with low Fo contents (Fo89) are seen to penetrate the high-Fo olivine cores. Minor elements are similar in the low-Fo zones and cores. The

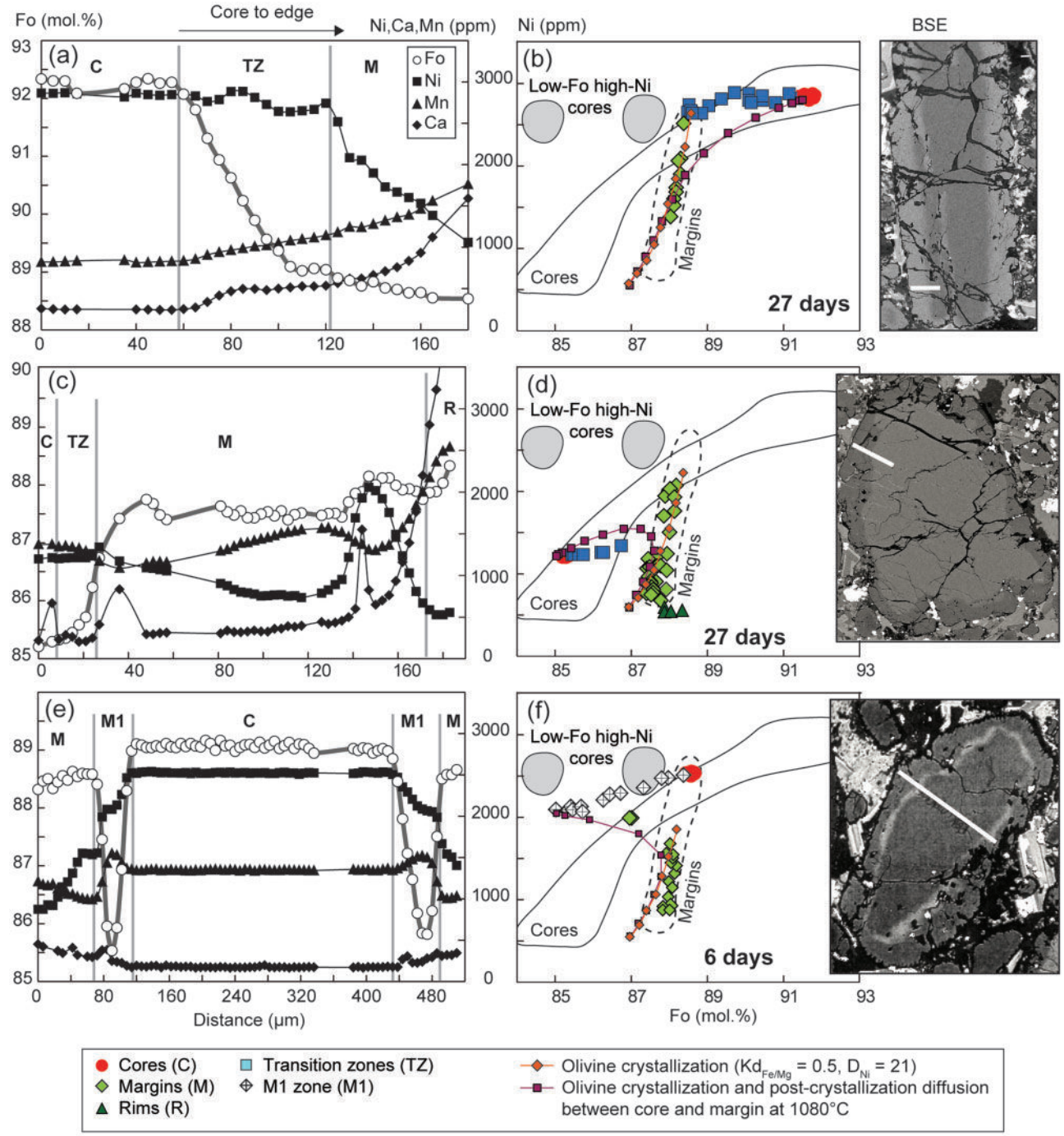

Fig. 4. Chemical profiles across marginal zones in olivine grains (a, c, e, g, i, k) and position of the data in Ni vs Fo diagrams (b, d, f, h, j, l). Position of the profiles is indicated on the back-scattered (BSE) electron images. Results of calculations for crystallization of olivine margin and post-crystallization diffusion between cores and margins during the indicated time intervals are shown in the right-hand panels.

(continued)

low-Fo zones are delimited on one side by lobate grain boundaries, which are marked by a sharp decrease in Fo and Ni contents and an increase in elements incompatible in olivine (Mn, Ca, Ti, Fig. 8). On the other side, the Fo content progressively increases to attain the high-Fo core composition, whereas the Ni content remains relatively constant. The lobate shape of internal grain boundaries, the asymmetric distribution of the low-Fo zones across the grain boundaries and their distinctive chemical gradients are characteristics of grain boundary zones.

Migrating grain boundaries and grain boundary zones are also identified in the low-Fo nodule illustrated in Fig. 7e and f. Mobile grain boundaries coexist with tablets and mosaic-textured grains but variations in olivine composition are restricted to the mobile grain

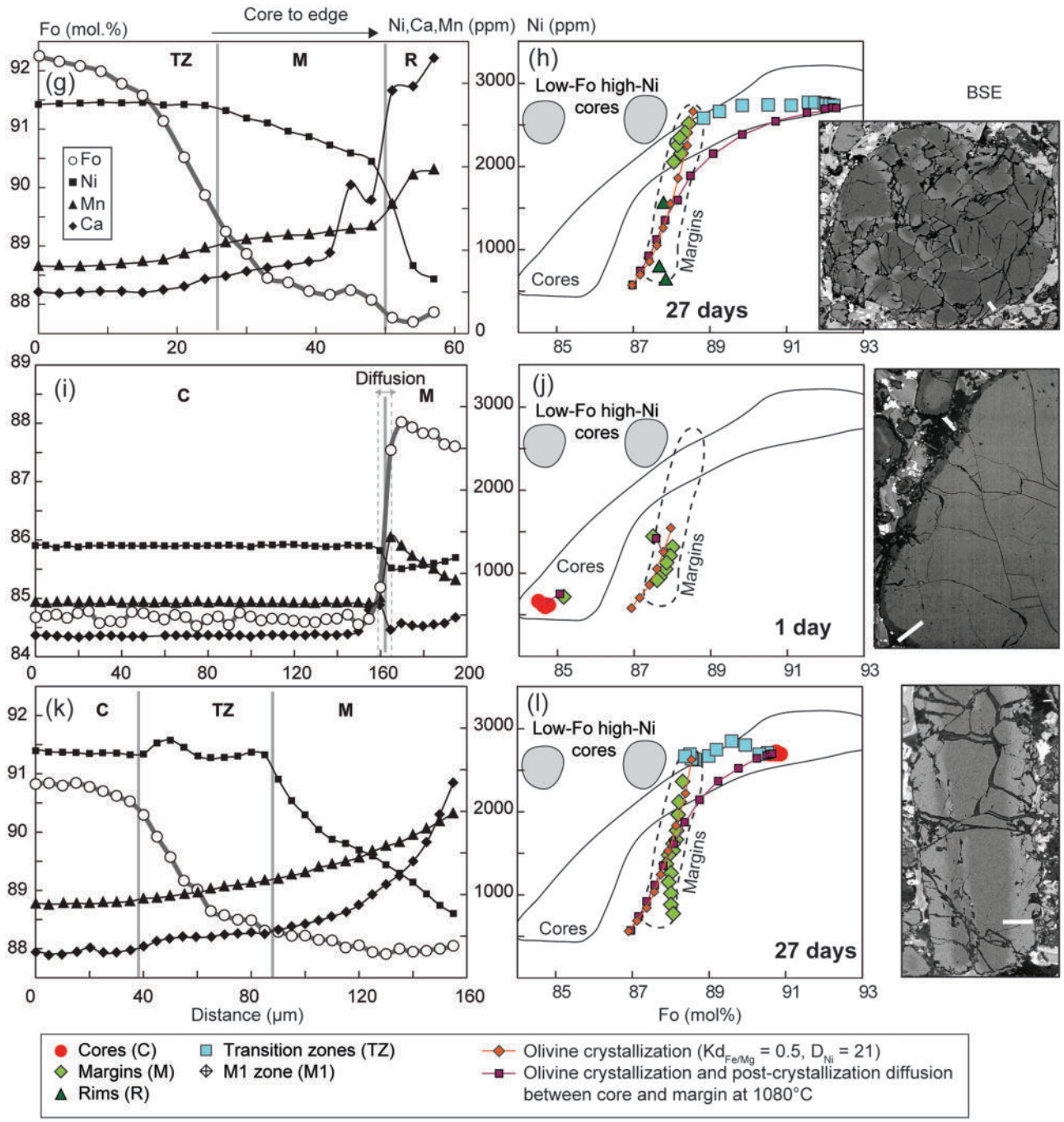

Fig. 4. Continued

boundaries. The grain boundary zone is asymmetric and marked by an increase of the Fo content in the bulging grain. The Ni content, like that of other minor elements, increases only slightly (Fig. 7e). In a Ni versus Fo diagram, the composition of the grain boundary zone lies on curving trends linking low-Fo core composition to the composition of the margin itself (Figs 5 and 7f).

KIMBERLITE MELT COMPOSITION

The composition of the kimberlite melt cannot be estimated directly from the bulk composition of sample NCR27 because of the high amount of xenocrystic olivine and the presence of large but rare ilmenite megacrysts (*c.* 60 vol. % olivine and 40 vol. % nodules; Arndt *et al.*, 2006). However, we can infer the parental melt composition from the chemical composition of NCR27 and that of another sample of the same dike (NCR29), which contains far less olivine (25 vol. % with 5 vol. % nodules; Arndt *et al.*, 2006). Two different values for the Fe–Mg distribution coefficient between olivine and melt ($Kd_{Fe–Mg}$) have been discussed in the literature (Kamenetsky *et al.*, 2008; Arndt *et al.*, 2010; Pilbeam *et al.*, 2013). A $Kd_{Fe–Mg}$ value of 0·3 is normally adopted

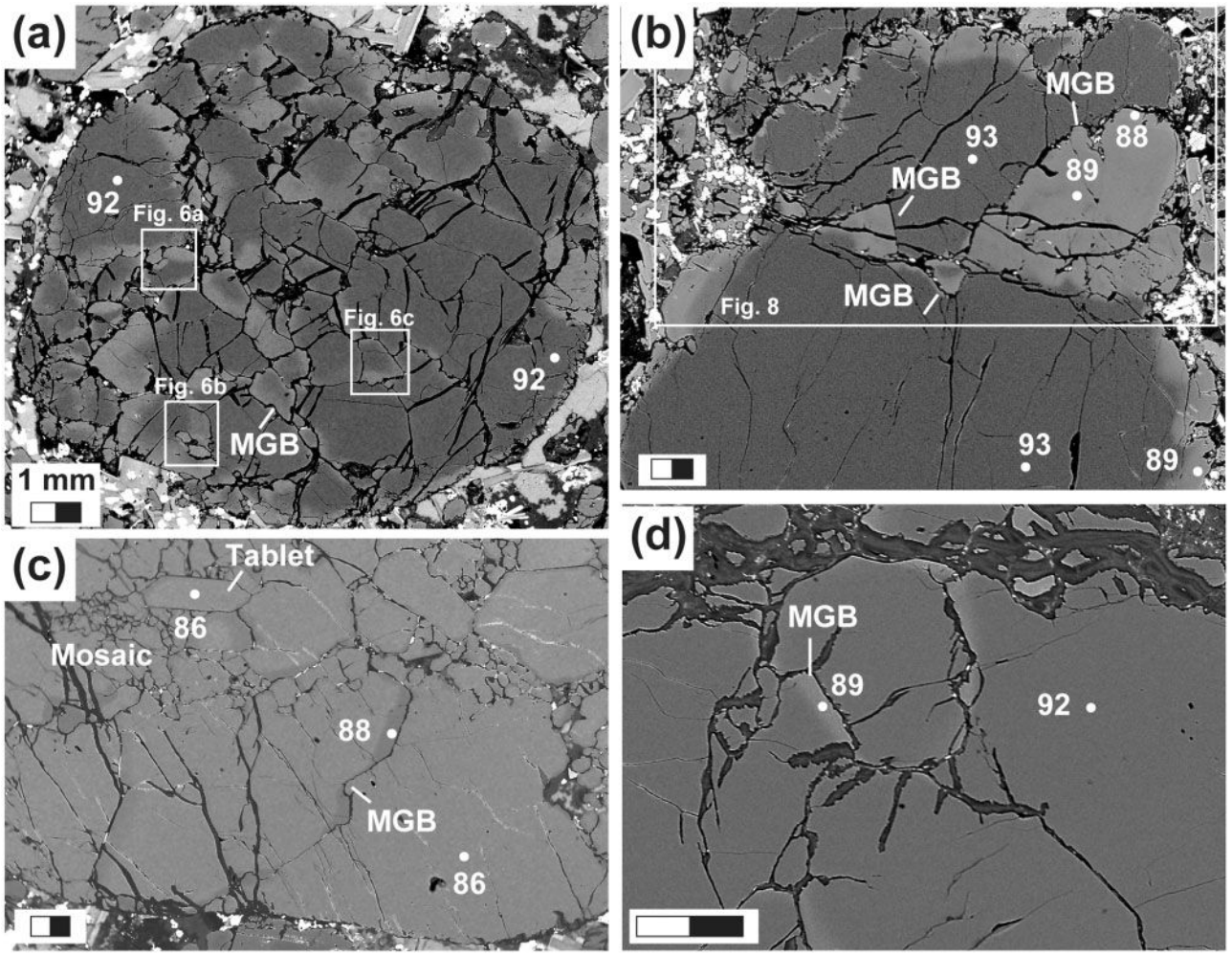

Fig. 5. Back-scattered electron images of mobile grain boundaries (MGB) in four nodules from sample NCR27. Light grey indicates Fo-poor compositions. Fo content (mol %) in olivine is indicated. Squares show the areas in which the compositions have been mapped (Figs 6 and 8). Scale bar in (b), (c) and (d) 200 μm.

for basaltic melts (Roeder & Emslie, 1970), whereas a value of 0·5 has been proposed for CO_2-rich kimberlite melts (Dalton & Wood, 1993; Girnis *et al.*, 2005). All iron can be considered to be FeO because of the reduced state of kimberlite magmas (ΔNNO = –3 to –2, where NNO is nickel–nickel oxide; Fedortchouk & Canil, 2004).

The MgO content of the parental melt can be determined graphically in an FeO versus MgO diagram (Fig. 9). The values are MgO = 20 wt % for $Kd_{Fe–Mg}$ of 0·3 and 30 wt % for $Kd_{Fe–Mg}$ of 0·5. These MgO values can then be used to estimate the concentrations of the other major and minor elements in the parental melt (Table 2) using trends between NCR27 and NCR29 samples in element versus MgO diagrams. For both $Kd_{Fe–Mg}$ values, the calculated parental melts have magnesium-rich silicocarbonatite composition (SiO_2 = 30–32 wt %, MgO = 20–30 wt % and FeO = 14–15 wt %, normalized to 100 wt %, without volatiles, Table 2). The new analyses allow us to determine the Ni contents: 120 ppm for the 30 wt % MgO melt and 770 ppm for the 20 wt % MgO melt.

To reproduce the compositions of the NCR29 and NCR27 samples, which both contain xenocrystic olivine, we added olivine (+ ilmenite) to the parental melt composition (Fig. 9; Table 2). The xenocryst assemblage is dominated by olivine (94 wt %), with a bulk Fe–Mg value very close to the average composition of all xenocryst cores analysed in NCR27 (Fig. 9). A small amount of xenocrystic ilmenite is required to account for the high TiO_2 content of NCR27. Calculated xenocryst versus melt proportions change depending on the $Kd_{Fe–Mg}$ value (Table 2). The xenocryst proportions obtained using a value of 0·3 (53 vol. % in NCR27 and 29 vol. % in NCR29) agree well with the amount of olivine (nodule + matrix olivine) observed in thin section (60 vol. % in NCR27 and 25 vol. % NCR29; Arndt *et al.*, 2010). Previous studies of the chemical and microstructural characteristics of matrix olivine grains have shown that a large proportion of these grains is xenocrystic (Brett *et al.*, 2009; Arndt *et al.*, 2010), supporting the view that the kimberlite melt is in equilibrium with olivine with a $Kd_{Fe–Mg}$ value of 0·3.

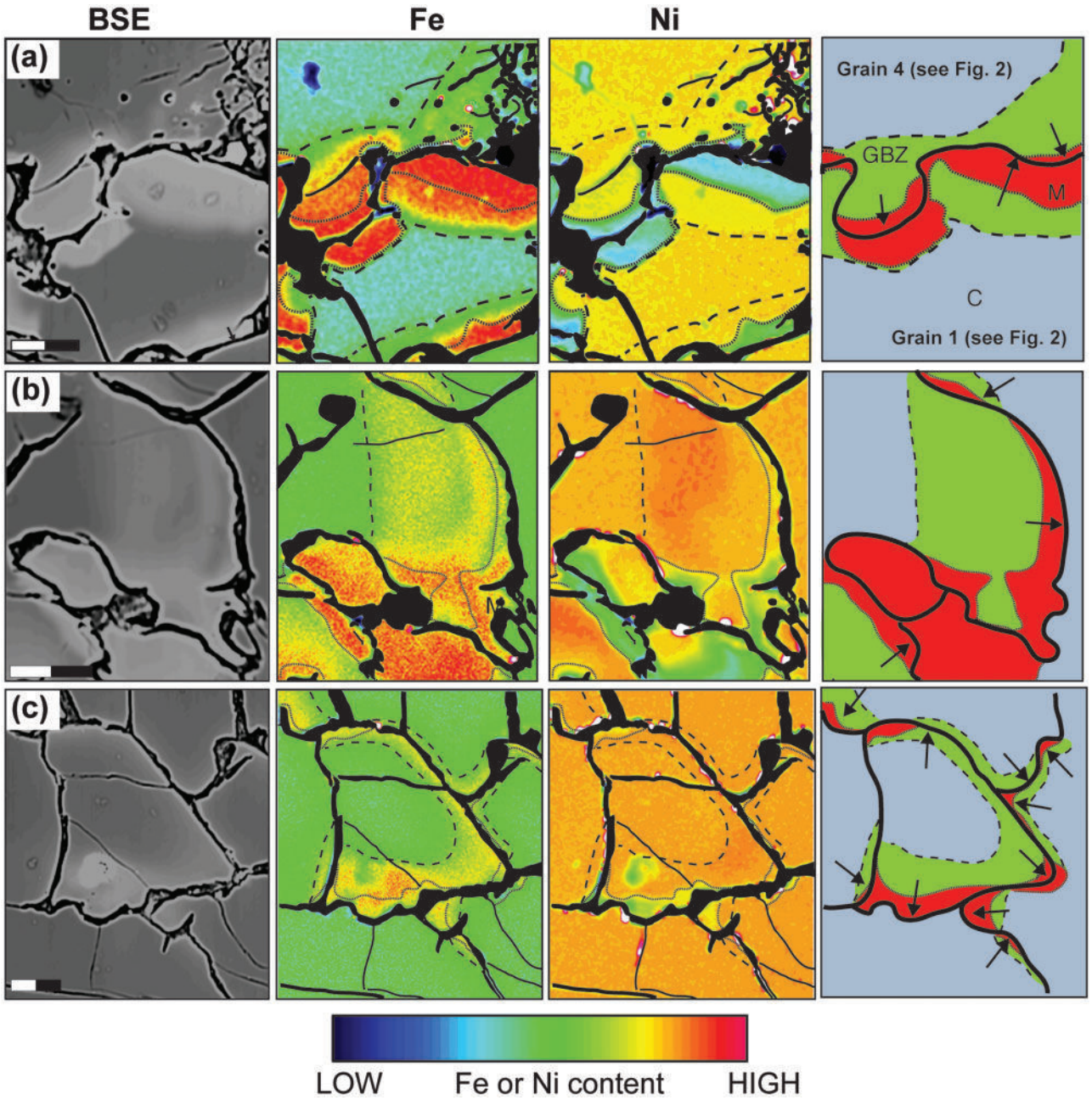

Fig. 6. Back-scattered electron (BSE) images and Fe and Ni distribution maps of the grain boundary zones (GBZ) in the multigranular nodule shown in Figs 2 and 5a. Scale bar 50 μm. Sketches (right) indicate the distribution of the core (blue), margin (red) and grain boundary zone (green) across the mobile grain boundary. The direction of migration is arrowed. The variation of thickness of the grain boundary zone between grown and consumed grains and in a single grain should be noted.

OLIVINE COMPOSITION: CRYSTALLIZATION VERSUS MELT REACTION

Is digestion of orthopyroxene coupled to margin crystallization?

The olivine margins that crystallized from the kimberlite melt have near-constant Fo contents (~Fo88) but variable minor element contents, most notably showing a dramatic decrease in Ni (Fig. 3a). The buffering of the Fo content in cognate olivine has been attributed by Kamenetsky *et al.* (2008) and Arndt *et al.* (2010) to a higher $Kd_{Fe/Mg}$ value than usually assumed for basaltic melts, and by Pilbeam *et al.* (2013) to concomitant crystallization of olivine and assimilation of orthopyroxene ('digestion fractional crystallization'). To test these possibilities we modelled the variations of olivine composition using incremental mass-balance calculations based on the two kimberlite-like parental melts listed in Table 2 and on a low-silica carbonatitic liquid (Pilbeam *et al.*, 2013).

We found no evidence of co-crystallization of high-Ni phases such as spinel, ilmenite or sulfide during margin crystallization. Cognate margins are typically devoid of

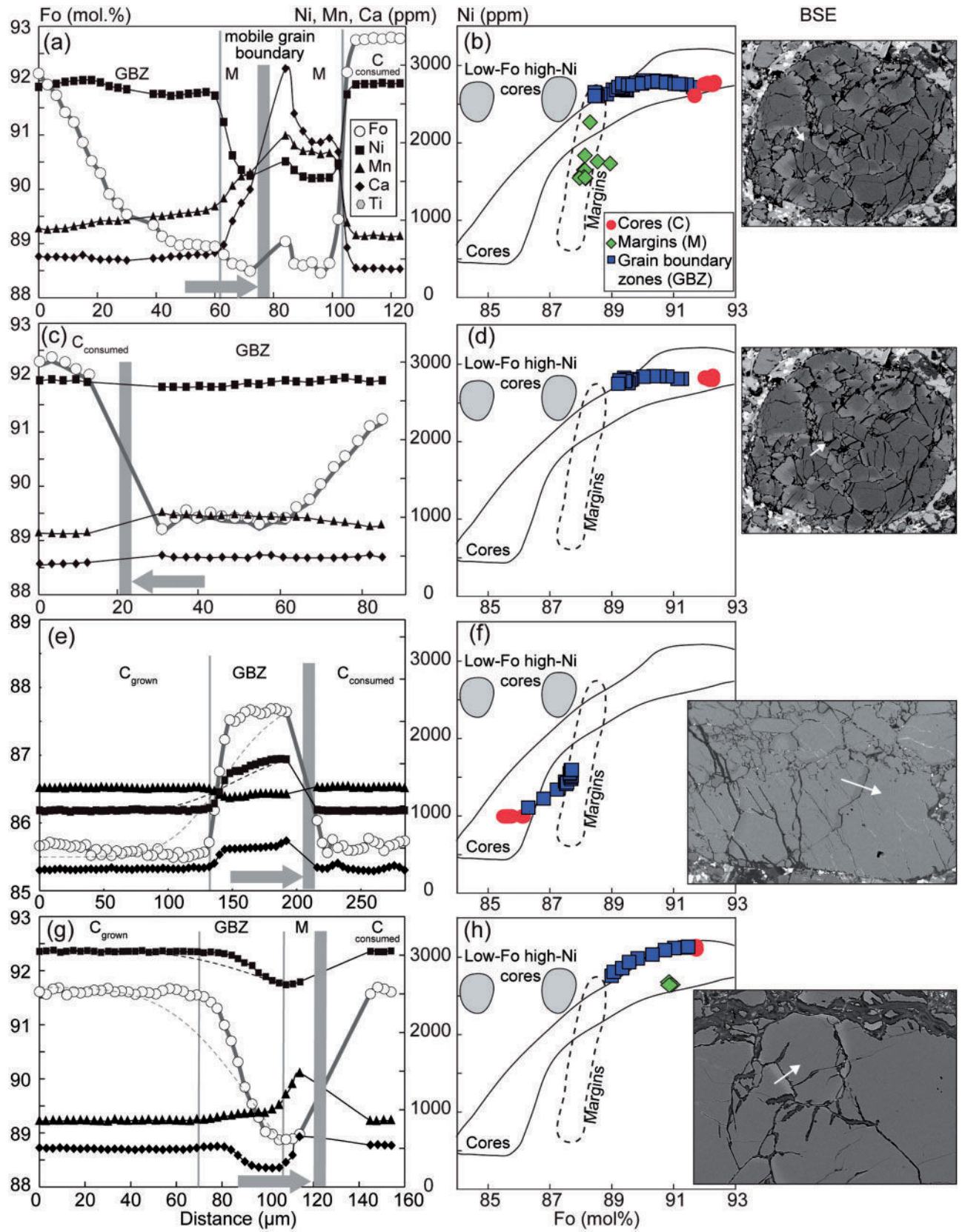

Fig. 7. Chemical profiles (a, c, e, g) across mobile grain boundaries and position of the analyses (b, d, f, h) in a Ni vs Fo diagram. The position of the profiles is indicated on the BSE images. Direction of migration is shown on the profiles by the grey arrows. Results of calculations for diffusive equilibration over 3 days between core and grain boundary zone at mantle temperature (1400°C) and pressure (1 GPa) are shown in (e) and (g) for Fo (grey dashed line) and Ni (black dashed line).

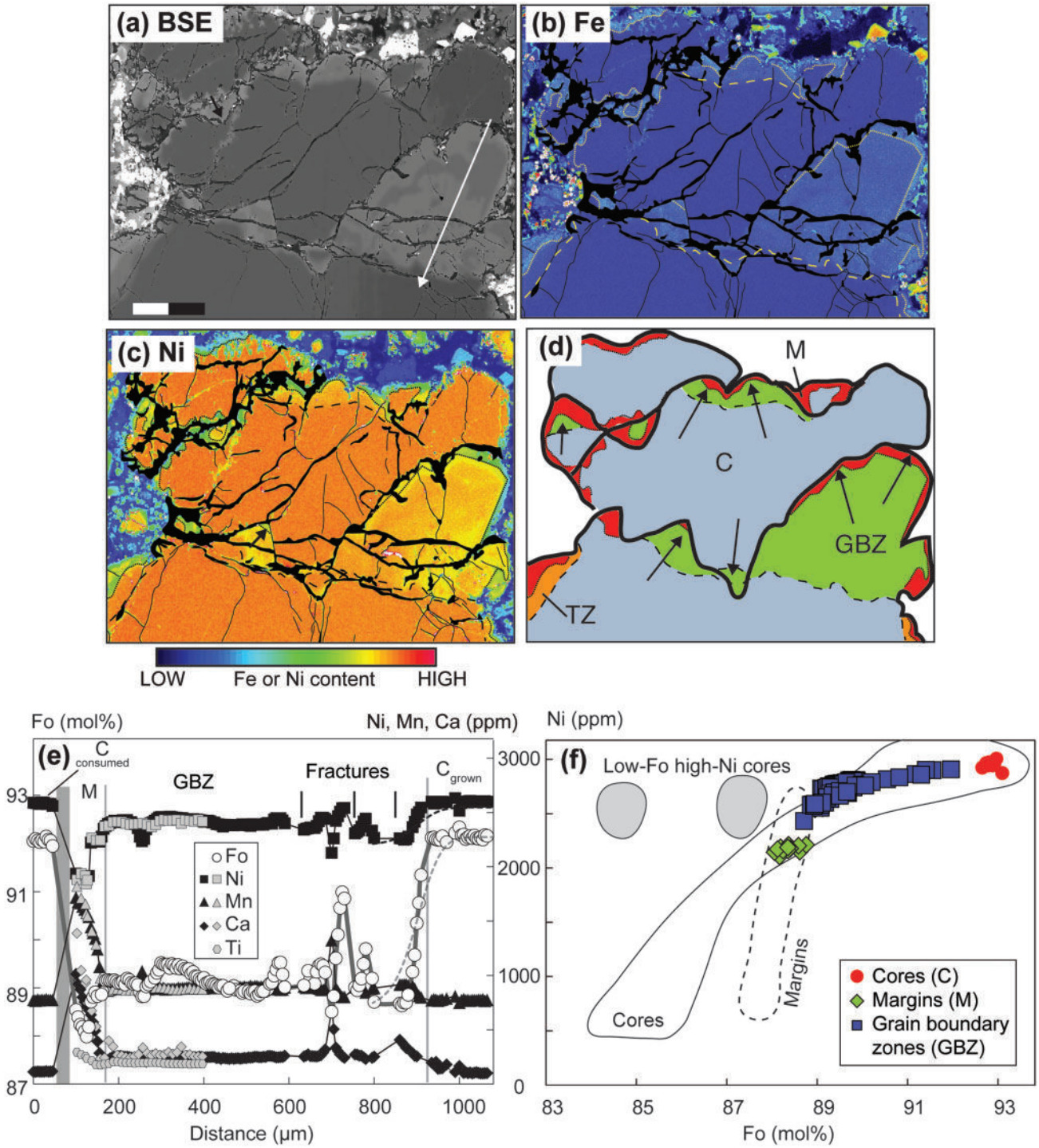

Fig. 8. Grain boundary zones (GBZ) in the multigranular nodule shown in Fig. 5b. (a–d) BSE images and Fe and Ni distribution maps. Scale bar 400 μm. Sketch in (d) indicates the distribution of the core (C, blue), margin (M, red), grain boundary zone (GBZ, green) and transition zone (TZ, orange). The direction of migration is arrowed. (e, f) Chemical profile along the transect shown in (a) and position of the analyses in the Ni vs Fo diagram. Minor elements plus Ti were analyzed using a high-resolution procedure (see text), as shown on the left side of the profile (grey symbols). Results of calculations for diffusive equilibration over 7 days between core and grain boundary zone at mantle temperature (1400°C) and pressure (1 GPa) are shown in (e) for Fo (grey dashed line) and Ni (black dashed line).

oxide inclusions and, when measured, the TiO_2 content increases within the margins (Fig. 8e), precluding ilmenite co-crystallization. We thus assumed that olivine was the only phase to crystallize. Assimilation of orthopyroxene coupled to fractional crystallization of olivine was modelled using the formulation of DePaolo (1981) and the parameters given in Table 3. Orthopyroxene has the highest potential to contaminate

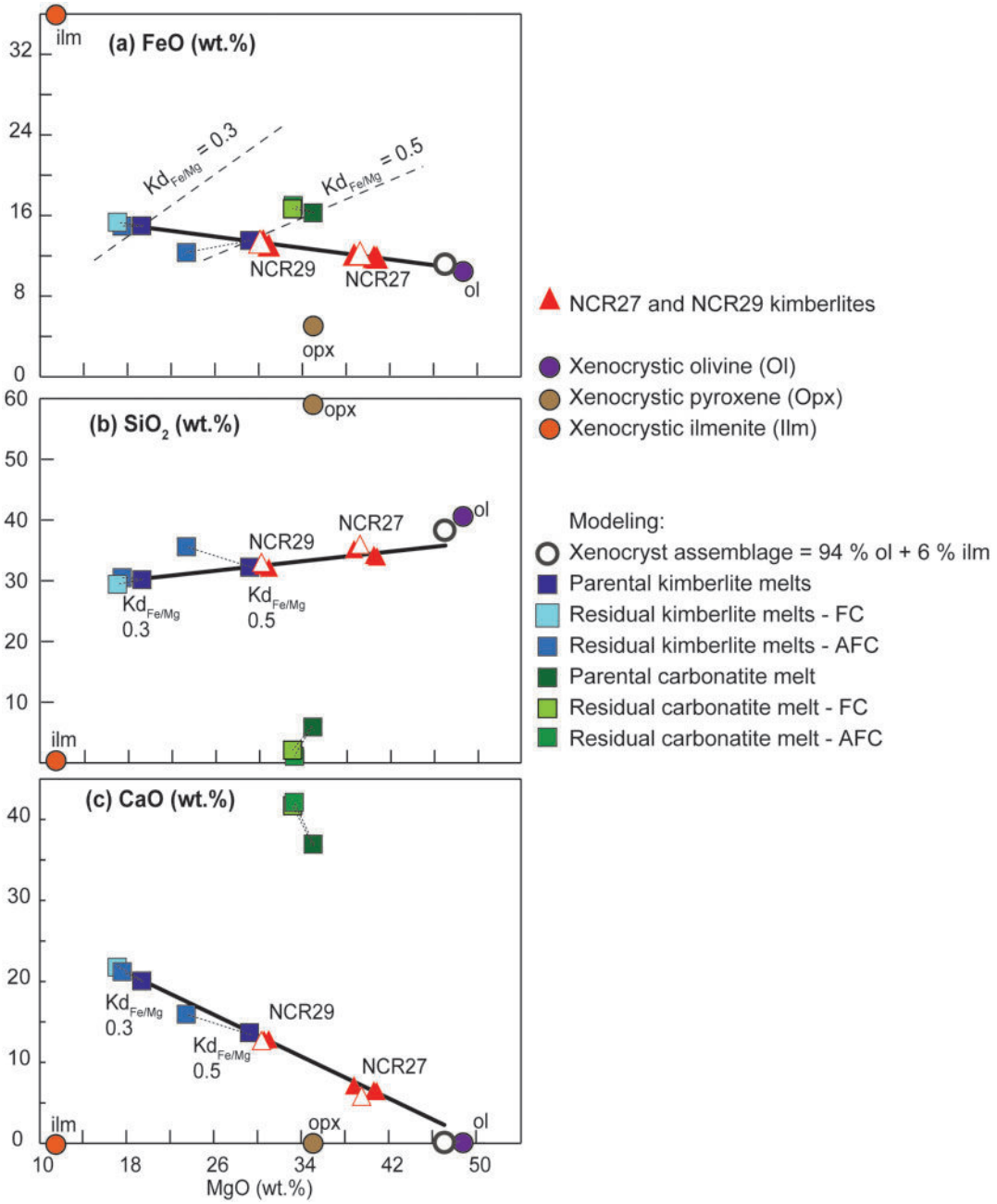

Fig. 9. Variation of FeO (a), SiO_2 (b) and CaO (c) vs MgO (wt %) in NCR27 and NCR29 kimberlite samples (40 and 5 vol. % olivine nodules, respectively) and in computed parental and residual melts. The xenocrystic line (bold line) connects the nodule-rich NCR27 sample and the nodule-poor NRC29 sample and shows the effect of addition of the xenocryst assemblage (94% olivine + 6% ilmenite). The composition of the xenocrystic olivine is the average of the analyzed core compositions; the compositions of xenocrystic ilmenite and orthopyroxene are from Nielsen & Sand (2008). The $Kd_{Fe/Mg}$ sloping dashed lines in (a) represent the FeO/MgO ratio of melts in equilibrium with olivine margin composition considering $Kd_{Fe/Mg}$ values of 0·3 and 0·5. The intersection of the $Kd_{Fe/Mg}$ lines and the xenocrystic line gives the MgO and FeO contents of the parental kimberlite melt (Table 2). The proportion of xenocrysts in NCR27 and NCR29 is back-calculated from the composition of the parental melts, xenocryst assemblage and kimberlite samples. The carbonatite-like parental melt composition is from Pilbeam *et al.* (2013). The dotted line connects the parental melts and the residual melts obtained by fractional crystallization of olivine (FC) and by orthopyroxene assimilation coupled with fractional crystallization (AFC). (See text and Table 3 for further details.)

the kimberlite melt because the reactivity of mantle minerals with a low-silica melt decreases from orthopyroxene to clinopyroxene to olivine (Luth, 2009; Russell *et al.*, 2012).

In mafic and ultramafic magmas the partition coefficient of Ni in olivine (D_{Ni}) depends on melt composition, in particular the MgO content (e.g. Hart & Davies, 1978; Li *et al.*, 2001). The compositional dependence of D_{Ni} in alkali-rich carbonatite melts with variable MgO contents has not been investigated experimentally, but we assumed that D_{Ni} is negatively correlated with the MgO content of the melt (Table 3). The D_{Ni} values were

Table 2: Volatile-free major element composition (wt %) of the kimberlite, carbonatitic and basaltic parental melts considered for the modeling of margin crystallization

	SiO_2 (wt %)	TiO_2 (wt %)	Al_2O_3 (wt %)	FeO^T (wt %)	MnO (wt %)	MgO (wt %)	CaO (wt %)	Ni (ppm)	vol. %* NCR27	vol. %* NCR29
Kimberlite†										
Ol $Kd_{Fe/Mg} = 0{\cdot}5$	32·2	3·4	3·4	13·5	0·3	29·2	13·7	767	40	5
Ol $Kd_{Fe/Mg} = 0{\cdot}3$	30·2	3·2	5·4	14·9	0·3	19·4	20·0	130	53	29
Carbonatite‡	5·9	2·2	0·6	16·2	0·18	35·0	37·0	208		
Basalt	48·7	1·1	15·1	9·6	0·2	10·6	12·8	280		

*Proportions of xenocryst assemblage (94% olivine plus 6% ilmenite) that have to be added to the melt to reproduce the compositions of NCR27 and NCR29. Proportions are converted to vol. % using densities of 3200, 4720 and 2450 kg m^{-3} for olivine, ilmenite and kimberlite melts, respectively.
†Kimberlite parental melt determined from Fig. 9 (see text).
‡Carbonatite parental melt from Pilbeam *et al.* (2013).

Table 3: Parameters used in crystallization models

Parental melt*	Kimberlite	Kimberlite	Carbonatite	Basalt
Fe^{2+}/Fe^{tot}	1	1	1	0·85
Ol $Kd_{Fe/Mg}$	0·5	0·3	0·5	0·3†
Cpx $Kd_{Fe/Mg}$	–	–	–	0·27†
Ol D_{Ni}‡	4	21	13	7–12
f‡	105	400	450	–
Cpx D_{Ni}	–	–	–	1
FC	–	ol	ol	ol + cpx
Cum. %§	–	9	14	16
Ni in ol (ppm)	–	575	575	2045
Fo in ol	–	86·9	87·5	84·7
AFC	ol–opx	ol–opx	ol–opx	–
Cum. %§	37	10	15	–
Opx %§	22	4	3	–
r§	0·6	0·4	0·2	–
Ni in ol (ppm)	800	535	513	–
Fo in ol	87·2	87·4	87·7	–

*Parental melt compositions are given in Table 2.
†$Kd_{Fe/Mg}$ values from Roeder & Emslie (1970) and Irving (1984).
‡Partition coefficients for Ni in olivine. In kimberlite and carbonatite melts, $D_{Ni} = f$/MgO. In basaltic melt, ln $D_{Ni} = 5{\cdot}67–1{\cdot}38$ ln MgO – 0·25 (FeO/MgO) (Li *et al.*, 2001).
§Cum. %, weight per cent of crystallized cumulate; opx %, weight per cent of assimilated opx; r, ratio of assimilation rate to crystallization rate (DePaolo, 1981).

evaluated from equilibrium between the parental melts and the margins with the highest Ni content. D_{Ni} varies depending on the $Kd_{Fe/Mg}$ used for the parental melt calculation, with D_{Ni} values ranging from three for $Kd_{Fe/Mg} = 0{\cdot}5$ to 21 for $Kd_{Fe/Mg} = 0{\cdot}3$ (Table 3). A combination of high $Kd_{Fe/Mg}$ with high D_{Ni} does not reproduce the chemical variations observed in olivine margins when kimberlite-like melts are considered (Table 3).

The D_{Ni} values are well above the range proposed for basaltic melts (e.g. 3·8–5 at 1400–1550°C; Matzen *et al.*, 2013) but are realistic in view of the following characteristics of kimberlite melts: (1) they are rich in carbonate and D_{Ni} up to 19 has been proposed for silicocarbonatite melts (Sweeney *et al.*, 1995; Girnis *et al.*, 2013); (2) they are rich in potassium ($K_2O \sim Al_2O_3$; SD Electronic Appendix Table EA1) and a D_{Ni} up to 40 has been proposed for highly potassic rocks (Foley *et al.*, 2011); (3) they crystallized at lower temperatures (1080–1170°C; Fedortchouk & Canil, 2004) than basaltic melts and D_{Ni} increases with decreasing temperature, at least in basaltic systems (Matzen *et al.*, 2013).

The modelled chemical trends are compared with margin compositions in Ni versus Fo diagrams (Figs 4 and 10). We used the composition of the two kimberlite samples with different xenocryst proportions to check that the modelled residual melts plot on similar trends to the bulk-rocks and xenocrystic assemblage in major element versus MgO diagrams (Fig. 9). Models considering a carbonatitic parental melt succeed in reproducing the margin olivine composition but the residual melts have too low SiO_2 and too high CaO to explain the compositions of the NCR27 and NCR29 samples by olivine (+ ilmenite) addition.

Both crystallization models based on parental kimberlite melts give residual melts consistent with the bulk compositional trends, but the cognate olivine compositions are different. The model with high $Kd_{Fe/Mg}$ and low D_{Ni} (Table 3) reproduces the buffering of Fo content only if orthopyroxene is simultaneously assimilated. However, unrealistically high proportions of crystallized olivine (37 wt %) and assimilated orthopyroxene (22 wt %, Table 3) are needed to reproduce the low Ni contents at the end of the trends. The proportion of margin olivine is only 7 vol. % (~6 wt %) in NCR27 and only 4 wt % in other kimberlite samples (e.g. Brett *et al.*, 2009). Reconciling model and observation would require the presence of a large amount of cognate olivine in the kimberlite matrix, which is inconsistent with the low observed proportion of phenocrysts (less than 1 vol. %, Brett *et al.*, 2009).

If a low $Kd_{Fe/Mg}$ and high D_{Ni} are adopted, however, the required amount of olivine crystallization is low (8–9 wt %, Table 3) and consistent with the proportion of olivine margins. The cognate olivine composition can be reproduced considering fractional crystallization of olivine only (Fig. 10) or olivine crystallization accompanied by the assimilation of a negligible amount of orthopyroxene (<5 wt %, Table 3).

Olivine crystallization from basaltic melt

A single complexly zoned grain in the matrix contains an unusual M1 zone between core and margin,

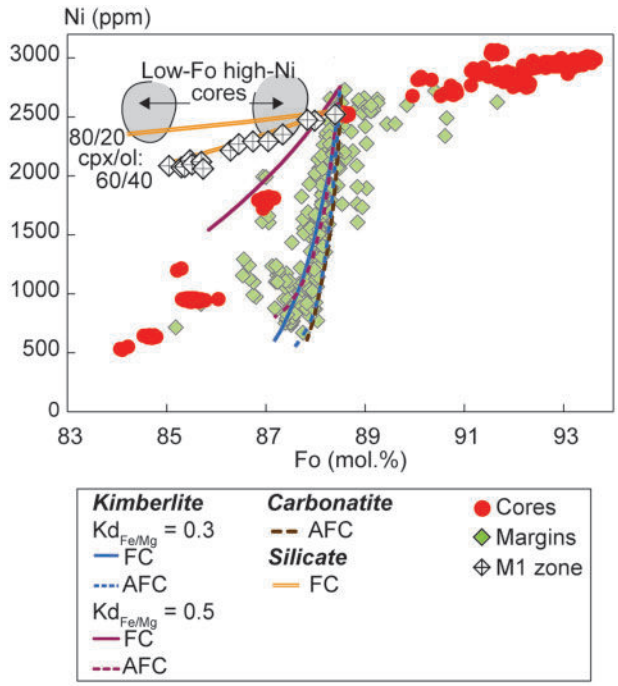

Fig. 10. Ni vs Fo diagram showing the margin crystallization models summarized in Table 3. For crystallization of the silicate melt, two trends are drawn for two ratios of crystallizing clinopyroxene and olivine.

characterized by low Fo contents but high Ni and Mn contents (Figs 4e, f and 10). In contrast to the other marginal zones, in which Ni contents drop rapidly, in this zone the Ni content decreases only from 2500 to 2100 ppm as the Fo content decreases from 89·2 to 85·5. The latter value is lower than any other values in zoned olivine grains, except for the low-Fo high-Ni population (Type 3 olivine) identified by Pilbeam *et al.* (2013). We attribute this trend to crystallization of olivine from a basaltic (Tables 2 and 3), rather than an ultramafic melt. At high pressure clinopyroxene crystallizes together with olivine and because the Ni partition coefficient in clinopyroxene is lower (e.g. $D_{Ni} = 2{\cdot}8$; Laubier *et al.*, 2014) than that for olivine, co-precipitation of the two phases results in only a subdued drop in the Ni content of the residual liquid. We could obtain a fit with the M1 zone composition considering a partition coefficient in clinopyroxene of unity (see Table 3 and Fig. 10). This value is slightly lower than those proposed for basaltic systems at atmospheric pressure (e.g. 2·8, Laubier *et al.*, 2014), but by comparison with the partitioning of Ni in olivine, the value must be lower at high mantle temperature and pressure (e.g. Matzen *et al.*, 2013). The M1 zone also has low Ca contents (Fig. 3c), a feature consistent with co-crystallization of calcic clinopyroxene. The core of the complexly zoned grain shares the low Fo, high Ni, high Mn and low Ca contents of the M1 zone that surrounds it. In this sense, it differs radically from the other olivine cores in the NCR27 sample, but it is similar to the rare (<1 vol. %) Type 3 low-Fo high-Ni cores reported by Pilbeam *et al.* (2013) in other Greenland kimberlites (Fig. 3). This may indicate that both the core and the M1 zone crystallized from a basaltic melt. The M1 zone is mantled outward by typical margins, suggesting that the crystallization of basaltic melt preceded kimberlite crystallization. If this interpretation is correct, we have evidence that kimberlite magmas interacted with deep-seated basalts in the lithosphere, before crystallization of the margin from the kimberlite melt.

Do transition zones result from diffusive equilibration?

Pilbeam *et al.* (2013) attributed the transition zones to diffusive equilibration after crystallization of the margins. Two observations oppose this interpretation: (1) the Fo content in the transition zones varies significantly from core to margin composition whereas Ni remains constant and similar to the core composition; (2) the evolution from transition zone to margin is sharp with the preservation of abrupt changes in minor element contents, notably Ni.

The continuous change of the Fo content in the transition zones would require a high degree of diffusive equilibration, if produced by this process. Like Pilbeam *et al.* (2013), we calculated a duration of equilibration of 1 month for a 60 μm thick transition zone (Fig. 4), using the parameterization of Dohmen & Chakraborty (2007) for the Fe–Mg inter-diffusion coefficient along the [001] crystallographic axis at atmospheric pressure and 1080°C (Fedortchouk & Canil, 2004). The diffusion time is reduced to 10 days if a higher crystallization temperature is considered (1170°C, Fedortchouk & Canil, 2004), but this duration is still significantly longer than the total ascent time of the kimberlite magma to the surface (less than 10 h; Canil & Fedortchouk, 1999; Wilson & Head, 2007; Russell *et al.*, 2012).

Given that Ni and the Fe–Mg pair have similar diffusion rates (Petry *et al.*, 2004), during the time required to produce continuous variations of Fo through the transition zones, Ni would also have diffused, producing correlated variations of Ni and Fo in the transition zones; such variations are not observed in the nodules (Fig. 4).

Some post-crystallization diffusion no doubt occurred but we believe that the effects on olivine are limited. One example can be seen in Fig. 4i and j. In this low-Fo low-Ni grain, a transition zone is absent and core and margin are in sharp contact. Any diffusion was limited to less than 10 μm at the boundary between core and margin (Fig. 4i). In the Fo versus Ni diagram (Fig. 4j), diffusion may have produced the observed minor deviations from core and margin compositions but certainly does not create the continuous chemical trend observed in the transition zones.

To summarize, post-crystallization diffusion between cores and margins cannot explain the 60 μm thick transition zones with the continuous variation in Fo content, the lack of equilibration between transition zones and margins, and the characteristic decoupling between Fo

and minor elements. This suggests that transition zones record a magmatic process that modified the olivine composition at the nodule and grain borders, before crystallization of the margins.

Grain boundary zones: grain-scale fluid percolation

In this section, we examine the chemical variations across mobile grain boundaries, and explore how they shed light on the origin of the grain boundary zones and what this tells us about the origin of olivine in kimberlites. The most distinctive features of the grain boundary zones are (i) the decoupling of Fo and minor elements, as observed in transition zones, (ii) the asymmetric chemical gradients across grain boundaries, with a systematically larger zone in the concave grain and thinner (or absent) zone in the convex grain, and (iii) their association with lobate migrating grain boundaries formed during dynamic recrystallization. Grain boundary zones are often, but not always, lined with margins.

As demonstrated for the transition zones, the gradients observed in the grain boundary zones cannot have resulted from post-crystallization diffusion. The asymmetric distribution of the grain boundary zones across the grain boundaries would require faster diffusion in the concave grains than in the convex grains. Diffusion rates of Fe–Mg and Ni do indeed depend on the crystallographic orientation, but for this to have produced the asymmetry would require a large difference in crystallographic orientation across the grain boundaries. This is inconsistent with the orientations shown in Fig. 2 (e.g. grains 1 and 4), which are not sufficiently different ($\sim$20°) to cause strong differences in diffusion rate (difference of less than a factor of 1·3). Likewise, the width of the grain boundary zone varies within single grains, within which the crystallographic orientation is constant, (misorientation $<$15°, Fig. 2). So, as proposed for transition zones, grain boundary zones do not result from post-crystallization diffusion and thus formed before margin crystallization.

Two observations confirm that grain boundary migration, which is stress-induced, could not have occurred in the kimberlite magma during its ascent to the surface: (1) the tablet-shaped grains, which result from static olivine recrystallization (i.e. annealing) during kimberlite melt ascent (Guéguen, 1979; Nermond, 1994), locally cross-cut the mobile grain boundaries; (2) the margins are free of deformation microstructures; they show only growth dislocation features (Arndt *et al.*, 2010).

We are not aware of previous studies reporting similar asymmetric chemical gradients associated with mobile grain boundaries in natural peridotite xenoliths or in kimberlite nodules. Experimental studies of grain boundary migration in olivine, carbonates and quartz show that asymmetric chemical gradients across mobile grain boundaries develop only when fluid is present (Evans *et al.*, 1986; Nakamura *et al.*, 2005; Ohuchi *et al.*, 2010). The asymmetric grain boundary zones thereby document intergranular percolation of fluid in dynamically deforming lithospheric mantle.

The chemical gradients in the grain boundary zones, which are less than 100 μm in thickness, have been preserved from diffusive equilibration with the host olivine. The sharp Fo gradient between the core and grain boundary zones would not have survived for more than a few days (Figs 7 and 8) at high mantle temperatures (1400°C) and pressures (1 GPa), particularly in the presence of fluids. The high ascent rate of the kimberlite magmas compared with basaltic magmas explains why the chemical gradients are preserved in our kimberlite samples and not in mantle xenoliths. The important conclusion that emerges from this discussion is that fluid or melt percolation in the lithospheric mantle must have occurred shortly before nodule entrainment into the kimberlite magma.

Decoupling of Fo and Ni in kimberlite olivine: a tracer for fluid–peridotite reaction in the lithospheric mantle?

The lithospheric mantle beneath old cratons has a refractory composition dominated by Fo-rich olivine (Boyd, 1989). The mantle beneath the Kaapvaal, Siberia, Slave and Tanzania cratons is unusual in that it contains a relatively high proportion of orthopyroxene, whereas the mantle beneath Greenland is dunitic (Bernstein *et al.*, 2007) and thus resembles the lithology of nodules in kimberlites. However, in marked contrast to the homogeneous composition of olivines in Archean lithospheric peridotites (Fo92–94; Boyd, 1989; Bernstein *et al.*, 2007), the Fo content of olivine in kimberlites varies significantly from nodule to nodule (Fo84–94, this study; Fo85–94, Kamenetsky *et al.*, 2008; Fo84–93, Arndt *et al.*, 2010; Fo88–94, Moore, 2012). This indicates that the nodules in kimberlites cannot simply be equated with the residue left after high-degree melting ($>$40%) as proposed for the shallow cratonic mantle (e.g. Boyd, 1989; Menzies, 1990; Herzberg, 2004; Bernstein *et al.*, 2007). Instead, we propose that the dunitic lithology and the variations in Fo content in the kimberlite nodules were both produced during the elimination of orthopyroxene and other mantle minerals through interaction with silica-undersaturated fluids or melts (Mitchell, 1986, 2008; Kamenetsky *et al.*, 2008; Brett *et al.*, 2009, 2015; Arndt *et al.*, 2010; Russell *et al.*, 2012; Pilbeam *et al.*, 2013; Kamenetsky & Yaxley, 2015).

An important result of our study is the demonstration of the similarity in Fo and minor element contents of olivine in the transition zones, the grain boundary zones, and the core population as a whole (Fig. 4). All three populations show the same chemical range and trends, with large variations in Fo content, whereas Ni, which usually correlates with Fo in olivine, remains relatively constant. The most plausible explanation is that the chemical variability of olivine in these three zones records a similar process.

Experimental and numerical simulations of interaction between silica-undersaturated melt or fluid and lherzolite or harzburgite have demonstrated that the dissolution of pyroxene commonly is coupled with a change in olivine chemistry. The Fo content decreases gradually when approaching the paths of percolating fluids, whereas the mineralogical front that marks the elimination of pyroxene is sharp (Morgan & Liang, 2003; Tursack & Liang, 2012). This interaction leads to the formation of replacive dunite (Kelemen & Dick, 1995) with olivine with variable Fo content (variations of Fo of up to 10 mole units), whereas compatible trace elements, such as Ni, are buffered by the peridotite composition (Tursack & Liang, 2012).

In sample NCR27, we have evidence, at the grain scale, of variations in Fo but near-uniform Ni content in the grain boundary zones adjacent to mobile grain boundaries, which we believe acted as fluid or melt percolation paths. We propose that the unusual decoupling between Fo and Ni within olivine cores, grain boundary zones, and transition zones is a diagnostic feature of interaction between olivine and fluid or melt and, by comparison with chemical gradients in replacive dunites, that this interaction removed the mineral phases other than olivine. The interaction, notably orthopyroxene dissolution, simultaneously modifies the melt composition; in particular, it increases its SiO_2 content (Russell *et al.*, 2012). An important observation is that in high-Fo nodules, the decrease in Fo that we attribute to fluid–rock interaction ends precisely at Fo89, the most magnesian composition observed in olivine margins (Fig. 4). This observation suggests that fluid–rock interaction proceeded until olivine saturation was achieved and thus would pre-date olivine crystallization.

The fluid or melt that interacted with the peridotite was not strictly kimberlitic in composition. The silica-poor carbonatite-like melt previously proposed as 'proto-kimberlite' melt (Kamenetsky *et al.*, 2008; Russell *et al.*, 2012) would be an excellent candidate as it has the low dihedral wetting angle and low viscosity required for efficient percolation along grain boundaries (Minarik & Watson, 1995; Hammouda & Laporte, 2000).

A TEMPORAL FRAMEWORK FOR FLUID–ROCK INTERACTIONS

Mitchell (1986, 2008), Kamenetsky *et al.* (2008), Brett *et al.* (2009, 2015), Russell *et al.* (2012), Pilbeam *et al.* (2013) and Kamenetsky & Yaxley (2015) all proposed that the interaction between peridotite and silica-poor fluid or melt, and the elimination of orthopyroxene, occurred during the transport of the nodules in the kimberlite magma whereas Arndt *et al.* (2010) saw the process happening in the lithospheric mantle prior to xenolith entrainment. Information about the temporal sequence of the processes that occurred in the lithospheric mantle or during the passage of the kimberlite magma from the mantle to the surface comes from textural and chemical features of olivines in sample NCR27, as summarized below.

1. Only a small amount of orthopyroxene assimilation (less than 5 wt %, Table 3) is needed to buffer the Fo content of the margins (Figs 4 and 10). This conclusion removes the requirement that a large amount of orthopyroxene was resorbed during the ascent of the kimberlite magma (15–20%; Le Roex *et al.*, 2003; Mitchell, 2008; Kopylova *et al.*, 2007; Russell *et al.*, 2012; Pilbeam *et al.*, 2013). In our model, the dissolution of orthopyroxene in the mantle gives to the melt and to the crystallized olivine the chemical signature of orthopyroxene, as will dissolution during olivine crystallization.
2. Given that grain boundary zones and transition zones do not result from diffusive equilibration between core and margin but record melt–rock interactions coupled to orthopyroxene dissolution, the position of these zones between cores and margins requires that they formed before crystallization of the margins. This conclusion is supported, first, by the chemical gradients in both zones (together with the cores of the nodules), which indicate that the modification of the olivine composition pre-dated the margin crystallization, and, second, by the fact that grain boundary zones are cross-cut by tablets that developed during magma ascent to the surface.
3. The grain boundary zones document fluid percolation at the grain scale coupled with dynamic recrystallization and grain boundary migration. Dynamic recrystallization cannot have occurred in the low-stress environment of the kimberlite magma during its ascent to the surface (Arndt *et al.*, 2010; Jones *et al.*, 2014) and must have occurred in the solid, deforming lithospheric mantle. The sharp contrasts in composition in the grain boundary zones would have been rapidly degraded by diffusion; the preservation of these zones indicates that fluid percolation occurred shortly (less than a few days) before nodule entrapment into the kimberlite magma.
4. The grain boundary zones are observed in nodules whose compositions range from Fo86 to Fo93, suggesting that they were derived from dunite that was heterogeneous in terms of olivine Fo content. The formation of these zones was contemporaneous with or shortly followed the event that removed any orthopyroxene and other minerals that may have been present and generated the range of olivine compositions in the lithospheric mantle.

In the light of the above observations and interpretations, we believe that peridotite–fluid interaction occurred in the deforming lithospheric mantle, before the dunitic nodules were entrained into the kimberlite melt. At a small scale, the carbonatite-like proto-kimberlite melt percolated along grain boundaries, which migrated simultaneously to accommodate the deformation under high stress. The fluid-assisted

recrystallization led to the development of the grain boundary zones distributed asymmetrically on the two sides of some grain boundaries. Simultaneously, at a scale far greater than the size of the nodules, interactions between peridotite and carbonatite-like protokimberlite melt resulted in the removal of orthopyroxene (and possibly other phases of the peridotites) and the formation of dunite. Within the percolation zones, the olivine composition was uniform at the centimetre scale but variable at a larger scale, depending on the position relative to the percolation zone. The presence of rare low-Fo high-Ni grains could indicate that liquids of different composition—some carbonate-rich, others basaltic—invaded that portion of the lithospheric mantle that was subsequently sampled by the kimberlitic magma. A parallel scenario, implying a kimberlite melt invading the lithosphere, has been invoked to explain the occurrence of megacrysts of garnet, clinopyroxene, orthopyroxene and olivine in the Jericho kimberlite (Kopylova *et al.*, 2009), which resemble our nodules in terms of their polycrystalline nature and textural evidence for recrystallization.

CO_2 exsolution and buoyancy increase resulting from orthopyroxene dissolution (Russell *et al.*, 2012; Kamenetsky & Yaxley, 2015), together with mantle compaction processes (Grégoire *et al.*, 2006), could then have triggered kimberlite melt segregation and ascent. The kimberlite magma entrained dunite xenoliths whose composition records their position in the sheaths of replacive dunite lining the fluid percolation channels in the lithosphere. Disaggregation of xenoliths during their incorporation into the kimberlite melt or during its ascent may be enhanced by fractures or grain boundaries along which the melt previously percolated. Fluid–nodule interaction probably continued at the nodule edges shortly after their entrapment to form the transition zone. When the saturation of olivine was achieved, the margins crystallized without significant concomitant orthopyroxene assimilation.

OLIVINE NODULES IN OTHER KIMBERLITES

Although this study focuses entirely on the Kangamiut kimberlites, many of the same distinctive features are found in kimberlites worldwide. The interpretations we propose here to explain the chemical variations in olivine apply equally well to the monomineralic, polygranular nodules observed in kimberlites from locations such as Majuagaa (Pilbeam *et al.*, 2013), Diavik (Brett *et al.*, 2009; Russell *et al.*, 2012), Ekati, Snap Lake and Botswana (Arndt *et al.*, 2010), and Sover, Monastery and Letseng-la-terai (Moore, 2012). Olivines in kimberlites from other regions (e.g. Udachnaya, Kamenetsky *et al.*, 2008; Lac de Gras, Fedortchouk & Canil, 2004) occur mainly as rounded, sub- to euhedral isolated grains or broken fragments and lack the more distinctive features of the olivines in the locations cited above. However, the lack of associated orthopyroxene and other mantle silicates, and the wide range of Fo contents in olivine cores, suggests that they could also have formed through fluid reaction in the lithospheric mantle. The 'megacrysts' in the Jericho kimberlite described by Kopylova *et al.* (2009) are polymineralic, but they too are proposed to have formed by metasomatism in the lithosphere shortly before kimberlite emplacement.

CONCLUSIONS

We conducted a detailed study of compositions and deformation microstructures in olivine in kimberlite sample NCR27 from the Kangamiut region, Greenland. Monomineralic dunitic nodules make up more than 50% of this sample. The morphology and composition of olivine in the nodules record a combination of processes that occurred during reactive porous flow and metasomatism in the lithospheric mantle, and subsequent xenolith disaggregation and margin crystallization during the ascent of the kimberlite melt.

The composition of olivine in the nodules covers a wide range from high Fo and high Ni (Fo94, 3000 ppm Ni) to low Fo and low Ni (Fo86, 500 ppm Ni), and includes a third, minor population with low Fo but high Ni (Fo88, 2500 ppm Ni). The dunitic lithology and the wide range of olivine compositions result from transformation of mantle peridotite through the dissolution in carbonate-rich liquids of orthopyroxene and other mantle minerals.

Thin margins surround the nodules and the matrix grains. Their compositions, notably the buffering of the Fo content associated with a sharp decrease in Ni, can be reproduced if a high distribution coefficient between olivine and melt is adopted ($D_{Ni} > 20$); concomitant orthopyroxene digestion during magma ascent is not required.

We report chemical gradients across mobile grain boundaries for the first time in a natural peridotite sample. These gradients were preserved from diffusive equilibration because of the short travel time of the nodules in the kimberlite melt. The grain boundary zones are interpreted to have formed by melt–fluid percolation at the grain scale, coupled with dynamic recrystallization in the deforming lithospheric mantle. Grain boundary zones occur in both high- and low-Fo nodules. These relations require that fluid-assisted recrystallization occurred during reactive porous flow and orthopyroxene dissolution, shortly (a few days) before entrainment of the dunite nodules by the kimberlite melt. Because grain boundary zones and high-Fo cores are distributed along similar trends in chemical variation diagrams, we propose that the zoning associated with grain boundaries mimics, on a small scale, the chemical diversity of the dunite that was the source of most of the olivine in the Greenland kimberlites.

ACKNOWLEDGEMENTS

We would like to thank Llewellyn Pilbeam and James Russell, who read and made comments on a first draft of this paper. We also thank Michel Grégoire, Don

Francis and an anonymous reviewer for their very constructive comments, and Marjorie Wilson for her editorial work.

FUNDING

This work was supported by a grant from Labex OSUG@2020 (Investissements d'avenir—ANR10 LABX56). The EPMA facility was purchased and installed at ISTerre via Chair of Excellence grant ANR-09-CEXC-003-01 from the Agence Nationale de la Recherche, France.

SUPPLEMENTARY DATA

Supplementary data for this paper are available at *Journal of Petrology* online.

REFERENCES

Arndt, N. T., Boullier, A. M., Clement, J. P., Dubois, M. & Schissel, D. (2006). What olivine, the neglected mineral, tells us about kimberlite petrogenesis. *eEarth Discuss* **1**, 15–21.

Arndt, N. T., Guitreau, M., Boullier, A. M., Le Roex, A., Tommasi, A., Cordier, P. & Sobolev, A. (2010). Olivine, and the origin of kimberlite. *Journal of Petrology* **51**, 573–602.

Bernstein, S., Kelemen, P. B. & Hanghøj, K. (2007). Consistent olivine Mg number in cratonic mantle reflects Archean mantle melting to the exhaustion of orthopyroxene. *Geology* **35**, 459–462.

Boullier, A.-M. & Nicolas, A. (1975). Classification of textures and fabrics of peridotite xenoliths from south African kimberlites. *Physics and Chemistry of the Earth* **9**, 467–475.

Boyd, F. R. (1989). Compositional distinction between oceanic and cratonic lithosphere. *Earth and Planetary Science Letters* **96**, 15–26.

Brett, R. C., Russell, J. K. & Moss, S. (2009). Origin of olivine in kimberlite: Phenocryst or impostor? *Lithos* **112**, 201–212.

Brett, R., Russell, J., Andrews, G. & Jones, T. (2015). The ascent of kimberlite: Insights from olivine. *Earth and Planetary Science Letters* **424**, 119–131.

Canil, D., & Fedortchouk, Y. (1999). Garnet dissolution and the emplacement of kimberlites. *Earth and Planetary Science Letters* **167**, 227–237.

Chauvel, C., Bureau, S. & Poggi, C. (2011). Comprehensive chemical and isotopic analyses of basalt and sediment reference materials. *Geostandards and Geoanalytical Research* **35**, 125–143.

Clement, C. R. (1982). A comparative geological study of some major kimberlite pipes in the Northern Cape and Orange Free State. PhD Thesis, University of Cape Town, 407 pp.

Dalton, J. A. & Wood, B. J. (1993). The partitioning of Fe and Mg between olivine and carbonate and the stability of carbonate under mantle conditions. *Contributions to Mineralogy and Petrology* **114**, 501–509.

DePaolo, D. J. (1981). Trace element and isotopic effects of combined wallrock assimilation and fractional crystallization. *Earth and Planetary Science Letters* **53**, 189–202.

Dohmen, R. & Chakraborty, S. (2007). Fe–Mg diffusion in olivine II: point defect chemistry, change of diffusion mechanisms and a model for calculation of diffusion coefficients in natural olivine. *Physics and Chemistry of Minerals* **34**, 409–430.

Drury, M. R. & Urai, J. L. (1990). Deformation-related recrystallization processes. *Tectonophysics* **172**, 235–253.

Drury, M. R. & van Roermund, H. L. M. (1988). Metasomatic origin for Fe–Ti-rich multiphase inclusions in olivine from kimberlite xenoliths. *Geology* **16**, 1035–1038.

Drury, M. R. & van Roermund, H. L. M. (1989). Fluid assisted recrystallization in upper mantle peridotite xenoliths from kimberlites. *Journal of Petrology* **30**, 133–152.

Evans, B., Hay, R. S. & Shimizu, N. (1986). Diffusion-induced grain-boundary migration in calcite. *Geology* **14**, 60–63.

Fedortchouk, Y. & Canil, D. (2004). Intensive variables in kimberlite magmas, Lac de Gras, Canada and implications for diamond survival. *Journal of Petrology* **45**, 1725–1745.

Foley, S. F., Jacob, D. E. & O'Neill, H. S. C. (2011). Trace element variations in olivine phenocrysts from Ugandan potassic rocks as clues to the chemical characteristics of parental magmas. *Contributions to Mineralogy and Petrology* **162**, 1–20.

Girnis, A. V., Bulatov, V. K. & Brey, G. P. (2005). Transition from kimberlite to carbonatite melt under mantle parameters: an experimental study. *Petrology* **13**, 1–15.

Girnis, A. V., Bulatov, V. K., Brey, G. P., Gerdes, A. & Höfer, H. E. (2013). Trace element partitioning between mantle minerals and silico-carbonate melts at 6–12 GPa and applications to mantle metasomatism and kimberlite genesis. *Lithos* **160–161**, 183–200.

Grégoire, M., Rabinowicz, M. & Janse, A. J. A. (2006). Mantle mush compaction; a key to understand the mechanisms of concentration of kimberlite melts and initiation of swarms of kimberlite dykes. *Journal of Petrology* **47**, 631–646.

Guéguen, Y. (1977). Dislocations in mantle peridotite nodules. *Tectonophysics* **39**, 231–254.

Guéguen, Y. (1979). Dislocations in naturally deformed terrestrial olivine: classification, interpretation, applications. *Bulletin de Minéralogie* **102**, 178–183.

Hammouda, T. & Laporte, D. (2000). Ultrafast mantle impregnation by carbonatite melts. *Geology* **28**, 283–285.

Hart, S. R. & Davis, K. E. (1978). Nickel partitioning between olivine and silicate melt. *Earth and Planetary Science Letters* **40**, 203–219.

Herzberg, C. (2004). Geodynamic information in peridotite petrology. *Journal of Petrology* **45**, 2507–2530.

Irving (1984). Trace element abundances in megacrysts and their host basalts: Constraints on partition coefficients and megacryst genesis. *Geochimica et Cosmochimica Acta* **48**, 1201–1221.

Jarosewitch, E. J., Nelen, J. A. & Norberg, J. A. (1980). Reference samples for microprobe analysis. *Geostandards Newsletter* **4**, 43–47.

Jones, T. J., Russell, J. K., Porritt, L. A. & Brown, R. J. (2014). Morphology and surface features of olivine in kimberlite: implications for ascent processes. *Solid Earth* **5**, 313–326.

Kamenetsky, V. S. & Yaxley, G. M. (2015). Carbonate–silicate liquid immiscibility in the mantle propels kimberlite magma ascent. *Geochimica et Cosmochimica Acta* **158**, 48–56.

Kamenetsky, V. S., Kamenetsky, M. B., Sobolev, A. V., Golovin, A. V., Demouchy, S., Faure, K., Sharygin, V. V. & Kuzmin, D. V. (2008). Olivine in the Udachnaya-East kimberlite (Yakutia, Russia): types, compositions and origins. *Journal of Petrology* **49**, 823–839.

Kelemen, P. B. & Dick, H. J. B. (1995). Focused melt flow and localized deformation in the upper mantle: Juxtaposition of replacive dunite and ductile shear zones in the Josephine peridotite, SW Oregon. *Journal of Geophysical Research* **100**, 423–438.

Kopylova, M. G., Matveev, S. & Raudsepp, M. (2007). Searching for parental kimberlite melt. *Geochimica et Cosmochimica Acta* **71**, 3616–3629.

Kopylova, M., Nowell, G., Pearson, D. & Markovic, G. (2009). Crystallization of megacrysts from protokimberlitic fluids: Geochemical evidence from high-Cr megacrysts in the Jericho kimberlite. *Lithos* **112**, 284–295.

Laubier, M., Grove, T. L. & Langmuir, C. H. (2014). Trace element mineral/melt partitioning for basaltic and basaltic andesitic melts: An experimental and laser ICP-MS study with application to the oxidation state of mantle source regions. *Earth and Planetary Science Letters* **392**, 265–278.

Le Roex, A. P., Bell, D. R. & Davis, P. (2003). Petrogenesis of Group I kimberlites from Kimberley, South Africa: Evidence from bulk-rock geochemistry. *Journal of Petrology* **44**, 2261–2286.

Li, C., Maier, W. D. & de Waal, S. A. (2001). Magmatic Ni–Cu versus PGE deposits: Contrasting genetic controls and exploration implications. *South African Journal of Geology* **104**, 309–318.

Luth, R. W. (2009). The activity of silica in kimberlites, revisited. *Contributions to Mineralogy and Petrology* **158**, 283–294.

Matzen, A. K., Baker, M. B., Beckett, J. R. & Stolper, E. M. (2013). The temperature and pressure dependence of nickel partitioning between olivine and silicate melt. *Journal of Petrology* **54**, 2521–2545.

Menzies, M. (1990). Archaean, Proterozoic and Phanerozoic lithosphere. In: Menzies, M. (ed.). *Continental Mantle*. Oxford: Oxford University Press, pp. 67–86.

Mercier, J.-C. C. & Nicolas, A. (1975). Textures and fabrics of upper-mantle peridotites as illustrated by xenoliths from basalts. *Journal of Petrology* **16**, 454–487.

Minarik, W. G. & Watson, E. (1995). Interconnectivity of carbonate melt at low melt fraction. *Earth and Planetary Science Letters* **133**, 423–437.

Mitchell, R. H. (1986). *Kimberlites: Mineralogy, Geochemistry, and Petrology*. New York: Plenum, 442 pp.

Mitchell, R. H. (2008). Petrology of hypabyssal kimberlites: relevance to primary magma compositions. *Journal of Volcanology and Geothermal Research* **174**, 1–8.

Moore, A. E. (1988). Olivine: a monitor of magma evolutionary paths in kimberlites and olivine melilitites. *Contributions to Mineralogy and Petrology* **99**, 238–248.

Moore, A. E. (2012). The case for a cognate, polybaric origin for kimberlitic olivines. *Lithos* **128**, 1–10.

Morgan, Z. & Liang, Y. (2003). An experimental and numerical study of the kinetics of harzburgite reactive dissolution with applications to dunite dike formation. *Earth and Planetary Science Letters* **214**, 59–74.

Nakamura, M., Yurimoto, H. & Watson, E. B. (2005). Grain growth control of isotope exchange between rocks and fluids. *Geology* **33**, 829–832.

Nermond, S. (1994). Etude expérimentale de la recristallisation statique et de la cinétique de croissance de l'olivine. PhD Thesis, Université de Paris 7, 204 pp.

Nielsen, T. F. & Sand, K. K. (2008). The Majuagaa kimberlite dike, Maniitsoq region, West Greenland: Constraints on an Mg-rich silicocarbonatitic melt composition from groundmass mineralogy and bulk compositions. *Canadian Mineralogist* **46**, 1043–1061.

Ohuchi, T., Nakamura, M. & Michibayashi, K. (2010). Effect of grain growth on cation exchange between dunite and fluid: implications for chemical homogenization in the upper mantle. *Contributions to Mineralogy and Petrology* **160**, 339–357.

Petry, C., Chakraborty, S. & Palme, H. (2004). Experimental determination of Ni diffusion coefficients in olivine and their dependence on temperature, composition, oxygen fugacity, and crystallographic orientation. *Geochimica et Cosmochimica Acta* **68**, 4179–4188.

Pilbeam, L. H., Nielsen, T. F. D. & Waight, T. E. (2013). Digestion fractional crystallization (DFC): an important process in the genesis of kimberlites. Evidence from olivine in the Majuagaa Kimberlite, southern West Greenland. *Journal of Petrology* **54**, 1399–1425.

Roeder, P. L. & Emslie, R. F. (1970). Olivine–liquid equilibria. *Contributions to Mineralogy and Petrology* **29**, 275–289.

Russell, J. K., Porritt, L. A., Lavallée, Y. & Dingwell, D. B. (2012). Kimberlite ascent by assimilation-fuelled buoyancy. *Nature* **481**, 352–356.

Skinner, E. M. W. (1989). Contrasting Group I and Group II kimberlite petrology: towards a genetic model. In: Ross, J. (ed.) *Kimberlites and Related Rocks: their Composition, Occurrence, Origin and Emplacement. Proceedings of the 4th International Kimberlite Conference. Geological Society of Australia, Special Publication* **29**, 528–544.

Skinner, E. M. W. & Clement, C. R. (1979). Mineralogical classification of southern African kimberlites. In: Boyd, F. R. & Meyer, H. O. A. (eds) *Kimberlite, Diatrems and Diamonds*. Washington, DC: American Geophysical Union, pp. 129–139.

Sweeney, R. J., Prozesky, V. & Przybylowicz, W. (1995). Selected trace and minor element partitioning between peridotite minerals and carbonatite melts at 18–46 kb pressure. *Geochimica et Cosmochimica Acta* **59**, 3671–3683.

Tommasi, A., Vauchez, A. & Ionov, D. A. (2008). Deformation, static recrystallization, and reactive melt transport in shallow subcontinental mantle xenoliths (Tok Cenozoic volcanic field, SE Siberia). *Earth and Planetary Science Letters* **272**, 65–77.

Tursack, E. & Liang, Y. (2012). A comparative study of melt–rock reactions in the mantle: laboratory dissolution experiments and geological field observations. *Contributions to Mineralogy and Petrology* **163**, 861–876.

Urai, J. L., Means, W. D. & Lister, G. S. (1986). Dynamic recrystallization of minerals. In: Hobbs, B. E. & Heard, H. C. (eds) *Mineral and Rock Deformation: Laboratory Studies*. Washington, DC: American Geophysical Union, pp. 161–199.

Wilson, L. and Head, J. W., III (2007). An integrated model of kimberlite ascent and eruption. *Nature* **447**, 53–57.

Annexe 3: Concentrations en éléments traces et majeurs et compositions isotopiques en cuivre ($\delta^{65}Cu$) et zinc ($\delta^{66}Zn$) mesurées dans neuf standards biologiques

NB: Pour des raisons de confidentialité, toutes ces données, n'étant pas encore publiées, ne sont pas fournies dans ce manuscrit.